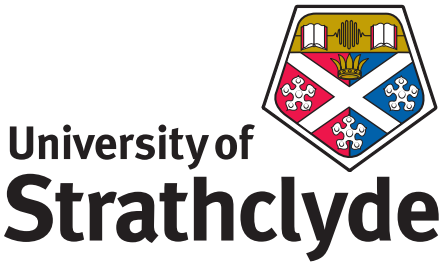

Reduced-order modelling of fluid flows using analytical and numerical methods

James Daniel Reilly
Department of Mathematics and Statistics
University of Strathclyde
Glasgow, UK

September 2023

This thesis is submitted to the University of Strathclyde for the degree of Doctor of Philosophy in the Faculty of Science.

Acknowledgements

I am extremely grateful to my supervisors, Professor Stephen Wilson and Dr Alexander Wray, for their support, guidance, and advice throughout my PhD. Thank you, Stephen, for helping me become a better writer and for your patience with my many mistakes along the way. Thank you, Alex, for your endless enthusiasm and encouragement, and for always being there to answer any of my questions (and for not getting annoyed when my questions were very basic!). I would like to thank the Carnegie Trust for the Universities of Scotland for their financial support during my PhD. I would also like to thank my examiners Dr David Pritchard and Dr Marc Pradas.

I owe a great deal of thanks to two of my former high school teachers: my Mathematics teacher Mr Keith Edwards who encouraged me to study Mathematics at University, and my Physics teacher Mr John Callan who encouraged my passion for problem solving.

I also owe an enormous thanks to my Carnegie Mentor, Professor Annie Tindley. Thank you, Annie, for all of your excellent advice and encouragement throughout my PhD, and for putting up with all of my complaining!

I am deeply indebted to my family and friends for their incredible support during my PhD: my parents and Christopher, for always being there for me; my grandparents, for letting me talk to them about what I had been working on; Erika, for your constant support, love, and patience; Becca and Andrew, I am extremely grateful to you for being able to share our PhD experience; Michael, for all of your moral support and advice; and Alistair, Ioana, Gary, Jayne, David, Michael, and Laura, for making the last few years more enjoyable with your friendship. Thank you.

Abstract

Coating the exterior of a cylinder with a layer of fluid is a fundamental problem in fluid mechanics and occurs in numerous natural processes and industrial applications, such as heat and mass transfer and the production of orthopaedic implants. This thesis formulates and analyses novel models for two different coating flow problems which are not restricted by the common assumptions that the cylinder has circular cross-section and/or that the film is thin.

The first problem involves the unsteady, two-dimensional flow on the exterior of a uniformly rotating horizontal cylinder with elliptical cross-section. By using a long-wave approximation we derive a thick-film model, and by using a thin-film approximation we derive a thin-film model. Both models incorporate the effects of cylinder eccentricity, rotation, gravity, centrifugation, viscosity, and surface tension. By studying the thin-film model, we demonstrate both analytically and numerically that the behaviour of the film coating the elliptical cylinder significantly differs from that in the circular case. In particular, it is shown that even a relatively mild departure from circularity produces significant qualitative and quantitative differences from the behaviour in the circular case.

The second problem involves the unsteady, three-dimensional flow of a thick film on the exterior of a vertical fibre with circular cross-section. By using a long-wave approximation and the method of weighted residuals, we derive a thick-film weighted-residual model, which incorporates the effects of gravity, viscosity, surface tension, and inertia. We study the thick-film weighted-residual model in the linear regime in order to elucidate the mechanics that determine both the stability and the axisymmetry of the flow. We demonstrate that these results in the linear regime, in general, correctly predict the results of the linear calculations of the Navier–Stokes equations and the results of numerical simulations of the thick-film weighted-residual model in the nonlinear regime.

Contents

Chapter 1

Introduction

In this chapter, we introduce the background theory underpinning the work described in this thesis, and we review the relevant existing literature. In Section 1.1, we discuss and give examples of free surface flows and, more specifically, coating flows. In Section 1.2, we outline the reduced-order modelling techniques that we use throughout this thesis. In Section 1.3, we discuss the important distinction that we draw between a "thin-film" approximation and a "long-wave" approximation, and discuss how to model the flow of a thick film. We then review the relevant literature for the two coating flow problems which will be discussed in this thesis, namely the coating of a horizontal cylinder in Sections 1.4 and 1.5, and the coating of a vertical fibre in Section 1.6. We then outline the contents of this thesis in Section 1.7, before concluding with a list of presentations of the work contained in this thesis in Section 1.8.

1.1 Free surface flows

"Free surface flows" are a specific category of fluid flows in which one or more of the surfaces bounding the fluid are not confined by a solid wall or boundary and are therefore free to move. Understanding the dynamics of free surface flows is a fundamental problem in fluid mechanics, and, as such, has been the subject of multiple major reviews [1–12]. Free surface flows are commonplace in numerous natural processes and industrial applications. For example, free surface flows are present in lava flow [13–15], avalanches [16–18], the flow of ice sheets [19–21],

safety features of hydroelectric power dams (as shown in Figure 1.1, which shows the spillway of the Höljes dam in Sweden, before and after refurbishment) [22], soap bubbles (as shown in Figure 1.2, which shows the freezing of a soap bubble deposited on an ice disk) [23; 24], the survival of COVID-19 in respiratory droplets [25], heat and mass transfer [26; 27], and microfluidics [28; 29].

Of particular interest to this thesis are "coating flows", in which a layer of fluid is applied to the surface of a solid object. Coating flows have also been the subject of multiple major reviews [30–32], and occur in many natural processes and industrial applications. For example, coating flows are present in harvesting moisture from desert air [33; 34], the lining of lungs and airways [35], the coating of the cornea of the eye [36–38], the production of protective films used in product packaging [39, Chapter 2], the coating of television screens [40], the manufacture of microelectronic devices [41], the production of aluminium foil [42], the production of solar cells [43; 44], moisture collection from fog and mist in plants [45], moisture collection from fog and mist in spider silk (as shown in Figure 1.3, which shows spider silk collecting moisture from mist) [46], moisture collection from fog and mist in cactus spines (as shown in Figure 1.4, which shows cactus spines at various angles collecting moisture from fog) [47–49], artificial moisture collection from fog and mist inspired by spider silk [50], and artificial moisture collection from fog and mist inspired by cactus spines (as shown in Figure 1.5, which shows a cactus-inspired moisture collection device) [51].

1.2 Reduced-order modelling

The flow of a viscous fluid is governed by the Navier–Stokes equations, which are a system of nonlinear partial differential equations. The Navier–Stokes equations are famously intractable, since performing any form of analysis often proves either difficult or impossible, either numerical via Direct Numerical Simulations (DNS), which can have a high computational cost, or analytical, which may only be possible in certain limits and/or special cases. However, there are a range of mathematical simplifications which can be applied to make the Navier–Stokes equations more amenable to analysis.

A useful (and perhaps the most common) method of analysing the behaviour of the solutions of the Navier–Stokes equations is via the use of a linear stability

Figure 1.1: The spillway of the Höljes dam (Sweden) with the original layout with two gate openings (left) and after refurbishment with a new 17 m gate opened next to the existing gates to accommodate increased discharge (right). Reproduced with permission, Copyright 2019, Yang et al. [22].

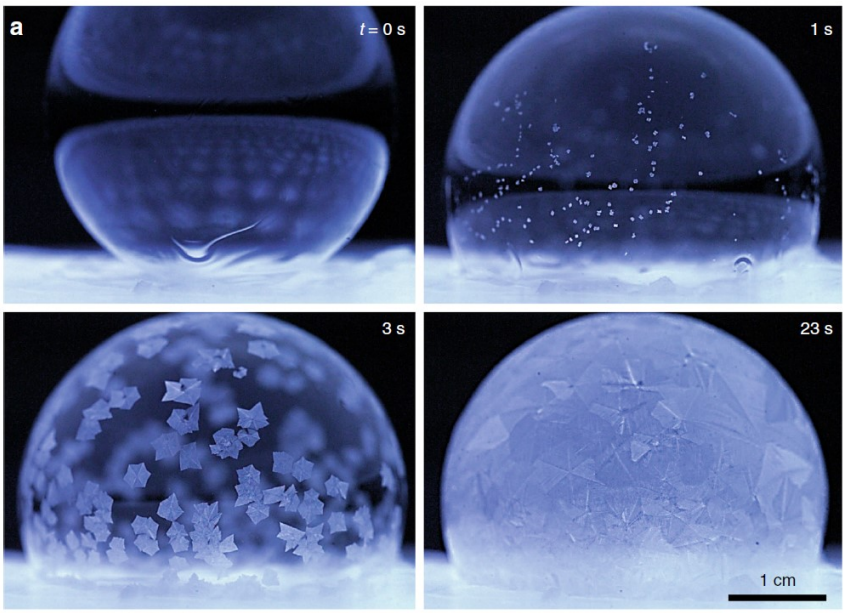

Figure 1.2: The freezing of a soap bubble deposited on an ice disk. Reproduced with permission, Copyright 2019, Ahmadi et al. [24].

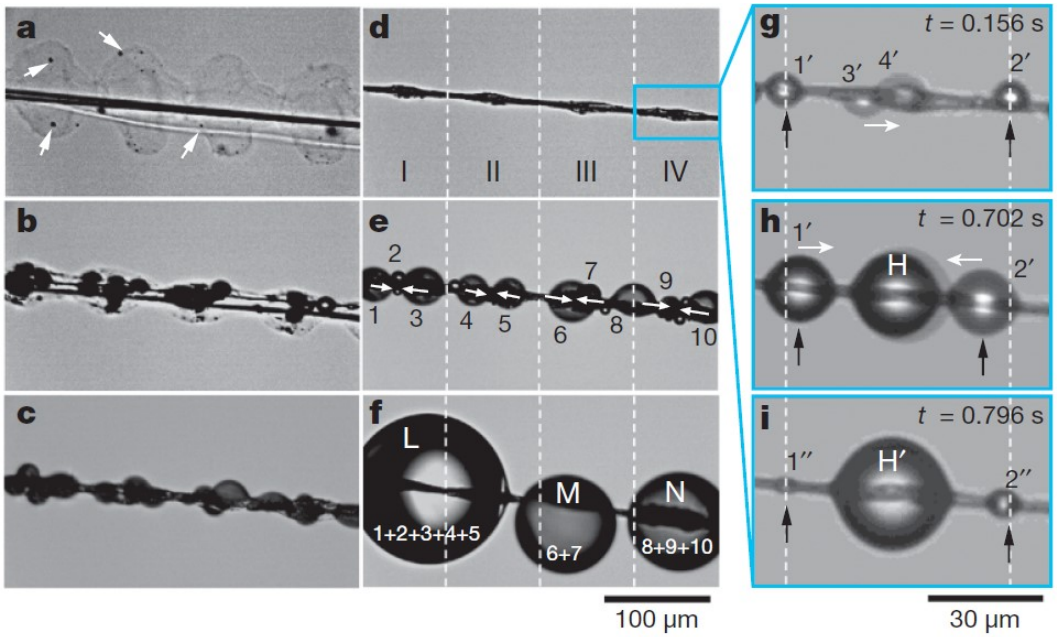

Figure 1.3: Microscopic observation of moisture collection on spider silk in mist. (a) Tiny water droplets (indicated by arrows) condense on the semi-transparent puffs of dry spider silk. (b)–(c) As more water condenses, the puffs shrink to opaque bumps, (d) which finally form periodic spindle-knots. (e) Smaller drops condense on the spider silk (denoted 1–10). (f) Small drops 1–5, 6–7, and 8–10 coalesce to form large drops denoted L, M, and N, respectively. (g)–(i) A more detailed view of the directional drop movement on an individual spindle-knot. Reproduced with permission from Springer Nature, Copyright 2010, Zheng et al. [46].

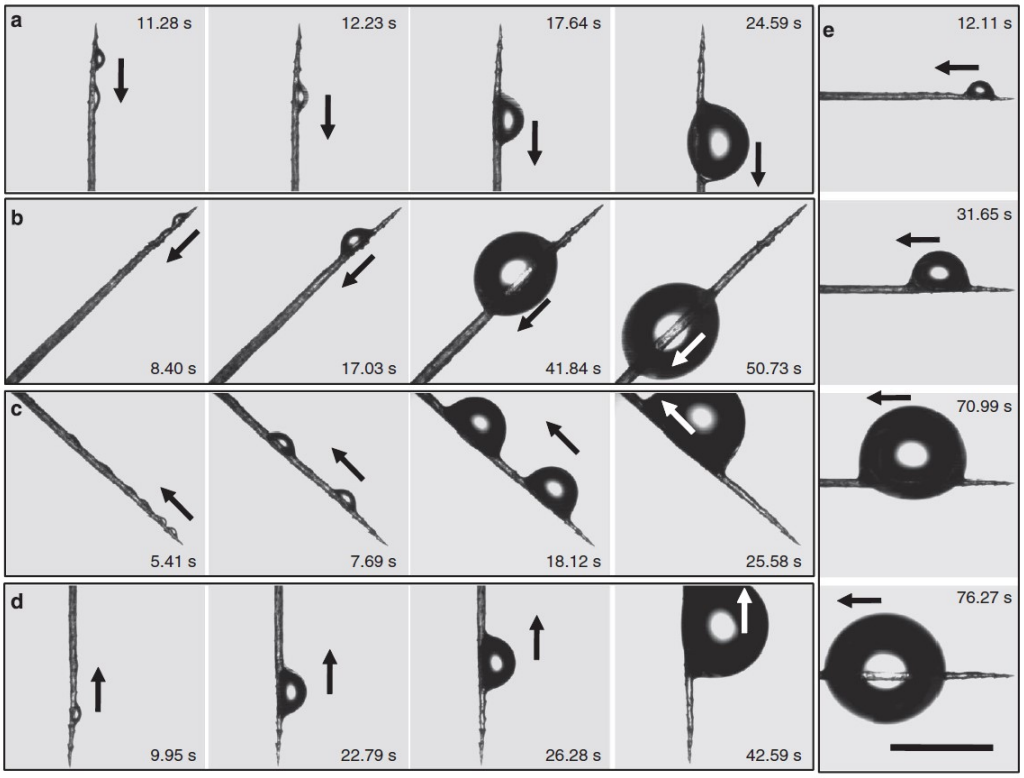

Figure 1.4: A cactus spine placed in fog at various angles and viewed under a microscope. Panels (a)–(e) show tilt angles of 90°, 45°, −45°, −90°, and 0°, respectively. Water droplets condense on the line and are driven towards the base of the spine. The scale bar indicates 500 μm. Reproduced with permission, Copyright 2012, Ju et al. [48].

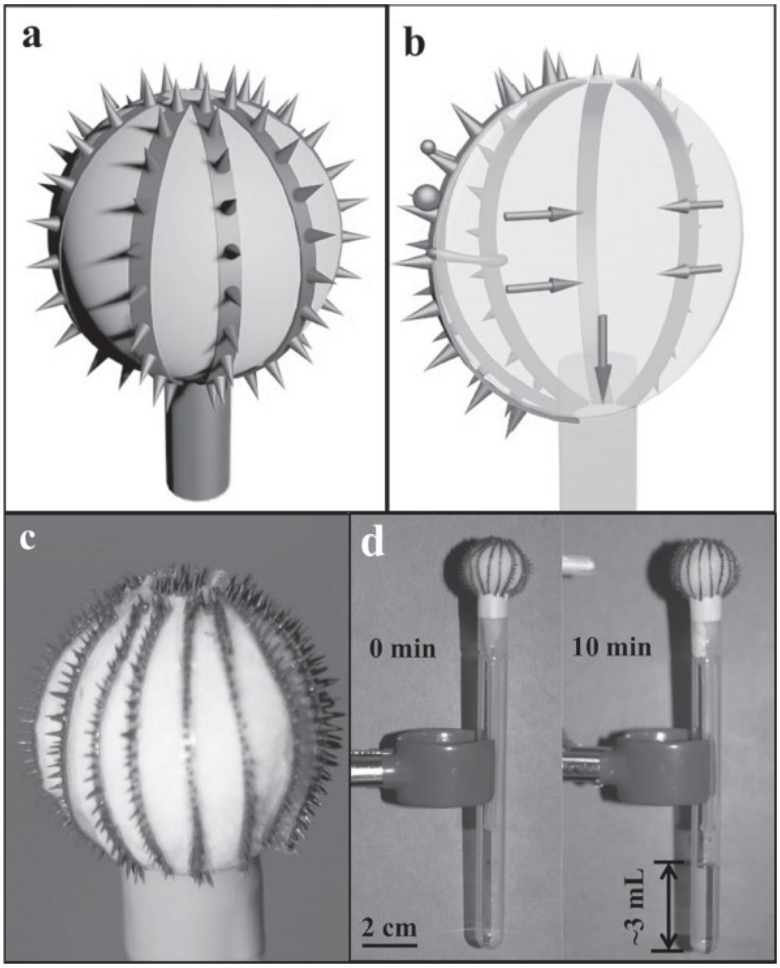

Figure 1.5: (a) An illustration of the cactus-inspired moisture collection device. (b) An illustration of the water transportation pathway. (c) A photograph of the cactus-inspired moisture collection device. (d) The moisture collection process. Reproduced with permission from John Wiley and Sons, Copyright 2014, Cao et al. [51].

analysis. Linear stability analysis involves analysing the linear growth rates associated with perturbations to some base-state solution (e.g. a uniform film coating the surface of an inclined plane). These perturbations either decay with time (in which case the base-state solution is linearly stable), grow with time (in which case the base-state solution is linearly unstable), or neither grow nor decay with time (in which case the base-state solution is linearly neutrally stable).

1.2.1 Hierarchy of reduced-order models

Linear stability analysis is an extremely useful tool which can be used to uncover some very important and interesting behaviours of a fluid system. However, the linear stability analysis is, of course, only valid in the linear regime (i.e. close to the base-state solution), and so is not able to capture the nonlinear mechanisms behind the full range of behaviour which can be exhibited by a fluid system. Therefore, we require other techniques if we wish to be able to analyse the nonlinear behaviour of a fluid system. A very fruitful approach is to develop a *reduced-order model* which captures the nonlinear behaviour of a fluid system, by exploiting a disparity between the length scales of the flow.

A typical procedure for implementing this reduced-order modelling approach is to define a small aspect ratio (sometimes also referred to as a slenderness parameter) $\delta = H/\lambda \ll 1$, where H is a characteristic length scale in the cross-stream direction (usually a characteristic film thickness), and λ is a characteristic length scale in the streamwise direction (usually a characteristic wavelength of the film). This technique is referred to as a "long-wave" or a "thin-film" approximation (we will discuss this approximation further in Section 1.3).

We will discuss various methods of developing reduced-order models for the simple case of two-dimensional flow down an inclined plane. However, the methods which we shall discuss can be readily extended to three-dimensional flow [52; 53] and/or flow over a non-planar geometry [54–58].

1.2.1.1 Gradient expansion method

Applying a long-wave approximation to the Navier–Stokes equations, we obtain a system of equations which may be solved order-by-order via a standard perturba-

tion method. This procedure is often referred to as a *gradient expansion* method in the literature associated with weighted residual modelling [52; 53; 55; 59–66] (discussed further in Section 1.2.1.4), and we use this terminology consistently here to aid making a clear distinction with other techniques. This is the technique used by Benney in their pioneering work [67] to derive a single evolution equation for the film thickness for flow down an inclined plane, which has come to be known as the Benney equation, namely

$$\frac{\partial h}{\partial t} + \frac{\partial}{\partial x}\left[\frac{1}{3}h^3 + \delta\left(\frac{2}{15}h^6\frac{\partial h}{\partial x} - \frac{\cot\beta}{3}h^3\frac{\partial h}{\partial x} + \frac{\Gamma}{3}h^3\frac{\partial^3 h}{\partial x^3}\right)\right] = 0, \tag{1.2.1}$$

where $h(x,t)$, t, x, and $\Gamma = \gamma\rho^{1/3}H^2/(\mu^{4/3}(g\sin\beta)^{1/3}\lambda^2)$ denote the dimensionless film thickness, the dimensionless time, the dimensionless streamwise coordinate, and the dimensionless surface tension parameter, respectively, where γ, ρ, μ, g, and β denote the surface tension coefficient, density, viscosity, acceleration due to gravity, and angle of inclination of the substrate to the horizontal, respectively. The terms in the square brackets (from left to right) correspond to the convective effect of gravity, the destabilising effect of inertia, the stabilising effect of gravity, and the stabilising effect of surface tension, respectively. Note that in the original work by Benney [67], the surface tension terms first appear at third order in δ, and were neglected. However, subsequent works have shown that it is crucial to retain surface tension at first order in δ in equation (1.2.1) [1; 2].

In the linear regime, equation (1.2.1) predicts the exact same threshold for instability as the linearised Navier–Stokes equations (i.e. the Orr–Sommerfeld equations) [59, Chapters 3 and 5]. However, for moderate to large inertial effects, the solutions of equation (1.2.1) are known to suffer "blowup" in a finite time (i.e. the thickness of the film becomes infinite in a finite time) [68–71]. This is of course an unphysical prediction and is not observed in DNS of the Navier–Stokes equations [72; 73] or in physical experiments [53].

1.2.1.2 Weakly nonlinear method

Equation (1.2.1) can be simplified by considering the limit of small interfacial perturbations. For simplicity, we consider the case of a vertical plane (i.e. $\beta = \pi/2$).

Setting $h(x,t) = 1 + \delta\breve{h}(x,t)$ and neglecting third-order terms yields

$$\delta\left(\frac{\partial\breve{h}}{\partial t} + \frac{\partial\breve{h}}{\partial x}\right) + \delta^2\left(2\breve{h}\frac{\partial\breve{h}}{\partial x} + \frac{2}{15}\frac{\partial^2\breve{h}}{\partial x^2} + \frac{\Gamma}{3}\frac{\partial^4\breve{h}}{\partial x^4}\right) = 0. \tag{1.2.2}$$

To change the system from the laboratory frame to a moving frame of reference (i.e. removing the terms which represent convection), we set $\breve{x} = x - t$ and $\breve{t} = \delta t$ to obtain

$$\delta^2\left(\frac{\partial\breve{h}}{\partial\breve{t}} + 2\breve{h}\frac{\partial\breve{h}}{\partial\breve{x}} + \frac{2}{15}\frac{\partial^2\breve{h}}{\partial\breve{x}^2} + \frac{\Gamma}{3}\frac{\partial^4\breve{h}}{\partial\breve{x}^4}\right) = 0. \tag{1.2.3}$$

By rescaling $\breve{x}$, $\breve{t}$, and $\breve{h}$ in (1.2.3) as

$$\breve{x} = \sqrt{\frac{5\Gamma}{2}}X, \quad \breve{t} = \frac{75\Gamma}{4}T, \quad \breve{h} = \frac{1}{15}\sqrt{\frac{2}{5\Gamma}}H, \tag{1.2.4}$$

and dividing by δ^2, we recover the Kuramoto–Sivashinsky equation, namely

$$\frac{\partial H}{\partial T} + H\frac{\partial H}{\partial X} + \frac{\partial^2 H}{\partial X^2} + \frac{\partial^4 H}{\partial X^4} = 0. \tag{1.2.5}$$

The second, third, and fourth terms in the Kuramoto–Sivashinsky equation (1.2.5) correspond to the convective effect of gravity (relative to the moving frame), the destabilising effect of inertia, and the stabilising effect of surface tension, respectively. The process of deriving equation (1.2.5) from equation (1.2.1) is known as *weak nonlinearisation*, where the second term is the only nonlinear term which remains in equation (1.2.5). Weakly nonlinear equations are more amenable to analytical and numerical analysis than fully nonlinear equations. Solutions of the Kuramoto–Sivashinsky equation (1.2.5) can also exhibit chaotic solutions [74–76]. The Kuramoto–Sivashinsky equation (1.2.5) is applicable in a variety of contexts such as interfacial flows [54; 76–79], two-phase flow in cylindrical pipes [80], flame front propagation [81–84], chemical reaction dynamics [85; 86], and has also been used extensively in control theory [87–90].

1.2.1.3 Integral boundary layer method

As the effects of inertia become more significant, an improved reduced-order model is needed whose solution does not experience unphysical blowup. An alternative to the gradient expansion method used to derive equation (1.2.1) is the Integral

Boundary Layer (IBL) method. Note that the terminology "boundary-layer" is something of a misnomer as there are, in fact, no boundary layers present, however this terminology is now commonly used in the literature associated with weighted residual modelling [52; 53; 55; 59–66], and so we (reluctantly) use it in the present work. In Section 1.2.1.4 we show that the IBL method is a special case of weighted residual modelling.

The IBL method yields a two-equation model for the dimensionless film thickness $h(x,t)$, and the dimensionless volume flux $q(x,t)$, namely,

$$\frac{\partial h}{\partial t} + \frac{\partial q}{\partial x} = 0, \tag{1.2.6}$$

$$\frac{5}{2h^2}q - \frac{5}{6}h + \delta\left[\frac{5}{6}\frac{\partial q}{\partial t} + \frac{2}{h}q\frac{\partial q}{\partial x} + \left(\frac{5\cot\beta}{6}h - \frac{q^2}{h^2}\right)\frac{\partial h}{\partial x} - \frac{5\Gamma}{6}\frac{\partial^3 h}{\partial x^3}\right] = 0. \tag{1.2.7}$$

Equations (1.2.6) and (1.2.7) are sometimes referred to as Shkadov's model [91]. The solutions of equations (1.2.6) and (1.2.7) do not experience blowup, which is an improvement on the Benney equation (1.2.1). However, when performing a gradient expansion on the flux in equations (1.2.6) and (1.2.7) (by expanding the flux in powers of δ), the Benney equation (1.2.1) is not recovered, and thus equations (1.2.6) and (1.2.7) do not predict the same threshold for instability as the Orr–Sommerfeld equations [59, Chapters 3 and 6].

1.2.1.4 Weighted residuals integral boundary layer method

A method for developing a reduced-order model which does not experience unphysical blowup and yet does predict the same threshold for instability as the Orr–Sommerfeld equations is the Weighted Residuals Integral Boundary Layer (WRIBL) method, pioneered by Ruyer-Quil and Manneville [52]. The WRIBL method is a separation of variables approach, combined with the selection of suitable weight functions during the computation of the residuals.

To implement the WRIBL method, we begin by applying a long-wave approximation to the Navier–Stokes equations to obtain a boundary-layer equation for

the dimensionless streamwise velocity $u(x, y, t)$, namely

$$\begin{aligned}\mathcal{B}(u) \equiv & \frac{\partial^2 u}{\partial y^2} + 1 - \delta\left(\frac{\partial u}{\partial t} + u\frac{\partial u}{\partial x} + v\frac{\partial u}{\partial y}\right) \\ & + \delta\left(\Gamma\frac{\partial^3 h}{\partial x^3} - \cot\beta\frac{\partial h}{\partial x}\right) + \delta^2\left[2\frac{\partial^2 u}{\partial x^2} + \frac{\partial}{\partial x}\left(\frac{\partial u}{\partial x}\bigg|_{y=h}\right)\right] + \mathcal{O}\left(\delta^3\right) = 0,\end{aligned} \tag{1.2.8}$$

where $v(x, y, t)$ and y denote the dimensionless cross-stream velocity and the dimensionless cross-stream coordinate, respectively. Note that by using the continuity equation we can express v in terms of u.

First, we will discuss the process of using the WRIBL method to derive a first-order model [52]. We seek a solution of the boundary-layer equation (1.2.8) in the form of the expansion

$$u = a_0\left(x, t\right) g_0\left(y; h\right) + \delta\sum_{i=1}^{N} a_i\left(x, t\right) g_i\left(y; h\right) + \mathcal{O}\left(\delta^2\right), \tag{1.2.9}$$

where

$$g_0(y; h) = hy - \frac{y^2}{2} \tag{1.2.10}$$

is the leading-order solution for u with coefficient $a_0(x, t)$, and $g_i(y; h)$ is a set of suitably-chosen basis functions (which are closed under the differentiations and products present in the boundary-layer equation (1.2.8)) with coefficients $a_i(x, t)$ for $i = 1, \ldots, N$, where $N + 1$ is the total number of coefficients. In principle, the expansion (1.2.9) can be substituted into the boundary-layer equation (1.2.8) and explicit expressions for the coefficients can be determined by matching in powers of y, however this is a cumbersome process, even at first order in δ (for algebraic details, see Ruyer-Quil and Manneville [52] and Wray et al. [62]), and so instead we use a weighted residuals approach to solve the boundary-layer equation (1.2.8) [52; 62]. We use weight functions $W_j(x, y, t)$ and define the residuals $\mathscr{R}_j$ for $j = 0, \ldots, M$ as

$$\mathscr{R}_j(x, t) = \left\langle W_j, \mathcal{B}\left(a_0 g_0 + \delta\sum_{i=1}^{N} a_i g_i\right)\right\rangle \tag{1.2.11}$$

for $j = 0, 1, \ldots, M$, and where

$$\langle \alpha, \beta \rangle = \int_0^h \alpha\beta \, \mathrm{d}y \tag{1.2.12}$$

is an inner product. In general, Ruyer-Quil and Manneville [52] show that the number of weights required, $M+1$, is the same as the number of basis functions, $N+1$ (i.e. $M = N$). We set the residuals $\widetilde{\mathscr{R}}_j$ (1.2.11), for $j = 0, 1, \ldots, N$, equal to zero to obtain a system of $N+1$ equations to be solved for the coefficients a_i for $i = 0, 1, \ldots, N$. While different weights will yield different systems of equations, all will yield the same coefficients when the number of basis functions is sufficiently large [63]. However, judicious choices of weights can make the evaluation of the coefficients substantially simpler, as we now show.

When computing the residuals (1.2.11) at first order in δ, we notice that the coefficients a_i, for $i = 1, \ldots, N$ of the expansion (1.2.9) only enter the problem via the leading-order viscous term in the boundary-layer equation (1.2.8). Evaluating the residual of the viscous term explicitly yields

$$\int_0^h W_j \frac{\partial^2}{\partial y^2}(a_i g_i) \, \mathrm{d}y = -\left(W_j \frac{\partial}{\partial y}(a_i g_i) \right) \Big|_{y=0} - \left(a_i g_i \frac{\partial W_j}{\partial y} \right) \Big|_{y=h} + \int_0^h a_i g_i \frac{\partial^2 W_j}{\partial y^2} \, \mathrm{d}y, \tag{1.2.13}$$

for $i = 0, 1, \ldots, N$ and $j = 0, 1, \ldots, N$, where we have used integration by parts, and applied the no-slip condition and the tangential stress balance in the streamwise direction. The evaluation of terms on the right-hand side of (1.2.13) can be made independent of terms involving a_i, for $i = 1, \ldots, N$ (thus negating the need to determine the a_i, or even the g_i, for $i = 1, \ldots, N$) by a suitable choice of W_j for $j = 0, 1, \ldots, N$. However, as we are about to show, only one weight function W_0 (i.e. $M = N = 0$) is required if we choose this weight function such that

$$W_0|_{y=0} = 0, \quad \frac{\partial W_0}{\partial y} \Big|_{y=h} = 0, \quad \frac{\partial^2 W_0}{\partial y^2} = A, \tag{1.2.14}$$

where A is a (non-zero) constant. The first two conditions on W_0 in (1.2.14) allow us to eliminate the first two terms on the right-hand side of (1.2.13), while the final condition on W_0 in (1.2.14) allows the remaining integral on the right-hand

side of (1.2.13) to be written so as to be proportional to

$$\int_0^h u \, \mathrm{d}y = q. \tag{1.2.15}$$

By making this particular choice of W_0, which satisfies the conditions (1.2.14), only one basis function, namely g_0, is required (and thus only one residual $\mathscr{R}_0$ must be evaluated) to derive a first-order model. In particular, when $A = -1$ in equation (1.2.14), the weight function W_0 is

$$W_0 = g_0 = hy - \frac{y^2}{2}, \tag{1.2.16}$$

where g_0 is defined by equation (1.2.10). In this case, the WRIBL method in fact coincides with the Galerkin approach, in which the weight functions and basis functions are identical [52; 63; 64]. Other applications of the WRIBL method, while following the same procedure outlined in the present section, do not use the Galerkin approach [55; 60]. Evaluating $\mathscr{R}_0 = \langle W_0, \mathcal{B}(a_0 g_0) \rangle = 0$ at first order, with this choice of W_0 (1.2.16), results in a single equation involving only a_0 and h. However, the coefficient a_0 (which has no physical meaning) can be eliminated in favour of q, which is a physically measurable quantity, by substituting the expansion (1.2.9) into equation (1.2.15), truncating at first-order, and obtaining an expression for a_0 in terms of q. Therefore, eliminating a_0 in favour of q yields

$$\frac{5}{2h^2}q - \frac{5}{6}h + \delta\left[\frac{\partial q}{\partial t} + \frac{17}{7h}q\frac{\partial q}{\partial x} + \left(\frac{5\cot\beta}{6}h - \frac{9}{7h^2}q^2\right)\frac{\partial h}{\partial x} - \frac{5\Gamma}{6}\frac{\partial^3 h}{\partial x^3}\right] = 0, \tag{1.2.17}$$

which, with the kinematic condition (1.2.6), yields a closed system of two coupled evolution equations for h and q.

Note that equation (1.2.17) has terms of the same form as equation (1.2.7) but with different coefficients for three of the terms (namely the third, fourth, and sixth terms of equations (1.2.7) and (1.2.17)). In particular, if we were to choose $W_0 = 1$ instead of (1.2.16), then evaluating $\mathscr{R}_0 = \langle 1, \mathcal{B}(a_0 g_0) \rangle = 0$ would yield equation (1.2.7) instead of equation (1.2.17) [63]. The first-order model (1.2.6) and (1.2.17) does not experience blowup and does recover the Benney equation (1.2.1) when a gradient expansion is performed on the flux, and hence correctly predicts the same threshold for instability as the Orr–Sommerfeld equations [59, Chapters 3 and 6; 52]. The first-order model (1.2.6) and (1.2.17) incorporates the

effects of gravity, viscosity, inertia, surface tension, and the angle of inclination of the substrate to the horizontal, but does not include the effects of second-order viscous terms. Note that the second-order viscous terms have a dispersive effect on the linear wave speed, and hence we will refer to them as (second-order) viscous dispersion terms, in line with standard terminology in the literature associated with weighted residual modelling [59]. If we wish to include the effect of viscous dispersion, we must proceed to second order.

To derive a second-order model, we extend the expansion of u (1.2.9) to second order

$$u = a_0(x,t)\, g_0(y;h) + \delta \sum_{i=1}^{N} a_i(x,t)\, g_i(y;h) + \delta^2 \sum_{k=1}^{N^*} a_k^*(x,t)\, g_k^*(y;h) + \mathcal{O}\left(\delta^3\right). \tag{1.2.18}$$

Similar to the first-order case, a suitable choice of W_j for $j = 0, 1, \ldots, N + N^*$, negates the need to determine the a_k^*, or even the g_k^*, for $k = 1, \ldots, N^*$. However, an expression for u at first order is required, and so some of the a_i and g_i for $i = 1, \ldots, N$ must be determined. In particular, Ruyer-Quil and Manneville [52] were able to show that, at first order, u could be written as

$$u = a_0(x,t)\, f_0(y;h) + \delta\left[a_1(x,t)\, f_1(y;h) + a_2(x,t)\, f_2(y;h)\right], \tag{1.2.19}$$

where $f_0 = g_0$, and f_1 and f_2 are linear combinations of g_0, g_1, g_2 and g_0, g_1, g_2, g_3, g_4, respectively (for algebraic details, see Ruyer-Quil and Manneville [52] and Wray et al. [62]).

The expression for u at first order (1.2.19) involves three basis functions, namely f_i for $i = 0, 1, 2$, and thus requires three weight functions, $W_j = f_j$ for $j = 0, 1, 2$, with three residuals to evaluate, namely $\mathscr{R}_j = \langle W_j, \mathcal{B}(a_0 f_0 + \delta\left[a_1 f_1 + a_2 f_2\right])\rangle = 0$ for $j = 0, 1, 2$ (i.e. $M = N = 2$). Evaluating $\mathscr{R}_j = \langle W_j, \mathcal{B}(a_0 f_0 + \delta\left[a_1 f_1 + a_2 f_2\right])\rangle = 0$ for $j = 0, 1, 2$, results in three equations involving only a_i for $i = 1, 2, 3$ and h. The coefficients a_i for $i = 1, 2, 3$ (which have no physical meaning) can be eliminated in favour of $q(x,t)$, $s_1(x,t)$, and $s_2(x,t)$, where s_1 and s_2 are additional variables which describe the deviation of the velocity profile from the leading-order semi-parabolic profile (1.2.10) [52]. Therefore, the second-order model is a coupled system of four equations for $h(x,t)$, $q(x,t)$, $s_1(x,t)$, and $s_2(x,t)$ [52]. The equations comprising the second-order model are lengthy, and are not reproduced here, but

are given by equations (11) and (38)–(40) in Ruyer-Quil and Manneville [52]. The second-order model includes the effect of viscous dispersion, which was absent in the first-order model (1.2.6) and (1.2.17).

While the second-order model does not experience blowup and is second-order accurate in δ, its complexity limits its amenability to either analytical or numerical analysis. The second-order model can be simplified by the ad hoc elimination of s_1 and s_2, by assuming that these terms are higher-order in the velocity expansion (1.2.9). With this assumption, only the leading-order term of the velocity expansion (1.2.18) (and thus only the leading-order basis function) is required. Therefore, evaluating $\mathscr{R}_0 = \langle W_0, \mathcal{B}(a_0 g_0)\rangle = 0$, with W_0 given by (1.2.16), but with the *second-order boundary-layer equation* (1.2.8) yields

$$\begin{aligned}\frac{5}{2h^2}q - \frac{5}{6}h + \delta\left[\frac{\partial q}{\partial t} + \frac{17}{7h}q\frac{\partial q}{\partial x} + \left(\frac{5\cot\beta}{6}h - \frac{9}{7h^2}q^2\right)\frac{\partial h}{\partial x} - \frac{5\Gamma}{6}\frac{\partial^3 h}{\partial x^3}\right] \\ - \delta^2\left[\frac{4}{h^2}q\left(\frac{\partial h}{\partial x}\right)^2 - \frac{9}{2h}\frac{\partial q}{\partial x}\frac{\partial h}{\partial x} - \frac{6}{h}q\frac{\partial^2 h}{\partial x^2} + \frac{9}{2}\frac{\partial^2 q}{\partial x^2}\right] = 0,\end{aligned} \tag{1.2.20}$$

which, with the kinematic condition (1.2.6), yields a closed system of two coupled evolution equations for h and q, and is referred to as the *simplified second-order model* by Ruyer-Quil and Manneville [52]. The simplified second-order model (1.2.6) and (1.2.20) includes the effect of viscous dispersion at second order, but does not include any of the second-order inertial effects which are associated with s_1 and s_2.

While the simplified second-order model is no longer second-order accurate (in particular, as it does not recover the Benney equation (1.2.1) at second order when a gradient expansion is performed on the flux), it is much more amenable to analytical and numerical analysis than the *full second-order model* (equations (11) and (38)–(40) in Ruyer-Quil and Manneville [52]). Additionally, the results of computations of the simplified second-order model in the linear and nonlinear regime have both been found to be accurate when compared to experimental results [64; 92; 93] and DNS computations [55; 60; 62; 94]. Thus, many studies adopt the simplified second-order model rather than the full second-order model [53; 55; 60–62; 64–66], however, finding the best two-equation model is still an open and active problem [95].

Reduced-order models can also be analysed using analytical techniques which

are not applicable to the Navier–Stokes equations. One such analytical technique is the Whitham wave hierarchy, which we will use in Chapter 5, and is described in the following subsection.

1.2.2 Whitham wave hierarchy

For equations of a specific structure, the onset of the instability of a flow in the linear regime can be understood via the Whitham wave hierarchy, as introduced by Whitham [96, Chapter 10]. The Whitham wave hierarchy has been applied in many contexts such as traffic flows [96, Chapter 3], two-phase flows [97], flood waves [96, Chapter 3], and falling film flows [59; 64–66; 98; 99]. The Whitham wave hierarchy provides a mathematical framework for discussing and understanding the physical mechanisms of wave dynamics and, in particular, how the dynamics of the waves relate to the linear stability of the flow.

The Whitham wave hierarchy is applicable to linearised equations of the form [96, Chapter 10; 98],

$$d_0\left(\frac{\partial}{\partial t}+c_k\frac{\partial}{\partial x}\right)\breve{h}+d_1\left(\frac{\partial}{\partial t}+c_{d_-}\frac{\partial}{\partial x}\right)\left(\frac{\partial}{\partial t}+c_{d_+}\frac{\partial}{\partial x}\right)\breve{h}=0, \tag{1.2.21}$$

where d_0 and d_1 are positive constants and c_k and $c_{d_\pm}$ are the kinematic and dynamic wave speeds [100], respectively. The kinematic waves are those formed in response to deformations of the free surface, and the dynamic waves are those formed in response to variations in momentum. When two-equation reduced-order models (such as those developed using the WRIBL method) are linearised around a constant base-state solution, then the linear governing equation may be able to be rewritten in the form of equation (1.2.21) [59, Chapter 7], and, to illustrate this process, we will use the first-order WRIBL model (1.2.6) and (1.2.17). To linearise equations (1.2.6) and (1.2.17), we decompose h and q as

$$h(x,t)=1+\xi\breve{h}(x,t), \tag{1.2.22}$$

$$q(x,t)=\bar{q}+\xi\breve{q}(x,t), \tag{1.2.23}$$

where $\xi\ll 1$, $\bar{q}$ is the base-state solution for the flux, and the terms with checks denote the perturbations to the base-state solutions. We substitute (1.2.22) and (1.2.23) into equations (1.2.6) and (1.2.17). At first order in ξ, we differentiate the

expression arising from equation (1.2.17) with respect to x and use the expression arising from equation (1.2.6) to eliminate $\partial\breve{q}/\partial x$ (and thus also eliminating $\breve{q}$) to leave a single equation for $\breve{h}$ of the form (1.2.21). The Whitham wave hierarchy can be extended to include derivatives of a higher order in equation (1.2.21) [59, Chapter 7; 64–66; 97–99], and we shall consider this extension in Chapter 5. Equations of the form (1.2.21) are referred to as having a "two-wave structure" [99] and the flow that equations of this form describe is stable when the stability criterion

$$c_{d_-} \leq c_k \leq c_{d_+} \tag{1.2.24}$$

is satisfied [96]. The stability criterion (1.2.24) can be justified by solving equation (1.2.21). To do this, we decompose $\breve{h}$ as

$$\breve{h}(x,t) = \widetilde{h}\mathrm{e}^{ikx+\sigma t}, \tag{1.2.25}$$

where k and σ denote the (real) streamwise wavenumber and the (complex) linear growth rate, respectively. Substituting (1.2.25) into (1.2.21) yields

$$d_0\left(ic_k k + \sigma\right) - d_1\left(c_{d_-}k - i\sigma\right)\left(c_{d_+}k - i\sigma\right) = 0. \tag{1.2.26}$$

When the linear growth rate is unstable for $k \to 0^+$ (i.e. for disturbances with a long wavelength), then this mode of instability is referred to as "long-wave instability" [101]. The mode of instability for the flow described by equation (1.2.21) is long-wave instability, thus an expansion of the linear growth rate of the form

$$\sigma = \sigma_0 + k\sigma_1 + k^2\sigma_2 + \mathcal{O}(k^3) \tag{1.2.27}$$

is used, for $k \ll 1$. Substituting (1.2.27) into (1.2.26) and solving order-by-order in k yields

$$\sigma_0 = 0, \quad \sigma_1 = -ic_k, \quad \sigma_2 = -\frac{d_1}{d_0}\left(c_{d_-} - c_k\right)\left(c_k - c_{d_+}\right). \tag{1.2.28}$$

Therefore, the stability is governed by the sign of σ_2, as $\sigma_0 = 0$ and σ_1 is purely imaginary, and thus does not affect the stability. The sign of σ_2 is negative when the stability criterion (1.2.24) is satisfied. Note that there is a second linear growth

rate of the form (1.2.27) namely

$$\sigma_0 = -\frac{d_0}{d_1}, \quad \sigma_1 = i(c_k - c_{d_+} - c_{d_-}), \quad \sigma_2 = \frac{d_1}{d_0}\left(c_{d_-} - c_k\right)\left(c_k - c_{d_+}\right), \tag{1.2.29}$$

which is always negative for small k and thus is always stable.

We will now provide a physical interpretation for the stability criterion (1.2.24) in the context of a signalling problem with a localised initial condition. Kinematic waves appear due to first-order derivatives in equation (1.2.21), and dynamic waves appear due to second-order derivatives. We can explore the roles of the two waves individually by examining equation (1.2.21) in the limits of $d_1 \to \infty$ and $d_1 \to 0^+$ (or equivalently, $d_0 \to 0^+$ and $d_0 \to \infty$). First, consider the limit $d_1 \to \infty$, in which equation (1.2.21) reduces to

$$\left(\frac{\partial}{\partial t} + c_{d_-}\frac{\partial}{\partial x}\right)\left(\frac{\partial}{\partial t} + c_{d_+}\frac{\partial}{\partial x}\right)\breve{h} = 0, \tag{1.2.30}$$

with the general solution

$$\breve{h} = \breve{h}_1(x - c_{d_-}t) + \breve{h}_2(x - c_{d_+}t). \tag{1.2.31}$$

Now, consider the limit $d_1 \to 0^+$, in which equation (1.2.21) reduces to

$$\left(\frac{\partial}{\partial t} + c_k\frac{\partial}{\partial x}\right)\breve{h} = 0, \tag{1.2.32}$$

with the general solution

$$\breve{h} = \breve{h}_0(x - c_k t). \tag{1.2.33}$$

A localised perturbation to the uniform base state produces a wavepacket which consists of both kinematic and dynamic waves. The early stages of the wavepacket evolution are governed by equation (1.2.30), where the wavefronts at the front and back of the wavepacket travel with speeds c_{d_+} and c_{d_-}, respectively. In other words, the dynamic waves carry the "first signal" at speeds c_{d_+} and c_{d_-} [96, Chapters 1 and 10]. The later stages of the wavepacket evolution are governed by equation (1.2.32), where the wavefronts travel with speed c_k. Here, the kinematic waves carry the "main disturbance" at speed c_k [96, Chapters 1 and 10]. Figure 1.6 shows a sketch of the characteristic curves of equations (1.2.30) and (1.2.32) for a wavepacket of length L. Figure 1.6(a) shows neutral stability ($c_{d_-} = c_k = c_{d_+}$)

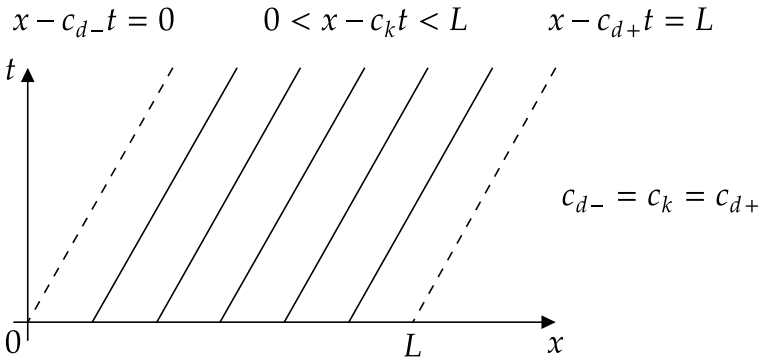

(a)

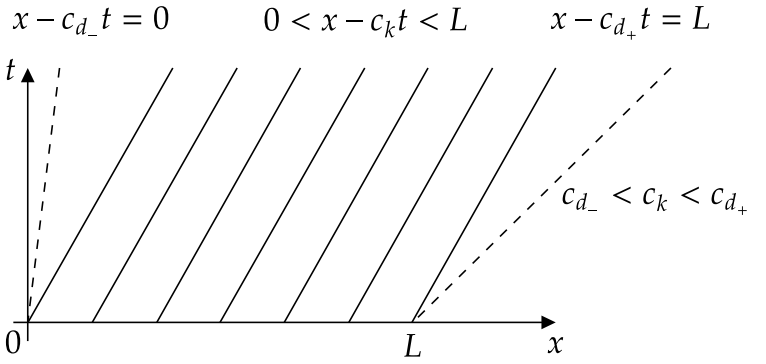

(b)

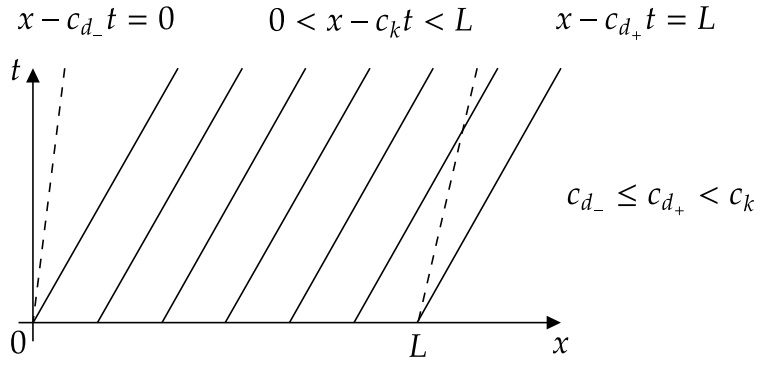

(c)

Figure 1.6: Sketch of the characteristic curves of equations (1.2.30) (dashed) and (1.2.32) (solid) for a wavepacket of length L. The cases sketched are (a) neutral stability ($c_{d_-} = c_k = c_{d_+}$), (b) stability ($c_{d_-} < c_k < c_{d_+}$), and (c) instability ($c_{d_-} \leq c_{d_+} < c_k$).

in which the wavepacket does not change shape. Figure 1.6(b) shows stability ($c_{d_-} < c_k < c_{d_+}$) in which the wavefront at the front of the wavepacket travels faster than the wavefronts in the middle of the wavepacket, which in turn, travels faster than the wavefront at the back of the wavepacket, thus the amplitude of the wavepacket decreases with time towards the uniform base state. Figure 1.6(c) shows instability ($c_{d_-} \leq c_{d_+} < c_k$) in which the wavefronts in the middle of the wavepacket travel faster than the wavefronts at the front and back of the wavepacket and the characteristics of the waves overlap, which causes the wavepacket to become multi-valued. When the wavepacket is multi-valued, equation (1.2.21) is no longer physically valid, and cannot describe the evolution of the wavepacket produced by a perturbation to the uniform base state.

By constructing a hierarchy of the lower-order (dynamic) waves and higher-order (kinematic) waves, we have a useful analytical technique which we will use to explore the mechanisms which govern the stability of the flow.

1.3 Thin-film and thick-film flows

In Section 1.2, we discussed the development of reduced-order models by exploiting a disparity in length scales of the flow. In the present section, we will discuss the relationship between length scales present for flow on a planar substrate, and then extend this discussion for flow on a curved substrate. Throughout this section, hats denote dimensional quantities.

1.3.1 Flow on a planar substrate

For flow on a planar substrate, only *two* length scales are present. These are the characteristic film thickness $\hat{H}$ (i.e. the length scale in the cross-stream direction), and a characteristic wavelength of the film $\hat{\lambda}$ (i.e. the length scale in the streamwise direction), as shown schematically in Figure 1.7.

There are two common techniques which are used to exploit a disparity in length scales of the flow. The first is a *thin-film approximation*, which assumes that $\hat{H}$ is small relative to $\hat{\lambda}$. The planar thin-film small aspect ratio δ_{plane} is

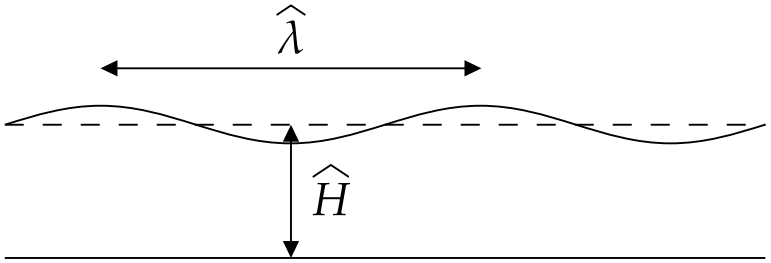

Figure 1.7: Schematic of the relationship between the two length scales present for flow on a planar substrate.

defined by

$$\delta_{\text{plane}} = \frac{\hat{H}}{\hat{\lambda}} \ll 1. \tag{1.3.1}$$

The second is a *long-wave approximation*, which assumes that $\hat{\lambda}$ is large relative to $\hat{H}$. However, in the present case, assuming that $\hat{\lambda}$ is large relative to $\hat{H}$ (i.e. a long-wave approximation) is equivalent to assuming that $\hat{H}$ is small relative to $\hat{\lambda}$ (i.e. a thin-film approximation). Thus, for flow on a planar substrate, the terms "thin-film" and "long-wave" are interchangeable. For the remainder of this section, for convenience, when discussing flow on a planar substrate, we choose to refer to the planar thin-film small aspect ratio δ_{plane}, defined by (1.3.1) as simply the *planar small aspect ratio* δ_{plane}.

1.3.2 Flow on a curved substrate

A curved substrate introduces two additional length scales, namely the two characteristic radii of curvature of the substrate. For simplicity, in the following discussions of flow on a curved substrate we will consider a substrate with only one characteristic radius of curvature $\hat{L}$ (e.g. a cylinder, where one of the two characteristic radii of curvature is the cylinder radius and the other is infinite and thus, similar to the radii of curvature in the planar case, can be ignored). However, the ideas discussed in the present section can be readily extended to curved substrates with two finite radii of curvature (e.g. an ellipsoid or a sphere). In this section, we use the characteristic radius of curvature $\hat{L}$ to nondimensionalise the length scales

$$H = \frac{\hat{H}}{\hat{L}}, \quad \lambda = \frac{\hat{\lambda}}{\hat{L}}, \quad L = \frac{\hat{L}}{\hat{L}}, \tag{1.3.2}$$

where H and λ are free parameters, and L is taken to be unity. While unconventional, we continue to include L explicitly in our discussion for the remainder of the present section.

As described, for example, by Wray et al. [55] and Wray and Cimpeanu [60], we draw a clear distinction between the terms "thin-film" and "long-wave" for flow on a curved substrate, which, as we shall explain, do not, in general, mean the same thing even though they are sometimes used interchangeably in the literature. For flow on a planar substrate, there is *one* small aspect ratio δ_{plane}, defined by (1.3.1), whereas for flow on a curved substrate, due to the presence of an additional length scale, there are *two* small aspect ratios, namely the thin-film small aspect ratio ε (which we shall define in Section 1.3.2.1), and the long-wave small aspect ratio δ (which we shall define in Section 1.3.2.2).

We will first discuss both a thin-film approximation and a long-wave approximation for flow on a curved substrate in Sections 1.3.2.1 and 1.3.2.2, respectively, and then discuss how a long-wave approximation can be used to develop reduced order models to describe the flow of a *thick film* on a curved substrate in Section 1.3.2.3. In particular, we define a thick film as one in which the characteristic film thickness is of the same order of magnitude as the characteristic radius of curvature.

1.3.2.1 Flow of a thin film on a curved substrate

On a curved substrate, a thin-film approximation assumes that the characteristic film thickness H is small compared to both a characteristic wavelength λ and the characteristic radius of curvature L. The thin-film small aspect ratio ε is defined by

$$\varepsilon = H \ll 1, \tag{1.3.3}$$

where $\lambda = \mathcal{O}(1)$. The relationship between the length scales present for the flow of a thin film on a curved substrate is shown schematically in Figure 1.8. The flow of a thin film on a curved substrate will be discussed in detail in Sections 1.4 and 1.5 for flow on a horizontal cylinder, and in Section 1.6 for flow on a vertical fibre.

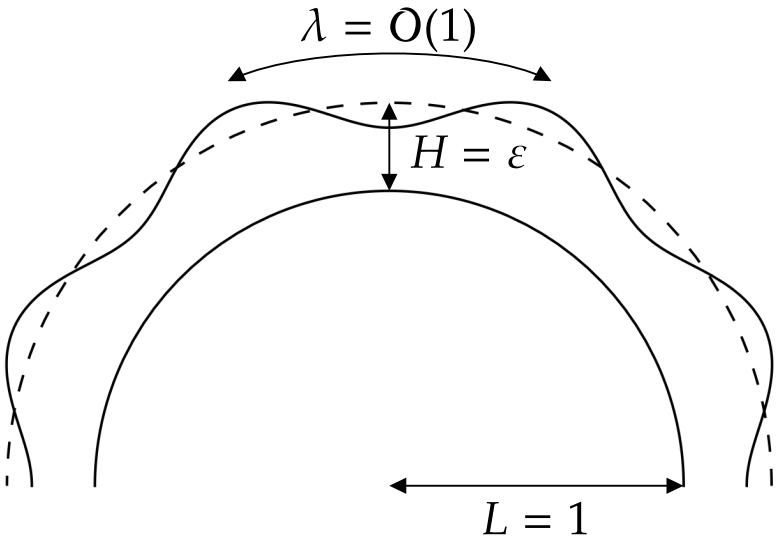

Figure 1.8: Schematic of the relationship between the three length scales for the flow of a thin film on a curved substrate with a thin-film approximation.

1.3.2.2 Flow of a thick film on a curved substrate

On a curved substrate, a long-wave approximation assumes that a characteristic wavelength λ is large compared to both the characteristic film thickness H and the characteristic radius of curvature L. The long-wave small aspect ratio δ is defined by

$$\delta = \lambda^{-1} \ll 1, \tag{1.3.4}$$

where $H = \mathcal{O}(1)$. The relationship between the length scales present for the flow of a thick film on a curved substrate is shown schematically in Figure 1.9. The flow of a thick film on a curved substrate will be discussed in detail in Section 1.4 for flow on a horizontal circular cylinder, and in Section 1.6 for flow on a vertical fibre.

1.3.2.3 Modelling the flow of a thick film on a curved substrate

Many studies of flow on a curved substrate have restricted themselves to using a thin-film approximation (i.e. assuming that $H \ll 1$) [102–108], however, by using a long-wave approximation, it is possible to relax the restriction that the film thickness must be small relative to the characteristic radius of curvature (i.e. allowing $H = \mathcal{O}(1)$ while maintaining the assumption that $\lambda^{-1} \ll 1$) in order to

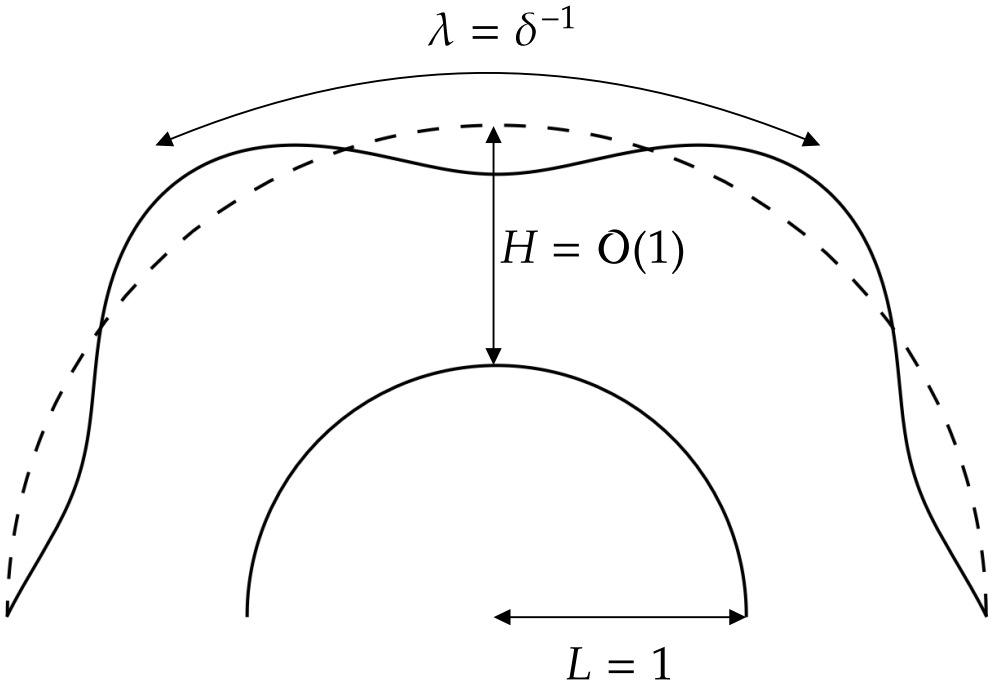

Figure 1.9: Schematic of the relationship between the three length scales for the flow of a thick film on a curved substrate with a long-wave approximation.

develop reduced-order models which are appropriate for a film thickness of order unity [55; 60; 64; 109; 110].

When the fluid film is thick, bulges which have a large interfacial curvature (relative to the characteristic radius of curvature) can form in the film. To accurately model these bulges, a common (albeit ad hoc) assumption is to retain the full form of the interfacial curvature κ [55; 60; 71; 109; 111–116]. Thus, terms in the full form of κ that are of higher order in δ are retained in order to effectively model these bulges.

Some reduced-order models have been developed using a thin-film approximation (i.e. assuming that $H \ll 1$) but are then used to model a flow in which the film thickness can exceed the range of validity of a thin-film approximation. As an example, we will discuss the flow of a thin film of fluid on a two-dimensional stationary horizontal circular cylinder. While the film is indeed initially thin, as the free surface evolves it can eventually exceed the range of validity of a thin-film approximation [113; 117]. Figure 1.10(a) shows a plot of the initial uniform free surface on a stationary circular cylinder and Figure 1.10(b) shows a plot of the free surface at $t = 150$, when the fluid has drained to form a bulge at the bottom

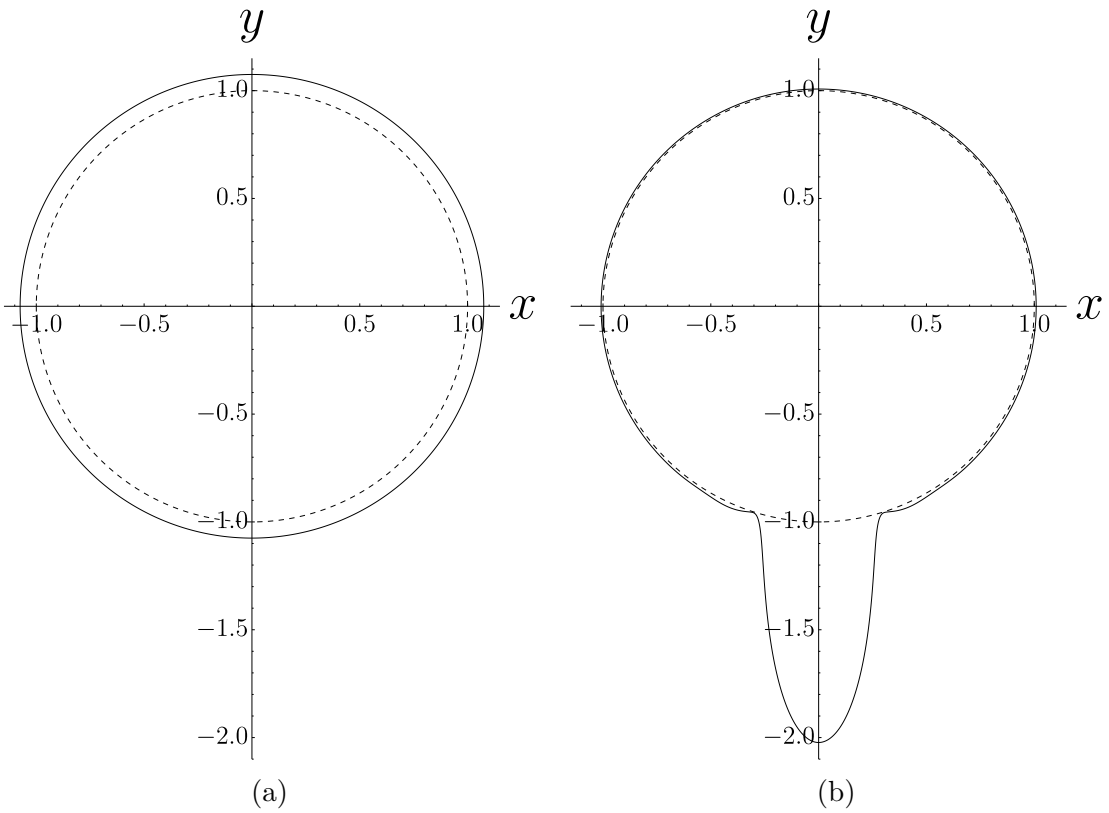

Figure 1.10: Plot of the unscaled free surface (solid) on a stationary horizontal circular cylinder (dashed) from the numerical solution of the two-dimensional case of equation (54) from Evans et al. [56] with $W = 0$, $M = 0.05$ (in the notation of Evans et al. [56]), $Bo = 100$, and $\varepsilon = 0.075$ (we defer the discussion of the work of Evans et al. [56] to Section 1.4.1.3). (a) The initial free surface is of uniform thickness, and (b) a bulge has formed in the free surface at the bottom of the cylinder due to gravity at $t = 150$.

of the cylinder, due to the effect of gravity (note that these results are generated from the numerical solution of the two-dimensional case of equation (54) from Evans et al. [56] which we will discuss in Section 1.4.1.3). The initial uniform free surface is clearly thin in Figure 1.10(a), whereas the free surface has become (locally) thick at the bottom of the cylinder in Figure 1.10(b) with the maximum film thickness being of the same order of magnitude as the cylinder radius. Thus, as the free surface evolves with time, the solution has violated the thin-film approximation. Therefore, to model a flow in which the free surface becomes (locally) thick, such as in the present example, it is not appropriate to use a reduced-order model derived using a thin-film approximation. However, despite the long-wave approximation also being violated in the present example, in which the (local) film

thickness, cylinder radius, and wavelength are all of a similar size, the results of a reduced-order model derived using a long-wave approximation can still provide a good agreement with the results of DNS, as we shall show in the remainder of this section.

A long-wave approximation has been successfully used to derive a reduced-order model for flow on a curved substrate with a fixed streamwise domain length. For example, we consider the case of a circular cylinder [55; 60] with azimuthal coordinate θ and a fixed azimuthal domain length of 2π. In this case, (following Wray et al. [55] and Wray and Cimpeanu [60]) applying a long-wave approximation to θ introduces the scaling

$$\frac{\partial}{\partial\theta} = \delta\frac{\partial}{\partial\tilde{\theta}}, \tag{1.3.5}$$

where $\delta \ll 1$. The scaling (1.3.5) follows from the assumption that variations are slow in the azimuthal direction. The long-wave scaling is applied to the variation of θ and not θ itself, since the azimuthal domain length is fixed at 2π, and thus cannot be assumed to be "long". As a consequence, the long-wave approximation for flow on a circular cylinder does not, in fact, constitute a formal asymptotic approach. Reduced-order models for flow on a circular cylinder (or more generally, for flow on a curved substrate with a fixed streamwise domain length) derived using a long-wave approximation can instead be treated as "data-driven" models in which validation of the results of the model are provided *a posteriori* against the results of the linear calculations and DNS of the Navier–Stokes equations [55; 60; 109].

Reduced-order models for flow on a circular cylinder derived using a long-wave approximation have been shown to provide good results in comparison with the results of both the linear calculations and DNS of the Navier–Stokes equations, even outside their range of formal validity. We demonstrate this point using an example from Wray et al. [55] for the problem of fluid coating the exterior of a two-dimensional uniformly rotating horizontal circular cylinder in the limit of zero gravity (in the absence of inertia). Figure 1.11 shows their plots of the linear growth rate s (in the notation of Wray et al. [55]) as a function of the unperturbed film radius $\bar{h}$ for the $n = 2$ mode (left), the $n = 4$ mode (middle), and the $n = 6$ mode (right), where n is the (integer) azimuthal wavenumber. The linear growth rates for the flow described by their second-order thick-film WRIBL model and the Stokes equations agree well, even at $\bar{h} = 2$ (when the film is as thick as the cylinder radius). Note that their second-order thick-film WRIBL model is

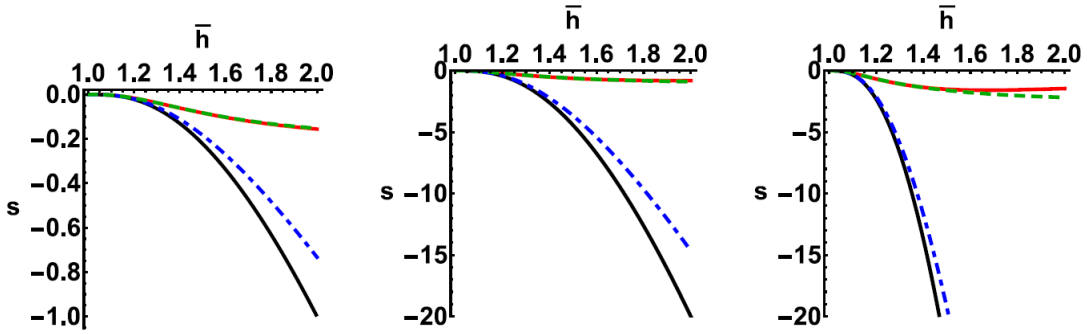

Figure 1.11: Plots of the linear growth rate s as a function of the unperturbed film radius $\bar{h}$, for the problem of fluid coating the exterior of a two-dimensional uniformly rotating horizontal circular cylinder in the limit of zero gravity (in the absence of inertia), for the $n = 2$ mode (left), the $n = 4$ mode (middle), and the $n = 6$ mode (right), where n is the azimuthal wavenumber. The dashed green, dash-dot blue, solid black, and solid red lines correspond to the linear growth rates for the flow described by their second-order thick-film WRIBL model (derived using a long-wave approximation), their first-order thick-film gradient-expansion model (derived using a long-wave approximation), their first-order thin-film gradient-expansion model (derived using a thin-film approximation), and the Stokes equations, respectively. Reproduced with permission from the Society for Industrial and Applied Mathematics, Copyright 2017, Wray et al. [55].

not a simplified second-order model (see Section 1.2.1.4) due to the absence of inertia. The linear growth rates for the flow described by their first-order thick-film gradient-expansion model and their first-order thin-film gradient-expansion model give poor agreement with the linear growth rates for the flow described by the Stokes equations, and the agreement becomes worse as $\bar{h}$ increases. In particular, Figure 1.11 shows that the linear growth rates of reduced-order models derived using a long-wave approximation accurately predict the linear growth rates of the Stokes equations, whereas the linear growth rates of reduced-order models derived using a thin-film approximation fails to predict the linear growth rates of the Stokes equations. The wavelengths of the $n = 6$ mode are not strictly "long", however the linear growth rate of the second-order thick-film WRIBL model still accurately predicts the linear growth rate of the Stokes equations, even outside the range of formal validity of the long-wave approximation, as shown in the rightmost part of Figure 1.11. We will discuss the results of Wray et al. [55] in more detail in Section 1.4.1.4.

1.4 Flow on circular cylinders

1.4.1 Flow on rotating circular cylinders

The pioneering work of Moffatt [57], which was inspired by both the question of what is the maximum load of honey which can be supported on a rotating knife [57], and a 1973 lecture delivered by V. V. Pukhnachev, has stimulated a large and growing body of work which has focused on improving our understanding of how fluid behaves when coating an object.

For mathematical convenience, the pioneering works by both Moffatt [57] and Pukhnachev [58] used a circular cylinder as a simple model for the knife. Nonetheless, fluids coating circular cylinders have been the subject of considerable interest in their own right as they are an important component in a variety of industrial processes, such as fluid transfer in printing processes [118], manufacturing functional films through nanoimprint lithography [119; 120] and ultraviolet imprint lithography [121], removing heat from an aero-engine bearing chamber [122], the application of radiation-curing coating materials to steel plates via a roller-coating process (as shown in Figure 1.12(a), which shows a sketch of the roller-coating process, and Figure 1.12(b), which shows the experimental apparatus used to test the performance of radiation-curing coating materials in response to vibrations) [123], and the manufacturing of lithium-ion battery electrodes via a slot-die coating process (as shown in Figure 1.13(a), which shows a schematic of the experimental set-up used for investigating the quality of the coating, and Figure 1.13(b), which shows a coating with no defects, a coating with bar-shaped defects, and a coating with a stripe defect).

1.4.1.1 The pioneering works of Moffatt [57] and Pukhnachev [58]

The work of Moffatt [57] uses a thin-film approximation to develop a reduced-order model of the form

$$\frac{\partial h}{\partial t} + \frac{\partial}{\partial \theta}\left(h - \frac{h^3}{3}\cos\theta\right) = 0, \tag{1.4.1}$$

where $h(\theta, t)$, t, and θ denote the dimensionless film thickness, the dimensionless time, and the azimuthal coordinate, respectively. Equation (1.4.1) is nonlinear and incorporates the effects of rotation and gravity (the first and second terms

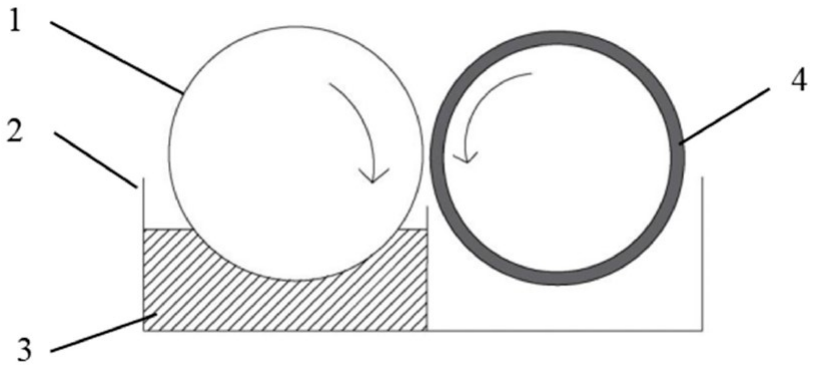

(a)

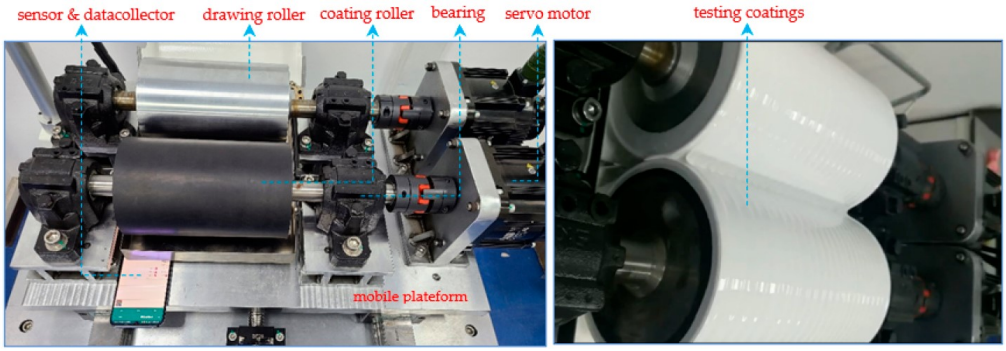

(b)

Figure 1.12: Roller-coating is a method used to apply radiation-curing coating materials to steel plates. (a) A sketch of the roller-coating process, where the drawing roller, coating materials box, coating fluid, and coating roller are indicated by 1, 2, 3, and 4, respectively. (b) Experimental apparatus used to test the performance of radiation-curing coating materials in response to vibrations (left), and the roller coating process performance experiment in operation (right). Reproduced with permssion, Copyright 2022, Lv et al. [123].

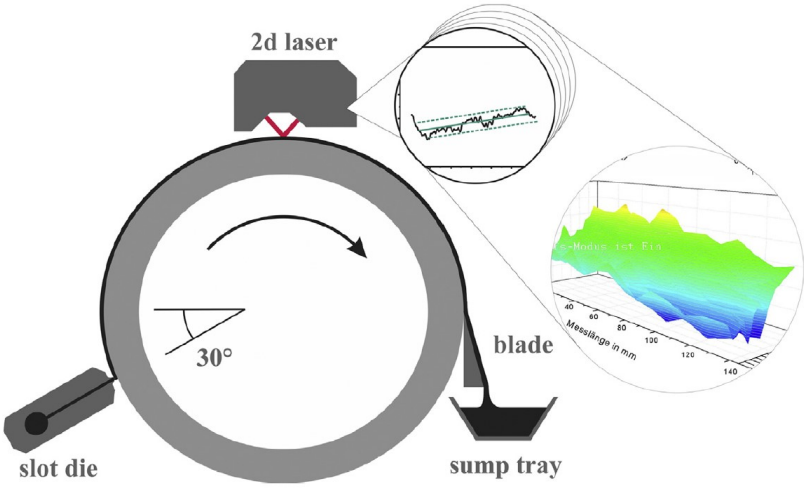

(a)

(b)

Figure 1.13: Slot-die coating is a commonly used method for the manufacturing of lithium-ion battery electrodes. (a) A schematic of the experimental set-up for investigating the quality of the coating applied to a rotating circular cylinder through a slot-die coating process. The topography of the coating is analysed by means of a laser triangulation system, and the coating is then removed from the cylinder by a blade. (b) When no defects are present, the coating is uniform (left), bar-shaped defects can occur in the coating at low flow rates (middle), and stripe defects can occur in the coating when large particles locally clog the coating gap (right). Reproduced with permission from Elsevier, Copyright 2013, Schmitt et al. [124].

in brackets, respectively), while neglecting the effect of surface tension. Equation (1.4.1) admits a steady solution when $\partial h/\partial t = 0$, i.e. when

$$h - \frac{h^3}{3}\cos\theta = q, \tag{1.4.2}$$

where $q(\theta, t)$ is the dimensionless volume flux (as the flow is steady, q is constant in both time and space). Moffatt [57] showed that (1.4.2) only admits a steady "full-film" solution (a single-valued solution for $\theta \in [0, 2\pi)$ for which the fluid wets the entire cylinder) when $0 < q \leq q_c$ where $q_c = 2/3$ is the critical value of the flux. The (dimensionless) maximum supportable load for the cylinder is $M_c \approx 4.443$ (which was incorrectly given by Moffatt [57] as $M_c \approx 4.428$), occurs at $q = q_c = 2/3$. We note here a confusing piece of terminology in the field: M_c is sometimes confusingly termed the "maximum supportable load" or "maximum load", even in studies with surface tension [125], when it would be better termed "the maximum supportable load in the absence of surface tension" (as, in the presence of surface tension, solutions do exist with $M > M_c$). For clarity, hereafter we always refer to M_c as the maximum supportable load in the absence of surface tension. The steady full-film solution of (1.4.2) is given explicitly by

$$h = \begin{cases} \dfrac{2}{\sqrt{|\cos\theta|}}\sinh\left(\dfrac{1}{3}\sinh^{-1}B\right) & \cos\theta < 0, \\ \dfrac{2}{\sqrt{\cos\theta}}\cos\left(\dfrac{2\pi}{3} - \dfrac{1}{3}\cos^{-1}B\right) & \cos\theta > 0, \\ q & \cos\theta = 0, \end{cases} \tag{1.4.3}$$

where

$$B = -q\frac{3}{2}\mathrm{sgn}(\cos\theta)\sqrt{|\cos\theta|}, \tag{1.4.4}$$

and $0 < q \leq q_c$, as shown by Duffy and Wilson [126]. Figure 1.14(a) shows a plot of the steady full-film solution (1.4.3) for various values of $0 < q \leq q_c$. The film is thickest at $\theta = 0$ (where the direction of gravity is tangential to the cylinder, and the effects of gravity and rotation oppose each other) and thinnest at $\theta = \pi$ (where the direction of gravity is tangential to the cylinder, and the effects of gravity and rotation are combined), and, for $0 < q < q_c = 2/3$ the solution is smooth, but for $q = q_c = 2/3$ the solution has a corner at $\theta = 0$. This corner can be seen clearly in Figure 1.14(b) which shows an example of the solution (1.4.3) for both the critical and a subcritical value of q on a cylinder rotating with constant angular velocity in

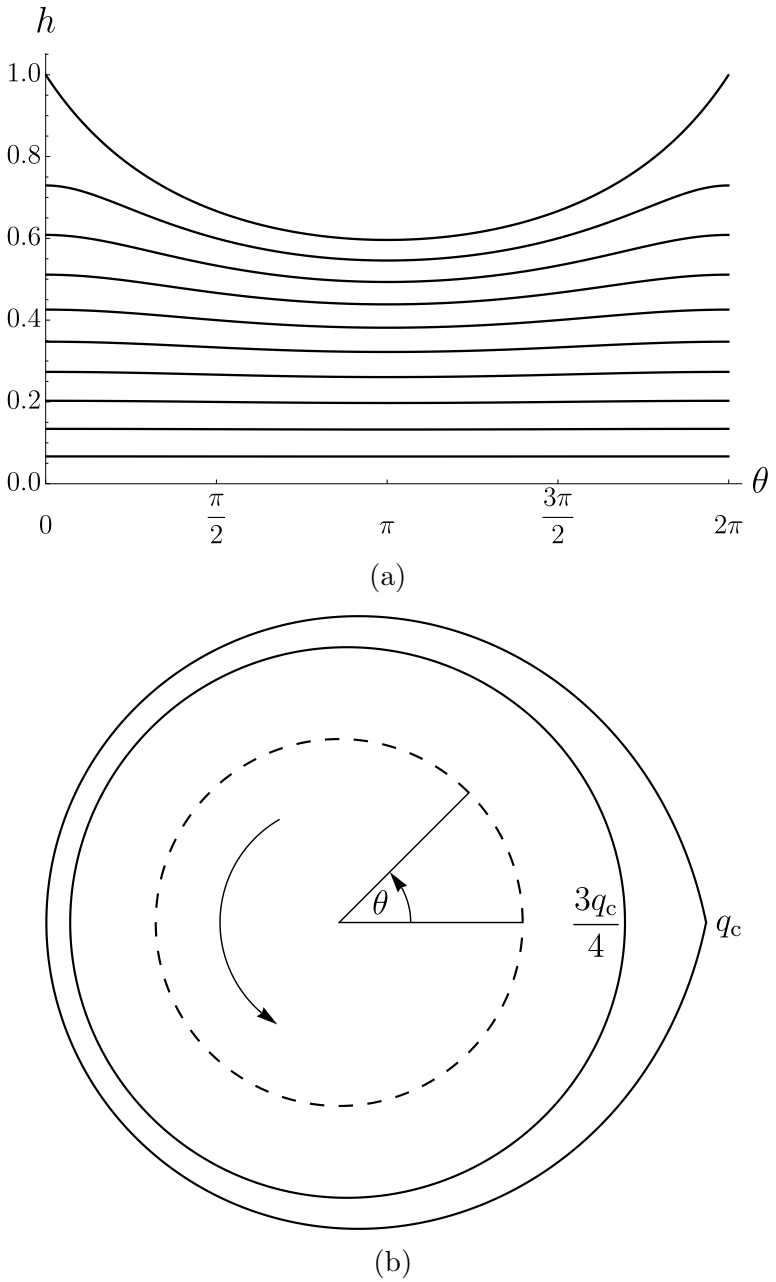

Figure 1.14: (a) Plot of the steady full-film solution (1.4.3) for $q = 1/15, 2/15, \ldots, q_c = 2/3$ (lowest to highest curve). (b) An example of the steady full-film solution (1.4.3) on the rotating circular cylinder (dashed) for $q = 3q_c/4 = 1/2$ and $q = q_c = 2/3$, where the cylinder rotates with constant angular velocity in the direction indicated by the arrow.

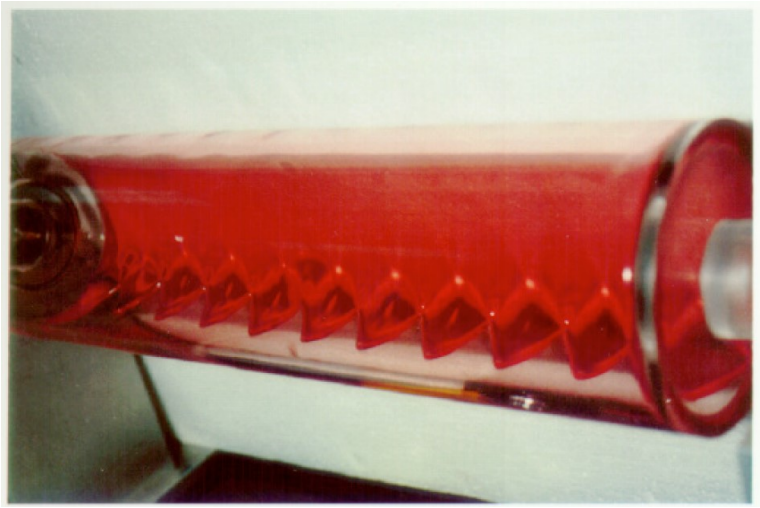

Figure 1.15: The shark-teeth-like pattern observed in the rimming flow experiments of Thoroddsen and Mahadevan [127]. Reproduced with permission from Springer Nature, Copyright 1997, Thoroddsen and Mahadevan [127].

the direction indicated by the arrow. A corner is, of course, not a physical feature of the free surface, and is no longer present when the effects of surface tension are included in the model. Pukhnachev [58] showed that there exists a unique steady solution for two-dimensional flow on the exterior of a rotating cylinder. Using a thin-film approximation, Pukhnachev [58] developed a reduced-order model of the form

$$\frac{\partial h}{\partial t} + \frac{\partial}{\partial \theta}\left(h - \omega \frac{h^3}{3}\cos\theta + \alpha \frac{h^3}{3}\frac{\partial}{\partial \theta}\left[h + \frac{\partial^2 h}{\partial \theta^2}\right]\right) = 0, \tag{1.4.5}$$

where $\omega = \varepsilon^2 \rho g R/(\Omega \mu)$, $\alpha = \varepsilon^3 \gamma/(\Omega \mu R)$, and $\varepsilon = H/R \ll 1$ denote the dimensionless gravity parameter, the dimensionless surface tension parameter, and the thin-film small aspect ratio (see Section 1.3.2.1), respectively, where R and H denote the cylinder radius and the characteristic film thickness, respectively. When the effect of surface tension is neglected in equation (1.4.5) (i.e. in the limit $\alpha \to 0^+$) equation (1.4.1) is recovered, up to a difference in scalings.

While both Moffatt [57] and Pukhnachev [58] considered flow on the exterior of a cylinder (coating flow), their leading-order equations are also applicable for flow on the interior of a cylinder (rimming flow). The problem of rimming flow has proven to be of great interest [127–136] with various different phenomena observed, such as the shark-teeth-like pattern observed in the experimental work of Thoroddsen and Mahadevan [127] as shown in Figure 1.15. However, the focus

of this thesis will be on coating flows.

1.4.1.2 Extensions to the works of Moffatt [57] and Pukhnachev [58]

There have been numerous studies on both coating and rimming flow which have built upon the pioneering works of Moffatt [57] and Pukhnachev [58] in a variety of ways.

Early work was motivated by trying to improve upon Moffatt's [57] value for the maximum supportable load in the absence of surface tension. The pioneering numerical investigation of Hansen and Kelmanson [137] studied steady two-dimensional coating flow on a rotating circular cylinder, without any restriction on the film thickness. Hansen and Kelmanson [137] found that the corner in Moffatt's [57] steady full-film solution (1.4.3) (see Figure 1.14) is never observed in practice (even in the absence of surface tension). Hansen and Kelmanson [137] used an integral-equation method and compared their numerical results with Moffatt's [57] analytical results. Hansen and Kelmanson [137] found that the film is always thickest at $\theta = 0$ and thinnest at $\theta = \pi$ (which agrees with Moffatt's [57] steady full-film solution (1.4.3)), and that the maximum supportable load in the absence of surface tension is close to, but always slightly above, Moffatt's [57] value.

Later, Kelmanson [138] tried to improve upon Moffatt's [57] value for the maximum supportable load in the absence of surface tension by using analytical and numerical methods. Kelmanson [138] developed a reduced-order model using a thin-film approximation which incorporates the effects of rotation and gravity at leading-order in the thin-film approximation (while neglecting the effect of surface tension), and retains a first-order term in the thin-film approximation corresponding to rotation. This approach yields a positive correction to Moffatt's [57] value for the maximum supportable load in the absence of surface tension, which results in an improved agreement with the numerical results of Hansen and Kelmanson [137].

Later, Wilson et al. [139] tried to further improve upon Moffatt's [57] value for the maximum supportable load in the absence of surface tension using analytical and numerical methods. Wilson et al. [139] found that if Kelmanson [138] had retained *all* first-order terms in the thin-film approximation, then the correction

to Moffatt's [57] value for the maximum supportable load in the absence of surface tension is actually negative, and therefore the agreement with the numerical results of Hansen and Kelmanson [137] is actually worse. By including terms which are formally of higher order in the thin-film approximation, the results of Wilson et al. [139] exhibited good agreement with the numerical results of Hansen and Kelmanson [137].

Johnson [132] considered the case of steady rimming flow and, by developing a reduced-order model using a thin-film approximation, found that four different free surface profiles are possible (two of which involve discontinuous "shock solutions") for various cylinder rotation speeds. Shock solutions are solutions in which there is a discontinuity in the free surface. Shock solutions have a fluid load which is greater than the maximum supportable load in the absence of surface tension found by Moffatt's [57] steady full-film solution (1.4.3). O'Brien and Gath [133] later determined the height and location of the shock solutions for rimming flow in the absence of surface tension.

Duffy and Wilson [126] extended the work of Moffatt [57] to include "curtain" solutions, which are unbounded at the top and bottom of the cylinder, where the fluid falls onto and off of the rotating circular cylinder, respectively.

Hinch and Kelmanson [140] analytically investigated the long-time dynamics of a reduced-order model which incorporates the effects of rotation, gravity, and surface tension (i.e. equation (1.4.5), up to a difference in scalings). Using the method of multiple scales, they found that perturbations to the free surface slowly decay towards a steady state, where the film is thickest at $\theta = 0$ and thinnest at $\theta = \pi$. As the perturbations decay, they experience a gravity-induced phase lag due to the complex interactions between gravity, rotation, and surface tension.

Benilov and O'Brien [141], Noakes et al. [142], and Kelmanson [143] all extended the work of Moffatt [57] and Pukhnachev [58] to include the effects of both surface tension and inertia.

Lopes et al. [144] investigated steady coating and rimming flow using DNS and by using a variational approach [145] (which ultimately leads to the retention of the full form of the interfacial curvature) to develop a reduced-order model, which they termed the "variational lubrication model" (VLM). The VLM retains the full form of the free energy which, in the case of Lopes et al. [144] consists of surface

energy (via the surface tension terms) and potential energy (via the gravitational term). Using the VLM, Lopes et al. [144] were able to capture regimes with weak surface tension in which there are multiple solutions, for both coating and rimming flow, for a single set of parameters. Classical (leading-order) models did not predict such multiplicity of solutions for a single set of parameters, and Lopes et al. [144] attributed this to the fact that classical models used a simplified form of the interfacial curvature.

1.4.1.3 The work of Evans et al. [56]

Thus far we have primarily discussed the maximum supportable load in the absence of surface tension on a cylinder which is rotating at a given speed, M_c, which is, of course, analogous to the minimum rotation speed needed to support a given load in the absence of surface tension. However, we have not yet discussed the behaviour of the free surface as the rotation speed is varied parametrically. Evans et al. [56] theoretically investigated the effect of parametrically varying the rotation speed on two-dimensional coating flow. This study uses one of the most complete models and most extensive parametric studies (as we are about to describe). Since we compare some of the results we obtain in Chapters 2 and 3 with the work of Evans et al. [56], we discuss their results in some detail.

Evans et al. [56] developed a reduced-order model using a thin-film approximation, which includes terms that are of first order in the thin-film approximation. The model of Evans et al. [56] is fully three-dimensional and includes the effects of gravity, viscosity, rotation, surface tension, and centrifugation. We will focus on the two-dimensional case, which is described by a reduced-order model of the form

$$(1+\varepsilon h)\frac{\partial h}{\partial t}+\frac{\partial}{\partial\theta}\left[U_\Omega\left(h+\varepsilon\frac{h^2}{2}\right)+\varepsilon\frac{1}{Bo}\frac{h^3}{3}\frac{\partial}{\partial\theta}\left(h+\frac{\partial^2 h}{\partial\theta^2}\right)\right.$$
$$\left.-\cos\theta\left(\frac{h^3}{3}+\varepsilon\frac{h^4}{2}\right)+\varepsilon\left[W^2-\sin\theta\right]\left(\frac{h^3}{3}\frac{\partial h}{\partial\theta}\right)\right]=0, \tag{1.4.6}$$

where $Bo = \rho g R^2/\gamma$, $W = \Omega R^{1/2}/g^{1/2}$, $M = \mu/(\rho g^{1/2}R^{3/2})$ (in the notation of Evans et al. [56]), and $U_\Omega = V_\Omega/(\varepsilon^2 V) = WM/\varepsilon^2 = \mu\Omega R/(\rho g H^2)$ denote a Bond number, a dimensionless rotation speed, a dimensionless viscosity, and a

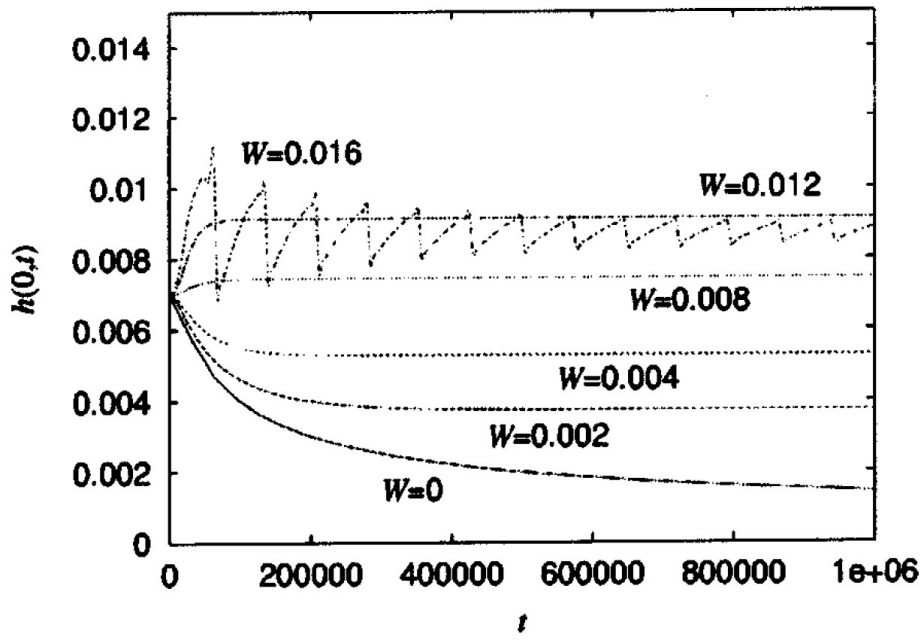

Figure 1.16: The film thickness at $\theta = 0$ plotted as a function of t for $W = 0$, 0.002, 0.004, 0.008, 0.012, and 0.016. Reproduced with permission from AIP Publishing, Copyright 2004, Evans et al. [56].

dimensionless ratio of the velocity of the surface of the cylinder ($V_\Omega = \Omega R$) to the characteristic velocity ($V = \rho g R^2/\mu$), respectively.

To simplify their numerical scheme, Evans et al. [56] neglected three of the terms which appear at first order in ε in equation (1.4.6), namely the second and fourth terms on the first line and the second term on the second line. The results of Evans et al. [56] are expressed in terms non-dimensional, but otherwise unscaled variables.

The key result of Evans et al. [56] is a parametric study on the rotation speed W, which is increased monotonically from $W = 0$. In the notation of Evans et al. [56], the (dimensionless) minimum rotation speed needed to support a given load in the absence of surface tension is denoted by W_c (where $W_c \approx 0.0141$ for the parameter values used by Evans et al. [56]). Figure 1.16 shows their plot of the film thickness at $\theta = 0$ as a function of t for several values of W. In what follows, we discuss the results of their parametric study for a stationary cylinder, a subcritical rotation speed, the critical rotation speed, and a supercritical rotation speed, respectively

When the cylinder is stationary (i.e. when $W = 0$), a bulge is formed on the bottom of the cylinder due to gravity and is supported by surface tension. As the free surface evolves, the film thickness at the top of the cylinder decreases, but the film does not reach zero thickness in a finite time.

When $0 < W < W_c$, corresponding to a load greater than M_c, a bulge is formed on the underside of the cylinder due to gravity, and is held in a steady state due to the effects of surface tension (see the curves for $0.002 \leq W \leq 0.012$ in Figure 1.16, which asymptote to a constant value). Figure 1.17(a) shows their plot of the maximum film thickness and minimum film thickness for the steady state on the underside of the cylinder plotted as a function of W (for $0 < W < W_c$), and Figure 1.17(b) shows their plot of the location of the maximum film thickness and the location of the minimum film thickness for the steady state on the underside of the cylinder plotted as a function of W (for $0 < W < W_c$). As W increases towards W_c in Figure 1.17(a), the maximum film thickness decreases while the minimum film thickness increases. This is a result of more fluid being carried around the rotating cylinder, and less fluid accumulating in the bulge. As W increases towards W_c in Figure 1.17(b), the location of the maximum film thickness moves further up the cylinder, i.e. towards $\theta = 0$, and, in particular, the film thickness at $\theta = 0$ increases. As W increases towards $W \approx 0.01$ in Figure 1.17(b), the location of the minimum film thickness also moves further up the cylinder until there is a jump in the location of the minimum film thickness at $W \approx 0.01$. As W increases from $W \approx 0.01$ towards W_c in Figure 1.17(b), the location of the minimum film thickness is now $\theta = \pi$. The jump in Figure 1.17(b) is due to the minimum film thickness changing from being located at a "capillary ripple" to being located at $\theta = \pi$. Capillary ripples have been described in the pioneering work of Wilson and Jones [146] for flow down a vertical wall into a pool of fluid. Since then, capillary ripples have also been studied in many other situations, such as falling films down inclined planes [147], drops on inclined planes [148], and fluid draining on the exterior of a stationary circular cylinder [149]. Figure 1.18 shows a plot of the free surface for the steady state on the underside of the cylinder from the numerical solution of equation (1.4.6), where the dashed boxes highlight the location of the capillary ripples, and the crosses denote the location for the minimum film thickness. Figure 1.18(a) shows a plot of the free surface for $W = 0.008$ (i.e. to the left of the jump seen in Figure 1.17(b)), in which the capillary ripple at $\theta \approx 3\pi/2$ is the location

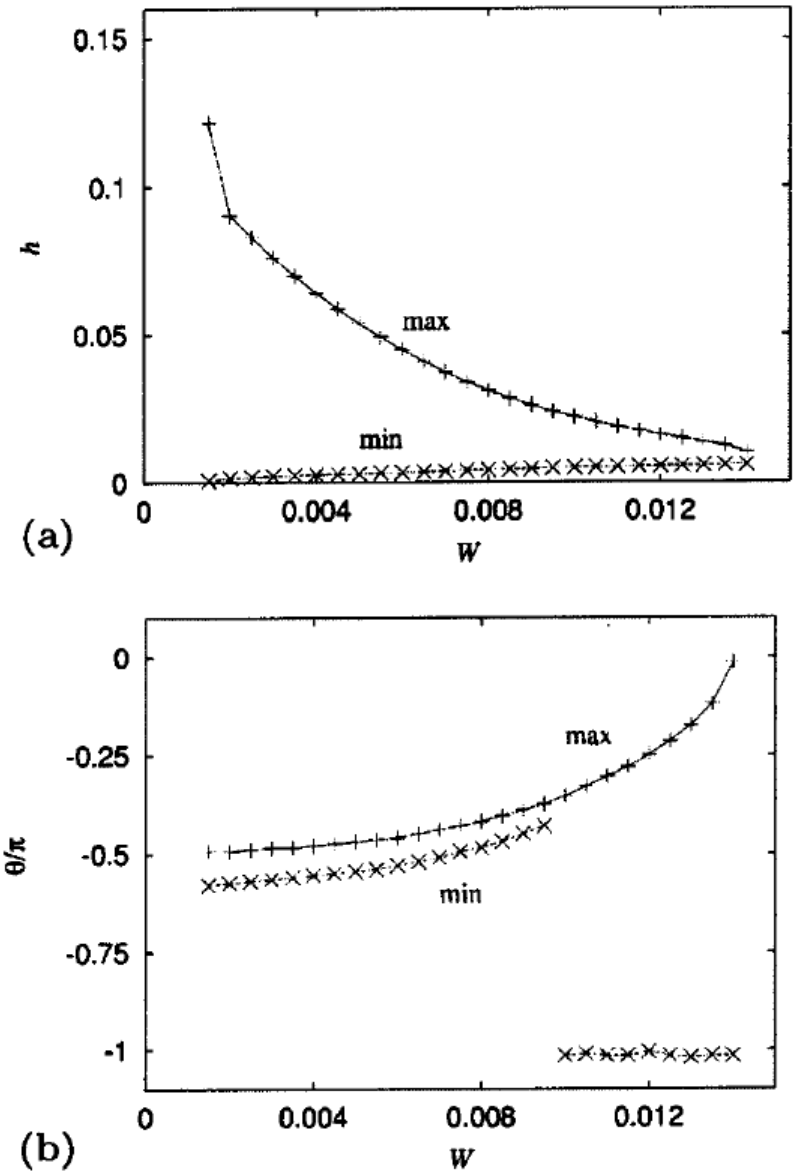

Figure 1.17: Plots of (a) the maximum film thickness and minimum film thickness for the steady state on the underside of the cylinder plotted as a function of W (for $0 < W < W_c$) and (b) the location of the maximum film thickness and the location of the minimum film thickness for the steady state on the underside of the cylinder plotted as a function of W (for $0 < W < W_c$). The maximum and minimum values are marked by "+" and "×", respectively. Reproduced with permission from AIP Publishing, Copyright 2004, Evans et al. [56].

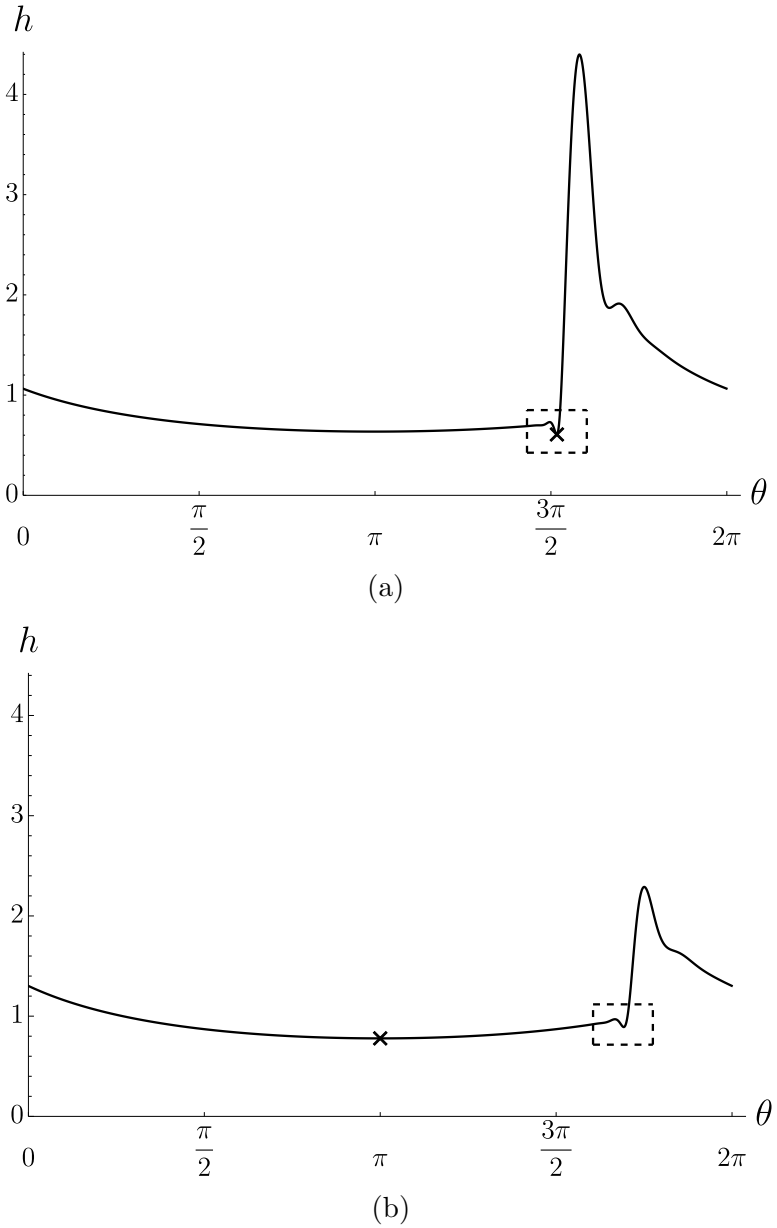

Figure 1.18: Plot of the free surface for the steady state on the underside of the cylinder from the numerical solution of equation (1.4.6) with $M = 0.007$ (in the notation of Evans et al. [56]), $Bo = 100$, $\varepsilon = 0.007$ and $t = 4900$ (i.e. the same parameter values used by Evans et al. [56] in Figure 1.16) for (a) $W = 0.008$, and (b) $W = 0.012$. Note that Evans et al. [56] used unscaled variables, and so the final time in Figure 1.16 is equivalent to the time used in the present figure when scaled with ε^2. The dashed boxes highlight the location of the capillary ripples, and the crosses denote the location of the minimum film thickness.

for the minimum film thickness, and Figure 1.18(b) shows a plot of the free surface for $W = 0.012$ (i.e. to the right of the jump seen in Figure 1.17(b)), in which $\theta = \pi$ is now the location of the minimum film thickness.

For $W = W_c$, corresponding to a load equal to M_c, there is still a bulge formed by gravity which reaches a steady state in which the film is thickest at $\theta = 0$ and thinnest at $\theta = \pi$, with a near-top-to-bottom symmetry. In practice, the subtle interplay of the effects of rotation, gravity, and surface tension will prevent the top-to-bottom symmetry of this steady state.

For $W > W_c$, corresponding to a load less than M_c, there is still a bulge formed by gravity, but it is now carried around the cylinder in the direction of rotation, but at a speed slower than the rotation of the cylinder. As the bulge is carried around the cylinder, its amplitude decays due to surface tension (see the curve for $W = 0.016$ in Figure 1.16, which has a decaying saw-tooth-like pattern) and the bulge approaches a steady state, with the maximum and minimum film thickness at $\theta = 0$ and $\theta = \pi$, respectively. However, in practice, due to the subtle interplay of the effects of rotation, gravity, and surface tension, the timescale required to reach this steady state may be large, as shown analytically by Hinch and Kelmanson [140]. Evans et al. [56] numerically investigated the long-time behaviour of the solution when $W = 0.016 > W_c$, by comparing the free surface at two (unscaled) times, namely $t = 10^6$ (after approximately 17.8 cylinder revolutions), and $t = 5 \times 10^6$ (after approximately 89.1 cylinder revolutions), to Moffatt's [57] steady full-film solution (1.4.3). Evans et al. [56] found that their solution at $t = 10^6$ is close to Moffatt's [57] steady full-film solution (1.4.3), however at $t = 5 \times 10^6$ their solution (which has near-top-to-bottom symmetry) is nearly identical to Moffatt's [57] steady full-film solution (1.4.3).

Evans et al. [56] also investigated the behaviour of the free surface in the limit of zero gravity (which is equivalent to the limit of rapid rotation and strong surface tension, as we shall describe in Chapter 3). Equation (1.4.6) has been nondimensionalised using the characteristic velocity $V = \rho g R^2/\mu$, which is no longer an appropriate choice for the characteristic velocity in the limit of zero gravity. Therefore, to nondimensionalise equation (1.4.6) in the limit of zero gravity, an appropriate choice of characteristic velocity is $V_{zg} = \gamma/\mu$. Recall that Evans et al. [56] neglected three of the first-order terms in equation (1.4.6), and so, in the limit

of zero gravity, the simplified version of equation (1.4.6) is

$$\frac{\partial h}{\partial t} + Ca_\Omega \frac{\partial h}{\partial \theta} + \varepsilon \frac{\partial}{\partial \theta}\left[\frac{h^3}{3}\left\{\frac{\partial}{\partial \theta}\left(h + \frac{\partial^2 h}{\partial \theta^2}\right) + We\frac{\partial h}{\partial \theta}\right\}\right] = 0, \tag{1.4.7}$$

where $Ca_\Omega = \mu V_{\mathrm{zg}}/\gamma = \mu\Omega R/\gamma$ and $We = W^2 Bo = \rho\Omega^2 R^3/\gamma$ denote a capillary number based on the velocity of the surface of the cylinder, and a Weber number, respectively. When We is large, the effects of centrifugation dominate the effects of surface tension, and when We is small, the effects of surface tension dominate the effects of centrifugation. In the limit of zero gravity, a film of uniform thickness is a steady solution of (1.4.7). Evans et al. [56] performed a linear stability analysis on this steady solution by decomposing h as

$$h(\theta, t) = \bar{h} + \xi\widetilde{h}\mathrm{e}^{in\theta+\sigma t}, \tag{1.4.8}$$

where $\xi \ll 1$ with $\bar{h}$, $\xi\widetilde{h}$, n, and σ denoting the uniform base-state solution, the (initial) amplitude of the disturbance, the (integer) azimuthal wavenumber, and the (complex) linear growth rate, respectively, which yields

$$\sigma = -Ca_\Omega ni + \varepsilon\bar{h}^3\frac{n^2}{3}\left(1 - n^2 + We\right). \tag{1.4.9}$$

For the $n = 1$ mode, the real parts of the linear growth rate (1.4.9) are neutrally stable for $We = 0$ and are unstable for $We > 0$. As We increases from $We = 0$, the real parts of the linear growth rate (1.4.9) are unstable for $n = 1$ and are also unstable for a finite range of n extending from $n = 1$. For $We > 0$ the perturbations grow due to the effects of centrifugation and form distinct bulges which are separated by thin films of fluid. Figure 1.19 shows their plot of the free surface in the limit of zero gravity at a time after these distinct bulges have formed when $We = 50$ in Figure 1.19(a) and when $We = 100$ in Figure 1.19(b). The number of distinct bulges which form is accurately predicted by the fastest-growing wavenumber. Specifically, a good approximation for the number of distinct bulges which can form is given by

$$N \approx \left[\sqrt{\frac{1 + We}{2}}\right], \tag{1.4.10}$$

where the square brackets give the greatest integer less than the argument [125].

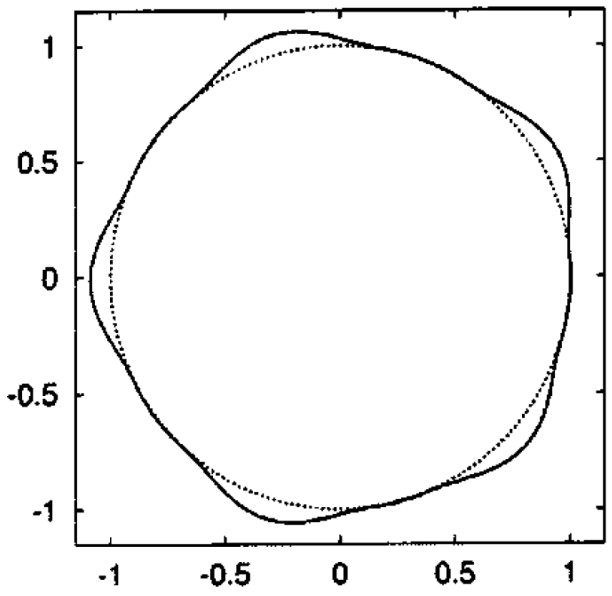

(a)

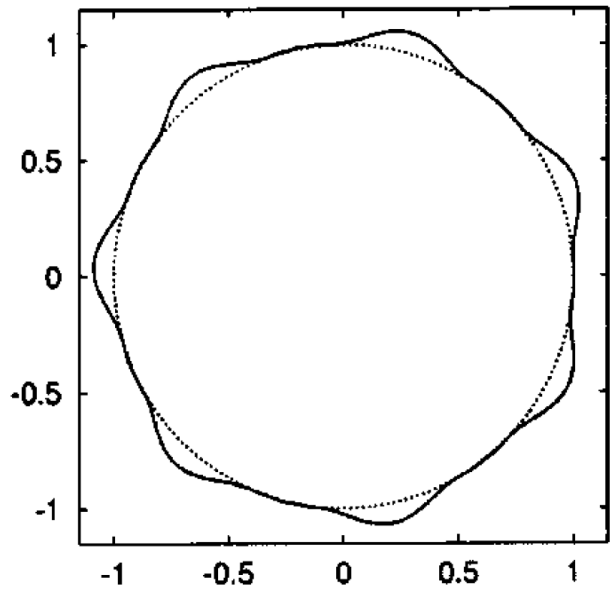

(b)

Figure 1.19: Plot of the free surface in the limit of zero gravity (where the dotted lines denote the circular cylinder) after the distinct bulges have formed for (a) $We = 50$ at $t = 10000$, and (b) $We = 100$ at $t = 2000$. Reproduced with permission from AIP Publishing, Copyright 2004, Evans et al. [56].

For $We = 50$ and $We = 100$ we have $N \approx [5.0498] = 5$ and $N \approx [7.1063] = 7$, respectively, which is indeed the number of distinct bulges which are shown in Figure 1.19(a) and Figure 1.19(b), respectively.

Evans et al. [150] later extended their investigations to the three-dimensional case. Three-dimensional effects have also been the subject of various theoretical and experimental investigations [57; 127; 150; 151].

1.4.1.4 Thick-film flow on rotating circular cylinders

Thus far, we have primarily restricted our attention to situations in which the film coating the cylinder is thin. The problem of a thin film of fluid coating a circular cylinder has been extended to include other physical effects, such as the effect of an irrotational airflow [152; 153], dewetting effects [154; 155], non-isothermal effects [156; 157], the effects of a magnetic field [115], surfactant effects [114; 158], and the effect of drying on a film laden with colloidal particles [159], however of particular interest to this thesis is the study of a thick-film flow on a rotating circular cylinder.

Wray et al. [55] and Wray and Cimpeanu [60] have developed reduced-order models, which are appropriate for a film thickness of order unity (see Section 1.3.2.2), by applying a long-wave approximation, and then applying the WRIBL method to derive a second-order model. Specifically, Wray and Cimpeanu [60] derived a simplified second-order model, as discussed in Section 1.2.1.4, whereas the second-order model derived by Wray et al. [55] is not a simplified second-order model due to the absence of inertia. The reduced-order model of Wray et al. [55] includes the effects of gravity, viscosity, rotation, surface tension, and viscous dispersion, while the reduced-order model of Wray and Cimpeanu [60] also includes the effect of inertia.

The key result of Wray et al. [55] for modelling the flow of a thick film on a curved substrate, is that the results of the thick-film models (i.e. reduced-order models developed using a long-wave approximation) give better agreement with the results of DNS than the results of thin-film models (i.e. reduced-order models developed using a thin-film approximation). A demonstration of this is given in Figure 1.20. The left image in Figure 1.20 shows their plot of a thick film hanging from a rotating circular cylinder when the free surface has reached a steady state

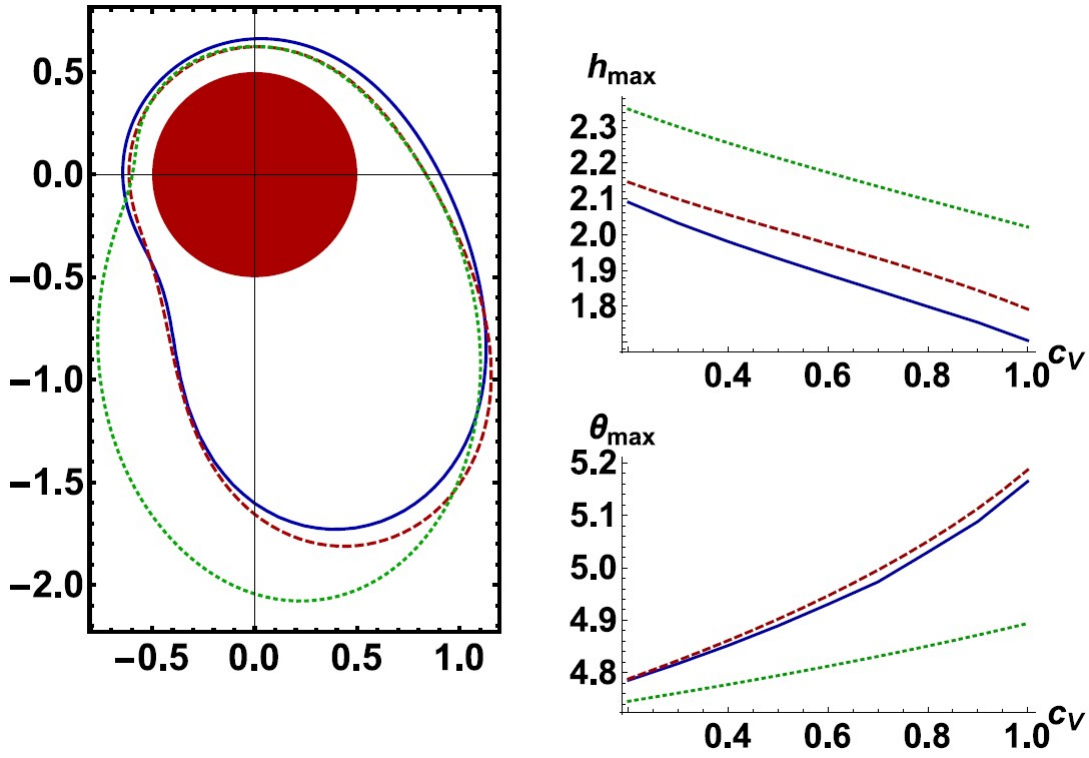

Figure 1.20: Plot of a thick film hanging from a rotating circular cylinder when the free surface has reached a steady state after an initial transient phase (left), a plot of the maximum film thickness as a function of the rotation speed c_V (top right), and a plot of the location of the maximum film thickness as a function of the rotation speed c_V (bottom right) for the second-order thick-film WRIBL model (dashed red), the thin-film model (dotted green), and DNS of the Stokes equations (solid blue). Reproduced with permission from the Society for Industrial and Applied Mathematics, Copyright 2017, Wray et al. [55].

after an initial transient phase, for the second-order thick-film WRIBL model (dashed red), the thin-film model (dotted green), and DNS of the Stokes equations (solid blue). The second-order thick-film WRIBL model and the DNS of the Stokes equations agree well, whereas the thin-film model fails to accurately capture the free surface. The top right and bottom right images in Figure 1.20 show their plots of the maximum film thickness as a function of the rotation speed c_V (in the notation of Wray et al. [55]) and the location of the maximum film thickness as a function of the rotation speed, respectively. The agreement between the second-order thick-film WRIBL model and the DNS of the Stokes equations is again good, with a maximum error of 5% for maximum film thickness, and a maximum error of 0.025 radians for the location of the maximum film thickness. Again, the thin-film model gives weaker agreement with the DNS of the Stokes equations, with a maximum error of 18% for maximum film thickness, and a maximum error of 0.22 radians for the location of the maximum film thickness.

The work of Wray and Cimpeanu [60] extended the work of Wray et al. [55] by including the effect of inertia and investigating regimes previously inaccessible to thin-film models, which reveals a rich variety of behaviours. Figure 1.21 shows their results of a parametric study of the behaviour of the free surface in c_R–c_V parameter space (where c_R denotes the film radius in the notation of Wray and Cimpeanu [60]) where solid lines correspond to the delineation between flow regimes as predicted by the simplified second-order thick-film WRIBL model, and symbols correspond to DNS of the Navier–Stokes equations, for two values of the Weber number $We = \rho g R^2/\gamma$. Figures 1.21(a) and Figure 1.21(b) show regimes in which the effect of surface tension is strong relative to the effect of inertia and where the effect of surface tension is weak relative to the effect of inertia, respectively. Figure 1.21(a) shows each of the three possible behaviours of the free surface, namely a steady state, a periodic state, and a multivalued free surface, however, Figure 1.21(b) only shows a periodic state and a multivalued free surface as, in this case, the surface tension is too weak to allow the free surface to exhibit steady states. For sufficiently large film thicknesses and/or rotation speeds, the free surface always becomes multivalued. Wray and Cimpeanu [60] used both their simplified second-order thick-film WRIBL model and DNS to explore the regimes which allow steady states and periodic states. However, only DNS can capture the dynamics of the regime in which a multivalued free surface occurs.

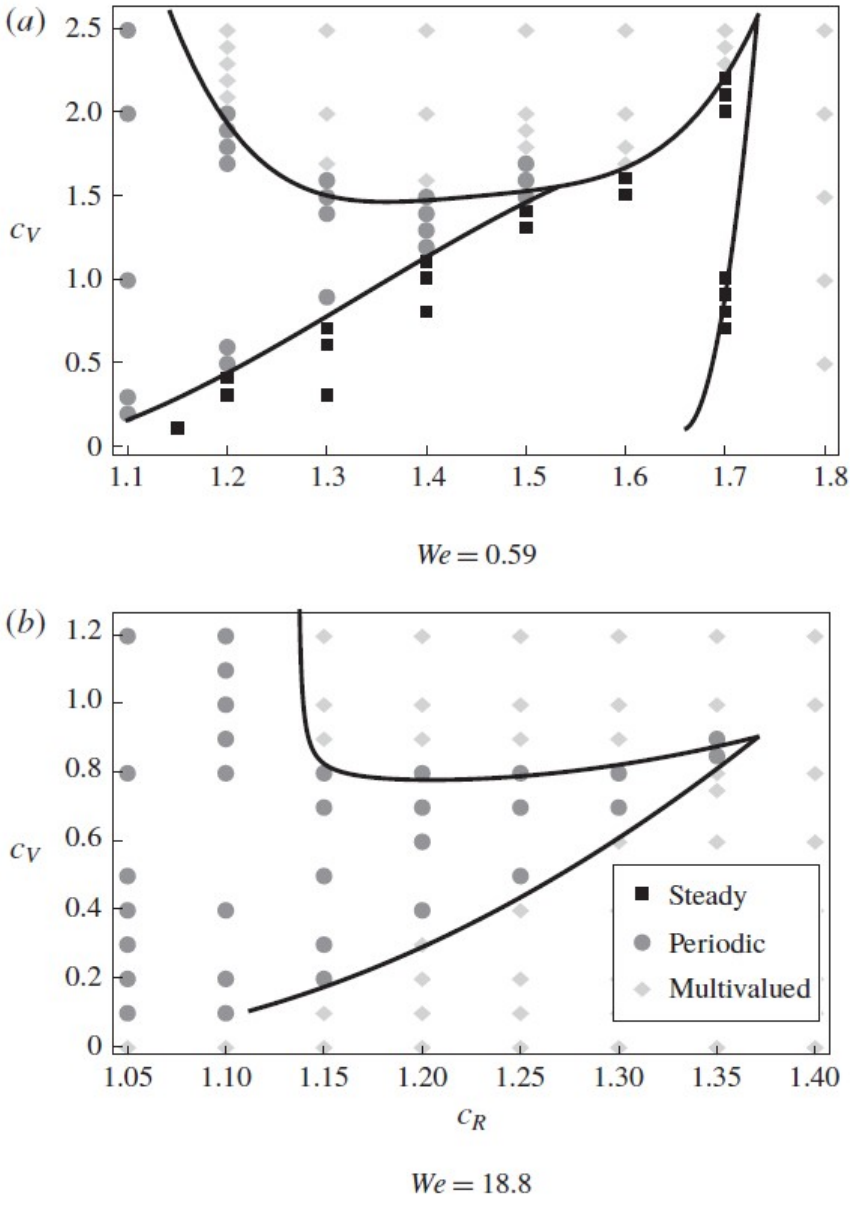

Figure 1.21: Plot of the results of a parametric study of the behaviour of the free surface in c_R–c_V parameter space, where c_R and c_V denote the film radius and cylinder rotation speed, respectively for (a) $We = 0.59$ (surface tension is strong relative to inertia), and (b) $We = 18.8$ (surface tension is weak relative to inertia), where We is the Weber number. Solid lines correspond to the delineation between flow regimes as predicted by the simplified second-order thick-film WRIBL model, and symbols correspond to DNS of the Navier–Stokes equations with squares, circles, and diamonds representing flow regimes where the behaviour of the free surface is a steady state, a periodic state, and a multivalued free surface, respectively. Reproduced with permission, Copyright 2020, Wray and Cimpeanu [60].

1.4.2 Flow on stationary circular cylinders

Thus far, we have restricted our attention to situations where the cylinder is rotating, however the problem of fluid coating a stationary cylinder has also been the subject of previous works.

Reisfeld and Bankoff [157] investigated the unsteady two-dimensional flow of a thin film of fluid coating the exterior of a uniformly heated or cooled stationary horizontal circular cylinder. Their reduced-order model includes the effects of gravity, viscosity, surface tension, thermocapillarity, and intermolecular forces. We will only discuss their results for cases in which the film is isothermal and intermolecular forces are negligible. Reisfeld and Bankoff [157] found that a steady state is only possible in the limit of strong surface tension (i.e. the limit of zero gravity). When the effects of gravity are reintroduced to the limit of strong surface tension, the fluid begins to drain and a bulge is formed at the bottom of the cylinder. When the effect of surface tension is negligible, the fluid drains and experiences blowup in finite time.

Weidner et al. [113] investigated the unsteady three-dimensional flow of a thin film of fluid coating the exterior of a stationary horizontal circular cylinder. Weidner et al. [113] determined the maximum volume of fluid which can be supported as a bulge on three-dimensional stationary horizontal cylinders of various radii by developing a reduced-order model, which includes the effects of gravity, viscosity, and surface tension. Weidner et al. [113] found that for large cylinder radii the bulge is localised at the bottom of the cylinder, whereas for sufficiently small cylinder radii the bulge can wrap around the entire cylinder, forming a part pendant, part sessile bulge. Weidner et al. [113] noted that it was necessary to use the full form of the interfacial curvature in order to predict the shape of the bulges which form at the bottom of the cylinder, when the amplitude of the bulge is sufficiently large.

Cachile et al. [117] investigated the unsteady flow of a thin film of fluid coating the exterior of a three-dimensional stationary horizontal cylinder, both theoretically (via a reduced-order model which includes the effects of gravity, viscosity, and surface tension) and experimentally. Their theoretical predictions agreed with their experimental results, and Cachile et al. [117] found that the film thickness at the top and bottom of the cylinder decreased monotonically and increased mono-

tonically, respectively. Cachile et al. [117] also determined the fastest-growing wavelength of the Rayleigh–Taylor instability, which destabilises the coating at the bottom of the cylinder in the axial direction.

McKinlay et al. [149] recently investigated the unsteady two-dimensional flow of a thin film of fluid on the exterior of a stationary horizontal circular cylinder. Specifically, McKinlay et al. [149] investigated the late-time draining of this flow by developing a reduced-order model which includes the effects of gravity, viscosity, and surface tension, and by using a combination of analytical and numerical techniques. At late times, three regions of qualitatively different behaviour emerge, namely the "draining region" on the upper part of the cylinder, the "pendant-drop region" on the lower part of the cylinder, and the "inner region" on the narrow intermediate region between the draining and pendant-drop regions. In the draining region, the effect of gravity dominates the effect of surface tension, resulting in a draining flow which causes the film in this region to thin. In particular, McKinlay et al. [149] showed that the film thickness in the draining region decreases as $t^{-1/2}$, where t denotes (dimensionless) time. In the pendant-drop region, the effects of gravity and surface tension balance, resulting in the formation of a quasistatic pendant droplet. The inner region has a capillary ripple structure and consists of an infinite sequence of alternating "dimples" (i.e. narrow regions in which the film thickness has a local minimum) and "ridges" (i.e. narrow regions in which the film thickness has a local maximum).

1.5 Flow on non-circular cylinders

Since the pioneering works of Moffatt [57] and Pukhnachev [58], the problem of coating a circular cylinder has been extended in numerous ways and still remains an active area of research. However, in many applications (such as the production of microelectronic devices [41], medical implants [160], orthopaedic implants [161], dental implants [162], and the coating of chocolate bars [163]), the substrate may not be perfectly circular. While the coating of circular cylinders has been well studied in recent years, there has been surprisingly little work on non-circular cylinders, even though a relatively mild departure from circularity can cause a radical difference in the behaviour compared to the perfectly circular case [125].

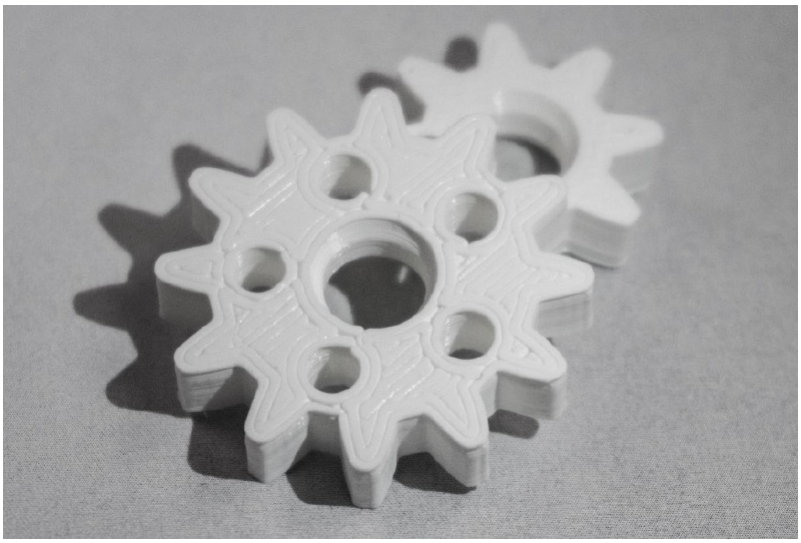

Figure 1.22: Photograph of 3D printed gears, which serves as an example of a topographically patterned cylinder. Reproduced with permission from the American Physical Society, Copyright 2017, Li et al. [165].

1.5.1 Flow on topographically patterned cylinders

Sahu and Kumar [164] were the first to study the problem of a thin film of fluid coating a uniformly rotating horizontal topographically patterned cylinder. Figure 1.22 shows a photograph of a 3D printed gear, which is an example of a topographically patterned cylinder. Sahu and Kumar [164] developed a reduced-order model which includes the effects of gravity, viscosity, rotation, surface tension, centrifugation, topographical pattern amplitude, and topographical pattern frequency, but assumed that the amplitude of the topographical pattern is small. When the effect of gravity is significant, the free surface never reaches a steady state. In the limit of zero gravity, the free surface does reach a steady state, the behaviour of which depends on the rotation speed. For low rotation speeds, the fluid accumulates in the troughs of the pattern, while for high rotation speeds, the fluid accumulates at the crests of the pattern.

Li et al. [165] later considered this same problem using DNS. Li et al. [165] also derived a corrected version of the reduced-order model of Sahu and Kumar [164] who erroneously multiplied two terms at first-order in the thin-film approximation by an extra factor of 2, namely one of the terms representing the effect of gravity and the term representing the effect of centrifugation. However, the qualitative conclusions of Sahu and Kumar [164] remain valid for this problem as the results

of the corrected reduced-order model of Li et al. [165] qualitatively agree with the results of the reduced-order model of Sahu and Kumar [164]. Li et al. [165] found that, when the interfacial curvature was sufficiently small, the results of DNS agreed with the results of their reduced-order model. However, as the amplitude of the topographical patterns increases, the agreement between the reduced-order model and DNS worsens as the interfacial curvature becomes larger.

Parrish et al. [166] considered three-dimensional cylinders with azimuthal topographical patterns (see Figure 1.22), axial topographical patterns, and screw-shaped cylinders (a combination of both azimuthal and axial topographical patterns), both theoretically and experimentally. Parrish et al. [166] developed a reduced-order model which includes the effects of gravity, viscosity, rotation, surface tension, centrifugation, topographical pattern amplitude, and topographical pattern frequency, but assumed that the amplitude of the topographical pattern is small. In the limit of zero gravity, for cylinders which are topographically patterned in the axial direction, for low rotation speeds, the fluid accumulates in the pattern troughs and is stable to disturbances in the azimuthal direction. In particular, the free surface will not show any noticeable variation in film thickness in the azimuthal direction while the fluid remains in the pattern troughs. In the limit of zero gravity, for cylinders which are topographically patterned in the axial direction, for high rotation speeds, the fluid accumulates at the crests of the pattern and is unstable to disturbances in the azimuthal direction. In particular, the fluid forms a stream of bulges in the azimuthal direction, which are separated by thin-films of fluid, and a good approximation of the number of bulges which can form is given by (1.4.10). In the limit of zero gravity, for cylinders which are topographically patterned in the azimuthal direction, for low rotation speeds, the fluid accumulates in the pattern troughs and is stable to disturbances in the axial direction. In particular, the free surface does not show any noticeable variation in film thickness in the axial direction while the fluid remains in the pattern troughs. In the limit of zero gravity, for cylinders which are topographically patterned in the azimuthal direction, for high rotation speeds, the fluid accumulates at the crests of the pattern and is unstable to disturbances in the axial direction. In particular, the fluid forms a stream of bulges in the axial direction, which are separated by thin-films of fluid. In the limit of zero gravity, for cylinders which are screw-shaped, for low rotation speed, the fluid accumulates in the troughs of the

pattern and is stable to both axial and azimuthal disturbances, whereas, for high rotation speeds, the fluid accumulates at the crests of the pattern and is unstable to both axial and azimuthal disturbances. The theoretical results of Parrish et al. [166] agreed well with their experimental results.

Parrish et al. [167] later developed a thin-film reduced-order model which includes the effects of gravity, viscosity, rotation, surface tension, centrifugation, pattern amplitude, and pattern frequency, but relaxes the assumption made by previous works that the amplitude of the topographical pattern is small [164–166]. This reduced-order model was applied to both topographically patterned and elliptical cylinders (we will discuss the results of Parrish et al. [167] for elliptical cylinders in Section 1.5.2), and the results of DNS were compared with the results of the reduced-order model. Parrish et al. [167] found that, for topographically patterned cylinders with pattern amplitude of the order of the radius of the cylinder, the results of DNS give good agreement with their reduced-order model, whereas a simplified reduced-order model which assumes that the pattern amplitude is small [165] gives weaker agreement.

1.5.2 Flow on elliptical cylinders

The first to study the problem of a layer of fluid coating a rotating elliptical cylinder, which is one of the two main subjects of this thesis, was Hunt [168]. The length of the semi-major and semi-minor axes of the elliptical cylinder are denoted by a and b, respectively, where $b \leq a$. The works discussed in this section use the length of the semi-major axis a as the characteristic length scale to nondimensionalise the governing equations, thus a is taken to be unity and b is a free parameter. The eccentricity of the cylinder decreases as b increases (i.e. the cylinder becomes less elliptical), with the special cases of a circular cylinder and a flat plate recovered when $b = 1$ and $b \to 0^+$, respectively. The work of Hunt [168] incorporated the effects of viscosity, gravity, rotation, and cylinder eccentricity, but neglected surface tension and inertial effects (including centrifugation, the Coriolis force, and convective inertia). Hunt [168] used DNS to determine the maximum supportable load in the absence of surface tension for an elliptical cylinder, again denoted by M_{c}.

Figure 1.23 shows their plot of the maximum supportable load in the absence of

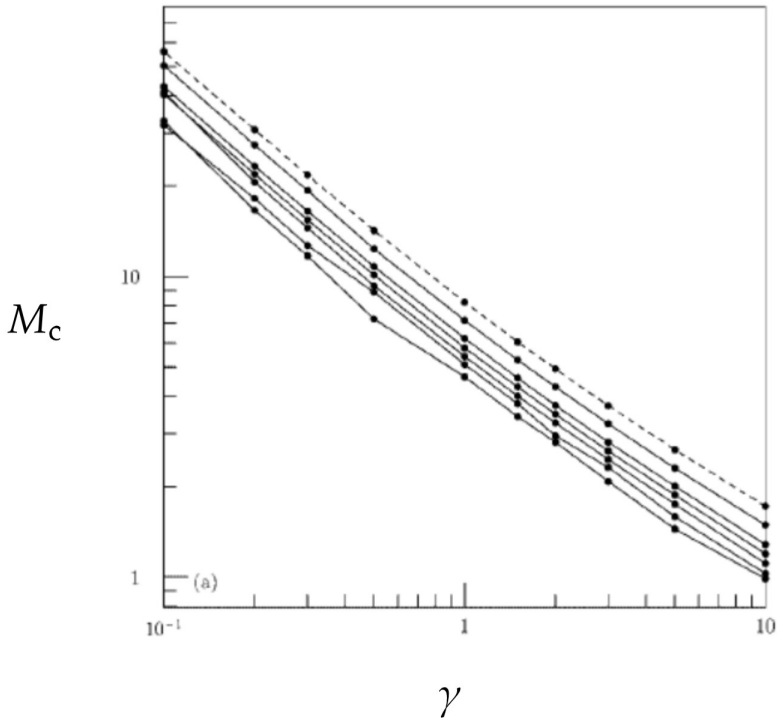

Figure 1.23: The maximum supportable load in the absence of surface tension M_c plotted as a function of the Stokes number γ for various eccentricities of elliptical cylinder on a log-log scale. The cylinder eccentricity decreases from bottom to top ($b = 0.2, 0.3, 0.4, 0.5, 0.6, 0.8, 1$), where the top curve (dotted) corresponds to the maximum supportable load in the absence of surface tension for a circular cylinder (i.e. $b = 1$). Adapted with permission from John Wiley and Sons, Copyright 2008, Hunt [168].

surface tension M_c as a function of the Stokes number, denoted by $\gamma = \rho g a/(\mu\Omega)$ in the notation of Hunt [168], on a log-log scale for various eccentricities of elliptical cylinder (where the top dotted curve corresponds to a circular cylinder). As γ increases, the effect of gravity becomes more significant, which corresponds to stronger gravity-driven drainage, resulting in a decreased M_c. Figure 1.23 also shows that as the cylinder becomes more eccentric M_c decreases, therefore a circular cylinder can support a greater load of fluid than an elliptical cylinder (in the absence of surface tension).

Figure 1.24 shows their plot of the free surface for the first half-rotation of the cylinder when the initial load is greater than M_c for an elliptical cylinder with $b = 0.5$. The leftmost panel shows the initial free surface, and the subsequent

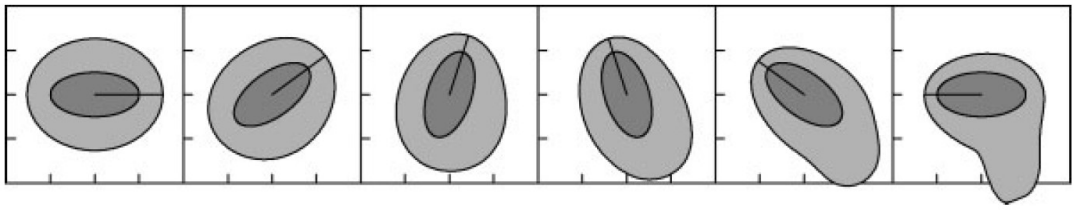

Figure 1.24: Plot of the free surface for the first half-rotation of the cylinder when the initial load is greater than M_c for $b = 0.5$. Reproduced with permission from John Wiley and Sons, Copyright 2008, Hunt [168].

panels show the free surface over the course of the first half-rotation of the cylinder. As the cylinder rotates, the fluid flows towards the underside of the cylinder and then falls off the cylinder after about one half-rotation. This is a consequence of surface tension being absent in Hunt's [168] work.

Li et al. [125] expanded on the work of Hunt [168] by performing DNS including the effects of surface tension and centrifugation (while neglecting the effects of the Coriolis force and convective inertia). By including the effects of surface tension, Li et al. [125] were able to obtain solutions for which the initial load was greater than M_c (analogous to the earlier discussion in Section 1.4.1.3 of the results of Evans et al. [56] for a circular cylinder). In this case, a bulge is formed on the underside of the cylinder, and is held in a periodic state which oscillates with each half-rotation of the cylinder. Li et al. [125] term a free surface characterised by this behaviour a "coating with a liquid bulge". When the initial load is less than M_c, a bulge is formed and is carried around the cylinder. As the bulge is carried around the cylinder, its amplitude decays due to surface tension. Li et al. [125] term a free surface characterised by this behaviour a "smooth coating". This regime was previously studied by Hunt [168] in the absence of surface tension. The transition between a free surface which is characterised by a "smooth coating", and a free surface which is characterised by a "coating with a liquid bulge" is how Li et al. [125] determine M_c (i.e. when a bulge is no longer formed on the underside of the cylinder). Figure 1.25 shows their plot of M_c plotted as a function of the Stokes number γ on a log-log scale for an elliptical cylinder with $b = 0.5$ (the solid line and symbols correspond to the results of Hunt [168] and Li et al. [125], respectively) and a circular cylinder ($b = 1$) (dotted line and dashed line correspond to the results of Moffatt [57] and Kelmanson [138], respectively). In particular, Figure 1.25 shows that the results of Li et al. [125] and Hunt [168] agree well for the

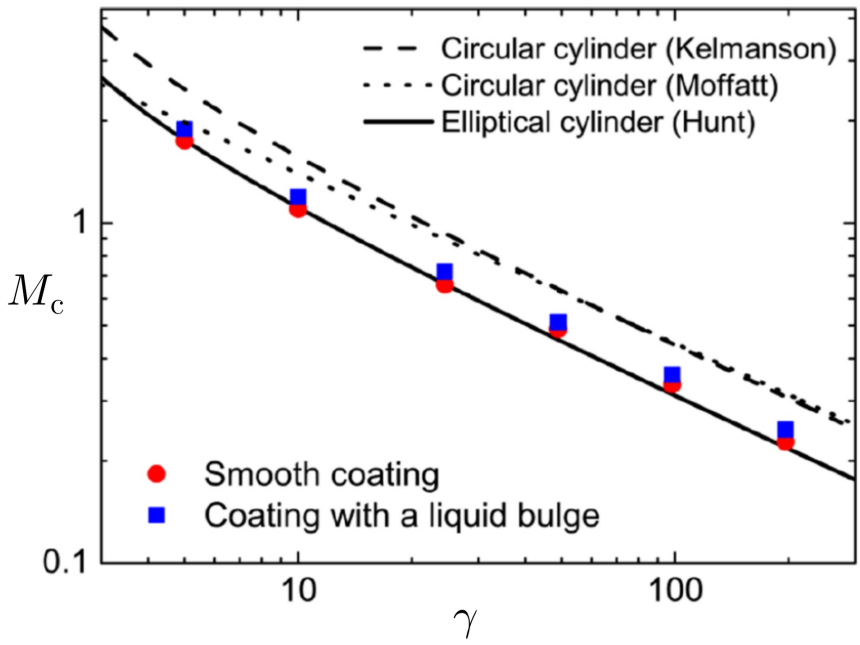

Figure 1.25: The maximum supportable load in the absence of surface tension M_c plotted as a function of the Stokes number γ on a log-log scale. The solid line and symbols correspond to the results of Hunt [168] and Li et al. [125], respectively, for M_c for an elliptical cylinder with $b = 0.5$, and the dotted line and dashed line correspond to the results of Moffatt [57] and Kelmanson [138], respectively, for M_c for a circular cylinder ($b = 1$). Adapted with permission from the American Physical Society, Copyright 2017, Li et al. [125].

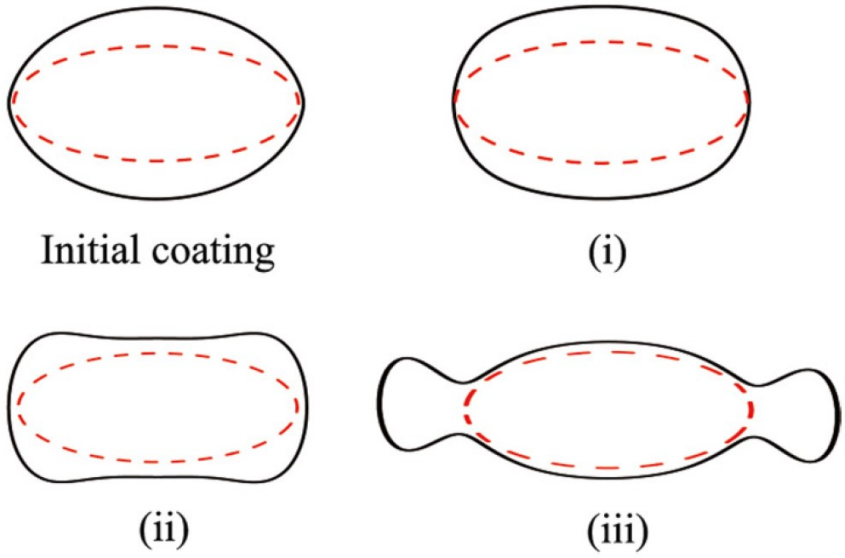

Figure 1.26: Plot of the free surface in the limit of zero gravity for a cylinder with $b = 0.2$. Figures (i) to (iii) show snapshots of the free surface at $t = 750$, 1750, and 2750, respectively. Reproduced with permission from the American Physical Society, Copyright 2017, Li et al. [125].

parameter regime chosen by Li et al. [125].

Li et al. [125] also examined the behaviour of the free surface in the limit of zero gravity. Figure 1.26 shows their plot of the free surface in the limit of zero gravity for an elliptical cylinder with $b = 0.2$. In the parameter regime chosen by Li et al. [125], the effects of centrifugation are stronger than the effects of surface tension, and so the fluid flows towards the tips of the cylinder as time increases from Figure 1.26(i) to Figure 1.26(iii). Li et al. [125] also examined the case of a nearly-circular ellipse in the limit of zero gravity. Figure 1.27 shows their plot of the free surface in the limit of zero gravity with $We = W^2Bo = 160$ (in the notation of Evans et al. [56]). The cylinder in the leftmost part of Figure 1.27 is circular with $b = 1$, and equation (1.4.10) predicts that there will be eight distinct bulges, which is exactly how many are present. The cylinder in the middle part of Figure 1.27 is nearly circular, with $b = 0.99$. The effect of centrifugation causes fluid to collect towards the tips of the ellipse, and so, while there are still eight bulges, they are now unevenly spaced, with two bulges forming on the tips of the ellipse and four bulges forming closer to the tips of the ellipse. Despite the cylinder in the middle part of Figure 1.27 being nearly circular, the behaviour is radically different when

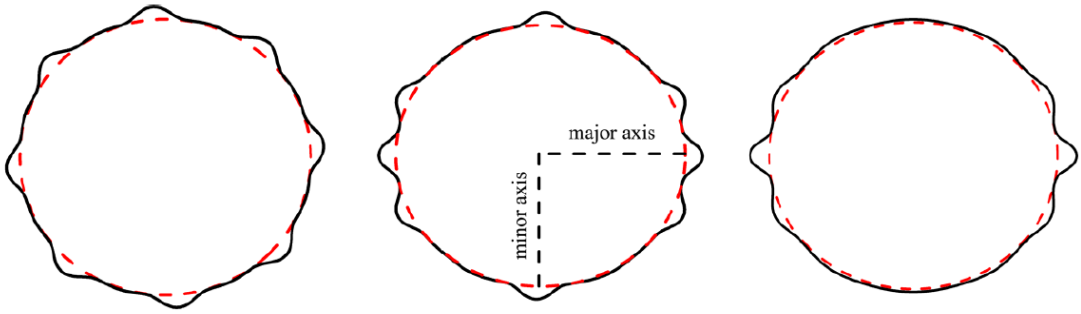

Figure 1.27: Plot of the free surface in the limit of zero gravity for cylinders with (left) $b = 1$ (circular), (middle) $b = 0.99$, and (right) $b = 0.95$, for $We = W^2Bo = 160$ (in the notation of Evans et al. [56]). Reproduced with permission from the American Physical Society, Copyright 2017, Li et al. [125].

compared to the perfectly circular case in the leftmost part of Figure 1.27. The cylinder in the rightmost part of Figure 1.27 has $b = 0.95$, and here only six visible bulges are formed, with the amplitude of the bulges on the tips of the ellipse being larger than that of the bulges formed elsewhere on the ellipse. Thus, Li et al. [125] showed that even a slight eccentricity can significantly change the behaviour of the free surface when compared with the perfectly circular case.

Parrish et al. [167] have also applied their reduced-order model to elliptical cylinders. They compared the results of their reduced-order model against DNS and found that they are in good agreement. Parrish et al. [167] performed a parametric study of the behaviour of the fluid coating for a fixed Stokes number γ as the initial fluid load is varied. This parametric study revealed four characteristic behaviours of the free surface for an elliptical cylinder with $b = 0.5$, as shown in Figure 1.28. In Figure 1.28(a) gravitational effects are dominant, in Figure 1.28(d) surface tension effects are dominant, and in Figure 1.28(b) and Figure 1.28(c) gravitational and surface tension effects are in competition. Figure 1.28(a) shows the characteristic behaviour of the regime previously studied by Li et al. [125] (i.e. an initial load above M_c), and Figure 1.28(b) shows the characteristic behaviour of the regime previously studied by Hunt [168] (in the absence of surface tension and centrifugation) and Li et al. [125] (i.e. an initial load slightly below M_c). In Figure 1.28(c), surface tension drives the fluid away from the tips of the cylinder. The fluid forms an asymmetric coating, where the bulges, which are formed at opposite ends of the cylinder, oscillate with the cylinder rotation. In Figure 1.28(d), surface tension dominates, driving the fluid away from the tips of the cylinder. However,

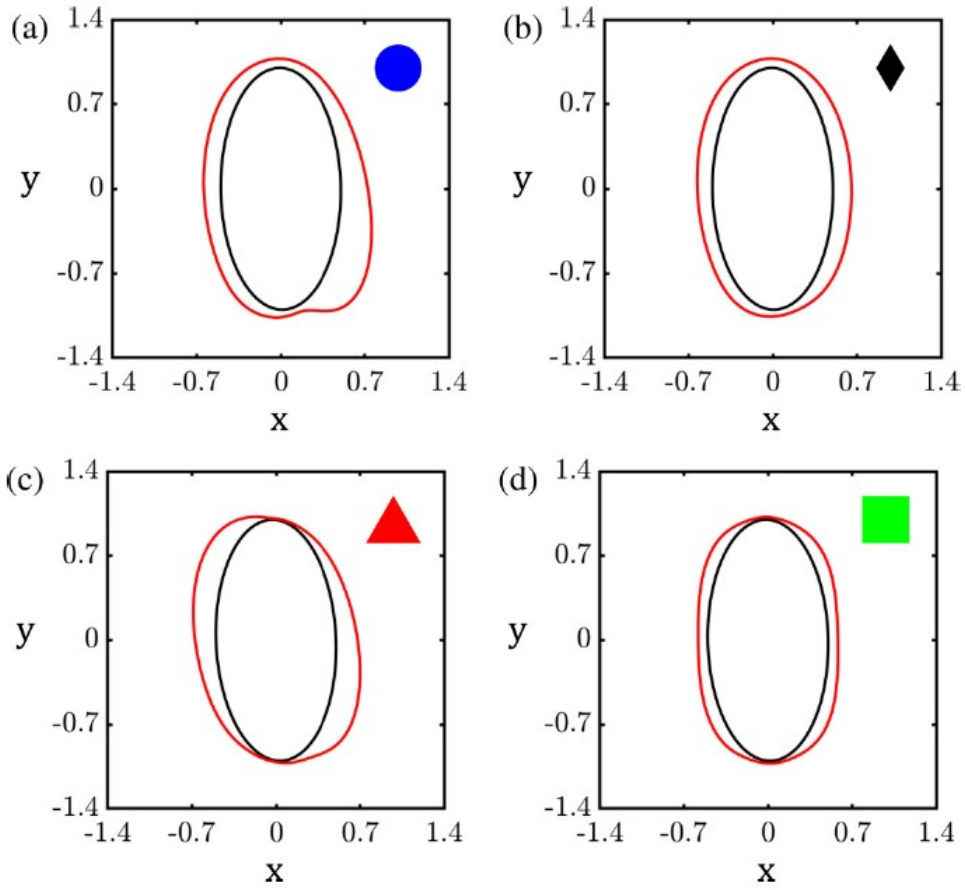

Figure 1.28: Plot of each of the four characteristic behaviours of the free surface from a parametric study of the initial load for $b = 0.5$. The initial load decreases from (a) through (d). The initial load is greater than M_c in (a), and less than M_c in (b) to (d). Reproduced with permission from the American Physical Society, Copyright 2022, Parrish et al. [167].

unlike the regime characterised by Figure 1.28(c), in this regime, the coating is symmetric as the effect of surface tension is strong enough to prevent the bulges from oscillating with the cylinder rotation. The characteristic behaviours shown in Figure 1.28(c) and Figure 1.28(d) were not observed by Li et al. [125], who studied the case of moderate surface tension, or Hunt [168], who neglected surface tension.

The three previous studies of elliptical cylinders have highlighted the radical difference in the behaviour of the free surface compared to the perfectly circular case [125; 167; 168]. Among these previous studies, only the work of Parrish et al. [167] involves a reduced-order model. However, despite this, they do not present any analytical results, which is surprising. Additionally, none of these previous studies consider the special case of a stationary cylinder or the effect of parametrically varying the rotation rate (i.e. extending the work of Evans et al. [56] discussed in Section 1.4.1.3).

1.6 Fibre flow

Fibre flows have been the subject of considerable interest as they are an important component in a variety of industrial and natural processes such as heat and mass transfer (as shown in Figure 1.29(a), which shows multiple dew drops covering the *Geranium robertianum* fruit, and Figure 1.29(b), which shows the break up of a layer of silicone oil coating a conical fibre into a stream of bulges which flow away from the apex of the conical fibre) [169–176], desalination [177], distillation [178], water and oil separation [179], wastewater treatment [180], microfluidics (as shown in Figure 1.30, which shows a droplet interacting with the intersection of two nylon fibres, where the intersection acts as a fluidic diode) [181], moisture collection from fog and mist [182; 183], and falling film bioreactors [184]. The plethora of natural processes and industrial applications which involve fibre flows has naturally led to many experimental and theoretical investigations of the dynamics of this type of flow.

1.6.1 Axisymmetric fibre flow

Much of the prior research on fibre flows has assumed that the flow is axisymmetric (i.e. that there are no variations of the flow in the azimuthal direction).

(a)

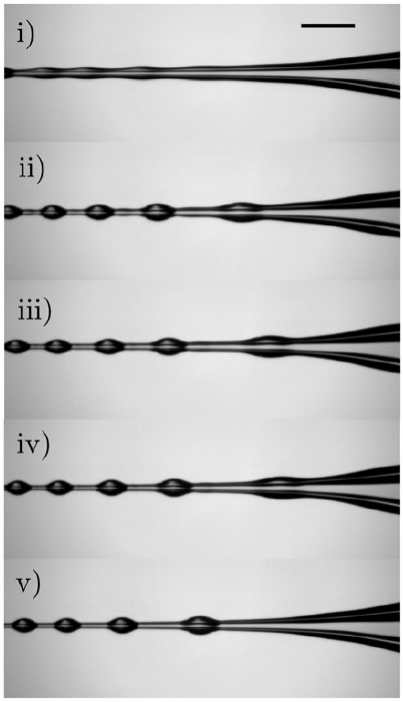

(b)

Figure 1.29: (a) Multiple dew drops covering the *Geranium robertianum* fruit. (b) A conical fibre (inspired by the shape of the *Geranium robertianum* fruit) coated with a thin layer of silicone oil viewed under a microscope, where the scale bar indicates 1 mm. Panels (i)–(v) show snapshots of the break up of the film into a stream of bulges which flow from left to right along the conical fibre (away from the apex) at 19.2 s, 44.8 s, 58.0 s, 73.6 s, 117.8 s, respectively. Reproduced with permission of the Royal Society of Chemistry, Copyright 2022, Lee et al. [176]; permission conveyed through Copyright Clearance Center, Inc.

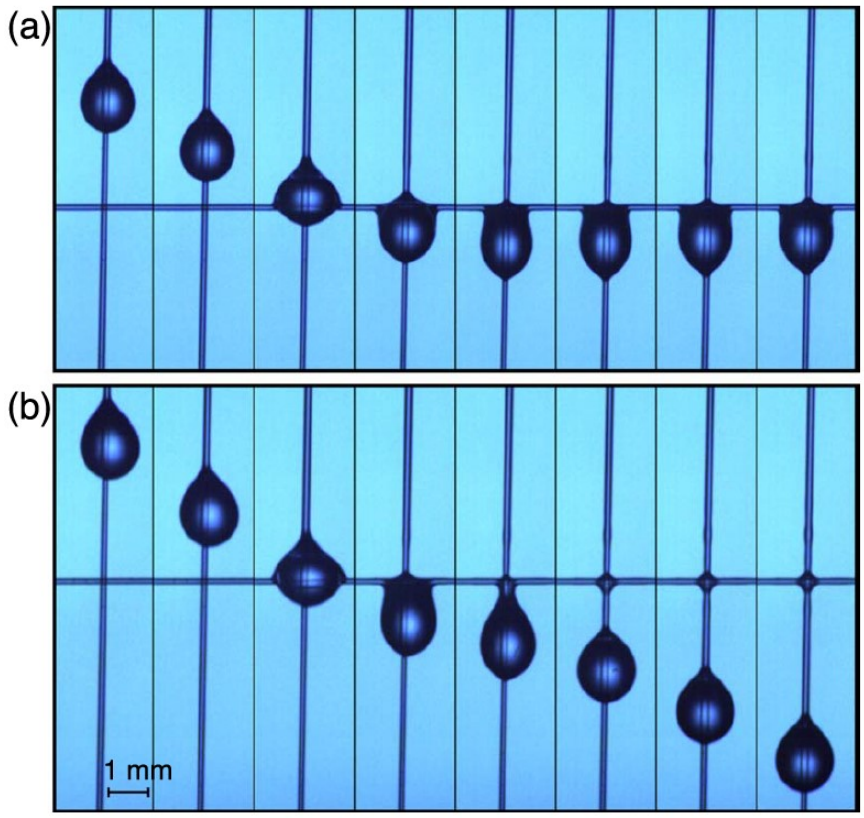

Figure 1.30: A droplet interacting with the intersection of two nylon fibres of radius 70 μm, where the intersection acts as a fluidic diode. Snapshots are taken every 10 ms. (a) A small droplet is pinned on the intersection, (b) while a large droplet crosses the intersection, leaving behind a tiny amount of fluid. Reproduced with permission from AIP Publishing, Copyright 2009, Gilet et al. [181].

1.6.1.1 Thin-film regime

In addition to assuming axisymmetry, many investigations were also restricted to the thin-film regime. Assuming that the flow is both axisymmetric and thin significantly simplifies the governing equations, which has led to the development of various reduced-order models. One such reduced-order model is that of Hammond [108], which has the form

$$\frac{\partial h}{\partial t} + \frac{\partial}{\partial z}\left[\frac{h^3}{3}\frac{\partial}{\partial z}\left(\frac{h}{a^2} + \frac{\partial^2 h}{\partial z^2}\right)\right] = 0, \tag{1.6.1}$$

where $h(z,t)$, t, z, and a denote the dimensionless film thickness, the dimensionless time, the dimensionless axial coordinate, and the dimensionless fibre radius, respectively. Equation (1.6.1) is nonlinear and includes the effects of viscosity and surface tension, while neglecting the effect of gravity. In particular, equation (1.6.1) captures the competing effects of the azimuthal and axial components of surface tension (the first and second terms in the round brackets, respectively). A film of uniform thickness is a steady solution of (1.6.1). We perform a linear stability analysis on this steady solution by decomposing h as

$$h(z,t) = 1 + \xi\widetilde{h}\mathrm{e}^{ikz+\sigma t}, \tag{1.6.2}$$

where $\xi \ll 1$ with k, σ, and $\xi\widetilde{h}$ denoting the (real) axial wavenumber, the (complex) linear growth rate, and the (initial) amplitude of the disturbance, respectively, which yields

$$\sigma = \frac{k^2}{3}\left(\frac{1}{a^2} - k^2\right). \tag{1.6.3}$$

The linear growth rate (1.6.3) is purely real as there is no convective flow due to the absence of gravity. The linear growth rate (1.6.3) is unstable for a finite range of k extending from $k = 0$ to $k = 1/a^2$ but is stable for $k > 1/a^2$. Therefore, unlike flow down an inclined plane (as described, for example, by the Benney equation (1.2.1)) which is linearly stable in the absence of inertia, the flow described by equation (1.6.1) is linearly long-wave unstable, even in the absence of inertia.

When the film is planar, surface tension acts as a stabilising mechanism to counter destabilising mechanisms, such as inertia in the Benney equation (1.2.1), for example. However, when the film is cylindrical, the free surface experiences

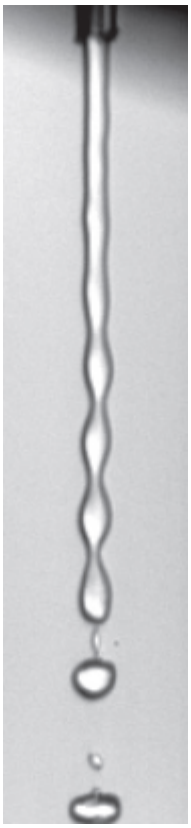

Figure 1.31: A cylindrical jet of fluid emanating from a nozzle experiences the Rayleigh–Plateau instability and breaks up into a stream of beads. Adapted with permission, Copyright 2020, Speirs et al. [186].

the Rayleigh–Plateau mode of instability [185], which is an instability driven by the azimuthal component of surface tension, and is often observed in the context of fluid jets [112]. An example of a fluid jet experiencing the Rayleigh–Plateau instability is shown in Figure 1.31. Surface tension acts so as to minimise surface area by causing the fluid to break up into a stream of beads, and the Rayleigh–Plateau instability is a consequence of this surface area minimisation. The flow described by equation (1.6.1) also experiences the Rayleigh–Plateau instability, which causes the fluid film coating the fibre to break up into a stream of bulges separated by thin films of fluid. The regions between the bulges demonstrate asymptotic thinning, which is where the fluid continues to drain from the thin films of fluid separating the bulges and accumulates in the bulges themselves [187].

Frenkel [188] extended the work of Hammond [108] to develop a reduced-order

model of the form

$$\frac{\partial h}{\partial t} + \frac{\partial}{\partial z}\left[\frac{h^3}{3}\left\{1 + \frac{\partial}{\partial z}\left(\frac{h}{a^2} + \frac{\partial^2 h}{\partial z^2}\right)\right\}\right] = 0. \tag{1.6.4}$$

Equation (1.6.4) is identical to equation (1.6.1) apart from the inclusion of the convective effect of gravity (the first term in the braces). The real parts of the (complex) linear growth rate of equation (1.6.4) coincides with the real linear growth rate of equation (1.6.1), however, the inclusion of gravity provides a mechanism for nonlinear stabilisation via the mean flow down the fibre, which can prevent the asymptotic thinning observed by Hammond [108]. In order to investigate the nonlinear mechanism for how small disturbances to the free surface evolve to form bulges, Kalliadasis and Chang [189] rescaled equation (1.6.4) to yield

$$\frac{\partial h}{\partial t} + \frac{\partial}{\partial z}\left[\frac{h^3}{3}\left\{1 + \frac{\partial}{\partial z}\left(\beta h + \frac{\partial^2 h}{\partial z^2}\right)\right\}\right] = 0, \tag{1.6.5}$$

where $\beta = (\gamma H/\rho g R^3)^{2/3}$ is a dimensionless parameter which represents the relative importance of azimuthal and axial curvature effects (note that $\beta \to 0^+$ corresponds to the planar limit). Kalliadasis and Chang [189] found the critical value $\beta = \beta_c \approx 1.413$, which denotes the transition between the two characteristic bulge formation behaviours. These two characteristic behaviours are shown schematically in Figure 1.32 for a thin film flowing down a vertical fibre. For $\beta < \beta_c$, the mean flow prevents the amplitude of the bulge from growing to become of the same order as the characteristic film thickness, as shown schematically on the left of Figure 1.32. For $\beta > \beta_c$, highly localised bulges with thickness of the same order as the characteristic film thickness form on the free surface due to the Rayleigh–Plateau instability overwhelming the convective effect of the mean flow. These highly localised bulges flow down the fibre with leading capillary ripples, as shown schematically on the right of Figure 1.32.

The assumptions that the flow is both axisymmetric and thin lead to many simplifications, however, despite the rather restrictive assumptions there have been experimental works in this regime which have shown good agreement between theory and experiments [190]. Thin-film equations of the form (1.6.1), (1.6.4), and (1.6.5) have since been extended to include other physical effects, such as electric fields [191], thermal effects [192; 193], a self-rewetting film [194], the effects of wall slippage [195], a thermoviscous fluid [196], and the effects of suction [197].

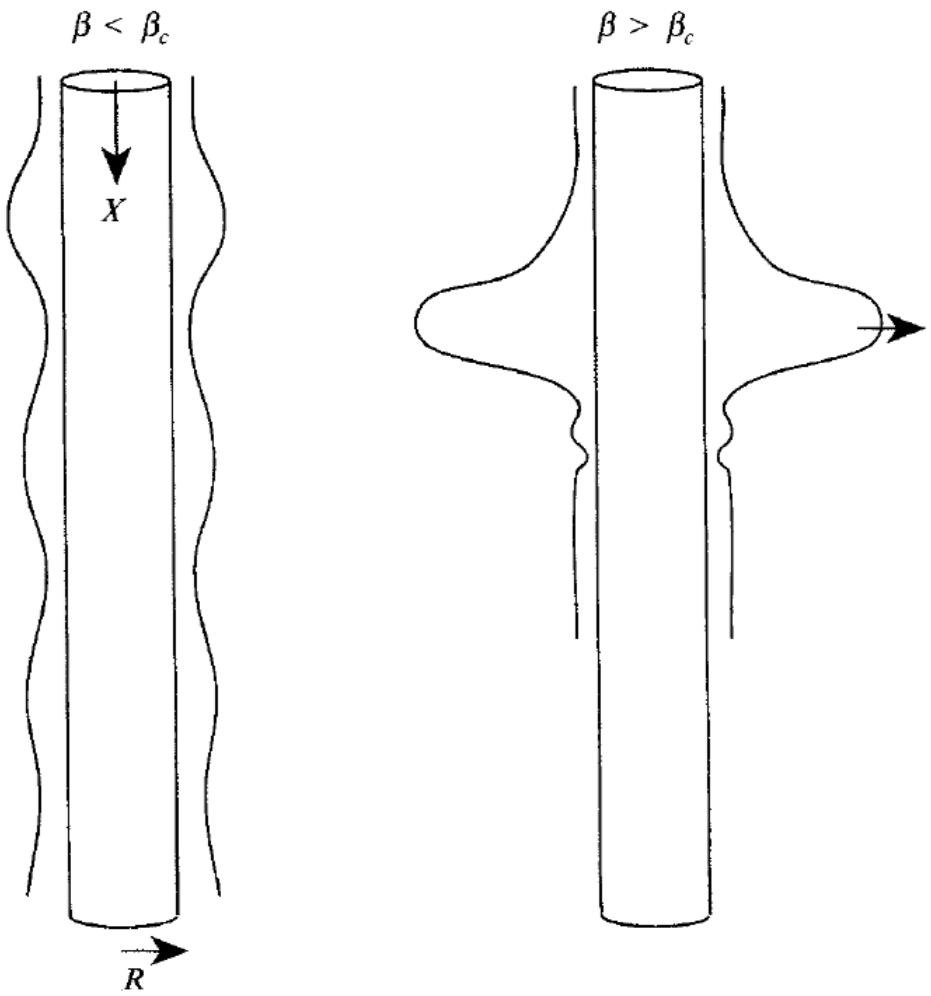

Figure 1.32: Schematic of the two characteristic bulge formation behaviours on a thin film flowing down a vertical fibre for $\beta < \beta_c$ (left) and $\beta > \beta_c$ (right). Reproduced with permission from Cambridge University Press, Copyright 1994, Kalliadasis and Chang [189].

1.6.1.2 Thick-film regime

More recent works have aimed to remove the assumption that the film is thin, while retaining the assumption that the flow is axisymmetric.

Kliakhandler et al. [109] performed experiments for thick film flow down a fibre (where the film thickness is at least double the fibre radius) and developed a reduced-order model using a long-wave approximation (as discussed in Section 1.3.2.2) to model their experimental observations. From their experiments, Kliakhandler et al. [109] observed three distinct flow patterns, in which the onset of bulges is triggered by the Rayleigh–Plateau instability, which they termed "regime a", "regime b", and "regime c", as shown in Figures 1.33(a), (b), and (c), respectively. These flow patterns are shown in Figure 1.33, where the flow rate decreases from (a) to (c). Figure 1.33(a) shows regime a which is characterised by large bulges flowing rapidly down the fibre. The film between the bulges is nearly uniform and is thick relative to the fibre radius. The average distance between the bulges is long, although the distance between each individual bulge varies. The large bulges can sometimes collide with each other in an irregular fashion, and the collision process is fast. Figure 1.33(b) shows regime b which is characterised by regularly-spaced periodic bulges flowing down the fibre. The speed, shape, and distance between bulges do not change over time. The speed and size of a bulge in regime b is smaller than in regime a. Figure 1.33(c) shows regime c which is characterised by large primary bulges separated by smaller secondary bulges flowing down the fibre. The size and speed of a primary bulge in regime c is larger than a bulge in regime b. The primary bulges collide with and coalesce with the secondary bulges in front of them. During the collision and coalescence process, the primary bulge moves faster, and as a result, the speed of the primary bulge changes periodically in time.

The reduced-order model of Kliakhandler et al. [109] includes the effects of viscosity, gravity, and surface tension, and has the form

$$S\frac{\partial S}{\partial t}+\frac{\partial}{\partial z}\left[\frac{-a^4+4a^2S^2-3S^4+4S^4\log\left(S/a\right)}{16}\left\{1+\frac{\partial\kappa}{\partial z}\right\}\right]=0, \qquad (1.6.6)$$

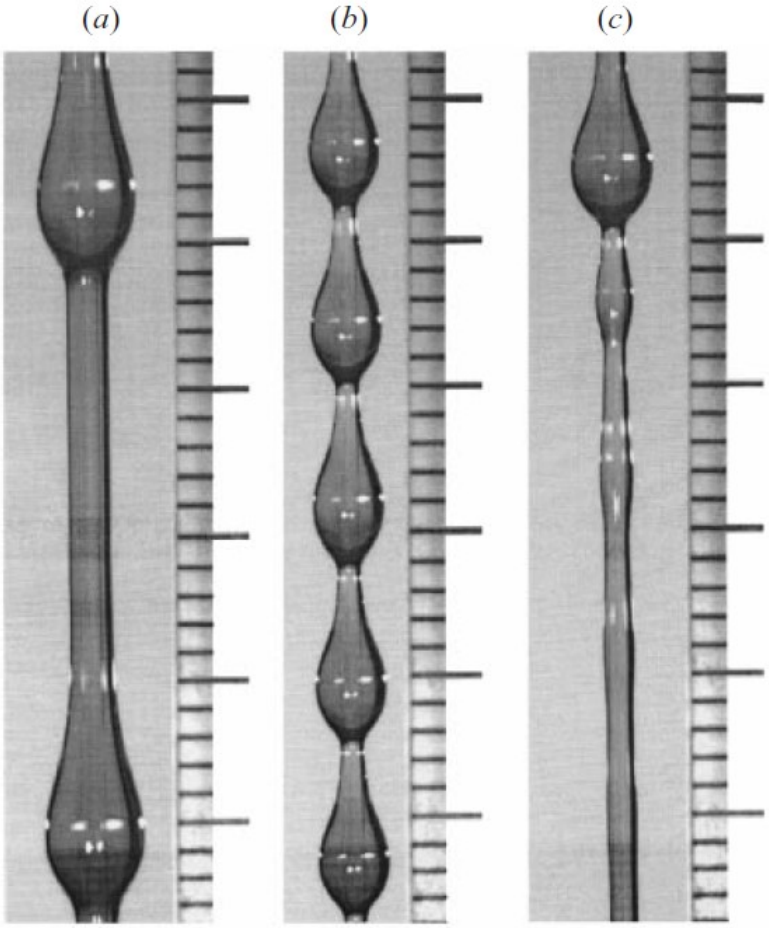

Figure 1.33: Experimental observations of the three distinct flow patterns which occur at different flow rates. The flow rate decreases from (a) to (c). The small marks on the ruler are 1mm apart. Reproduced with permission from Cambridge University Press, Copyright 2001, Kliakhandler et al. [109].

with

$$\kappa = \frac{S\dfrac{\partial^2 S}{\partial z^2} - 1 - \left(\dfrac{\partial S}{\partial z}\right)^2}{S\left[1 + \left(\dfrac{\partial S}{\partial z}\right)^2\right]^{3/2}}, \tag{1.6.7}$$

where $S(z,t)$ and $\kappa(z,t)$ are the dimensionless film radius and the (full form of the) interfacial curvature, respectively. The $h^3/3$ mobility coefficient in equations in the thin-film regime (such as equations (1.6.1), (1.6.4), and (1.6.5)) is replaced by the first term in the square brackets in the thick film regime. In order to model the large bulges observed in their experiments, Kliakhandler et al. [109] retained the full form of the interfacial curvature κ in equation (1.6.6) (see Section 1.3.2.3). They showed that, in the linear regime, the real parts of the linear growth rate of equation (1.6.6) compare well with the real parts of the linear growth rate of the Stokes equations. In the nonlinear regime, Kliakhandler et al. [109] captured the characteristic behaviours of both regime b and regime c from their numerical solution of equation (1.6.6). Figure 1.34 shows their plot of the free surface profiles for regime b (left) and regime c (right) from the numerical solution of equation (1.6.6). The free surface profile for regime b resembles the flow pattern shown in Figure 1.33(b), however, despite having clear primary and secondary bulges, the resemblance of the free surface profile for regime c being (in the words of Kliakhandler et al. [109]) "close to that observed" in Figure 1.33(c) is dubious. Kliakhandler et al. [109] were also unable to capture the main feature of regime a, namely the nearly uniform film separating large bulges, with their numerical solution of equation (1.6.6).

Later, Craster and Matar [110] developed a reduced-order model which includes the effects of viscosity, gravity, and surface tension, and has the form

$$S\frac{\partial S}{\partial t} + \frac{\partial}{\partial z}\left[\frac{-a^4 + 4a^2S^2 - 3S^4 + 4S^4\log(S/a)}{16}\left\{1 - \frac{\partial}{\partial z}\left(\frac{1}{S} - \delta^2\frac{\partial^2 S}{\partial z^2}\right)\right\}\right] = 0, \tag{1.6.8}$$

where $\delta = \mathcal{R}/\mathcal{L} \ll 1$ denotes the long-wave small aspect ratio (see Section 1.3.2.2), where $\mathcal{R}$ and $\mathcal{L} = \gamma/(\rho g \mathcal{R})$ denote the characteristic film radius, and the characteristic length scale in the streamwise direction, respectively. Equation (1.6.8) is identical to equation (1.6.6) (up to a difference in scalings) apart from the approximation of the full form of the interfacial curvature (1.6.7). The term in equation

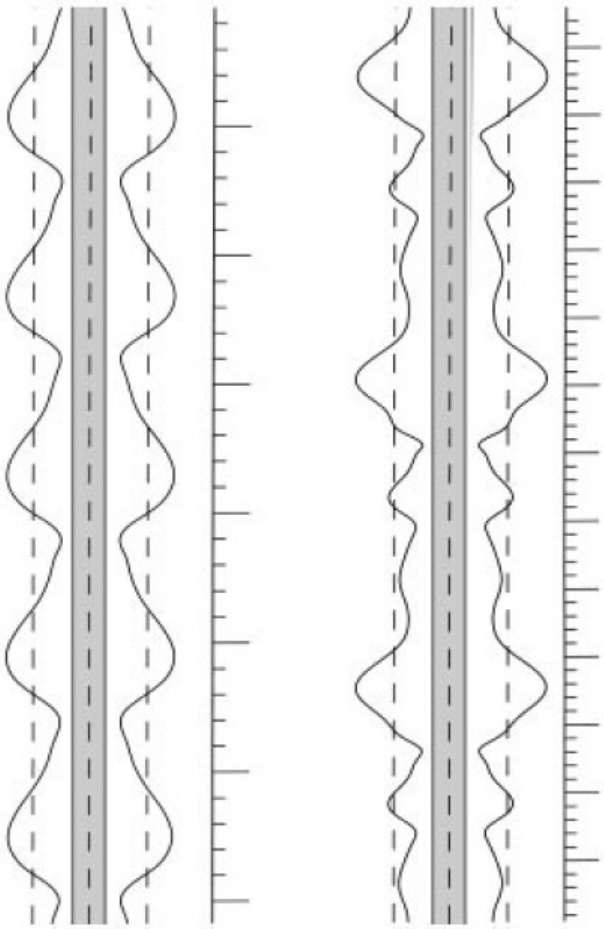

Figure 1.34: Free surface profiles for regime b (left) and regime c (right) from the numerical solution of equation (1.6.6). Reproduced with permission from Cambridge University Press, Copyright 2001, Kliakhandler et al. [109].

(1.6.8) which represents the axial component of surface tension (the second term in the curved brackets inside the braces) is formally of a higher order in δ, but is retained in order to provide a stabilising effect on the flow. In the nonlinear regime, Craster and Matar [110] computed travelling wave solutions of equation (1.6.8) and compared these solutions with the experimental observations of Kliakhandler et al. [109]. Figure 1.35 shows their plot of the free surface profiles of the travelling wave solution of (1.6.8) for each of the three regimes observed in the experiments of Kliakhandler et al. [109]. The free surface profiles shown in Figure 1.35 are in good agreement with the flow patterns shown in Figure 1.33. In particular, Figure 1.35(c) bears a much closer resemblance to the flow pattern shown in Figure 1.33(c) than Figure 1.34(b) does.

Craster and Matar [110] did not perform any further comparisons with the experimental results of Kliakhandler et al. [109], but instead performed their own experiments, with which they then compared the numerical solution of (1.6.8). The experimental results of Craster and Matar [110] only showed the characteristic behaviours of regime a and regime c, and they noted that the characteristic behaviour of regime b was only observed near the inlet. Craster and Matar [110] showed that the travelling wave solution and the numerical solution of equation (1.6.8) compared well to their experimental results in regime a and regime c, respectively.

Thick-film equations of the form (1.6.6) and (1.6.8) have since been extended to include other physical effects such as electric fields [198; 199], thermal effects [200; 201], a self-rewetting film [202], a rotating fibre [203], the effect of curvature elasticity [204], and porosity of the fibre [205–207].

Thus far, each of the works described in the present section has assumed that inertia is negligible and therefore could not account for the Kapitza mode of instability. The Kapitza instability is an inertia-driven instability which is often observed in the context of falling films on inclined planes [59; 208]. The Kapitza instability causes the fluid film to break into continuously interacting solitary waves. Figure 1.36 shows a schematic representation of the characteristic shape of two pulses flowing from left to right down a vertical wall under gravity. The two pulses in Figure 1.36 are excited by the Kapitza instability, with capillary ripples due to surface tension. Unlike the Rayleigh–Plateau instability, the Kapitza instability cannot occur if there is no mean flow down the fibre.

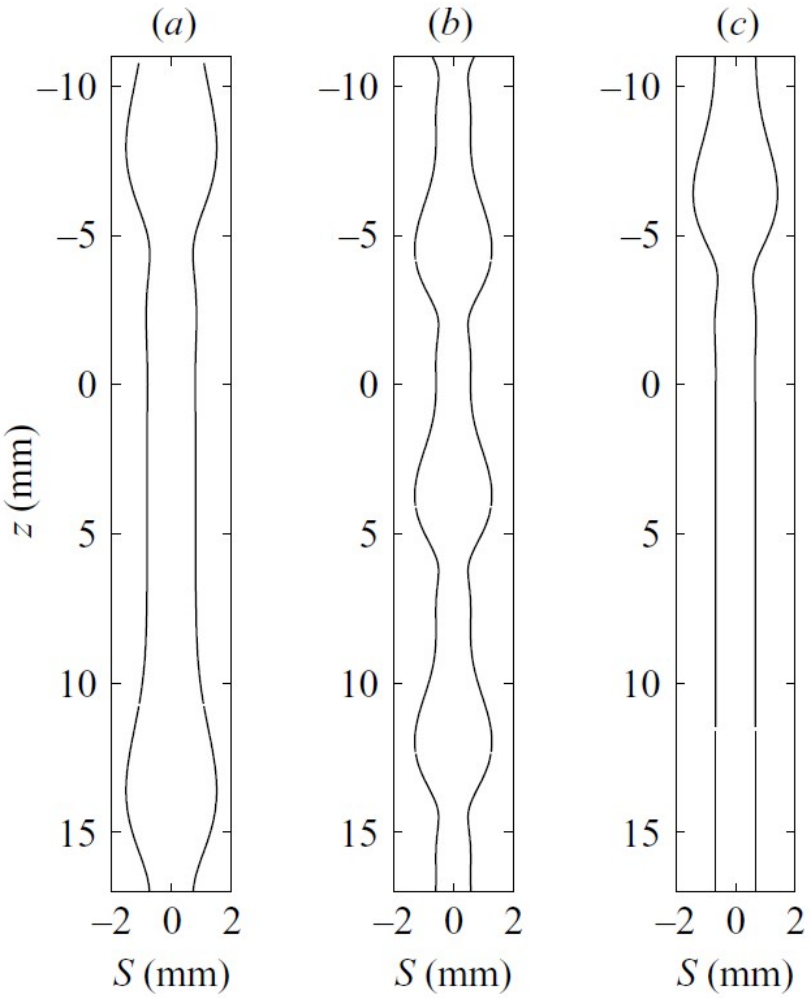

Figure 1.35: Free surface profiles of the travelling wave solution of (1.6.8) for (a) regime a, (b) regime b, and (c) regime c, as observed in the experiments of Kliakhandler et al. [109]. Reproduced with permission from Cambridge University Press, Copyright 2006, Craster and Matar [110].

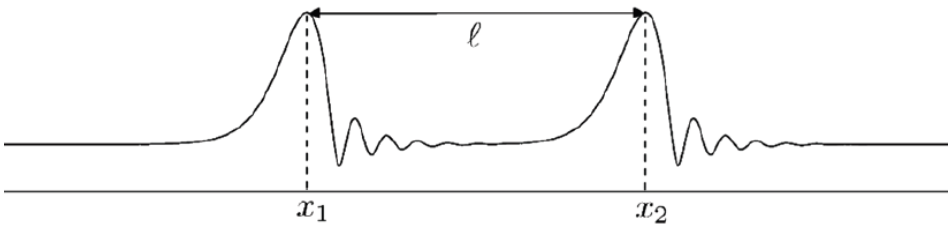

Figure 1.36: Schematic representation of the characteristic shape of two pulses, separated by a distance l, and located at x_1 and x_2, flowing from left to right down a vertical wall under gravity. The pulses are excited by the Kapitza instability, with capillary ripples due to surface tension. Reproduced with permission from Oxford University Press, Copyright 2012, Pradas et al. [208].

Ruyer-Quil et al. [64] developed a reduced-order model for the axisymmetric flow of a thick film down a vertical fibre by applying a long-wave approximation, and then applying the WRIBL method. The reduced-order model of Ruyer-Quil et al. [64] includes the effects of viscosity, gravity, surface tension, viscous dispersion, and inertia, and is a simplified second-order model (see Section 1.2.1.4). The equations comprising this reduced-order model are lengthy, and are not reproduced here, but are given by equation (4.16) in Ruyer-Quil et al. [64].

In the linear regime, Ruyer-Quil et al. [64] used the framework of the Whitham wave hierarchy (as discussed in Section 1.2.2) to show that the effects of viscous dispersion and axial surface tension have a stabilising effect on the flow, whereas the effects of inertia and azimuthal surface tension have a destabilising effect on the flow. In the nonlinear regime, Ruyer-Quil et al. [64] computed travelling wave solutions of both their equation (4.16) and the equation of Craster and Matar [110] (1.6.8) for each of the three regimes observed in the experiments of Kliakhandler et al. [109]. Figure 1.37 shows their plot of the free surface profiles and streamlines of the travelling wave solution of equation (4.16) in Ruyer-Quil et al. [64] and equation (1.6.8). The travelling wave solutions of both equation (4.16) in Ruyer-Quil et al. [64] and equation (1.6.8) are in good agreement with the flow patterns shown in Figure 1.33. The only noticeable difference between the travelling wave solutions of both equation (4.16) in Ruyer-Quil et al. [64], and equation (1.6.8) is the absence of capillary ripples in the travelling wave solutions of equation (4.16) in Ruyer-Quil et al. [64], in agreement with the experimental observations of Kliakhandler et al. [109].

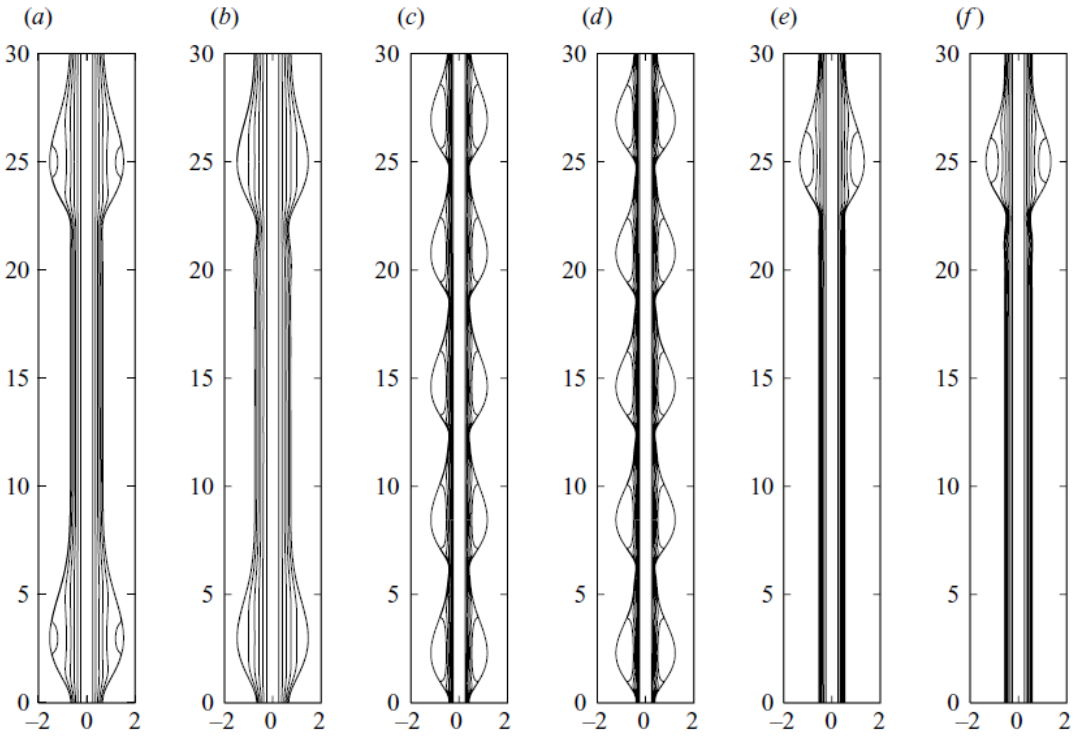

Figure 1.37: Free surface profiles and streamlines of the travelling wave solution of (a, c, e) equation (4.16) of Ruyer-Quil et al. [64] and (b, d, f) the equation of Craster and Matar [110] (1.6.8). (a, b), (c, d), and (c, f) correspond to regime a, regime b, and regime c, as observed in the experiments of Kliakhandler et al. [109], respectively. Reproduced with permission from Cambridge University Press, Copyright 2008, Ruyer-Quil et al. [64].

Ruyer-Quil et al. [64] also compared the numerical solution of both equation (4.16) in Ruyer-Quil et al. [64] and equation (1.6.8) with the experimental observations of Kliakhandler et al. [109]. Ruyer-Quil et al. [64] found that the numerical solution of their equation (4.16) gives better agreement with the experimental observations of Kliakhandler et al. [109] than the numerical solution of equation (1.6.8). In particular, in regime a, the numerical solution of equation (4.16) in Ruyer-Quil et al. [64] displays bulge coalescence events and predicts a bulge amplitude and bulge spacing in agreement with the experimental observations of Kliakhandler et al. [109], whereas the numerical solution of equation (1.6.8) does not display bulge coalescence events and predicts a bulge spacing approximately three times smaller than the experimental observations of Kliakhandler et al. [109]. However, the numerical solution of both equation (4.16) in Ruyer-Quil et al. [64] and equation (1.6.8) cannot capture the behaviour of regime c. Ruyer-Quil et al. [64] also showed that their numerical solutions are in good agreement with the experimental observations of Duprat et al. [209], in which the effect of inertia is non-negligible.

Despite improving upon equations (1.6.6) and (1.6.8), the travelling wave solution of equation (4.16) in Ruyer-Quil et al. [64] does not accurately capture the dynamics in every regime observed in the experiments of Kliakhandler et al. [109]. In particular, the travelling wave solution of regime c shown in Figure 1.37(e) does not capture the secondary bulges observed in the flow pattern shown in Figure 1.33(c), and the travelling wave solution of each regime does not accurately predict *all* of the experimental measurements Kliakhandler et al. [109] (i.e. the bulge speed and the maximum and minimum bulge height). Finding the best reduced-order model to effectively capture the dynamics of every regime observed in the experiments of Kliakhandler et al. [109] is still an open and active problem [210–212].

1.6.2 Non-axisymmetric fibre flow

In the previous section, we have discussed various theoretical and experimental studies which have assumed that the flow is axisymmetric, in both the thin-film regime and the thick-film regime. However, the classical experimental work of Binnie [213] observed a flow that is non-axisymmetric. Figure 1.38 shows the

experimental observations of Binnie [213] in which non-axisymmetric bulges have formed on the free surface of a thin film of fluid flowing down the exterior of a vertical fibre. Despite the observation of non-axisymmetric flow in this classical experimental work of Binnie [213], situations in which the flow is non-axisymmetric have, surprisingly, remained relatively unstudied. Non-axisymmetric flow down a vertical fibre is one of the two main subjects of this thesis.

The first theoretical study of non-axisymmetric fibre flow was performed by Shlang and Sivashinsky [54] who developed a weakly nonlinear reduced-order model in the moving frame of reference of the form

$$\frac{\partial \breve{h}}{\partial t} + \breve{h}\frac{\partial \breve{h}}{\partial z} + Re\frac{\partial^2 \breve{h}}{\partial z^2} + \nabla^2\left(\frac{\breve{h}}{a^2} + \nabla^2 \breve{h}\right) = 0, \tag{1.6.9}$$

where $\breve{h}(\theta, z, t)$ and $Re = \rho^2 g H^3/\mu^2$ denote small deviations in the dimensionless film thickness from the uniform base-state solution and a Reynolds number, respectively. The second and third terms of equation (1.6.9) correspond to the convective effect of gravity (relative to the moving frame) and inertia, respectively, and the terms in the brackets correspond to the azimuthal and axial components of surface tension, respectively. Equation (1.6.9) is a generalised form of the Kuramoto–Sivashinsky equation (1.2.5). In addition to being weakly nonlinear, equation (1.6.9) is also only applicable in the thin-film regime. Shlang and Sivashinsky [54] only explored the dynamics of equation (1.6.9) in the linear regime. We perform a linear stability analysis by decomposing $\breve{h}$ as

$$\breve{h}(\theta, z, t) = \widetilde{h}\mathrm{e}^{ikz+in\theta+\sigma t}, \tag{1.6.10}$$

where n is the (integer) azimuthal wavenumber, which yields the (purely real) linear growth rate

$$\sigma_{(n)} = Rek^2 + \frac{k^2\left(1-2n^2\right)}{a^2} - k^4 + \frac{n^2\left(1-n^2\right)}{a^4}. \tag{1.6.11}$$

For the $n = 0$ (axisymmetric) mode, the linear growth rate (1.6.11) is

$$\sigma_{(0)} = \left(Re + \frac{1}{a^2}\right)k^2 - k^4, \tag{1.6.12}$$

and for the $n = 1$ (first non-axisymmetric) mode, the linear growth rate (1.6.11)

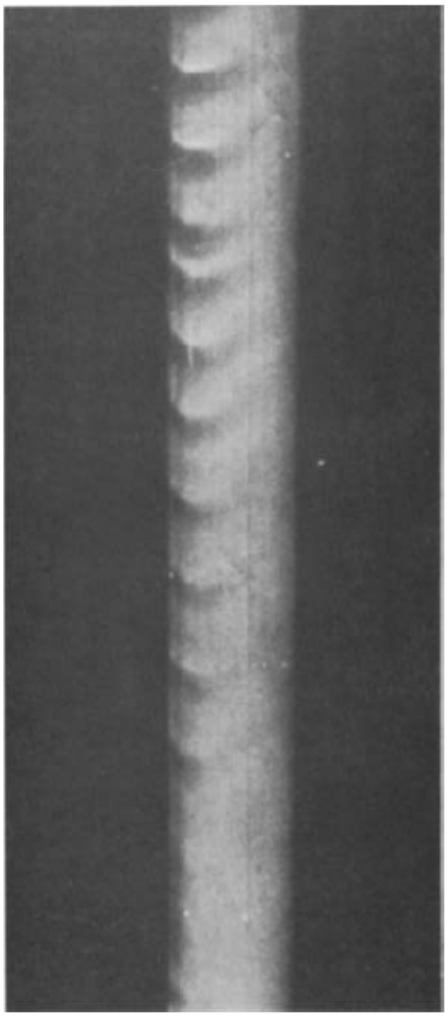

Figure 1.38: Experimental observations of non-axisymmetric bulges which have formed on the free surface of a thin film of fluid flowing down the exterior of a vertical fibre. Reproduced with permission from Cambridge University Press, Copyright 1957, Binnie [213].

is

$$\sigma_{(1)} = \left(Re - \frac{1}{a^2} \right) k^2 - k^4. \tag{1.6.13}$$

The linear growth rate for the $n = 0$ mode (1.6.12) is long-wave unstable, even in the absence of inertia, which is in agreement with the works discussed in Section 1.6.1. However, the linear growth rate for the $n = 1$ mode (1.6.13) is long-wave unstable when $Re > 1/a^2$ (i.e. increasing Re and/or increasing a destabilises the $n = 1$ mode). Therefore, for non-axisymmetric flow to occur, a destabilising effect, such as inertia in the present case, has to be included. Higher azimuthal wavenumbers (i.e. $n \geq 2$) can also be destabilised by further increasing Re and/or increasing a. However, the $n = 1$ mode will already have been destabilised for values of Re and a which are large enough to destabilise the $n \geq 2$ modes, and so the flow will already be non-axisymmetric. We are only interested in the onset of non-axisymmetric instabilities, therefore, we are able to ignore the $n \geq 2$ modes and focus only on the (in)stability of both the $n = 0$ mode and the $n = 1$ mode. Figures 1.39(a) and 1.39(b) show a sketch of the characteristic shape of the $n = 0$ mode and the $n = 1$ mode, respectively, viewed from above as a two-dimensional cross-section of the fibre. Figures 1.39(c) and 1.39(d) show a sketch of the flow down a fibre when excited by the $n = 0$ mode and the $n = 1$ mode, respectively.

Later, Dávalos-Orozco and Ruiz-Chavarría [214] studied the non-axisymmetric flow down a rotating fibre by investigating the linear stability of the Navier–Stokes equations. In what follows, we discuss their results for the case of a stationary fibre with a uniform base-state solution. While analytical progress is not possible in general in the linear regime, it is possible to make certain approximations in order to allow analytical progress. Two such approximations which Dávalos-Orozco and Ruiz-Chavarría [214] made in order to obtain analytical solutions for the linear growth rate were to take the limit of small Reynolds number ($Re \to 0^+$), and the limit of small axial wavenumbers ($k \to 0^+$), i.e. long waves. In the limit of small Reynolds number, Dávalos-Orozco and Ruiz-Chavarría [214] found that the $n = 0$ mode is always unstable, while the $n = 1$ mode is always stable, while in the limit of small axial wavenumbers, they found that the $n = 0$ mode is always unstable (which agrees with the results of Shlang and Sivashinsky [54] mentioned previously). The $n = 1$ mode in the limit of small axial wavenumbers was not considered analytically until the later paper by Ruiz-Chavarría and Dávalos-Orozco [215]. Ruiz-Chavarría and Dávalos-Orozco [215] found that the $n = 1$ mode was

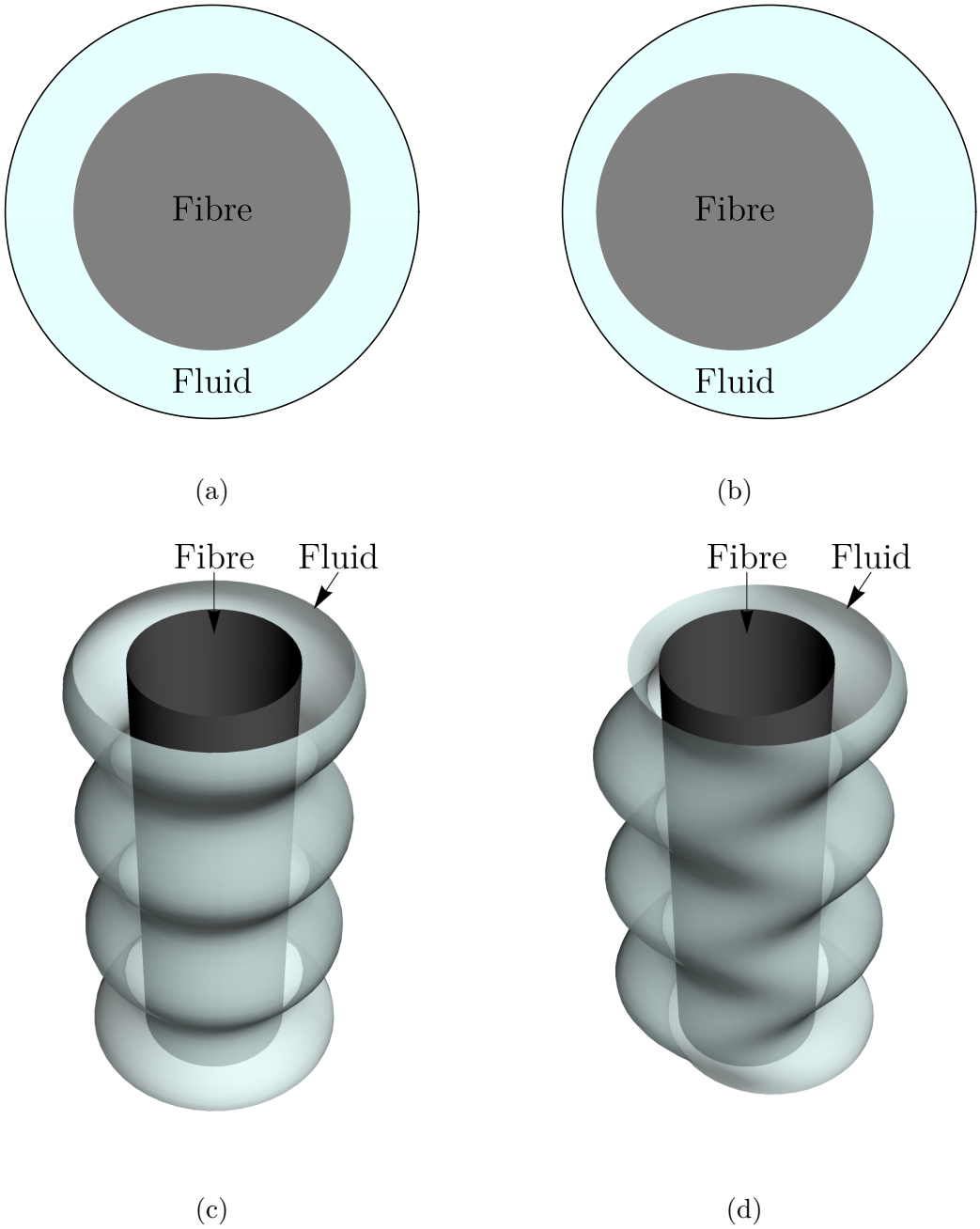

Figure 1.39: Sketch of the characteristic shape of (a) the $n = 0$ (axisymmetric) mode and (b) the $n = 1$ (first non-axisymmetric) mode viewed from above as a two-dimensional cross-section of the fibre. Sketch of the flow down a fibre when excited by (c) the $n = 0$ mode and (d) the $n = 1$ mode. Note that the size of the disturbance in (b) has been exaggerated for illustrative purposes.

stabilised by increasing the strength of surface tension, and destabilised by increasing the fibre radius and/or increasing the effect of inertia (which also agrees with the results of Shlang and Sivashinsky [54] mentioned previously). Later, Ruiz-Chavarría and Dávalos-Orozco [216] considered the linear stability of the Navier–Stokes equations for general axial wavenumbers numerically. The numerical results of Ruiz-Chavarría and Dávalos-Orozco [216] validated the analytical results of their previous papers [214; 215].

Much of the work on non-axisymmetric flow down a fibre was confined to either the linear or weakly nonlinear regime, however, a nonlinear reduced-order model for non-axisymmetric flow down a fibre was developed by Frenkel et al. [188] using a thin-film approximation. This reduced-order model includes the effects of viscosity, gravity, and surface tension, and has the form

$$\frac{\partial h}{\partial t} + \frac{\partial}{\partial z}\left(\frac{h^3}{3}\right) + \nabla \cdot \left[\frac{h^3}{3}\nabla\left(\frac{h}{a^2} + \nabla^2 h\right)\right] = 0, \tag{1.6.14}$$

where $h(\theta, z, t)$ is the dimensionless film thickness. Frenkel et al. [188] only explored the dynamics of (1.6.14) in the linear regime. We perform a linear stability analysis by decomposing h as

$$h(\theta, z, t) = 1 + \xi \widetilde{h} \mathrm{e}^{ikz + in\theta + \sigma t}, \tag{1.6.15}$$

where $\xi \ll 1$, which yields the linear growth rate

$$\sigma_{(n)} = -ik + \frac{1}{3}\left(\frac{k^2\left(1 - 2n^2\right)}{a^2} - k^4 + \frac{n^2\left(1 - n^2\right)}{a^4}\right). \tag{1.6.16}$$

The real parts of the linear growth rate (1.6.16) is identical to the linear growth rate (1.6.11) when $Re = 0$, up to a difference in scalings. Therefore, the flow described by equation (1.6.14) is axisymmetric, as there are no effects present which will destabilise the $n = 1$ mode.

More recently, thin-film equations of the form (1.6.14) have since been extended to include other non-axisymmetric instability-inducing effects, such as fingering instability due to a gravity-driven contact line [217; 218], electric fields [219], thermal effects [220], and fibre inclination [221].

Despite there being surprisingly little theoretical work, the problem of non-axisymmetric flow down a fibre is still an active area of research, with two recent experimental works investigating situations in which the flow is non-axisymmetric

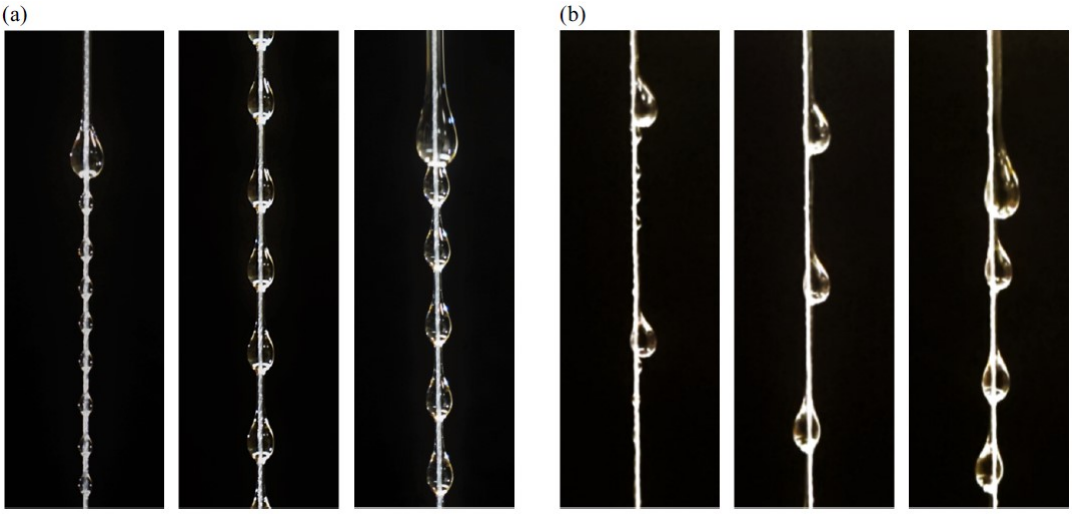

Figure 1.40: Experimental observations of the three distinct flow patterns originally observed by Kliakhandler et al. [109] (from left to right: regime a, regime b, and regime c) for (a) axisymmetric flow, and (b) non-axisymmetric flow. Reproduced with permission from the American Physical Society, Copyright 2021, Gabbard and Bostwick [222].

[222; 223].

The first of these works is the experiments performed by Gabbard and Bostwick [222] on the non-axisymmetric instability experienced by the flow down a vertical fibre. Gabbard and Bostwick [222] found that the three distinct flow patterns observed experimentally by Kliakhandler et al. [109] for an axisymmetric flow (namely, regime a, regime b, and regime c) are also observed in a non-axisymmetric flow, as shown in Figure 1.40. In their experiments, Gabbard and Bostwick [222] applied the fluid to the side of the fibre (i.e. the flow is initially non-axisymmetric) and examined the transition from a non-axisymmetric flow to an axisymmetric flow. Figure 1.41 shows a plot of their results of an experimental parametric study for the transition from a non-axisymmetric flow to an axisymmetric flow, showing how it depends upon the fibre diameter and surface tension. Gabbard and Bostwick [222] found that decreasing the fibre diameter and/or decreasing the strength of surface tension caused the (initially) non-axisymmetric flow to become axisymmetric. Gabbard and Bostwick [222] also found that non-axisymmetric flow has more predictable dynamics than axisymmetric flow. Figure 1.42 shows their plot of the bulge frequency as a function of the flow rate for both non-axisymmetric (red circles) and axisymmetric (blue triangles) flows. The bulge frequency for non-

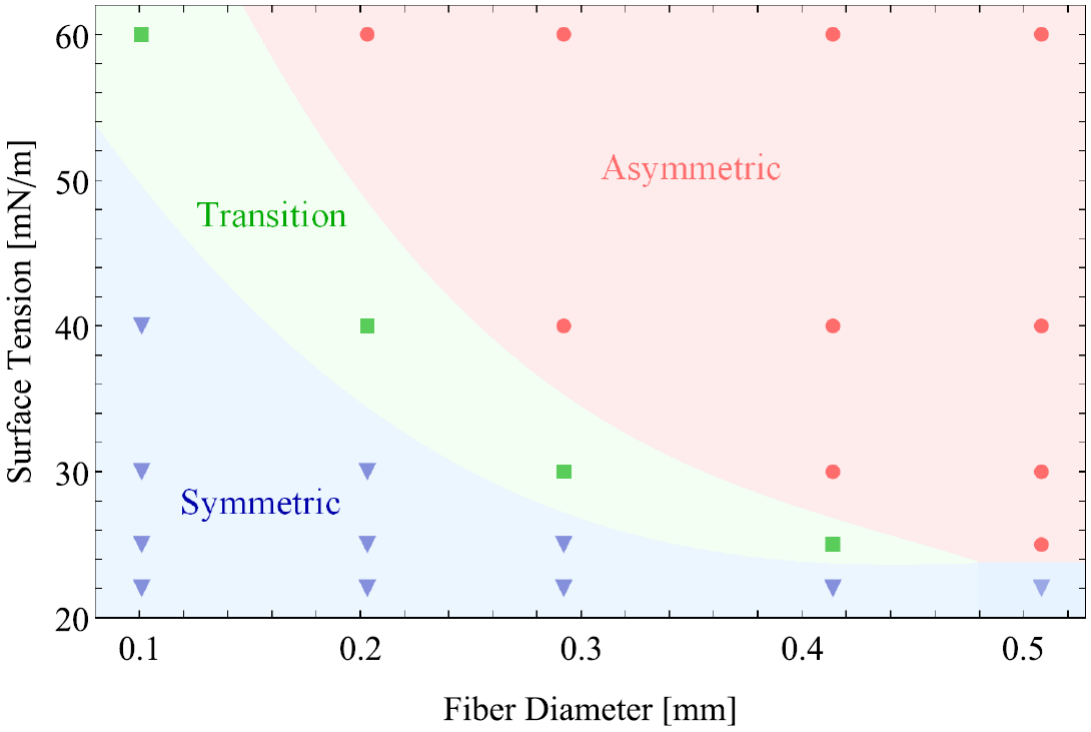

Figure 1.41: The results of an experimental parametric study for the transition from a non-axisymmetric flow to an axisymmetric flow, showing how it depends upon the fibre diameter and surface tension. Circles, triangles, and squares correspond to parameter values for which the flow remained non-axisymmetric, transitioned to an axisymmetric flow, and randomly transitioned back and forth between a non-axisymmetric flow and an axisymmetric flow. Reproduced with permission from the American Physical Society, Copyright 2021, Gabbard and Bostwick [222].

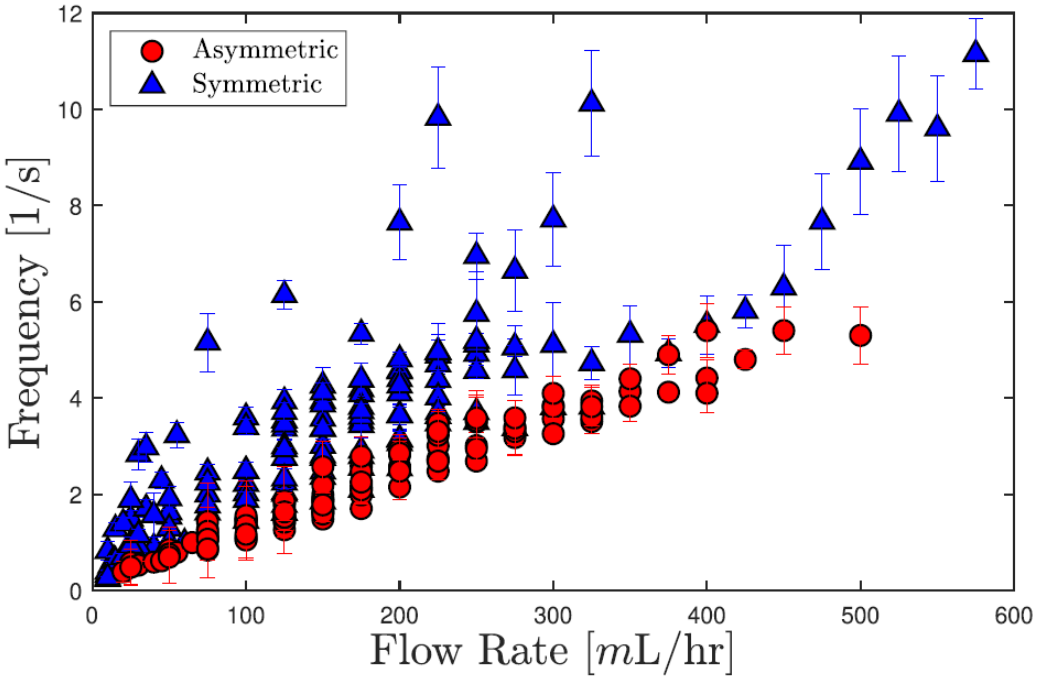

Figure 1.42: Plot of the bulge frequency (the speed of the bulge divided by the spacing between bulges) as a function of the flow rate from the experimental results of Gabbard and Bostwick [222]. Red circles and blue triangles correspond to experiments where the flow is non-axisymmetric and axisymmetric, respectively. Reproduced with permission from the American Physical Society, Copyright 2021, Gabbard and Bostwick [222].

axisymmetric flow increases almost linearly with the flow rate, whereas the bulge frequency for axisymmetric flow is more spread out. The predictable dynamics of non-axisymmetric flow, as observed experimentally by Gabbard and Bostwick [222], are, of course, extremely beneficial in industrial processes which involve fibre flow. In particular, Gabbard and Bostwick [222] note that the optimal desalination process occurs when the flow has a regular pattern of bulges with a maximal bulge frequency [177].

The second of these works is the experiments performed by Eghbali et al. [223] which examined the effect of fibre eccentricity on the flow. Fibre eccentricity is where the fibre is placed in a position away from the centre of the flow. These experiments showed the existence of two unstable modes, which Eghbali et al. [223] termed the "pearl" and "whirl" modes, as shown in Figure 1.43. The pearl mode (shown in the left column of Figure 1.43) is characterised by the flow of non-axisymmetric fluid bulges down one side of the fibre, whereas the whirl mode (shown in the right column of Figure 1.43) is characterised by the fluid forming a single helix which "whirls" around the axial direction as the fluid flows down the fibre. Eghbali et al. [223] found that both decreasing the strength of surface tension and decreasing the fibre radius promotes the whirl mode over the pearl mode.

The works discussed in Section 1.6.1 explored both the thin-film regime and the thick-film regime for axisymmetric flow down a fibre. In particular, the work of Ruyer-Quil et al. [64] used the WRIBL method to derive a thick-film reduced-order model which incorporates the effect of inertia. The works discussed in Section 1.6.2 explored non-axisymmetric flow down a fibre. Much of this work has been confined to the linear [214–216] and weakly nonlinear regimes [54]. Frenkel et al. [188] derived a nonlinear thin-film reduced-order model, however, this model did not incorporate any effects (such as inertia [54; 215; 216] or other physical effects [217–221]) which would induce a non-axisymmetric instability. For non-axisymmetric flow down a fibre, there have been no previous works in the nonlinear regime when the non-axisymmetric instability-inducing effect of inertia is incorporated. Additionally, there have been no previous works in the thick-film regime for non-axisymmetric flow down a fibre.

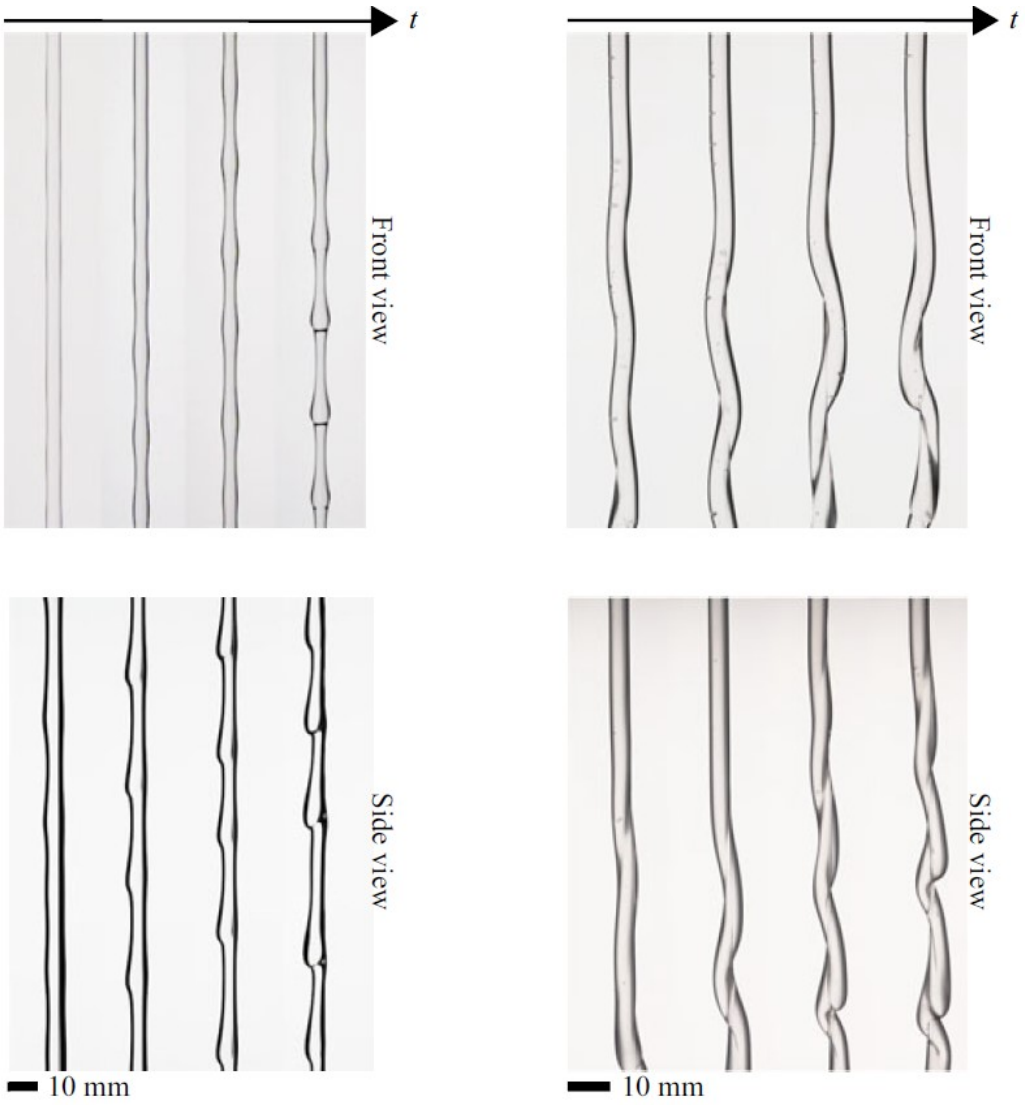

Figure 1.43: Experimental observations of the flow down an eccentric fibre excited by (a) the pearl mode and (b) the whirl mode, viewed from the front (top row) and the side (bottom row). In each part, the time increases from left to right. The front and side views are not synchronous. Reproduced with permission, Copyright 2022, Eghbali et al. [223].

1.7 Outline of thesis

In Chapter 2 we derive a reduced-order model using a long-wave approximation and a reduced-order model using a thin-film approximation for flow on a two-dimensional uniformly rotating horizontal elliptical cylinder.

In Chapter 3 we analyse the analytical and numerical results of the thin-film reduced-order model derived in Chapter 2 by performing a parametric study on the rotation speed. We also investigate the special case of a stationary cylinder and the asymptotic limits of strong surface tension, rapid rotation, and a nearly-circular ellipse.

In Chapter 4 we derive a reduced-order model for the non-axisymmetric coating of a vertical fibre by a thick film of fluid by applying a long-wave approximation, and then applying the WRIBL method. We also recover generalisations of reduced-order models previously studied by other authors in the thick-film regime and the thin-film regime.

In Chapter 5 we analyse the results of reduced-order models derived in Chapter 4 in both the linear and nonlinear regimes. We compare these results with the results of the Navier–Stokes equations in the linear regime and with the experimental results of Gabbard and Bostwick [222].

In Chapter 6 we provide some concluding remarks and discuss possible directions for future work.

1.8 Presentations

The work contained in this thesis has been presented by me (both virtually and in person) at several local, national, and international meetings and conferences.

Aspects of Chapter 1 have been presented by me as a poster presentation at the Carnegie PhD Scholars' Gathering 2019, February 2019, Royal College of Physicians and Surgeons of Glasgow, Glasgow.

Aspects of Chapters 2 and 3 have been presented by me as a poster presentation at the 62nd British Applied Mathematics Colloquium (joint with British Mathematical Colloquium), April 2021, University of Glasgow (virtually), as a pre-

recorded oral presentation at the 73rd Annual Meeting of the American Physical Society Division of Fluid Dynamics, November 2020, Chicago (virtually), and as an oral presentation at the Carnegie PhD Scholars' Gathering 2020, February 2020, Discovery Point, Dundee; at the Continuum Mechanics and Industrial Mathematics (CMIM) Research Group Seminar, February 2020, University of Strathclyde, Glasgow; at the 34th Scottish Fluid Mechanics Meeting, May 2021, Robert Gordon University (virtually); at the 14th European Coating Symposium, September 2021, Université Libre de Bruxelles, Brussels (virtually); at the 35th Scottish Fluid Mechanics Meeting, May 2022, Scottish Association for Marine Science, Oban; and at the 14th European Fluid Mechanics Conference, September 2023, Megaron Athens International Conference Centre, Athens.

Aspects of Chapters 4 and 5 have been presented by me as an oral presentation at the 63rd British Applied Mathematics Colloquium, April 2022, Loughborough University, Loughborough (virtual); at the 35th Scottish Fluid Mechanics Meeting, May 2022, Scottish Association for Marine Science, Oban; and at the 1st Spanish Fluid Mechanics Conference, June 2022, University of Cádiz, Cádiz.

Part of the work in Chapter 2 and the work in Chapter 3 is currently being prepared for publication in a peer-reviewed journal.

Chapter 2

Formulation of reduced-order models for the coating of a uniformly rotating horizontal elliptical cylinder by a thick film of fluid and a thin film of fluid

In this chapter, we derive a thick-film reduced-order model and a thin-film reduced-order model, for flow on a two-dimensional uniformly rotating horizontal elliptical cylinder. In particular, in Section 2.1 we introduce the system which we will be investigating and describe the coordinate system. We then derive and nondimensionalise the governing equations and boundary conditions in this coordinate system. In Section 2.2 we derive a thick-film model using a long-wave approximation (see Sections 1.3.2.2 and 1.3.2.3), and recover the special cases of a circular cylinder and a flat plate in Section 2.2.2. In Section 2.3 we derive a thin-film model using a thin-film approximation (see Section 1.3.2.1), and again recover the special cases of a circular cylinder and a flat plate in Section 2.3.2.

2.1 Problem formulation and geometry

We consider the unsteady, two-dimensional coating flow of an incompressible Newtonian fluid of constant density $\hat{\rho}$ and constant viscosity $\hat{\mu}$ on the exterior of a uniformly rotating horizontal elliptical cylinder. Throughout, hats denote dimensional quantities. The length of the semi-major and semi-minor axes of the ellipse are denoted by $\hat{a}$ and $\hat{b}$, respectively, where $\hat{b} \leq \hat{a}$. The cylinder rotates about its axis in the anti-clockwise direction with constant angular velocity $\hat{\Omega}$. The fluid is surrounded by an inviscid, hydrodynamically-passive gas at constant pressure $\hat{p}_a$, and the gas-fluid free surface has constant surface tension $\hat{\gamma}$. The characteristic film thickness is denoted by $\hat{H}$, a characteristic wavelength is denoted by $\hat{\lambda}$, and the mass of the fluid per unit width is denoted by $\hat{M}$.

We work in a non-inertial frame of reference that rotates with the cylinder, and which has its origin located at the axis of the cylinder. In this rotating frame of reference, the surface of the cylinder is located at $\hat{r} = \hat{r}_{\mathrm{e}}(\widetilde{\theta})$, where $(\hat{r}, \widetilde{\theta})$ are the usual polar coordinates, and

$$\hat{r}_{\mathrm{e}}(\widetilde{\theta}) = \frac{\hat{a}\hat{b}}{\sqrt{\hat{a}^2 \sin^2 \widetilde{\theta} + \hat{b}^2 \cos^2 \widetilde{\theta}}}. \tag{2.1.1}$$

The elliptical cylinder is aligned such that the semi-major axis is on $\widetilde{\theta} = 0$.

2.1.1 Body-fitted curvilinear coordinate system

We make use of a body-fitted curvilinear coordinate system $(\widetilde{\theta}, \hat{y})$ as described by Roy et al. [103] (see also Roberts and Li [102] and Wray et al. [55]), as opposed to Parrish et al. [167] (see Section 1.5.2), who used a cylindrical polar coordinate system. As shown in Figure 2.1, $\mathbf{e}_1$ and $\mathbf{e}_3$ are unit vectors in the directions parallel and perpendicular to the surface of the cylinder, respectively. In particular, the coordinate $(\widetilde{\theta}, \hat{y})$ corresponds to a point which is a distance $\hat{y}$ in the direction $\mathbf{e}_3$ from (i.e. perpendicular to) the surface of the cylinder at the point $\hat{r} = \hat{r}_{\mathrm{e}}(\widetilde{\theta})$, where

$$\mathbf{e}_1 = \frac{-\hat{a} \sin \widetilde{\theta} \mathbf{e}_X + \hat{b} \cos \widetilde{\theta} \mathbf{e}_Y}{\hat{m}}, \quad \mathbf{e}_3 = \frac{\hat{b} \cos \widetilde{\theta} \mathbf{e}_X + \hat{a} \sin \widetilde{\theta} \mathbf{e}_Y}{\hat{m}}, \tag{2.1.2}$$

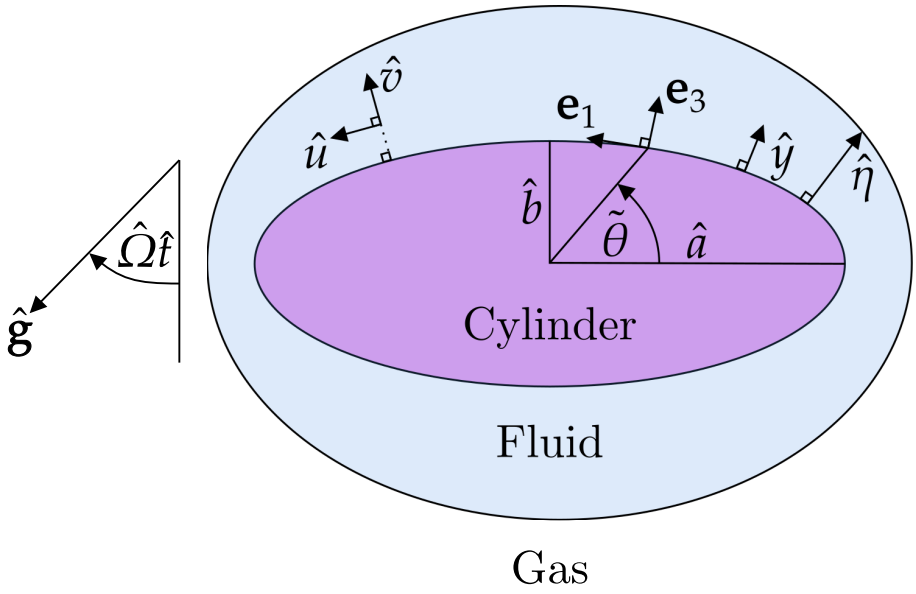

Figure 2.1: Schematic of the elliptical cylinder in a body-fitted curvilinear coordinate system in the rotating frame of reference.

in which

$$\hat{m}(\widetilde{\theta}) = \sqrt{\hat{a}^2 \sin^2 \widetilde{\theta} + \hat{b}^2 \cos^2 \widetilde{\theta}} \tag{2.1.3}$$

is the metric scale factor, and $\mathbf{e}_X$ and $\mathbf{e}_Y$ are the unit vectors in the horizontal and vertical directions, respectively. The metric scale factor ensures that each $\Delta\widetilde{\theta}$ results in the same $\Delta\hat{s}$ (where $\hat{s}$ denotes an arc length) regardless of the current value of $\widetilde{\theta}$, and the spatial scale factor, namely

$$\hat{h}(\widetilde{\theta}, \hat{y}) = \hat{m} + \frac{\hat{a}\hat{b}\hat{y}}{\hat{m}^2}, \tag{2.1.4}$$

extends this into the fluid layer. Hence, the surface of the cylinder is located at $\hat{y} = 0$, and the free surface is denoted by $\hat{y} = \hat{\eta}(\widetilde{\theta}, \hat{t})$, where $\hat{t}$ is time. The velocities in the $\mathbf{e}_1$ and $\mathbf{e}_3$ direction are denoted by $\hat{u}(\widetilde{\theta}, \hat{y}, \hat{t})$ and $\hat{v}(\widetilde{\theta}, \hat{y}, \hat{t})$, respectively. A schematic of this body-fitted curvilinear coordinate system in the rotating frame of reference is shown in Figure 2.1.

2.1.2 Governing equations in vector form

The fluid satisfies the continuity and Navier–Stokes equations, which in this reference frame are [224, Chapter 3]

$$\nabla\cdot\hat{\mathbf{u}} = 0, \quad \hat{\rho}\left(\hat{\mathbf{u}}_{\hat{t}} + \hat{\mathbf{u}}\cdot\nabla\hat{\mathbf{u}}\right) = -\nabla\hat{p} + \hat{\mu}\nabla^2\hat{\mathbf{u}} - \hat{\rho}\hat{\boldsymbol{\Omega}}\times\left(\hat{\boldsymbol{\Omega}}\times\hat{\mathbf{x}}\right) - 2\hat{\rho}\hat{\boldsymbol{\Omega}}\times\hat{\mathbf{u}} + \hat{\rho}\hat{\mathbf{g}}, \tag{2.1.5}$$

where $\hat{\boldsymbol{u}} = (\hat{u}(\widetilde{\theta},\hat{y},\hat{t}),\hat{v}(\widetilde{\theta},\hat{y},\hat{t}))$ and $\hat{p}(\widetilde{\theta},\hat{y},\hat{t})$ are the velocity and pressure of the fluid, respectively, $\hat{\mathbf{g}}$ is the acceleration due to gravity, $\hat{\boldsymbol{\Omega}} = \hat{\Omega}\mathbf{e}_Z$ where $\mathbf{e}_Z$ is the unit vector parallel to the axis of the cylinder, and

$$\hat{\mathbf{x}} = \hat{a}\cos\widetilde{\theta}\mathbf{e}_X + \hat{b}\sin\widetilde{\theta}\mathbf{e}_Y + \hat{y}\mathbf{e}_3 \tag{2.1.6}$$

is the spatial position. The boundary conditions are no-slip and impermeability conditions at the surface of the cylinder, $\hat{y} = 0$,

$$\hat{\mathbf{u}} = \mathbf{0}, \tag{2.1.7}$$

and the tangential and normal stress balance conditions at the free surface, $\hat{y} = \hat{\eta}$,

$$\left[\hat{\mathbf{n}}\cdot\hat{\mathbf{T}}\cdot\hat{\mathbf{t}}\right]_F^G = 0, \quad \left[\hat{\mathbf{n}}\cdot\hat{\mathbf{T}}\cdot\hat{\mathbf{n}}\right]_F^G = \hat{\gamma}\hat{\kappa}, \tag{2.1.8}$$

where $[\cdot]_F^G$ represents the jump in a quantity at the free surface between the fluid and gas regions. The total stress tensor is given by

$$\hat{\mathbf{T}} = -\hat{p}\mathbf{I} + \hat{\mu}\left[\nabla\hat{\mathbf{u}} + (\nabla\hat{\mathbf{u}})^{\mathrm{T}}\right], \tag{2.1.9}$$

where $\mathbf{I}$ is the identity tensor, the unit normal and tangential vectors to the free surface are

$$\hat{\mathbf{n}} = \frac{-\dfrac{\partial\hat{\eta}}{\partial\widetilde{\theta}}\mathbf{e}_1 + \hat{h}\mathbf{e}_3}{\sqrt{\hat{h}^2 + \left(\dfrac{\partial\hat{\eta}}{\partial\widetilde{\theta}}\right)^2}}, \quad \hat{\mathbf{t}} = \frac{\hat{h}\mathbf{e}_1 + \dfrac{\partial\hat{\eta}}{\partial\widetilde{\theta}}\mathbf{e}_3}{\sqrt{\hat{h}^2 + \left(\dfrac{\partial\hat{\eta}}{\partial\widetilde{\theta}}\right)^2}}, \tag{2.1.10}$$

respectively, and the interfacial curvature is given by

$$\hat{\kappa}(\widetilde{\theta},\hat{t}) = \nabla\cdot\hat{\mathbf{n}}. \tag{2.1.11}$$

The system (2.1.5)–(2.1.11) is closed by the kinematic condition at the free surface

$$\frac{D}{D\hat{t}}\left(\hat{y}-\hat{\eta}\right)=0, \tag{2.1.12}$$

where $D/D\hat{t}=\partial/\partial\hat{t}+\hat{\mathbf{u}}\cdot\nabla$ is the material derivative.

2.1.3 Governing equations in coordinate form

The system (2.1.5)–(2.1.12) is nondimensionalised using

$$\begin{gathered}\hat{y}=\hat{a}\widetilde{y},\quad \hat{\eta}=\hat{a}\widetilde{\eta},\quad \hat{u}=\hat{V}\widetilde{u},\quad \hat{v}=\hat{V}\widetilde{v},\quad \hat{p}=\frac{\hat{\mu}\hat{V}}{\hat{a}}\widetilde{p},\quad \hat{t}=\frac{\hat{a}}{\hat{V}}\widetilde{t}\\ \hat{\kappa}=\frac{1}{\hat{a}}\widetilde{\kappa},\quad \hat{M}=\hat{\rho}\hat{a}^2\widetilde{M},\quad \hat{m}=\hat{a}\widetilde{m},\quad \hat{h}=\hat{a}\widetilde{h}\end{gathered} \tag{2.1.13}$$

where $\hat{V}=\hat{\rho}\hat{g}\hat{a}^2/\hat{\mu}$ is a characteristic velocity for gravitational drainage. This gives rise to six dimensionless parameters, namely

$$Ca=\frac{\hat{\mu}\hat{V}}{\hat{\gamma}},\quad Re=\frac{\hat{\rho}\hat{V}\hat{a}}{\hat{\mu}},\quad W=\hat{\Omega}\sqrt{\frac{\hat{a}}{\hat{g}}},\quad b=\frac{\hat{b}}{\hat{a}},\quad H=\frac{\hat{H}}{\hat{a}},\quad \lambda=\frac{\hat{\lambda}}{\hat{a}}, \tag{2.1.14}$$

representing a capillary number, a Reynolds number, the dimensionless rotation speed, and dimensionless measures of the length of the semi-minor axis, the characteristic film thickness, and a characteristic wavelength, respectively.

In this novel application of a body-fitted curvilinear coordinate system (as described by Roy et al. [103], and discussed in Section 2.1.1) to flow on a two-dimensional uniformly rotating horizontal elliptical cylinder, the continuity equation and the azimuthal and radial components of the Navier–Stokes equations (2.1.5) for flow on a uniformly rotating horizontal elliptical cylinder are

$$\frac{\partial\widetilde{u}}{\partial\widetilde{\theta}}+\frac{\partial(\widetilde{h}\widetilde{v})}{\partial\widetilde{y}}=0, \tag{2.1.15}$$

$$
\begin{aligned}
&Re\left(\frac{\partial\widetilde{u}}{\partial\widetilde{t}}+\frac{\widetilde{u}}{\widetilde{h}}\frac{\partial\widetilde{u}}{\partial\widetilde{\theta}}+\widetilde{v}\frac{\partial\widetilde{u}}{\partial\widetilde{y}}+\frac{\widetilde{u}\widetilde{v}b}{\widetilde{h}\widetilde{m}^2}\right)\\
=&-\frac{1}{\widetilde{h}}\frac{\partial\widetilde{p}}{\partial\widetilde{\theta}}+\frac{2}{\widetilde{h}^2}\frac{\partial\widetilde{h}}{\partial\widetilde{y}}\frac{\partial\widetilde{v}}{\partial\widetilde{\theta}}-\frac{1}{\widetilde{h}^2}\frac{\partial\widetilde{h}}{\partial\widetilde{\theta}}\frac{\partial\widetilde{u}}{\partial\widetilde{\theta}}+\frac{1}{\widetilde{h}}\frac{\partial}{\partial\widetilde{\theta}}\left(\frac{1}{\widetilde{h}}\frac{\partial\widetilde{h}}{\partial\widetilde{y}}\right)\widetilde{v}+\frac{1}{\widetilde{h}^2}\frac{\partial^2\widetilde{u}}{\partial\widetilde{\theta}^2}\\
&+\frac{\partial}{\partial\widetilde{y}}\left(\frac{1}{\widetilde{h}}\frac{\partial(\widetilde{h}\widetilde{u})}{\partial\widetilde{y}}\right)-W^2\frac{(1-b^2)}{2\widetilde{m}}\sin 2\widetilde{\theta}-2W\sqrt{Re}\widetilde{v}\\
&-\frac{1}{\widetilde{m}}\left[b\cos\widetilde{\theta}\cos\left(\widetilde{V}_\Omega\widetilde{t}\right)-\sin\widetilde{\theta}\sin\left(\widetilde{V}_\Omega\widetilde{t}\right)\right],
\end{aligned}
\tag{2.1.16}
$$

$$
\begin{aligned}
&Re\left(\frac{\partial\widetilde{v}}{\partial\widetilde{t}}+\frac{\widetilde{u}}{\widetilde{h}}\frac{\partial\widetilde{v}}{\partial\widetilde{\theta}}+\widetilde{v}\frac{\partial\widetilde{v}}{\partial\widetilde{y}}-\frac{b\widetilde{u}^2}{\widetilde{h}\widetilde{m}^2}\right)\\
=&-\frac{\partial\widetilde{p}}{\partial\widetilde{y}}-\frac{1}{\widetilde{h}^2}\frac{\partial\widetilde{h}}{\partial\widetilde{\theta}}\frac{\partial\widetilde{v}}{\partial\widetilde{\theta}}+\frac{1}{\widetilde{h}^2}\frac{\partial^2\widetilde{v}}{\partial\widetilde{\theta}^2}-\frac{1}{\widetilde{h}}\frac{\partial}{\partial\widetilde{\theta}}\left(\frac{1}{\widetilde{h}}\frac{\partial\widetilde{h}}{\partial\widetilde{y}}\right)\widetilde{u}-\frac{1}{\widetilde{h}^2}\frac{\partial\widetilde{h}}{\partial\widetilde{y}}\frac{\partial\widetilde{u}}{\partial\widetilde{\theta}}\\
&+\frac{2}{\widetilde{h}}\frac{\partial\widetilde{h}}{\partial\widetilde{y}}\frac{\partial\widetilde{v}}{\partial\widetilde{y}}+\frac{\partial^2\widetilde{v}}{\partial\widetilde{y}^2}+W^2\left(\frac{b}{\widetilde{m}}+\widetilde{y}\right)+2W\sqrt{Re}\widetilde{u}\\
&-\frac{1}{\widetilde{m}}\left[\sin\widetilde{\theta}\cos\left(\widetilde{V}_\Omega\widetilde{t}\right)+b\cos\widetilde{\theta}\sin\left(\widetilde{V}_\Omega\widetilde{t}\right)\right],
\end{aligned}
\tag{2.1.17}
$$

respectively, where

$$
\widetilde{V}_\Omega=\frac{W}{\sqrt{Re}}=\frac{\hat{\Omega}\hat{a}}{\hat{V}} \tag{2.1.18}
$$

is the dimensionless ratio of the cylinder velocity to the characteristic velocity. At the surface of the cylinder, $\widetilde{y}=0$, we have the no-slip and impermeability conditions (2.1.7)

$$
\widetilde{u}=\widetilde{v}=0. \tag{2.1.19}
$$

The total stress tensor (2.1.9) becomes

$$
\widetilde{\mathbf{T}}=\begin{bmatrix}\dfrac{2}{\widetilde{h}}\dfrac{\partial\widetilde{u}}{\partial\widetilde{\theta}}+\dfrac{2b}{\widetilde{h}\widetilde{m}^2}\widetilde{v}-\widetilde{p} & \dfrac{1}{\widetilde{h}}\dfrac{\partial\widetilde{v}}{\partial\widetilde{\theta}}+\dfrac{\partial\widetilde{u}}{\partial\widetilde{y}}-\dfrac{b}{\widetilde{h}\widetilde{m}^2}\widetilde{u}\\ \dfrac{1}{\widetilde{h}}\dfrac{\partial\widetilde{v}}{\partial\widetilde{\theta}}+\dfrac{\partial\widetilde{u}}{\partial\widetilde{y}}-\dfrac{b}{\widetilde{h}\widetilde{m}^2}\widetilde{u} & 2\dfrac{\partial\widetilde{v}}{\partial\widetilde{y}}-\widetilde{p}\end{bmatrix}, \tag{2.1.20}
$$

At the free surface, $\widetilde{y}=\widetilde{\eta}$, we have the tangential stress balance (2.1.8)

$$
4\widetilde{h}^2\frac{\partial\widetilde{\eta}}{\partial\widetilde{\theta}}\frac{\partial\widetilde{v}}{\partial\widetilde{y}}+\left[\frac{\partial\widetilde{v}}{\partial\widetilde{\theta}}+\widetilde{h}^2\frac{\partial}{\partial\widetilde{y}}\left(\frac{\widetilde{u}}{\widetilde{h}}\right)\right]\left[1-\left(\frac{\partial\widetilde{\eta}}{\partial\widetilde{\theta}}\right)^2\right]=0, \tag{2.1.21}
$$

the normal stress balance (2.1.8)

$$\left[\frac{\widetilde{\kappa}}{Ca}-\widetilde{p}\right]\left[\widetilde{h}^2+\left(\frac{\partial\widetilde{\eta}}{\partial\widetilde{\theta}}\right)^2\right]+2\frac{\partial\widetilde{v}}{\partial\widetilde{y}}\left[\widetilde{h}^2-\left(\frac{\partial\widetilde{\eta}}{\partial\widetilde{\theta}}\right)^2\right]-2\frac{\partial\widetilde{\eta}}{\partial\widetilde{\theta}}\left[\frac{\partial\widetilde{v}}{\partial\widetilde{\theta}}+\widetilde{h}^2\frac{\partial}{\partial\widetilde{y}}\left(\frac{\widetilde{u}}{\widetilde{h}}\right)\right]=0, \tag{2.1.22}$$

where the interfacial curvature (2.1.11) becomes

$$\widetilde{\kappa}=\frac{\frac{b}{\widetilde{m}^2}\widetilde{h}^2+\frac{\partial\widetilde{\eta}}{\partial\widetilde{\theta}}\left(\frac{b}{\widetilde{m}^2}\frac{\partial\widetilde{\eta}}{\partial\widetilde{\theta}}+\frac{\partial\widetilde{h}}{\partial\widetilde{\theta}}\right)-\widetilde{h}\frac{\partial^2\widetilde{\eta}}{\partial\widetilde{\theta}^2}}{\left[\widetilde{h}^2+\left(\frac{\partial\widetilde{\eta}}{\partial\widetilde{\theta}}\right)^2\right]^{3/2}}, \tag{2.1.23}$$

and the kinematic condition (2.1.12)

$$\frac{\partial\widetilde{\eta}}{\partial\widetilde{t}}+\frac{\widetilde{u}}{\widetilde{h}}\frac{\partial\widetilde{\eta}}{\partial\widetilde{\theta}}-\widetilde{v}=\frac{\partial\widetilde{\eta}}{\partial\widetilde{t}}+\frac{1}{\widetilde{h}}\frac{\partial}{\partial\widetilde{\theta}}\int_0^{\widetilde{\eta}}\widetilde{u}\,\mathrm{d}\widetilde{y}=0. \tag{2.1.24}$$

The mass of the fluid is

$$\widetilde{M}=\int_0^{2\pi}\widetilde{m}\widetilde{\eta}+\frac{1}{2}\frac{b}{\widetilde{m}^2}\widetilde{\eta}^2\,\mathrm{d}\widetilde{\theta}. \tag{2.1.25}$$

2.2 Thick-film equations

In this section we exploit the fact that a characteristic wavelength in the azimuthal direction is large compared to both a characteristic film thickness and the length of the semi-major axis in order to derive a reduced-order model in the thick-film regime, which we refer to as the *thick-film ellipse equation*.

2.2.1 Thick-film ellipse equation

We examine the thick-film regime in which the long-wave small aspect ratio is $\delta = 1/\lambda \ll 1$ (and $H = \mathcal{O}(1)$, as discussed in Section 1.3.2.2). In particular, we

use the long-wave scalings

$$\begin{aligned}\frac{\partial}{\partial\widetilde{\theta}} = \delta\frac{\partial}{\partial\theta}, \quad \widetilde{y} = y, \quad \widetilde{\eta} = \eta, \quad \widetilde{u} = u, \quad \widetilde{v} = \delta v, \quad \widetilde{p} = p,\\ \widetilde{t} = \frac{t}{\delta}, \quad \widetilde{\kappa} = \kappa, \quad \widetilde{M} = M, \quad \widetilde{m} = m, \quad \widetilde{h} = h.\end{aligned} \tag{2.2.1}$$

The scaling of the variation of θ follows from the assumption that variations are slow in the azimuthal direction compared to variations in the radial direction. Note that we have (as discussed in Section 1.3.2.3) chosen to scale the variation of θ and not θ itself, following Wray et al. [55] and Wray and Cimpeanu [60], since the azimuthal domain length is fixed at 2π, and thus cannot be assumed to be "long". The scaling on v is chosen in order to balance the radial and azimuthal components of velocity at leading order in the continuity equation (2.1.15). The scaling on t is chosen in order to retain the time derivative by balancing leading order terms in the kinematic condition (2.1.24).

In order to derive the thick-film ellipse equation correct to first order in δ, we require equations (2.1.15) and (2.1.16) correct to first order, namely

$$\frac{\partial u}{\partial\theta} + v\frac{\partial h}{\partial y} + h\frac{\partial v}{\partial y} = 0, \tag{2.2.2}$$

$$\begin{aligned}-\delta\frac{1}{h}\frac{\partial p}{\partial\theta} + \frac{\partial}{\partial y}\left(\frac{1}{h}\frac{\partial\left(hu\right)}{\partial y}\right) - W^2\frac{(1-b^2)}{2m}\sin 2\theta\\ - \frac{1}{m}\left[b\cos\theta\cos\left(V_\Omega^{(\text{thick})}t\right) - \sin\theta\sin\left(V_\Omega^{(\text{thick})}t\right)\right] + \mathcal{O}(\delta^2) = 0,\end{aligned} \tag{2.2.3}$$

and equation (2.1.17) to leading order, namely

$$-\frac{\partial p}{\partial y} + W^2\left(\frac{b}{m} + y\right) - \frac{1}{m}\left[\sin\theta\cos\left(V_\Omega^{(\text{thick})}t\right) + b\cos\theta\sin\left(V_\Omega^{(\text{thick})}t\right)\right] + \mathcal{O}(\delta) = 0, \tag{2.2.4}$$

where

$$V_\Omega^{(\text{thick})} = \frac{W}{\delta\sqrt{Re}} = \frac{\hat{\Omega}\hat{a}^2}{\hat{\lambda}\hat{V}} \tag{2.2.5}$$

is the dimensionless ratio of the cylinder velocity to the characteristic velocity (in the thick-film regime). In deriving (2.2.2)–(2.2.4), we retain the effect of centrifugation while the effects of both convective inertia and the Coriolis force have been neglected by assuming that Re is at most $\mathcal{O}(\delta)$ and that $W\sqrt{Re}$ is at most $\mathcal{O}(\delta)$, respectively, which then allows for $V_\Omega^{(\text{thick})}$ to be at most $\mathcal{O}(\delta^{-1})$.

At the surface of the cylinder, $y = 0$, the no-slip and impermeability conditions (2.1.19) are

$$u = v = 0. \tag{2.2.6}$$

At the free surface, $y = \eta$, the tangential stress balance (2.1.21) is required correct to first order

$$h\frac{\partial u}{\partial y} - u\frac{\partial h}{\partial y} + \mathcal{O}(\delta^2) = 0, \tag{2.2.7}$$

and the normal stress balance (2.1.22) is required correct to leading order

$$p = \frac{\kappa}{Ca} + \mathcal{O}(\delta), \tag{2.2.8}$$

where the interfacial curvature (2.1.23) is now

$$\kappa = \frac{\dfrac{b}{m^2}h^2 + \delta^2\dfrac{\partial\eta}{\partial\theta}\left(\dfrac{b}{m^2}\dfrac{\partial\eta}{\partial\theta} + \dfrac{\partial h}{\partial\theta}\right) - \delta^2 h\dfrac{\partial^2\eta}{\partial\theta^2}}{\left[h^2 + \delta^2\left(\dfrac{\partial\eta}{\partial\theta}\right)^2\right]^{3/2}}, \tag{2.2.9}$$

while the kinematic condition (2.1.24) becomes

$$\frac{\partial\eta}{\partial t} + \frac{1}{h}\frac{\partial}{\partial\theta}\int_0^\eta u \, \mathrm{d}y = 0. \tag{2.2.10}$$

As discussed in Section 1.3.2.3, we retain the full form of the interfacial curvature κ (2.2.9) here. The mass of the fluid (2.1.25) is now

$$M = \int_0^{2\pi} m\eta + \frac{1}{2}\frac{b}{m^2}\eta^2 \, \mathrm{d}\theta. \tag{2.2.11}$$

The leading order pressure p can be determined by solving the leading-order radial component of the Navier–Stokes equation (2.2.4) subject to the leading-order normal stress balance (2.2.8) to yield,

$$\begin{aligned} p = \frac{\kappa}{Ca} + W^2\left(\frac{b}{m}(y-\eta) + \frac{y^2-\eta^2}{2}\right) \\ - \frac{y-\eta}{m}\left[\sin\theta\cos\left(V_\Omega^{(\text{thick})}t\right) + b\cos\theta\sin\left(V_\Omega^{(\text{thick})}t\right)\right]. \end{aligned} \tag{2.2.12}$$

Substituting the leading order solution for p (2.2.12) into the first-order azimuthal

component of the Navier–Stokes equation (2.2.3) yields

$$\begin{aligned}
&\frac{\partial}{\partial y}\left\{\frac{m^3}{(m^3+by)}\frac{\partial}{\partial y}\left[\left(1+\frac{by}{m^3}\right)u\right]\right\} \qquad (2.2.13)\\
&=\frac{\delta m^2}{(m^3+by)}\frac{1}{Ca}\frac{\partial\kappa}{\partial\theta}+\frac{\delta W^2 m^2}{(m^3+by)}\frac{\partial}{\partial\theta}\left[\frac{b}{m}(y-\eta)+\frac{y^2-\eta^2}{2}\right]\\
&\quad-\frac{\delta m^2}{(m^3+by)}\frac{\partial}{\partial\theta}\left[\frac{y-\eta}{m}\left(\sin\theta\cos\left(V_\Omega^{(\text{thick})}t\right)+b\cos\theta\sin\left(V_\Omega^{(\text{thick})}t\right)\right)\right]\\
&\quad+W^2\frac{(1-b^2)}{2m}\sin 2\theta+\frac{1}{m}\left[b\cos\theta\cos\left(V_\Omega^{(\text{thick})}t\right)-\sin\theta\sin\left(V_\Omega^{(\text{thick})}t\right)\right].
\end{aligned}$$

The azimuthal velocity u can be determined up to first order by solving (2.2.13) subject to the no-slip condition (2.2.6) and the first-order tangential stress balance (2.2.7). The resulting expression for u can then be substituted into the kinematic condition (2.2.10) to determine the first-order evolution equation for thick-film flow on the exterior of a uniformly rotating horizontal elliptical cylinder (i.e. the thick-film ellipse equation), namely

$$\begin{aligned}
&\frac{m^4}{2b}\frac{\partial}{\partial t}\left(\Gamma^2\right)+\frac{\partial}{\partial\theta}\left\{\frac{m^{11}}{72b^4}\left(\delta\frac{9bM_1}{m^3}\frac{\partial}{\partial\theta}\left[\frac{1}{Ca}\kappa-W^2\left(m^2(\Gamma-1)+\frac{m^6(\Gamma-1)^2}{2b^2}\right)\right.\right.\right.\\
&\qquad\left.+\frac{m^2(\Gamma-1)}{b}\left(\sin\theta\cos\left(V_\Omega^{(\text{thick})}t\right)+b\cos\theta\sin\left(V_\Omega^{(\text{thick})}t\right)\right)\right]\\
&+\frac{2bM_2}{m^2}\left[\frac{1}{m}\left(b\cos\theta\cos\left(V_\Omega^{(\text{thick})}t\right)-\sin\theta\sin\left(V_\Omega^{(\text{thick})}t\right)\right)+W^2\frac{(1-b^2)}{2m}\sin 2\theta\right]\\
&\left.\left.+\delta(2M_2-9M_1)\frac{\partial}{\partial\theta}\left[W^2\frac{b}{m}-\frac{1}{m}\left(\sin\theta\cos\left(V_\Omega^{(\text{thick})}t\right)+b\cos\theta\sin\left(V_\Omega^{(\text{thick})}t\right)\right)\right]\right)\right\}=0, \qquad (2.2.14)
\end{aligned}$$

where

$$\Gamma(\theta,t)=1+\frac{b}{m(\theta)^3}\eta(\theta,t), \qquad (2.2.15)$$

and $M_1(\theta,t)$ and $M_2(\theta,t)$ are mobility coefficients defined by

$$M_1=1-\Gamma^4+4\Gamma^2\log\Gamma \qquad (2.2.16)$$

and

$$M_2=2-6\Gamma^2-3\Gamma^5+\Gamma^3(7+6\log\Gamma), \qquad (2.2.17)$$

respectively. The thick-film ellipse equation (2.2.14) incorporates the effects of cylinder eccentricity, rotation, gravity, centrifugation, viscosity, and surface tension, and is appropriate for a film thickness of order unity (see Section 1.3.2.3).

In order to solve thick-film equations, such as the thick-film ellipse equation (2.2.14), we work in non-dimensional, but otherwise unscaled, variables [55; 60]. However, due to time constraints, we do not study the results of the thick-film ellipse equation (2.2.14) in the present work.

2.2.2 Special cases of the thick-film ellipse equation

Two special cases of equation (2.2.14) are of particular interest. In the case $b = 1$ the cylinder is circular, and equation (2.2.14) becomes

$$\frac{1}{2}\frac{\partial}{\partial t}\left(S^2\right) + \frac{1}{72}\frac{\partial}{\partial \theta}\Bigg\{\delta 9 M_1^* \frac{\partial}{\partial \theta}\left[\frac{1}{Ca}\kappa - W^2\frac{S^2}{2} + S\sin\left(\theta + V_\Omega^{(\text{thick})}t\right)\right] + 2\left(1-\delta\right)M_2^*\cos\left(\theta + V_\Omega^{(\text{thick})}t\right)\Bigg\} = 0, \tag{2.2.18}$$

where

$$S(\theta, t) = 1 + \eta(\theta, t), \tag{2.2.19}$$

and $M_1^*(\theta, t)$ and $M_2^*(\theta, t)$ are mobility coefficients defined by

$$M_1^* = 1 - S^4 + 4S^2\log S \tag{2.2.20}$$

and

$$M_2^* = 2 - 6S^2 - 3S^5 + S^3\left(7 + 6\log S\right), \tag{2.2.21}$$

respectively, with

$$\kappa = \frac{2\delta^2\left(\dfrac{\partial S}{\partial \theta}\right)^2 + S\left(S - \delta^2\dfrac{\partial^2 S}{\partial \theta^2}\right)}{\left[S^2 + \delta^2\left(\dfrac{\partial S}{\partial \theta}\right)^2\right]^{3/2}}. \tag{2.2.22}$$

Equation (2.2.18) matches, for example, equation (3.18) of Wray and Cimpeanu [60] up to differences in scaling, when expressed in the rotating frame.

In the case $b \to 0^+$ the cylinder is a flat plate. Making the transformation

$x = -\cos\theta$, equation (2.2.14) becomes

$$\frac{\partial \eta}{\partial t} + \frac{\partial}{\partial x}\left[\frac{\eta^3}{3}\left(-\delta\frac{1}{Ca}\frac{\partial \kappa}{\partial x} + \sin\left(V_\Omega^{(\text{thick})}t\right) + W^2 x \right.\right. \\ \left.\left. - \delta\cos\left(V_\Omega^{(\text{thick})}t\right)\frac{\partial \eta}{\partial x} - \delta W^2 \eta \frac{\partial \eta}{\partial x}\right)\right] = 0, \tag{2.2.23}$$

where

$$\kappa = -\frac{\delta^2 \dfrac{\partial^2 \eta}{\partial x^2}}{\left[1 + \delta^2\left(\dfrac{\partial \eta}{\partial x}\right)^2\right]^{3/2}}. \tag{2.2.24}$$

However, perhaps more well known is the equation for an inclined flat plate, which we can also recover from equation (2.2.23) in the stationary case by the ad hoc replacement of $V_\Omega^{(\text{thick})}t$ with a constant. In the case $W = 0$ and setting $V_\Omega^{(\text{thick})}t \equiv \alpha$ to be a constant, the flat plate is stationary and inclined at the angle α to the horizontal, and equation (2.2.23) becomes

$$\frac{\partial \eta}{\partial t} + \frac{\partial}{\partial x}\left[\frac{\eta^3}{3}\left(-\delta\frac{1}{Ca}\frac{\partial \kappa}{\partial x} + \sin\alpha - \delta\cos\alpha\frac{\partial \eta}{\partial x}\right)\right] = 0. \tag{2.2.25}$$

Equation (2.2.25) matches, for example, the Benney equation (1.2.1) up to differences in scaling (and in the absence of inertia).

2.3 Thin-film equations

In this section we exploit the fact that the characteristic film thickness is small compared to both a characteristic wavelength in the azimuthal direction and the length of the semi-major axis in order to derive a reduced-order model in the thin-film regime, which we refer to as the *thin-film ellipse equation*.

2.3.1 Thin-film ellipse equation

We now examine the thin-film regime in which the thin-film small aspect ratio is $\varepsilon = H \ll 1$ (and $\lambda = \mathcal{O}(1)$, as discussed in Section 1.3.2.1). In particular, we use

the thin-film scalings

$$\begin{gathered}\widetilde{\theta}=\theta, \quad \widetilde{y}=\varepsilon y, \quad \widetilde{\eta}=\varepsilon\eta, \quad \widetilde{u}=\varepsilon^2 u, \quad \widetilde{v}=\varepsilon^3 v, \quad \widetilde{p}=\varepsilon p, \\ \widetilde{t}=\frac{t}{\varepsilon^2}, \quad \widetilde{\kappa}=\kappa, \quad \widetilde{M}=\varepsilon M, \quad \widetilde{m}=m, \quad \widetilde{h}=h.\end{gathered} \tag{2.3.1}$$

The scalings (2.3.1) are the same as those used by Evans et al. [56; 150], Li et al. [165], and Li and Kumar [225]. Due to the difference of coordinate systems, the scalings of Parrish et al. [167], who used a cylindrical polar coordinate system, appear different but are consistent with the present scalings (2.3.1) for a body-fitted curvilinear coordinate system.

In order to derive the thin-film ellipse equation correct to first order in ε, we require equations (2.1.15) and (2.1.16) correct to first order, namely

$$\frac{\partial u}{\partial\theta}+\varepsilon v\frac{b}{m^2}+\left(m+\varepsilon\frac{b}{m^2}y\right)\frac{\partial v}{\partial y}=0, \tag{2.3.2}$$

$$\begin{aligned}&-\varepsilon\frac{1}{h}\frac{\partial p}{\partial\theta}+\frac{\partial}{\partial y}\left(\frac{1}{h}\frac{\partial\left(hu\right)}{\partial y}\right)-W^2\frac{(1-b^2)}{2m}\sin 2\theta \\ &\quad-\frac{1}{m}\left[b\cos\theta\cos\left(V_\Omega^{(\text{thin})}t\right)-\sin\theta\sin\left(V_\Omega^{(\text{thin})}t\right)\right]+\mathcal{O}(\varepsilon^2)=0,\end{aligned} \tag{2.3.3}$$

and equation (2.1.17) to leading order, namely

$$-\frac{\partial p}{\partial y}+W^2\frac{b}{m}-\frac{1}{m}\left[\sin\theta\cos\left(V_\Omega^{(\text{thin})}t\right)+b\cos\theta\sin\left(V_\Omega^{(\text{thin})}t\right)\right]+\mathcal{O}(\varepsilon)=0, \tag{2.3.4}$$

where

$$V_\Omega^{(\text{thin})}=\frac{W}{\varepsilon^2\sqrt{Re}}=\frac{\hat{\Omega}\hat{a}^3}{\hat{H}^2\hat{V}} \tag{2.3.5}$$

is the dimensionless ratio of the cylinder velocity to the characteristic velocity (in the thin-film regime). In deriving (2.3.2)–(2.3.4), we retain the effect of centrifugation while the effect of both convective inertia and the Coriolis force have been neglected by assuming that Re is at most $\mathcal{O}(\varepsilon^{-2})$ and that $W\sqrt{Re}$ is at most $\mathcal{O}(\varepsilon^{-1})$, respectively, which then allows for $V_\Omega^{(\text{thin})}$ to be at most $\mathcal{O}(\varepsilon^{-1})$.

At the surface of the cylinder, $y=0$, the no-slip and impermeability conditions (2.1.19) are

$$u=v=0. \tag{2.3.6}$$

At the free surface, $y=\eta$, the tangential stress balance (2.1.21) is required correct

to first order

$$\frac{\partial u}{\partial y} - \varepsilon \frac{b\eta}{m^3}\frac{\partial u}{\partial y} - \varepsilon \frac{b}{m^3}u + \mathcal{O}(\varepsilon^2) = 0, \tag{2.3.7}$$

and the normal stress balance (2.1.22) is required correct to leading order

$$p = \frac{1}{Ca}\left[\frac{1}{\varepsilon}\frac{b}{m^3} + \frac{1}{m^6}\left(m^3\frac{\mathrm{d}m}{\mathrm{d}\theta}\frac{\partial \eta}{\partial \theta} - b^2\eta - m^4\frac{\partial^2 \eta}{\partial \theta^2}\right)\right] + \mathcal{O}(\varepsilon), \tag{2.3.8}$$

while the kinematic condition (2.1.24) becomes

$$\left(m + \varepsilon\frac{b}{m^2}\eta\right)\frac{\partial \eta}{\partial t} + \frac{\partial}{\partial \theta}\int_0^\eta u \ \mathrm{d}y = 0. \tag{2.3.9}$$

The mass of the fluid (2.1.25) is now

$$M = \int_0^{2\pi} m\eta + \frac{\varepsilon}{2}\frac{b}{m^2}\eta^2 \ \mathrm{d}\theta. \tag{2.3.10}$$

The leading order pressure p can be determined by solving the leading-order radial component of the Navier–Stokes equation (2.3.4) subject to the leading-order normal stress balance (2.3.8) to yield,

$$\begin{aligned} p = \frac{1}{Ca}\left[\frac{1}{\varepsilon}\frac{b}{m^3} + \frac{1}{m^6}\left(m^3\frac{\mathrm{d}m}{\mathrm{d}\theta}\frac{\partial \eta}{\partial \theta} - b^2\eta - m^4\frac{\partial^2 \eta}{\partial \theta^2}\right)\right] + W^2\frac{b}{m}(y-\eta) \\ - \frac{y-\eta}{m}\left[\sin\theta\cos\left(V_\Omega^{(\mathrm{thin})}t\right) + b\cos\theta\sin\left(V_\Omega^{(\mathrm{thin})}t\right)\right]. \end{aligned} \tag{2.3.11}$$

Substituting the leading order solution for p (2.3.11) into the first-order azimuthal component of the Navier–Stokes equation (2.3.3) yields

$$\begin{aligned} &\left(m + \varepsilon\frac{b}{m^2}y\right)\frac{\partial}{\partial y}\left\{\frac{m^3}{(m^3+\varepsilon by)}\frac{\partial}{\partial y}\left[\left(1+\varepsilon\frac{by}{m^3}\right)u\right]\right\} \\ =&\frac{1}{Ca}\frac{\partial}{\partial \theta}\left[\frac{b}{m^3} + \frac{\varepsilon}{m^6}\left(m^3\frac{\mathrm{d}m}{\mathrm{d}\theta}\frac{\partial \eta}{\partial \theta} - b^2\eta - m^4\frac{\partial^2 \eta}{\partial \theta^2}\right)\right] + \varepsilon W^2\frac{\partial}{\partial \theta}\left[\frac{b}{m}(y-\eta)\right] \\ &- \varepsilon\frac{\partial}{\partial \theta}\left[\frac{y-\eta}{m}\left(\sin\theta\cos\left(V_\Omega^{(\mathrm{thin})}t\right) + b\cos\theta\sin\left(V_\Omega^{(\mathrm{thin})}t\right)\right)\right] \\ &+ W^2\left(1+\varepsilon\frac{b}{m^3}y\right)\frac{(1-b^2)}{2}\sin 2\theta \\ &+ \left(1+\varepsilon\frac{b}{m^3}y\right)\left[b\cos\theta\cos\left(V_\Omega^{(\mathrm{thin})}t\right) - \sin\theta\sin\left(V_\Omega^{(\mathrm{thin})}t\right)\right]. \end{aligned} \tag{2.3.12}$$

The azimuthal velocity u can be determined up to first order by solving (2.3.12) subject to the no-slip condition (2.3.6) and the first-order tangential stress balance (2.3.7). The resulting expression for u can then be substituted into the kinematic condition (2.3.9) to determine the first-order evolution equation for thin-film flow on the exterior of a uniformly rotating horizontal elliptical cylinder (i.e. the thin-film ellipse equation), namely

$$\begin{aligned}\left(m+\varepsilon\frac{b}{m^2}\eta\right)\frac{\partial\eta}{\partial t}+\frac{\partial}{\partial\theta}\Bigg\{&\frac{1}{Ca}\frac{b(1-b^2)\eta^3}{2m^6}\sin 2\theta\left[1+\varepsilon\frac{b\eta}{2m^3}\right]-\frac{\eta^3}{3m}\left[1+\varepsilon\frac{9b\eta}{8m^3}\right]\times\\&\left[W^2\frac{(1-b^2)}{2}\sin 2\theta+b\cos\theta\cos\left(V_\Omega^{(\text{thin})}t\right)-\sin\theta\sin\left(V_\Omega^{(\text{thin})}t\right)\right]\\&-\varepsilon\frac{1}{Ca}\frac{\eta^3}{3m}\frac{\partial}{\partial\theta}\left[\frac{1}{m^6}\left(\frac{m^2(1-b^2)}{2}\sin 2\theta\frac{\partial\eta}{\partial\theta}-b^2\eta-m^4\frac{\partial^2\eta}{\partial\theta^2}\right)\right]\\&+\varepsilon\frac{\eta^3}{3m^2}\left[\frac{3\eta(1-b^2)}{16m^2}\sin 2\theta-\frac{\partial\eta}{\partial\theta}\right]\times\\&\left[\sin\theta\cos\left(V_\Omega^{(\text{thin})}t\right)+b\cos\theta\sin\left(V_\Omega^{(\text{thin})}t\right)-W^2b\right]\\&-\varepsilon\frac{\eta^4}{8m^2}\left(\cos\theta\cos\left(V_\Omega^{(\text{thin})}t\right)-b\sin\theta\sin\left(V_\Omega^{(\text{thin})}t\right)\right)\Bigg\}=0.\end{aligned}\tag{2.3.13}$$

The thin-film ellipse equation (2.3.13) incorporates the effects of cylinder eccentricity, rotation, gravity, centrifugation, viscosity, and surface tension. If we undo the long-wave scalings (2.2.1) in the thick-film ellipse equation (2.2.14), apply the thin-film scalings (2.3.1), and neglect terms of second-order in ε, we recover the thin-film ellipse equation (2.3.13).

2.3.2 Special cases of the thin-film ellipse equation

Two special cases of equation (2.3.13) are of particular interest. In the case $b=1$ the cylinder is circular, and equation (2.3.13) becomes

$$\begin{aligned}(1+\varepsilon\eta)\frac{\partial\eta}{\partial t}+\frac{\partial}{\partial\theta}\Bigg[&\varepsilon\frac{1}{Ca}\frac{\eta^3}{3}\frac{\partial}{\partial\theta}\left(\eta+\frac{\partial^2\eta}{\partial\theta^2}\right)-\cos\left(\theta+V_\Omega^{(\text{thin})}t\right)\left(\frac{\eta^3}{3}+\varepsilon\frac{\eta^4}{2}\right)\\&+\varepsilon\left[W^2-\sin\left(\theta+V_\Omega^{(\text{thin})}t\right)\right]\left(\frac{\eta^3}{3}\frac{\partial\eta}{\partial\theta}\right)\Bigg]=0.\end{aligned}\tag{2.3.14}$$

This recovers, for example, equation (54) of Evans et al. [56] when expressed in the rotating frame. If we undo the long-wave scalings (2.2.1) in the thick-film circle equation (2.2.18), apply the thin-film scalings (2.3.1), and neglect terms of second-order in ε, we recover the thin-film circle equation (2.3.14).

In the case $b \to 0^+$ the cylinder is a flat plate. Making the transformation $x = -\cos\theta$, equation (2.3.13) becomes

$$\frac{\partial \eta}{\partial t} + \frac{\partial}{\partial x}\left[\frac{\eta^3}{3}\left(\varepsilon \frac{1}{Ca}\frac{\partial^3 \eta}{\partial x^3} + \sin\left(V_\Omega^{(\text{thin})} t\right) + W^2 x - \varepsilon \cos\left(V_\Omega^{(\text{thin})} t\right)\frac{\partial \eta}{\partial x}\right)\right] = 0. \tag{2.3.15}$$

If we undo the long-wave scalings (2.2.1) in the thick-film rotating flat plate equation (2.2.23), apply the thin-film scalings (2.3.1), and neglect terms of second-order in ε, we recover the thin-film rotating flat plate equation (2.3.15). For flow on a rotating flat plate, the effects of rotation and centrifugation arise differently in the long-wave approximation than they do in the thin-film approximation. Therefore, despite the substrate being planar, the thick-film rotating flat plate equation (2.2.23) is not equivalent to the thin-film rotating flat plate equation (2.3.15). However, as we now show, these equations are equivalent when the flat plate is stationary.

We recover the equation for an inclined flat plate from equation (2.3.15) by the ad hoc replacement of $V_\Omega^{(\text{thin})} t$ with a constant. In the case $W = 0$ and setting $V_\Omega^{(\text{thin})} t \equiv \alpha$ to be a constant, the flat plate is stationary and inclined at an angle α to the horizontal, and equation (2.3.15) becomes

$$\frac{\partial \eta}{\partial t} + \frac{\partial}{\partial x}\left[\frac{\eta^3}{3}\left(\varepsilon \frac{1}{Ca}\frac{\partial^3 \eta}{\partial x^3} + \sin\alpha - \varepsilon \cos\alpha \frac{\partial \eta}{\partial x}\right)\right] = 0. \tag{2.3.16}$$

This matches, for example, the Benney equation (1.2.1) up to differences in scaling (and in the absence of inertia). The thick-film inclined flat plate equation (2.2.25) is equivalent to the thin-film inclined flat plate equation (2.3.16) as the long-wave small aspect ratio δ, and the thin-film small aspect ratio ε, are equivalent for flow on a (stationary) planar substrate (see Section 1.3.1).

2.4 Conclusions

In this chapter, we derived two novel evolution equations for flow on a two-dimensional uniformly rotating horizontal elliptical cylinder, namely the thick-film ellipse equation (2.2.14), and the thin-film ellipse equation (2.3.13).

In Section 2.1, we introduced and described the problem and the body-fitted curvilinear coordinate system, as shown schematically in Figure 2.1.

In Section 2.2, using a long-wave approximation, we derived a thick-film reduced-order model, namely the thick-film equation (2.2.14), which is appropriate for a film thickness of order unity. We also recovered the special cases of a circular cylinder when $b = 1$ (i.e. equation (2.2.18)) and a flat plate when $b \to 0^+$ (i.e. equations (2.2.23) and (2.2.25)).

In Section 2.3, using a thin-film approximation, we derived a thin-film reduced-order model, namely the thin-film ellipse equation (2.3.13). We also recovered the special cases of a circular cylinder when $b = 1$ (i.e. equation (2.3.14)) and a flat plate when $b \to 0^+$ (i.e. equations (2.3.15) and (2.3.16)). The thin-film ellipse equation (2.3.13), the thin-film circle equation (2.3.14), and the thin-film rotating flat plate equation (2.3.15) are recovered as a special case of the thick-film ellipse equation (2.2.14), the thick-film circle equation (2.2.18), and the thick-film rotating flat plate equation (2.2.23), respectively, and the thick-film inclined flat plate equation (2.2.25) is equivalent to the thin-film inclined flat plate equation (2.3.16).

Chapter 3

Analysis of the thin-film reduced-order model for flow on a uniformly rotating horizontal elliptical cylinder

In this chapter, we analyse the analytical and numerical results of the thin-film ellipse equation (2.3.13) for flow on a two-dimensional uniformly rotating horizontal elliptical cylinder. We provide a variety of analytical results in this chapter, whereas the three previous studies of elliptical cylinders [125; 167; 168], surprisingly, do not present any analytical results (see Section 1.5.2). We also explore a different region of parameter space than these previous studies, and examine the previously uninvestigated special case of a stationary elliptical cylinder. In Section 3.1 we describe the results of a parametric study on the dimensionless rotation speed. In Section 3.2 we analytically explore the effects of small cylinder eccentricity on the steady full-film solution first described by Moffatt [57] (1.4.3). In Sections 3.3–3.6 we investigate the behaviour of the free surface as the dimensionless rotation speed monotonically increases from $W = 0$. Finally, in Section 3.7 we examine the effect of cylinder eccentricity on the results of the parametric study on the dimensionless rotation speed described in Section 3.1.

3.1 Parametric study of the thin-film ellipse equation

3.1.1 Outline of parametric study

The behaviour of the solutions of the thin-film ellipse equation (2.3.13) depends on the unscaled mass $\widetilde{M}$ (via ε), the length of the semi-minor axis b, a Reynolds number Re, a capillary number Ca, and the dimensionless rotation speed W. In light of the high dimensionality of this parameter space, we simplify the task of understanding the behaviour of (2.3.13) by fixing the parameter values

$$\widetilde{M} = 0.3, \quad b = 0.9, \quad Re = 400, \quad Ca = 80, \tag{3.1.1}$$

and then performing a parametric study on the dimensionless rotation speed W. These are the default parameter values that will be used throughout, except where noted otherwise. These parameter values were chosen during an earlier phase of exploratory calculations, which suggested that interesting behaviour would be seen in this area of parameter space. The value of b given in (3.1.1) was selected to ensure that the cylinder was close to circular, thereby highlighting the different behaviours introduced by even a small eccentricity. In particular, we shall find that even a relatively mild departure from circularity can produce significant qualitative and quantitative differences from the behaviour in the circular case (we will explore the effects of a small cylinder eccentricity in Sections 3.2 and 3.7.2). For the parameter values given in (3.1.1), equation (2.3.10) gives $\varepsilon = 0.04899$. The value of Re was chosen to be of $\mathcal{O}(\varepsilon^{-2})$ in line with the discussion in Section 2.3.1. The value of Ca was chosen to ensure that surface tension does not overwhelm the other effects so that a distinct bulge may form in the film.

In Sections 3.3, 3.6, and 3.7, the effects of varying b and Ca will be elucidated via both analytical and numerical studies. In the cases where the solutions of the thin-film ellipse equation (2.3.13) are compared when b is varied, the unscaled mass $\widetilde{M}$ is kept fixed in our numerical studies to allow for consistent comparisons. To achieve this, we vary ε, which consequently affects the final scaled time $t = t_f$ via the scalings (2.3.1). While we choose to fix the final unscaled time $\widetilde{t} = \widetilde{t}_f$ in our comparisons, it should be noted that, alternatively, we could fix $t = t_f$, provided a

sufficiently long final time (either scaled or unscaled) is chosen to ensure that any initial transient phase has concluded.

In contrast to the case for a circular cylinder, in which both steady and time-periodic states are found depending on the value of W (as discussed in Section 1.4.1), we do not anticipate there being any steady states in the general case of an elliptical cylinder $b \in (0,1)$. However, as we describe in Section 3.1.2, several characteristically different behaviours are observed. One metric we use to distinguish these different behaviours is by tracking the centre of mass of the fluid. The Cartesian coordinates in the rotating frame are denoted by $\left(X^{(\mathrm{r})}, Y^{(\mathrm{r})}\right)$, and in the laboratory frame by (X, Y). Then the centre of mass is at $\left(X^{(\mathrm{r})}, Y^{(\mathrm{r})}\right) = \left(X_{\mathrm{c}}^{(\mathrm{r})}, Y_{\mathrm{c}}^{(\mathrm{r})}\right)$, where

$$\begin{aligned} MX_c^{(\mathrm{r})} &= \int_0^{2\pi} \int_0^{\eta} h \left(1 + \varepsilon \frac{b}{m} y\right) \cos\theta \, \mathrm{d}y \, \mathrm{d}\theta \\ &= \int_0^{2\pi} \left(m\eta + \varepsilon(m^2+1)\frac{b}{2m^2}\eta^2\right) \cos\theta \, \mathrm{d}\theta + \mathcal{O}(\varepsilon^2), \end{aligned} \tag{3.1.2}$$

$$\begin{aligned} MY_c^{(\mathrm{r})} &= \int_0^{2\pi} \int_0^{\eta} h \left(b + \varepsilon \frac{1}{m} y\right) \sin\theta \, \mathrm{d}y \, \mathrm{d}\theta \\ &= \int_0^{2\pi} \left(bm\eta + \varepsilon(m^2+b^2)\frac{1}{2m^2}\eta^2\right) \sin\theta \, \mathrm{d}\theta + \mathcal{O}(\varepsilon^2). \end{aligned} \tag{3.1.3}$$

Throughout the present chapter, we only use the unscaled centre of mass (hereafter referred to as simply the "centre of mass"). In order to aid understanding, we transform the centre of mass in the rotating frame back to recover the centre of mass $\left(\widetilde{X}, \widetilde{Y}\right) = \left(\widetilde{X}_{\mathrm{c}}, \widetilde{Y}_{\mathrm{c}}\right)$ in the laboratory frame via the standard rotation,

$$\begin{bmatrix} \widetilde{X}_{\mathrm{c}} \\ \widetilde{Y}_{\mathrm{c}} \end{bmatrix} = \begin{bmatrix} \cos\left(\widetilde{V}_{\Omega}\widetilde{t}\right) & -\sin\left(\widetilde{V}_{\Omega}\widetilde{t}\right) \\ \sin\left(\widetilde{V}_{\Omega}\widetilde{t}\right) & \cos\left(\widetilde{V}_{\Omega}\widetilde{t}\right) \end{bmatrix}^{-1} \begin{bmatrix} \widetilde{X}_{\mathrm{c}}^{(\mathrm{r})} \\ \widetilde{Y}_{\mathrm{c}}^{(\mathrm{r})} \end{bmatrix}, \tag{3.1.4}$$

where $\widetilde{V}_{\Omega}\widetilde{t}$ is the angle of inclination of the semi-major axis to the horizontal at time $\widetilde{t}$. Therefore, we denote by $\left(\widetilde{X}, \widetilde{Y}\right) = \left(\widetilde{X}_{\mathrm{c}}^{\mathrm{av}}, \widetilde{Y}_{\mathrm{c}}^{\mathrm{av}}\right)$ the time-averaged centre of

mass in the laboratory frame,

$$\left(\widetilde{X}_{\mathrm{c}}^{\mathrm{av}}, \widetilde{Y}_{\mathrm{c}}^{\mathrm{av}}\right) = \frac{1}{\widetilde{t}_f} \int_0^{\widetilde{t}_f} \left(\widetilde{X}_{\mathrm{c}}, \widetilde{Y}_{\mathrm{c}}\right) \, \mathrm{d}\widetilde{t}. \tag{3.1.5}$$

3.1.2 Numerical investigation of the thin-film ellipse equation

Numerical simulations were performed using a well-tested C++ code [55; 60] (see Appendix A.1).

Figure 3.1 shows plots of the time-averaged centre of mass in the laboratory frame $\widetilde{X}_{\mathrm{c}}^{\mathrm{av}}$ and $\widetilde{Y}_{\mathrm{c}}^{\mathrm{av}}$ as a function of W. This figure is divided into four regions corresponding to the four different characteristic behaviours of the free surface we observed, which we have chosen to denote, according to the respective rotation speeds, as "low", "low-moderate", "high-moderate", and "high". These four characteristic behaviours are:

- at low rotation speed ($0 < W < W_1(b)$) a single main bulge (and sometimes a smaller secondary bulge), which hangs below the cylinder due to gravity, and which is found to oscillate periodically (described in Section 3.4),
- at low-moderate rotation speed ($W_1(b) \leq W \leq W_2(b)$) a single main bulge (and smaller secondary bulges) formed by gravity and centrifugation which travels around the cylinder (described in Section 3.5.1),
- at high-moderate rotation speed ($W_2(b) < W < W_3(b)$) multiple main bulges formed at the tips of the ellipse by centrifugation which travel around the cylinder (described in Section 3.5.2),
- at high rotation speed ($W \geq W_3(b)$) two main bulges formed and held at the tips of the ellipse by centrifugation (described in Section 3.6).

We examine the special case of a stationary cylinder ($W = 0$) in Section 3.3.

For the parameter values studied in the present work (3.1.1), the transition between low and low-moderate rotation speed regimes occurs at $W = W_1(0.9) \approx 0.105$, which corresponds to the lowest value of W for which $\widetilde{Y}_{\mathrm{c}}^{\mathrm{av}} = 0$. For $0 < W < W_1(0.9) \approx 0.105$ the time-averaged centre of mass lies below the horizontal

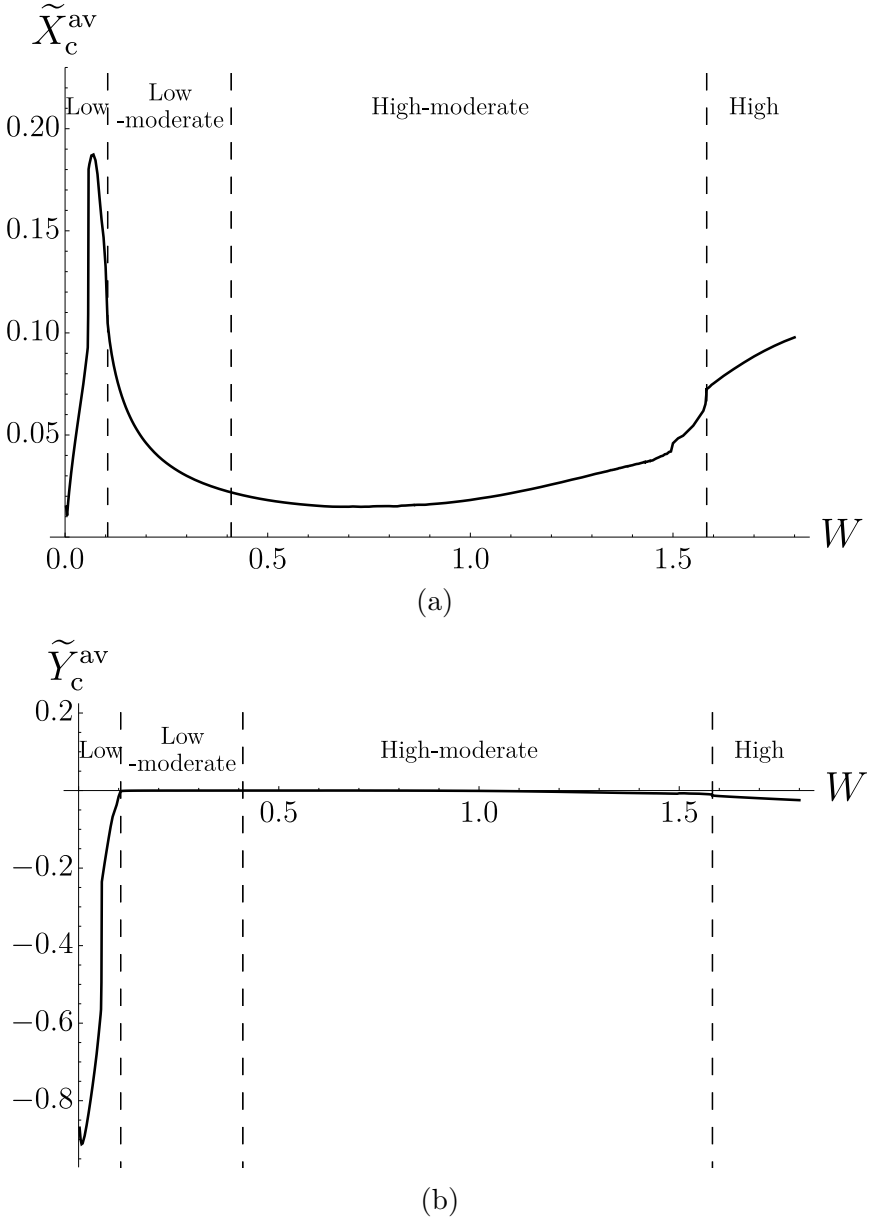

Figure 3.1: Plots of (a) $\widetilde{X}_{\rm c}^{\rm av}$ and (b) $\widetilde{Y}_{\rm c}^{\rm av}$, the time-averaged centre of mass in the laboratory frame, as functions of $W \in [0.0025, 1.8]$ from $\widetilde{t} = 0$ to $\widetilde{t} = \widetilde{t}_f = 5 \times 10^4$. The four characteristic parameter regimes described in Section 3.1.2 are indicated. The other parameters are as given in (3.1.1).

axis $\widetilde{Y} = 0$, i.e. $\widetilde{Y}_{\rm c}^{\rm av} < 0$, corresponding to a single main bulge, which hangs below the cylinder due to gravity. This transition is analogous to the transition observed on a circular cylinder by Evans et al. [56] at $W = W_{\rm c}$ as discussed in Section 1.4.1.3. The transition between low-moderate and high-moderate rotation speed regimes occurs at $W = W_2(0.9) \approx 0.410$. As this transition corresponds to the effect of gravity (which is primarily responsible for energy in the $n = 1$ mode of the Fourier transform of the free surface) being overwhelmed by centrifugation (which is primarily responsible for energy in the $n = 2$ mode of the Fourier transform of the free surface), we define the transition as taking place at the point at which these two energies are equal: this is made more precise in Section 3.5. Finally, the transition between high-moderate and high rotation speed regimes occurs at $W = W_3(0.9) \approx 1.583$. This corresponds to the point at which centrifugation becomes dominant, holding the fluid at the tips of the ellipse (i.e. at $\theta = 0$ and $\theta = \pi$) so that the system moves in approximately solid body rotation: this is made more precise in Section 3.6.

The values of $W_1(0.9)$, $W_2(0.9)$, and $W_3(0.9)$ quoted in the present section depend on the parameters given in (3.1.1). In particular, these values correspond to $b = 0.9$. In Section 3.7.1 we discuss the effect that varying b has on $W_1(b)$, $W_2(b)$, and $W_3(b)$ by examining the case of a highly eccentric ellipse (i.e. $b = 0.5$, with the other parameters as given in (3.1.1)). In particular, we perform a second parametric study on W to determine values of $W_1(0.5)$, $W_2(0.5)$ and $W_3(0.5)$ in this case. In Section 3.7.2 we examine the case of a nearly-circular ellipse (i.e. $b = 0.999$, with the other parameters as given in (3.1.1)) in the low and high rotation speed regimes.

3.2 Asymptotic solution for a nearly-circular ellipse

While it is not possible, in general, to obtain a closed form analytical solution to (2.3.13), significant progress can be made in understanding the dependence of its solution on the values of the parameters in certain limits. In particular, it is possible to derive an asymptotic solution to the leading-order (in ε) version of

(2.3.13), namely

$$m\frac{\partial\eta}{\partial t} - \frac{\partial}{\partial\theta}\left\{\frac{\eta^3}{3m}\left[\left(W^2 - \frac{3b}{m^5}\frac{1}{Ca}\right)\frac{(1-b^2)}{2}\sin 2\theta \right.\right.$$
$$\left.\left. + b\cos\theta\cos\left(V_\Omega^{(\text{thin})}t\right) - \sin\theta\sin\left(V_\Omega^{(\text{thin})}t\right)\right]\right\} = 0, \quad (3.2.1)$$

for a nearly-circular ellipse in the limit of small flux. First, equation (3.2.1) is recast in canonical form [57] via the rescalings

$$t = \frac{\breve{t}}{V_\Omega^{(\text{thin})}}, \quad \eta = \sqrt{V_\Omega^{(\text{thin})}}\breve{\eta}, \quad (3.2.2)$$

to yield

$$m\frac{\partial\breve{\eta}}{\partial\breve{t}} - \frac{\partial}{\partial\theta}\left\{\frac{\breve{\eta}^3}{3m}\left[\left(W^2 - \frac{3b}{m^5}\frac{1}{Ca}\right)\frac{(1-b^2)}{2}\sin 2\theta + b\cos\theta\cos\breve{t} - \sin\theta\sin\breve{t}\right]\right\} = 0, \quad (3.2.3)$$

which now has only four parameters, namely b, Ca, W, and $\breve{\eta}_\text{I}$, where $\breve{\eta}_\text{I} = \breve{\eta}|_{\breve{t}=0}$ is the uniform initial film thickness.

3.2.1 Nearly-circular limit

In the case $b = 1$ we recover the case of a circular cylinder which has a steady full-film solution (i.e. a single-valued solution for which the fluid wets the entire cylinder) when the fluid mass is below a critical value (see Section 1.4.1.1). We can analyse the nearly-circular limit by considering $b = 1 - \xi$ with $\xi \ll 1$, and expanding $\breve{\eta}$ as

$$\breve{\eta}(\theta,\breve{t}) = \breve{\eta}_0(\theta,\breve{t}) + \xi\breve{\eta}_1(\theta,\breve{t}) + \mathcal{O}(\xi^2), \quad (3.2.4)$$

to yield

$$\frac{\partial\breve{\eta}_0}{\partial\breve{t}} - \frac{\partial}{\partial\theta}\left[\frac{\breve{\eta}_0^3}{3}\cos(\theta+\breve{t})\right] + \xi\left\{\frac{\partial\breve{\eta}_1}{\partial\breve{t}} - \cos^2\theta\frac{\partial\breve{\eta}_0}{\partial\breve{t}}\right. \quad (3.2.5)$$
$$\left. + \frac{\partial}{\partial\theta}\left[\left(\frac{6}{Ca} + \sin(\theta+\breve{t}) - 2W^2\right)\frac{\breve{\eta}_0^3}{6}\sin 2\theta - \breve{\eta}_0^2\breve{\eta}_1\cos(\theta+\breve{t})\right]\right\} + \mathcal{O}(\xi^2) = 0.$$

We can move into the laboratory frame using the Galilean transformation

$$\phi = \phi(\theta, \breve{t}) = \theta + \breve{t}, \quad T = T(\theta, \breve{t}) = \breve{t}. \tag{3.2.6}$$

Under the transformation (3.2.6), the leading-order evolution equation (3.2.3) is

$$m\frac{\partial \breve{\eta}}{\partial T} + m\frac{\partial \breve{\eta}}{\partial \phi} + \frac{\partial}{\partial \phi}\left\{ \frac{\breve{\eta}^3}{3m}\left[\xi\left(W^2 - \frac{3}{Ca}\right)\sin\left(2\phi - 2T\right) \right.\right. \tag{3.2.7}$$
$$\left.\left. - \Big((1-\xi)\cos\left(\phi - T\right)\cos T - \sin\left(\phi - T\right)\sin T\Big)\right]\right\} = 0.$$

Under the transformation (3.2.6), the leading-order (in ξ) version of (3.2.5) is

$$\frac{\partial \breve{\eta}_0}{\partial T} + \frac{\partial \breve{\eta}_0}{\partial \phi} - \frac{\partial}{\partial \phi}\left(\frac{\breve{\eta}_0^3}{3}\cos\phi\right) = 0, \tag{3.2.8}$$

which, as expected, is the same as equation (1.4.1) (i.e. equation (29) of Moffatt [57]) up to differences in scaling. Equation (3.2.8) admits a steady solution when $\partial\breve{\eta}_0/\partial T = 0$, i.e. when

$$\breve{\eta}_0 - \frac{\breve{\eta}_0^3}{3}\cos\phi = \breve{Q}, \tag{3.2.9}$$

where $\breve{Q}$ is the (dimensionless) volume flux. As discussed in Section 1.4.1.1, Moffatt [57] showed that (3.2.9) only admits a steady full-film solution when $\breve{Q}$ satisfies the constraint $0 < \breve{Q} \leq 2/3$, and the corresponding exact solutions for $\breve{\eta}_0$ are well known [126; 133; 226] (1.4.3).

Under the transformation (3.2.6), the first order (in ξ) terms in (3.2.5) may be expressed in characteristic form as

$$\frac{\mathrm{d}\breve{\eta}_1}{\mathrm{d}T} = G(\phi, T) \quad \text{on the characteristics} \quad \frac{\mathrm{d}\phi}{\mathrm{d}T} = F(\phi), \tag{3.2.10}$$

where

$$F(\phi) = 1 - \breve{\eta}_0^2\cos\phi, \tag{3.2.11}$$

$$G(\phi, T) = \breve{\eta}_1\frac{\mathrm{d}}{\mathrm{d}\phi}\left(\breve{\eta}_0^2\cos\phi\right) + \cos^2\left(\phi - T\right)\frac{\mathrm{d}\breve{\eta}_0}{\mathrm{d}\phi}$$
$$+ \frac{\partial}{\partial\phi}\left[\frac{\breve{\eta}_0^3}{6}\left(2W^2 - \sin\phi - \frac{6}{Ca}\right)\sin\left(2\phi - 2T\right)\right]. \tag{3.2.12}$$

While (3.2.10) cannot be solved exactly, it can be solved in the limit of small flux $\breve{Q} \to 0^+$.

3.2.2 Small flux limit

In order to determine the asymptotic behaviour of the leading-order solution $\breve{\eta}_0$ of (3.2.9) in the limit of small flux $\breve{Q} \to 0^+$ it is, in principle, possible to expand the exact solution given by Duffy and Wilson [126] (i.e. equation (1.4.3)), but in practice it is easier to seek an asymptotic solution in the form

$$\breve{\eta}_0 = \zeta_0 + \breve{Q}\zeta_1 + \breve{Q}^2\zeta_2 + \breve{Q}^3\zeta_3 + \breve{Q}^4\zeta_4 + \breve{Q}^5\zeta_5 + \mathcal{O}(\breve{Q}^6). \tag{3.2.13}$$

Substituting (3.2.13) into (3.2.9) and solving at each order of $\breve{Q}$ yields

$$\breve{\eta}_0 \sim \eta_0' = \breve{Q} + \frac{\breve{Q}^3}{3}\cos\phi + \frac{\breve{Q}^5}{3}\cos^2\phi + \mathcal{O}(\breve{Q}^7). \tag{3.2.14}$$

In order to solve (3.2.10), $\mathrm{d}\phi/\mathrm{d}T = F(\phi)$ is first expanded in the limit $\breve{Q} \to 0^+$ to find the characteristics, yielding

$$F(\phi) = 1 - \eta_0'^2\cos\phi = 1 - \breve{Q}^2\cos\phi + \mathcal{O}(\breve{Q}^4), \tag{3.2.15}$$

whence

$$\phi + \breve{Q}^2\sin\phi - \phi_0 - \breve{Q}^2\sin\phi_0 + \mathcal{O}(\breve{Q}^4) = T, \tag{3.2.16}$$

where $\phi(0) = \phi_0$ is the initial value of ϕ, which parametrises the characteristics. Inverting (3.2.16) (i.e. solving (3.2.16) for ϕ at leading order in $\breve{Q}$ and substituting into the second-order terms, and then repeat for ϕ_0) yields the relations

$$\phi = \phi_0 + T + \breve{Q}^2\left[\sin\phi_0 - \sin\left(\phi_0 + T\right)\right] + \mathcal{O}(\breve{Q}^4), \tag{3.2.17}$$

$$\phi_0 = \phi - T + \breve{Q}^2\left[\sin\phi - \sin\left(\phi - T\right)\right] + \mathcal{O}(\breve{Q}^4), \tag{3.2.18}$$

which allow expressions for $\breve{\eta}_1$ to be transformed between having ϕ_0 or ϕ as the independent variable. The equation $\mathrm{d}\breve{\eta}_1/\mathrm{d}T = G(\phi, T)$ from (3.2.10) can be rewritten in the form

$$\frac{\mathrm{d}\breve{\eta}_1}{\mathrm{d}T} + P(\phi)\breve{\eta}_1 = L(\phi, T), \tag{3.2.19}$$

where

$$P(\phi) = -\frac{\mathrm{d}}{\mathrm{d}\phi}\left(\eta_0'^2 \cos\phi\right), \tag{3.2.20}$$

$$L(\phi, T) = \cos^2(\phi - T)\frac{\mathrm{d}\eta_0'}{\mathrm{d}\phi} - \frac{\partial}{\partial\phi}\left[\frac{\eta_0'^3}{6}\left(2W^2 - \sin\phi - \frac{6}{Ca}\right)\sin(2\phi - 2T)\right]. \tag{3.2.21}$$

To facilitate integration with respect to T, (3.2.18) is used to write $P(\phi) \equiv P^*(T;\phi_0)$ and $L(\phi, T) \equiv L^*(T;\phi_0)$, where

$$P^*(T;\phi_0) = \breve{Q}^2 \sin(\phi_0 + T) + \mathcal{O}(\breve{Q}^4), \tag{3.2.22}$$

$$\begin{aligned} &L^*(T;\phi_0) \\ &= \frac{\breve{Q}^3}{12}\Bigg\{8\left(W^2 - \frac{3}{Ca}\right)\cos(2\phi_0) + 2\sin(\phi_0 - T) - 2\sin(\phi_0 + T) - 4\sin(3\phi_0 + T) \\ &\quad + \breve{Q}^2\Bigg[2\left(W^2 - \frac{3}{Ca}\right)\Big(4\cos(3\phi_0) - 4\cos\phi_0 + 5\cos(\phi_0 - T) - \cos(3\phi_0 + T)\Big) \\ &\quad - 7\sin(2\phi_0) + \sin(2\phi_0 - T) + 2\sin T - \sin(2T) + \sin(2\phi_0 + 2T) \\ &\quad + 5\sin(2\phi_0 + T) + 4\sin(4\phi_0 + 2T) - 6\sin(4\phi_0 + T)\Bigg]\Bigg\} + \mathcal{O}(\breve{Q}^7). \end{aligned} \tag{3.2.23}$$

Equation (3.2.19) may then be solved via the use of an integrating factor to yield

$$\breve{\eta}_1 = \frac{\int_0^T I(T)L^*(T)\,\mathrm{d}T}{I(T)}, \tag{3.2.24}$$

where

$$I(T) = \mathrm{e}^{\int P^*(T)\,\mathrm{d}T} = 1 - \breve{Q}^2\cos(\phi_0 + T) + \mathcal{O}(\breve{Q}^4). \tag{3.2.25}$$

Evaluating (3.2.24) gives

$$\breve{\eta}_1 = \frac{\breve{Q}^3}{6}\Bigg\{4T\left(W^2-\frac{3}{Ca}\right)\cos(2\phi_0)+\cos(\phi_0-T) \tag{3.2.26}$$
$$+\cos(\phi_0+T)-2\cos(\phi_0)-2\cos(3\phi_0)+2\cos(3\phi_0+T)\Bigg\}$$
$$+\frac{\breve{Q}^5}{12}\Bigg\{12\left[W^2-\frac{3}{Ca}\right]\Bigg[\Big(\cos\phi_0-\cos(\phi_0+T)\Big)\sin(2\phi_0)$$
$$+\frac{2T}{3}\Big(\cos(3\phi_0)-\cos\phi_0+\cos(2\phi_0)\cos(\phi_0+T)\Big)\Bigg]$$
$$+3+8\cos(2\phi_0)-3\cos(4\phi_0)-\cos(2\phi_0-T)-4\cos T+\cos(2T)$$
$$-7\cos(2\phi_0+T)-\cos(4\phi_0+2T)+4\cos(4\phi_0+T)-6T\sin(2\phi_0)\Bigg\}+\mathcal{O}(\breve{Q}^7),$$

which can be expressed in terms of ϕ and T via (3.2.18) as

$$\breve{\eta}_1 = \breve{Q}^3\Bigg\{\frac{2T}{3}\left[W^2-\frac{3}{Ca}\right]\cos(2\phi-2T) \tag{3.2.27}$$
$$-\frac{2}{3}\sin\left(\frac{T}{2}\right)\left[\cos(\phi-T)\sin\left(\frac{T}{2}\right)+\sin\left(3\phi-\frac{5T}{2}\right)\right]\Bigg\}$$
$$+\frac{\breve{Q}^5}{12}\Bigg\{12\left[W^2-\frac{3}{Ca}\right]\Bigg(T\left[\cos(3\phi-2T)-\frac{1}{3}\cos(\phi-2T)\right]$$
$$+\sin\left(\frac{T}{2}\right)\left[\cos\left(\phi-\frac{3T}{2}\right)-\cos\left(3\phi-\frac{5T}{2}\right)\right]\Bigg)$$
$$-8\cos(4\phi-3T)-4\cos(2\phi-T)+3\cos(4\phi-4T)+5\cos(4\phi-2T)$$
$$+\cos(2\phi)-\cos(2\phi-2T)+4\cos(2\phi-3T)-6T\sin(2\phi-2T)\Bigg\}+\mathcal{O}(\breve{Q}^7).$$

The solution (3.2.27) may be verified via direct substitution into (3.2.10). The solution (3.2.27) contains several secular terms. These are the terms on the first and third lines involving W^2-3/Ca (which are a particular combination of the centrifugation and surface tension terms), and the final term on the final line. As a result, the terms in the solution (3.2.27) will become disordered when $T=\mathcal{O}(\breve{Q}^{-2})$,

limiting the validity of this expansion. The structure of the centrifugation and surface tension terms in the solution (3.2.27) indicates that, in the present limit, the two have exactly opposing effects, and will cancel one another out when $W^2Ca = 3$.

Figure 3.2 shows plots of the $\mathcal{O}(\breve{Q}^3)$ truncation of (3.2.27) (multiplied by $1/\breve{Q}^3$), the numerical solutions to the first-order PDE (3.2.10), and the full PDE (3.2.7) for various values of Ca and for $T = 21\pi \approx 66.0$. This choice of T is motivated by the fact that, in the special case in which $W^2Ca = 3$, the $\mathcal{O}(\breve{Q}^3)$ truncation of (3.2.27) is identically equal to zero at $T = 2n\pi$, and so we will examine times of the form $T = (2n+1)\pi$, where n is an integer. We impose $\breve{\eta}_1|_{T=0} = 0$ and $\breve{\eta}_{\mathrm{I}} = \breve{\eta}_0$ (where $\breve{\eta}_0$ is the exact solution to (3.2.8)) with $\breve{Q} = 0.1$ as initial conditions for (3.2.7) and (3.2.10), respectively. Figure 3.2(a) corresponds to a region of parameter space in which surface tension is stronger than centrifugation ($W^2Ca < 3$) and shows that the fluid collects away from the tips of the ellipse (i.e. near $\phi = \pi/2$ and $\phi = 3\pi/2$) which is the characteristic behaviour of strong surface tension trying to return the free surface to circular. We will explore strong surface tension effects in more detail in Sections 3.3.3 and 3.6.3. Figure 3.2(b) corresponds to the special case $W^2Ca = 3$ in which (in this limit) surface tension and centrifugation cancel each other out identically, so that the flow is driven purely by gravity and rotation. The $\mathcal{O}(\breve{Q}^3)$ truncation of (3.2.27) clearly gives inaccurate predictions: the solution is in fact 2π-periodic in time at this order. However, the first-order PDE (3.2.10) performs better as it retains some of the higher-order behaviours which only become significant on a longer timescale, such as the secondary effects of gravity and rotation (which manifest as, for example, the final secular term in (3.2.27)). Figure 3.2(c) corresponds to a region of parameter space in which surface tension is weaker than centrifugation ($W^2Ca > 3$) and shows that the fluid collects towards the tip of the ellipse at $\phi = 0$. At this time, the effect of gravity is preventing the fluid from collecting at the other tip of the ellipse at $\phi = \pi$.

Figure 3.3 shows plots of the $\mathcal{O}(\breve{Q}^3)$ truncation of (3.2.27) (multiplied by $1/\breve{Q}^3$), the $\mathcal{O}(\breve{Q}^5)$ truncation of (3.2.27) (multiplied by $1/\breve{Q}^3$), the numerical solutions to the first-order PDE (3.2.10), and the full PDE (3.2.7) for $T = 41\pi \approx 128.8$. At this time, the solution (3.2.27) has become disordered, and the $\mathcal{O}(\breve{Q}^3)$ truncation of (3.2.27) gives inaccurate predictions, however the $\mathcal{O}(\breve{Q}^5)$ truncation of (3.2.27) performs better. In particular, the $\mathcal{O}(\breve{Q}^5)$ truncation of (3.2.27) is not 2π-periodic

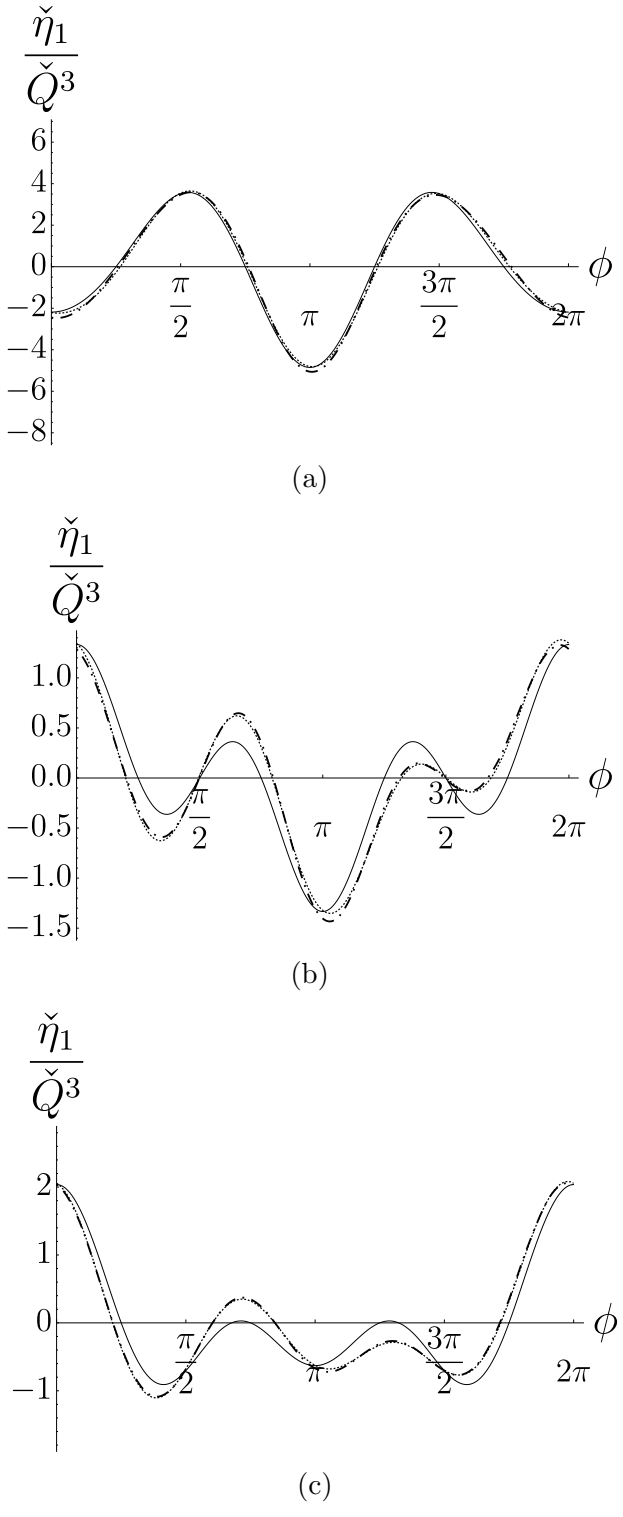

Figure 3.2: Plot of the $\mathcal{O}(\breve{Q}^3)$ truncation of (3.2.27) (multiplied by $1/\breve{Q}^3$) (solid), the numerical solutions to the first-order PDE (3.2.10) with $\breve{\eta}_1|_{T=0} = 0$ (dotted), and the full PDE (3.2.7) with $\breve{\eta}_{\text{I}} = \breve{\eta}_0$ (where $\breve{\eta}_0$ is the exact solution to (3.2.8)) when $\xi = 0.01$ (dot-dashed) at $T = 21\pi \approx 66.0$ with $\breve{Q} = 0.1$, $W = 0.2$ and (a) $Ca = 25$, (b) $Ca = 75$, and (c) $Ca = 125$. Note that the plots are shown on different scales.

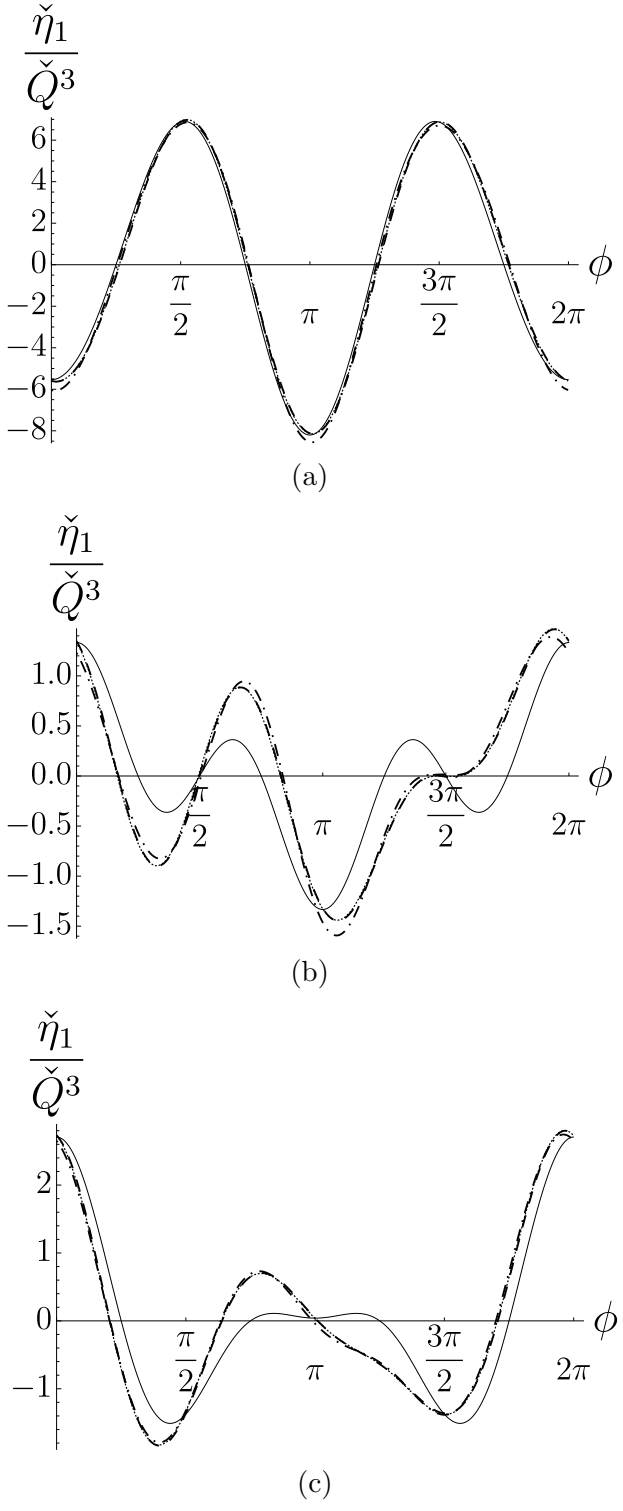

Figure 3.3: Plot of the $\mathcal{O}(\breve{Q}^3)$ truncation of (3.2.27) (multiplied by $1/\breve{Q}^3$) (solid), the $\mathcal{O}(\breve{Q}^5)$ truncation of (3.2.27) (multiplied by $1/\breve{Q}^3$) (dashed), the numerical solutions to the first-order PDE (3.2.10) with $\breve{\eta}_1|_{T=0} = 0$ (dotted), and the full PDE (3.2.7) with $\breve{\eta}_{\text{I}} = \breve{\eta}_0$ (where $\breve{\eta}_0$ is the exact solution to (3.2.8)) when $\xi = 0.01$ (dot-dashed) at $T = 41\pi \approx 128.8$ with $\breve{Q} = 0.1$, $W = 0.2$ and (a) $Ca = 25$, (b) $Ca = 75$, and (c) $Ca = 125$. Note that the plots are shown on different scales.

in time at this order, and so the agreement of the $\mathcal{O}(\breve{Q}^5)$ truncation of (3.2.27) with the full PDE (3.2.7) in the special case of $W^2Ca = 3$ is better than the agreement of the $\mathcal{O}(\breve{Q}^3)$ truncation of (3.2.27) with the full PDE (3.2.7) due to the single $\mathcal{O}(\breve{Q}^5)$ secular term in this case. Additionally, at this time, Figure 3.3(c) shows that the fluid now collects towards both tips of the ellipse (i.e. near $\phi = 0$ and $\phi = \pi$, although the effect in the latter case is less pronounced due to the effect of gravity). This behaviour is characteristic of high rotation speed, and will be explored in more detail in Section 3.6.

3.3 Stationary cylinder

In this section we analyse the special case in which the cylinder is stationary. We therefore set $W = 0$ in the thin-film ellipse equation (2.3.13), yielding

$$\begin{aligned}\left(m+\varepsilon\frac{b}{m^2}\eta\right)\frac{\partial\eta}{\partial t}+\frac{\partial}{\partial\theta}\Bigg\{&\frac{1}{Ca}\frac{b(1-b^2)\eta^3}{2m^6}\sin 2\theta\left[1+\varepsilon\frac{b\eta}{2m^3}\right]-\frac{b\eta^3}{3m}\cos\theta \\ &-\varepsilon\frac{1}{Ca}\frac{\eta^3}{3m}\frac{\partial}{\partial\theta}\left[\frac{1}{m^6}\left(\frac{m^2(1-b^2)}{2}\sin 2\theta\frac{\partial\eta}{\partial\theta}-b^2\eta-m^4\frac{\partial^2\eta}{\partial\theta^2}\right)\right] \\ &+\varepsilon\left[\frac{\eta^3}{3m^2}\left(\frac{3\eta(1-b^2)}{16m^2}\sin 2\theta-\frac{\partial\eta}{\partial\theta}\right)\sin\theta-\frac{\eta^4}{8m^2}\left(1+\frac{3b^2}{m^2}\right)\cos\theta\right]\Bigg\}=0,\end{aligned} \tag{3.3.1}$$

where the terms in the braces involving Ca correspond to the effect of surface tension, and the rest of the terms in the braces correspond to the effect of gravity. When the cylinder is stationary, we are able to exploit the symmetry of the system to impose the symmetry conditions

$$\left.\frac{\partial\eta}{\partial\theta}\right|_{\theta=\pi/2}=\left.\frac{\partial\eta}{\partial\theta}\right|_{\theta=3\pi/2}=0. \tag{3.3.2}$$

The cylinder is fixed as being horizontal (i.e. with the tips of the ellipse being at the same height in the laboratory frame). While different configurations are possible, understanding the flow even in this configuration is already significantly more complicated than the equivalent situation for a circular cylinder, and so other configurations are not considered in the present work.

In Sections 3.3.1 and 3.3.2 we analytically and numerically examine the be-

haviour at leading order in ε of (3.3.1) in the limit $Ca \to \infty$, and in the case $Ca = \mathcal{O}(1)$, respectively. In Section 3.3.3 we analytically examine behaviour of (3.3.1) in the limit $Ca \to 0^+$ and the nearly-circular limit. Finally, in Section 3.3.4 we numerically investigate the behaviour of (3.3.1) in general.

3.3.1 Stationary cylinder in the limit of large capillary number

Reisfeld and Bankoff [157] showed that, for a stationary circular cylinder in the limit of large capillary number, the fluid drains down the sides of the cylinder and the solution blows up (i.e. the film thickness approaches infinity) in finite time. We examine the equivalent situation for an elliptical cylinder; in particular, we examine (3.3.1) at leading order in ε in the limit $Ca \to \infty$, which yields

$$m\frac{\partial \eta}{\partial t} - \frac{\partial}{\partial \theta}\left(\frac{b\eta^3}{3m}\cos\theta\right) = 0. \tag{3.3.3}$$

Up to differences in scaling, in the special case $b = 1$ this recovers equation (5.8) of Reisfeld and Bankoff [157]. Equation (3.3.3) can be written in characteristic form as

$$\frac{\mathrm{d}\eta}{\mathrm{d}t} = \frac{b\eta^3}{3m}\frac{\mathrm{d}}{\mathrm{d}\theta}\left(\frac{\cos\theta}{m}\right) \quad \text{on the characteristics} \quad \frac{\mathrm{d}\theta}{\mathrm{d}t} = -\frac{b\eta^2}{m^2}\cos\theta, \tag{3.3.4}$$

which can be solved exactly to yield

$$\eta = \begin{cases} \sqrt{\dfrac{3}{3+2bt}} & \theta = \dfrac{\pi}{2}, \\ \sqrt{\dfrac{3}{3-2bt}} & \theta = \dfrac{3\pi}{2}, \\ \left(\dfrac{\cos\theta_0\sqrt{\sin^2\theta + b^2\cos^2\theta}}{\cos\theta\sqrt{\sin^2\theta_0 + b^2\cos^2\theta_0}}\right)^{1/3} & 0 \le \theta \le 2\pi,\ \theta \neq \dfrac{\pi}{2},\ \theta \neq \dfrac{3\pi}{2}, \end{cases} \tag{3.3.5}$$

where $\theta(0) = \theta_0$ is the initial value of θ, which parametrises the characteristics. When $b = 1$, (3.3.5) reduces to the corresponding solution for a circular cylinder given by equation (5.11a) of Reisfeld and Bankoff [157], up to differences in scalings.

The solution (3.3.5) experiences blowup due to a singularity at $\theta = 3\pi/2$ at

$$t = t_{\text{blowup}} = \frac{3}{2b}. \tag{3.3.6}$$

This blowup is unphysical and occurs because the stabilising effect of surface tension, represented by the fourth-order derivative in equation (3.3.1), is not present in equation (3.3.3) (i.e. at leading order in ε in the limit $Ca \to \infty$).

Preliminary investigations of the numerical solution of (3.3.4) have shown that for $b_{\text{c}} \leq b \leq 1$ the characteristics do not cross. However, for $0 < b < b_{\text{c}}$ the characteristics cross for some $t < t_{\text{blowup}}$ (3.3.6). Here, b_{c} denotes the transition between the cases where the characteristics cross and do not cross. By performing a parametric study on b for the numerical solution of (3.3.4), we determined that $b_{\text{c}} \approx 0.867$. The solutions in which the characteristic cross must be interpreted with care as the free surface has been parametrised as being a single-valued function of θ. Therefore, the solutions obtained by the method of characteristics are only valid while the solution remains single-valued (i.e. when the characteristics do not cross). In the case where the characteristics do cross, instead of becoming multi-valued (which is unphysical), a shock forms in the solution of equation (3.3.3).

Figure 3.4 shows plots of the numerical solution of (3.3.3). Figures 3.4(a) and 3.4(b) show plots of the free surface on a Cartesian plot for $b = 0.9$ and $b = 0.5$, respectively, and Figures 3.4(c) and 3.4(d) shows plots of the unscaled free surface on the ellipse for $b = 0.9$ and $b = 0.5$, respectively. Figures 3.4(a) and 3.4(c) show a case where the characteristics do not cross. In this case, the solution of (3.3.3) experiences blowup at $\theta = 3\pi/2$ at $t = t_{\text{blowup}} \approx 1.67$ (3.3.6). This blowup is characterised by the spike in Figures 3.4(a) and 3.4(c) which occurs due to the omission of the stabilising effect of surface tension in equation (3.3.3). Figures 3.4(b) and 3.4(d) show a case where the characteristics do cross. In this case, a shock forms in the solution of equation (3.3.3) at $t < t_{\text{blowup}}$ (3.3.6). The formation of the shock can perhaps be seen more clearly in Figure 3.4(b) as steep fronts are formed in the free surface either side of $\theta = 3\pi/2$. The formation of the shock in the solution of (3.3.3) makes it difficult for us to plot the free surface at a time closer to $t = t_{\text{blowup}} = 3$ (3.3.6). We expect that the inclusion of the stabilising effect of surface tension in equation (3.3.3) would smooth this shock [128].

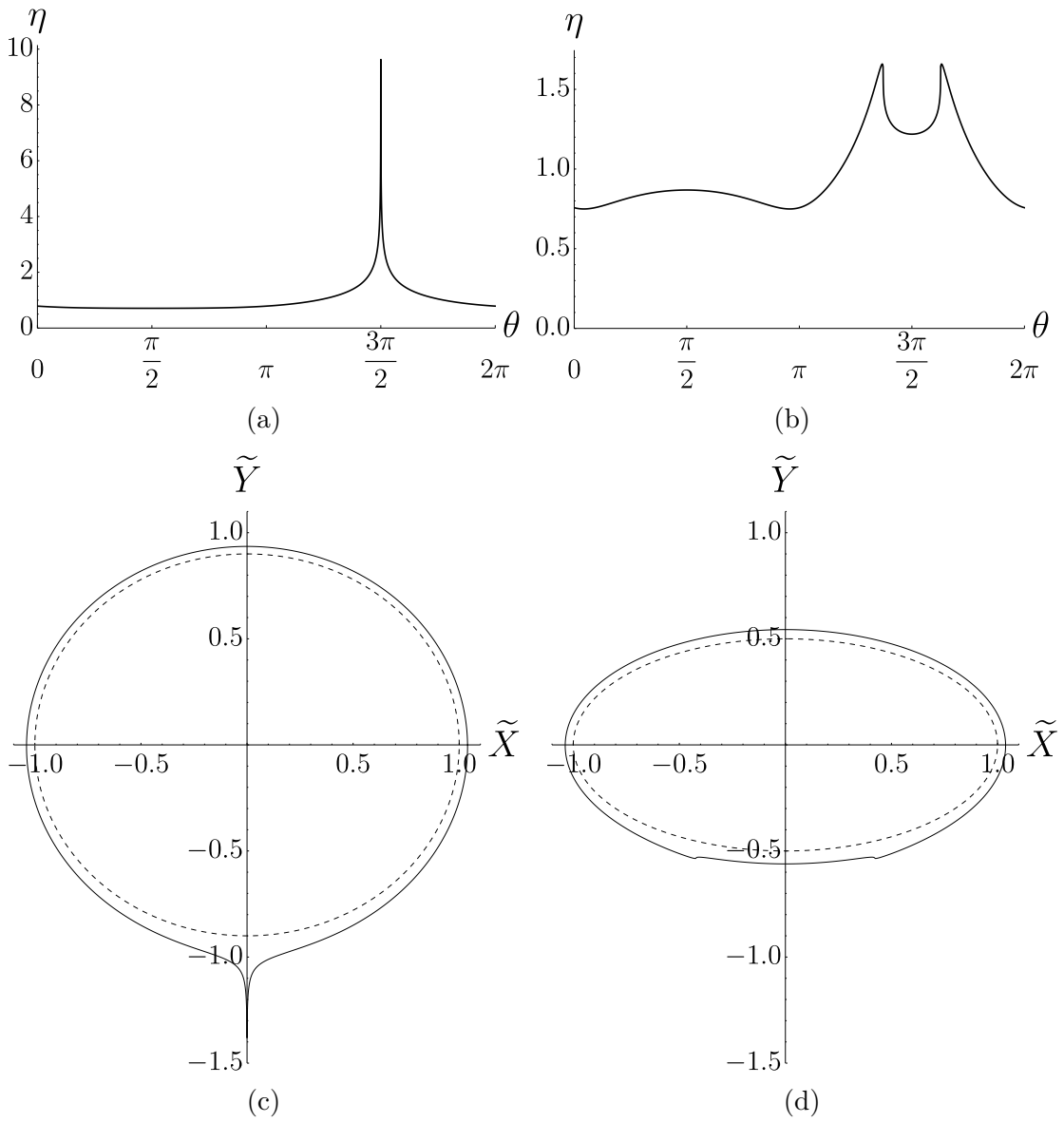

Figure 3.4: Plots of the numerical solution of (3.3.3) for a stationary cylinder for (a, c) $b = 0.9$ at time $t = 0.99t_{\text{blowup}} \approx 1.65$ (b, d) $b = 0.5$ at time $t = 0.98 < t_{\text{blowup}} = 3$, for t_{blowup} predicted by (3.3.6). The plots (a, b) show the free surface on a Cartesian plot, and the plots (c, d) show the unscaled free surface (solid lines) on the ellipse, plotted for $\varepsilon = 0.05$. The dashed lines in (c, d) are the ellipse. Note that the scale of the vertical axis is different in part (a) and (b).

3.3.2 Stationary cylinder with order unity capillary number

We examine (3.3.1) at leading order in ε in the case $Ca = \mathcal{O}(1)$, which yields

$$m\frac{\partial \eta}{\partial t} - \frac{\partial}{\partial \theta}\left(\frac{b\eta^3}{3m}\cos\theta - \frac{b(1-b^2)\eta^3 \sin 2\theta}{2m^6 Ca}\right) = 0. \tag{3.3.7}$$

This can be written in characteristic form as

$$\frac{\mathrm{d}\eta}{\mathrm{d}t} = \frac{b\eta^3}{3m}\left[\frac{\mathrm{d}}{\mathrm{d}\theta}\left(\frac{\cos\theta}{m}\right) - \frac{3(1-b^2)}{2Ca}\frac{\mathrm{d}}{\mathrm{d}\theta}\left(\frac{\sin 2\theta}{m^6}\right)\right] \tag{3.3.8}$$

on the characteristics

$$\frac{\mathrm{d}\theta}{\mathrm{d}t} = -\frac{b\eta^2}{m^2}\left(\cos\theta - \frac{3(1-b^2)\sin 2\theta}{2m^5 Ca}\right). \tag{3.3.9}$$

While (3.3.8) and (3.3.9) cannot, in general, be solved analytically, they can be solved along the characteristic curves starting at $\theta_0 = \pi/2$ and $\theta_0 = 3\pi/2$. Specifically, on the characteristic starting at $\theta_0 = \pi/2$,

$$\eta = \left[1 - 2b\left(\frac{(1-b^2)}{Ca} - \frac{1}{3}\right)t\right]^{-1/2}, \tag{3.3.10}$$

while on the characteristic starting at $\theta_0 = 3\pi/2$,

$$\eta = \left[1 - 2b\left(\frac{(1-b^2)}{Ca} + \frac{1}{3}\right)t\right]^{-1/2}, \tag{3.3.11}$$

both of which recover the corresponding solutions in (3.3.5) in the limit $Ca \to \infty$ (and in the limit $Ca \to 0^+$, as we show in Section 3.6.3.1).

The solution (3.3.11) blows up due to a singularity at $\theta = 3\pi/2$ at

$$t = t_{\text{blowup}} = \frac{3Ca}{2b(3(1-b^2)+Ca)}. \tag{3.3.12}$$

This blowup is unphysical and occurs because the stabilising effect of surface tension, represented by the fourth-order derivative in equation (3.3.1), is not present in equation (3.3.7) (i.e. at leading order in ε with $Ca = \mathcal{O}(1)$). The solution

(3.3.10) can also blow up due to a singularity at $\theta = \pi/2$ at

$$t = \frac{3Ca}{2b(3(1-b^2) - Ca)}, \tag{3.3.13}$$

however, this always occurs after (3.3.12). This is due to the fact that at $\theta = 3\pi/2$ surface tension and gravity work in concert, whereas at $\theta = \pi/2$ surface tension and gravity work in opposition. Note that this is only the case for $Ca = \mathcal{O}(1)$, as (3.3.12) and (3.3.13) coincide in the limit $Ca \to 0^+$ (we explore the limit $Ca \to 0^+$ further in Section 3.6.3.1), and in the previously examined case of $Ca \to \infty$ there is, of course, no surface tension.

While we are unable to obtain an analytical solution of (3.3.8) and (3.3.9) along other characteristic curves, preliminary investigations of the numerical solution of (3.3.8) and (3.3.9) have shown that these solutions exhibit the same qualitative behaviour as the solutions in Section 3.3.1. Specifically, for $b_c \leq b \leq 1$ the characteristics do not cross and so the solution of (3.3.7) will experience blowup at $\theta = 3\pi/2$ at $t = t_{\text{blowup}}$ (3.3.12). However, for $0 < b < b_c$ the characteristics cross and so a shock is formed in the solution of (3.3.7) for some $t < t_{\text{blowup}}$ (3.3.12). Due to time constraints and equation (3.3.7) being more complicated than equation (3.3.3), we have been unable to perform a similar parametric study on b in the present section to determine b_c as we did in Section 3.3.1.

Figure 3.5 shows plots of the numerical solution of (3.3.7). Figures 3.5(a) and 3.5(b) show plots of the free surface on a Cartesian plot for $b = 0.9$ and $b = 0.5$, respectively, and Figures 3.5(c) and 3.5(d) shows plots of the unscaled free surface on the ellipse for $b = 0.9$ and $b = 0.5$, respectively. Figures 3.5(a) and 3.5(c) show a case where the characteristics do not cross. In this case, the solution of (3.3.7) experiences blowup at $\theta = 3\pi/2$ at $t = t_{\text{blowup}} \approx 1.06$ (3.3.12). This blowup is characterised by the spike in Figures 3.5(a) and 3.5(c) which occurs due to the omission of the stabilising effect of surface tension in equation (3.3.7). Figures 3.5(b) and 3.5(d) show a case where the characteristics do cross. In this case, a shock forms in the solution of equation (3.3.7) at $t < t_{\text{blowup}}$ (3.3.12). The formation of the shocks can perhaps be seen more clearly in Figure 3.5(b) as steep fronts are formed in the free surface either side of $\theta = \pi/2$ and $\theta = 3\pi/2$. The formation of the shocks in the solution of (3.3.7) makes it difficult for us to plot the free surface at a time closer to $t = t_{\text{blowup}} \approx 0.92$ (3.3.12). As mentioned previously,

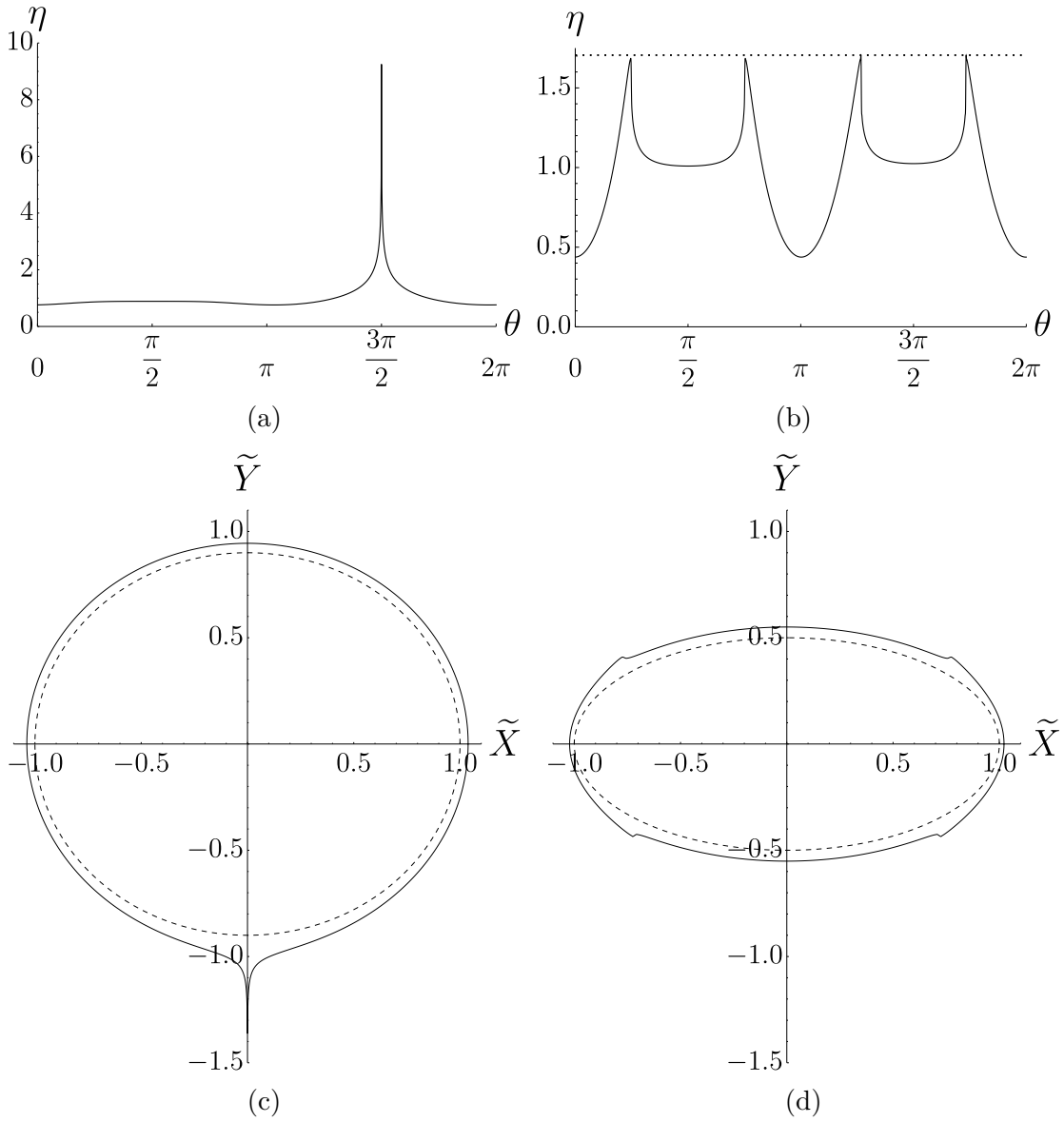

Figure 3.5: Plots of the numerical solution of (3.3.7) for a stationary cylinder with $Ca = 1$ for (a, c) $b = 0.9$ at time $t = 0.99t_{\text{blowup}} \approx 1.05$, and (b, d) $b = 0.5$ at time $t = 0.044 < t_{\text{blowup}} \approx 0.92$, for t_{blowup} predicted by (3.3.12). The plots (a, b) show the free surface on a Cartesian plot, and the plots (c, d) show the unscaled free surface (solid lines) on the ellipse, plotted for $\varepsilon = 0.05$. The dashed lines in (c, d) are the ellipse and the dotted line in (b) shows the maximum film thickness. Note that the scale of the vertical axis is different in part (a) and (b).

the blowup will occur at $\theta = 3\pi/2$ due to the combined effects of surface tension and gravity, and not at $\theta = \pi/2$ where the effects of surface tension and gravity are in opposition. To highlight this, a dotted line showing the maximum film thickness has been added Figure 3.5(b) to show that the film on the bottom of the cylinder is thicker than the film on the top. We expect that the inclusion of the stabilising effect of surface tension in equation (3.3.7) would smooth these shocks [128].

3.3.3 Nearly-circular stationary ellipse in the limit of small capillary number

We examine (3.3.1) in the limit of strong surface tension $Ca \to 0^+$ with $\varepsilon^2 \ll Ca \ll \varepsilon \ll 1$. While it is not possible to obtain an analytical solution in this limit for a general b, analytical progress can be made in the nearly-circular case in which $b = 1 - Ca$. Introducing a fast time $\breve{t} = (\varepsilon/Ca)t$ in order to capture the rapid dynamics due to the strong surface tension, (3.3.1) becomes

$$\frac{\partial \eta}{\partial \breve{t}} + \frac{\partial}{\partial \theta}\left[\frac{\eta^3}{3}\frac{\partial}{\partial \theta}\left(\eta + \frac{\partial^2 \eta}{\partial \theta^2}\right) + \frac{Ca}{\varepsilon}\eta^3\left(\sin 2\theta - \frac{\cos\theta}{3}\right)\right] + \mathcal{O}(\varepsilon) = 0. \qquad (3.3.14)$$

The first and second terms in the final curved bracket of equation (3.3.14) are due to surface tension and gravity, respectively. In the circular case, the surface tension terms only appear at first order in ε (see equation (2.3.14)), and so we could simply rescale Ca as, for example, $Ca = \varepsilon\breve{Ca}$ (where $\breve{Ca} = \mathcal{O}(1)$) to promote the surface tension terms to leading order in ε [157]. However, equation (3.3.14) has surface tension terms at both leading and first order in ε, and so, the reason we consider this specific limit is to retain the stabilising surface tension effect (represented by the fourth-order derivative in equation (3.3.14)) while neglecting $\mathcal{O}(\varepsilon)$ terms.

As might be expected, in the absence of gravity, (3.3.14) has a steady solution corresponding to a circular free surface, namely

$$\eta(\theta, \breve{t}) = \bar{\eta}(\theta) = 1 - \frac{Ca}{\varepsilon}\frac{1}{2}\cos 2\theta. \qquad (3.3.15)$$

However, in the presence of gravity, unsteady draining will inevitably take place. Therefore, in Sections 3.3.3.1 and 3.3.3.2 we examine two analytically tractable situations, namely the linear stability of the free surface in the absence of gravity,

and early-time behaviour in the presence of gravity, respectively.

3.3.3.1 Linear stability in the absence of gravity

We can examine the linear stability of the steady solution (3.3.15) in the absence of gravity by substituting $\eta(\theta,\breve{t}) = \bar{\eta}(\theta) + \zeta\eta^*(\theta,\breve{t})$ with $\zeta \ll 1$ into (3.3.14) and linearising to find

$$\begin{aligned}\frac{\partial\eta^*}{\partial\breve{t}} + \left(\frac{1}{3} - \frac{Ca}{\varepsilon}\frac{1}{2}\cos 2\theta\right)\frac{\partial^2}{\partial\theta^2}\left(\eta^* + \frac{\partial^2\eta^*}{\partial\theta^2}\right)\\ + \frac{Ca}{\varepsilon}\sin 2\theta\frac{\partial}{\partial\theta}\left(\eta^* + \frac{\partial^2\eta^*}{\partial\theta^2}\right) + \mathcal{O}\left(\left(\frac{Ca}{\varepsilon}\right)^2, \zeta^2\right) = 0.\end{aligned} \tag{3.3.16}$$

The linear PDE (3.3.16) has solution

$$\begin{aligned}\eta^* = &\sum_{n=0}^{\infty}(a_n\cos n\theta + b_n\sin n\theta)\exp\left[-\frac{1}{3}n^2(n^2-1)\breve{t}\right]\\ &+ \frac{Ca}{\varepsilon}\eta'(\theta,\breve{t}) + \mathcal{O}\left(\left(\frac{Ca}{\varepsilon}\right)^2, \zeta^2\right),\end{aligned} \tag{3.3.17}$$

where η' satisfies

$$\begin{aligned}&\frac{\partial\eta'}{\partial\breve{t}} + \frac{1}{3}\frac{\partial^2}{\partial\theta^2}\left(\eta' + \frac{\partial^2\eta'}{\partial\theta^2}\right)\\ =&\sum_{n=0}^{\infty} n(n^2-1)\exp\left[-\frac{1}{3}n^2(n^2-1)\breve{t}\right]\\ &\times\frac{2\sin 2\theta(-a_n\sin n\theta + b_n\cos n\theta) + n\cos 2\theta(a_n\cos n\theta + b_n\sin n\theta)}{2},\end{aligned} \tag{3.3.18}$$

which has solution

$$\begin{aligned}\eta' = &\sum_{n=0}^{\infty}\frac{3n}{8\left(4n^4-4n^2+9\right)}\exp\left[-\frac{1}{3}n^2\left(n^2-1\right)\breve{t}\right]\\ &\times\Big[\left(2n^4-5n^2-6\right)\sin 2\theta(b_n\cos n\theta - a_n\sin n\theta)\\ &\qquad - n\left(2n^2-11\right)\cos 2\theta(a_n\cos n\theta + b_n\sin n\theta)\Big].\end{aligned} \tag{3.3.19}$$

The solution (3.3.17) and (3.3.19) shows that the $n = 0$ and $n = 1$ modes are neutrally stable, and that all higher modes are stable. The $n = 1$ mode corresponds to a translation of the circular free surface (3.3.15) (rather than a deformation of it), and so it is to be expected that both the $n = 0$ and $n = 1$ modes are neutrally stable in both the circular case and nearly-circular case. However, the decay rates of the higher modes are different in the nearly-circular case than in the circular case due to the influence of the non-circular substrate.

3.3.3.2 Early-time behaviour in the presence of gravity

The early-time behaviour of (3.3.14) can be examined by setting

$$\eta(\theta, \breve{t}) = 1 + \frac{Ca}{\varepsilon}\breve{\eta}_1(\theta, \breve{t}) + \left(\frac{Ca}{\varepsilon}\right)^2 \breve{\eta}_2(\theta, \breve{t}) + \mathcal{O}\left(\left(\frac{Ca}{\varepsilon}\right)^3\right) \tag{3.3.20}$$

and solving for $\breve{\eta}_1$ and $\breve{\eta}_2$ to yield

$$\begin{aligned}\eta =& 1 + \frac{Ca}{\varepsilon}\left[\frac{1}{2}\cos 2\theta(\mathrm{e}^{-4\breve{t}} - 1) - \frac{\breve{t}}{3}\sin\theta\right] \\ &+ \left(\frac{Ca}{\varepsilon}\right)^2\left[\left(\frac{\breve{t}}{4} - \frac{3}{32} + \frac{1}{8}\mathrm{e}^{-4\breve{t}}\left(\breve{t} + \frac{3}{4}\right)\right)\sin\theta\right. \\ &\quad + \left(\frac{1}{32} + \frac{3}{40}\mathrm{e}^{-4\breve{t}}\left(\breve{t} - \frac{11}{20}\right) + \frac{1}{100}\mathrm{e}^{-24\breve{t}}\right)\sin 3\theta \\ &\quad + \left(\frac{1}{48}(1 - \mathrm{e}^{-4\breve{t}}) - \frac{\breve{t}}{12}\right)\cos 2\theta \\ &\quad \left. + \left(\frac{3}{76}\mathrm{e}^{-4\breve{t}} - \frac{1}{24}\mathrm{e}^{-8\breve{t}} + \frac{1}{456}\mathrm{e}^{-80\breve{t}}\right)\cos 4\theta\right] + \mathcal{O}\left(\left(\frac{Ca}{\varepsilon}\right)^3\right).\end{aligned} \tag{3.3.21}$$

The terms in the solution (3.3.21) become disordered when $\breve{t} = \mathcal{O}(\varepsilon/Ca) \gg 1$. Two modes of disturbance are present. The first, due to the $\sin 2\theta$ forcing term in (3.3.14), generates terms of the form $\cos 2n\theta, n \in \mathbb{N}$ in (3.3.21), which correspond to thinning of the film at the tips of the ellipse due to surface tension attempting to drive the free surface towards circularity. The second, due to the $-\cos\theta/3$ forcing term in (3.3.14), generates terms of the form $\sin(2n+1)\theta, n \in \mathbb{N}$ in (3.3.21), which correspond to draining due to gravity. Figure 3.6 shows plots of the asymptotic solution (3.3.21) and the numerical solution to the PDE (3.3.14) for $\varepsilon = 0.001$ and

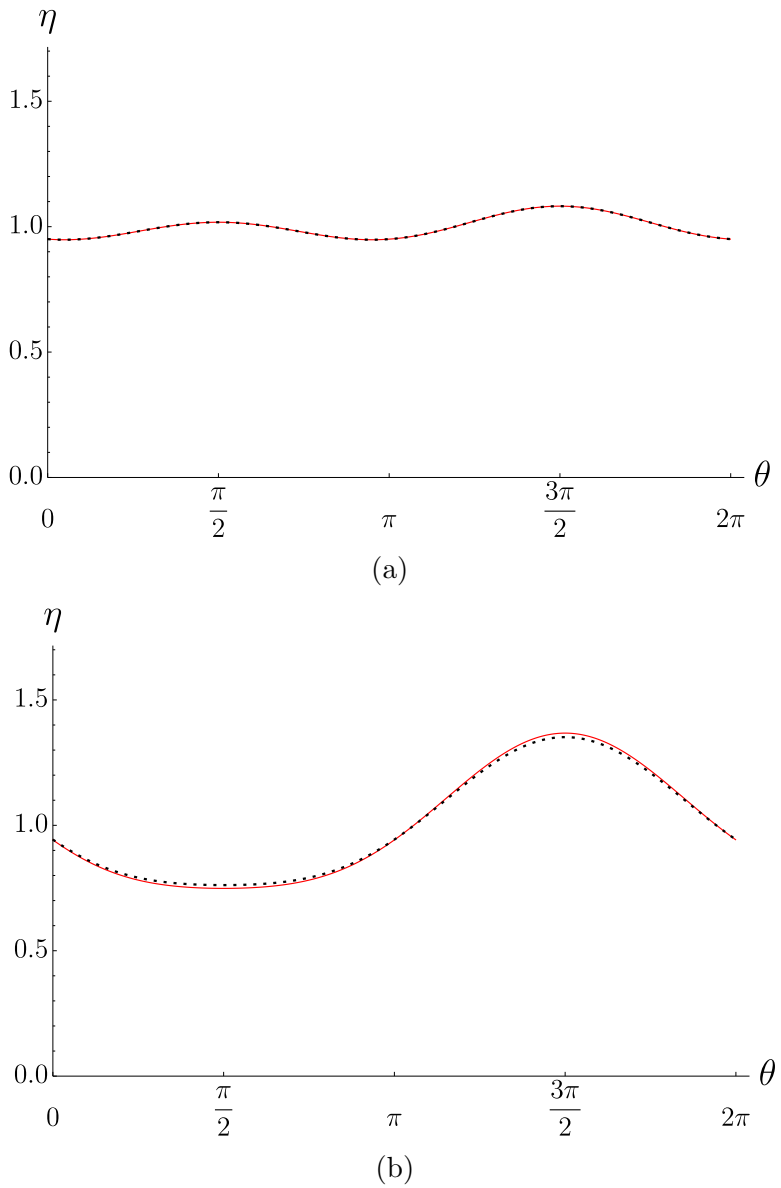

Figure 3.6: Plots of the asymptotic solution (3.3.21) (solid red line) and the numerical solution of the PDE (3.3.14) (dotted black line) with $\varepsilon = 0.001$ and $Ca = 0.0001$ at (a) $\breve{t} = 1$ and (b) $\breve{t} = 10$.

$Ca = 0.0001$ at times $\breve{t} = 1$ and $\breve{t} = 10$. As seen in Figure 3.6(a), thinning initially occurs at $\theta = 0$ and $\theta = \pi$, i.e. at the tips of the ellipse, due to the effect of surface tension, with corresponding thickening at $\theta = \pi/2$ and $\theta = 3\pi/2$ due to mass conservation. As seen in Figure 3.6(b), the thickening at $\theta = 3\pi/2$ subsequently becomes more pronounced than that at $\pi/2$ due to draining due to gravity, as can be inferred from the first-order solution in (3.3.21). At early times, the agreement between (3.3.21) and (3.3.14) is excellent, however, despite the terms in (3.3.21) becoming disordered at $\breve{t} = \mathcal{O}(\varepsilon/Ca) = \mathcal{O}(10)$ the agreement in Figure 3.6(b) (i.e. at $\breve{t} = 10$) is still very good.

3.3.4 Numerical study of draining flow on a stationary ellipse

In Sections 3.3.1–3.3.3 we examined equation (3.3.1) both analytically and numerically in various limits. Now we numerically examine the behaviour of equation (3.3.1) in general. In particular, we will show that two parameter sets which differ only in their value of b, namely

$$\widetilde{M} = 0.15, \quad b = 0.15 \text{ and } 0.45, \quad Re = 400, \quad Ca = 20, \tag{3.3.22}$$

result in qualitatively different behaviours. The unscaled mass $\widetilde{M} = 0.15$ is the same for both values of b with $\varepsilon = 0.03540$ and $\varepsilon = 0.03113$ for $b = 0.15$ and $b = 0.45$, respectively.

Figure 3.7 shows plots of the free surface corresponding to the parameters (3.3.22) at time $\widetilde{t} = \widetilde{t}_f = 2.5 \times 10^8$. Figures 3.7(a) and 3.7(b) shows plots of the free surface on a Cartesian plot for $b = 0.15$ and $b = 0.45$, respectively, and Figures 3.7(c) and 3.7(d) shows plots of the unscaled free surface on the ellipse for $b = 0.15$ and $b = 0.45$, respectively. The free surfaces exhibit local minima, which are denoted by crosses. Figures 3.7(a) and 3.7(c) show that there is a portion of the fluid trapped on the top of the ellipse between the local minima for $b = 0.15$, while Figures 3.7(b) and 3.7(d) show that there is no fluid trapped between the local minima for $b = 0.45$. This is shown more clearly in Figure 3.8. Figure 3.8(a) shows the fluid mass between the two local minima as a function of time, namely

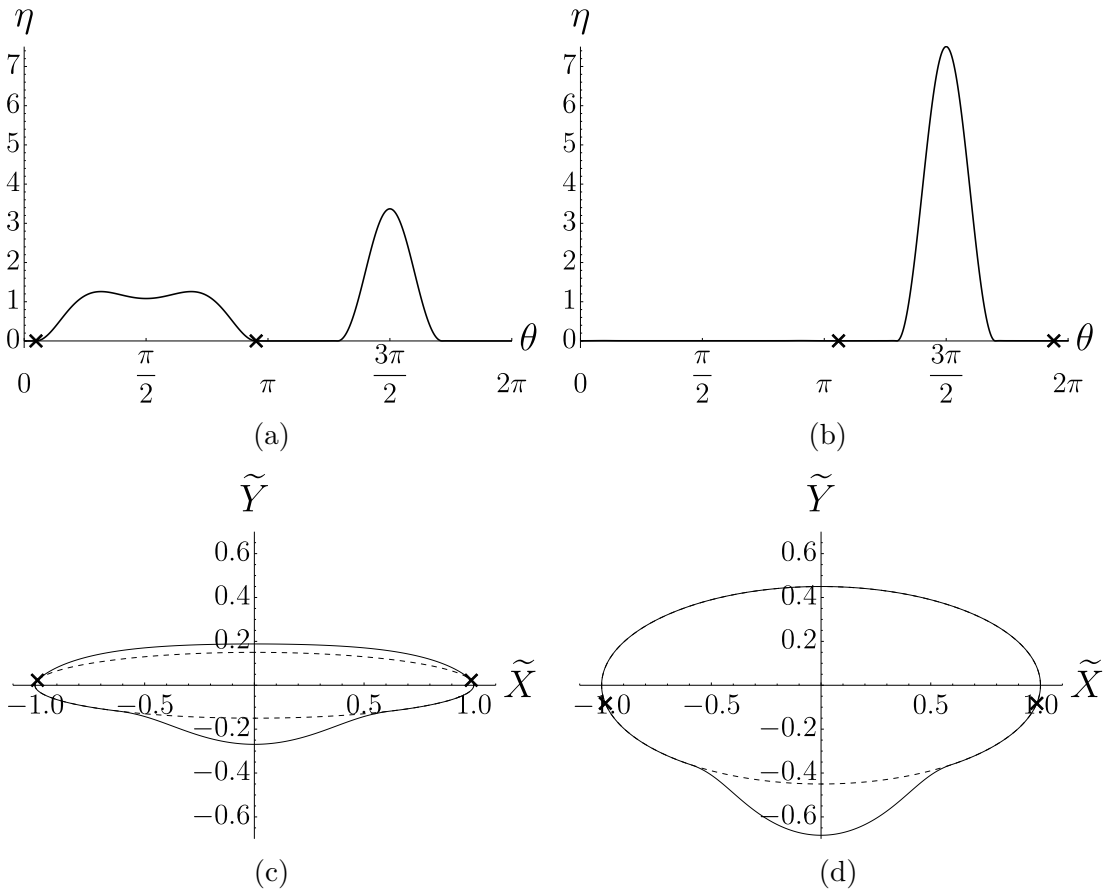

Figure 3.7: Plots of the free surface with $b = 0.15$ (left column) and $b = 0.45$ (right column) at $\widetilde{t} = \widetilde{t}_f = 2.5 \times 10^8$. The other parameters are as given in (3.3.22). The plots (a, b) show the free surface on a Cartesian plot, and the plots (c, d) show the unscaled free surface (solid lines) on the ellipse. The dashed lines in (c, d) are the ellipse. The crosses denote the positions of the local minima of the free surfaces.

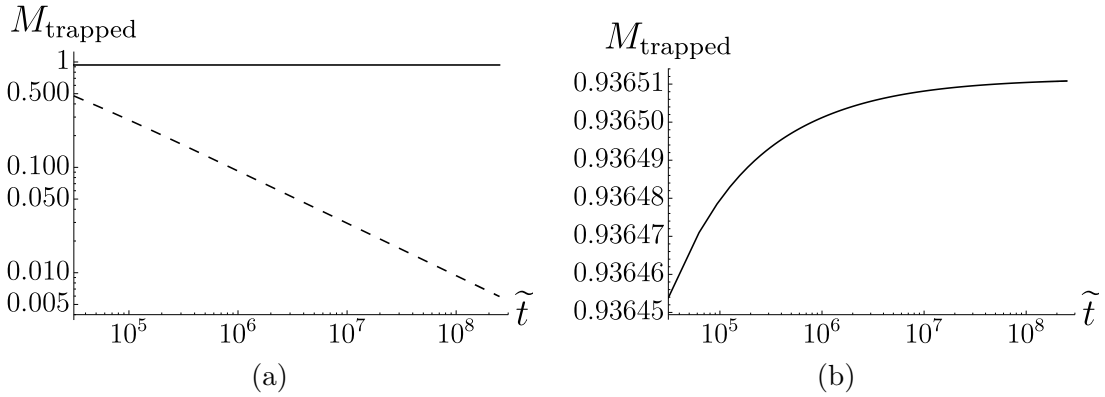

Figure 3.8: Plots of (a) the fluid mass between the local minima, M_{trapped} (3.3.23), for $b = 0.15$ (solid) and $b = 0.45$ (dashed) on a log-log plot, and (b) a zoom of the $b = 0.15$ curve. M_{trapped} is calculated to $\widetilde{t} = \widetilde{t}_f = 2.5 \times 10^8$ and the other parameters are as given in (3.3.22). The gradients of the lines are 1.285×10^{-6} and -0.497 for $b = 0.15$ and $b = 0.45$, respectively.

$$M_{\text{trapped}}(\widetilde{t}) = \int_{\theta_1}^{\theta_2} m\eta + \frac{\varepsilon}{2}\frac{b}{m^2}\eta^2 \, \mathrm{d}\theta, \tag{3.3.23}$$

where θ_1 and θ_2 ($> \theta_1$) are the positions of the local minima, for both $b = 0.15$ and $b = 0.45$ on a log-log plot. Figure 3.8(b) shows a zoom of the $b = 0.15$ curve. For $b = 0.45$, the log-log plot in Figure 3.8(a) has a gradient of -0.497, indicating that the film drains like $\mathcal{O}(\widetilde{t}^{-1/2})$. This temporal scaling agrees well with the $\widetilde{t}^{-1/2}$ scaling predicted by Takagi and Huppert [227], Qin et al. [228], and McKinlay et al. [149], suggesting that draining takes place in the same way as on circular cylinders and spheres. In contrast, for $b = 0.15$ the log-log plot in Figure 3.8(a) has a gradient of 1.285×10^{-6} (i.e. effectively zero), which indicates that fluid is indeed trapped between the two local minima.

In order to investigate this trapped fluid further, we examine the film thickness at various points on the surface of the ellipse for both $b = 0.15$ and $b = 0.45$ in Figure 3.9. Figure 3.9(a) shows the film thickness at the top of the ellipse, i.e. at $\theta = \pi/2$, as a function of time on a log-log plot and, in the case $b = 0.45$, the film thickness decreases with a gradient of -0.500, again in agreement with Takagi and Huppert [227], Qin et al. [228] and McKinlay et al. [149]. Figure 3.9(b) shows a zoom of the $b = 0.15$ curve from Figure 3.9(a). In contrast, for $b = 0.15$ the log-log plot in Figure 3.9(a) has a gradient of 1.541×10^{-5} (i.e. again, effectively zero), which indicates that the film thickness approaches a constant value. Figure 3.9(c)

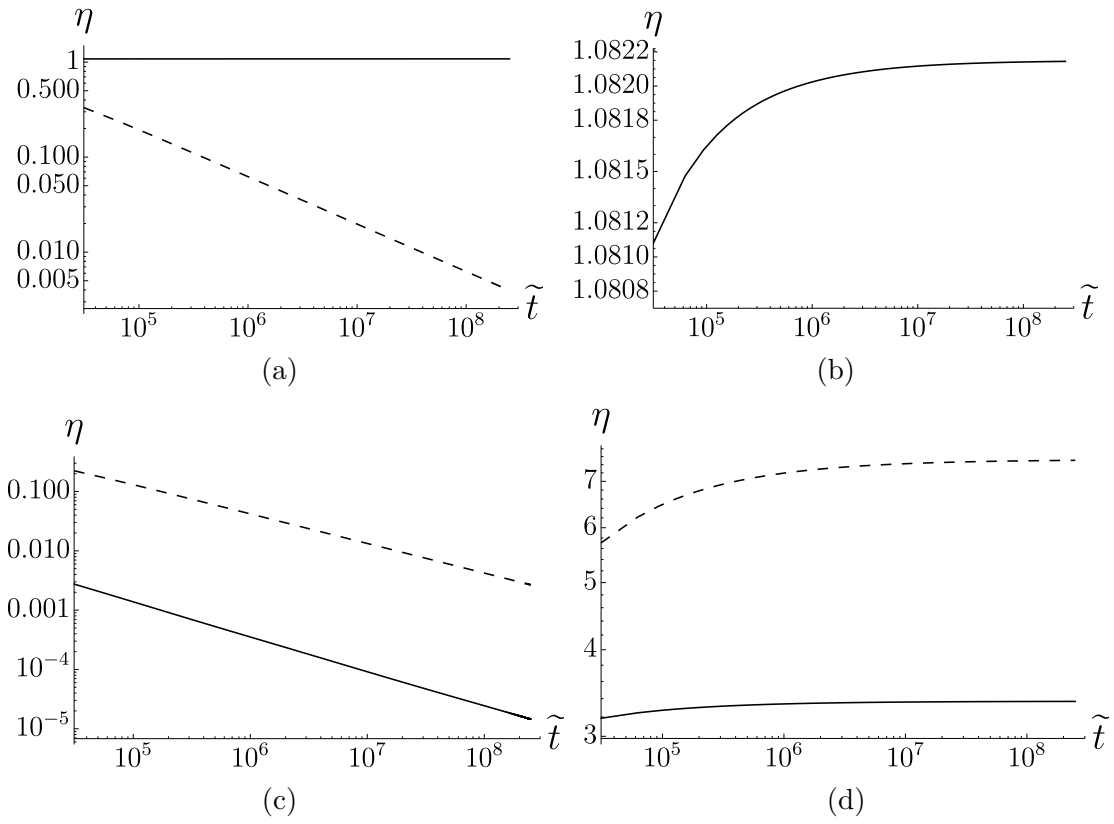

Figure 3.9: Plots of the film thickness for $b = 0.15$ (solid) and $b = 0.45$ (dashed) (a) at $\theta = \pi/2$, (b) a zoom of the $b = 0.15$ curve from (a), (c) at the local minima, and (d) at $\theta = 3\pi/2$. The thickness is calculated to $\widetilde{t} = \widetilde{t}_f = 2.5\times10^8$ and the other parameters are as given in (3.3.22). The gradients of the lines are (a) 1.541×10^{-5} and -0.500, (c) -0.574 and -0.499, (d) 1.077×10^{-3} and 5.482×10^{-3} for $b = 0.15$ and $b = 0.45$, respectively. Note that these plots use different scales.

shows the film thickness at the local minima (denoted by crosses in Figure 3.7) as a function of time on a log-log plot. Both curves are decreasing, but the gradient of the curve corresponding to $b = 0.15$ (-0.574) is slightly steeper than that of the curve corresponding to $b = 0.45$ (-0.499). This might be expected as, in order to trap fluid, one might anticipate that the film thickness at the local minima for the case $b = 0.15$ would approach zero more quickly than for the case $b = 0.45$ in which complete draining occurs. Figure 3.9(d) shows the film thickness at the bottom of the ellipse, i.e. at $\theta = 3\pi/2$, as a function of time on a log-log plot. As expected, the log-log plots for both $b = 0.15$ and $b = 0.45$ (with gradients of 1.077×10^{-3} and 5.482×10^{-3}, respectively) approach a constant value asymptotically in the limit of large time. This limiting value is larger for $b = 0.45$, corresponding to a greater film thickness as, in this case, all of the fluid drains into the bottom bulge, unlike in the $b = 0.15$ case, in which some of the fluid is trapped on top of the ellipse.

In this section, for the parameter values given in (3.3.23), we have presented a case in which fluid is trapped for $b = 0.15$ and a case in which complete draining occurs for $b = 0.45$. For $0 < b \leq 0.15$ we expect that we would observe the case of trapped fluid, and for $0.45 \leq b \leq 1$ we expect that we would observe the case of complete draining. However, we have not been able to find a critical value of b for the transition between these two cases for $0.15 < b < 0.45$.

3.4 Low rotation speed

In Sections 3.4–3.6 we examine the characteristic behaviour of the free surface in each of the four regions introduced in Section 3.1.2 for the parameter values given in (3.1.1).

In the low rotation speed regime ($0 < W < W_1(0.9) \approx 0.105$) there is a single main bulge (and sometimes a smaller secondary bulge, as we show in the present section), which hangs below the cylinder due to gravity and oscillates periodically due to the rotation of the cylinder. This regime was studied by Li et al. [125] and Parrish et al. [167], but was not studied by Hunt [168] due to the absence of surface tension in this work (as discussed in Section 1.5.2). Figure 3.10 shows the unscaled free surface in the laboratory frame when the semi-major axis of the ellipse is perpendicular to the direction of gravity and when it is parallel to the direction of gravity. The single main bulge located in the lower right-hand quadrant

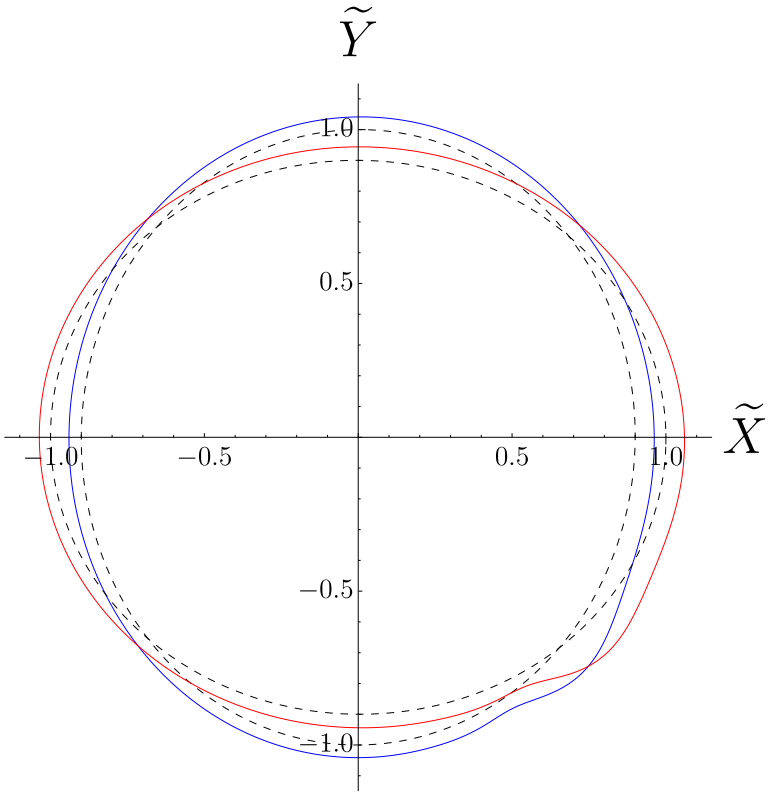

Figure 3.10: The unscaled free surface on the ellipse in the laboratory frame when the semi-major axis is perpendicular to the direction of gravity (red line) and when it is parallel to the direction of gravity (blue line) for $W = 0.09$. The dashed lines are the ellipse at the corresponding times. The other parameters are as given in (3.1.1).

shown in Figure 3.10 oscillates as the cylinder rotates due to the eccentricity of the cylinder. Figure 3.11 shows the location of the centre of mass in the laboratory frame for $W = 0.09$. Figure 3.11(a) shows the location for the centre of mass from $\widetilde{t} = 0$ to $\widetilde{t} = \widetilde{t}_f = 5 \times 10^4$ and shows that the centre of mass has an initial transient phase before converging to a periodic orbit. Figure 3.11(b) shows the location of the centre of mass from $\widetilde{t} = 7.5 \times 10^3$ to $\widetilde{t} = \widetilde{t}_f = 5 \times 10^4$ (i.e. after the initial transient phase). In Figure 3.11, a circle has been fitted to the periodic orbit, showing that the orbit is almost, but not quite, circular. One period of the single main bulge corresponds to one half rotation of the cylinder. Figure 3.12 shows a space-time plot for the free surface in the rotating frame from $\widetilde{t} = 4.5 \times 10^4$ to $\widetilde{t} = \widetilde{t}_f = 5 \times 10^4$ for $W = 0.09$, in which the single main bulge, which does not grow or decay over time, is clearly visible.

Figure 3.13(a) shows a plot of E_n, the time-averaged integral (up to $\widetilde{t} = \widetilde{t}_f = 5 \times 10^4$) of the absolute value of the n^{th} mode of the Fourier transform of the free surface for $n = 1, \ldots, 5$ as a function of W, i.e.,

$$E_n = \frac{1}{\widetilde{t}_{\text{f}}} \int_0^{\widetilde{t}_{\text{f}}} \left| \frac{1}{2\pi} \int_0^{2\pi} \eta(\theta, \widetilde{t}) \mathrm{e}^{-in\theta} \, \mathrm{d}\theta \right| \, \mathrm{d}\widetilde{t}. \tag{3.4.1}$$

For brevity, we term E_n the "energy" of the n^{th} Fourier mode. The energies of the higher modes are smaller and are omitted for clarity. Loosely speaking, E_n corresponds to the significance of the n^{th} mode in the shape of the free surface. For example, for $W = 0.09$ the dominance of the $n = 1$ mode evident in Figure 3.13(a) corresponds to the single main bulge which hangs below the cylinder, as shown in Figure 3.12. In particular, Figure 3.13(a) shows that for all W in this regime E_1 is dominant, corresponding to the free surface having a single main bulge which hangs below the cylinder. Figure 3.13(a) shows that there is an abrupt decrease in energy at $W \approx 0.058$. Above this value of W, all of the energies are lower than they were for smaller values of W, but E_1 is proportionally even more dominant than it is below this value. Figure 3.13(b) shows a plot of the time-averaged maximum film thickness and the time-averaged minimum film thickness as a function of W. Figure 3.13(b) shows that there is also an abrupt decrease in the time-averaged maximum film thickness (and a small increase in the time-averaged minimum film thickness) at $W \approx 0.058$.

Figure 3.14 shows a plot of the free surface at $\widetilde{t} = 3.5 \times 10^3$ (dashed lines) and

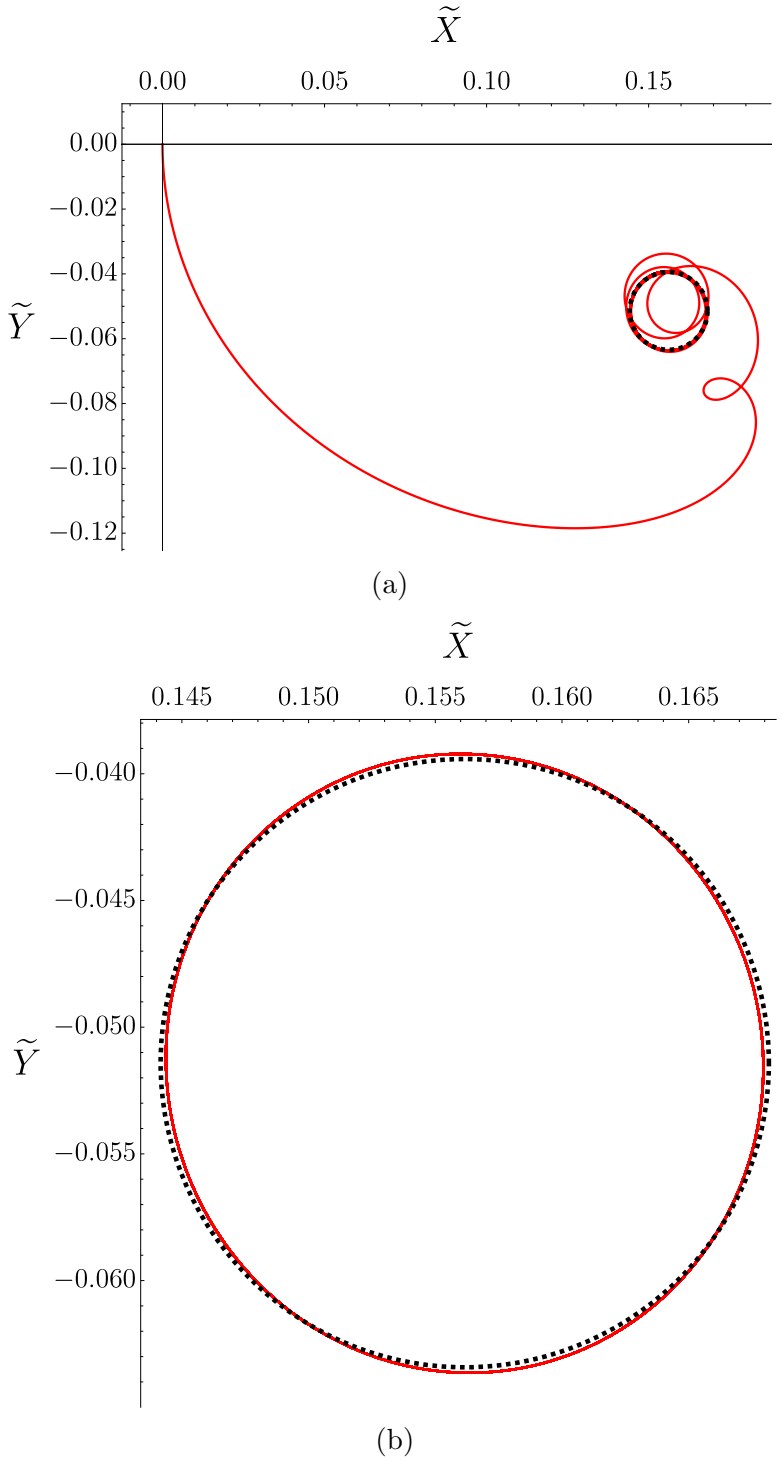

Figure 3.11: The location of the centre of mass in the laboratory frame (solid red line) (a) from $\widetilde{t} = 0$ to $\widetilde{t} = 5 \times 10^4$ and (b) from $\widetilde{t} = 7.5 \times 10^3$ to $\widetilde{t} = 5 \times 10^4$ for $W = 0.09$. A circle (shown with a dotted black line) has been fitted to the periodic orbit. The other parameters are as given in (3.1.1).

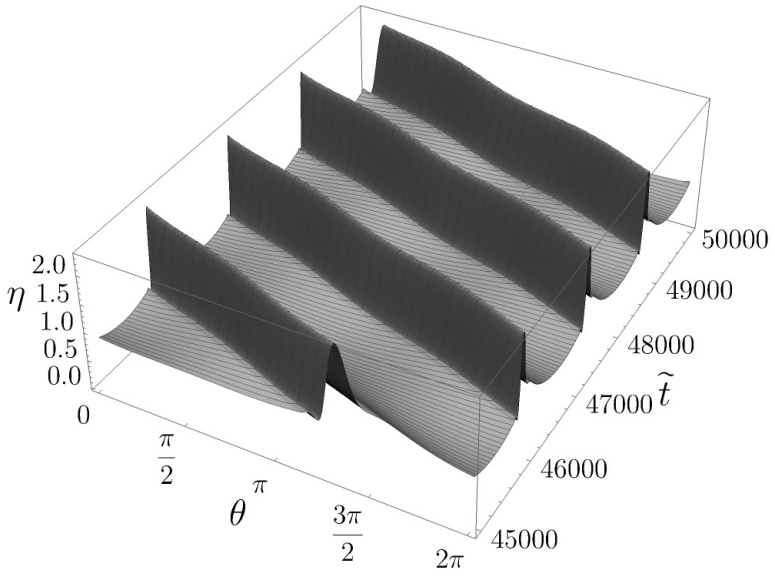

Figure 3.12: Space-time plot in the low rotation speed regime ($0 < W < W_1(0.9) \approx 0.105$) for the free surface in the rotating frame from $\widetilde{t} = 4.5\times10^4$ to $\widetilde{t} = \widetilde{t}_f = 5\times10^4$ for $W = 0.09$. The other parameters are as given in (3.1.1).

$\widetilde{t} = 4.7 \times 10^4$ (solid lines) for two values of W, one on either side of $W \approx 0.058$. Figure 3.14(a), shows a plot of the free surface for $W = 0.056$. For this value of W, at $\widetilde{t} = 3.5 \times 10^3$ a single main bulge is formed in the free surface, with a smaller secondary bulge formed to the right. However, by $\widetilde{t} = 4.7 \times 10^4$ the fluid has drained from the secondary bulge into the single main bulge, significantly increasing (decreasing) the maximum (minimum) film thickness. The fluid draining from the secondary bulge into the single main bulge corresponds to a larger value of E_1 in Figure 3.13(a) and a higher (lower) value of the time-averaged maximum (minimum) film thickness in Figure 3.13(b). Figure 3.14(b) shows a plot of the free surface for $W = 0.060$. Again, for this value of W, at $\widetilde{t} = 3.5 \times 10^3$, a single main bulge is formed in the free surface, with a smaller secondary bulge formed to the right. However, by $\widetilde{t} = 4.7 \times 10^4$, unlike in Figure 3.14(a), the secondary bulge remains (i.e. the fluid has not drained from the secondary bulge into the single main bulge), and the maximum and minimum film thickness does not vary significantly. In particular, Figure 3.14(b) shows that more fluid is being carried around with the rotating cylinder, corresponding to a thicker film elsewhere, and a lower proportion of the fluid accumulating in both the single main bulge and the secondary bulge. The fluid not draining from the secondary bulge into the single main bulge, as well as more fluid being carried around with the rotating cylinder,

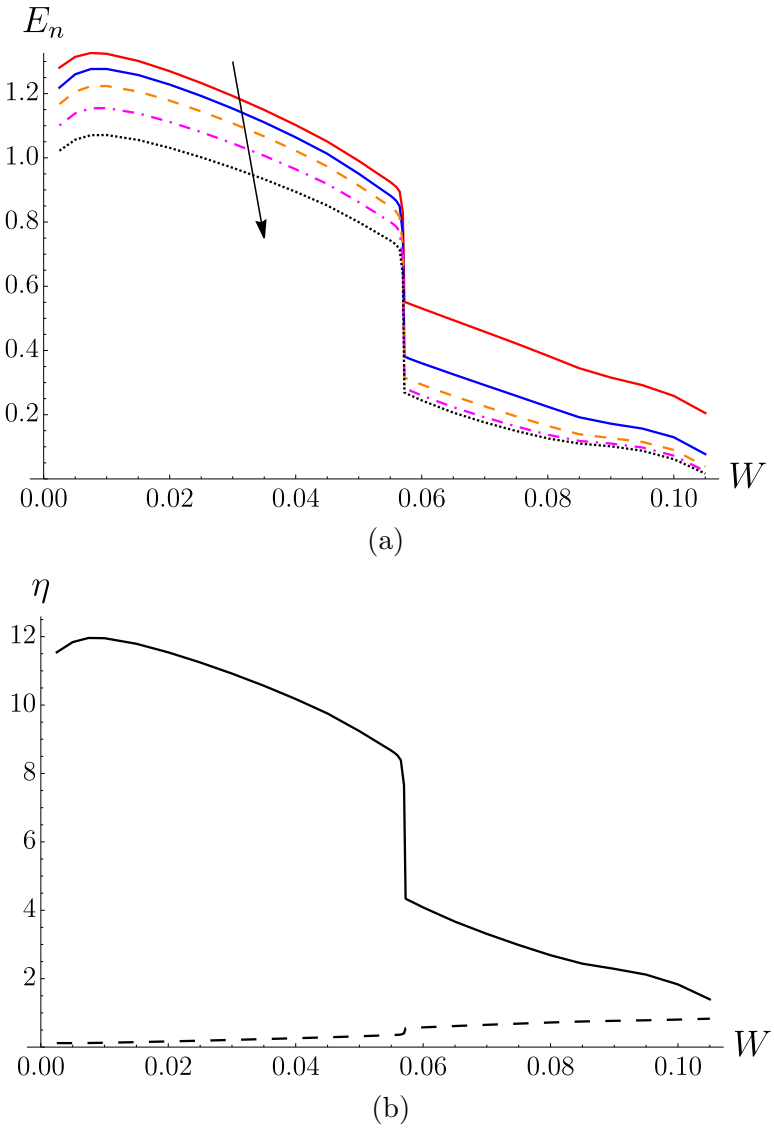

Figure 3.13: For all values of W in the low rotation speed regime ($0 < W < W_1(0.9) \approx 0.105$). (a) The energy of the n^{th} Fourier mode E_n for $n = 1, \ldots, 5$, plotted as a function of W. The $n = 1, \ldots, 5$ modes are shown with solid red, solid blue, dashed orange, dot-dashed purple, and dotted black lines, respectively, and the arrow indicates the direction of increasing n. (b) The time-averaged maximum film thickness (solid) and the time-averaged minimum film thickness (dashed) plotted as functions of W. Both (a) and (b) are calculated to $\widetilde{t} = \widetilde{t}_f = 5 \times 10^4$. The other parameters are as given in (3.1.1).

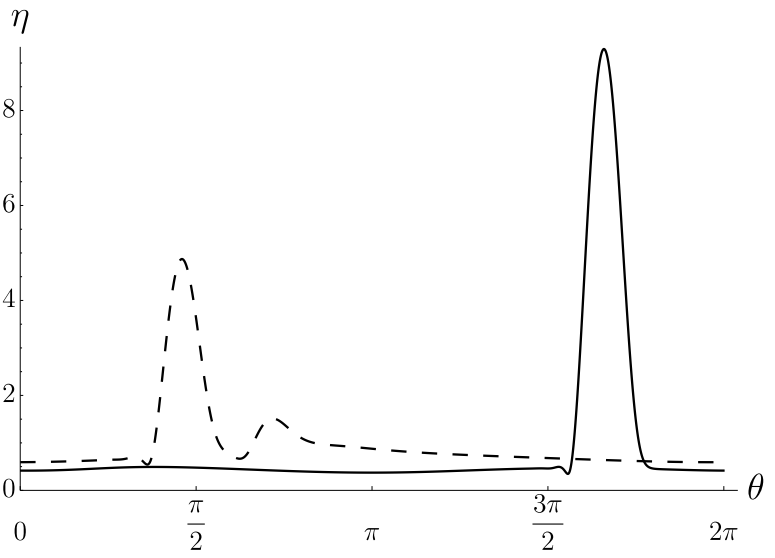

(a)

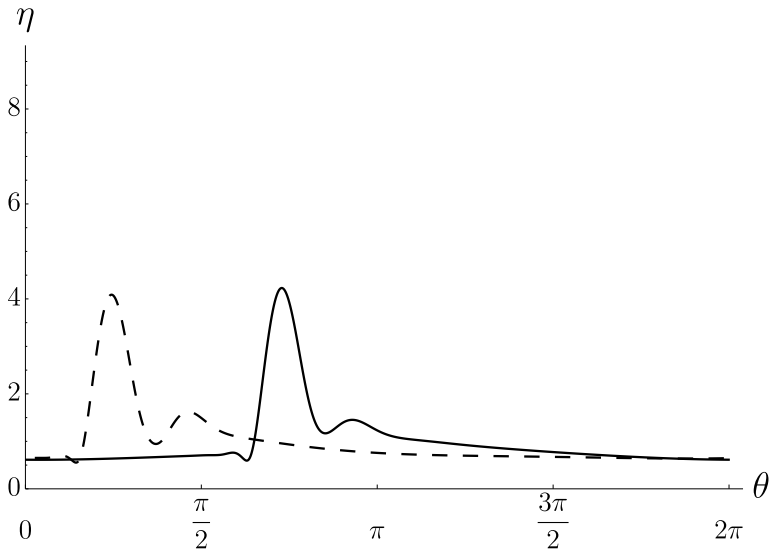

(b)

Figure 3.14: Plots of the free surface in the rotating frame for (a) $W = 0.056$ and (b) $W = 0.060$. The dashed lines and solid lines show the free surface in the rotating frame at $\widetilde{t} = 3.5 \times 10^3$ and $\widetilde{t} = 4.7 \times 10^4$, respectively. The other parameters are as given in (3.1.1).

corresponds to a smaller value of E_1 in Figure 3.13(a) and a lower (higher) value of the time-averaged maximum (minimum) film thickness in Figure 3.13(b). Figure 3.15 shows the location of the centre of mass in the laboratory frame for two values of W, one on either side of $W \approx 0.058$. Figure 3.15(a) shows the location of the centre of mass for $W = 0.056$. For this value of W, the location of the centre of mass initially oscillates around $(\widetilde{X}_c^{av}, \widetilde{Y}_c^{av}) \approx (0.18, -0.25)$ (i.e. fluid is held in the secondary bulge) before converging to a periodic orbit (shown by the dashed black line) around $(\widetilde{X}_c^{av}, \widetilde{Y}_c^{av}) \approx (0.09, -0.62)$ (i.e. fluid has drained from the secondary bulge into the single main bulge). Figure 3.15(b) shows the location of the centre of mass for $W = 0.060$. For $W = 0.060$, the location of the centre of mass oscillates around $(\widetilde{X}_c^{av}, \widetilde{Y}_c^{av}) \approx (0.185, -0.225)$ in a periodic orbit (shown by the dashed black line) but, in contrast to the case $W = 0.056$, does not subsequently move to $(0.09, -0.62)$.

As the value of W increases from $W = 0.058$ towards $W_1(0.9) \approx 0.105$, the secondary bulge coalesces with the single main bulge, as shown in Figure 3.16 which shows a plot of the free surface at $\widetilde{t} = 4.7 \times 10^4$ for $W = 0.09$. As the value of W increases from $W = 0.058$ towards $W_1(0.9) \approx 0.105$, the average position of the single main bulge moves higher up the upward-moving side of the cylinder in the laboratory frame. As a result, as W approaches $W_1(b)$ from below the time-averaged $\widetilde{Y}$ position of the centre of mass, $\widetilde{Y}_c^{av}$, shown in Figure 3.1(b) increases until it reaches the horizontal $\widetilde{X}$ axis, corresponding to the transition to the low-moderate rotation speed regime, which occurs at $W = W_1(b)$ (where $W_1(0.9) \approx 0.105$).

3.5 Moderate rotation speed

We now discuss the low-moderate rotation speed regime in Section 3.5.1, and the high-moderate rotation speed regime in Section 3.5.2. The transition between the two regimes, which occurs at $W = W_2(0.9) \approx 0.410$, will be made precise in terms of the energy in Fourier modes.

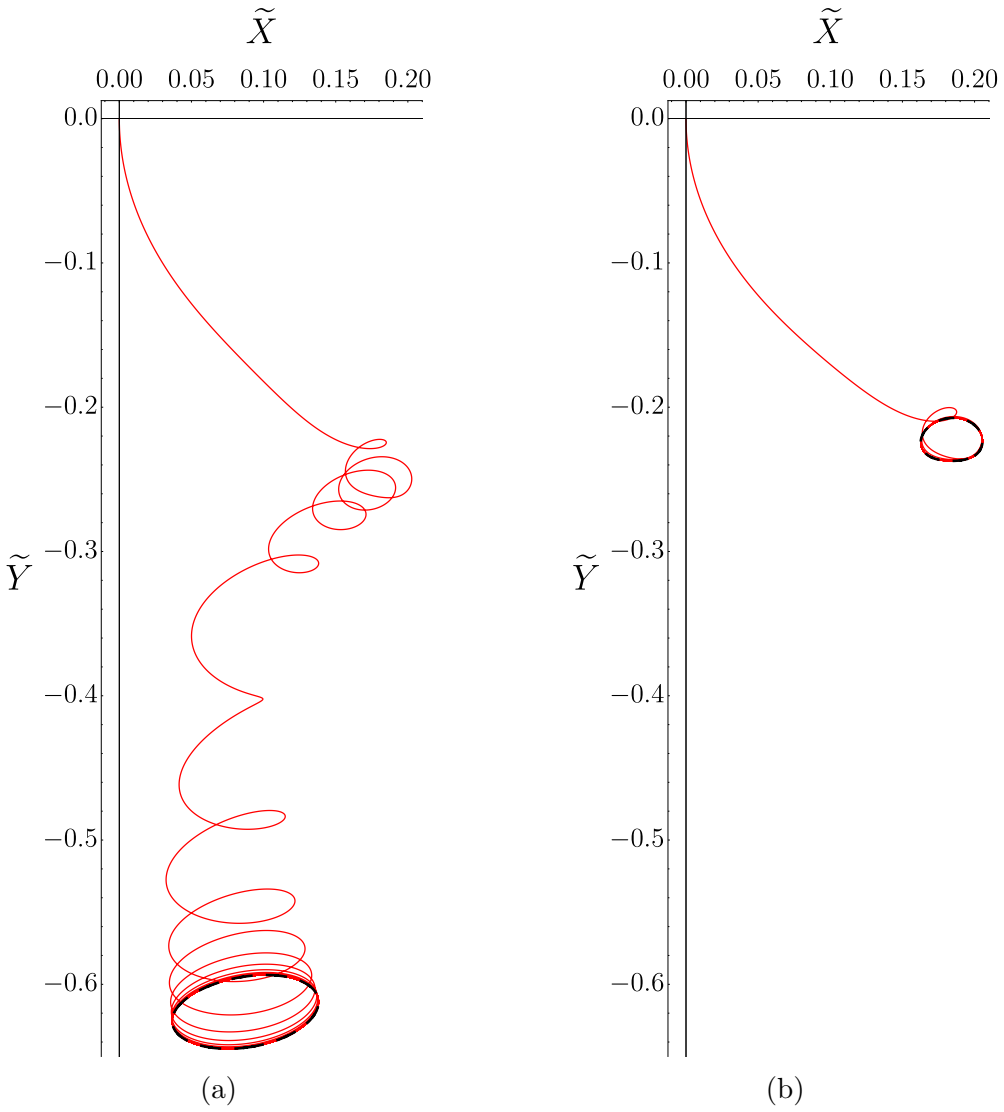

Figure 3.15: The location of the centre of mass in the laboratory frame (solid red line) for (a) $W = 0.056$ and (b) $W = 0.060$ in the low rotation speed regime ($0 < W < W_1(0.9) \approx 0.105$) from $\widetilde{t} = 0$ to $\widetilde{t} = \widetilde{t}_f = 5 \times 10^4$. The dashed black line shows the periodic orbit. The other parameters are as given in (3.1.1).

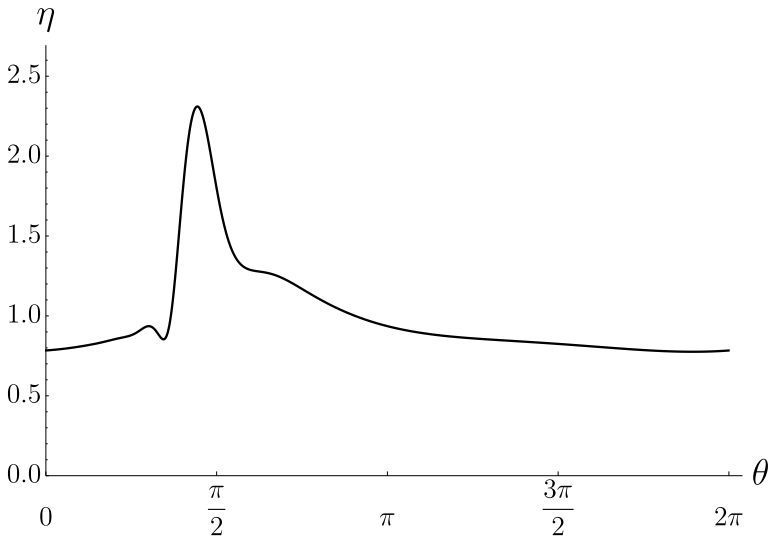

Figure 3.16: Plot of the free surface in the rotating frame for $W = 0.09$ at $\widetilde{t} = 4.7 \times 10^4$. The other parameters are as given in (3.1.1).

3.5.1 Low-moderate rotation speed

In the low-moderate rotation speed regime ($0.105 \approx W_1(0.9) \leq W \leq W_2(0.9) \approx 0.410$) a single main bulge (and smaller secondary bulges) is formed due to a combination of gravity and centrifugation. The single main bulge is carried past the horizontal $\widetilde{X}$ axis in the laboratory frame, travels anti-clockwise with the rotation of the cylinder, and grows, decays and occasionally coalesces with the secondary bulges. This regime was studied by Hunt [168] (in the absence of surface tension and centrifugation), Li et al. [125], and Parrish et al. [167] (as discussed in Section 1.5.2). Figure 3.17(a) shows a plot of E_n for $n = 1, \ldots, 5$ as a function of W. Figure 3.17(b) shows a plot of the time-averaged maximum film thickness and the time-averaged minimum film thickness as functions of W.

As W is increased towards 0.410, E_1 decreases, and the time-averaged maximum film thickness and time-averaged minimum film thickness approach one another. We therefore define $W_2(b)$ (where $W_2(0.9) \approx 0.410$) to be the critical value of W at which E_1 and E_2 coincide.

Figure 3.18 shows space-time plots in the rotating frame for $W = 0.32$ which demonstrate the characteristic behaviour in the low-moderate rotation speed regime. Figure 3.18(a) shows the space-time plot for the free surface in the rotating frame from $\tilde{t} = 1.5 \times 10^4$ to $\tilde{t} = \tilde{t}_f = 5 \times 10^4$. The single main bulge which travels

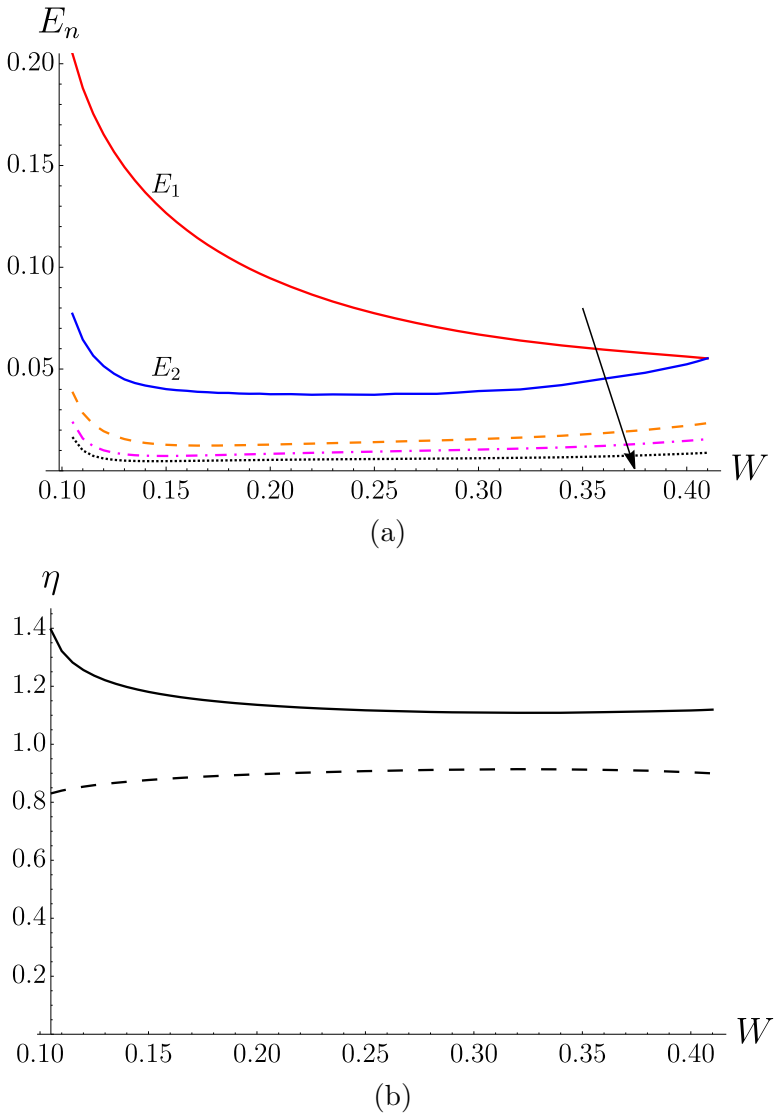

Figure 3.17: For all values of W in the low-moderate rotation speed regime ($0.105 \approx W_1(0.9) \leq W \leq W_2(0.9) \approx 0.410$). (a) The energy of the n^{th} Fourier mode E_n for $n = 1, \ldots, 5$, plotted as a function of W. The $n = 1, \ldots, 5$ modes are shown with solid red, solid blue, dashed orange, dot-dashed purple, and dotted black lines, respectively, and the arrow indicates the direction of increasing n. (b) The time-averaged maximum film thickness (solid) and the time-averaged minimum film thickness (dashed) plotted as functions of W. Both (a) and (b) are calculated to $\widetilde{t} = \widetilde{t}_f = 5 \times 10^4$. The other parameters are as given in (3.1.1).

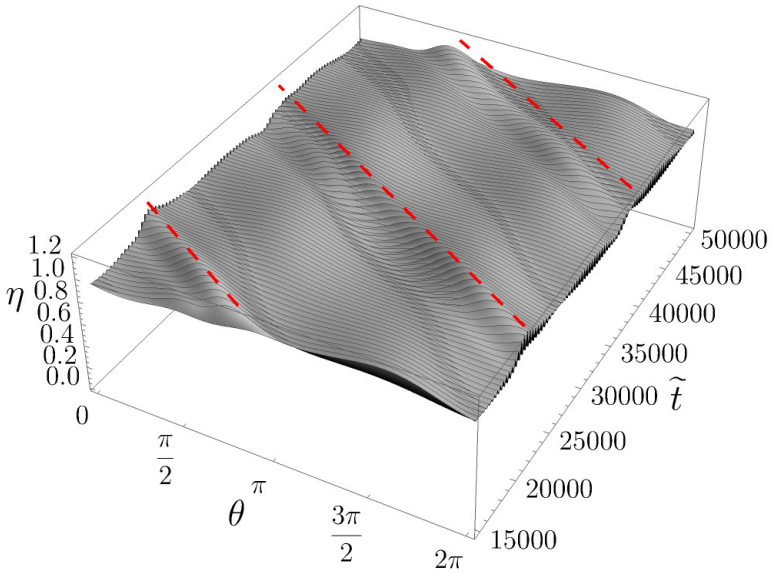

(a)

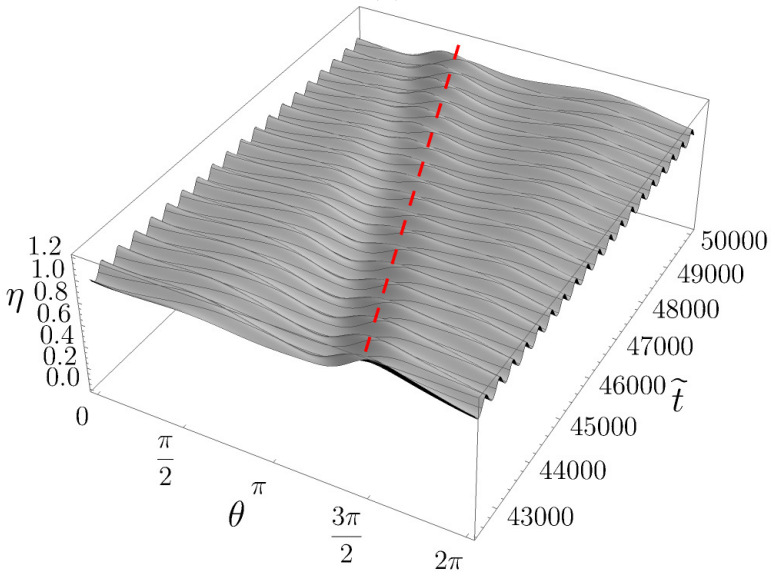

(b)

Figure 3.18: Space-time plot in the low-moderate rotation speed regime ($0.105 \approx W_1(0.9) \leq W \leq W_2(0.9) \approx 0.410$) for the free surface in the rotating frame (a) from $\tilde{t} = 1.5\times10^4$ to $\tilde{t} = \tilde{t}_f = 5\times10^4$ and (b) from $\tilde{t} = 4.25\times10^4$ to $\tilde{t} = \tilde{t}_f = 5\times10^4$ for $W = 0.32$. The dashed red lines in (a) and (b) highlight the single main bulge. The other parameters are as given in (3.1.1).

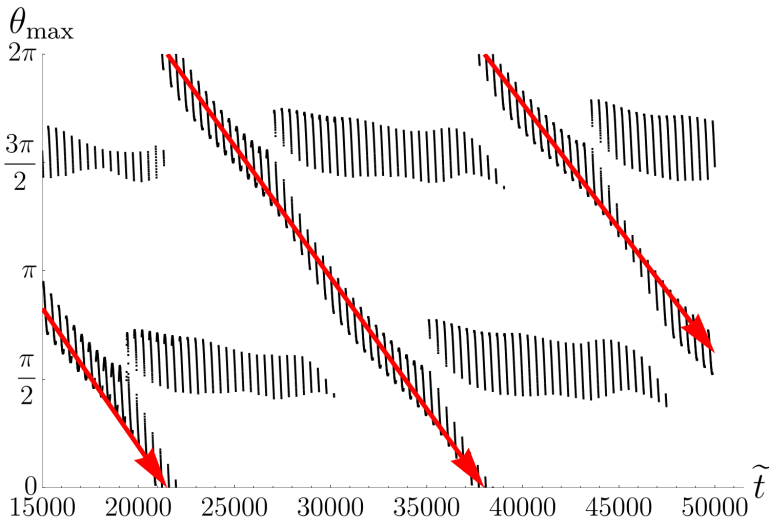

Figure 3.19: Plot of the location of the maximum film thickness in the rotating frame $\theta_{\max}$ as a function of time from $\tilde{t} = 1.5\times10^4$ to $\tilde{t} = \tilde{t}_f = 5\times10^4$ for $W = 0.32$, where the arrows indicate the direction that the single main bulge travels. The other parameters are as given in (3.1.1).

anti-clockwise with the rotation of the cylinder is highlighted by the dashed red lines. Figure 3.18(b) shows a zoom of the region between $\tilde{t} = 4.25 \times 10^4$ and $\tilde{t} = \tilde{t}_f = 5 \times 10^4$, at which scale two timescales are visible. The fast timescale corresponds to the rotation of the cylinder (i.e. the film being thicker on the upward-moving side of the cylinder) and the slow timescale corresponds to the single main bulge which travels anti-clockwise with the rotation of the cylinder (highlighted by the dashed red line). In particular, Figure 3.18 shows that the single main bulge travels anti-clockwise with the rotation of the cylinder, but at a speed slower than the rotation of the cylinder. Figure 3.19 shows a plot of the location of the maximum film thickness in the rotating frame $\theta_{\max}$ as a function of time from $\tilde{t} = 1.5 \times 10^4$ to $\tilde{t} = \tilde{t}_f = 5 \times 10^4$ for $W = 0.32$. Figure 3.19 shows that $\theta_{\max}$ alternates between three locations, namely near $\theta = \pi/2$ and $\theta = 3\pi/2$ (i.e. near the top and bottom of the cylinder), and the single main bulge (indicated by the arrows) which results in the "striped" pattern. For a fixed location on the vertical axis, each horizontal stripe corresponds to one rotation of the cylinder, i.e. the fast timescale. The slow timescale corresponding to the single main bulge travelling anti-clockwise with the rotation of the cylinder (indicated by the arrows), but at a speed slower than the rotation of the cylinder. The tendency for $\theta_{\max}$ to be located near $\theta = \pi/2$ and $\theta = 3\pi/2$ is due to the effect of surface

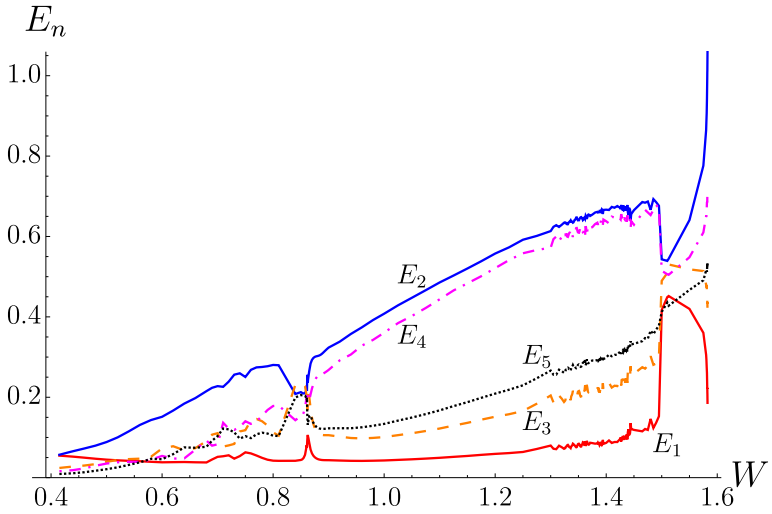

Figure 3.20: For all values of W in the high-moderate rotation speed regime ($0.410 \approx W_2(0.9) < W < W_3(0.9) \approx 1.583$), the energy of the n^{th} Fourier mode E_n for $n = 1, \ldots, 5$, plotted as a function of W, and calculated to $\widetilde{t} = \widetilde{t}_f = 5 \times 10^4$. The $n = 1, \ldots, 5$ modes are shown with solid red, solid blue, dashed orange, dot-dashed purple, and dotted black lines, respectively. The other parameters are as given in (3.1.1).

tension. Specifically, surface tension is attempting to drive the free surface towards circularity, and so the film will become thinner at $\theta = 0$ and $\theta = \pi$ (i.e. the tips of the ellipse) and thicker at $\theta = \pi/2$ and $\theta = 3\pi/2$ (i.e. the top and bottom of the ellipse). The sketch shown in Figure 2.1 is an example of this drive towards circularity.

3.5.2 High-moderate rotation speed

In the high-moderate rotation speed regime ($0.410 \approx W_2(0.9) < W < W_3(0.9) \approx 1.583$) multiple main bulges are formed at the tips of the ellipse due to a combination of gravity and centrifugation. The main bulges again travel anti-clockwise with the rotation of the cylinder, but at a speed slower than the rotation of the cylinder. This regime was not studied by Hunt [168], Li et al. [125], or Parrish et al. [167], as they did not explore this region of parameter space. Figure 3.20 shows a plot of E_n for $n = 1, \ldots, 5$ as a function of W. As W is increased from $W_2(0.9) \approx 0.410$, E_2 increases due to the stronger effect of centrifugation. The overall trend across the high-moderate rotation speed regime is that E_2 and E_4 increase approximately linearly, corresponding to the fact that the free surface

exhibits alternating configurations of two and four main bulges, which increase in amplitude with increasing W. Figure 3.21(a) shows the space-time plot of the free surface in the rotating frame for $W = 1.2$ which demonstrates the alternation between two and four main bulges, which is the most common behaviour in the high-moderate rotation speed regime. Figure 3.21(b) shows two cross-sections of Figure 3.21(a) showing two main bulges at $\widetilde{t} = 4.36 \times 10^4$ and four main bulges at $\widetilde{t} = 4.28 \times 10^4$. However, there are three exceptions to this behaviour, which we now discuss in turn.

First, close to $W \approx 0.86$, E_2 and E_4 decrease while E_3 and E_5 increase. Here instead of alternating between two and four main bulges the free surface alternates between three and five main bulges. Second, close to $W \approx 1.5$, E_2 decreases and E_1 increases. Here, the two main bulges are initially held at the tips of the ellipse. As the size of the two main bulges increase, the effect of gravity effectively overpowers the effect of centrifugation, and so the two main bulges begin to travel around the cylinder in the same direction as the cylinder rotation (as they can no longer be held at the tips of the ellipse) and eventually coalesce into a single main bulge. The third and final exception is at the upper limit $W = W_3(0.9) \approx 1.583$, at which E_2 increases significantly. The closer W is to $W_3(0.9) \approx 1.583$, the longer the two main bulges are held at the tips before they begin to travel around the cylinder and coalesce into a single main bulge.

Figures 3.22(a), 3.23(a), and 3.23(b) show space-time plots of the free surface in the rotating frame for $W = 0.86$, $W = 1.5$, and $W = 1.575$, respectively, corresponding to the three exceptions discussed above. Figure 3.22(a) shows a space-time plot in the rotating frame for the first exception, corresponding to $W = 0.86$. In this case, the free surface alternates between three and five main bulges. Figure 3.22(b) shows two cross-sections of Figure 3.22(a) showing three main bulges at $\widetilde{t} = 4.49 \times 10^4$ and five main bulges at $\widetilde{t} = 4.21 \times 10^4$. Figure 3.23(a) shows a space-time plot in the rotating frame for the second exception, corresponding to $W = 1.5$. In this case, the two main bulges are held at the tips of the ellipse until $\widetilde{t} \approx 9 \times 10^3$ when they begin to travel around the cylinder and coalesce into a single main bulge by $\widetilde{t} \approx 1.7 \times 10^4$. Figure 3.23(b) shows a space-time plot in the rotating frame for the third exception, corresponding to $W = 1.575$. In this case, the two main bulges are held at the tips of the ellipse until $\widetilde{t} \approx 2.5 \times 10^4$, at which point the two main bulges begin to travel around the

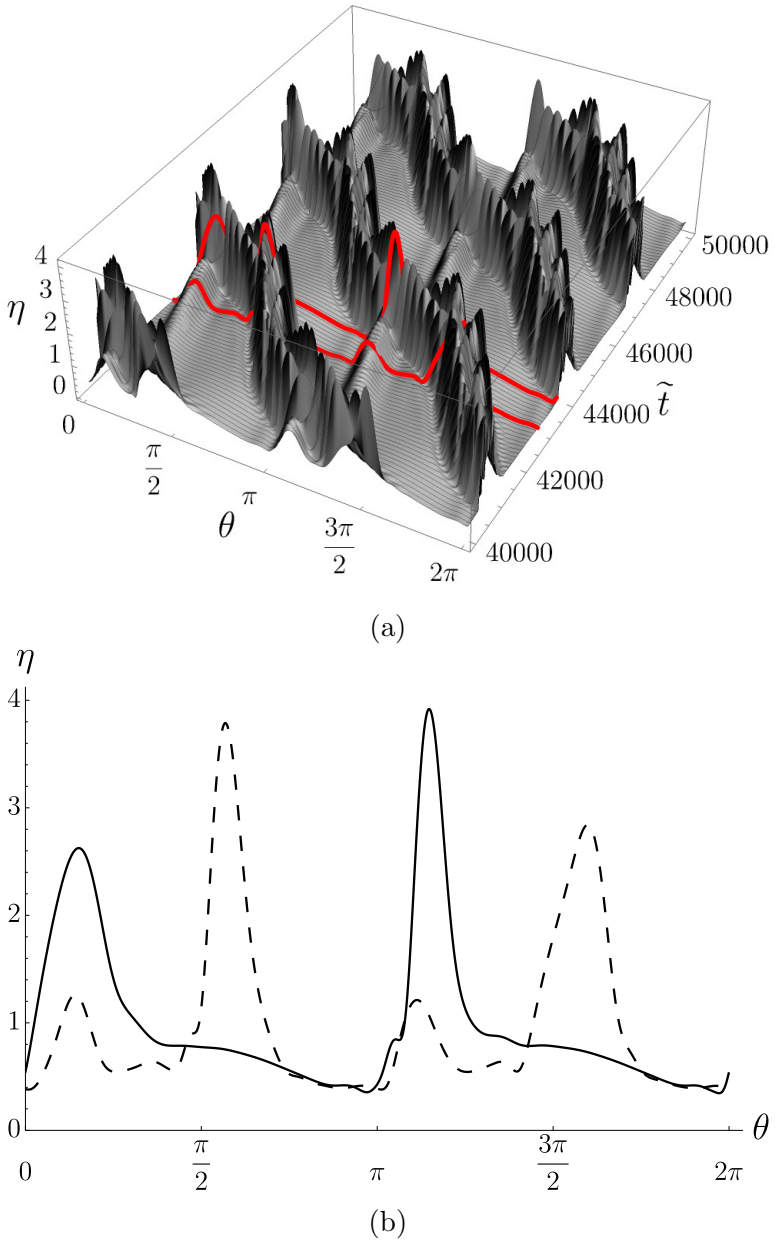

Figure 3.21: (a) Space-time plot in the high-moderate rotation speed regime ($0.410 \approx W_2(0.9) < W < W_3(0.9) \approx 1.583$) for the free surface in the rotating frame from $\widetilde{t} = 4\times10^4$ to $\widetilde{t} = \widetilde{t}_f = 5\times10^4$ for $W = 1.2$. (b) Two cross-sections of (a) corresponding to the free surface at $\widetilde{t} = 4.28 \times 10^4$ (dashed line) and $\widetilde{t} = 4.36 \times 10^4$ (solid line). The thick red lines in (a) highlight the cross-sections in (b). The other parameters are as given in (3.1.1).

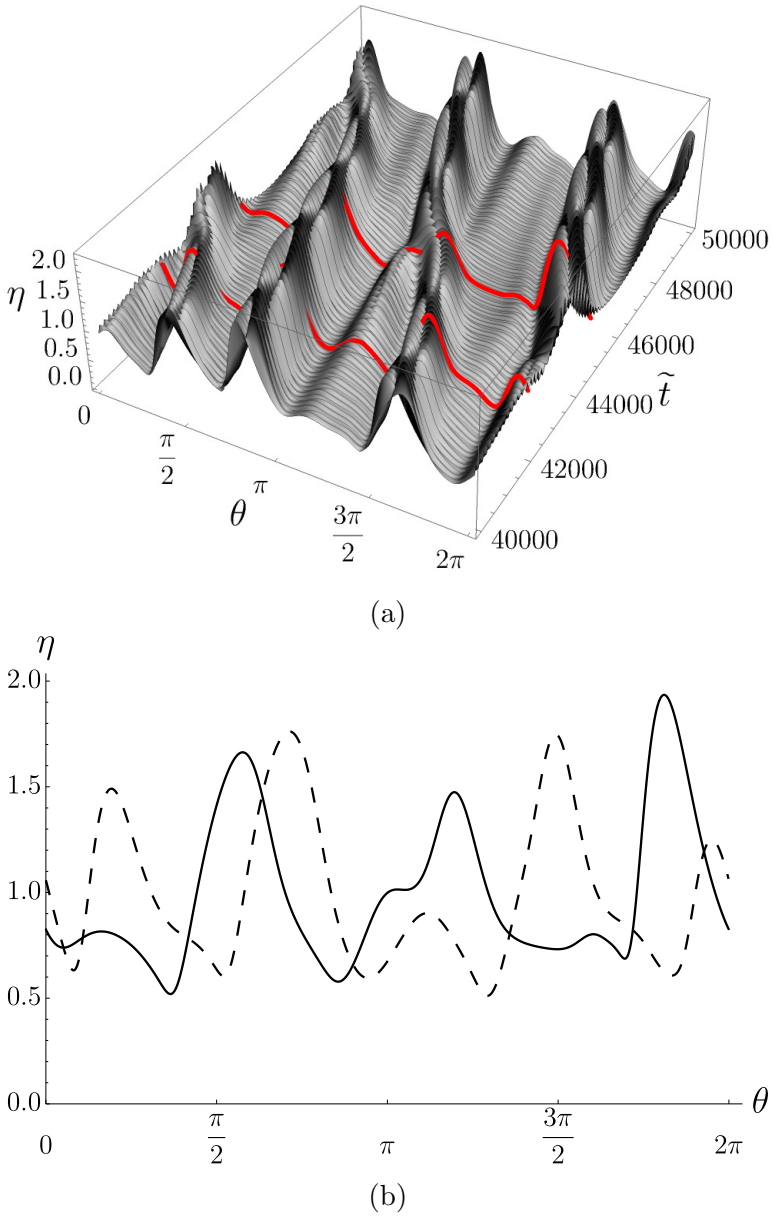

Figure 3.22: (a) Space-time plot in the high-moderate rotation speed regime ($0.410 \approx W_2(0.9) < W < W_3(0.9) \approx 1.583$) for the free surface in the rotating frame from $\widetilde{t} = 4 \times 10^4$ to $\widetilde{t} = \widetilde{t}_f = 5 \times 10^4$ for $W = 0.86$. (b) Two cross-sections of (a) corresponding to the free surface at $\widetilde{t} = 4.21 \times 10^4$ (dashed line) and $\widetilde{t} = 4.49 \times 10^4$ (solid line). The thick red lines in (a) highlight the cross-sections in (b). The other parameters are as given in (3.1.1).

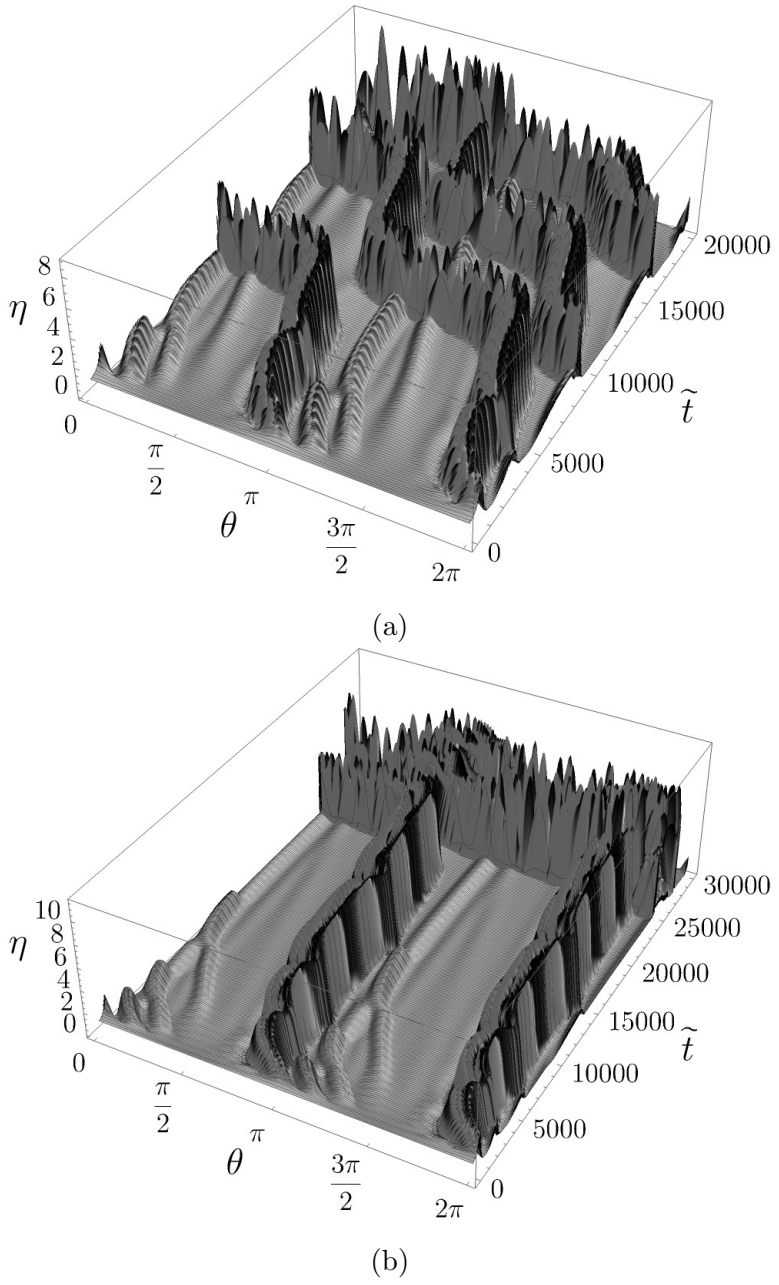

Figure 3.23: Space-time plot in the high-moderate rotation speed regime ($0.410 \approx W_2(0.9) < W < W_3(0.9) \approx 1.583$) for the free surface in the rotating frame (a) from $\widetilde{t} = 0$ to $\widetilde{t} = 2 \times 10^4$ for $W = 1.5$ and (b) from $\widetilde{t} = 0$ to $\widetilde{t} = 3 \times 10^4$ for $W = 1.575$. The other parameters are as given in (3.1.1).

cylinder and eventually coalesce into a single main bulge.

3.6 High rotation speed

In the high rotation speed regime ($W \geq W_3(0.9) \approx 1.583$) the rotation speed is large enough that centrifugation is the dominant effect, resulting in two main bulges that form and are held at the tips of the ellipse. This regime was not studied by Hunt [168], Li et al. [125], or Parrish et al. [167], as they did not explore this region of parameter space. We define the transition from the high-moderate to high rotation speed regime to be the point at which the system is essentially in solid body rotation, with the mass being predominantly held at the tips of the ellipse, with little to no fluid being exchanged across $\theta = \pi/2$ or $\theta = 3\pi/2$. Therefore, to define $W_3(b)$ we first define the mass on the left half of the cylinder in the rotating frame to be

$$M_{1/2}(\widetilde{t}) = \int_{\pi/2}^{3\pi/2} m\eta + \frac{\varepsilon}{2}\frac{b}{m^2}\eta^2 \, \mathrm{d}\theta. \tag{3.6.1}$$

Then $W_3(b)$ is defined to be the value of W above which $M_{1/2}$ varies by less than 1% across the time interval $\widetilde{t} \in [2 \times 10^4, \widetilde{t}_f = 5 \times 10^4]$ (i.e. a suitably long time interval which begins well after the initial transient phase has ended).

3.6.1 Numerical results

In the present section, the maximum value of W we consider is $W = 1.8$, however, in Section 3.6.2.2 we show that the free surface exhibits the same qualitative behaviour in the limit $W \to \infty$ as it does in the high rotation speed regime.

Figure 3.24(a) shows a plot of E_n for $n = 1, \ldots, 5$ as a function of W. For every value of W in this regime, E_2 is dominant. This reflects the characteristic behaviour of the free surface in the high rotation speed regime (i.e. two main bulges form and are held at the tips of the ellipse). Figure 3.24(b) shows a plot of the time-averaged locations of the maxima of the two main bulges in the rotating frame as functions of W. These time-averaged maxima positions are near the tips of the ellipse and, as W increases, they move closer to the tips of the ellipse, where the dotted lines highlight the position of π and 2π (i.e. the tips of the ellipse). In Section 3.6.2 we show that, in the limit $W \to \infty$, the maxima of the two main

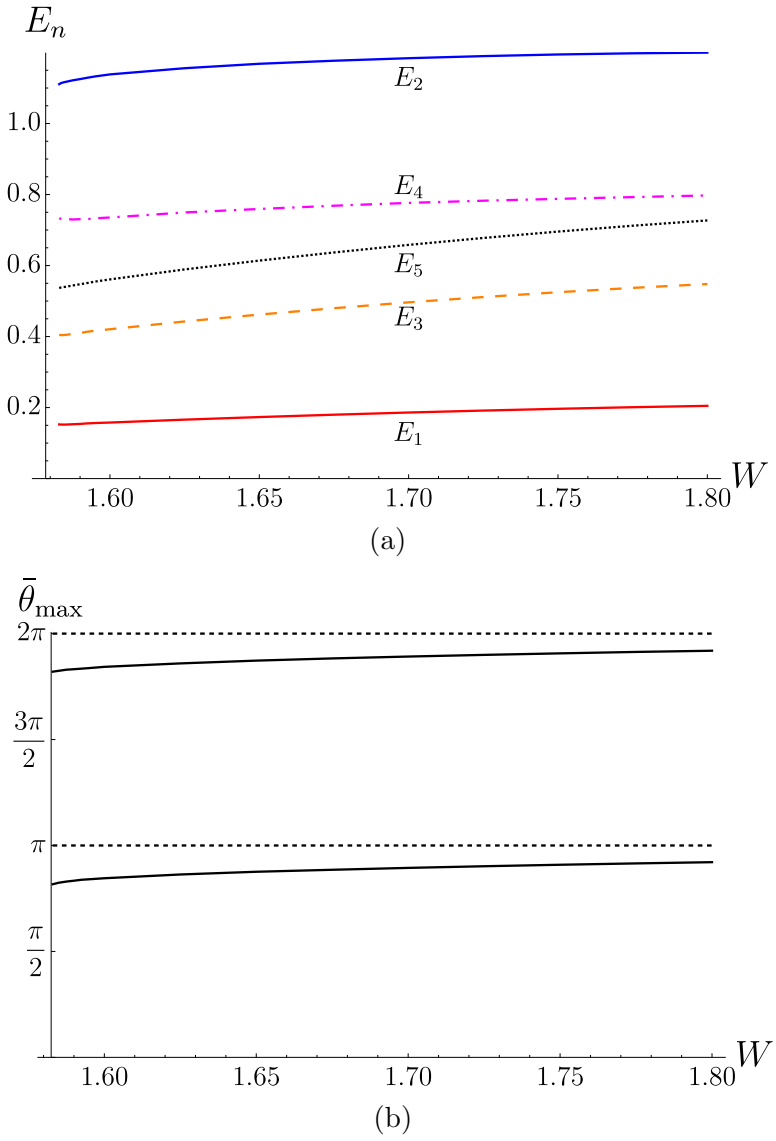

Figure 3.24: For all values of W in the high rotation speed regime ($1.583 \approx W_3(0.9) \leq W \leq 1.8$). (a) The energy of the n^{th} Fourier mode E_n for $n = 1, \ldots, 5$, plotted as a function of W. The $n = 1, \ldots, 5$ modes are shown with solid red, solid blue, dashed orange, dot-dashed purple, and dotted black lines, respectively. (b) The time-averaged location of the maxima of the two main bulges in the rotating frame $\bar{\theta}_{\max}$ plotted as a function of W, where the dotted lines highlight the location of π and 2π. Both (a) and (b) are calculated to $\widetilde{t} = \widetilde{t}_f = 5 \times 10^4$. The other parameters are as given in (3.1.1).

bulges lie exactly on the tips of the ellipse.

Figure 3.25 shows space-time plots in the rotating frame for $W = 1.8$. Figure 3.25(a) shows the two main bulges forming and being held near the tips of the ellipse. Figure 3.25(b) shows a zoom of the region between $\widetilde{t} = 4.95 \times 10^4$ and $\widetilde{t} = \widetilde{t}_f = 5 \times 10^4$, at which scale the high frequency oscillations of the two main bulges (due to the rotation of the cylinder) are clearer. The oscillation of the two main bulges causes the position of the maximum value to vary over time, which is why we plot the time-averaged location of the maxima of the two main bulges in Figure 3.24(b). Figure 3.26 shows a plot of the unscaled free surface on the ellipse in the laboratory frame when the semi-major axis is perpendicular to the direction of gravity. The unscaled free surface in Figure 3.26 is a cross-section corresponding to the thick red line in Figure 3.25 at $\widetilde{t} = 4.9707 \times 10^4$. In the high rotation speed regime, $\widetilde{X}_c^{\text{av}}$ and $\widetilde{Y}_c^{\text{av}}$ increase and decrease, respectively, as W increases. The film is thicker on the upward-moving side of the cylinder in the laboratory frame (as shown in the lower right-hand quadrant of Figure 3.26), which is why $\widetilde{X}_c^{\text{av}}$ increases in Figure 3.1(a) and the small decrease in $\widetilde{Y}_c^{\text{av}}$ in Figure 3.1(b) is due to gravity acting on the two main bulges.

3.6.2 Solutions in the limit of $W \to \infty$

We examine the thin-film ellipse equation (2.3.13) in the limit $W \to \infty$, which we refer to as the rapid rotation limit. To obtain a PDE in the rapid rotation limit we set

$$W = \zeta \breve{W}, \quad t = \breve{t}/\zeta^2, \tag{3.6.2}$$

where $\breve{t}$ is a suitable fast time chosen to capture the rapid dynamics of the system, and we examine the limit $\zeta \to \infty$. We apply the scalings (3.6.2) to the thin-film ellipse equation (2.3.13) to obtain a PDE in the rapid rotation limit. However, to facilitate comparisons between the solutions of the thin-film ellipse equation (2.3.13) and the solutions of the PDE in the rapid rotation limit, we apply the scalings (3.6.2) and then present the resulting equation in the original variables used in the thin-film ellipse equation (2.3.13). In the rapid rotation limit ($W \to$

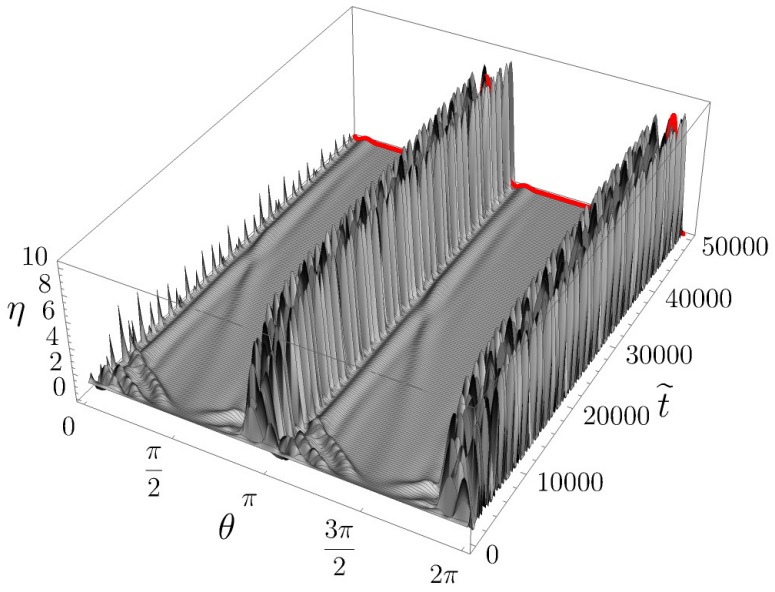

(a)

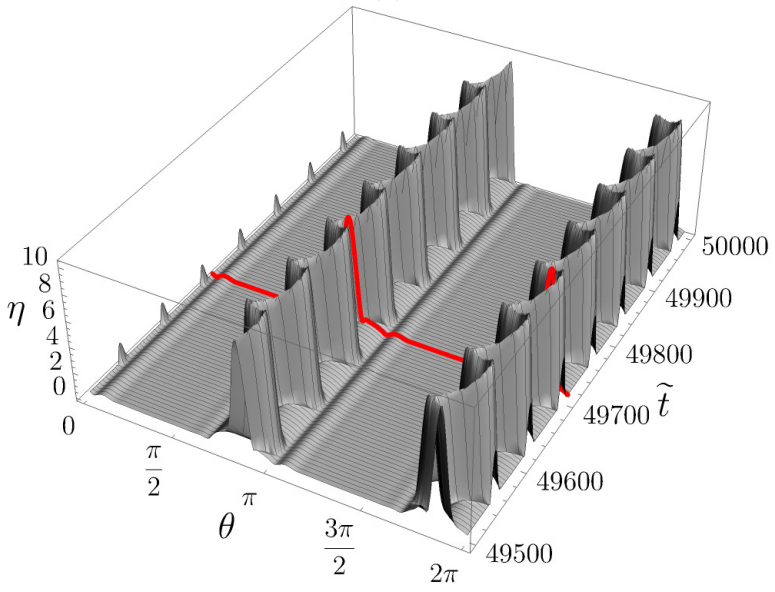

(b)

Figure 3.25: Space-time plot in the high rotation speed regime ($1.583 \approx W_3(0.9) \leq W \leq 1.8$) for the free surface in the rotating frame (a) from $\widetilde{t} = 0$ to $\widetilde{t} = \widetilde{t}_f = 5\times10^4$ and (b) zoomed in on the region from $\widetilde{t} = 4.95\times10^4$ to $\widetilde{t} = \widetilde{t}_f = 5\times10^4$ for $W = 1.8$. The thick red line in (a) and (b) highlights the cross-section in plotted in Figure 3.26. The other parameters are as given in (3.1.1).

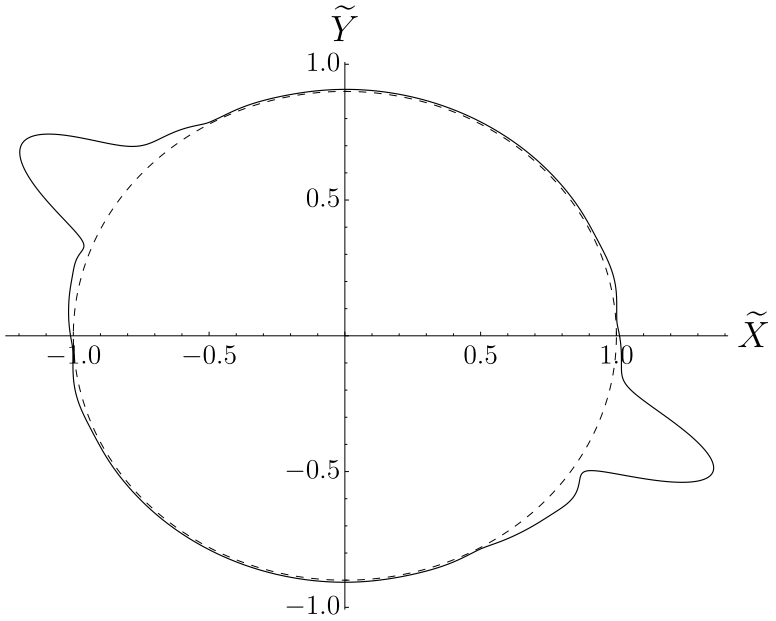

Figure 3.26: Plot of the unscaled free surface on the ellipse in the laboratory frame for $W = 1.8$ at $\widetilde{t} = 4.9707 \times 10^4$ when the semi-major axis is perpendicular to the direction of gravity, where the dashed line is the ellipse. The other parameters are as given in (3.1.1).

∞), the thin-film ellipse equation (2.3.13) becomes

$$\left(m + \varepsilon \frac{b}{m^2}\eta\right) \frac{\partial \eta}{\partial t} - \frac{\partial}{\partial \theta}\left\{ W^2 \frac{(1-b^2)\eta^3}{6m} \sin 2\theta \left[1 + \varepsilon \frac{9b\eta}{8m^3}\right] + \varepsilon W^2 \frac{b\eta^3}{3m^2}\left[\frac{3\eta(1-b^2)}{16m^2}\sin 2\theta - \frac{\partial \eta}{\partial \theta}\right]\right\} = 0. \quad (3.6.3)$$

We anticipate that the solution of (3.6.3) will experience blowup at some finite time. This is because the effect of surface tension is absent in the present limit, and so cannot balance the effect of centrifugation.

While the first-order PDE in the rapid rotation limit (3.6.3) is too complex to solve analytically to first order in ε, it is analytically tractable at leading order via the method of characteristics, which we examine in Section 3.6.2.1. We then numerically examine the first-order PDE in the rapid rotation limit (3.6.3) in Section 3.6.2.2. Specifically, we compare the solution of the first-order PDE in the rapid rotation limit (3.6.3) with the solution of thin-film ellipse equation (2.3.13) for three eccentricities, namely $b = 0.75$, 0.5, and 0.25.

3.6.2.1 Asymptotic solutions in the rapid rotation limit to leading order in ε

At leading order in ε the first-order PDE in the rapid rotation limit (3.6.3) is

$$m\frac{\partial \eta}{\partial t} - \frac{\partial}{\partial \theta}\left(W^2\frac{(1-b^2)\,\eta^3}{6m}\sin 2\theta\right) = 0. \tag{3.6.4}$$

Hence,

$$\frac{\mathrm{d}\eta}{\mathrm{d}t} = W^2\frac{(1-b^2)\eta^3}{6m}\frac{\mathrm{d}}{\mathrm{d}\theta}\left(\frac{\sin 2\theta}{m}\right) \tag{3.6.5}$$

on the characteristics

$$\frac{\mathrm{d}\theta}{\mathrm{d}t} = -W^2\frac{(1-b^2)\eta^2}{2m^2}\sin 2\theta, \tag{3.6.6}$$

with solution

$$\eta = \begin{cases} \sqrt{\dfrac{3b^2}{3b^2 - 2W^2(1-b^2)t}} & \theta = 0,\ \theta = \pi, \\ \sqrt{\dfrac{3}{3 + 2W^2(1-b^2)t}} & \theta = \dfrac{\pi}{2},\ \theta = \dfrac{3\pi}{2}, \\ \left(\dfrac{(\sin^2\theta + b^2\cos^2\theta)(\cos\theta_0\sin\theta_0)^2}{(\cos\theta\sin\theta)^2(\sin^2\theta_0 + b^2\cos^2\theta_0)}\right)^{1/6} & 0 < \theta < 2\pi,\ \theta \neq \dfrac{\pi}{2},\ \theta \neq \pi,\ \theta \neq \dfrac{3\pi}{2}, \end{cases} \tag{3.6.7}$$

where $\theta(0) = \theta_0$ is the initial value of θ, which parametrises the characteristics. The solution (3.6.7) always blows up due to a singularity at $\theta = 0$ and $\theta = \pi$ at

$$t = t_{\text{blowup}} = \frac{3b^2}{2W^2(1-b^2)}. \tag{3.6.8}$$

This blowup is unphysical and occurs because the stabilising effect of surface tension is not present in this limit. Preliminary investigations of the numerical solution of (3.6.5) and (3.6.6) have shown that the characteristics do not cross for any $b \in (0,1)$. Therefore, in the present limit, there is never a situation in which a shock will form in the solution of equation (3.6.4), unlike in Sections 3.3.1 and 3.3.2.

Figure 3.27 shows plots of the numerical solution of (3.6.4). Figure 3.27(a) shows a plot of the free surface on a Cartesian plot, and Figure 3.27(b) shows a plot of the unscaled free surface on the ellipse. The free surface exhibits large curvatures over the tips of the ellipse before the solution blows up in finite time

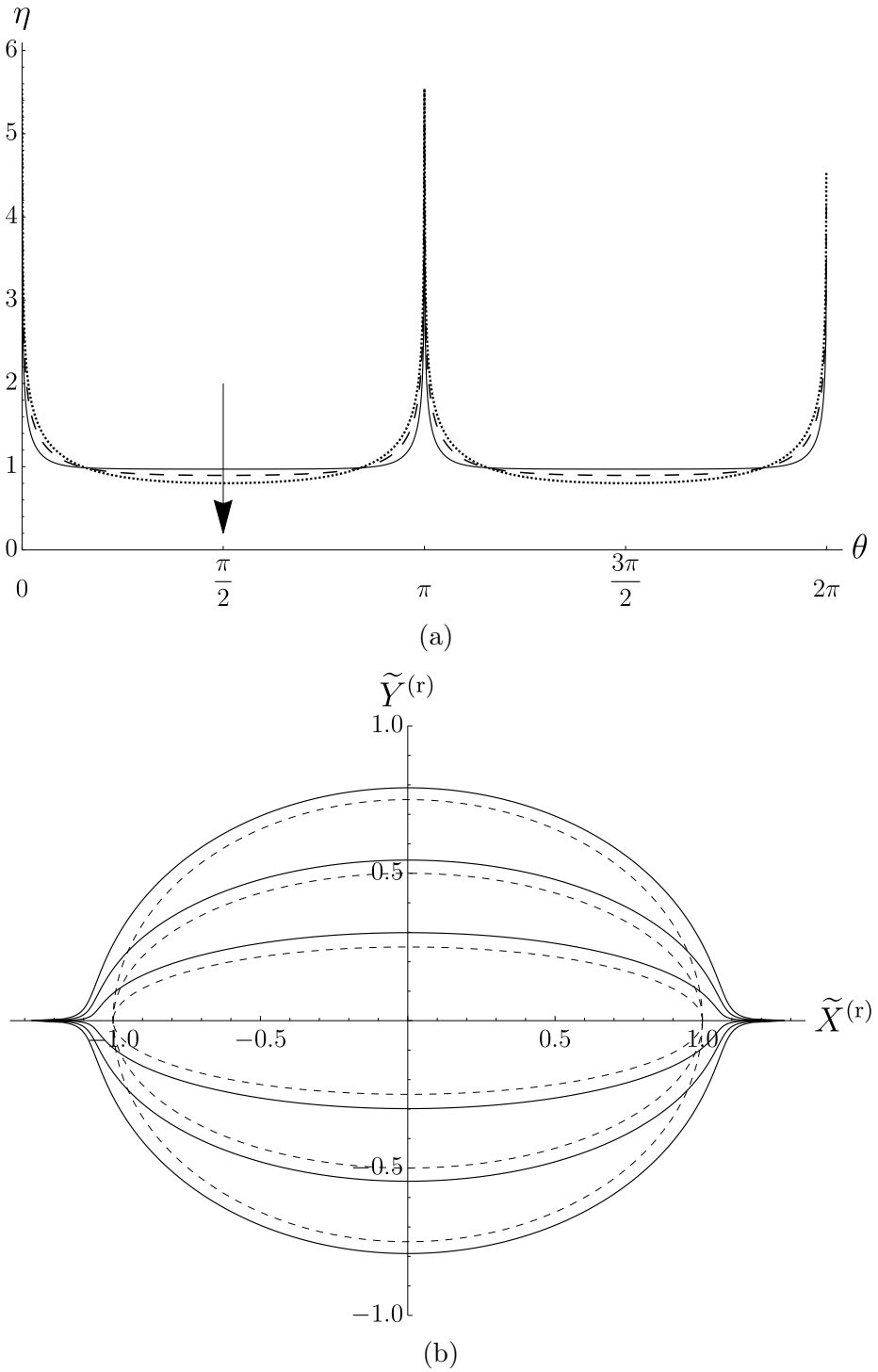

Figure 3.27: Plots of the numerical solution of (3.6.4) with $W = 10$ for $b = 0.25, t = 0.99t_{\text{blowup}} = 9.9 \times 10^{-4}$; $b = 0.5, t = 0.99t_{\text{blowup}} = 4.95 \times 10^{-3}$; $b = 0.75, t = 0.99t_{\text{blowup}} \approx 0.019$, for t_{blowup} predicted by (3.6.8). The arrow in (a) indicates the direction of increasing b. The plot (a) shows the free surface on a Cartesian plot, and the plot (b) show the unscaled free surface (solid lines) on the ellipse, plotted for $\varepsilon = 0.05$. The dashed lines in (b) are the ellipse.

at $t = t_{\text{blowup}}$ (3.6.8). The large curvatures of the free surface over the tips of the ellipse is due to the absence of surface tension in this limit.

3.6.2.2 Numerical solutions in the rapid rotation limit to first order in ε

We now numerically examine the first-order PDE in the rapid rotation limit (3.6.3). Figure 3.28 shows plots comparing the free surfaces in the rotating frame at $t = 10^{-5}$ for the solution of the thin-film ellipse equation (2.3.13) and the solution of the first-order PDE in the rapid rotation limit (3.6.3). Figure 3.28(a) shows a plot of the free surface on a Cartesian plot, and Figure 3.28(b) shows a plot of the unscaled free surface on the ellipse. For each eccentricity, the fluid collects at the tips of the ellipse and forms two main bulges. There is no surface tension to support the film in the rapid rotation limit, and so the solution of (3.6.3) will blow up in finite time. In particular, the film thickness at the tips of the ellipse grows rapidly and so, in the absence of the stabilising effect of surface tension, the free surfaces are plotted at early times before numerical instabilities can manifest. Although the thin-film ellipse equation (2.3.13) incorporates the effect of surface tension, it is dominated by the effect of centrifugation. The solutions of the first-order PDE in the rapid rotation limit (3.6.3) compare well with the solutions of the thin-film ellipse equation (2.3.13).

3.6.3 Solutions in the limit of $Ca \to 0^+$

We examine the thin-film ellipse equation (2.3.13) in the limit $Ca \to 0^+$, which we refer to as the strong surface tension limit. To obtain a PDE in the strong surface tension limit we set

$$Ca = \breve{Ca}/\zeta^2, \quad t = \breve{t}/\zeta^2, \tag{3.6.9}$$

where $\breve{t}$ is a suitable fast time chosen to capture the dynamics of the system, and we examine the limit $\zeta \to \infty$. We apply the scalings (3.6.9) to the thin-film ellipse equation (2.3.13) to obtain a PDE in the strong surface tension limit. Again, to facilitate comparisons between the solutions of the thin-film ellipse equation (2.3.13) and the solutions of the PDE in the strong surface tension limit, we apply the scalings (3.6.9) and then present the resulting equation in the original variables

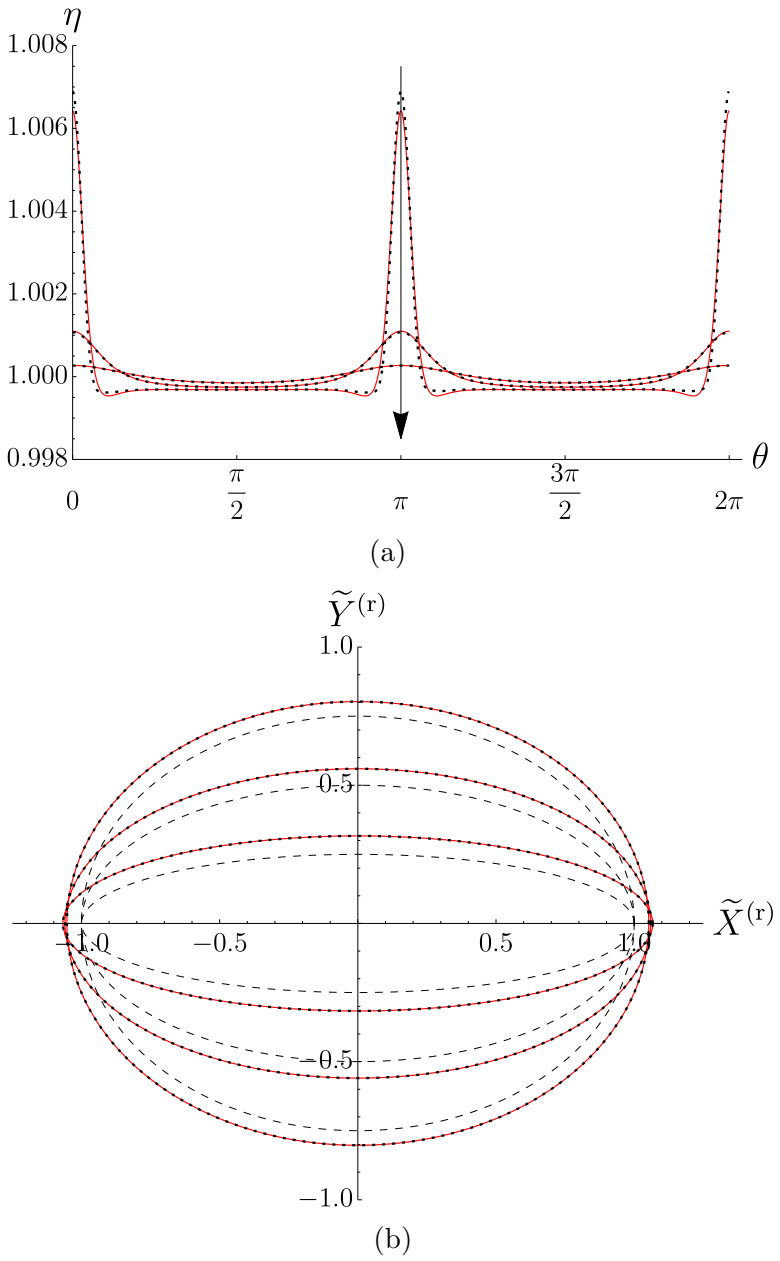

Figure 3.28: Comparison of the solutions of the thin-film ellipse equation (2.3.13) ($Ca = 10, Re = 1$) (dashed black lines) and the solution of the first-order PDE in the rapid rotation limit (3.6.3) (solid red lines) in the rotating frame with $W = 10$, $t = 10^{-5}$, $\widetilde{M} = 0.3$ for $b = 0.25$, $\varepsilon = 0.06669$; $b = 0.5$, $\varepsilon = 0.05965$; $b = 0.75$, $\varepsilon = 0.05271$, where the arrow in (a) indicates the direction of increasing b. The plot (a) shows the free surface on a Cartesian plot, and the plot (b) shows the unscaled free surface on the ellipse. The dashed lines in (b) are the ellipse.

used in the thin-film ellipse equation (2.3.13). In the strong surface tension limit ($Ca \to 0^+$), the thin-film ellipse equation (2.3.13) becomes

$$\left(m + \varepsilon\frac{b}{m^2}\eta\right)\frac{\partial\eta}{\partial t} - \frac{\partial}{\partial\theta}\Bigg\{ - \frac{1}{Ca}\frac{b(1-b^2)\eta^3}{2m^6}\sin 2\theta\left[1 + \varepsilon\frac{b\eta}{2m^3}\right] + \varepsilon\frac{1}{Ca}\frac{\eta^3}{3m}\frac{\partial}{\partial\theta}\left[\frac{1}{m^6}\left(\frac{m^2(1-b^2)}{2}\sin 2\theta\frac{\partial\eta}{\partial\theta} - b^2\eta - m^4\frac{\partial^2\eta}{\partial\theta^2}\right)\right]\Bigg\} = 0. \tag{3.6.10}$$

We anticipate that the solution of (3.6.10) will exhibit rapid thinning at the tips of the ellipse. This is because the effect of centrifugation is absent in the present limit, and so cannot balance the effect of surface tension.

While the first-order PDE in the strong surface tension limit (3.6.10) is too complex to solve analytically to first order in ε, it is analytically tractable at leading order via the method of characteristics, which we examine in Section 3.6.3.1. We then numerically examine the first-order PDE in the strong surface tension limit (3.6.10) in Section 3.6.3.2. Specifically, we compare the solution of the first-order PDE in the strong surface tension limit (3.6.10) with the solution of thin-film ellipse equation (2.3.13) for three eccentricities, namely $b = 0.75$, 0.5, and 0.25.

3.6.3.1 Asymptotic solutions in the strong surface tension limit to leading order in ε

At leading order in ε the first-order PDE in the strong surface tension limit (3.6.10) is

$$m\frac{\partial\eta}{\partial t} + \frac{\partial}{\partial\theta}\left(\frac{1}{Ca}\frac{b\,(1-b^2)\,\eta^3}{2m^6}\sin 2\theta\right) = 0, \tag{3.6.11}$$

which coincides with (3.3.7) in the absence of gravity. Hence,

$$\frac{\mathrm{d}\eta}{\mathrm{d}t} = -\frac{b(1-b^2)\eta^3}{2mCa}\frac{\mathrm{d}}{\mathrm{d}\theta}\left(\frac{\sin 2\theta}{m^6}\right) \tag{3.6.12}$$

on the characteristics

$$\frac{\mathrm{d}\theta}{\mathrm{d}t} = \frac{3b(1-b^2)\eta^2}{2m^7Ca}\sin 2\theta, \tag{3.6.13}$$

with solution

$$\eta = \begin{cases} \sqrt{\dfrac{b^6 Ca}{b^6 Ca + 2(1-b^2)t}} & \theta = 0,\ \theta = \pi, \\ \sqrt{\dfrac{Ca}{Ca - 2b(1-b^2)t}} & \theta = \dfrac{\pi}{2},\ \theta = \dfrac{3\pi}{2}, \\ \left(\dfrac{(\sin^2\theta + b^2\cos^2\theta)^3(\cos\theta_0 \sin\theta_0)}{(\cos\theta\sin\theta)(\sin^2\theta_0 + b^2\cos^2\theta_0)^3}\right)^{1/3} & 0 < \theta < 2\pi,\ \theta \neq \dfrac{\pi}{2},\ \theta \neq \pi,\ \theta \neq \dfrac{3\pi}{2}, \end{cases} \tag{3.6.14}$$

where $\theta(0) = \theta_0$ is the initial value of θ, which parametrises the characteristics.

The solution blow up due to a singularity at $\theta = \pi/2$ and $\theta = 3\pi/2$ at

$$t = t_{\text{blowup}} = \frac{Ca}{2b(1-b^2)}, \tag{3.6.15}$$

This blowup is unphysical and occurs because the stabilising effect of surface tension is not present at leading order in ε in equation (3.6.11).

Preliminary investigations of the numerical solution of (3.6.12) and (3.6.13) have shown that these solutions exhibit the same qualitative behaviour as in Sections 3.3.1 and 3.3.2. Specifically, for $b_c \leq b < 1$ the characteristics do not cross and so the solution of (3.6.11) will experience blowup at $\theta = \pi/2$ and $\theta = 3\pi/2$ at $t = t_{\text{blowup}}$ (3.6.15). However, for $0 < b < b_c$ the characteristics cross and a shock is formed in the solution of (3.6.11) for some $t < t_{\text{blowup}}$ (3.6.15). Due to time constraints and equation (3.6.11) being more complicated than equation (3.3.3), we have been unable to perform a similar parametric study on b in the present section to determine b_c as we did in Section 3.3.1.

Figure 3.29 shows plots of the numerical solution of (3.6.11). Figures 3.29(a) and 3.29(b) show plots of the free surface on a Cartesian plot for $b = 0.9$ and $b = 0.5$, respectively, and Figures 3.29(c) and 3.29(d) shows plots of the unscaled free surface on the ellipse for $b = 0.9$ and $b = 0.5$, respectively. Figures 3.29(a) and 3.29(c) show a case where the characteristics do not cross. In this case, the solution of (3.6.11) experiences blowup at $\theta = \pi/2$ and $\theta = 3\pi/2$ at $t = t_{\text{blowup}} \approx 0.292$ (3.6.15). This blowup is characterised by the spikes in Figures 3.29(a) and 3.29(c) which occur due to the omission of the stabilising effect of surface tension in equation (3.6.11). Figures 3.29(b) and 3.29(d) show a case where the characteristics do cross. In this case, a shock forms in the solution of

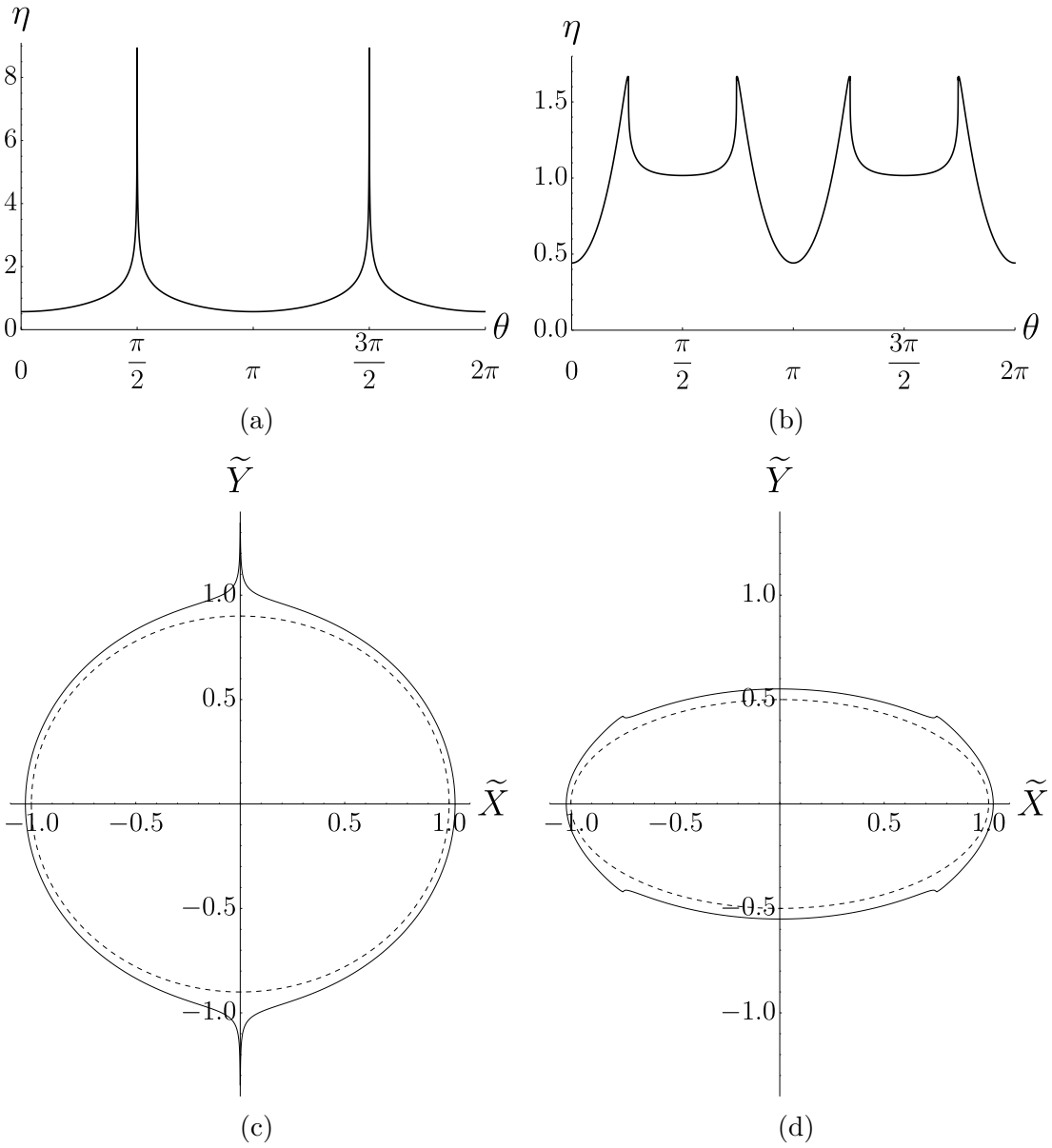

Figure 3.29: Plots of the numerical solution of (3.6.11) with $Ca = 0.1$ for (a, c) $b = 0.9$ at time $t = 0.99t_{\text{blowup}} \approx 0.289$, and (b, d) $b = 0.5$ are shown at time $t = 0.0043 < t_{\text{blowup}} \approx 0.133$, for t_{blowup} predicted by (3.6.15). The plots (a, b) show the free surface on a Cartesian plot, and the plots (c, d) show the unscaled free surface (solid lines) on the ellipse, plotted for $\varepsilon = 0.05$. The dashed lines in (c, d) are the ellipse. Note that the scale of the vertical axis is different in part (a) and (b).

equation (3.6.11) at $t < t_{\text{blowup}}$ (3.6.15). The formation of the shocks can perhaps be seen more clearly in Figure 3.29(b) as steep fronts are formed in the free surface either side of $\theta = \pi/2$ and $\theta = 3\pi/2$. The formation of the shocks in the solution of (3.6.11) makes it difficult for us to plot the free surface at a time closer to $t = t_{\text{blowup}} \approx 0.133$ (3.6.15). We expect that the inclusion of the stabilising effect of surface tension in equation (3.6.11) would smooth these shocks [128].

3.6.3.2 Numerical solutions in the strong surface tension to first order in ε

We now numerically examine the first-order PDE in the strong surface tension limit (3.6.10). Figure 3.30 shows plots comparing the free surfaces in the rotating frame at $t = 0.015$ for the solution of the thin-film ellipse equation (2.3.13) and the solution of the first-order PDE in the strong surface tension limit (3.6.10). Figure 3.30(a) shows a plot of the free surface on a Cartesian plot, and Figure 3.30(b) shows a plot of the unscaled free surface on the ellipse. For each eccentricity, the fluid collects at the top and bottom of the ellipse. There is no centrifugation to force the fluid towards the tips in the strong surface tension limit, and so the solution of (3.6.10) will exhibit rapid thinning at the tips of the ellipse (as shown in Figure 3.30 for $b = 0.25$) as the effect of surface tension drives the fluid away from the tips of the ellipse and towards a circular film. Although the thin-film ellipse equation (2.3.13) incorporates the effect of centrifugation, it is dominated by the effect of surface tension. The solutions of the first-order PDE in the strong surface tension limit (3.6.10) compare well with the solutions of the thin-film ellipse equation (2.3.13).

This behaviour was studied by Parrish et al. [167] in their parametric study of the initial fluid load (see Figure 1.28(d)).

3.6.4 Solutions in the limit of $W \to \infty$ and $Ca \to 0^+$

We examine the thin-film ellipse equation (2.3.13) in the limit $W \to \infty$ and $Ca \to 0^+$, which we refer to as the combined rapid rotation and strong surface tension limit. To obtain a PDE in the combined rapid rotation and strong surface tension

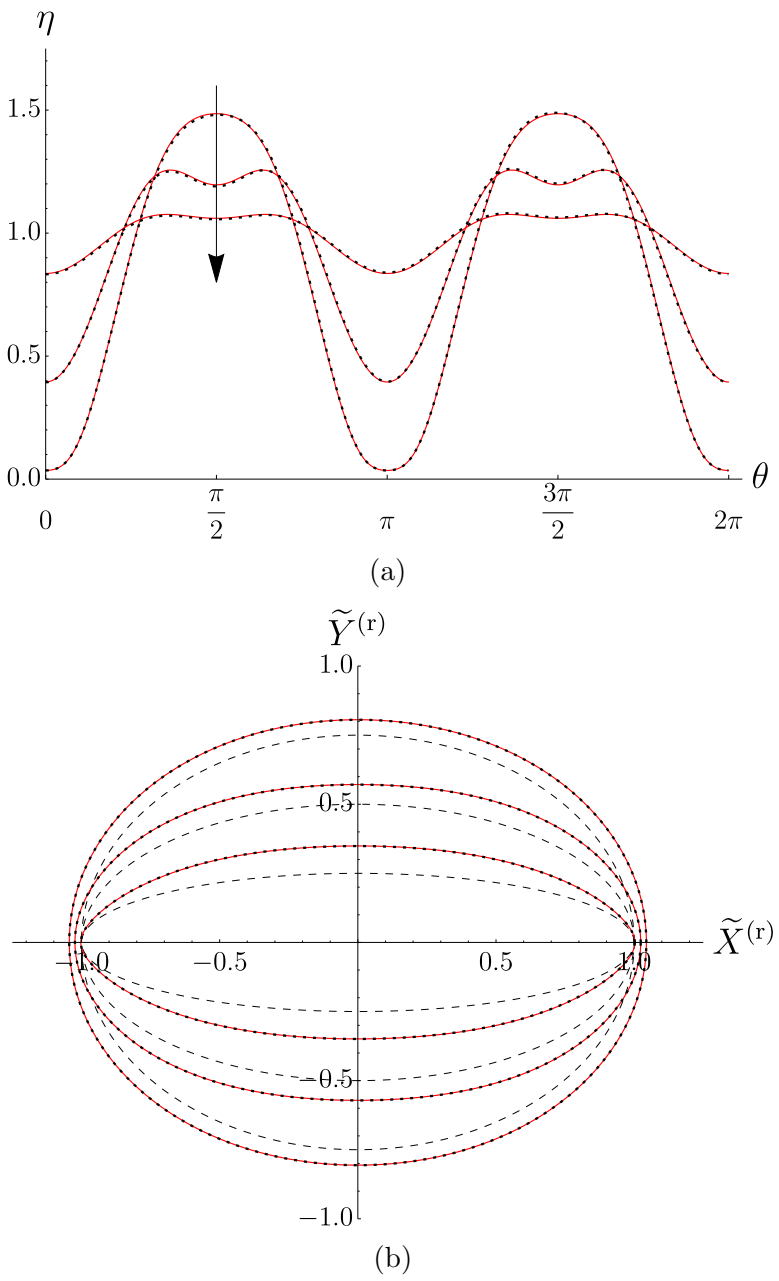

Figure 3.30: Comparison of the solutions of the thin-film ellipse equation (2.3.13) ($W = 0.25, Re = 1$) (dashed black) and the solution of the first-order PDE in the strong surface tension limit (3.6.10) (solid red) in the rotating frame with $Ca = 0.1$, $t = 0.015$, $\widetilde{M} = 0.3$ for $b = 0.25$, $\varepsilon = 0.06669$, $b = 0.5$, $\varepsilon = 0.05965$ and $b = 0.75$, $\varepsilon = 0.05271$, where the arrow in (a) indicates the direction of increasing b. The plot (a) shows the free surface on a Cartesian plot, and the plot (b) shows the unscaled free surface on the ellipse. The dashed lines in (b) are the ellipse.

limit we set

$$W = \zeta\breve{W}, \quad Ca = \breve{Ca}/\zeta^2, \quad t = \breve{t}/\zeta^2, \tag{3.6.16}$$

where $\breve{t}$ is a suitable fast time chosen to capture the dynamics of the system, and we examine the limit $\zeta \to \infty$. We apply the scalings (3.6.16) to the thin-film ellipse equation (2.3.13) to obtain a PDE in the combined rapid rotation and strong surface tension limit. Again, to facilitate comparisons between the solutions of the thin-film ellipse equation (2.3.13) and the solutions of the PDE in the combined rapid rotation and strong surface tension limit, we apply the scalings (3.6.16) and then present the resulting equation in the original variables used in the thin-film ellipse equation (2.3.13). In the combined rapid rotation and strong surface tension limit ($W \to \infty$ and $Ca \to 0^+$), the thin-film ellipse equation (2.3.13) becomes

$$\begin{aligned}\left(m + \varepsilon\frac{b}{m^2}\eta\right)\frac{\partial \eta}{\partial t} - \frac{\partial}{\partial \theta}\Bigg\{ & W^2\frac{(1-b^2)\eta^3}{6m}\sin 2\theta\left[1 + \varepsilon\frac{9b\eta}{8m^3}\right] \\ & + \varepsilon W^2\frac{b\eta^3}{3m^2}\left[\frac{3\eta(1-b^2)}{16m^2}\sin 2\theta - \frac{\partial \eta}{\partial \theta}\right] \\ & + \varepsilon\frac{1}{Ca}\frac{\eta^3}{3m}\frac{\partial}{\partial \theta}\left[\frac{1}{m^6}\left(\frac{m^2(1-b^2)}{2}\sin 2\theta\frac{\partial \eta}{\partial \theta} - b^2\eta - m^4\frac{\partial^2 \eta}{\partial \theta^2}\right)\right] \\ & - \frac{1}{Ca}\frac{b(1-b^2)\eta^3}{2m^6}\sin 2\theta\left[1 + \varepsilon\frac{b\eta}{2m^3}\right]\Bigg\} = 0. \end{aligned} \tag{3.6.17}$$

Equation (3.6.17) is equivalent to the zero-gravity limit of the thin-film ellipse equation (2.3.13) up to a rescaling in t. We anticipate that the solution of (3.6.17) will neither experience blowup at some finite time nor exhibit rapid thinning at the tips of the ellipse. This is because the effects of centrifugation and surface tension are balanced in the present limit.

While the first-order PDE in the combined rapid rotation and strong surface tension limit (3.6.17) is too complex to solve analytically to first order in ε, it is analytically tractable at leading order via the method of characteristics, which we examine in Section 3.6.4.1. We then numerically examine the first-order PDE in the combined rapid rotation and strong surface tension limit (3.6.17) in Section 3.6.4.2. Specifically, we compare the solution of the first-order PDE in the combined rapid rotation and strong surface tension limit (3.6.17) with the solution of thin-film ellipse equation (2.3.13) for three eccentricities, namely $b = 0.75$, 0.5, and 0.25.

3.6.4.1 Asymptotic solutions in the combined rapid rotation and strong surface tension limit to leading order in ε

At leading order in ε the first-order PDE in the combined rapid rotation and strong surface tension limit (3.6.17) is

$$m\frac{\partial \eta}{\partial t} + \frac{\partial}{\partial \theta}\left(\frac{1}{Ca}\frac{b\,(1-b^2)\,\eta^3}{2m^6}\sin 2\theta\right) - \frac{\partial}{\partial \theta}\left(W^2\frac{(1-b^2)\,\eta^3}{6m}\sin 2\theta\right) = 0. \tag{3.6.18}$$

Hence,

$$\frac{\mathrm{d}\eta}{\mathrm{d}t} = \frac{(1-b^2)\eta^3}{6m}\left(W^2\frac{\mathrm{d}}{\mathrm{d}\theta}\left(\frac{\sin 2\theta}{m}\right) - \frac{3b}{Ca}\frac{\mathrm{d}}{\mathrm{d}\theta}\left(\frac{\sin 2\theta}{m^6}\right)\right) \tag{3.6.19}$$

on the characteristics

$$\frac{\mathrm{d}\theta}{\mathrm{d}t} = \left(\frac{3b}{m^5 Ca} - W^2\right)\frac{(1-b^2)\eta^2}{m^2}\sin 2\theta. \tag{3.6.20}$$

While (3.6.19)–(3.6.20) cannot, in general, be solved analytically, they can be solved along the characteristic curves starting at $\theta_0 = 0$ and $\theta_0 = \pi/2$ (which are equivalent to the $\theta_0 = \pi$ and $\theta_0 = 3\pi/2$ characteristic curves by symmetry), where $\theta(0) = \theta_0$ is the initial value of θ, which parametrises the characteristics. On the characteristic curve starting at $\theta_0 = 0$ we have the solution

$$\eta = \sqrt{\frac{3b^6}{3b^6 - 2(1-b^2)\left(b^4W^2 - \dfrac{3}{Ca}\right)t}}, \tag{3.6.21}$$

and on the characteristic curve starting at $\theta_0 = \pi/2$ we have the solution

$$\eta = \sqrt{\frac{3}{3 + 2(1-b^2)\left(W^2 - \dfrac{3b}{Ca}\right)t}}. \tag{3.6.22}$$

The solution (3.6.21) blows up due to a singularity at $\theta = 0$ and $\theta = \pi$ at

$$t = t^{(\mathrm{i})}_{\mathrm{blowup}} = \frac{3b^6 Ca}{2(1-b^2)(b^4W^2Ca - 3)}, \tag{3.6.23}$$

while the solution (3.6.22) blows up due to a singularity at $\theta = \pi/2$ and $\theta = 3\pi/2$ at

$$t = t^{(\mathrm{ii})}_{\mathrm{blowup}} = \frac{3Ca}{2(1-b^2)(3b - W^2 Ca)}. \tag{3.6.24}$$

Depending on the choice of b, W, and Ca, we can have a case where the solution of equation (3.6.18) will experience blowup at $\theta = 0$ and $\theta = \pi$ at $t = t^{(\mathrm{i})}_{\mathrm{blowup}}$ (3.6.23), or at $\theta = \pi/2$ and $\theta = 3\pi/2$ at $t = t^{(\mathrm{ii})}_{\mathrm{blowup}}$ (3.6.24). This blowup is unphysical and occurs because the stabilising effect of surface tension is not present at leading order in ε in equation (3.6.18).

Preliminary investigations of the numerical solution of (3.6.19) and (3.6.20) have shown that these solutions exhibit the same qualitative behaviour as in Sections 3.3.1, 3.3.2, 3.6.2.1, and 3.6.3.1. Specifically, for $b_{\mathrm{c}} \leq b < 1$ the characteristics do not cross and so the solution of (3.6.18) will experience blowup at $\theta = 0$ and $\theta = \pi$ at $t = t^{(\mathrm{i})}_{\mathrm{blowup}}$ (3.6.23) or at $\theta = \pi/2$ and $\theta = 3\pi/2$ at $t = t^{(\mathrm{ii})}_{\mathrm{blowup}}$ (3.6.24). However, for $0 < b < b_{\mathrm{c}}$ the characteristics cross and a shock is formed in the solution of (3.6.11) at the top and bottom of the cylinder for some $t \notin \{t^{(\mathrm{i})}_{\mathrm{blowup}}, t^{(\mathrm{ii})}_{\mathrm{blowup}}\}$ (for $t^{(\mathrm{i})}_{\mathrm{blowup}}$ and $t^{(\mathrm{ii})}_{\mathrm{blowup}}$ predicted by (3.6.23) and (3.6.24), respectively). In the present limit, the balance of the effects of centrifugation and surface tension is also important. Other preliminary investigations of the numerical solution of (3.6.19) and (3.6.20) have shown that for some b, W, and Ca, the characteristics do not cross and the solution of (3.6.18) will experience blowup at $\theta \in (0, 2\pi) \setminus \{\pi/2, \pi, 3\pi/2\}$ at $t \notin \{t^{(\mathrm{i})}_{\mathrm{blowup}}, t^{(\mathrm{ii})}_{\mathrm{blowup}}\}$ (for $t^{(\mathrm{i})}_{\mathrm{blowup}}$ and $t^{(\mathrm{ii})}_{\mathrm{blowup}}$ predicted by (3.6.23) and (3.6.24), respectively). Due to time constraints and equation (3.6.18) being more complicated than equation (3.3.3), we have been unable to perform a similar parametric study on b in the present section to determine b_{c} as we did in Section 3.3.1. We have also been unable to determine the t_{blowup} in the case where the solution of (3.6.18) experiences blowup at $\theta \in (0, 2\pi) \setminus \{\pi/2, \pi, 3\pi/2\}$ at $t \notin \{t^{(\mathrm{i})}_{\mathrm{blowup}}, t^{(\mathrm{ii})}_{\mathrm{blowup}}\}$ (for $t^{(\mathrm{i})}_{\mathrm{blowup}}$ and $t^{(\mathrm{ii})}_{\mathrm{blowup}}$ predicted by (3.6.23) and (3.6.24), respectively).

Figure 3.31 shows plots of the numerical solution of (3.6.18). Figures 3.31(a) and 3.29(b) shows plots of the free surface on a Cartesian plot for $b = 0.9$ and $b = 0.5$, respectively, and Figures 3.31(c) and 3.31(d) shows plots of the unscaled free surface on the ellipse for $b = 0.9$ and $b = 0.5$, respectively. Figures 3.31(a) and 3.31(c) show a case where the characteristics do not cross. In this case, the solution of (3.6.18) experiences blowup at $\theta = 0$ and $\theta = \pi$ at $t = t^{(\mathrm{i})}_{\mathrm{blowup}} \approx 0.118$

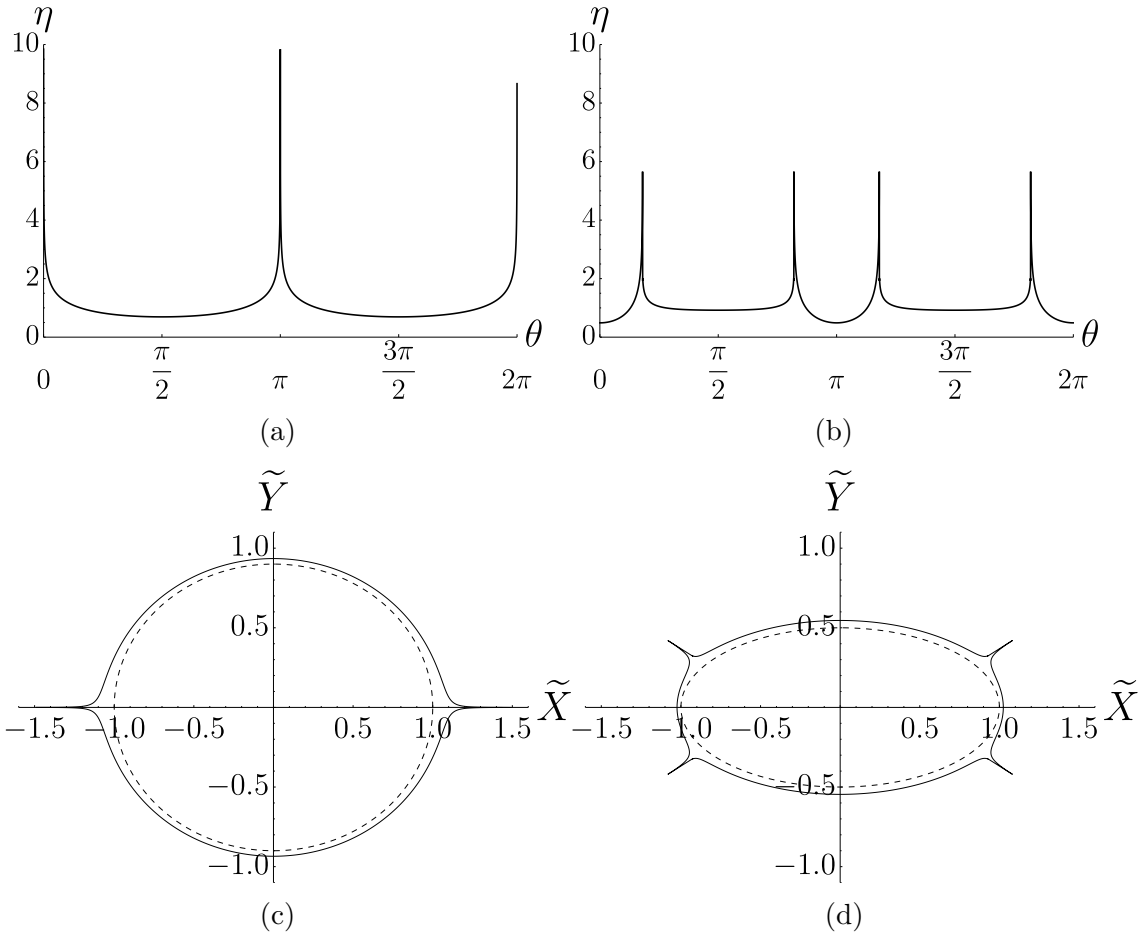

Figure 3.31: Plots of the numerical solution of (3.6.18) with $W = 10$ and $Ca = 0.1$ for (a, c) $b = 0.9$ at time $t = 0.99t^{(\mathrm{i})}_{\mathrm{blowup}} \approx 0.117$, and (b, d) $b = 0.5$ at time $t = 4.2 \times 10^{-3} \notin \{t^{(\mathrm{i})}_{\mathrm{blowup}}, t^{(\mathrm{ii})}_{\mathrm{blowup}}\}$, for $t^{(\mathrm{i})}_{\mathrm{blowup}}$ and $t^{(\mathrm{ii})}_{\mathrm{blowup}}$ predicted by (3.6.23) and (3.6.24), respectively. The plots (a, b) show the free surface on a Cartesian plot, and the plots (c, d) show the unscaled free surface (solid lines) on the ellipse, plotted for $\varepsilon = 0.05$. The dashed lines in (c, d) are the ellipse. Note that the scale of the vertical axis is different in part (a) and (b).

(3.6.23). This blowup is characterised by the spikes in Figures 3.31(a) and 3.31(c) which occur due to the omission of the stabilising effect of surface tension in equation (3.6.18). In particular, the behaviour shown in Figures 3.31(a) and 3.31(c) is characteristic of the rapid rotation limit (see Section 3.6.2.1). Figures 3.31(b) and 3.31(d) also show a case where the characteristics do not cross, despite their similarity to Figures 3.29(b) and 3.29(d). In this case, the solution of (3.6.18) experiences blowup at $\theta \in (0, 2\pi) \setminus \{\pi/2, \pi, 3\pi/2\}$ at $t \notin \{t^{(\mathrm{i})}_{\mathrm{blowup}}, t^{(\mathrm{ii})}_{\mathrm{blowup}}\}$ (for $t^{(\mathrm{i})}_{\mathrm{blowup}}$ and $t^{(\mathrm{ii})}_{\mathrm{blowup}}$ predicted by (3.6.23) and (3.6.24), respectively). Again, this blowup is characterised by the spikes in Figures 3.31(a) and 3.31(c) which occur due to the omission of the stabilising effect of surface tension in equation (3.6.18). The blowup occurring at $\theta \in (0, 2\pi) \setminus \{\pi/2, \pi, 3\pi/2\}$ is due to the effect of surface tension opposing the effect of centrifugation. We expect that, by increasing (decreasing) the effect of surface tension and/or decreasing (increasing) the effect of centrifugation, then the blowup would occur closer towards the top and bottom (tips) of the ellipse. We also expect that, by further increasing the effect of surface tension and/or decreasing the effect of centrifugation, we would begin to see behaviour characteristic of the strong surface tension limit (see Section 3.6.3.1), where a shock forms in the solution of equation (3.6.18) with steep fronts formed in the free surface either side of $\theta = \pi/2$ and $\theta = 3\pi/2$ (see Figure 3.29(b)). Again, we expect that the inclusion of the stabilising effect of surface tension in equation (3.6.18) would smooth these shocks [128].

3.6.4.2 Numerical solutions in the combined rapid rotation and strong surface tension limit to first order in ε

We now numerically examine the first-order PDE in the combined rapid rotation and strong surface tension limit (3.6.17). Figure 3.32 shows plots comparing the free surfaces in the rotating frame at $t = 0.1$ for the solution of the thin-film ellipse equation (2.3.13) and the solution of the first-order PDE in the combined rapid rotation and strong surface tension limit (3.6.17). Figure 3.32(a) shows a plot of the free surface on a Cartesian plot, and Figure 3.32(b) shows a plot of the unscaled free surface on the ellipse. For each eccentricity, the fluid collects at the tips of the ellipse, which is the characteristic behaviour of the high rotation speed regime and the rapid rotation limit. However, in the combined rapid rotation and strong surface tension limit, unlike in the rapid rotation limit, the solution of

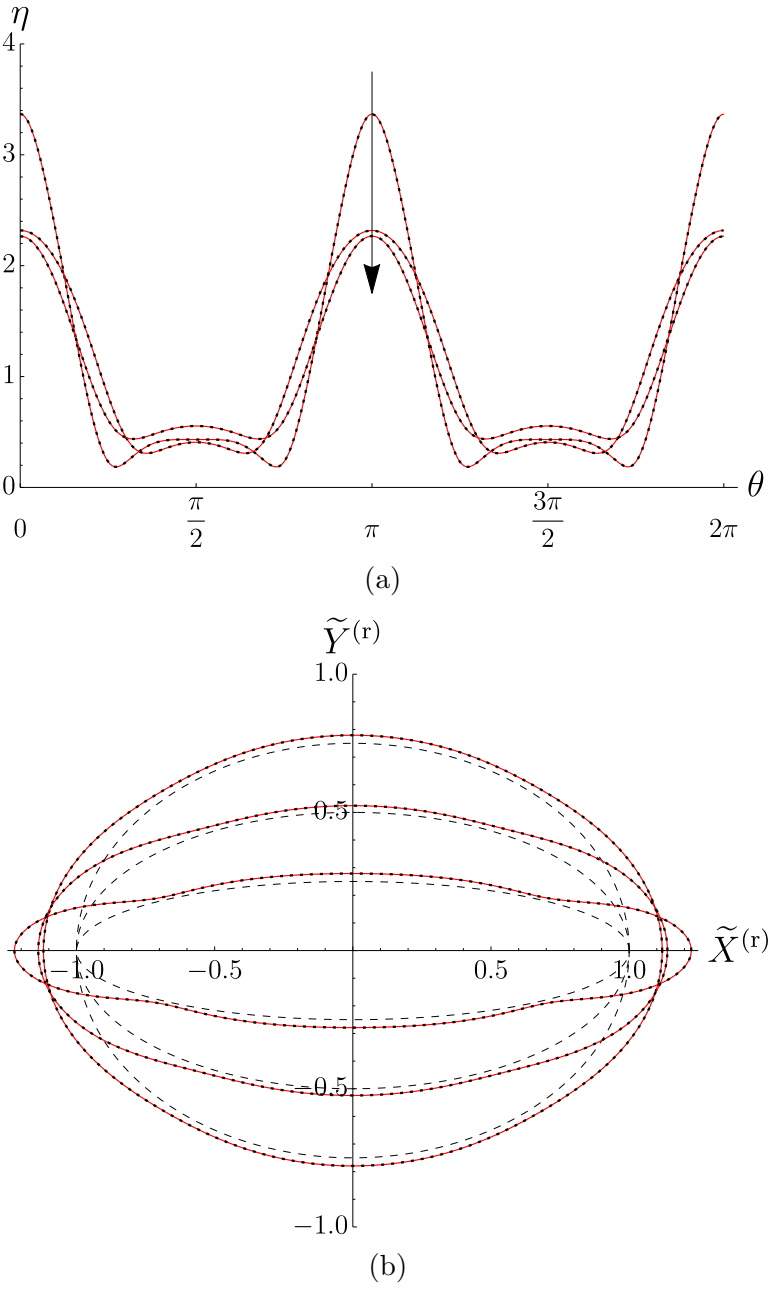

Figure 3.32: Comparison of the solutions of the thin-film ellipse equation (2.3.13) ($Re = 1$) (dashed black) and the first-order PDE in the combined rapid rotation and strong surface tension limit (3.6.17) (solid red) in the rotating frame with $W = 10$, $Ca = 0.1$, $t = 0.1$, $\widetilde{M} = 0.3$ for $b = 0.25$, $\varepsilon = 0.06669$, $b = 0.5$, $\varepsilon = 0.05965$ and $b = 0.75$, $\varepsilon = 0.05271$, where the arrow in (a) indicates the direction of increasing b. The plot (a) shows the free surface on a Cartesian plot, and the plot (b) shows the unscaled free surface on the ellipse. The dashed lines in (b) are the ellipse.

(3.6.17) will not experience blow up at some finite time due to the balancing effect of surface tension. The solutions of the first-order PDE in the combined rapid rotation and strong surface tension limit (3.6.17) compare well with the solutions of the thin-film ellipse equation (2.3.13).

Of course, in the combined rapid rotation and strong surface tension limit, the balance of the effects of centrifugation and surface tension is important. Figure 3.32 is an example of a case where the effect of centrifugation is stronger than (but does not dominate) the effect of surface tension. However, by decreasing the effect of centrifugation and/or increasing the effect of surface tension, we hypothesise that we would have a case in which the effect of surface tension is stronger than (but does not dominate) the effect of centrifugation. Specifically, we predict that the fluid would flow away from the tips of the ellipse, but the film would not exhibit rapid thinning at the tips of the ellipse due to the balancing effect of centrifugation.

3.7 Effect of cylinder eccentricity

We now examine the effect of varying the eccentricity of the cylinder. In particular, we examine the case of a highly eccentric ellipse ($b = 0.5$, corresponding to $\varepsilon = 0.05965$) in Section 3.7.1 and a nearly-circular ellipse ($b = 0.999$, corresponding to $\varepsilon = 0.04668$) in Section 3.7.2. The other parameters are as given in (3.1.1).

3.7.1 Highly eccentric ellipse $b = 0.5$

In Sections 3.4–3.6 we determined the transitions $W_i(0.9)$ for $i = 1, 2, 3$, i.e. for $b = 0.9$. We now find that

$$0.183 \approx W_1(0.5) > W_1(0.9) \approx 0.105, \tag{3.7.1}$$

$$0.196 \approx W_2(0.5) < W_2(0.9) \approx 0.410, \tag{3.7.2}$$

$$1.000 \approx W_3(0.5) < W_3(0.9) \approx 1.583. \tag{3.7.3}$$

Figure 3.33 shows plots of the time-averaged centre of mass in the laboratory frame $\widetilde{X}_{\mathrm{c}}^{\mathrm{av}}$ and $\widetilde{Y}_{\mathrm{c}}^{\mathrm{av}}$ as a function of W for $b = 0.5$ (Figure 3.1 shows the corresponding plot for $b = 0.9$), while Figure 3.34 shows a plot of E_n for $n = 1, \ldots, 5$ as a function of W for $b = 0.5$ (Figures 3.13(a), 3.17(a), 3.20, and 3.24(a) show the

corresponding plots for $b = 0.9$). We now discuss each of the transitions $W_i(0.5)$ for $i = 1, 2, 3$ in turn.

Firstly, for the lowest transition $W_1(b)$ now occurs for a higher value of W as b decreases from 0.9 to 0.5: $0.183 \approx W_1(0.5) > W_1(0.9) \approx 0.105$. Figure 3.35(a) shows the unscaled free surface in the laboratory frame when the semi-major axis is perpendicular to the direction of gravity and when it is parallel to the direction of gravity for $b = 0.5$. Figure 3.35(b) shows the location of the centre of mass in the laboratory frame for $b = 0.5$. In particular, the solid red line shows the location of the centre of mass from $\widetilde{t} = 0$ to $\widetilde{t} = \widetilde{t}_f = 5 \times 10^4$, demonstrating that the centre of mass again has an initial transient phase before converging to a periodic orbit. This periodic orbit is shown by the dashed black line in Figure 3.35(b). One period of the single main bulge corresponds to one half rotation of the cylinder. A decrease in b results in an increase in ε ($\widetilde{M}$ is unchanged), corresponding to a thicker initial film, and hence the single main bulge is larger due to the effect of gravity. Note that for the same value of $W = 0.09$, the single main bulge hangs almost vertically downwards when the semi-major axis of ellipse is parallel to gravity for $b = 0.5$ (see Figure 3.35(a)), whereas the single main bulge was still substantially displaced to the side for $b = 0.9$ (see Figure 3.10). Consequently, a higher rotation speed is needed to overcome this increase in ε and raise $\widetilde{Y}_{\mathrm{c}}^{\mathrm{av}}$ to 0, corresponding to a larger value of $W_1(b)$ for $b = 0.5$ than for $b = 0.9$.

Conversely, the second transition $W_2(b)$ now occurs for a lower value of W as b decreases from 0.9 to 0.5: $0.196 \approx W_2(0.5) < W_2(0.9) \approx 0.410$. This is due to the more pronounced effect of centrifugation for a more eccentric ellipse. The relevant term in (2.3.13) is

$$W^2 \frac{(1 - b^2)}{2} \sin 2\theta. \tag{3.7.4}$$

This term promotes an $n = 2$ instability, and $1 - b^2 = 0.19$ for $b = 0.9$, but $1 - b^2 = 0.75$ for $b = 0.5$. As a result, the switch from E_1 to E_2 dominance occurs substantially earlier for $b = 0.5$ (see Figure 3.34) than for $b = 0.9$ (see Figure 3.17(a)).

The third and final transition $W_3(b)$ similarly occurs for a lower value of W as b decreases from 0.9 to 0.5: $1.000 \approx W_3(0.5) < W_3(0.9) \approx 1.583$. The relevant term in 2.3.13 is again (3.7.4). As b decreases, the effect of centrifugation which holds the fluid at the tips of the ellipse becomes dominant at a lower value of W.

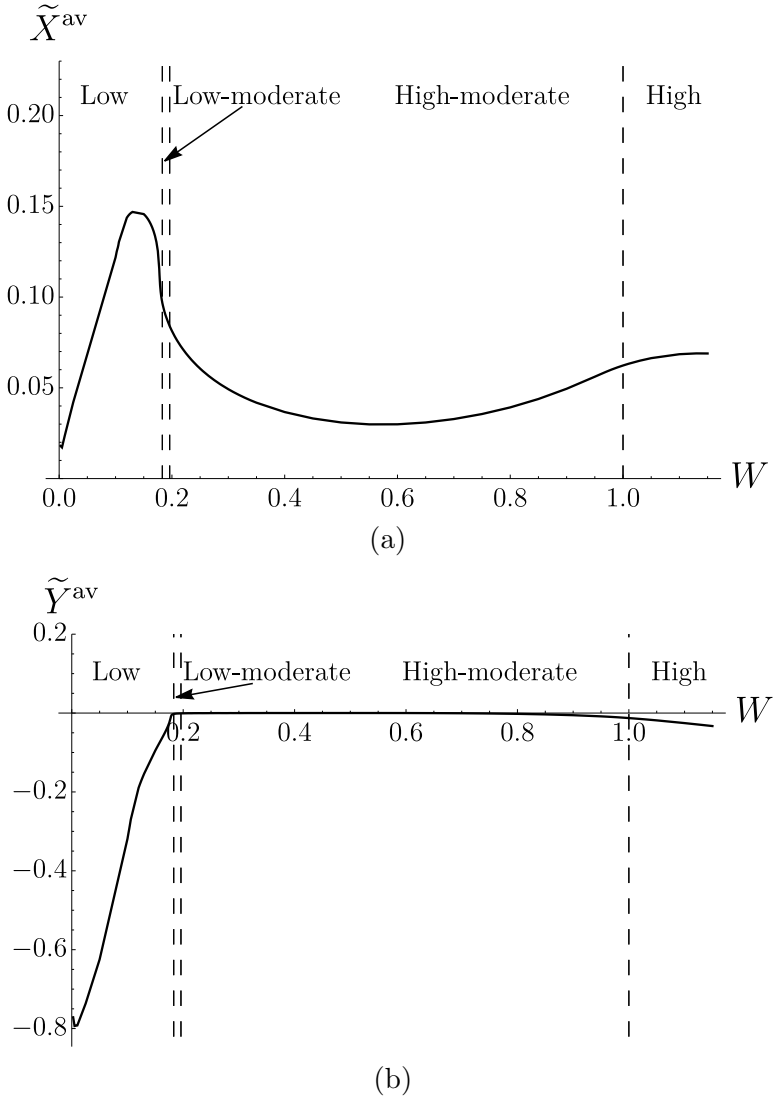

Figure 3.33: Plots of (a) $\widetilde{X}_{\rm c}^{\rm av}$ and (b) $\widetilde{Y}_{\rm c}^{\rm av}$, the time-averaged centre of mass in the laboratory frame, as functions of $W \in [0.0025, 1.15]$ from $\widetilde{t} = 0$ to $\widetilde{t} = \widetilde{t}_f = 5 \times 10^4$ for $b = 0.5$ and $\varepsilon = 0.05965$. The four characteristic parameter regimes described in Section 3.1.2 are indicated. The other parameters are as given in (3.1.1).

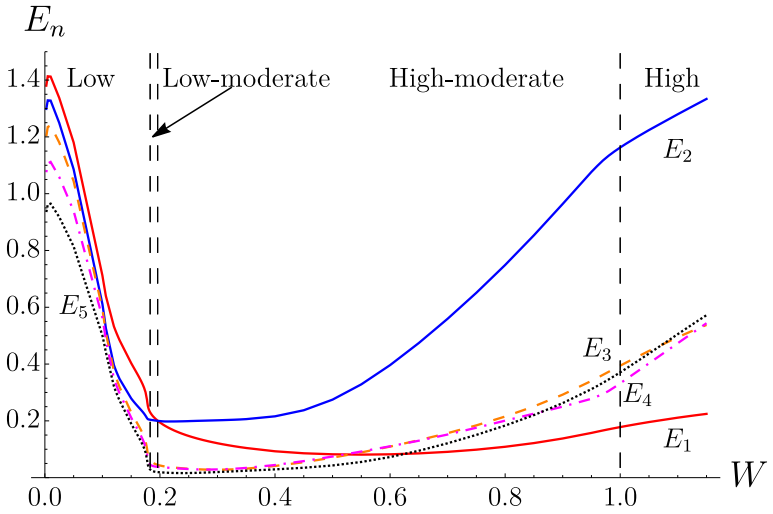

Figure 3.34: The energy of the n^{th} Fourier mode E_n for $n = 1, \ldots, 5$, plotted as a function of $W \in [0.0025, 1.15]$ and calculated to $\widetilde{t} = \widetilde{t}_f = 5 \times 10^4$ for $b = 0.5$ and $\varepsilon = 0.05965$. The $n = 1, \ldots, 5$ modes are shown with solid red, solid blue, dashed orange, dot-dashed purple, and dotted black lines, respectively. The four characteristic parameter regimes described in Section 3.1.2 are indicated. The other parameters are as given in (3.1.1).

Figure 3.36 shows a space-time plot in the rotating frame for $b = 0.5$ for $W = 1.5$ (which is in the high-moderate rotation speed regime for $b = 0.9$, but is clearly in the high rotation speed regime for $b = 0.5$, as evidenced by the two main bulges at the tips of the ellipse). Note that for $b = 0.5$ and $W = 1.5$ in Figure 3.36 the two main bulges are held much closer to the tips of the ellipse than they are for $b = 0.9$ and $W = 1.8$ (see Figure 3.25).

3.7.2 Nearly-circular ellipse $b = 0.999$

We examined the behaviour of a film on a nearly-circular ellipse in the limit of small flux at leading order in ε in Section 3.2. We found that at early times the limit $b \to 1^-$ (corresponding to $\xi \to 0^+$) was regular: the solution (3.2.27) converged to the appropriate limit of the Moffatt [57] steady full-film solution for a circle (3.2.14) as $b \to 1^-$. However, we also found that secular terms arise due to the effects of centrifugation and surface tension that, over longer times, disorder the solution (3.2.27). We also ignored a number of physical effects by discarding higher-order terms in ε (including the stabilising effect of surface tension, and the effect of increased film thickness) in this limit. In order to understand what is

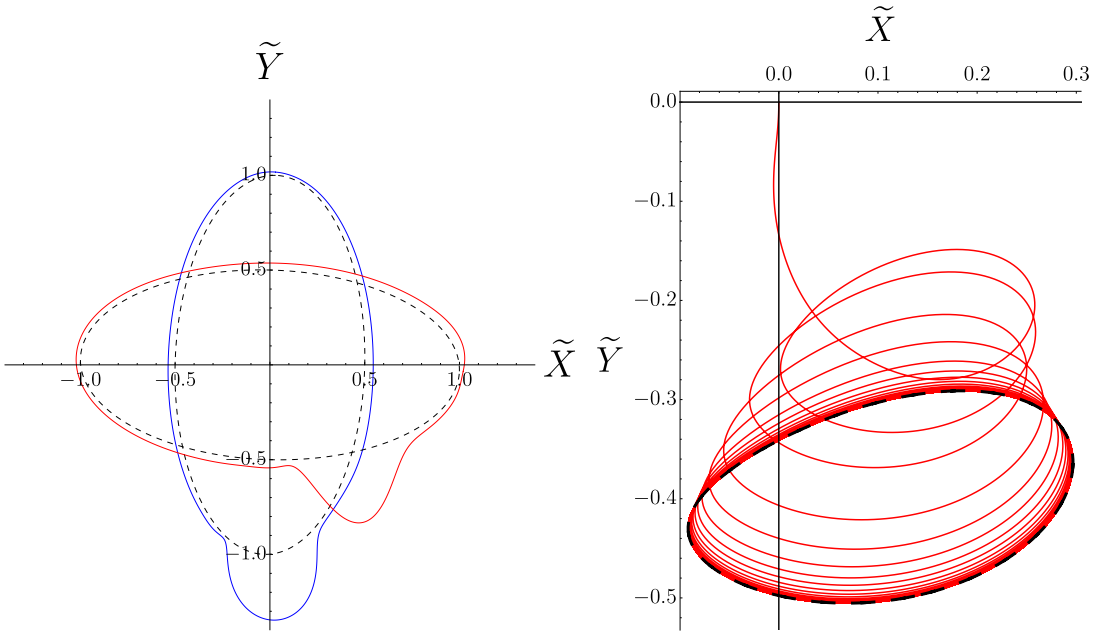

Figure 3.35: (a) The unscaled free surface on the ellipse in the laboratory frame when the semi-major axis is perpendicular to the direction of gravity (red line) and when it is parallel to the direction of gravity (blue line) for $W = 0.09$, $b = 0.5$, and $\varepsilon = 0.05965$. The dashed lines in (a) are the ellipse at the respective times. (b) The location of the centre of mass in the laboratory frame (solid red line) from $\widetilde{t} = 0$ to $\widetilde{t} = \widetilde{t}_f = 5 \times 10^4$ for $W = 0.09$, $b = 0.5$, and $\varepsilon = 0.05965$. The dashed black line in (b) shows the periodic orbit. The other parameters are as given in (3.1.1).

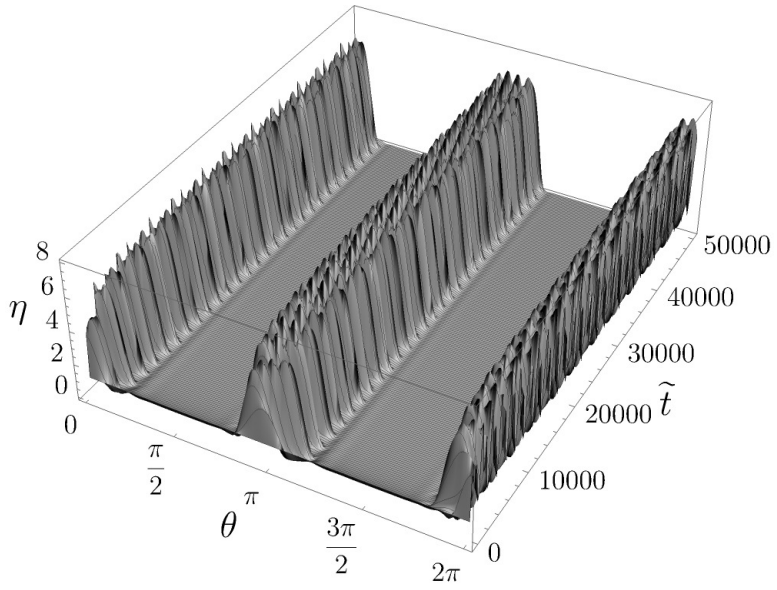

Figure 3.36: Space-time plot for the free surface in the rotating frame with $b = 0.5$ from $\widetilde{t} = 0$ to $\widetilde{t} = \widetilde{t}_f = 5 \times 10^4$ for $W = 1.5$ and $\varepsilon = 0.05965$. The other parameters are as given in (3.1.1).

happening when these effects are included, we now examine the thin-film ellipse equation (2.3.13) numerically in the case of a nearly-circular ellipse in the low and high rotation speed regimes. In Sections 3.4 and 3.6 we found pronounced effects due to eccentricity even when $b = 0.9$ in the low and high rotation speed regimes, respectively; we therefore examine the cases $b = 0.999$ (corresponding to $\varepsilon = 0.04668$) and $b = 1$ (corresponding to $\varepsilon = 0.04666$) which correspond to a nearly-circular ellipse and a circle, respectively.

We begin by examining the low rotation speed regime. Figure 3.37 shows the location of the centre of mass in the laboratory frame for $W = 0.09$ when $b = 0.999$. Figure 3.37(a) shows the location for the centre of mass from $\widetilde{t} = 0$ to $\widetilde{t} = \widetilde{t}_f = 10^5$ and shows that the centre of mass has an initial transient phase before converging to a periodic orbit. Figure 3.37(b) shows the location of the centre of mass from $\widetilde{t} = 5 \times 10^4$ to $\widetilde{t} = \widetilde{t}_f = 10^5$ (i.e. after the initial transient phase). In Figure 3.37(b), a circle has been fitted to the periodic orbit, showing that the orbit is almost, but not quite, circular. Figure 3.38 shows the location of the centre of mass in the laboratory frame for $W = 0.09$ when $b = 1$. Figure 3.38(a) shows the location for the centre of mass from $\widetilde{t} = 0$ to $\widetilde{t} = \widetilde{t}_f = 10^5$ and shows that the centre of mass has an initial transient phase before converging to a steady state. Figure

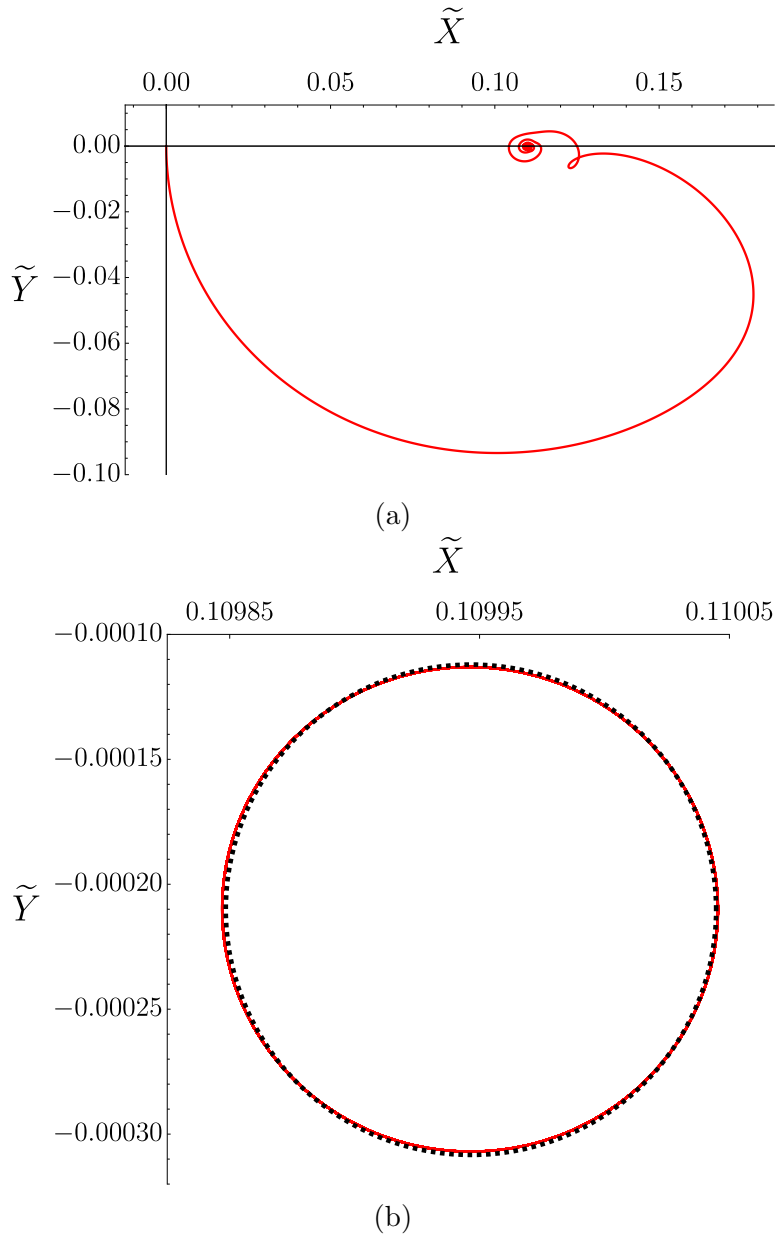

Figure 3.37: The location of the centre of mass in the laboratory frame (solid red line) for $W = 0.09$, $b = 0.999$ and $\varepsilon = 0.04668$ (a) from $\widetilde{t} = 0$ to $\widetilde{t} = \widetilde{t}_f = 10^5$, and (b) from $\widetilde{t} = 5 \times 10^4$ to $\widetilde{t} = \widetilde{t}_f = 10^5$ (i.e. as the location of the centre of mass converges to a periodic orbit). A circle (shown with a dotted black line) has been fitted to the periodic orbit in (b). The other parameters are as given in (3.1.1).

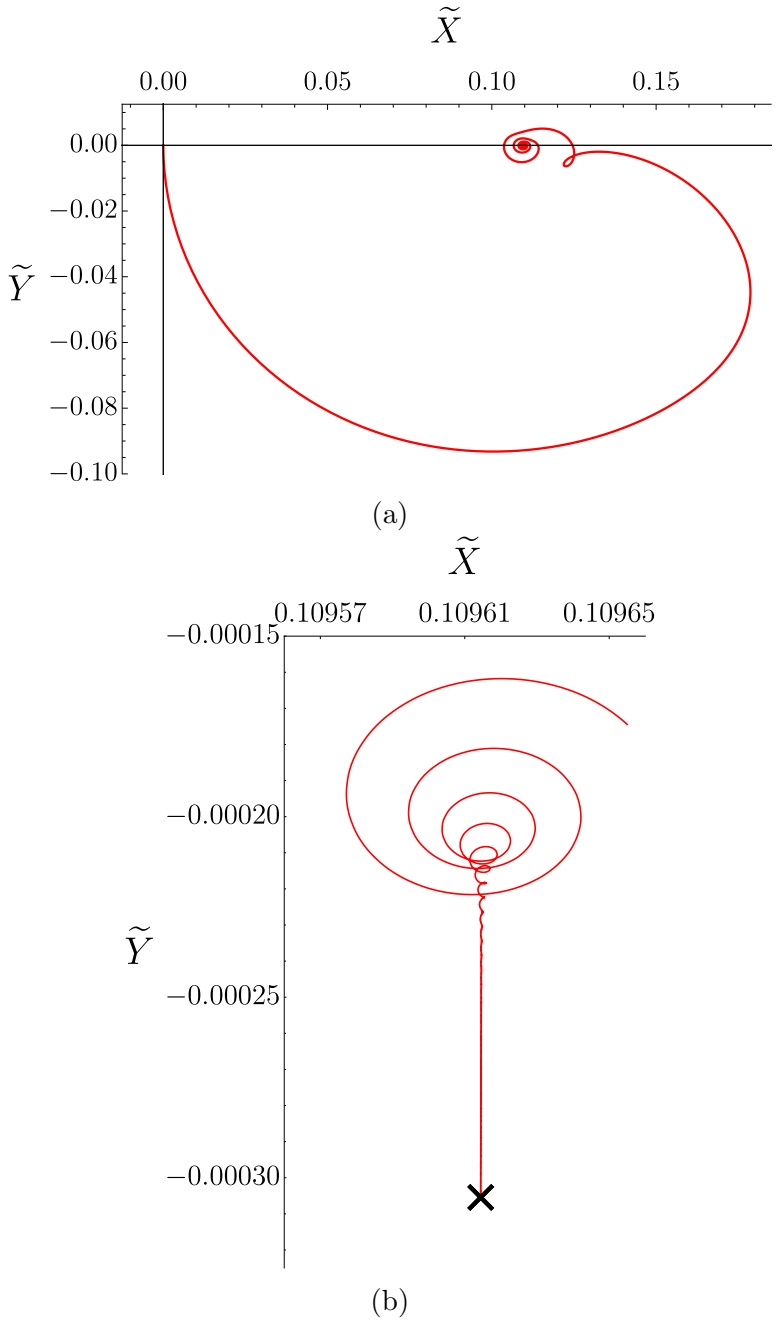

Figure 3.38: The location of the centre of mass in the laboratory frame (solid red line) for $W = 0.09$, $b = 1$ and $\varepsilon = 0.04666$ (a) from $\widetilde{t} = 0$ to $\widetilde{t} = \widetilde{t}_f = 10^5$, and (b) from $\widetilde{t} = 2.5 \times 10^4$ to $\widetilde{t} = \widetilde{t}_f = 10^5$ (i.e. as the location of the centre of mass converges to a steady state). A cross denotes the location of the centre of mass in the laboratory frame for a steady state in (b). The other parameters are as given in (3.1.1).

3.38(b) shows the location of the centre of mass from $\widetilde{t} = 2.5 \times 10^4$ to $\widetilde{t} = \widetilde{t}_f = 10^5$ (i.e. after the initial transient phase) as the centre of mass converges to a steady state, as observed by Evans et al. [56] (see Section 1.4.1.3). In Figure 3.38(b), a cross denotes the location of the steady state. Note that although Figures 3.37(a) and 3.38(a) are visually indistinguishable, corresponding to the previously noted regularity of the limit $b \to 1^-$, the final behaviour shown in Figures 3.37(b) and 3.38(b) is qualitatively different. In the case $b = 0.999$ the location of the centre of mass converges to a periodic orbit in Figure 3.37(b) which is almost, but not quite, circular, while in the case $b = 1$ the location of the centre of mass converges to a steady state in Figure 3.38(b). However, convergence to both of these final behaviours is exponentially slow (hence the need to take the simulations up to $\widetilde{t} = \widetilde{t}_f = 10^5$), and the size of the orbit shown in Figure 3.37(b) is extremely small.

We next examine the high rotation speed regime. Figure 3.39(a) shows a space-time plot in the rotating frame for $W = 1.5$ and $b = 0.999$. Figure 3.39(a) shows that there is substantially less preferential accumulation at the tips of the ellipse due to its near circularity when compared to the case $b = 0.9$ (see Figure 3.25). The relevant centrifugation term in (2.3.13), namely (3.7.4), has coefficient $W^2(1 - b^2) \approx 0.002W^2$ for $b = 0.999$. In particular, we do not observe the characteristic behaviour in the high rotation speed limit for $b = 0.999$ (i.e. two main bulges formed and held at the tips of the ellipse). Instead, we see behaviour closer to that of a film on a circular cylinder in the zero gravity limit [56; 125] in which small perturbations to the uniform film grow due to centrifugation (i.e. represented by the $W^2 b$ term in (2.3.13)) and form distinct bulges all over the surface of the cylinder which are separated by thin films of fluid (see Section 1.4.1.3). In the absence of any symmetry-breaking effect, including numerical noise, these bulges remain distinct. However, in the presence of gravity, we observe that the distinct bulges eventually coalesce into a single main bulge which travels around the cylinder in the same direction as the rotation, but at a speed slower than the rotation of the cylinder. Figure 3.39(b) shows two cross-sections of Figure 3.39(a) showing the distinct bulges at $\tilde{t} = 8 \times 10^3$ and the single main bulge at $\tilde{t} = 1.6 \times 10^4$. Figure 3.40(a) shows a space-time plot in the rotating frame for $W = 1.5$ and $b = 1$. Figure 3.40(a), of course, shows the characteristic behaviour of a film on a circular cylinder in the zero gravity limit [56] (see Section 1.4.1.3). Again, in the absence of any symmetry-breaking effect, including numerical noise, these bulges remain

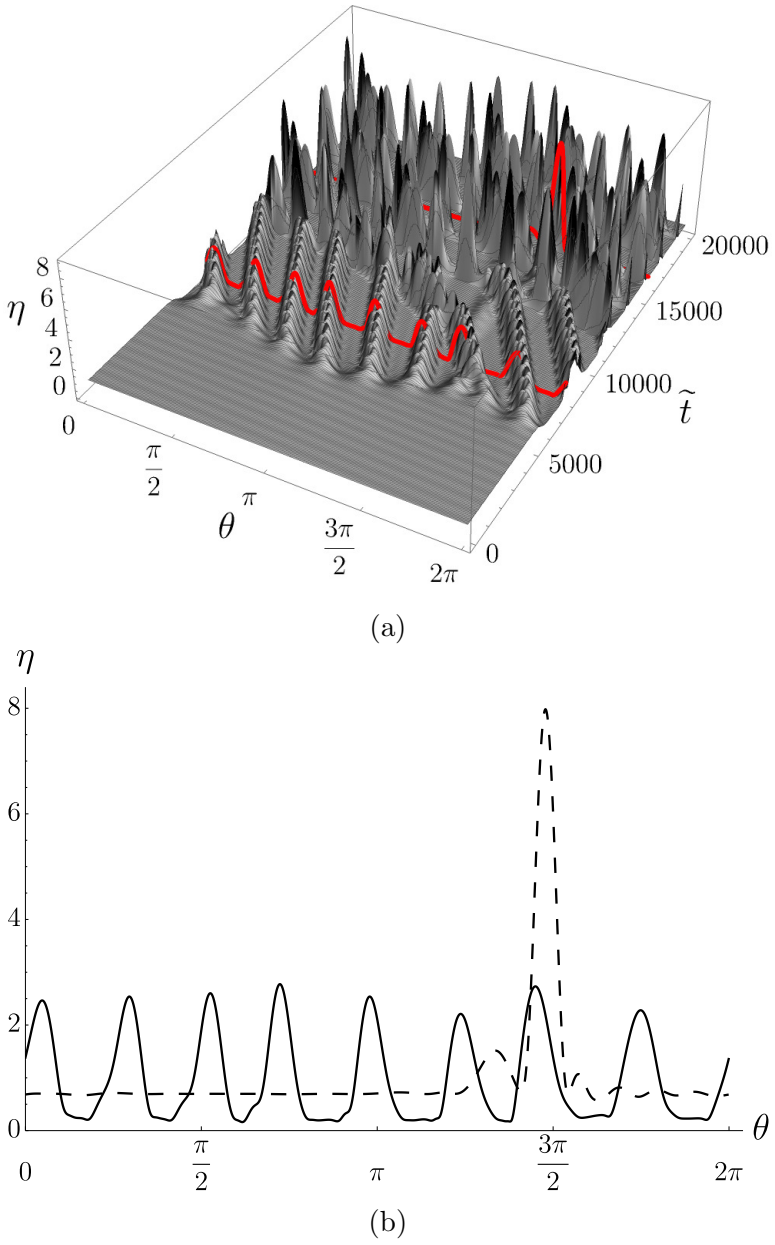

Figure 3.39: (a) Space-time time plot for the free surface in the rotating frame from $\tilde{t} = 0$ to $\tilde{t} = 2 \times 10^4$ for $W = 1.5$ and $b = 0.999$. (b) Two cross-sections of (a) corresponding to the free surface at $\tilde{t} = 8 \times 10^3$ (solid line) and $\tilde{t} = 1.6 \times 10^4$ (dashed line). The thick red lines in (a) highlight the cross-sections in (b). The other parameters are as given in (3.1.1).

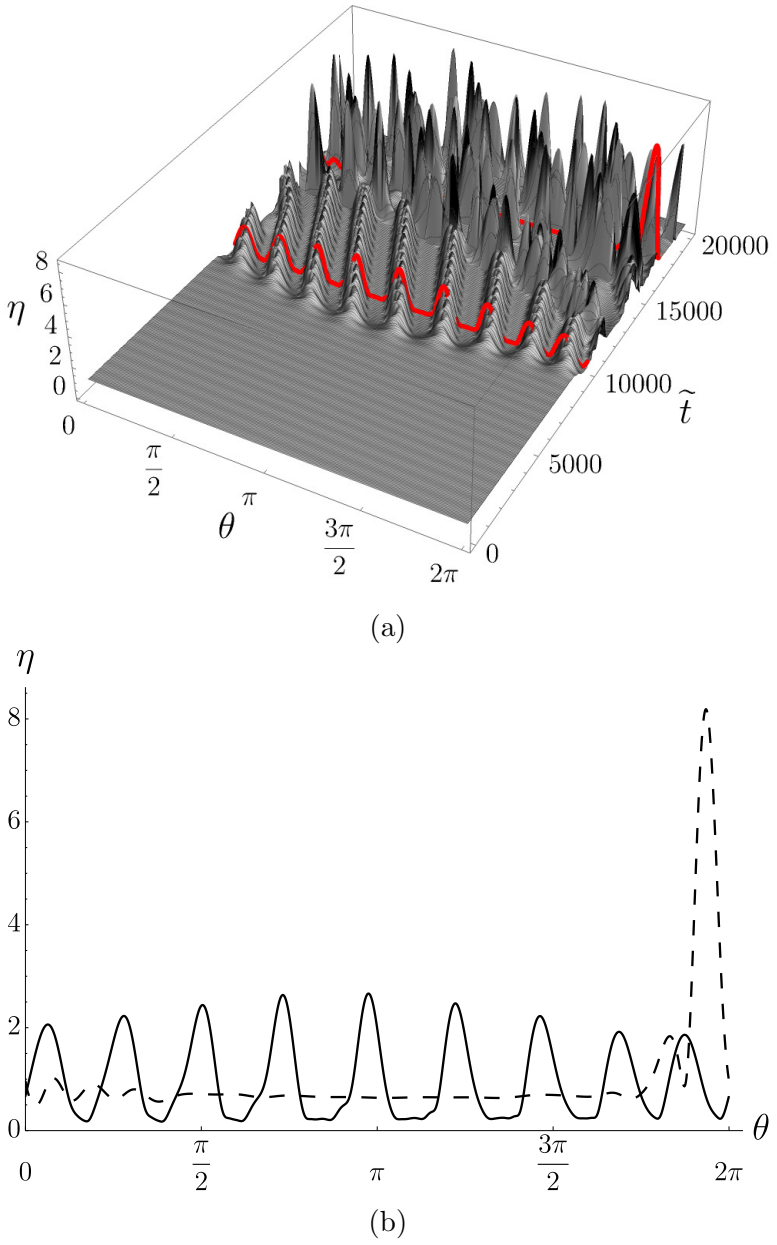

Figure 3.40: (a) Space-time time plot for the free surface in the rotating frame from $\tilde{t} = 0$ to $\tilde{t} = 2 \times 10^4$ for $W = 1.5$ and $b = 1$. (b) Two cross-sections of (a) corresponding to the free surface at $\tilde{t} = 10^4$ (solid line) and $\tilde{t} = 1.7 \times 10^4$ (dashed line). The thick red lines in (a) highlight the cross-sections in (b). The other parameters are as given in (3.1.1).

distinct. However, in the presence of gravity, we observe that the distinct bulges eventually coalesce into a single main bulge which travels around the cylinder in the same direction as the rotation, but at a speed slower than the rotation of the cylinder. Figure 3.40(b) shows two cross-sections of Figure 3.39(a) showing the distinct bulges at $\tilde{t} = 10^4$ and the single main bulge at $\tilde{t} = 1.7 \times 10^4$. There is relatively little difference between the behaviour in the case $b = 0.999$ shown in Figure 3.39 and the case $b = 1$ shown in Figure 3.40, again reflecting the regularity of the limit $b \to 1^-$. As discussed in Section 1.4.1.3, in the limit of zero gravity, the number of distinct bulges which form on the free surface for a circular cylinder can be predicted via a linear stability analysis by examining the fastest growing wavenumber. Specifically, a good approximation for the number of distinct bulges which form is given by (1.4.10). Applying (1.4.10) to the parameters used in Figures 3.39 and 3.40 gives $N \approx [9.51] = 9$ which is indeed the number of distinct bulges shown for $b = 1$ in Figure 3.39, and close to the number shown (namely eight) for $b = 0.999$ in Figure 3.40.

3.8 Conclusions

In this chapter, we analysed the analytical and numerical results of the thin-film ellipse equation for flow on a two-dimensional uniformly rotating horizontal elliptical cylinder (2.3.13). We explored a different region of parameter space than previous studies [125; 167; 168]. Our study was the first to provide analytical results for flow on a two-dimensional uniformly rotating horizontal elliptical cylinder. Additionally, we were the first to examine the special case of a stationary elliptical cylinder.

In Section 3.1 we described the results of a parametric study on the dimensionless rotation speed W for the parameters given in (3.1.1). In particular, we identified four characteristic behaviours of the free surface corresponding to their respective rotation speeds, namely low rotation speed, low-moderate rotation speed, high-moderate rotation speed, and high rotation speed.

In Section 3.2 we analytically explored the effects of small cylinder eccentricity on the steady full-film solution first described by Moffatt [57] (1.4.3). To make analytical progress, we considered the limit of a nearly-circular ellipse and the limit of small flux to obtain the solution (3.2.27). The solution (3.2.27) contains a

particular combination of centrifugation and surface tension terms, namely $W^2 - 3/Ca$, as well as a number of secular terms. The structure of solution (3.2.27) revealed three regions of parameter space and highlighted that even a relatively mild departure from circularity produces significant qualitative and quantitative differences from the behaviour in the circular case. When $W^2Ca < 3$ surface tension is dominant and the fluid collects away from the tips of the ellipse. When $W^2Ca = 3$ (in this limit) surface tension and centrifugation cancel out each other identically, and thus the flow is purely driven by gravity and rotation. When $W^2Ca > 3$ centrifugation is dominant and the fluid collects towards the tips of the ellipse.

In Section 3.3 we examined the special case of a stationary cylinder. In particular, in Sections 3.3.1–3.3.3 we investigated the qualitative change to the behaviour of the free surface as Ca is decreased. At leading order in ε in the limit $Ca \to \infty$ (Section 3.3.1) we used the method of characteristics to obtain an analytical solution (3.3.5). The characteristics do not cross for $0.867 \approx b_c \leq b \leq 1$, however they cross for $0 < b < b_c \approx 0.867$. When the characteristics do not cross, the solution of (3.3.3) experiences finite time blowup at $\theta = 3\pi/2$ at $t = t_{\text{blowup}}$ (3.3.6). When the characteristics cross, a shock forms in the solution of (3.3.3) either side of $\theta = 3\pi/2$ at $t < t_{\text{blowup}}$ (3.3.6). At leading order in ε for $Ca = \mathcal{O}(1)$ (Section 3.3.2), we again used the method of characteristics to obtain a solution along the characteristics starting at $\theta_0 = \pi/2$ and $\theta_0 = 3\pi/2$. The characteristics do not cross for $b_c \leq b \leq 1$, however they cross for $0 < b < b_c$, for some b_c. We found that the opposing effects of gravity and centrifugation prevent finite-time blowup at $\theta = \pi/2$, however the combined effect of gravity and centrifugation accelerate finite-time blowup at $\theta = 3\pi/2$ (when compared to the limit $Ca \to \infty$). Therefore, when the characteristics do not cross, the solution of (3.3.7) experiences finite time blowup at $\theta = 3\pi/2$ at $t = t_{\text{blowup}}$ (3.3.12), and when the characteristics cross, shocks form in the solution of (3.3.7) either side of $\theta = \pi/2$ and $\theta = 3\pi/2$ at $t < t_{\text{blowup}}$ (3.3.12). In the limit of $Ca \to 0^+$ and the nearly-circular limit (Section 3.3.3) we obtained a steady solution in the absence of gravity (3.3.15), which is neutrally stable for the $n = 0$ and $n = 1$ modes and stable for higher modes. We also obtained a solution for the early-time behaviour of the free surface in the presence of gravity, namely (3.3.21). Two modes of disturbances were observed in (3.3.21) corresponding to the effect of surface tension which drives the fluid away from the tips of the ellipse

and towards a circular film, and the effect of gravity which causes the fluid to drain towards the bottom of the ellipse. In Section 3.3.4 we investigated the case of draining flow on a stationary ellipse and two distinct behaviours were observed for two values of b, namely $b = 0.15$ and $b = 0.45$. For $b = 0.15$ a portion of the fluid was trapped on top of the ellipse, whereas for $b = 0.45$ there was no fluid trapped and instead the fluid accumulates in a single bulge at the bottom of the ellipse.

In Sections 3.4–3.6, for the parameter values given in (3.1.1), we examined the characteristic behaviour of the free surface in the low rotation speed regime, the low-moderate rotation speed regime, the high-moderate rotation speed regime, and the high rotation speed regime, respectively.

In Section 3.4 we examined the low rotation speed regime ($0 < W < W_1(0.9) \approx 0.105$). In this regime, there is a single main bulge (and sometimes a smaller secondary bulge), which hangs below the cylinder due to gravity and oscillates periodically due to the rotation of the cylinder. The transition between the low and low-moderate rotation speed regimes occurs at $W = W_1(0.9) \approx 0.105$, which corresponds to the lowest value of W for which $\widetilde{Y}_{\mathrm{c}}^{\mathrm{av}} = 0$. This regime had been previously studied by Li et al. [125] and Parrish et al. [167].

In Section 3.5.1 we examined the low-moderate rotation speed regime ($0.105 \approx W_1(0.9) \leq W \leq W_2(0.9) \approx 0.410$). In this regime, a single main bulge (and smaller secondary bulges) is formed due to a combination of gravity and centrifugation. The single main bulge is carried past the horizontal $\widetilde{X}$ axis in the laboratory frame, travels anti-clockwise with the rotation of the cylinder (but at a speed slower than the rotation of the cylinder), and grows, decays and occasionally coalesces with the secondary bulge. The transition between the low-moderate and high-moderate rotation speed regimes occurs at $W = W_2(0.9) \approx 0.410$, which corresponds to the value of W at which E_1 and E_2 coincide. This regime had been previously studied by Hunt [168], Li et al. [125], and Parrish et al. [167].

In Section 3.5.2 we examined the high-moderate rotation speed regime ($0.410 \approx W_2(0.9) < W < W_3(0.9) \approx 1.583$). In this regime, multiple main bulges are formed at the tips of the ellipse due to a combination of gravity and centrifugation. The main bulges travel anti-clockwise with the rotation of the cylinder, but at a speed slower than the rotation of the cylinder. The transition between the high-moderate and high rotation speed regimes occurs at $W = W_3(0.9) \approx 1.583$, which

corresponds to the lowest value of W for which $M_{1/2}$, given by (3.6.1), varies by less than 1% across the time interval $\widetilde{t} \in [2 \times 10^4, \widetilde{t}_f = 5 \times 10^4]$ (i.e. a suitably long time interval which begins well after the initial transient phase has ended). This regime had not been previously studied.

In Section 3.6.1 we examined the high rotation speed regime ($W \geq W_3(0.9) \approx 1.583$). In this regime, the rotation speed is large enough that centrifugation is the dominant effect, resulting in two main bulges that form and are held at the tips of the ellipse. This regime had not been previously studied. In Sections 3.6.2, 3.6.3, and 3.6.4, we examined various limits of the thin-film ellipse equation (2.3.13), namely the rapid rotation limit ($W \to \infty$), the strong surface tension limit ($Ca \to 0^+$), and the combined rapid rotation and strong surface tension limit ($W \to \infty$ and $Ca \to 0^+$), respectively. We first examined the analytically-tractable leading-order case of each of these limits in Sections 3.6.2.1, 3.6.3.1, and 3.6.4.1. We then proceeded to numerically examine the first-order case of each limit and compared the solutions with that of the thin-film ellipse equation (2.3.13) in Sections 3.6.2.2, 3.6.3.2, and 3.6.4.2. The strong surface tension limit (Section 3.6.3) had been previously studied by Parrish et al. [167] in their parametric study of the initial fluid load (see Figure 1.28(d)).

In Section 3.7 we examined the effect of cylinder eccentricity on the results of the parametric study on the dimensionless rotation speed described in Section 3.1 In Section 3.7.1 we considered the case of a highly eccentric ellipse ($b = 0.5$) and determined the values of $W_i(b)$ for $i = 1, 2, 3$, at which transition between the regimes outlined in Section 3.1 occurs. The values of $W_i(b)$ for $i = 1, 2, 3$ for transition between the regimes for both $b = 0.9$ and $b = 0.5$ are summarised in (3.7.1)–(3.7.3). The change in $W_1(b)$ (see (3.7.1)) is due to the increase in ε ($\widetilde{M}$ is unchanged) as b decreases from 0.9 to 0.5, and the change in both $W_2(b)$ (see (3.7.2)) and $W_3(b)$ (see (3.7.3)) is due to the more pronounced effect of centrifugation as b deceases from 0.9 to 0.5. Finally, in Section 3.7.2 we examined the thin-film ellipse equation (2.3.13) in the case of a nearly-circular ellipse ($b = 0.999$) in the low and high rotation speed regimes. In the low rotation speed regime, the case $b = 0.999$ exhibits qualitatively distinct behaviour of the free surface (convergence to a periodic orbit) to the case $b = 1$ (convergence to a steady state). In the high rotation speed regime, there is relatively little difference between the $b = 0.999$ case and $b = 1$ case due to less preferential accumulation at the tips of

the ellipse.

There is only one regime from the parametric study of the initial fluid load by Parrish et al. [167], shown in their Figure 1.28(c), which we did not observe in the present work. In their study, Parrish et al. [167] observed a regime where gravitational and surface tension effects compete, leading to the formation of bulges at opposite ends of the cylinder that oscillate with the rotation of the cylinder. Parrish et al. [167] found that, in this regime, the effect of surface tension is not strong enough to dominate the effect of gravity, allowing the bulges to oscillate.

Chapter 4

Formulation of reduced-order models for the non-axisymmetric coating of a vertical fibre by a thick film of fluid

In this chapter, we derive a thick-film reduced-order model using the WRIBL method (see Sections 1.2.1.4 and 1.3.2.2) for non-axisymmetric flow on the exterior of a vertical fibre. In particular, in Section 4.1 we introduce the system which we will be investigating. We then derive and nondimensionalise the governing equations and boundary conditions for this system. In Section 4.2 we derive the thick-film weighted-residual model. Specifically, in Section 4.2.1 we apply a set of long-wave scalings to the governing equations to obtain boundary-layer equations for the azimuthal and axial velocities, and then (following Section 1.2.1.4) in Section 4.2.2 we expand the velocities and compute the weighted residuals. In Section 4.3 we derive reductions of the thick-film weighted-residual model. Specifically, in Section 4.3.1 we perform a gradient expansion to reduce the thick-film weighted residual model to a thick-film gradient-expansion model, and then in Section 4.3.2 we further reduce the thick-film weighted-residual model by applying a set of thin-film scalings to the thick-film gradient-expansion model to obtain a thin-film gradient-expansion model.

4.1 Problem formulation

We consider the unsteady, three-dimensional coating flow of an incompressible Newtonian fluid of constant density $\hat{\rho}$ and constant viscosity $\hat{\mu}$ on the exterior of a stationary vertical cylindrical fibre with circular cross-section of radius $\hat{a}$. Throughout, hats denote dimensional quantities. The fluid is surrounded by an inviscid, hydrodynamically-passive gas at constant pressure $\hat{p}_a$, and the gas-fluid free surface has constant surface tension $\hat{\gamma}$. The characteristic film thickness is denoted by $\hat{h}$, a characteristic wavelength is denoted by $\hat{\lambda}$, and a characteristic film radius is denoted by $\hat{s}$ (where $\hat{s} = \hat{a} + \hat{h}$). We use cylindrical polar coordinates $(\hat{r}, \theta, \hat{z})$, where $\hat{z}$ points vertically downwards. The surface of the fibre is therefore located at $\hat{r} = \hat{a}$, and the free surface is denoted by $\hat{r} = \hat{S}(\theta, \hat{z}, \hat{t}) = \hat{a} + \hat{H}(\theta, \hat{z}, \hat{t})$, where $\hat{S}$ is the film radius, $\hat{H}$ is the film thickness, and $\hat{t}$ is time. A schematic of this system is shown in Figure 4.1.

4.1.1 Governing equations in vector form

The fluid satisfies the continuity and Navier–Stokes equations, which are [224, Chapter 3]

$$\nabla \cdot \hat{\mathbf{u}} = 0, \quad \hat{\rho}\left(\hat{\mathbf{u}}_{\hat{t}} + \hat{\mathbf{u}} \cdot \nabla \hat{\mathbf{u}}\right) = -\nabla \hat{p} + \hat{\mu} \nabla^2 \hat{\mathbf{u}} + \hat{\rho} \hat{\mathbf{g}}, \tag{4.1.1}$$

where $\hat{\boldsymbol{u}} = (\hat{u}(\hat{r}, \theta, \hat{z}, \hat{t}), \hat{v}(\hat{r}, \theta, \hat{z}, \hat{t}), \hat{w}(\hat{r}, \theta, \hat{z}, \hat{t}))$ and $\hat{p}(\hat{r}, \theta, \hat{z}, \hat{t})$ are the velocity and pressure of the fluid, respectively, and $\hat{\mathbf{g}}$ is the acceleration due to gravity. The boundary conditions are no-slip and impermeability conditions at the surface of the fibre, $\hat{r} = \hat{a}$,

$$\hat{\mathbf{u}} = \mathbf{0}, \tag{4.1.2}$$

and the tangential stress balance condition in the azimuthal direction, the tangential stress balance condition in the axial direction, and the normal stress balance condition at the free surface, $\hat{r} = \hat{S}$,

$$\left[\hat{\mathbf{n}} \cdot \hat{\mathbf{T}} \cdot \hat{\mathbf{t}}_1\right]_F^G = 0, \qquad \left[\hat{\mathbf{n}} \cdot \hat{\mathbf{T}} \cdot \hat{\mathbf{t}}_2\right]_F^G = 0, \qquad \left[\hat{\mathbf{n}} \cdot \hat{\mathbf{T}} \cdot \hat{\mathbf{n}}\right]_F^G = \hat{\gamma}\hat{\kappa}, \tag{4.1.3}$$

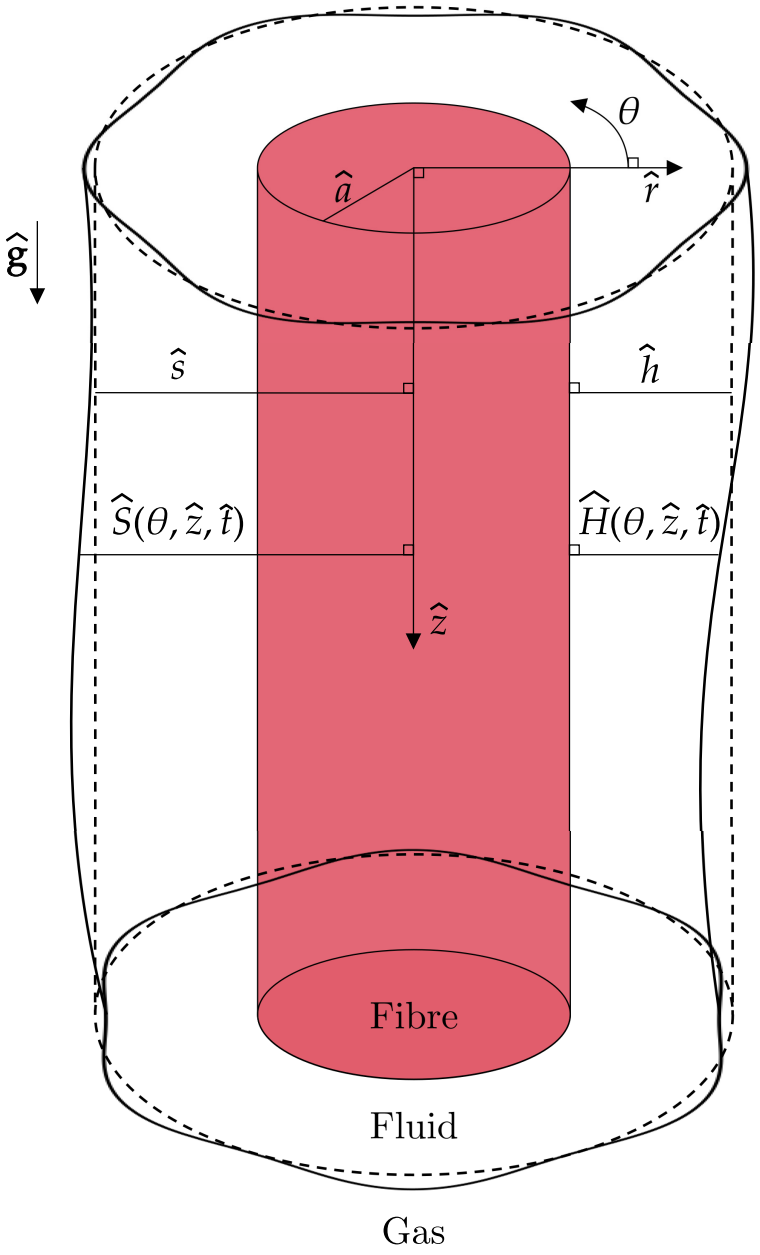

Figure 4.1: Schematic of an unsteady, non-axisymmetric, free-surface flow of fluid coating the exterior of a stationary vertical cylindrical fibre with circular cross-section. The solid lines denote the unsteady free surface with film radius $\hat{S}(\theta,\hat{z},\hat{t})$, and the dashed lines denote the steady free surface with film radius $\hat{s}$.

respectively, where $[\cdot]_F^G$ represents the jump in a quantity at the free surface between the fluid and gas regions. The total stress tensor is given by

$$\hat{\mathbf{T}} = -\hat{p}\mathbf{I} + \hat{\mu}\left[\nabla\hat{\mathbf{u}} + (\nabla\hat{\mathbf{u}})^{\mathrm{T}}\right], \tag{4.1.4}$$

where $\mathbf{I}$ is the identity tensor, the unit normal vector to the free surface is

$$\hat{\mathbf{n}} = \frac{\hat{S}\mathbf{e}_r - \dfrac{\partial\hat{S}}{\partial\theta}\mathbf{e}_\theta - \hat{S}\dfrac{\partial\hat{S}}{\partial\hat{z}}\mathbf{e}_z}{\sqrt{\left(\dfrac{\partial\hat{S}}{\partial\theta}\right)^2 + \hat{S}^2\left(1 + \left(\dfrac{\partial\hat{S}}{\partial\hat{z}}\right)^2\right)}}, \tag{4.1.5}$$

the unit tangential vectors to the free surface in the azimuthal and the axial directions are

$$\hat{\mathbf{t}}_1 = \frac{\dfrac{\partial\hat{S}}{\partial\theta}\mathbf{e}_r + \hat{S}\mathbf{e}_\theta}{\sqrt{\hat{S}^2 + \left(\dfrac{\partial\hat{S}}{\partial\theta}\right)^2}}, \quad \hat{\mathbf{t}}_2 = \frac{\dfrac{\partial\hat{S}}{\partial\hat{z}}\mathbf{e}_r + \mathbf{e}_z}{\sqrt{1 + \left(\dfrac{\partial\hat{S}}{\partial\hat{z}}\right)^2}}, \tag{4.1.6}$$

respectively, and the interfacial curvature is given by

$$\hat{\kappa}(\theta, \hat{z}, \hat{t}) = \nabla\cdot\hat{\mathbf{n}}. \tag{4.1.7}$$

The system (4.1.1)–(4.1.7) is closed by the kinematic condition at the free surface

$$\frac{D}{D\hat{t}}\left(\hat{r} - \hat{S}\right) = 0, \tag{4.1.8}$$

where $D/D\hat{t} = \partial/\partial\hat{t} + \hat{\mathbf{u}}\cdot\nabla$ is the material derivative.

4.1.2 Governing equations in coordinate form

The system (4.1.1)–(4.1.8) is nondimensionalised using

$$\begin{aligned} &\hat{r} = \hat{a}r, \quad \hat{z} = \hat{a}z, \quad \hat{S} = \hat{a}S, \quad \hat{H} = \hat{a}H, \quad \hat{u} = \hat{V}u, \\ &\hat{v} = \hat{V}v, \quad \hat{w} = \hat{V}w, \quad \hat{p} = \frac{\hat{u}\hat{V}}{\hat{a}}p, \quad \hat{t} = \frac{\hat{a}}{\hat{V}}t, \quad \hat{\kappa} = \frac{1}{\hat{a}}\kappa, \end{aligned} \tag{4.1.9}$$

where $\hat{V} = \hat{\rho}\hat{g}\hat{a}^2/\hat{\mu}$ is a characteristic velocity for gravitational drainage. This gives rise to four dimensionless parameters, namely

$$Re = \frac{\hat{\rho}\hat{V}\hat{a}}{\hat{\mu}}, \quad \Gamma = \frac{\hat{\gamma}}{\hat{\mu}\hat{V}}, \quad \bar{H} = \frac{\hat{h}}{\hat{a}}, \quad \lambda = \frac{\hat{\lambda}}{\hat{a}}, \tag{4.1.10}$$

representing a Reynolds number, a surface tension parameter, the characteristic film thickness (where $\bar{H} = \bar{S} - 1$), and a characteristic wavelength, respectively.

In the present coordinate system, the continuity equation and the radial, azimuthal, and axial components of the Navier–Stokes equations (4.1.1) for flow on a vertical fibre are

$$\frac{1}{r}\frac{\partial (ru)}{\partial r} + \frac{1}{r}\frac{\partial v}{\partial \theta} + \frac{\partial w}{\partial z} = 0, \tag{4.1.11}$$

$$\begin{aligned} &Re\left(\frac{\partial u}{\partial t} + u\frac{\partial u}{\partial r} + \frac{v}{r}\frac{\partial u}{\partial \theta} + w\frac{\partial u}{\partial z} - \frac{v^2}{r}\right) \\ &= -\frac{\partial p}{\partial r} + \frac{1}{r}\frac{\partial}{\partial r}\left(r\frac{\partial u}{\partial r}\right) - \frac{u}{r^2} + \frac{1}{r^2}\frac{\partial^2 u}{\partial \theta^2} - \frac{2}{r^2}\frac{\partial v}{\partial \theta} + \frac{\partial^2 u}{\partial z^2}, \end{aligned} \tag{4.1.12}$$

$$\begin{aligned} &Re\left(\frac{\partial v}{\partial t} + u\frac{\partial v}{\partial r} + \frac{v}{r}\frac{\partial v}{\partial \theta} + w\frac{\partial v}{\partial z} + \frac{uv}{r}\right) \\ &= -\frac{1}{r}\frac{\partial p}{\partial \theta} + \frac{1}{r}\frac{\partial}{\partial r}\left(r\frac{\partial v}{\partial r}\right) - \frac{v}{r^2} + \frac{1}{r^2}\frac{\partial^2 v}{\partial \theta^2} + \frac{2}{r^2}\frac{\partial u}{\partial \theta} + \frac{\partial^2 v}{\partial z^2}, \end{aligned} \tag{4.1.13}$$

$$\begin{aligned} &Re\left(\frac{\partial w}{\partial t} + u\frac{\partial w}{\partial r} + \frac{v}{r}\frac{\partial w}{\partial \theta} + w\frac{\partial w}{\partial z}\right) \\ &= -\frac{\partial p}{\partial z} + \frac{1}{r}\frac{\partial}{\partial r}\left(r\frac{\partial w}{\partial r}\right) + \frac{1}{r^2}\frac{\partial^2 w}{\partial \theta^2} + \frac{\partial^2 w}{\partial z^2} + 1, \end{aligned} \tag{4.1.14}$$

respectively. At the surface of the fibre, $r = 1$, we have the no-slip and impermeability conditions (4.1.2)

$$u = v = w = 0. \tag{4.1.15}$$

The total stress tensor (4.1.4) becomes

$$\mathbf{T} = \begin{bmatrix} 2\dfrac{\partial u}{\partial r} - p & \dfrac{1}{r}\dfrac{\partial u}{\partial \theta} + \dfrac{\partial v}{\partial r} - \dfrac{v}{r} & \dfrac{\partial u}{\partial z} + \dfrac{\partial w}{\partial r} \\ \dfrac{1}{r}\dfrac{\partial u}{\partial \theta} + \dfrac{\partial v}{\partial r} - \dfrac{v}{r} & \dfrac{2}{r}\dfrac{\partial v}{\partial \theta} + \dfrac{2u}{r} - p & \dfrac{\partial v}{\partial z} + \dfrac{1}{r}\dfrac{\partial w}{\partial \theta} \\ \dfrac{\partial u}{\partial z} + \dfrac{\partial w}{\partial r} & \dfrac{\partial v}{\partial z} + \dfrac{1}{r}\dfrac{\partial w}{\partial \theta} & 2\dfrac{\partial w}{\partial z} - p \end{bmatrix}. \tag{4.1.16}$$

At the free surface, $r = S$, we have the tangential stress balance in the azimuthal direction (4.1.3)

$$\left(\frac{\partial S}{\partial \theta}\right)^2 \left(\frac{\partial u}{\partial \theta} - v + S\frac{\partial v}{\partial r}\right) + S^2 \left(v - \frac{\partial u}{\partial \theta} - S\frac{\partial v}{\partial r} + S\frac{\partial S}{\partial z}\frac{\partial v}{\partial z} + \frac{\partial S}{\partial z}\frac{\partial w}{\partial \theta}\right) + S\frac{\partial S}{\partial \theta}\left[2u - 2S\frac{\partial u}{\partial r} + 2\frac{\partial v}{\partial \theta} + S\frac{\partial S}{\partial z}\left(\frac{\partial u}{\partial z} + \frac{\partial w}{\partial r}\right)\right] = 0, \tag{4.1.17}$$

the tangential stress balance in the axial direction (4.1.3)

$$\frac{\partial S}{\partial \theta}\left[\frac{\partial S}{\partial z}\left(\frac{\partial u}{\partial \theta} - v + S\frac{\partial v}{\partial r}\right) + S\frac{\partial v}{\partial z} + \frac{\partial w}{\partial \theta}\right] + S^2\left[\frac{\partial S}{\partial z}\left(2\frac{\partial w}{\partial z} + \frac{\partial S}{\partial z}\left[\frac{\partial u}{\partial z} + \frac{\partial w}{\partial r}\right] - 2\frac{\partial u}{\partial r}\right) - \frac{\partial u}{\partial z} - \frac{\partial w}{\partial r}\right] = 0, \tag{4.1.18}$$

the normal stress balance (4.1.3)

$$(\Gamma\kappa - p)\left[\left(\frac{\partial S}{\partial \theta}\right)^2 + S^2\left(1 + \left(\frac{\partial S}{\partial z}\right)^2\right)\right] + \frac{2}{S}\left(\frac{\partial S}{\partial \theta}\right)^2\left(u + \frac{\partial v}{\partial \theta}\right) - 2S\frac{\partial S}{\partial \theta}\left(\frac{\partial v}{\partial r} - \frac{\partial S}{\partial z}\frac{\partial v}{\partial z}\right) + 2\frac{\partial S}{\partial \theta}\left(v - \frac{\partial u}{\partial \theta} + \frac{\partial S}{\partial z}\frac{\partial w}{\partial \theta}\right) + 2S^2\left[\frac{\partial u}{\partial r} + \frac{\partial S}{\partial z}\left(\frac{\partial S}{\partial z}\frac{\partial w}{\partial z} - \frac{\partial u}{\partial z} - \frac{\partial w}{\partial r}\right)\right] = 0, \tag{4.1.19}$$

where the interfacial curvature (4.1.7) becomes

$$\kappa = \left[\left(\frac{\partial S}{\partial \theta}\right)^2 + S^2\left(1 + \left(\frac{\partial S}{\partial z}\right)^2\right)\right]^{-3/2}\left\{2\left(\frac{\partial S}{\partial \theta}\right)^2 - 2S\frac{\partial S}{\partial z}\frac{\partial S}{\partial \theta}\frac{\partial^2 S}{\partial \theta \partial z} - S\left[\frac{\partial^2 S}{\partial z^2}\left(S^2 + \left(\frac{\partial S}{\partial \theta}\right)^2\right) + \left(\frac{\partial^2 S}{\partial \theta^2} - S\right)\left(1 + \left(\frac{\partial S}{\partial z}\right)^2\right)\right]\right\}, \tag{4.1.20}$$

and the kinematic condition (4.1.8)

$$S\frac{\partial S}{\partial t} + v\frac{\partial S}{\partial \theta} + wS\frac{\partial S}{\partial z} - u = S\frac{\partial S}{\partial t} + \frac{\partial f}{\partial \theta} + \frac{\partial q}{\partial z} = 0, \tag{4.1.21}$$

where

$$f(\theta, z, t) = \int_1^S v \, \mathrm{d}r \tag{4.1.22}$$

is the dimensionless azimuthal volume flux and

$$q(\theta, z, t) = \int_1^S rw \, \mathrm{d}r \tag{4.1.23}$$

is the dimensionless axial volume flux.

4.2 Thick-film WRIBL equations

In this section we exploit the fact that a characteristic wavelength in the azimuthal and axial directions is large compared to both a characteristic film thickness and the fibre radius. In this novel application of a long-wave approximation to equations (4.1.11)–(4.1.23) we derive long-wave boundary-layer equations for the azimuthal velocity v and the axial velocity w. We then solve these boundary-layer equations using the WRIBL method (see Section 1.2.1.4) in order to derive a reduced-order model in the thick-film regime, which we refer to as the *thick-film WRIBL equations*.

4.2.1 Long-wave boundary-layer equations

We examine the thick-film regime in which the long-wave small aspect ratio is $\delta = 1/\lambda \ll 1$ (and $\bar{H} = \mathcal{O}(1)$, as discussed in Section 1.3.2.2). In particular, we use the long-wave scalings

$$\begin{gathered}\frac{\partial}{\partial \theta} = \delta\frac{\partial}{\partial \widetilde{\theta}}, \quad r = \widetilde{r}, \quad z = \frac{\widetilde{z}}{\delta}, \quad S = \widetilde{S}, \quad H = \widetilde{H}, \quad u = \delta\widetilde{u}, \quad v = \delta\widetilde{v}, \\ w = \widetilde{w}, \quad p = \widetilde{p}, \quad t = \frac{\widetilde{t}}{\delta}, \quad \kappa = \widetilde{\kappa}, \quad f = \delta\widetilde{f}, \quad q = \widetilde{q}.\end{gathered} \tag{4.2.1}$$

The scalings of both the variation of $\widetilde{\theta}$ and $\widetilde{z}$ follow from the assumption that variations are slow in both the azimuthal and axial directions compared to variations in the radial direction. Note that we have chosen to scale the variation of θ and not θ itself, following Wray et al. [55] and Wray and Cimpeanu [60], since the azimuthal domain length is fixed at 2π, and thus cannot be assumed to be "long" (as discussed in Section 1.3.2.3). We also note that while it is more plausible that variations in the azimuthal direction would be over a length scale comparable to variations in the radial direction, we proceed nevertheless with the current assumption as it builds directly on the work of Wray et al. [55; 62]. The scaling of $\widetilde{u}$ is chosen in order to balance the radial and axial components of velocity at leading order in the continuity equation (4.1.11). The scaling of $\widetilde{v}$ (and thus $\widetilde{f}$ via (4.1.22)) is chosen in order to balance the axial velocity and pressure at leading order in equation (4.1.13), which avoids a trivial solution for the azimuthal velocity at leading order. The scaling of $\widetilde{t}$ is chosen in order to retain the time derivative at leading order in the kinematic condition (4.1.21).

In order to derive the thick-film WRIBL equations correct to first order in δ, we require equations (4.1.11) and (4.1.14) correct to first order, namely

$$\frac{1}{\widetilde{r}}\frac{\partial(\widetilde{r}\widetilde{u})}{\partial\widetilde{r}} + \delta\frac{1}{\widetilde{r}}\frac{\partial\widetilde{v}}{\partial\widetilde{\theta}} + \frac{\partial\widetilde{w}}{\partial\widetilde{z}} = 0, \tag{4.2.2}$$

$$\delta Re\left(\frac{\partial\widetilde{w}}{\partial\widetilde{t}} + \widetilde{u}\frac{\partial\widetilde{w}}{\partial\widetilde{r}} + \widetilde{w}\frac{\partial\widetilde{w}}{\partial\widetilde{z}}\right) = -\delta\frac{\partial\widetilde{p}}{\partial\widetilde{z}} + \frac{1}{\widetilde{r}}\frac{\partial}{\partial\widetilde{r}}\left(\widetilde{r}\frac{\partial\widetilde{w}}{\partial\widetilde{r}}\right) + 1 + \mathcal{O}(\delta^2), \tag{4.2.3}$$

and equations (4.1.12) and (4.1.13) to leading order, namely

$$-\frac{\partial\widetilde{p}}{\partial\widetilde{r}} + \mathcal{O}(\delta) = 0, \tag{4.2.4}$$

$$-\frac{1}{\widetilde{r}}\frac{\partial\widetilde{p}}{\partial\widetilde{\theta}} + \frac{\partial}{\partial\widetilde{r}}\left(\frac{1}{\widetilde{r}}\frac{\partial(\widetilde{r}\widetilde{v})}{\partial\widetilde{r}}\right) + \mathcal{O}(\delta) = 0. \tag{4.2.5}$$

In Section 4.2.2 we show that $\widetilde{v}$ is only required to leading order, while $\widetilde{w}$ is required to first order.

At the surface of the fibre, $\widetilde{r} = 1$, the no-slip and impermeability conditions (4.1.15) are

$$\widetilde{u} = \widetilde{v} = \widetilde{w} = 0. \tag{4.2.6}$$

At the free surface, $\widetilde{r} = \widetilde{S}$, the tangential stress balance in the axial direction

(4.1.18) is required correct to first order

$$\frac{\partial \widetilde{w}}{\partial \widetilde{r}} + \mathcal{O}(\delta^2) = 0, \tag{4.2.7}$$

and the tangential stress balance in the azimuthal direction (4.1.17) and the normal stress balance (4.1.19) are required correct to leading order, namely

$$\widetilde{v} - \widetilde{S}\frac{\partial \widetilde{v}}{\partial \widetilde{r}} + \mathcal{O}(\delta) = 0, \tag{4.2.8}$$

$$\widetilde{p} = \Gamma\widetilde{\kappa} + \mathcal{O}(\delta) = 0, \tag{4.2.9}$$

respectively, where the interfacial curvature (4.1.20) is now

$$\begin{aligned}\widetilde{\kappa} = \left[\delta^2\left(\frac{\partial \widetilde{S}}{\partial \widetilde{\theta}}\right)^2 + \widetilde{S}^2\left(1 + \delta^2\left(\frac{\partial \widetilde{S}}{\partial \widetilde{z}}\right)^2\right)\right]^{-3/2} \Bigg\{2\delta^2\left(\frac{\partial \widetilde{S}}{\partial \widetilde{\theta}}\right)^2 - 2\delta^4\widetilde{S}\frac{\partial \widetilde{S}}{\partial \widetilde{z}}\frac{\partial \widetilde{S}}{\partial \widetilde{\theta}}\frac{\partial^2 \widetilde{S}}{\partial \widetilde{\theta}\partial \widetilde{z}} \\ - \widetilde{S}\left[\delta^2\frac{\partial^2 \widetilde{S}}{\partial \widetilde{z}^2}\left(\widetilde{S}^2 + \delta^2\left(\frac{\partial \widetilde{S}}{\partial \widetilde{\theta}}\right)^2\right) + \left(\delta^2\frac{\partial^2 \widetilde{S}}{\partial \widetilde{\theta}^2} - \widetilde{S}\right)\left(1 + \delta^2\left(\frac{\partial \widetilde{S}}{\partial \widetilde{z}}\right)^2\right)\right]\Bigg\},\end{aligned} \tag{4.2.10}$$

while the kinematic condition (4.1.21) becomes

$$\widetilde{S}\frac{\partial \widetilde{S}}{\partial \widetilde{t}} + \delta\frac{\partial \widetilde{f}}{\partial \widetilde{\theta}} + \frac{\partial \widetilde{q}}{\partial \widetilde{z}} = 0. \tag{4.2.11}$$

As discussed in Section 1.3.2.2, we retain the full form of the interfacial curvature $\widetilde{\kappa}$ (4.2.10) here.

The pressure $\widetilde{p}$ appears at first order in equation (4.2.3) and at leading order in equation (4.2.5), therefore we need only determine the leading-order pressure $\widetilde{p}$. The leading-order pressure $\widetilde{p}$ may be determined by solving the leading-order radial component of the Navier–Stokes equation (4.2.4) subject to the leading-order normal stress balance (4.2.9) to yield

$$\widetilde{p}(\widetilde{\theta}, \widetilde{z}, \widetilde{t}) = \Gamma\widetilde{\kappa}. \tag{4.2.12}$$

Substituting the leading-order solution for $\widetilde{p}$ (4.2.12) into the leading-order azimuthal component of the Navier–Stokes equation (4.2.5) and the first-order axial component of the Navier–Stokes equation (4.2.3) yields the leading-order boundary-

layer equation for the azimuthal velocity

$$\widetilde{\mathcal{B}}_\theta(\widetilde{v}) \equiv \frac{\Gamma}{\widetilde{r}}\frac{\partial\widetilde{\kappa}}{\partial\widetilde{\theta}} - \frac{\partial}{\partial\widetilde{r}}\left(\frac{1}{\widetilde{r}}\frac{\partial(\widetilde{r}\widetilde{v})}{\partial\widetilde{r}}\right) = 0, \tag{4.2.13}$$

and the first-order boundary-layer equation for the axial velocity

$$\widetilde{\mathcal{B}}_z(\widetilde{w}) \equiv -\frac{1}{\widetilde{r}}\frac{\partial}{\partial\widetilde{r}}\left(\widetilde{r}\frac{\partial\widetilde{w}}{\partial\widetilde{r}}\right) - 1 + \delta Re\left(\frac{\partial\widetilde{w}}{\partial\widetilde{t}} + \widetilde{u}\frac{\partial\widetilde{w}}{\partial\widetilde{r}} + \widetilde{w}\frac{\partial\widetilde{w}}{\partial\widetilde{z}}\right) + \delta\Gamma\frac{\partial\widetilde{\kappa}}{\partial\widetilde{z}} = 0, \tag{4.2.14}$$

respectively. Note that the radial velocity $\widetilde{u}$ only appears at first order in the boundary-layer equation for the axial velocity (4.2.14), and so we can use the continuity equation (4.2.2) to express $\widetilde{u}$ in terms of $\widetilde{w}$ at leading order.

4.2.2 Velocity expansion and computation of the weighted residuals

To use the WRIBL method, we first need to determine the leading-order solutions of the azimuthal velocity $\widetilde{v}$ and the axial velocity $\widetilde{w}$. The leading-order azimuthal velocity $\widetilde{v}$ can be determined by solving the leading-order boundary-layer equation for the azimuthal velocity (4.2.13) subject to the no-slip condition (4.2.6) and the leading-order tangential stress balance in the azimuthal direction (4.2.8) to yield

$$\widetilde{v} = \frac{\Gamma}{4\widetilde{r}}\frac{\partial\widetilde{\kappa}}{\partial\widetilde{\theta}}\left[2\widetilde{r}^2\log\widetilde{r} + \widetilde{S}^2\left(1-\widetilde{r}^2\right)\right], \tag{4.2.15}$$

and hence, from (4.1.22), the leading-order azimuthal flux is

$$\widetilde{f} = \frac{\Gamma}{8}\frac{\partial\widetilde{\kappa}}{\partial\widetilde{\theta}}\left(1 - \widetilde{S}^4 + 4\widetilde{S}^2\log\widetilde{S}\right). \tag{4.2.16}$$

Similarly, the leading-order axial velocity $\widetilde{w}$ can be determined by solving the boundary-layer equation for the axial velocity (4.2.14) at leading order, subject to the no-slip condition (4.2.6) and the tangential stress balance in the axial direction (4.2.7) at leading order to yield

$$\widetilde{w} = \frac{1-\widetilde{r}^2+2\widetilde{S}^2\log\widetilde{r}}{4}, \tag{4.2.17}$$

and hence, from (4.1.23), the leading-order azimuthal flux is

$$\widetilde{q} = \frac{-1 + 4\widetilde{S}^2 - 3\widetilde{S}^4 + 4\widetilde{S}^4 \log \widetilde{S}}{16}. \tag{4.2.18}$$

We are now able to seek an expansion of the form (1.2.9) for both $\widetilde{v}$ and $\widetilde{w}$. However, $\widetilde{v}$ only appears at first order (via $\widetilde{f}$) in the kinematic condition (4.2.11), whereas $\widetilde{w}$ (via $\widetilde{q}$) appears at leading order. Therefore, to obtain the thick-film WRIBL equations, the azimuthal velocity $\widetilde{v}$ (and azimuthal flux $\widetilde{f}$) are only required at leading order. In particular, with $\widetilde{f}$ given by (4.2.16) at leading order, the kinematic condition (4.2.11) becomes

$$\widetilde{S}\frac{\partial \widetilde{S}}{\partial \widetilde{t}} + \delta \frac{\Gamma}{8} \frac{\partial}{\partial \widetilde{\theta}} \left[\frac{\partial \widetilde{\kappa}}{\partial \widetilde{\theta}} \left(1 - \widetilde{S}^4 + 4\widetilde{S}^2 \log \widetilde{S} \right) \right] + \frac{\partial \widetilde{q}}{\partial \widetilde{z}} = 0. \tag{4.2.19}$$

We seek a solution of the first-order boundary-layer equation for the axial velocity (4.2.14) in the form

$$\widetilde{w} = \widetilde{a}_0(\widetilde{\theta}, \widetilde{z}, \widetilde{t})\widetilde{g}_0(\widetilde{r}; \widetilde{S}) + \delta \sum_{i=1}^{N} \widetilde{a}_i(\widetilde{\theta}, \widetilde{z}, \widetilde{t})\widetilde{g}_i(\widetilde{r}; \widetilde{S}) + \mathcal{O}(\delta^2), \tag{4.2.20}$$

where

$$\widetilde{g}_0(\widetilde{r}; \widetilde{S}) = \frac{1 - \widetilde{r}^2 + 2\widetilde{S}^2 \log \widetilde{r}}{4} \tag{4.2.21}$$

is the leading-order axial velocity $\widetilde{w}$ (4.2.17) with coefficient $\widetilde{a}_0(\widetilde{\theta}, \widetilde{z}, \widetilde{t})$, and $\widetilde{g}_i(\widetilde{r}; \widetilde{S})$ is a set of suitably-chosen basis functions with coefficients $\widetilde{a}_i(\widetilde{\theta}, \widetilde{z}, \widetilde{t})$ for $i = 1, \ldots, N$, where $N + 1$ is the number of coefficients. We use weight functions $\widetilde{W}_j(\widetilde{r}, \widetilde{\theta}, \widetilde{z}, \widetilde{t})$ for $j = 0, \ldots, M$, and define the residuals $\widetilde{\mathscr{R}}_j$ as

$$\widetilde{\mathscr{R}}_j(\widetilde{\theta}, \widetilde{z}, \widetilde{t}) = \left\langle \widetilde{W}_j, \widetilde{\mathcal{B}}_z \left(\widetilde{a}_0\widetilde{g}_0 + \delta \sum_{i=1}^{N} \widetilde{a}_i\widetilde{g}_i \right) \right\rangle \tag{4.2.22}$$

for $j = 0, 1, \ldots, M$, and where

$$\langle \alpha, \beta \rangle = \int_1^{\widetilde{S}} \widetilde{r}\alpha\beta \, \mathrm{d}\widetilde{r} \tag{4.2.23}$$

is the inner product in the present coordinate system. In general, Ruyer-Quil and Manneville [52] show that the number of weights required, $M + 1$, is the same

as the number of basis functions, $N+1$ (i.e. $M=N$). We set the residuals $\widetilde{\mathscr{R}}_j$ (4.2.22), for $j=0,1,\ldots,N$, equal to zero to obtain a system of $N+1$ equations to be solved for the coefficients $\widetilde{a}_i$ for $i=0,1,\ldots,N$. When computing the residuals (4.2.22), we notice that the coefficients $\widetilde{a}_i(\widetilde{\theta},\widetilde{z},\widetilde{t})$ for $i=1,\ldots,N$ only enter the first-order boundary-layer equation for the axial velocity (4.2.14) via the leading-order viscous terms (i.e. the second to last term of (4.2.14)). Evaluating the residual of the viscous term explicitly yields

$$\begin{aligned}&\int_1^{\widetilde{S}} \widetilde{r}\widetilde{W}_j\left[\frac{1}{\widetilde{r}}\frac{\partial}{\partial\widetilde{r}}\left(\widetilde{r}\frac{\partial}{\partial\widetilde{r}}(\widetilde{a}_i\widetilde{g}_i)\right)\right]\,\mathrm{d}\widetilde{r} \qquad (4.2.24)\\ &=-\left(\widetilde{W}_j\frac{\partial}{\partial\widetilde{r}}(\widetilde{a}_i\widetilde{g}_i)\right)\Big|_{\widetilde{r}=1}-\widetilde{S}\left(\widetilde{a}_i\widetilde{g}_i\frac{\partial\widetilde{W}_j}{\partial\widetilde{r}}\right)\Big|_{\widetilde{r}=\widetilde{S}}+\int_1^{\widetilde{S}}\widetilde{r}\widetilde{a}_i\widetilde{g}_i\left[\frac{1}{\widetilde{r}}\frac{\partial}{\partial\widetilde{r}}\left(\widetilde{r}\frac{\partial\widetilde{W}_j}{\partial\widetilde{r}}\right)\right]\,\mathrm{d}\widetilde{r},\end{aligned}$$

for $i=0,1,\ldots,N$ and $j=0,1,\ldots,N$, where we have used integration by parts, and applied the no-slip condition (4.2.6) and the leading-order tangential stress balance in the axial direction (4.2.7). The evaluation of terms on the right-hand side of (4.2.24) can be made independent of terms involving $\widetilde{a}_i$, for $i=1,\ldots,N$ by a suitable choice of $\widetilde{W}_j$ for $j=0,1,\ldots,N$. However, as we are about to show, only one weight function $\widetilde{W}_0$ (i.e. $M=N=0$) is required if we choose this weight function such that

$$\widetilde{W}_0\Big|_{\widetilde{r}=1}=0,\quad \frac{\partial\widetilde{W}_0}{\partial\widetilde{r}}\Big|_{\widetilde{r}=\widetilde{S}}=0,\quad \frac{1}{\widetilde{r}}\frac{\partial}{\partial\widetilde{r}}\left(\widetilde{r}\frac{\partial\widetilde{W}_0}{\partial\widetilde{r}}\right)=A, \qquad (4.2.25)$$

where A is a (non-zero) constant. The first two conditions on $\widetilde{W}_0$ in (4.2.25) allow us to eliminate the first two terms on the right-hand side of (4.2.24), while the final condition on $\widetilde{W}_0$ in (4.2.25) allows the remaining integral on the right-hand side of (4.2.24) to be written as

$$\widetilde{a}_0\int_1^{\widetilde{S}}\widetilde{r}\widetilde{g}_0\,\mathrm{d}\widetilde{r}+\delta\sum_{i=1}^{N}\widetilde{a}_i\int_1^{\widetilde{S}}\widetilde{r}\widetilde{g}_i\,\mathrm{d}\widetilde{r}=\int_1^{\widetilde{S}}\widetilde{r}\widetilde{w}\,\mathrm{d}\widetilde{r}=\widetilde{q}, \qquad (4.2.26)$$

using the definition of the axial flux (4.1.23). By making this particular choice of $\widetilde{W}_0$, which satisfies the conditions (4.2.25), only one basis function, namely $\widetilde{g}_0$, is required (and thus only one residual $\widetilde{\mathscr{R}}_0=\langle\widetilde{W}_0,\widetilde{\mathcal{B}}_z(\widetilde{a}_0\widetilde{g}_0)\rangle=0$ must be evaluated) to obtain the thick-film WRIBL equations. In particular, when $A=-1$ in equation

(4.2.25), the weight function $\widetilde{W}_0$ is

$$\widetilde{W}_0 = \widetilde{g}_0 = \frac{1 - \widetilde{r}^2 + 2\widetilde{S}^2 \log \widetilde{r}}{4}, \tag{4.2.27}$$

where $\widetilde{g}_0$ is defined in (4.2.21). Before we compute the residual $\widetilde{\mathscr{R}}_0 = \langle \widetilde{W}_0, \widetilde{\mathcal{B}}_z(\widetilde{a}_0 \widetilde{g}_0) \rangle = 0$, we first eliminate $\widetilde{a}_0$ in favour of $\widetilde{q}$ by rearranging (4.2.26) for $\widetilde{a}_0$ to obtain

$$\widetilde{a}_0 = \frac{1}{\widetilde{q}_0} \left(\widetilde{q} - \delta \sum_{i=1}^{N} \widetilde{a}_i \int_1^{\widetilde{S}} \widetilde{r} \widetilde{g}_i \, \mathrm{d}\widetilde{r} \right), \tag{4.2.28}$$

where

$$\widetilde{q}_0 = \int_1^{\widetilde{S}} \widetilde{r} \widetilde{g}_0 \, \mathrm{d}\widetilde{r}. \tag{4.2.29}$$

Our choice of $\widetilde{W}_0$ (4.2.27) removes the need to determine $\widetilde{a}_i$ for $i = 1, \ldots, N$. Therefore, substituting (4.2.28) into the expansion (4.2.20) yields

$$\widetilde{w} = \frac{\widetilde{q}}{\widetilde{q}_0} \widetilde{g}_0 + \mathcal{O}(\delta) = \frac{\widetilde{q}}{\widetilde{q}_0} \frac{1 - \widetilde{r}^2}{4} + \frac{\widetilde{q}\widetilde{S}^2}{\widetilde{q}_0} \frac{\log \widetilde{r}}{2} + \mathcal{O}(\delta). \tag{4.2.30}$$

Computing the residual

$$\widetilde{\mathscr{R}}_0 = \left\langle \widetilde{W}_0, \widetilde{\mathcal{B}}_z \left(\frac{\widetilde{q}}{\widetilde{q}_0} \frac{1 - \widetilde{r}^2}{4} + \frac{\widetilde{q}\widetilde{S}^2}{\widetilde{q}_0} \frac{\log \widetilde{r}}{2} \right) \right\rangle = 0 \tag{4.2.31}$$

yields

$$\begin{aligned} &\widetilde{q} + \left(\delta \Gamma \frac{\partial \widetilde{\kappa}}{\partial \widetilde{z}} - 1 \right) \widetilde{q}_0 \\ &+ \delta Re \left[\frac{\partial}{\partial \widetilde{t}} \left(\frac{\widetilde{q}}{\widetilde{q}_0} \right) \widetilde{q}_1 + \frac{\partial}{\partial \widetilde{t}} \left(\frac{\widetilde{q}\widetilde{S}^2}{\widetilde{q}_0} \right) \widetilde{q}_2 + \left(\frac{\widetilde{q}}{\widetilde{q}_0} \right) \frac{\partial}{\partial \widetilde{z}} \left(\frac{\widetilde{q}\widetilde{S}^2}{\widetilde{q}_0} \right) \widetilde{q}_3 \right. \\ &\left. + \left(\frac{\widetilde{q}\widetilde{S}^2}{\widetilde{q}_0} \right) \frac{\partial}{\partial \widetilde{z}} \left(\frac{\widetilde{q}\widetilde{S}^2}{\widetilde{q}_0} \right) \widetilde{q}_4 + \left(\frac{\widetilde{q}}{\widetilde{q}_0} \right) \frac{\partial}{\partial \widetilde{z}} \left(\frac{\widetilde{q}}{\widetilde{q}_0} \right) \widetilde{q}_5 + \left(\frac{\widetilde{q}\widetilde{S}^2}{\widetilde{q}_0} \right) \frac{\partial}{\partial \widetilde{z}} \left(\frac{\widetilde{q}}{\widetilde{q}_0} \right) \widetilde{q}_6 \right] = 0, \end{aligned} \tag{4.2.32}$$

where

$$\widetilde{q}_k = \int_1^{\widetilde{S}} \widetilde{r} \widetilde{W}_0(\widetilde{r}; \widetilde{S}) \widetilde{c}_k(\widetilde{r}) \, \mathrm{d}\widetilde{r}, \quad k = 0, 1, \ldots, 6 \tag{4.2.33}$$

in which

$$\widetilde{c}_0(\widetilde{r}) = 1, \tag{4.2.34}$$

$$\widetilde{c}_1(\widetilde{r}) = \frac{1-\widetilde{r}^2}{4}, \tag{4.2.35}$$

$$\widetilde{c}_2(\widetilde{r}) = \frac{\log\widetilde{r}}{2}, \tag{4.2.36}$$

$$\widetilde{c}_3(\widetilde{r}) = \frac{1-\widetilde{r}^2+2\log\widetilde{r}}{16}, \tag{4.2.37}$$

$$\widetilde{c}_4(\widetilde{r}) = \left(\frac{\log\widetilde{r}}{2}\right)^2 - \frac{1-\widetilde{r}^2+2\widetilde{r}^2\log\widetilde{r}}{16\widetilde{r}^2}, \tag{4.2.38}$$

$$\widetilde{c}_5(\widetilde{r}) = \frac{\left(1-\widetilde{r}^2\right)^2}{32}, \tag{4.2.39}$$

$$\widetilde{c}_6(\widetilde{r}) = \frac{\left(1-\widetilde{r}^2\right)^2}{32\widetilde{r}^2} + \frac{\left(1-\widetilde{r}^2\right)\log\widetilde{r}}{8}. \tag{4.2.40}$$

Equations (4.2.19) and (4.2.32) are the thick-film WRIBL equation, and they constitute a closed system of two coupled evolution equations for $\widetilde{S}$ and $\widetilde{q}$. The thick-film WRIBL equations (4.2.19) and (4.2.32) incorporate the effects of gravity, viscosity, inertia, and surface tension, allow for variations in the film in both the axial and azimuthal directions, and are appropriate for a film thickness of order unity (see Section 1.3.2.3).

The thick-film WRIBL equations (4.2.19) and (4.2.32) are a generalisation of the first-order model of Ruyer-Quil et al. [64] given by their equations (2.2) and (4.10), but not their simplified second-order model, which is the main focus of that work [64] (see Sections 1.2.1.4 and 1.6.1.2). Specifically, by approximating the full form of $\widetilde{\kappa}$ (4.1.20), and neglecting variations in the azimuthal direction, we recover equations (2.2) and (4.10) of Ruyer-Quil et al. [64] up to differences in scaling.

4.3 Gradient expansion equations

We now consider reductions of the thick-film WRIBL equations (4.2.19) and (4.2.32).

By performing a gradient expansion on the azimuthal flux $\widetilde{f}$ and axial flux $\widetilde{q}$ (see Section 1.2.1.4), we reduce the thick-film WRIBL equations (4.2.19) and (4.2.32) to a single evolution equation for $\widetilde{S}$ only. We refer to this reduction of the thick-film WRIBL equations (4.2.19) and (4.2.32) as the *thick-film gradient-*

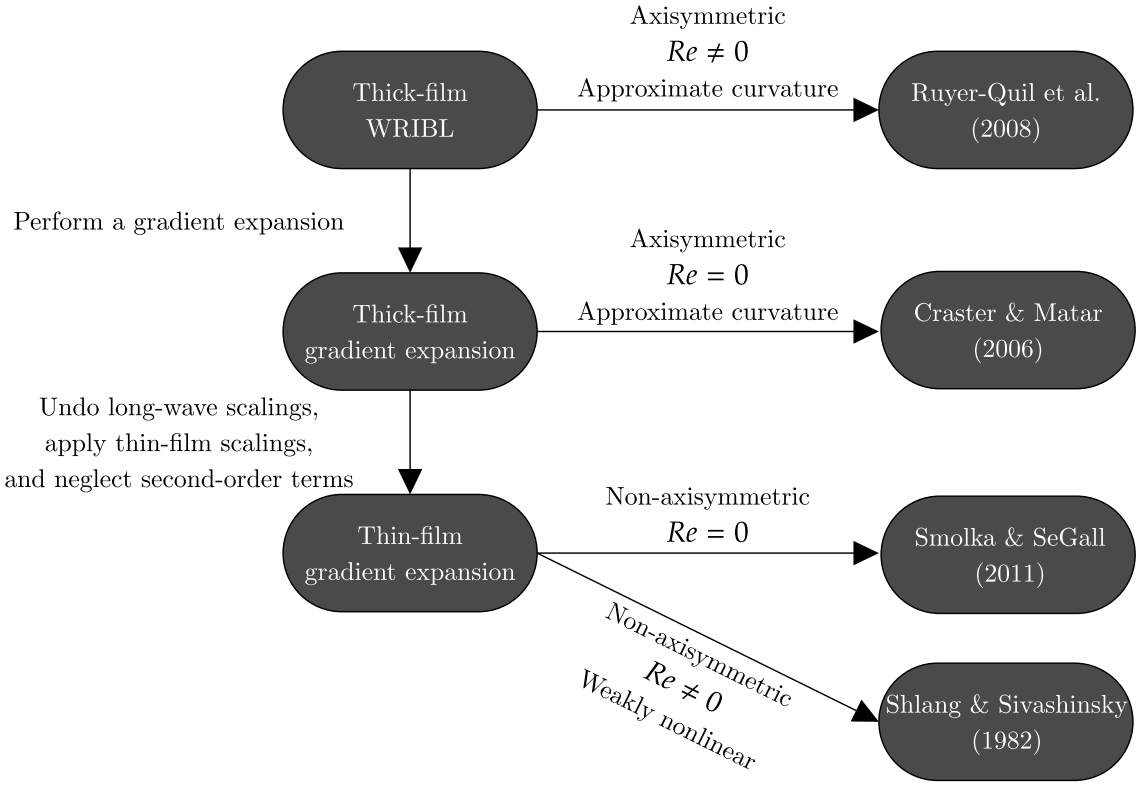

Figure 4.2: Sketch of the relationship between the thick-film WRIBL equations (4.2.19) and (4.2.32) and their reductions, and the models of Ruyer-Quil et al. [64], Craster and Matar [110], Smolka and SeGall [217], and Shlang and Sivashinsky [54].

expansion equation (see Section 4.3.1). We further reduce the thick-film WRIBL equations (4.2.19) and (4.2.32) by undoing the long-wave scalings (4.2.1) in the thick-film gradient-expansion equation, applying thin-film scalings, and neglecting terms of second-order in the thin-film small aspect ratio. We refer to this reduction of the thick-film WRIBL equations (4.2.19) and (4.2.32) and the thick-film gradient-expansion equation as the *thin-film gradient-expansion equation* (see Section 4.3.2). Both the thick-film gradient-expansion equation and the thin-film gradient-expansion equation are generalisations of existing equations [110; 217], however we defer this discussion to Sections 4.3.1 and 4.3.2, respectively.

The relationship between the thick-film WRIBL equations (4.2.19) and (4.2.32) and the reductions discussed above, and the models of Ruyer-Quil et al. [64], Craster and Matar [110], Smolka and SeGall [217], and Shlang and Sivashinsky [54] is summarised in Figure 4.2. The details of the relationships shown in Figure

4.2 will be given in Sections 4.3.1 and 4.3.2.

4.3.1 Thick-film gradient-expansion equation

We now reduce the thick-film WRIBL equations (4.2.19) and (4.2.32) by performing a gradient expansion on the azimuthal flux $\widetilde{f}$ and the axial flux $\widetilde{q}$ to obtain the thick-film gradient-expansion equation.

To perform a gradient expansion, we expand the azimuthal flux $\widetilde{f}$ and the axial flux $\widetilde{q}$ in powers of δ, namely

$$\widetilde{f}(\widetilde{\theta},\widetilde{z},\widetilde{t}) = \widetilde{F}_0(\widetilde{\theta},\widetilde{z},\widetilde{t})+\mathcal{O}(\delta), \quad \widetilde{q}(\widetilde{\theta},\widetilde{z},\widetilde{t}) = \widetilde{Q}_0(\widetilde{\theta},\widetilde{z},\widetilde{t})+\delta\widetilde{Q}_1(\widetilde{\theta},\widetilde{z},\widetilde{t})+\mathcal{O}(\delta^2). \quad (4.3.1)$$

Note that the azimuthal flux only appears in the kinematic condition (4.2.11) at leading order, hence only the leading-order term in the expansion for $\widetilde{f}$ (4.3.1) is required. Following the literature on weighted residuals [52; 60], $\widetilde{S}$ is not explicitly expanded in order to keep the evolution equations concise. Nonetheless, $\widetilde{S}$ remains accurate to first order in δ. The expansions (4.3.1) for $\widetilde{f}$ and $\widetilde{q}$ can be truncated at leading and first order, respectively, substituted into equations (4.2.19) and (4.2.32), and solved order-by-order in δ to yield

$$\widetilde{F}_0 = \frac{\Gamma}{8}\frac{\partial\widetilde{\kappa}}{\partial\widetilde{\theta}}\left(1-\widetilde{S}^4+4\widetilde{S}^2\log\widetilde{S}\right) \quad (4.3.2)$$

and

$$\widetilde{Q}_0 = \widetilde{q}_0, \quad \widetilde{Q}_1 = -\Gamma\widetilde{q}_0\frac{\partial\widetilde{\kappa}}{\partial\widetilde{z}} - 2Re\widetilde{S}\left[\widetilde{q}_2\frac{\partial\widetilde{S}}{\partial\widetilde{t}}+\left(\widetilde{q}_3+\widetilde{q}_4\widetilde{S}^2\right)\frac{\partial\widetilde{S}}{\partial\widetilde{z}}\right], \quad (4.3.3)$$

respectively. Substituting the solutions (4.3.2) and (4.3.3) into the kinematic condition (4.2.11) yields

$$\frac{\partial\widetilde{S}}{\partial\widetilde{t}}+\frac{\partial\widetilde{q}_0}{\partial\widetilde{z}} = 0 \quad (4.3.4)$$

at leading order. We use (4.3.4) to remove the time derivative from the expression for $\widetilde{Q}_1$ (4.3.3) in favour of the spatial derivative, which links the velocity (via $\widetilde{q}$) to the free surface. The solutions (4.3.2) and (4.3.3) are substituted into the

kinematic condition (4.2.19) to yield

$$\widetilde{S}\frac{\partial\widetilde{S}}{\partial\widetilde{t}}+\delta\frac{\Gamma}{8}\frac{\partial}{\partial\widetilde{\theta}}\left[\frac{\partial\widetilde{\kappa}}{\partial\widetilde{\theta}}\left(1-\widetilde{S}^4+4\widetilde{S}^2\log\widetilde{S}\right)\right] + \frac{\partial}{\partial\widetilde{z}}\left[\left(1-\delta\Gamma\frac{\partial\widetilde{\kappa}}{\partial\widetilde{z}}\right)\widetilde{q}_0\right]+2\delta Re\frac{\partial}{\partial\widetilde{z}}\left[\widetilde{S}\left(\widetilde{q}_3+\widetilde{q}_4\widetilde{S}^2\right)\frac{\partial\widetilde{S}}{\partial\widetilde{z}}-\widetilde{q}_2\frac{\partial\widetilde{q}_0}{\partial\widetilde{z}}\right]=0 \tag{4.3.5}$$

to first order.

By approximating the full form of $\widetilde{\kappa}$ (4.2.10), neglecting azimuthal variations, and neglecting the effects of inertia, we recover equation (2.17) of Craster and Matar [110] (i.e. equation (1.6.8)) from the thick-film gradient-expansion equation (4.3.5), up to differences in scalings.

4.3.2 Thin-film gradient-expansion equation

We now reduce the thick-film gradient-expansion equation (4.3.5) by undoing the long-wave scalings (4.2.1), applying thin-film scalings in which the thin-film small aspect ratio is $\varepsilon=\bar{H}\ll 1$ (and $\lambda=\mathcal{O}(1)$, as discussed in Section 1.3.2.1), and neglecting terms of second-order in ε. In particular, we use the thin-film scalings

$$S=1+\varepsilon\breve{H},\quad t=\frac{\breve{t}}{\varepsilon^2},\quad z=\breve{z},\quad \theta=\breve{\theta}. \tag{4.3.6}$$

The scaling of $\breve{t}$ is chosen in order to retain the time derivative in the thin-film gradient-expansion equation. We apply the thin-film scalings (4.3.6) to the unscaled thick-film gradient-expansion equation (4.3.5), and neglect terms of second-order in ε to yield

$$\left(1+\varepsilon\breve{H}\right)\frac{\partial\breve{H}}{\partial\breve{t}}+\frac{1}{3}\frac{\partial}{\partial\breve{z}}\left(\breve{H}^3+\varepsilon\breve{H}^4\right) + \varepsilon\frac{2\breve{Re}}{15}\frac{\partial}{\partial\breve{z}}\left(\breve{H}^6\frac{\partial\breve{H}}{\partial\breve{z}}\right)+\varepsilon\frac{\Gamma}{3}\nabla\cdot\left[\breve{H}^3\nabla\left(\breve{H}+\nabla^2\breve{H}\right)\right]=0 \tag{4.3.7}$$

to first order in ε, where we have rescaled $Re=\breve{Re}/\varepsilon^3$ in order to retain the destabilising effect of inertia (as discussed in Section 1.6.2).

By neglecting the effect of inertia, we recover equation (7) of Smolka and

SeGall [217] from the thin-film gradient-expansion equation (4.3.7). Finally, the thin-film gradient expansion-equation (4.3.7) is a fully-nonlinear generalisation of the weakly-nonlinear equation (3.5) of Shlang and Sivashinsky [54] (i.e. equation (1.6.9)), up to differences in scalings.

4.4 Conclusions

In this chapter, we derived the thick-film WRIBL equations (4.2.19) and (4.2.32) for non-axisymmetric flow on the exterior of a vertical fibre.

In Section 4.1 we introduced the system shown schematically in Figure 4.1, and obtained and nondimensionalised the governing equations and boundary conditions for this system.

In Section 4.2.1 we applied a set of long-wave scalings (4.2.1) to the governing equations to obtain a leading-order boundary-layer equation for the azimuthal velocity (4.2.13) and a first-order boundary-layer equation for the axial velocity (4.2.14). In Section 4.2.2 we obtained the leading-order solution of the azimuthal velocity $\widetilde{v}$ (4.2.15) and axial velocity $\widetilde{w}$ (4.2.17) (and the leading-order solution of the azimuthal flux $\widetilde{f}$ (4.2.16) and axial flux $\widetilde{q}$ (4.2.18)). The leading-order solution of $\widetilde{f}$ (4.2.16) is all that is needed to derive the thick-film WRIBL equations (4.2.19) and (4.2.32), however, in order to obtain a solution of the first-order boundary-layer equation for the axial velocity (4.2.14) we expanded the axial velocity $\widetilde{w}$ as (4.2.20). We determined the conditions (4.2.25), and then chose an appropriate weight function $\widetilde{W}_0$ (4.2.27). Finally, we computed the residual $\widetilde{\mathscr{R}}_0$ (4.2.31) to obtain (4.2.32) which, coupled with (4.2.19), constitutes the thick-film WRIBL equations.

In Section 4.3.1 we performed a gradient expansion on the azimuthal flux $\widetilde{f}$ and axial flux $\widetilde{q}$ to reduce the thick-film WRIBL equations (4.2.19) and (4.2.32) to a single evolution equation for $\widetilde{S}$ only, namely the thick-film gradient-expansion equation (4.3.5).

In Section 4.3.2 we further reduced the thick-film WRIBL equations (4.2.19) and (4.2.32) by applying a set of thin-film scalings (4.3.6) to the unscaled thick-film gradient-expansion equation (4.3.5). We then neglected terms of second-order in ε to obtain the thin-film gradient-expansion equation (4.3.7).

As summarised in Figure 4.2: the thick-film WRIBL equations (4.2.19) and (4.2.32) are a generalisation of equations (2.2) and (4.10) of Ruyer-Quil et al. [64], the thick-film gradient-expansion equation (4.3.5) is a generalisation of equation (2.17) of Craster and Matar [110], and the thin-film gradient-expansion equation (4.3.7) is a generalisation of equation (7) of Smolka and SeGall [217] and a fully-nonlinear generalisation of the weakly-nonlinear equation (3.5) of Shlang and Sivashinsky [54].

Chapter 5

Analysis of the thick-film reduced-order model for the non-axisymmetric coating of a vertical fibre

In this chapter, for the non-axisymmetric coating of a vertical fibre by a thick film of fluid, in the linear regime, we analyse the analytical and numerical results of the thick-film WRIBL equations (4.2.19) and (4.2.32), the thick-film gradient-expansion equation (4.3.5), and the thin-film gradient-expansion equation (4.3.7). We compare the results of these calculations with the results of the Navier–Stokes equations (4.1.11)–(4.1.21) in the linear regime. Comparing the results of the reduced-order models models with those of Navier–Stokes equations provides a useful check on which aspects of the dynamics can and cannot be captured by the reduced-order models In particular, we focus on the stability of the $n = 0$ (axisymmetric) and the $n = 1$ (first non-axisymmetric) modes, as discussed in Section 1.6.2. In the nonlinear regime, we analyse the numerical results of the thick-film WRIBL equations (4.2.19) and (4.2.32). We compare the results of the thick-film WRIBL equations (4.2.19) and (4.2.32) in the linear regime with the results of the numerical simulations of the thick-film WRIBL equations (4.2.19) and (4.2.32) in the nonlinear regime, and with the experimental results of Gabbard and Bostwick [222]. In Section 5.1 we perform a linear stability analysis of the flow

described by the thick-film WRIBL equations (4.2.19) and (4.2.32). In particular, we obtain an analytical expression for the linear growth rate of the $n = 0$ and $n = 1$ modes for small axial wavenumbers. In Section 5.2 we perform a linear stability analysis of the flow described by the Navier–Stokes equations (4.1.11)–(4.1.21). In particular, we obtain an analytical expression for the linear growth rate of the $n = 0$ and $n = 1$ modes for small axial wavenumbers. In Section 5.3 we perform a parametric study of the linear stability of the flow described by the thick-film WRIBL equations (4.2.19) and (4.2.32), the thick-film gradient-expansion equation (4.3.5), the thin-film gradient-expansion equation (4.3.7), and the Navier–Stokes equations (4.1.11)–(4.1.21), for general axial wavenumbers, for the $n = 0$ and $n = 1$ modes. In Section 5.4, in order to gain insight into the (in)stability of the $n = 0$ and $n = 1$ modes of the flow described by the thick-film WRIBL equations (4.2.19) and (4.2.32), we implement the Whitham wave hierarchy, as discussed in Section 1.2.2. In Section 5.5 we examine the solutions of the thick-film WRIBL equations (4.2.19) and (4.2.32) in the nonlinear regime, and we compare these solutions to the results from the linear calculations. In Section 5.6 we compare our results in Sections 5.1–5.5 with the experimental results of Gabbard and Bostwick [222], as discussed in Section 1.6.2

In order to compare the results of the thick-film WRIBL equations (4.2.19) and (4.2.32), the thick-film gradient-expansion equation (4.3.5), the thin-film gradient-expansion equation (4.3.7), and the Navier–Stokes equations (4.1.11)–(4.1.21), we work in non-dimensional, but otherwise unscaled, variables [55; 60]. By working in such variables, we are able to easily compare the results of equations which were originally derived by applying different scalings.

5.1 Linear stability of the flow described by the thick-film WRIBL equations

To perform the linear stability analysis of the flow described by the thick-film WRIBL equations (4.2.19) and (4.2.32), we decompose S and q as

$$S(\theta, z, t) = \bar{S} + \xi S^* \mathrm{e}^{ikz+in\theta+\sigma t}, \tag{5.1.1}$$

$$q(\theta, z, t) = \bar{q} + \xi q^* \mathrm{e}^{ikz+in\theta+\sigma t}, \tag{5.1.2}$$

where $\xi \ll 1$ with k, n, and σ representing the (real) axial wavenumber, the (integer) azimuthal wavenumber, and the (complex) linear growth rate, respectively. The terms $\bar{S}$ and $\bar{q}$ denote the base-state solutions for the film radius and axial flux, respectively, and the terms ξS^* and ξq^* represent the (initial) amplitudes of the disturbance. Substituting (5.1.1) and (5.1.2) into (4.2.19) and (4.2.32) yields the expression for $\bar{q}$ in terms of $\bar{S}$, namely

$$\bar{q} = \frac{-1 + 4\bar{S}^2 - 3\bar{S}^4 + 4\bar{S}^4 \log \bar{S}}{16}, \tag{5.1.3}$$

at leading order in ξ. The base-state solution (5.1.3) represents a steady unidirectional flow down the fibre. At first order in ξ we obtain the matrix problem

$$A \begin{bmatrix} S^* \\ q^* \end{bmatrix} = \mathbf{0}, \tag{5.1.4}$$

where the matrix A is

$$A = \begin{bmatrix} \Gamma \dfrac{X}{8\bar{S}^2} + \bar{S}\sigma & ik \\ \dfrac{i\Gamma k \bar{q}_0 \left(k^2\bar{S}^2 + n^2 - 1\right)}{\bar{S}^2} + \dfrac{\bar{S}^3 - 2\bar{S}^3 \log \bar{S} - \bar{S}}{2} + Re\dfrac{Y}{8\bar{q}_0} & 1 + Re\dfrac{Z}{\bar{q}_0} \end{bmatrix}, \tag{5.1.5}$$

where

$$\begin{aligned} X =& n^2 \left(\bar{S}^4 - 4\bar{S}^2 \log \bar{S} - 1\right)\left(k^2\bar{S}^2 + n^2 - 1\right), && (5.1.6)\\ Y =& \bar{S}\left(\bar{S}^2 - 1\right)\Big[\sigma\left(4\bar{q}_1 + \bar{q}_2\bar{S}^2 + \bar{q}_2\right) \\ &+ ik\left(\bar{S}^2[\bar{q}_3 + \bar{q}_4 + 4\bar{q}_6] + \bar{q}_3 + \bar{q}_4\bar{S}^4 + 4\bar{q}_5\right)\Big] && (5.1.7)\\ &- 4i\bar{S}^3 \log \bar{S}\left[k\bar{S}^2\left(\bar{q}_3 + \bar{q}_4\bar{S}^2 + 2\bar{q}_6\right) + 2k\bar{q}_5 - i\sigma\left(2\bar{q}_1 + \bar{q}_2\bar{S}^2\right)\right], \\ Z =& \sigma\left(\bar{q}_1 + \bar{q}_2\bar{S}^2\right) + ik\left[\bar{S}^2\left(\bar{q}_3 + \bar{q}_4\bar{S}^2 + \bar{q}_6\right) + \bar{q}_5\right], && (5.1.8) \end{aligned}$$

and $\bar{q}_k$ are the base-state solutions of q_k, given by (4.2.33), for $k = 0, 1, \ldots, 6$. To obtain a non-trivial solution of the matrix problem (5.1.4), we set $\det(A) = 0$ to obtain the dispersion relation for σ. The dispersion relation for σ is quadratic, with two solutions for σ.

Performing the corresponding linear stability analysis of the flow described

by the thick-film gradient-expansion equation (4.3.5) or the thin-film gradient-expansion equation (4.3.7) is much simpler than what we have just described for the thick-film WRIBL equations (4.2.19) and (4.2.32) since in both cases q does not have an independent evolution equation. Thus, in these cases, we substitute (5.1.1) into equations (4.3.5) and (4.3.7) and solve for σ at first order in ξ. This yields the linear growth rate of the flow described by the thick-film gradient-expansion equation (4.3.5)

$$\begin{aligned}\sigma =& - ik\frac{1-\bar{S}^2+2\bar{S}^2\log\bar{S}}{2}+\frac{2Re\,k^2}{768}\Bigg[13-27\bar{S}^2-45\bar{S}^4+59\bar{S}^6\\ &-12\bar{S}^2\left(-7+17\bar{S}^2\right)\log\bar{S}-120\bar{S}^4\left(-1+\bar{S}^2\right)\log^2\bar{S}+96\bar{S}^6\log^3\bar{S}\Bigg]\\ &-\Gamma\frac{(-1+n^2+k^2)\left[2n^2(-1+\bar{S}^4-4\bar{S}^2\log\bar{S})+k^2(-1+4\bar{S}^2-3\bar{S}^4+4\bar{S}^4\log\bar{S})\right]}{16\bar{S}^3},\end{aligned} \tag{5.1.9}$$

and the linear growth rate of the flow described by the thin-film gradient-expansion equation (4.3.7)

$$\begin{aligned}\sigma =& - ik\frac{\left(-1+\bar{S}\right)^2\left(-1+4\bar{S}\right)}{3\bar{S}}+2Re\,k^2\frac{\left(-1+\bar{S}\right)^6}{15\bar{S}}\\ &-\Gamma\frac{(-1+k^2+n^2)\left(k^2+n^2\right)\left(-1+\bar{S}\right)^3}{3\bar{S}}.\end{aligned} \tag{5.1.10}$$

5.1.1 Linear stability of the flow described by the thick-film WRIBL equations for small axial wavenumbers

In Section 5.3 we consider the linear behaviour of the flow described by the thick-film WRIBL equations (4.2.19) and (4.2.32) numerically for a general axial wavenumber k, however, in the present section, we consider only the analytically tractable case of small axial wavenumber k. For small k, we seek a linear growth rate of the form

$$\sigma = \sigma_{0(n)} + k\sigma_{1(n)} + k^2\sigma_{2(n)} + \mathcal{O}(k^3) \tag{5.1.11}$$

for $k \ll 1$. In this limit, one of the solutions for the linear growth rate of the flow described by the thick-film WRIBL equations (4.2.19) and (4.2.32) is always negative and thus is always stable, while the other solution can be either positive or negative and thus may lead to either stability or instability. Hence, we will only

examine the latter of these two solutions for the linear growth rate.

We begin by considering the $n = 0$ mode. Substituting (5.1.11) into the matrix problem (5.1.4) and solving $\det(A) = 0$ order-by-order in k for the $n = 0$ mode yields

$$\sigma_{0(0)} = 0, \quad \sigma_{1(0)} = -\frac{i}{2}\left(1 - \bar{S}^2 + 2\bar{S}^2 \log \bar{S}\right) \tag{5.1.12}$$

and

$$\begin{aligned}\sigma_{2(0)} =& \frac{Re}{768}\Big[13 - 27\bar{S}^2 - 45\bar{S}^4 + 59\bar{S}^6 + 12\bar{S}^2\left(7 - 17\bar{S}^2\right)\log \bar{S} \\ & - 120\bar{S}^4\left(-1 + \bar{S}^2\right)\log^2 \bar{S} + 96\bar{S}^6 \log^3 \bar{S}\Big] \\ & + \frac{\Gamma}{16\bar{S}^3}\left[4\bar{S}^2 - 1 - \bar{S}^4\left(3 - 4\log \bar{S}\right)\right].\end{aligned} \tag{5.1.13}$$

The stability is governed by the sign of $\sigma_{2(0)}$ (5.1.13) as $\sigma_{0(0)} = 0$ and $\sigma_{1(0)}$ is purely imaginary, and thus does not affect the stability. Both the inertia and azimuthal curvature terms are positive in $\sigma_{2(0)}$ (5.1.13), and thus destabilising.

We now consider the $n = 1$ mode. Substituting (5.1.11) into the matrix problem (5.1.4) and solving $\det(A) = 0$ order-by-order in k for the $n = 1$ mode yields

$$\sigma_{0(1)} = 0, \quad \sigma_{1(1)} = -\frac{i}{2}\left(1 - \bar{S}^2 + 2\bar{S}^2 \log \bar{S}\right) \tag{5.1.14}$$

and

$$\begin{aligned}\sigma_{2(1)} =& \frac{Re}{768}\Big[13 - 27\bar{S}^2 - 45\bar{S}^4 + 59\bar{S}^6 + 12\bar{S}^2\left(7 - 17\bar{S}^2\right)\log \bar{S} \\ & - 120\bar{S}^4\left(-1 + \bar{S}^2\right)\log^2 \bar{S} + 96\bar{S}^6 \log^3 \bar{S}\Big] \\ & - \frac{\Gamma}{8\bar{S}}\left[\bar{S}^4 - 1 - 4\bar{S}^2 \log \bar{S}\right].\end{aligned} \tag{5.1.15}$$

Again, the stability is governed by the sign of $\sigma_{2(1)}$ (5.1.15) as $\sigma_{0(0)} = \sigma_{0(1)} = 0$ and $\sigma_{1(0)} = \sigma_{1(1)}$ is purely imaginary, and thus does not affect the stability. The inertial terms (i.e. the terms multiplied by Re) in $\sigma_{2(0)}$ (5.1.13) and $\sigma_{2(1)}$ (5.1.15) are identical and are always positive and therefore destabilising. Thus, the only difference in $\sigma_{2(0)}$ (5.1.13) and $\sigma_{2(1)}$ (5.1.15) occurs in the terms that represent the azimuthal curvature (i.e. the terms multiplied by Γ). As mentioned previously, for the $n = 0$ mode, this term is always positive, therefore the effect of azimuthal curvature is destabilising. However, for the $n = 1$ mode, this term is always

negative, therefore the effect of azimuthal curvature is stabilising.

5.2 Linear stability of the flow described by the Navier–Stokes equations

To perform the linear stability analysis of the flow described by the Navier–Stokes equations (4.1.11)–(4.1.21), we decompose u, v, w, p, and S as

$$u(r,\theta,z,t) = \xi\breve{u}(r,\theta,z,t), \tag{5.2.1}$$
$$v(r,\theta,z,t) = \xi\breve{v}(r,\theta,z,t), \tag{5.2.2}$$
$$w(r,\theta,z,t) = \bar{w}(r,\theta,z) + \xi\breve{w}(r,\theta,z,t), \tag{5.2.3}$$
$$p(r,\theta,z,t) = \bar{p}(r,\theta,z) + \xi\breve{p}(r,\theta,z,t), \tag{5.2.4}$$
$$S(\theta,z,t) = \bar{S} + \xi\breve{S}(\theta,z,t), \tag{5.2.5}$$

where $\xi \ll 1$. The terms with an overbar denote the base-state solutions, and the terms with checks denote the perturbations to the base-state solutions. Substituting (5.2.1)–(5.2.4) into equations (4.1.11)–(4.1.14) yields the ODEs

$$\frac{\mathrm{d}\bar{p}}{\mathrm{d}r} = 0, \tag{5.2.6}$$
$$\frac{\mathrm{d}^2\bar{w}}{\mathrm{d}r^2} + \frac{1}{r}\frac{\mathrm{d}\bar{w}}{\mathrm{d}r} + 1 = 0 \tag{5.2.7}$$

at leading order in ξ. Substituting (5.2.1)–(5.2.5) into the boundary conditions (4.1.15)–(4.1.21) yields

$$\bar{w} = 0 \tag{5.2.8}$$

at the surface of the fibre, $r = 1$, and

$$\frac{\mathrm{d}\bar{w}}{\mathrm{d}r} = 0, \tag{5.2.9}$$
$$\Gamma - \bar{S}\bar{p} = 0 \tag{5.2.10}$$

at the unperturbed free surface, $r = \bar{S}$, at leading-order in ξ. To determine the base-state solution for the pressure, (5.2.6) is solved for $\bar{p}$, subject to (5.2.10) to

obtain

$$\bar{p} = \frac{\Gamma}{\bar{S}}, \tag{5.2.11}$$

which represents a pressure which is spatially uniform, and depends only on Γ and $\bar{S}$. To determine the base-state solution for the axial velocity, (5.2.7) is solved for $\bar{w}$, subject to (5.2.8) and (5.2.9), to obtain

$$\bar{w}(r) = \frac{1 - r^2 + 2\bar{S}^2 \log r}{4}, \tag{5.2.12}$$

which is independent of θ and z, and represents a steady unidirectional flow down the fibre.

Using the base-state solutions (5.2.11) and (5.2.12), substituting (5.2.1)–(5.2.4) into equations (4.1.11)–(4.1.14) yields the governing equations that describe the linear disturbances

$$\frac{\partial \breve{u}}{\partial r} + \frac{\partial \breve{w}}{\partial z} + \frac{1}{r}\left(\frac{\partial \breve{v}}{\partial \theta} + \breve{u}\right) = 0, \tag{5.2.13}$$

$$Re\left(\frac{\partial \breve{u}}{\partial t} + \bar{w}\frac{\partial \breve{u}}{\partial z}\right) = -\frac{\partial \breve{p}}{\partial r} + \frac{\partial^2 \breve{u}}{\partial r^2} + \frac{\partial^2 \breve{u}}{\partial z^2} + \frac{1}{r^2}\left(\frac{\partial^2 \breve{u}}{\partial \theta^2} - \breve{u} - 2\frac{\partial \breve{v}}{\partial \theta}\right) + \frac{1}{r}\frac{\partial \breve{u}}{\partial r}, \tag{5.2.14}$$

$$Re\left(\frac{\partial \breve{v}}{\partial t} + \bar{w}\frac{\partial \breve{v}}{\partial z}\right) = -\frac{1}{r}\frac{\partial \breve{p}}{\partial \theta} + \frac{\partial^2 \breve{v}}{\partial r^2} + \frac{\partial^2 \breve{v}}{\partial z^2} + \frac{1}{r^2}\left(\frac{\partial^2 \breve{v}}{\partial \theta^2} - \breve{v} + 2\frac{\partial \breve{u}}{\partial \theta}\right) + \frac{1}{r}\frac{\partial \breve{v}}{\partial r}, \tag{5.2.15}$$

$$Re\left(\frac{\partial \breve{w}}{\partial t} + \frac{\mathrm{d}\bar{w}}{\mathrm{d}r}\breve{u} + \bar{w}\frac{\partial \breve{w}}{\partial z}\right) = -\frac{\partial \breve{p}}{\partial z} + \frac{\partial^2 \breve{w}}{\partial r^2} + \frac{\partial^2 \breve{w}}{\partial z^2} + \frac{1}{r^2}\frac{\partial^2 \breve{w}}{\partial \theta^2} + \frac{1}{r}\frac{\partial \breve{w}}{\partial r} \tag{5.2.16}$$

at first order in ξ. Similarly, using the base-state solutions (5.2.11) and (5.2.12), substituting (5.2.1)–(5.2.5) into the boundary conditions (4.1.15)–(4.1.21) yields the boundary conditions for the linear disturbances at first order in ξ. At the surface of the fibre, $r = 1$, at first order in ξ, we have the no-slip and impermeability conditions

$$\breve{u} = \breve{v} = \breve{w} = 0. \tag{5.2.17}$$

At the unperturbed free surface, $r = \bar{S}$, at first order in ξ, we have the tangential stress balance in the azimuthal direction

$$\frac{\partial \breve{u}}{\partial \theta} + \bar{S}\frac{\partial \breve{v}}{\partial r} - \breve{v} = 0, \tag{5.2.18}$$

the tangential stress balance in the axial direction

$$\frac{\partial \breve{u}}{\partial z} + \frac{\partial \breve{w}}{\partial r} + \breve{S}\frac{\mathrm{d}^2 \bar{w}}{\mathrm{d}r^2} = 0, \tag{5.2.19}$$

the normal stress balance

$$\frac{\Gamma}{\bar{S}^2}\left(\breve{S} + \bar{S}^2\frac{\partial^2 \breve{S}}{\partial z^2} + \frac{\partial^2 \breve{S}}{\partial \theta^2}\right) + \breve{p} - 2\frac{\partial \breve{u}}{\partial r} = 0, \tag{5.2.20}$$

and the kinematic condition

$$\frac{\partial \breve{S}}{\partial t} - \breve{u} + \bar{w}\frac{\partial \breve{S}}{\partial z} = 0. \tag{5.2.21}$$

We have been unable to make analytical progress with the full problem (5.2.13)–(5.2.21) (i.e. for general axial wavenumbers k), however, as in Section 5.1.1, we can make analytical progress in the limit of small axial wavenumber k (as discussed in Section 1.6.2). In Section 5.3 we will consider the linear behaviour of the flow described by the Navier–Stokes equations (4.1.11)–(4.1.21) for general axial wavenumber k by using the Chebyshev–Tau method (see Appendix B).

5.2.1 Linear stability of the flow described by the Navier–Stokes equations for small axial wavenumbers

In the present section, we consider the analytically tractable case of small axial wavenumber k. In this limit, we are able to obtain analytical expressions for the linear growth rate of long waves. In order to obtain these analytical expressions for the linear growth rate of long waves, we follow Dávalos-Orozco and Ruiz-Chavarría [214] and Ruiz-Chavarría and Dávalos-Orozco [215] for the $n = 0$ mode and the $n = 1$ mode, respectively. While the work presented in this section is not novel, we include it to provide a more comprehensive account of the analysis, which was previously summarised in a condensed form by Dávalos-Orozco and Ruiz-Chavarría [214] and Ruiz-Chavarría and Dávalos-Orozco [215].

The thick-film WRIBL equations (4.2.19) and (4.2.32), the thick-film gradient-expansion equation (4.3.5), and the thin-film gradient-expansion equation (4.3.7) each exhibit only stability or long-wave instability, whereas, in the present chapter,

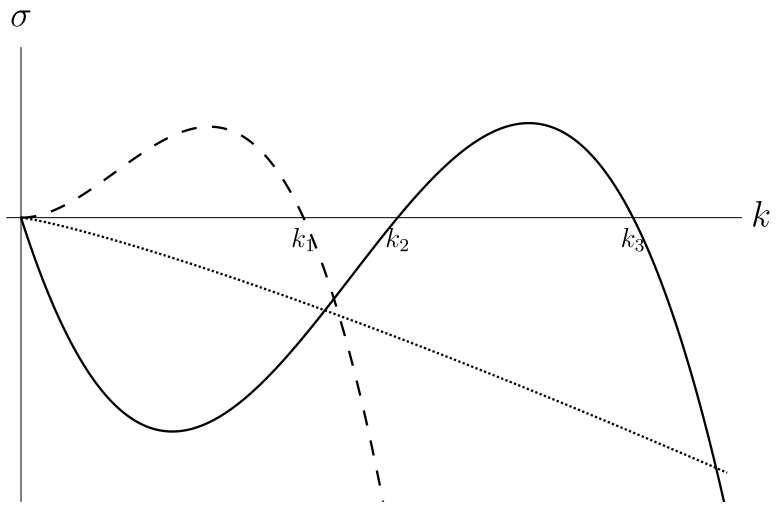

Figure 5.1: A sketch of each of the three possible behaviours we observe for the real parts of the linear growth rate of the flow described by the Navier–Stokes equations (4.1.11)–(4.1.21), namely stability (dotted line), long-wave instability (dashed line), and finite-wave instability (solid line).

we observe that the Navier–Stokes equations (4.1.11)–(4.1.21) can exhibit stability or long-wave instability or *finite-wave instability*. Figure 5.1 shows a sketch of the possible behaviours we observe for the real parts of the linear growth rate σ sketched as a function of k for the flow described by the Navier–Stokes equations (4.1.11)–(4.1.21). The dotted line represents the real parts of a linear growth rate which is negative for all $k > 0$ (stable). The dashed line represents the real parts of a linear growth rate which is positive for a finite range of k ($0 < k \leq k_1$) but negative for $k > k_1$ (long-wave unstable). The solid line represents the real parts of a linear growth rate which is positive for a finite range of k ($0 < k_2 < k < k_3$) and negative for both a finite range of k ($0 < k \leq k_2$) and for $k \geq k_3$ (finite-wave unstable). Other types of behaviour of the real parts of the linear growth rate of the flow described by the Navier–Stokes equations (4.1.11)–(4.1.21) are possible and have been observed in other works [198], however, the present work only observes the three behaviours sketched in Figure 5.1.

In order to obtain analytical expressions for the linear growth rate of long waves, following Dávalos-Orozco and Ruiz-Chavarría [214], we first eliminate $\breve{p}$ by

taking the curl of equations (5.2.14)–(5.2.16) to obtain

$$\begin{aligned} &Re\left[\bar{w}\frac{\partial^2\breve{v}}{\partial z^2}+\frac{\partial^2\breve{v}}{\partial t\partial z}-\frac{1}{r}\left(\frac{\mathrm{d}\bar{w}}{\mathrm{d}r}\frac{\partial\breve{u}}{\partial\theta}+\bar{w}\frac{\partial^2\breve{w}}{\partial\theta\partial z}+\frac{\partial^2\breve{w}}{\partial t\partial\theta}\right)\right] \\ &=-\frac{1}{r^3}\frac{\partial^3\breve{w}}{\partial\theta^3}-\frac{1}{r^2}\left(\frac{\partial\breve{v}}{\partial z}-2\frac{\partial^2\breve{u}}{\partial\theta\partial z}-\frac{\partial^3\breve{v}}{\partial\theta^2\partial z}+\frac{\partial^2\breve{w}}{\partial r\partial\theta}\right) \\ &\quad-\frac{1}{r}\left(\frac{\partial^3\breve{w}}{\partial\theta\partial z^2}-\frac{\partial^2\breve{v}}{\partial r\partial z}+\frac{\partial^3\breve{w}}{\partial r^2\partial\theta}\right)+\frac{\partial^3\breve{v}}{\partial z^3}+\frac{\partial^2\breve{v}}{\partial r^2\partial z}, \end{aligned} \tag{5.2.22}$$

$$\begin{aligned} &Re\left[\frac{\mathrm{d}^2\bar{w}}{\mathrm{d}r^2}\breve{u}+\frac{\mathrm{d}\bar{w}}{\mathrm{d}r}\left(\frac{\partial\breve{u}}{\partial r}+\frac{\partial\breve{w}}{\partial z}\right)+\bar{w}\left(\frac{\partial^2\breve{w}}{\partial r\partial z}-\frac{\partial^2\breve{u}}{\partial z^2}\right)-\frac{\partial^2\breve{u}}{\partial t\partial z}+\frac{\partial^2\breve{w}}{\partial t\partial r}\right] \\ &=-\frac{2}{r^3}\frac{\partial^2\breve{w}}{\partial\theta^2}+\frac{1}{r^2}\left(\frac{\partial\breve{u}}{\partial z}-\frac{\partial^3\breve{u}}{\partial\theta^2\partial z}+2\frac{\partial^2\breve{v}}{\partial\theta\partial z}-\frac{\partial\breve{w}}{\partial r}+\frac{\partial^3\breve{w}}{\partial r\partial\theta^2}\right) \\ &\quad+\frac{1}{r}\left(\frac{\partial^2\breve{w}}{\partial r^2}-\frac{\partial^2\breve{u}}{\partial r\partial z}\right)-\frac{\partial^3\breve{u}}{\partial z^3}-\frac{\partial^3\breve{u}}{\partial r^2\partial z}+\frac{\partial^3\breve{w}}{\partial r\partial z^2}+\frac{\partial^3\breve{w}}{\partial r^3}, \end{aligned} \tag{5.2.23}$$

$$\begin{aligned} &Re\left[\frac{1}{r}\left(\bar{w}\left[\frac{\partial^2\breve{u}}{\partial\theta\partial z}-\frac{\partial\breve{v}}{\partial z}\right]+\frac{\partial^2\breve{u}}{\partial t\partial\theta}-\frac{\partial\breve{v}}{\partial t}\right)-\frac{\mathrm{d}\bar{w}}{\mathrm{d}r}\frac{\partial\breve{v}}{\partial z}-\bar{w}\frac{\partial^2\breve{v}}{\partial r\partial z}-\frac{\partial^2\breve{v}}{\partial t\partial r}\right] \\ &=\frac{1}{r^3}\left(\frac{\partial\breve{u}}{\partial\theta}+\frac{\partial^3\breve{u}}{\partial\theta^3}-\frac{\partial^2\breve{v}}{\partial\theta^2}-\breve{v}\right)-\frac{1}{r^2}\left(\frac{\partial^2\breve{u}}{\partial r\partial\theta}-\frac{\partial\breve{v}}{\partial r}+\frac{\partial^3\breve{v}}{\partial r\partial\theta^2}\right) \\ &\quad+\frac{1}{r}\left(\frac{\partial^3\breve{u}}{\partial\theta\partial z^2}+\frac{\partial^3\breve{u}}{\partial r^2\partial\theta}-\frac{\partial^2\breve{v}}{\partial z^2}-2\frac{\partial^2\breve{v}}{\partial r^2}\right)-\frac{\partial^3\breve{v}}{\partial r\partial z^2}-\frac{\partial^3\breve{v}}{\partial r^3}. \end{aligned} \tag{5.2.24}$$

Then, again following Dávalos-Orozco and Ruiz-Chavarría [214], we introduce potential functions $\phi(r)$ and $\psi(r)$ and decompose $\breve{u}$, $\breve{v}$, and $\breve{w}$ as

$$\begin{aligned} (\breve{u},\breve{v},\breve{w}) &= \nabla\times\left(\psi(r)\mathrm{e}^{ikz+in\theta+\sigma t},\phi(r)\mathrm{e}^{ikz+in\theta+\sigma t},0\right) \\ &= \left(-ik\phi(r),ik\psi(r),\frac{\phi(r)-in\psi(r)+r\dfrac{\mathrm{d}\phi(r)}{\mathrm{d}r}}{r}\right)\mathrm{e}^{ikz+in\theta+\sigma t}. \end{aligned} \tag{5.2.25}$$

Both $\phi(r)$ and $\psi(r)$ are required as the flow is three-dimensional. Substituting

(5.2.25) into equations (5.2.22)–(5.2.24) yields

$$
\begin{aligned}
&Re\Bigg[-k^2\psi\left(\sigma+ik\bar{w}\right)+\frac{n}{r}\left[\frac{\mathrm{d}\phi}{\mathrm{d}r}\left(k\bar{w}-i\sigma\right)-k\phi\frac{\mathrm{d}\bar{w}}{\mathrm{d}r}\right]-\frac{n}{r^2}\left(\sigma+ik\bar{w}\right)\left(i\phi+n\psi\right)\Bigg]\\
&-\frac{n\left(-1+n^2\right)\left(i\phi+n\psi\right)}{r^4}-\frac{n}{r^3}\left(n\frac{\mathrm{d}\psi}{\mathrm{d}r}+i\left(1+n^2\right)\frac{\mathrm{d}\phi}{\mathrm{d}r}\right)\\
&+\frac{1}{r^2}\left(n\left[2i\frac{\mathrm{d}^2\phi}{\mathrm{d}r^2}+n\frac{\mathrm{d}^2\psi}{\mathrm{d}r^2}\right]-k^2\left[3in\phi+\left(1+2n^2\right)\psi\right]\right)\\
&+\frac{1}{r}\left[in\frac{\mathrm{d}^3\phi}{\mathrm{d}r^3}+k^2\left(\frac{\mathrm{d}\psi}{\mathrm{d}r}-in\frac{\mathrm{d}\phi}{\mathrm{d}r}\right)\right]+k^2\left(\frac{\mathrm{d}^2\psi}{\mathrm{d}r^2}-k^2\psi\right)=0,
\end{aligned}
\tag{5.2.26}
$$

$$
\begin{aligned}
&Re\Bigg[\left(\sigma+ik\bar{w}\right)\left(\frac{\mathrm{d}^2\phi}{\mathrm{d}r^2}-k^2\phi\right)-ik\phi\frac{\mathrm{d}^2\bar{w}}{\mathrm{d}r^2}-\frac{\left(\sigma+ik\bar{w}\right)\left(\phi-in\psi\right)}{r^2}\\
&+\frac{1}{r}\left[\left(\sigma+ik\bar{w}\right)\left(\frac{\mathrm{d}\phi}{\mathrm{d}r}-in\frac{\mathrm{d}\psi}{\mathrm{d}r}\right)+k\left(i\phi+n\psi\right)\frac{\mathrm{d}\bar{w}}{\mathrm{d}r}\right]\Bigg]\\
&-\frac{3\left(-1+n^2\right)\left(\phi-in\psi\right)}{r^4}-\frac{1}{r^3}\left(\left(3+n^2\right)\frac{\mathrm{d}\phi}{\mathrm{d}r}+in\left(-3+n^2\right)\frac{\mathrm{d}\psi}{\mathrm{d}r}\right)\\
&+\frac{1}{r^2}\left(k^2\left[3in\psi-\left(2+n^2\right)\phi\right]+\left(3+n^2\right)\frac{\mathrm{d}^2\phi}{\mathrm{d}r^2}-2in\frac{\mathrm{d}^2\psi}{\mathrm{d}r^2}\right)\\
&+\frac{1}{r}\left(k^2\left(2\frac{\mathrm{d}\phi}{\mathrm{d}r}-in\frac{\mathrm{d}\psi}{\mathrm{d}r}\right)-2\frac{\mathrm{d}^3\phi}{\mathrm{d}r^3}+in\frac{\mathrm{d}^3\psi}{\mathrm{d}r^3}\right)-k^4\phi+2k^2\frac{\mathrm{d}^2\phi}{\mathrm{d}r^2}-\frac{\mathrm{d}^4\phi}{\mathrm{d}r^4}=0,
\end{aligned}
\tag{5.2.27}
$$

$$
\begin{aligned}
&Re\Bigg[-i\left(\sigma+ik\bar{w}\right)\frac{\mathrm{d}\psi}{\mathrm{d}r}+k\psi\frac{\mathrm{d}\bar{w}}{\mathrm{d}r}+\frac{\left(\sigma+ik\bar{w}\right)\left(n\phi-i\psi\right)}{r}\Bigg]\\
&+\frac{\left(-1+n^2\right)\left(n\phi-i\psi\right)}{r^3}+\frac{1}{r^2}\left(n\frac{\mathrm{d}\phi}{\mathrm{d}r}-i\left(1+n^2\right)\frac{\mathrm{d}\psi}{\mathrm{d}r}\right)\\
&+\frac{1}{r}\left(k^2\left(n\phi-i\psi\right)-n\frac{\mathrm{d}^2\phi}{\mathrm{d}r^2}+2i\frac{\mathrm{d}^2\psi}{\mathrm{d}r^2}\right)-i\left(k^2\frac{\mathrm{d}\psi}{\mathrm{d}r}-\frac{\mathrm{d}^3\psi}{\mathrm{d}r^3}\right)=0.
\end{aligned}
\tag{5.2.28}
$$

Both $\breve{S}$ and $\breve{p}$ appear in the linearised boundary conditions (5.2.19)–(5.2.21)

thus, we decompose $\breve{S}$ and $\breve{p}$ as

$$\breve{S}(\theta, z, t) = S^* \mathrm{e}^{ikz+in\theta+\sigma t}, \tag{5.2.29}$$

$$\breve{p}(r, \theta, z, t) = p^*(r)\mathrm{e}^{ikz+in\theta+\sigma t}. \tag{5.2.30}$$

Substituting (5.2.25) and the expressions (5.2.29) and (5.2.30) into the boundary conditions (5.2.17)–(5.2.21) yields

$$\phi = \psi = \frac{\mathrm{d}\phi}{\mathrm{d}r} = 0 \tag{5.2.31}$$

at the surface of the fibre, $r = 1$, and

$$-in\phi + \bar{S}\frac{\mathrm{d}\psi}{\mathrm{d}r} - \psi = 0, \tag{5.2.32}$$

$$\left(1 - k^2\bar{S}^2\right)\phi - \bar{S}\left(-in\frac{\mathrm{d}\psi}{\mathrm{d}r} + \bar{S}\frac{\mathrm{d}^2\phi}{\mathrm{d}r^2} + \frac{\mathrm{d}\phi}{\mathrm{d}r} + \bar{S}S^*\frac{\mathrm{d}^2\bar{w}}{\mathrm{d}r^2}\right) - in\psi = 0, \tag{5.2.33}$$

$$\Gamma S^*\left(k^2\bar{S}^2 + n^2 - 1\right) - 2ik\bar{S}^2\frac{\mathrm{d}\phi}{\mathrm{d}r} - \bar{S}^2 p^* = 0, \tag{5.2.34}$$

$$ik\phi + S^*(\sigma + ik\bar{w}) = 0 \tag{5.2.35}$$

at the unperturbed free surface $r = \bar{S}$. In the expression (5.2.30), $p^*(r)$ is an unknown function of r which we wish to express as a function of $\phi(r)$ and $\psi(r)$, thus eliminating $p^*(r)$ from the boundary condition (5.2.34). We substitute (5.2.25) and the expression for $\breve{p}$ (5.2.30) into equations (5.2.15) and (5.2.16) and then solve for p^*. Thus, two expressions of the solution for p^* are obtained, namely

$$p_1^* = -Re\,\frac{kr\psi(\sigma + ik\bar{w})}{n} - \frac{k}{nr}\left[\psi\left(k^2r^2 + n^2 + 1\right) + 2in\phi - r\left(r\frac{\mathrm{d}^2\psi}{\mathrm{d}r^2} + \frac{\mathrm{d}\psi}{\mathrm{d}r}\right)\right] \tag{5.2.36}$$

and

$$\begin{aligned} p_2^* = {} & Re\left[\phi\frac{\mathrm{d}\bar{w}}{\mathrm{d}r} + \frac{1}{kr}(\sigma + ik\bar{w})\left(n\psi + ir\frac{\mathrm{d}\phi}{\mathrm{d}r} + i\phi\right)\right] \\ & + \frac{1}{kr^3}\left[ir\left(k^2r^2 + n^2 + 1\right)\frac{\mathrm{d}\phi}{\mathrm{d}r} + i\phi\left(k^2r^2 + n^2 - 1\right)\right. \\ & \left. + n\psi\left(k^2r^2 + n^2 - 1\right) - ir^2\left(-in\frac{\mathrm{d}^2\psi}{\mathrm{d}r^2} + r\frac{\mathrm{d}^3\phi}{\mathrm{d}r^3} + 2\frac{\mathrm{d}^2\phi}{\mathrm{d}r^2}\right) + nr\frac{\mathrm{d}\psi}{\mathrm{d}r}\right]. \end{aligned} \tag{5.2.37}$$

Now we substitute (5.2.36) and (5.2.37) into equation (5.2.34) to obtain

$$k\bar{S}\left[\psi\left(k^2\bar{S}^2+n^2+1\right)-\bar{S}\left(2in\frac{\mathrm{d}\phi}{\mathrm{d}r}+\bar{S}\frac{\mathrm{d}^2\psi}{\mathrm{d}r^2}+\frac{\mathrm{d}\psi}{\mathrm{d}r}\right)+2in\phi\right] \tag{5.2.38}$$
$$+\Gamma\, nS^*\left(k^2\bar{S}^2+n^2-1\right)+kRe\,\bar{S}^3\psi(\sigma+ik\bar{w})=0$$

and

$$\Gamma\, k\bar{S}S^*\left(k^2\bar{S}^2+n^2-1\right)+Re\,\bar{S}^2\left[(k\bar{w}-i\sigma)\left(-in\psi+\bar{S}\frac{\mathrm{d}\phi}{\mathrm{d}r}+\phi\right)-k\bar{S}\phi\frac{\mathrm{d}\bar{w}}{\mathrm{d}r}\right]$$
$$-i\Bigg[\bar{S}\left(\left(3k^2\bar{S}^2+n^2+1\right)\frac{\mathrm{d}\phi}{\mathrm{d}r}-in\left(\frac{\mathrm{d}\psi}{\mathrm{d}r}-\bar{S}\frac{\mathrm{d}^2\psi}{\mathrm{d}r^2}\right)-\bar{S}^2\frac{\mathrm{d}^3\phi}{\mathrm{d}r^3}-2\bar{S}\frac{\mathrm{d}^2\phi}{\mathrm{d}r^2}\right) \tag{5.2.39}$$
$$+\phi\left(k^2\bar{S}^2+n^2-1\right)-in\psi\left(k^2\bar{S}^2+n^2-1\right)\Bigg]=0,$$

respectively. The governing equations (5.2.26)–(5.2.28) and boundary conditions (5.2.31)–(5.2.33), (5.2.35), (5.2.38), and (5.2.39) now depend on r only via $\phi(r)$ and $\psi(r)$.

We expand $\phi(r)$, $\psi(r)$, and σ as

$$\phi(r)=\phi_{0(n)}(r)+k\phi_{1(n)}(r)+k^2\phi_{2(n)}(r)+\mathcal{O}(k^3), \tag{5.2.40}$$
$$\psi(r)=\psi_{0(n)}(r)+k\psi_{1(n)}(r)+k^2\psi_{2(n)}(r)+\mathcal{O}(k^3), \tag{5.2.41}$$
$$\sigma=\sigma_{0(n)}+k\sigma_{1(n)}+k^2\sigma_{2(n)}+\mathcal{O}(k^3) \tag{5.2.42}$$

for $k\ll 1$. We substitute (5.2.40)–(5.2.42) into the governing equations (5.2.26)–(5.2.28) and boundary conditions (5.2.31)–(5.2.33), (5.2.35), (5.2.38), and (5.2.39), and solve the resulting system order-by-order in k.

Note that from (5.2.35) $\sigma_{0(n)}=0$ for $n=0$ and $n=1$, and so $\sigma_{1(n)}$ is now the leading-order term in the expansion (5.2.42) for $n=0$ and $n=1$.

5.2.1.1 $n=0$ mode for small axial wavenumbers

We begin by examining the $n=0$ mode. When $n=0$, $\phi_{i(0)}$ and $\psi_{i(0)}$ for $i=0,1,2$ are decoupled. In particular, $\sigma_{1(0)}$ only appears at leading order in k in equation (5.2.35), therefore, to obtain the linear growth rate for the $n=0$ mode we need

only consider $\phi_{i(0)}$ for $i = 0, 1, 2$.

At leading order in k the governing equation (5.2.27) for $\phi_{0(0)}$ is

$$\frac{3\phi_{0(0)}}{r^3} - \frac{3}{r^2}\frac{\mathrm{d}\phi_{0(0)}}{\mathrm{d}r} + \frac{3}{r}\frac{\mathrm{d}^2\phi_{0(0)}}{\mathrm{d}r^2} - 2\frac{\mathrm{d}^3\phi_{0(0)}}{\mathrm{d}r^3} - r\frac{\mathrm{d}^4\phi_{0(0)}}{\mathrm{d}r^4} = 0, \tag{5.2.43}$$

subject to the boundary conditions

$$\phi_{0(0)} = \frac{\mathrm{d}\phi_{0(0)}}{\mathrm{d}r} = 0, \tag{5.2.44}$$

at the surface of the fibre, $r = 1$, (5.2.31) and

$$\phi_{0(0)} - \bar{S}\left(\frac{\mathrm{d}\phi_{0(0)}}{\mathrm{d}r} + \bar{S}\left(\frac{\mathrm{d}^2\phi_{0(0)}}{\mathrm{d}r^2} + S^*\frac{\mathrm{d}^2\bar{w}}{\mathrm{d}r^2}\right)\right) = 0, \tag{5.2.45}$$

$$i\phi_{0(0)} + S^*(\sigma_{1(0)} + i\bar{w}) = 0, \tag{5.2.46}$$

$$\phi_{0(0)} - \bar{S}\frac{\mathrm{d}\phi_{0(0)}}{\mathrm{d}r} + 2\bar{S}^2\frac{\mathrm{d}^2\phi_{0(0)}}{\mathrm{d}r^2} + \bar{S}^3\frac{\mathrm{d}^3\phi_{0(0)}}{\mathrm{d}r^3} = 0, \tag{5.2.47}$$

at the unperturbed free surface, $r = \bar{S}$, (5.2.33), (5.2.35), and (5.2.39). Equation (5.2.43) has the general solution

$$\phi_{0(0)} = \frac{A_1}{r} + A_2 r + A_3 r^3 + A_4 r\log r, \tag{5.2.48}$$

where A_i for $i = 1, \ldots, 4$ are unknown constants. We substitute the general solution (5.2.48) into the boundary conditions (5.2.44)–(5.2.47) to obtain the matrix problem

$$A_{0(0)}\mathbf{x}_{0(0)} = \mathbf{0}, \tag{5.2.49}$$

where the matrix $A_{0(0)}$ is given in Appendix C.1, and

$$\mathbf{x}_{0(0)} = (A_1, A_2, A_3, A_4, S^*)^{\mathrm{T}} \tag{5.2.50}$$

is the vector of unknowns. To obtain a non-trivial solution of the matrix problem (5.2.49), we set $\det(A_{0(0)}) = 0$ to obtain the dispersion relation for $\sigma_{1(0)}$. The dispersion relation for $\sigma_{1(0)}$ has solution

$$\sigma_{1(0)} = -\frac{i}{2}\left(1 - \bar{S}^2 + 2\bar{S}^2\log\bar{S}\right). \tag{5.2.51}$$

The linear growth rate $\sigma_{1(0)}$ given by (5.2.51) is identical to the linear growth rate of the flow described by the thick-film WRIBL equations (4.2.19) and (4.2.32) for small axial wavenumbers $\sigma_{1(0)}$ given by (5.1.12).

The linear growth rate $\sigma_{1(0)}$ (5.2.51) is purely imaginary and does not affect the stability of the flow, therefore we must now proceed to first order in k to obtain a form for $\sigma_{2(0)}$. However, to proceed to first order in k we need to determine the constants in the general solution for $\phi_{0(0)}$ (5.2.48). Therefore, imposing the boundary conditions (5.2.44)–(5.2.46) we obtain

$$\phi_{0(0)} = \frac{S^*\bar{S}}{4}\left(\frac{1}{r} - r + 2r\log r\right). \tag{5.2.52}$$

The solution (5.2.52) may be verified via direct substitution into (5.2.43).

At first order in k the governing equation (5.2.27) for $\phi_{1(0)}$ is

$$\begin{aligned}&\frac{3\phi_{1(0)}}{r^3} - \frac{3}{r^2}\frac{\mathrm{d}\phi_{1(0)}}{\mathrm{d}r} + \frac{3}{r}\frac{\mathrm{d}^2\phi_{1(0)}}{\mathrm{d}r^2} - 2\frac{\mathrm{d}^3\phi_{1(0)}}{\mathrm{d}r^3} - r\frac{\mathrm{d}^4\phi_{1(0)}}{\mathrm{d}r^4} \\ &= Re\left[\frac{\phi_{0(0)}\left(\sigma_{1(0)} + i\bar{w}\right)}{r} - \left(\sigma_{1(0)} + i\bar{w}\right)\frac{\mathrm{d}\phi_{0(0)}}{\mathrm{d}r}\right. \\ &\quad \left. - i\phi_{0(0)}\frac{\mathrm{d}\bar{w}}{\mathrm{d}r} - r\left(\left[\sigma_{1(0)} + i\bar{w}\right]\frac{\mathrm{d}^2\phi_{0(0)}}{\mathrm{d}r^2} - i\phi_{0(0)}\frac{\mathrm{d}^2\bar{w}}{\mathrm{d}r^2}\right)\right],\end{aligned} \tag{5.2.53}$$

subject to the boundary conditions

$$\phi_{1(0)} = \frac{\mathrm{d}\phi_{1(0)}}{\mathrm{d}r} = 0, \tag{5.2.54}$$

at the surface of the fibre, $r = 1$, (5.2.31) and

$$\phi_{1(0)} - \bar{S}\left(\frac{\mathrm{d}\phi_{1(0)}}{\mathrm{d}r} + \bar{S}\frac{\mathrm{d}^2\phi_{1(0)}}{\mathrm{d}r^2}\right) = 0, \tag{5.2.55}$$

$$i\phi_{1(0)} + S^*\sigma_{2(0)} = 0, \tag{5.2.56}$$

$$\begin{aligned}&Re\,\bar{S}\left[\left(-i\sigma_{1(0)} + \bar{w}\right)\left(\phi_{0(0)} + \bar{S}\frac{\mathrm{d}\phi_{0(0)}}{\mathrm{d}r}\right) - \bar{S}\phi_{0(0)}\frac{\mathrm{d}\bar{w}}{\mathrm{d}r}\right] - \Gamma\, S^* \\ &\quad + \frac{i}{\bar{S}}\left[\phi_{1(0)} + \bar{S}\left(-\frac{\mathrm{d}\phi_{1(0)}}{\mathrm{d}r} + \bar{S}\left(2\frac{\mathrm{d}^2\phi_{1(0)}}{\mathrm{d}r^2} + \bar{S}\frac{\mathrm{d}^3\phi_{1(0)}}{\mathrm{d}r^3}\right)\right)\right] = 0\end{aligned} \tag{5.2.57}$$

at the unperturbed free surface, $r = \bar{S}$, (5.2.33), (5.2.35), and (5.2.39). Equation

(5.2.53) has the general solution

$$\begin{aligned}\phi_{1(0)} =&\frac{B_1}{r} + B_2 r + B_3 r^3 + B_4 r \log r \\ &+ ReS^*\Bigg[- \frac{ir\bar{S}}{768}\left(r^4 + 12\bar{S}^2 - 3r^2\left[-5 + 22\bar{S}^2 + 20i\sigma_{1(0)}\right]\right) \\ &+ \frac{r^3\bar{S}}{64}\left(i - 6i\bar{S}^2 + 4\sigma_{1(0)}\right)\log r + \frac{ir\left(-1+r^2\right)\bar{S}^3}{32}\log^2 r\Bigg],\end{aligned} \tag{5.2.58}$$

where B_i for $i = 1, \ldots, 4$ are unknown constants. We substitute the general solution (5.2.58) into the boundary conditions (5.2.54)–(5.2.57) to obtain the matrix problem

$$A_{1(0)}\mathbf{x}_{1(0)} = \mathbf{0}, \tag{5.2.59}$$

where the matrix $A_{1(0)}$ is given in Appendix C.2, and

$$\mathbf{x}_{1(0)} = \left(B_1, B_2, B_3, B_4, S^*\right)^{\mathrm{T}} \tag{5.2.60}$$

is the vector of unknowns. To obtain a non-trivial solution of the matrix problem (5.2.59), we set $\det(A_{1(0)}) = 0$ to obtain the dispersion relation for $\sigma_{2(0)}$. The dispersion relation for $\sigma_{2(0)}$ has solution

$$\begin{aligned}\sigma_{2(0)} =& \frac{Re}{768}\Big[13 - 27\bar{S}^2 - 45\bar{S}^4 + 59\bar{S}^6 + 12\bar{S}^2\left(7 - 17\bar{S}^2\right)\log\bar{S} \\ &- 120\bar{S}^4\left(-1 + \bar{S}^2\right)\log^2\bar{S} + 96\bar{S}^6\log^3\bar{S}\Big] \\ &+ \frac{\Gamma}{16\bar{S}^3}\left[4\bar{S}^2 - 1 - \bar{S}^4\left(3 - 4\log\bar{S}\right)\right].\end{aligned} \tag{5.2.61}$$

The linear growth rate $\sigma_{2(0)}$ (5.2.61) is identical to the linear growth rate of the flow described by the thick-film WRIBL equations (4.2.19) and (4.2.32) for small axial wavenumbers $\sigma_{2(0)}$ given by (5.1.13), i.e. both the inertia and azimuthal curvature terms are positive in $\sigma_{2(0)}$ (5.2.61), and thus destabilising for the $n = 0$ mode, which agrees with the results of Dávalos-Orozco and Ruiz-Chavarría [214] in this limit (see Section 1.6.2).

5.2.1.2 $n = 1$ mode for small axial wavenumbers

We now examine the $n = 1$ mode. When $n = 1$, $\phi_{i(1)}$ and $\psi_{i(1)}$ for $i = 0, 1, 2$ are coupled.

At leading order in k the governing equations (5.2.26) and (5.2.28) for $\phi_{0(1)}$ and $\psi_{0(1)}$ are

$$-\frac{2i}{r^2}\frac{\mathrm{d}\phi_{0(1)}}{\mathrm{d}r} - \frac{1}{r^2}\frac{\mathrm{d}\psi_{0(1)}}{\mathrm{d}r} + \frac{2i}{r}\frac{\mathrm{d}^2\phi_{0(1)}}{\mathrm{d}r^2} + \frac{1}{r}\frac{\mathrm{d}^2\psi_{0(1)}}{\mathrm{d}r^2} + i\frac{\mathrm{d}^3\phi_{0(1)}}{\mathrm{d}r^3} = 0, \tag{5.2.62}$$

$$\frac{1}{r}\frac{\mathrm{d}\phi_{0(1)}}{\mathrm{d}r} - \frac{2i}{r}\frac{\mathrm{d}\psi_{0(1)}}{\mathrm{d}r} - \frac{\mathrm{d}^2\phi_{0(1)}}{\mathrm{d}r^2} + 2i\frac{\mathrm{d}^2\psi_{0(1)}}{\mathrm{d}r^2} + ir\frac{\mathrm{d}^3\psi_{0(1)}}{\mathrm{d}r^3} = 0, \tag{5.2.63}$$

subject to the boundary conditions

$$\phi_{0(1)} = \psi_{0(1)} = \frac{\mathrm{d}\phi_{0(1)}}{\mathrm{d}r} = 0, \tag{5.2.64}$$

at the surface of the fibre, $r = 1$, (5.2.31) and

$$-i\phi_{0(1)} - \psi_{0(1)} + \bar{S}\frac{\mathrm{d}\psi_{0(1)}}{\mathrm{d}r} = 0, \tag{5.2.65}$$

$$\phi_{0(1)} - i\psi_{0(1)} - \bar{S}\left(\frac{\mathrm{d}\phi_{0(1)}}{\mathrm{d}r} - i\frac{\mathrm{d}\psi_{0(1)}}{\mathrm{d}r} + \bar{S}\left(\frac{\mathrm{d}^2\phi_{0(1)}}{\mathrm{d}r^2} + S^*\frac{\mathrm{d}^2\bar{w}}{\mathrm{d}r^2}\right)\right) = 0, \tag{5.2.66}$$

$$i\phi_{0(1)} + S^*(\sigma_{1(1)} + i\bar{w}) = 0, \tag{5.2.67}$$

$$-2i\phi_{0(1)} - 2\psi_{0(1)} + \bar{S}\left(2i\frac{\mathrm{d}\phi_{0(1)}}{\mathrm{d}r} + \frac{\mathrm{d}\psi_{0(1)}}{\mathrm{d}r} + \bar{S}\frac{\mathrm{d}^2\psi_{0(1)}}{\mathrm{d}r^2}\right) = 0, \tag{5.2.68}$$

at the unperturbed free surface, $r = \bar{S}$, (5.2.32), (5.2.33), (5.2.35), and (5.2.38). While the procedure for solving the system of equations (5.2.62)–(5.2.68) is formally the same as the procedure for solving both previous systems of equations for the $n = 0$ mode (namely equations (5.2.43)–(5.2.47) and equations (5.2.53)–(5.2.57)), the algebraic details are more complicated. To obtain the general solution of the governing equations (5.2.62) and (5.2.63) we assume that the solution

can be expressed as an infinite series in powers of r and $\log r$, namely

$$\phi_{0(1)} = \sum_{i=-\infty}^{\infty} \sum_{j=0}^{\infty} A_{i,j} r^i \log^j r, \tag{5.2.69}$$

$$\psi_{0(1)} = \sum_{i=-\infty}^{\infty} \sum_{j=0}^{\infty} B_{i,j} r^i \log^j r, \tag{5.2.70}$$

where $A_{i,j}$ and $B_{i,j}$ are unknown constants. We substitute (5.2.69) and (5.2.70) into the governing equations (5.2.62) and (5.2.63) and equate powers of r and $\log r$ to obtain the general solutions

$$\phi_{0(1)} = A_{0,0} + A_{2,0} r^2 - \frac{i B_{-2,0}}{r^2} + i B_{0,1} \log r, \tag{5.2.71}$$

$$\psi_{0(1)} = B_{0,0} + B_{2,0} r^2 + \frac{B_{-2,0}}{r^2} + B_{0,1} \log r, \tag{5.2.72}$$

where $A_{0,0}$, $A_{2,0}$, $B_{0,0}$, $B_{2,0}$, $B_{-2,0}$, and $B_{0,1}$ are unknown constants. We substitute the general solutions (5.2.71) and (5.2.72) into the boundary conditions (5.2.64)–(5.2.68) to obtain the matrix problem

$$A_{0(1)} \mathbf{x}_{0(1)} = \mathbf{0}, \tag{5.2.73}$$

where the matrix $A_{0(1)}$ is given in Appendix C.3, and

$$\mathbf{x}_{0(1)} = (A_{0,0}, A_{2,0}, B_{0,0}, B_{2,0}, B_{-2,0}, B_{0,1}, S^*)^{\mathrm{T}} \tag{5.2.74}$$

is the vector of unknowns. To obtain a non-trivial solution of the matrix problem (5.2.73), we set $\det(A_{0(1)}) = 0$ to obtain the dispersion relation for $\sigma_{1(1)}$. The dispersion relation for $\sigma_{1(1)}$ has solution

$$\sigma_{1(1)} = -\frac{i}{4} \left(1 - \bar{S}^2 + 2\bar{S}^2 \log \bar{S} + \frac{\bar{S}^2 \left(1 - \bar{S}^2 \left(4 - 3\bar{S}^2\right) - 2\left(1 + \bar{S}^4\right) \log \bar{S}\right)}{2\left(1 + \bar{S}^4\right)} \right). \tag{5.2.75}$$

The linear growth rate $\sigma_{1(1)}$ (5.2.75) is purely imaginary and does not affect the stability of the flow, therefore we must proceed to first order in k to obtain a form for $\sigma_{2(1)}$. However, to proceed to first order in k we need to determine the constants in the general solutions for $\phi_{0(1)}$ (5.2.71) and $\psi_{0(1)}$ (5.2.72). Therefore,

imposing the boundary conditions (5.2.64)–(5.2.68) we obtain

$$\phi_{0(1)} = \frac{S^*\bar{S}^2}{8\left(1+\bar{S}^4\right)}\Bigg[1+4\bar{S}^2-\bar{S}^4-\left(1+2\bar{S}^2\right)r^2 + \frac{\bar{S}^2\left(-2+\bar{S}^2\right)}{r^2}+2\left(1+\bar{S}^4\right)\log r\Bigg], \tag{5.2.76}$$

$$\psi_{0(1)} = \frac{iS^*\bar{S}^2}{8\left(1+\bar{S}^4\right)}\Bigg[-11+4\bar{S}^2-\bar{S}^4+\frac{16}{1+\bar{S}^2}+\left(11-2\bar{S}^2-\frac{16}{1+\bar{S}^2}\right)r^2 + \frac{\bar{S}^2\left(-2+\bar{S}^2\right)}{r^2}-2\left(1+\bar{S}^4\right)\log r\Bigg]. \tag{5.2.77}$$

The solutions (5.2.76) and (5.2.77) may be verified via direct substitution into (5.2.71) and (5.2.72).

At first order in k the governing equations (5.2.26) and (5.2.28) for $\phi_{1(1)}$ and $\psi_{1(1)}$ are

$$\begin{aligned}&-\frac{2i}{r^2}\frac{\mathrm{d}\phi_{1(1)}}{\mathrm{d}r}-\frac{1}{r^2}\frac{\mathrm{d}\psi_{1(1)}}{\mathrm{d}r}+\frac{2i}{r}\frac{\mathrm{d}^2\phi_{1(1)}}{\mathrm{d}r^2}+\frac{1}{r}\frac{\mathrm{d}^2\psi_{1(1)}}{\mathrm{d}r^2}+i\frac{\mathrm{d}^3\phi_{1(1)}}{\mathrm{d}r^3}\\ &=Re\left[\phi_{0(1)}\frac{\mathrm{d}\bar{w}}{\mathrm{d}r}+\left(i\sigma_{1(1)}-\bar{w}\right)\frac{\mathrm{d}\phi_{0(1)}}{\mathrm{d}r}-\frac{\left(\bar{w}-i\sigma_{1(1)}\right)\left(\phi_{0(1)}-i\psi_{0(1)}\right)}{r}\right],\end{aligned} \tag{5.2.78}$$

$$\begin{aligned}&\frac{1}{r}\frac{\mathrm{d}\phi_{1(1)}}{\mathrm{d}r}-\frac{2i}{r}\frac{\mathrm{d}\psi_{1(1)}}{\mathrm{d}r}-\frac{\mathrm{d}^2\phi_{1(1)}}{\mathrm{d}r^2}+2i\frac{\mathrm{d}^2\psi_{1(1)}}{\mathrm{d}r^2}+ir\frac{\mathrm{d}^3\psi_{1(1)}}{\mathrm{d}r^3}\\ &=-Re\left[\left(\phi_{0(1)}-i\psi_{0(1)}\right)\left(\sigma_{1(1)}+i\bar{w}\right)+r\left(\left(\bar{w}-i\sigma_{1(1)}\right)\frac{\mathrm{d}\psi_{0(1)}}{\mathrm{d}r}+\psi_{0(1)}\frac{\mathrm{d}\bar{w}}{\mathrm{d}r}\right)\right],\end{aligned} \tag{5.2.79}$$

subject to the boundary conditions

$$\phi_{1(1)}=\psi_{1(1)}=\frac{\mathrm{d}\phi_{1(1)}}{\mathrm{d}r}=0, \tag{5.2.80}$$

at the surface of the fibre, $r = 1$, (5.2.31) and

$$-i\phi_{1(1)} - \psi_{1(1)} + \bar{S}\frac{\mathrm{d}\psi_{1(1)}}{\mathrm{d}r} = 0, \tag{5.2.81}$$

$$\phi_{1(1)} - i\psi_{1(1)} - \bar{S}\left(\frac{\mathrm{d}\phi_{1(1)}}{\mathrm{d}r} - i\frac{\mathrm{d}\psi_{1(1)}}{\mathrm{d}r} + \bar{S}\frac{\mathrm{d}^2\phi_{1(1)}}{\mathrm{d}r^2}\right) = 0, \tag{5.2.82}$$

$$i\phi_{1(1)} + S^*\sigma_{2(1)} = 0, \tag{5.2.83}$$

$$\begin{aligned} Re\,\bar{S}\psi_{0(1)}\left(\sigma_{1(1)} + i\bar{w}\right) + \Gamma\,\bar{S}S^* + 2i\phi_{1(1)} + 2\psi_{1(1)} \\ - \bar{S}\left(2i\frac{\mathrm{d}\phi_{1(1)}}{\mathrm{d}r} + \frac{\mathrm{d}\psi_{1(1)}}{\mathrm{d}r} + \bar{S}\frac{\mathrm{d}^2\psi_{1(1)}}{\mathrm{d}r^2}\right) = 0, \end{aligned} \tag{5.2.84}$$

at the unperturbed free surface, $r = \bar{S}$, (5.2.32), (5.2.33), (5.2.35), and (5.2.38). The procedure for solving the system of equations (5.2.78)–(5.2.84) is the same as described previously for solving the system (5.2.62)–(5.2.68). However, due to the increased difficulty of the algebraic details, we consider the homogeneous and non-homogeneous problem of equations (5.2.78)–(5.2.79) separately. We begin with the homogeneous problem (i.e. when the right-hand side of equations (5.2.78)–(5.2.79) is equal to zero). We assume that the general solutions of the homogeneous problem can be expressed as an infinite series in powers of r and $\log r$, namely

$$\phi_{1(1)_{\mathrm{HS}}} = \sum_{i=-\infty}^{\infty}\sum_{j=0}^{\infty} C_{i,j} r^i \log^j r, \tag{5.2.85}$$

$$\psi_{1(1)_{\mathrm{HS}}} = \sum_{i=-\infty}^{\infty}\sum_{j=0}^{\infty} D_{i,j} r^i \log^j r, \tag{5.2.86}$$

where $C_{i,j}$ and $D_{i,j}$ are unknown constants. We substitute (5.2.85) and (5.2.86) into the homogeneous governing equations (5.2.78) and (5.2.79) and equate powers of r and $\log r$ to obtain the general homogeneous solutions

$$\phi_{1(1)_{\mathrm{HS}}} = C_{0,0} + C_{2,0}r^2 - \frac{iD_{-2,0}}{r^2} + iD_{0,1}\log r, \tag{5.2.87}$$

$$\psi_{1(1)_{\mathrm{HS}}} = D_{0,0} + D_{2,0}r^2 + \frac{D_{-2,0}}{r^2} + D_{0,1}\log r. \tag{5.2.88}$$

We now obtain the particular integral of the non-homogeneous problem. We assume that the general solutions of the non-homogeneous problem can be expressed

as an infinite series in powers of r and $\log r$, namely

$$\phi_{1(1)_{\rm PI}} = \sum_{i=0}^{\infty} \sum_{j=-\infty}^{\infty} E_{i,j} r^i \log^j r, \tag{5.2.89}$$

$$\psi_{1(1)_{\rm PI}} = \sum_{i=0}^{\infty} \sum_{j=-\infty}^{\infty} F_{i,j} r^i \log^j r, \tag{5.2.90}$$

where $E_{i,j}$ and $F_{i,j}$ are unknown constants. We substitute the (5.2.89) and (5.2.90) into the governing equations (5.2.78) and (5.2.79) and equate powers of r and $\log r$ to obtain

$$\begin{aligned}
\phi_{1(1)_{\rm PI}} = Re\, S^* \bar{S}^2 \Bigg[& - \frac{r^4}{4608\left(1+\bar{S}^2\right)\left(1+\bar{S}^4\right)} \Big\{ 24\left(3+3\bar{S}^2+4\bar{S}^4\right)\sigma_{1(1)} \\
& + i\left[-41+2r^2+40\bar{S}^2+2\left(8+r^2\right)\bar{S}^4+39\bar{S}^6\right] \Big\} \\
& + \frac{r^2 \log r}{384\left(1+\bar{S}^2\right)\left(1+\bar{S}^4\right)} \Big\{ 12\left(5+\bar{S}^2\right)\left(1+\bar{S}^4\right)\sigma_{1(1)} \\
& - i\Big[15+r^2-2\left(21+r^2\right)\bar{S}^2-2\left(3+r^2\right)\bar{S}^4 \\
& - 3\left(10+r^2\right)\bar{S}^6+3\bar{S}^8\Big] \Big\} \\
& - \frac{i\bar{S}^2 \log^2 r}{64}\left(\frac{2r^2}{1+\bar{S}^2}+\frac{\bar{S}^2\left(-2+\bar{S}^2\right)}{1+\bar{S}^4}\right) \Bigg],
\end{aligned} \tag{5.2.91}$$

$$\begin{aligned}
\psi_{1(1)_{\rm PI}} = Re\, S^* \bar{S}^2 \Bigg[& \frac{r^4}{4608\left(1+\bar{S}^2\right)\left(1+\bar{S}^4\right)} \Big\{ -24i\left(9-15\bar{S}^2+4\bar{S}^4\right)\sigma_{1(1)} \\
& - 113+202\bar{S}^2-182\bar{S}^4+39\bar{S}^6+2r^2\left(11-18\bar{S}^2+5\bar{S}^4\right) \Big\} \\
& + \frac{r^2 \log r}{384\left(1+\bar{S}^2\right)\left(1+\bar{S}^4\right)} \Big\{ -12i\left(-1+3\bar{S}^2\right)\left(1+\bar{S}^4\right)\sigma_{1(1)} \\
& + 3+30\bar{S}^2+6\bar{S}^4+6\bar{S}^6+15\bar{S}^8 \\
& + r^2\left(1-8\bar{S}^2+16\bar{S}^4-3\bar{S}^6\right) \Big\} \\
& + \frac{\bar{S}^4 \log^2 r}{64}\left(-\frac{2r^2}{1+\bar{S}^2}+\frac{2-\bar{S}^2}{1+\bar{S}^4}\right) \Bigg].
\end{aligned} \tag{5.2.92}$$

Thus, the governing equations (5.2.78) and (5.2.79) have the general solutions

$$\phi_{1(1)} = \phi_{1(1)_{\mathrm{HS}}} + \phi_{1(1)_{\mathrm{PI}}}, \tag{5.2.93}$$

$$\psi_{1(1)} = \psi_{1(1)_{\mathrm{HS}}} + \psi_{1(1)_{\mathrm{PI}}}. \tag{5.2.94}$$

We substitute the general solutions (5.2.93) and (5.2.94) into the boundary conditions (5.2.80)–(5.2.84) to obtain the matrix problem

$$A_{1(1)}\mathbf{x}_{1(1)} = \mathbf{0}, \tag{5.2.95}$$

where the matrix $A_{1(1)}$ is given in Appendix C.4, and

$$\mathbf{x}_{1(1)} = (C_{0,0}, C_{2,0}, D_{0,0}, D_{2,0}, D_{-2,0}, D_{0,1}, S^*)^{\mathrm{T}} \tag{5.2.96}$$

is the vector of unknowns. To obtain a non-trivial solution of the matrix problem (5.2.95), we set $\det(A_{1(1)}) = 0$ to obtain the dispersion relation for $\sigma_{2(1)}$. The dispersion relation for $\sigma_{2(1)}$ has solution

$$\begin{aligned}
\sigma_{2(1)} =& \frac{Re\bar{S}^2}{4608\left(1+\bar{S}^2\right)\left(1+\bar{S}^4\right)^3}\Bigg[13 + 188\bar{S}^2 - 326\bar{S}^4 + 1354\bar{S}^6 - 1452\bar{S}^8 \\
&+ 1742\bar{S}^{10} - 2142\bar{S}^{12} + 1426\bar{S}^{14} - 957\bar{S}^{16} + 154\bar{S}^{18} \\
&+ 6\bar{S}^2\left(1+\bar{S}^4\right)\Big(12 + 69\bar{S}^2 + 51\bar{S}^4 \\
&+ 308\bar{S}^6 - 120\bar{S}^8 + 139\bar{S}^{10} - 19\bar{S}^{12}\Big)\log\bar{S} \\
&- 36\bar{S}^4\left(1+\bar{S}^4\right)^2\left(9 - 13\bar{S}^2 + 5\bar{S}^4 + 3\bar{S}^6\right)\log^2\bar{S} \\
&+ 72\bar{S}^4\left(1+\bar{S}^2\right)\left(1+\bar{S}^4\right)^3\log^3\bar{S}\Bigg] \\
&+ \frac{\Gamma\bar{S}}{8\left(1+\bar{S}^4\right)}\left[\bar{S}^4 - 1 - 2\left(1+\bar{S}^4\right)\log\bar{S}\right].
\end{aligned} \tag{5.2.97}$$

The azimuthal curvature terms in $\sigma_{2(1)}$ (5.2.97) are always negative and so, unlike for the $n = 0$ mode, azimuthal curvature is stabilising for the $n = 1$ mode. The inertial terms in $\sigma_{2(1)}$ (5.2.97) can be either positive or negative and so, unlike for the $n = 0$ mode, there is a range of values of $\bar{S}$, Re, and Γ for which inertia is stabilising for the $n = 1$ mode. Note that this stabilising effect of inertia

only occurs for small axial wavenumbers (we will examine stability for general axial wavenumbers in Section 5.3.1). However, in general, increasing $\bar{S}$ and/or Re and/or decreasing Γ destabilises the $n = 1$ mode, which is analogous to the results of Ruiz-Chavarría and Dávalos-Orozco [215] in this limit (see Section 1.6.2).

5.3 Parametric study of the linear stability of the flow

In Sections 5.1.1 and 5.2.1 we have considered the linear stability of the flow for small axial wavenumbers. Whilst this allows us to obtain analytical expressions for the linear growth rates which describe the onset of long-wave instability, of course, this long-wave analysis cannot tell us anything about the behaviour for other larger axial wavenumbers. To rectify this, in the present section, we numerically investigate the linear stability of the flow for the $n = 0$ and $n = 1$ modes for general axial wavenumbers. In particular, we compare the predictions of the linear stability analysis of the flow described by the thick-film WRIBL equations (4.2.19) and (4.2.32) with the linear stability analysis of the flow described by the thick-film gradient-expansion equation (4.3.5), the thin-film gradient-expansion equation (4.3.7), and the Navier–Stokes equations (4.1.11)–(4.1.21), for general axial wavenumbers, for both the $n = 0$ and $n = 1$ modes.

5.3.1 Parametric study of the linear stability of the $n = 0$ mode

We begin our numerical investigation of the linear stability of the flow for general axial wavenumbers by examining the stability of the $n = 0$ mode.

Figure 5.2 shows the results of our parametric study of the linear stability of the $n = 0$ mode of the flow plotted in $\bar{S} - \Gamma$ parameter space for the thick-film WRIBL equations (4.2.19) and (4.2.32), the thick-film gradient-expansion equation (4.3.5), the thin-film gradient-expansion equation (4.3.7), and the Navier–Stokes equations (4.1.11)–(4.1.21). In particular, Figure 5.2 (trivially) shows that the $n = 0$ mode is always long-wave unstable (as correctly predicted by all models).

Figure 5.3 shows the real parts of the linear growth rate σ plotted as a function

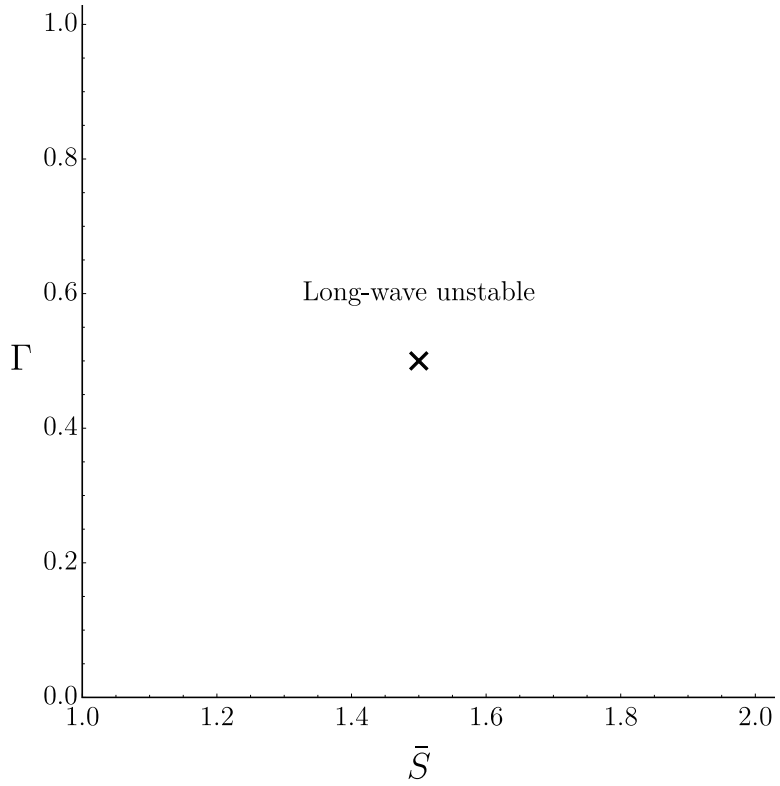

Figure 5.2: The results of our parametric study of the linear stability of the $n = 0$ mode of the flow plotted in $\bar{S} - \Gamma$ parameter space with $Re = 2$ for the thick-film WRIBL equations (4.2.19) and (4.2.32), the thick-film gradient-expansion equation (4.3.5), the thin-film gradient-expansion equation (4.3.7), and the Navier–Stokes equations (4.1.11)–(4.1.21). The cross corresponds to the parameter values used to plot the real parts of the linear growth rates in Figure 5.3.

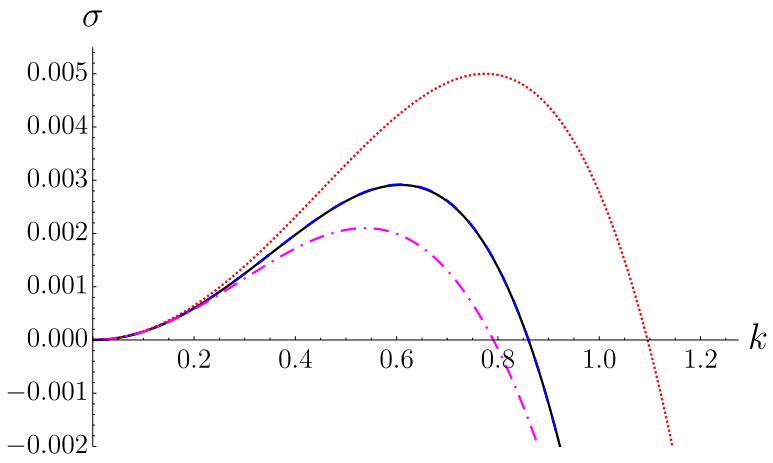

Figure 5.3: The real parts of the linear growth rate σ plotted as a function of k for the $n = 0$ mode for the thick-film WRIBL equations (4.2.19) and (4.2.32) (solid black), the thick-film gradient-expansion equation (4.3.5) (dashed blue), the thin-film gradient-expansion equation (4.3.7) (dotted red), and the Navier–Stokes equations (4.1.11)–(4.1.21) (dot-dashed purple) with $Re = 2$, $\Gamma = 0.5$, and $\bar{S} = 1.5$.

of k for the $n = 0$ mode for the thick-film WRIBL equations (4.2.19) and (4.2.32) (solid black), the thick-film gradient-expansion equation (4.3.5) (dashed blue), the thin-film gradient-expansion equation (4.3.7) (dotted red), and the Navier–Stokes equations (4.1.11)–(4.1.21) (dot-dashed purple). The parameter values used correspond to the point denoted by a cross in Figure 5.2, and each of the real parts of the linear growth rates in Figure 5.3 are long-wave unstable. As expected, for small k, the real parts of the linear growth rates are indistinguishable from each other. In particular, the agreement between the real parts of the linear growth rates of the thick-film WRIBL equations (4.2.19) and (4.2.32) and the Navier–Stokes equations (4.1.11)–(4.1.21) for small k in Figure 5.3 corroborates our analytical expressions for the linear growth rates for long waves in Sections 5.1.1 and 5.2.1 in which the linear growth rates for small axial wavenumbers for the thick-film WRIBL equations (5.1.12) and (5.1.13) and the Navier–Stokes equations (5.2.51) and (5.2.61) were shown to be identical for the $n = 0$ mode. As k is increased from $k = 0$, the real parts of the linear growth rates predicted by the thick-film WRIBL equations (4.2.19) and (4.2.32) and the thick-film gradient-expansion equation (4.3.5) are virtually indistinguishable, and are in good agreement with the real parts of the linear growth rates predicted by the Navier–Stokes equations (4.1.11)–(4.1.21), whereas the real parts of the linear growth rate for the thin-film gradient-expansion equation (4.3.7) overpredicts both the magnitude of the real

parts of the linear growth rate and the range of unstable axial wavenumbers.

5.3.2 Parametric study of the linear stability of the $n = 1$ mode

We now focus our attention on the $n = 1$ mode, for which we show that there are both stable and unstable regions of $\bar{S} - \Gamma$ parameter space.

Figure 5.4 shows plots of the results of our parametric study of the linear stability of the $n = 1$ mode in $\bar{S} - \Gamma$ parameter space, in which neutral stability curves are plotted for the thick-film WRIBL equations (4.2.19) and (4.2.32), the thick-film gradient-expansion equation (4.3.5), the thin-film gradient-expansion equation (4.3.7), and the Navier–Stokes equations (4.1.11)–(4.1.21). The stability boundaries in Figure 5.4 were obtained using the built-in `RegionPlot` function of the symbolic computational software Mathematica [229]. `RegionPlot` is used to visualise regions where an inequality is satisfied. In this case, the inequality is the real part of the linear growth rate being greater than or equal to zero. The linear growth rates for the thick-film WRIBL equations (4.2.19) and (4.2.32), the thick-film gradient-expansion equation (4.3.5), and the thin-film gradient-expansion equation (4.3.7) were input analytically. Conversely, the linear growth rate for the Navier–Stokes equations (4.1.11)–(4.1.21) was determined numerically using the Chebyshev–Tau method (see Appendix B). To verify the accuracy of these plots, we calculated the linear growth rates for the thick-film WRIBL equations (4.2.19) and (4.2.32), the thick-film gradient-expansion equation (4.3.5), the thin-film gradient-expansion equation (4.3.7), and the Navier–Stokes equations (4.1.11)–(4.1.21) at various points surrounding the stability boundaries in Figure 5.4. Figure 5.4(a) shows the neutral stability curves for the thick-film WRIBL equations (4.2.19) and (4.2.32), the thick-film gradient-expansion equation (4.3.5), and the thin-film gradient-expansion equation (4.3.7). The regions of $\bar{S} - \Gamma$ parameter space to the left and right of the neutral stability curves correspond to stability and long-wave instability, respectively, for the $n = 1$ mode. The neutral stability curves for the thick-film WRIBL equations (4.2.19) and (4.2.32) (solid) and the thick-film gradient-expansion equation (4.3.5) (dashed) are virtually indistinguishable. Figure 5.4(a) shows that, as $\bar{S}$ increases, the $n = 1$ mode is destabilised, whereas as Γ increases, the $n = 1$ mode is stabilised. Figure 5.4(b)

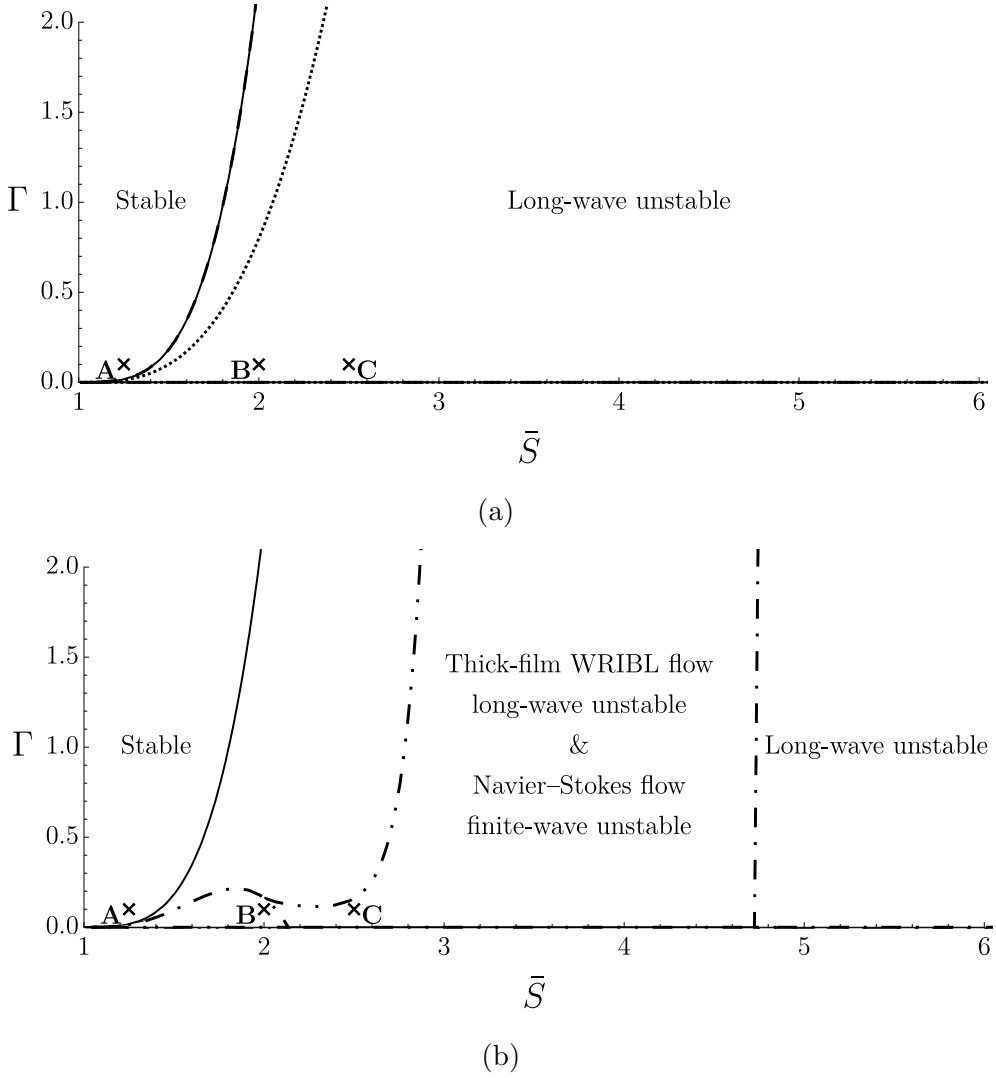

Figure 5.4: The results of our parametric study of the linear stability of the $n = 1$ mode of the flow plotted in $\bar{S} - \Gamma$ parameter space for $Re = 2$. Neutral stability curves are plotted for (a) the thick-film WRIBL equations (4.2.19) and (4.2.32) (solid), the thick-film gradient-expansion equation (4.3.5) (dashed), the thin-film gradient-expansion equation (4.3.7) (dotted), and (b) the thick-film WRIBL equations (4.2.19) and (4.2.32) (solid), the Navier–Stokes equations (4.1.11)–(4.1.21) for long-wave instabilities (dot-dashed), and the Navier–Stokes equations (4.1.11)–(4.1.21) for finite-wave instabilities (dot-dot-dashed). The crosses (labelled A, B, and C) correspond to the parameter values used to plot the real parts of the linear growth rates in Figure 5.5.

shows the neutral stability curves for the thick-film WRIBL equations (4.2.19) and (4.2.32) and the Navier–Stokes equations (4.1.11)–(4.1.21). Figure 5.4(b) shows that, for the $n = 1$ mode, the flow described by the Navier–Stokes equations (4.1.11)–(4.1.21) is stable for parameter values in the region containing point A, long-wave unstable for parameter values in the region containing point B, finite-wave unstable for parameter values in the region containing point C, and long-wave unstable in the region to the right of the dot-dashed curve (which is nearly vertical) that emanates from $\bar{S} \approx 4.725$, $\Gamma = 0$. In particular, Figure 5.4(b) shows that for the flow described by the Navier–Stokes equations (4.1.11)–(4.1.21), there are two distinct regions of long-wave instability, separated by a region of finite-wave instability, whereas, for the thick-film WRIBL equations (4.2.19) and (4.2.32), the instability is always long wave. While the flow described by the Navier–Stokes equations (4.1.11)–(4.1.21) is, in general, also stabilised by decreasing $\bar{S}$ and/or increasing Γ, there exists a region of $\bar{S} - \Gamma$ parameter space in Figure 5.4(b) where this is not the case. Specifically, the parameter values surrounding point B exhibit a non-monotonic stability boundary along the $\bar{S}$ axis. For $\sigma_{2(1)}$ given by (5.2.97), we have already seen that both the inertial and surface tension terms stabilise long waves for a range of values of $\bar{S}$, Re, and Γ, specifically the parameter values containing point C in Figure 5.4(b), however waves of a finite length are still unstable. The thick-film WRIBL equations (4.2.19) and (4.2.32) overpredict the range of unstable parameter values when compared with the Navier–Stokes equations (4.1.11)–(4.1.21).

Figure 5.5 shows the real parts of the linear growth rate σ plotted as a function of k for the $n = 1$ mode for the thick-film WRIBL equations (4.2.19) and (4.2.32) (solid black), the thick-film gradient-expansion equation (4.3.5) (dashed blue), the thin-film gradient-expansion equation (4.3.7) (dotted red), and the Navier–Stokes equations (4.1.11)–(4.1.21) (dot-dashed purple) for various values of $\bar{S}$. The parameter values used in Figure 5.5 correspond to the points A, B, and C denoted by the crosses in Figure 5.4. In particular, each part of Figure 5.5 shows one of the three possible behaviours we observe for the real parts of the linear growth rate of the flow described by the Navier–Stokes equations (4.1.11)–(4.1.21) (i.e. stability, long-wave instability, and finite-wave instability, as shown in Figure 5.1). Figure 5.5(a) shows a situation in which each of the real parts of the linear growth rates are stable for all k. For larger values of $\bar{S}$, Figure 5.5(b) shows a

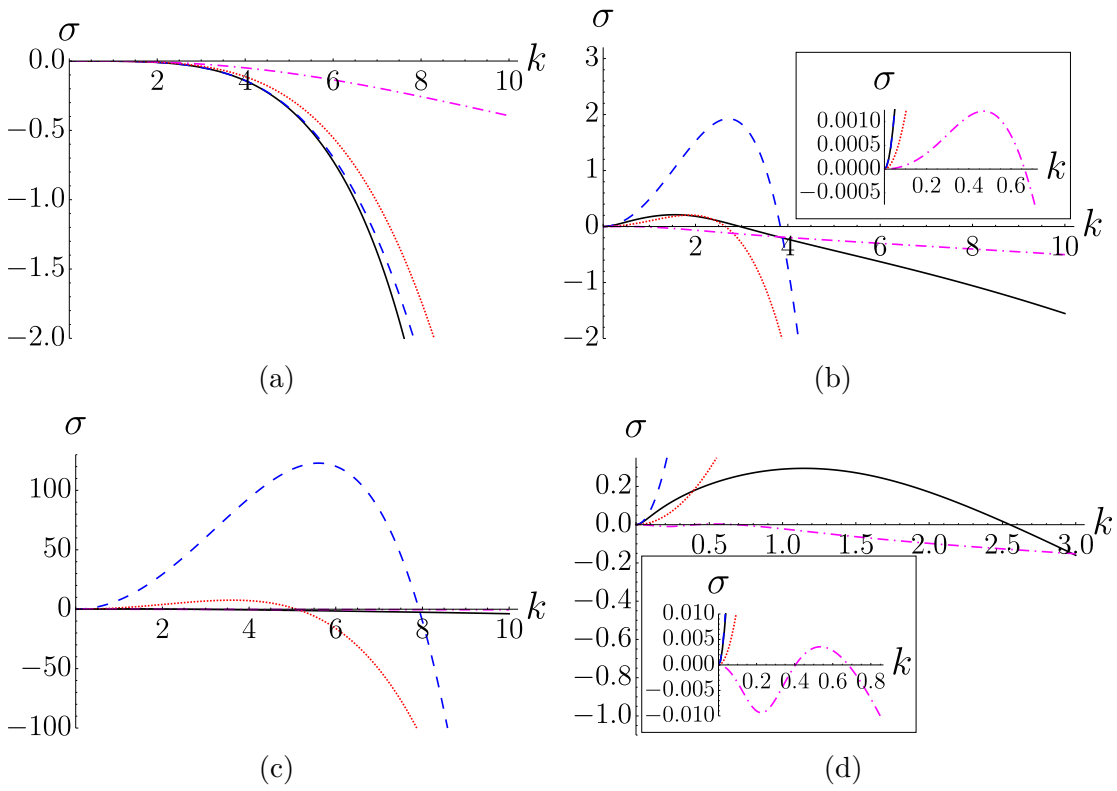

Figure 5.5: The real parts of the linear growth rate σ plotted as a function of k for the $n = 1$ mode for the thick-film WRIBL equations (4.2.19) and (4.2.32) (solid black), the thick-film gradient-expansion equation (4.3.5) (dashed blue), the thin-film gradient-expansion equation (4.3.7) (dotted red), and the Navier–Stokes equations (4.1.11)–(4.1.21) (dot-dashed purple) with $Re = 2$, $\Gamma = 0.1$ for (a) $\bar{S} = 1.25$, (b) $\bar{S} = 2$, (c) $\bar{S} = 2.5$, and (d) a zoom of (c). In (b) and (d) the insets show a zoom showing the real parts of the linear growth rates near $k = 0$ in greater detail. Note that the scale of the vertical axis is different in each part and also that the horizontal axis scale in part (d) is different from the horizontal axis scale in parts (a), (b), and (c).

situation in which each of the real parts of the linear growth rates are long-wave unstable. The real parts of the linear growth rates predicted by the thick-film WRIBL equations (4.2.19) and (4.2.32), the thick-film gradient-expansion equation (4.3.5), and the thin-film gradient-expansion equation (4.3.7) overpredict both the magnitude of the real parts of the linear growth rate and the range of unstable axial wavenumbers when compared to that predicted by the Navier–Stokes equations (4.1.11)–(4.1.21). For an even larger value of $\bar{S}$, Figures 5.5(c) and 5.5(d) show an example of a case where the real parts of the linear growth rate predicted by the Navier–Stokes equations (4.1.11)–(4.1.21) are finite-wave unstable, while those predicted by the thick-film WRIBL equations (4.2.19) and (4.2.32), the thick-film gradient-expansion equation (4.3.5), and the thin-film gradient-expansion equation (4.3.7) are long-wave unstable. The real parts of the linear growth rates predicted by the thick-film WRIBL equations (4.2.19) and (4.2.32), the thick-film gradient-expansion equation (4.3.5), and the thin-film gradient-expansion equation (4.3.7) are in poor agreement with that predicted by the Navier–Stokes equations (4.1.11)–(4.1.21). In particular, the Navier–Stokes equations (4.1.11)–(4.1.21) predict a finite-wave instability which none of the other models are able to capture.

The results of the parametric study of the linear stability of the $n = 1$ mode in Figure 5.4(b) show that the thick-film WRIBL equations (4.2.19) and (4.2.32) significantly overpredict the range of unstable parameter values when compared with the Navier–Stokes equations (4.1.11)–(4.1.21). In Section 6.2.2, we suggest potential improvements to the thick-film WRIBL equations (4.2.19) and (4.2.32) as future work to enhance their agreement with the Navier–Stokes equations (4.1.11)–(4.1.21) in the linear and nonlinear regimes. Despite the discrepancy observed, the thick-film WRIBL equations (4.2.19) and (4.2.32) do, in general, correctly predict the effect that increasing $\bar{S}$ and Γ has on the stability of the $n = 1$ mode. Therefore, in order to gain insight into the mechanisms for the (in)stability of the $n = 0$ and $n = 1$ modes, we use the thick-film WRIBL equations (4.2.19) and (4.2.32) to implement the Whitham wave hierarchy (see Section 1.2.2).

5.4 Whitham wave hierarchy

In Section 5.3 we have performed a numerical parametric study of the linear stability of the flow described by the thick-film WRIBL equations (4.2.19) and

(4.2.32), the thick-film gradient-expansion equation (4.3.5), the thin-film gradient-expansion equation (4.3.7), and the Navier–Stokes equations (4.1.11)–(4.1.21), for general axial wavenumbers. From this study, we have found that the $n = 0$ mode is always long-wave unstable, whereas, depending on the choice of parameter values, the $n = 1$ mode can either be stable or long-wave unstable (or finite-wave unstable in the case of the Navier–Stokes equations (4.1.11)–(4.1.21)). In particular, the $n = 1$ mode is stabilised by increasing Γ and/or decreasing $\bar{S}$. In order to gain insight into the mechanisms for the (in)stability of the $n = 0$ and $n = 1$ modes, we derive explicit expressions for the kinematic and dynamic wave speeds for these modes and use the framework of the Whitham wave hierarchy (discussed in Section 1.2.2).

In order to implement the Whitham wave hierarchy, we require a single linear equation for the film radius of the general form (1.2.21) (i.e. with time and space derivatives of second order). From the equations describing the flow we have considered thus far in the present chapter, only the thick-film WRIBL equations (4.2.19) and (4.2.32) can be linearised around a constant base-state solution and then rewritten in the form of equation (1.2.21) (see Section 1.2.2). To begin, we decompose S and q in the thick-film WRIBL equations (4.2.19) and (4.2.32) as

$$S(\theta, z, t) = \bar{S} + \xi \breve{S}(\theta, z, t), \tag{5.4.1}$$

$$q(\theta, z, t) = \bar{q} + \xi \breve{q}(\theta, z, t), \tag{5.4.2}$$

where $\xi \ll 1$, terms with an overbar denote the base-state solutions (in particular, with $\bar{q}$ given by (5.1.3)) and the terms with checks denote the perturbations to the base-state solutions. Next, we substitute (5.4.1) and (5.4.2) into the thick-film WRIBL equations (4.2.19) and (4.2.32). At first order in ξ, we differentiate the expression arising from equation (4.2.32) with respect to z and use the expression arising from equation (4.2.19) to eliminate $\partial\breve{q}/\partial z$ (and thus also eliminating $\breve{q}$) to leave a single equation for $\breve{S}$. In order to investigate the behaviour of a single azimuthal mode, we set

$$\breve{S}(\theta, z, t) = S'(z, t)\mathrm{e}^{in\theta}. \tag{5.4.3}$$

Note that in order to simplify the algebra, we have decomposed θ using normal modes but not z and t. Finally, we will only consider the cases in which $n = 0$

and $n = 1$, namely

$$\alpha_1 \frac{\partial S'}{\partial t} + Re\,\alpha_2 \frac{\partial^2 S'}{\partial t^2} + \alpha_3 \frac{\partial S'}{\partial z} + Re\,\alpha_4 \frac{\partial^2 S'}{\partial z \partial t} + (\Gamma\,\alpha_5 + Re\,\alpha_6) \frac{\partial^2 S'}{\partial z^2} + \Gamma\,\alpha_7 \frac{\partial^4 S'}{\partial z^4} = 0 \tag{5.4.4}$$

when $n = 0$, and

$$\begin{aligned} \alpha_1 \frac{\partial S'}{\partial t} + Re\,\alpha_2 \frac{\partial^2 S'}{\partial t^2} + \alpha_3 \frac{\partial S'}{\partial z} + Re\,\alpha_4 \frac{\partial^2 S'}{\partial z \partial t} - (\Gamma\,\beta_5 - Re\,\alpha_6) \frac{\partial^2 S'}{\partial z^2} \\ + \Gamma\,\alpha_7 \frac{\partial^4 S'}{\partial z^4} - Re\,\Gamma\,\beta_8 \frac{\partial^3 S'}{\partial z^2 \partial t} - Re\,\Gamma\,\beta_9 \frac{\partial^3 S'}{\partial z^3} = 0 \end{aligned} \tag{5.4.5}$$

when $n = 1$, where

$$\alpha_1(\bar{S}) = \bar{S}, \tag{5.4.6}$$

$$\alpha_2(\bar{S}) = \frac{\bar{S}\left(\bar{q}_1 + \bar{q}_2 \bar{S}^2\right)}{\bar{q}_0}, \tag{5.4.7}$$

$$\alpha_3(\bar{S}) = \frac{\bar{S} - \bar{S}^3 + 2\bar{S}^3 \log \bar{S}}{2}, \tag{5.4.8}$$

$$\begin{aligned} \alpha_4(\bar{S}) = & \frac{\bar{S}\left[\bar{q}_1 - 4\bar{q}_0\bar{q}_2 + 2\bar{q}_5 + \bar{S}^2\left(-\bar{q}_1 + \bar{q}_2 + 2\left(\bar{q}_3 + \bar{q}_6\right)\right) - \bar{S}^4\left(\bar{q}_2 - 2\bar{q}_4\right)\right]}{2\bar{q}_0} \\ & + \frac{\bar{S}^3\left(\bar{q}_1 + \bar{q}_2\bar{S}^2\right)\log \bar{S}}{\bar{q}_0}, \end{aligned} \tag{5.4.9}$$

$$\alpha_5(\bar{S}) = \frac{\bar{q}_0}{\bar{S}^2}, \tag{5.4.10}$$

$$\alpha_6(\bar{S}) = -\frac{\bar{S}\left[4\bar{q}_0\left(\bar{q}_3 + \bar{q}_4\bar{S}^2\right) + \left(-1 + \bar{S}^2 - 2\bar{S}^2\log \bar{S}\right)\left(\bar{S}^2\left(\bar{q}_3 + \bar{q}_6\right) + \bar{q}_4\bar{S}^4 + \bar{q}_5\right)\right]}{2\bar{q}_0}, \tag{5.4.11}$$

$$\alpha_7(\bar{S}) = \bar{q}_0, \tag{5.4.12}$$

$$\beta_5(\bar{S}) = \frac{-1 + \bar{S}^4 - 4\bar{S}^2 \log \bar{S}}{8}, \tag{5.4.13}$$

$$\beta_8(\bar{S}) = \frac{\left(\bar{q}_1 + \bar{q}_2\bar{S}^2\right)\left(-1 + \bar{S}^4 - 4\bar{S}^2\log \bar{S}\right)}{8\bar{q}_0}, \tag{5.4.14}$$

$$\beta_9(\bar{S}) = \frac{\left[\bar{q}_5 + \bar{S}^2\left(\bar{q}_3 + \bar{q}_6 + \bar{q}_4\bar{S}^2\right)\right]\left(-1 + \bar{S}^4 - 4\bar{S}^2\log \bar{S}\right)}{8\bar{q}_0} \tag{5.4.15}$$

are positive functions of $\bar{S}$, where $\bar{q}_k$ are the base-state solutions of q_k, given by (4.2.33), for $k = 0, 1, \ldots, 6$.

5.4.1 Wave speed for small axial wavenumbers

As shown in Section 5.3, the mode of instability for the flow described by the thick-film WRIBL equations (4.2.19) and (4.2.32) is long-wave instability. To determine the mechanism for this instability, we first consider explicit expressions for the kinematic and dynamic wave speeds for the case of small axial wavenumbers. Following Ruyer-Quil et al. [64], to study the behaviour of small axial wavenumbers, for the time being we discard the third and fourth-order derivatives in equations (5.4.4) and (5.4.5), which are negligible for small axial wavenumbers. However, we include these terms in Section 5.4.2 where we obtain explicit expressions for the kinematic and dynamic wave speeds for the case of general axial wavenumbers.

5.4.1.1 $n = 0$ mode for small axial wavenumbers

We begin by considering the $n = 0$ mode for small axial wavenumbers. We begin by discarding third and fourth-order derivatives in order to rewrite equation (5.4.4) in the form of equation (1.2.21) as

$$\alpha_1 \left(\frac{\partial}{\partial t} + c_k \frac{\partial}{\partial z} \right) S' + Re\, \alpha_2 \left(\frac{\partial}{\partial t} + c_{d_-} \frac{\partial}{\partial z} \right) \left(\frac{\partial}{\partial t} + c_{d_+} \frac{\partial}{\partial z} \right) S' = 0, \tag{5.4.16}$$

with kinematic wave speed

$$c_k = \frac{\alpha_3}{\alpha_1} \tag{5.4.17}$$

and dynamic wave speeds

$$c_{d_\pm} = \frac{\alpha_4}{2\alpha_2} \pm \sqrt{\frac{\alpha_4^2}{4\alpha_2^2} - \frac{\Gamma\, \alpha_5}{Re\, \alpha_2} - \frac{\alpha_6}{\alpha_2}}. \tag{5.4.18}$$

In the present section, we denote all wave speeds by c and specify the particular wave speed (i.e. kinematic or dynamic) with a subscript. For a planar geometry, the dynamic wave speeds $c_{d_\pm}$ are purely real [59; 65; 66; 97–99]. However, for a fibre, the dynamic wave speeds $c_{d_\pm}$ for the $n = 0$ mode, given by (5.4.18), can have both real and imaginary parts due to the effect of the azimuthal curvature [64] (i.e. the term α_5 in (5.4.18)). The Whitham wave hierarchy can only be applied when the wave speeds are purely real, therefore we do not attempt to apply the Whitham wave hierarchy in any region of parameter space in which the wave speeds become complex.

Figure 5.6(a) shows the real parts of the linear growth rate σ plotted as a function of k for the $n = 0$ mode for the thick-film WRIBL equations (4.2.19) and (4.2.32) with $\bar{S} = 2$ which is long-wave unstable. Figure 5.6(b) shows the wave speed c as a function of $\bar{S}$ for the $n = 0$ mode, specifically the kinematic wave speed c_k (5.4.17) (solid black) and the dynamic wave speeds c_{d_+} and c_{d_-} (5.4.18) (dot-dashed blue and dot-dashed red, respectively). The dynamic wave speeds in Figure 5.6(b) emanate from $\bar{S} \approx 2.39$ and $\Gamma \approx 1.14$. Dynamic wave speeds are complex to the left of this point, and thus the Whitham wave hierarchy is not applicable. However, our previous results in the present chapter have confirmed that the $n = 0$ mode is always long-wave unstable. Therefore, when the Whitham wave hierarchy is not applicable, we need to determine the real part of the linear growth rate σ directly, as demonstrated in Figure 5.6(a). Figure 5.6(b) shows that the kinematic wave speed (5.4.17) is always greater than the dynamic wave speeds (5.4.18) (when the dynamic wave speeds are purely real), which violates the stability criterion (1.2.24), and thus the $n = 0$ mode for the flow described by the thick-film WRIBL equations (4.2.19) and (4.2.32) is long-wave unstable.

To confirm the general results given above, we now consider the behaviour of the kinematic wave speed (5.4.17) and the dynamic wave speeds (5.4.18) in the limit of a thin base state ($\bar{S} \to 1^+$), and in the limit of a thick base state ($\bar{S} \to \infty$). For a thin base state

$$c_k \sim (-1 + \bar{S})^2 \quad \text{in the limit} \quad \bar{S} \to 1^+, \tag{5.4.19}$$

however, in this limit, the dynamic wave speeds are complex and the Whitham wave hierarchy is not applicable. For a thick base state

$$c_k \sim \bar{S}^2 \log \bar{S} \quad \text{and} \quad c_{d_\pm} \sim \frac{1}{2}\bar{S}^2 \log \bar{S} \quad \text{in the limit} \quad \bar{S} \to \infty, \tag{5.4.20}$$

which clearly violates the stability criterion (1.2.24). The wave speeds in the limit of a thin base state (5.4.19) and in the limit of a thick base state (5.4.20) are independent of both surface tension and inertia, and are therefore purely gravity driven. In particular, for a thin base state, the base-state solution for the axial velocity (5.2.12) at the unperturbed free surface, $r = \bar{S}$, is

$$\bar{w} \sim \frac{(-1 + \bar{S})^2}{2} \quad \text{in the limit} \quad \bar{S} \to 1^+, \tag{5.4.21}$$

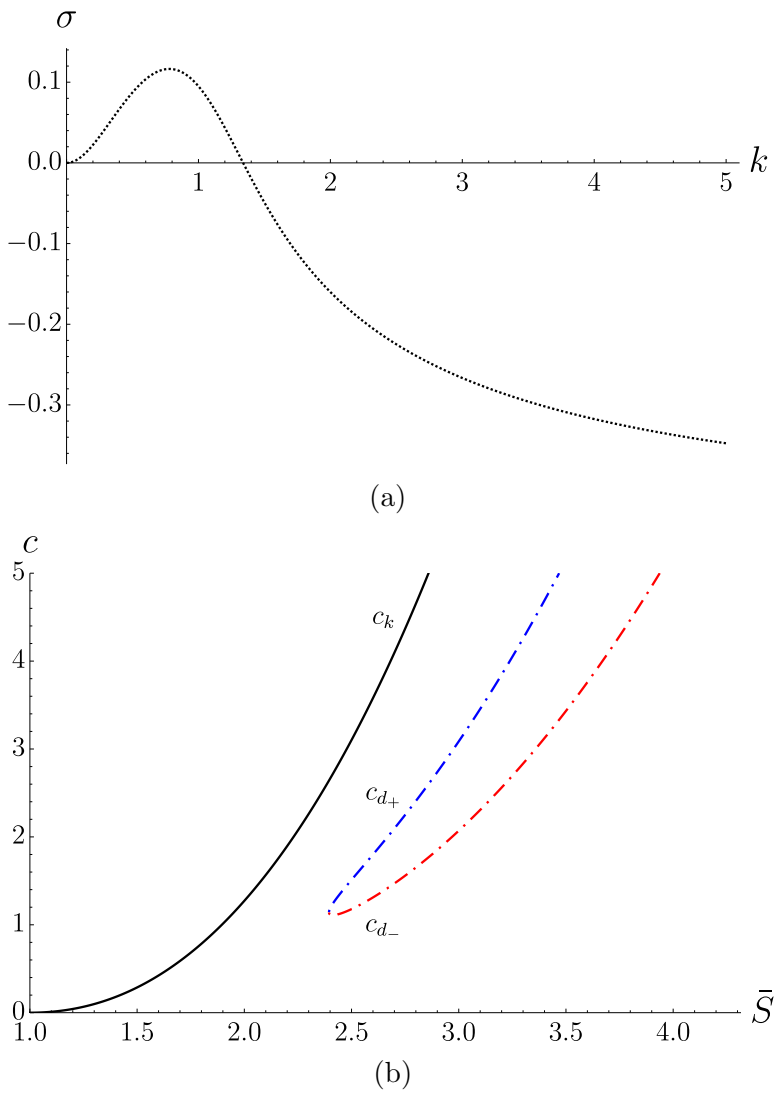

Figure 5.6: (a) The real parts of the linear growth rate σ plotted as a function of k for the $n = 0$ mode for the thick-film WRIBL equations (4.2.19) and (4.2.32) for $\bar{S} = 2$, $Re = 2$, and $\Gamma = 1$. (b) The wave speed c as a function of $\bar{S}$ for the $n = 0$ mode, specifically the kinematic wave c_k (5.4.17) (solid black) and the dynamic wave speeds c_{d_+} and c_{d_-} (5.4.18) (dot-dashed blue and dot-dashed red, respectively), for $Re = 2$ and $\Gamma = 1$.

which is half of the kinematic wave speed in the limit of a thin base state (5.4.19). Additionally, in the limit of a thick base state, the base-state solution for the axial velocity (5.2.12) at the unperturbed free surface, $r = \bar{S}$, is

$$\bar{w} \sim \frac{1}{2}\bar{S}^2 \log \bar{S} \quad \text{in the limit} \quad \bar{S} \to \infty, \tag{5.4.22}$$

which is half of the kinematic wave speed in the limit of a thick base state and equal to the dynamic wave speeds in the limit of a thick base state (5.4.20).

The stability criterion (1.2.24) for the $n = 0$ mode can be recast as a stability criterion based on the ratio Γ/Re, which measures the relative importance of surface tension compared to inertia. The kinematic wave speed c_k (5.4.17) and the dynamic wave speed c_{d_+} (5.4.18) can be substituted into the stability criterion (1.2.24) to yield the stability criterion

$$\frac{\Gamma}{Re} \leq \zeta_{(0)}, \quad \text{where} \quad \zeta_{(0)} = -\frac{\alpha_2}{\alpha_5}\left(\left(\frac{\alpha_3}{\alpha_1} - \frac{\alpha_4}{2\alpha_2}\right)^2 + \frac{\alpha_6}{\alpha_2} - \frac{\alpha_4^2}{2\alpha_2^2}\right) \leq 0, \tag{5.4.23}$$

for the $n = 0$ mode. In particular, equation (5.4.23) confirms that the $n = 0$ mode is long-wave unstable for all (physically reasonable) values of Γ/Re.

5.4.1.2 $n = 1$ mode for small axial wavenumbers

Now we consider the $n = 1$ mode for small axial wavenumbers. Again, discarding third and fourth-order derivatives, equation (5.4.5) can be rewritten in the form of equation (1.2.21) as

$$\alpha_1\left(\frac{\partial}{\partial t} + c_k\frac{\partial}{\partial z}\right)S' + Re\,\alpha_2\left(\frac{\partial}{\partial t} + c_{d_-}\frac{\partial}{\partial z}\right)\left(\frac{\partial}{\partial t} + c_{d_+}\frac{\partial}{\partial z}\right)S' = 0, \tag{5.4.24}$$

with kinematic wave speed

$$c_k = \frac{\alpha_3}{\alpha_1} \tag{5.4.25}$$

and dynamic wave speeds

$$c_{d_\pm} = \frac{\alpha_4}{2\alpha_2} \pm \sqrt{\frac{\alpha_4^2}{4\alpha_2^2} + \frac{\Gamma\,\beta_5}{Re\,\alpha_2} - \frac{\alpha_6}{\alpha_2}}. \tag{5.4.26}$$

The dynamic wave speeds (5.4.26) for the $n = 1$ mode are purely real for all $\bar{S}$, unlike the previous case for the $n = 0$ mode in Section 5.4.1.1.

Figure 5.7(a) shows the real parts of the linear growth rate σ plotted as a function of k for the $n = 1$ mode for the thick-film WRIBL equations (4.2.19) and (4.2.32), showing that the solid curve for $\bar{S} = 1.5$ is stable and the dotted curve for $\bar{S} = 2.5$ is long-wave unstable. Figure 5.7(b) shows the wave speed c as a function of $\bar{S}$ for the $n = 1$ mode, specifically the kinematic wave speed c_k (5.4.25) (solid black) and the dynamic wave speeds c_{d_+} and c_{d_-} (5.4.26) (dot-dashed blue and dot-dashed red, respectively). For values of $\bar{S}$ to the left of the vertical dashed line at $c_k = c_{d_+}$ shown in Figure 5.7(b), the kinematic wave speed c_k (5.4.25) lies between the two dynamic wave speeds c_{d_+} and c_{d_-} (5.4.26), and satisfies the stability criterion (1.2.24). This agrees with the solid curve for $\bar{S} = 1.5$ in Figure 5.7(a) which shows stability. Conversely, for values of $\bar{S}$ to the right of the vertical dashed line at $c_k = c_{d_+}$ shown in Figure 5.7(b), the kinematic wave speed c_k (5.4.25) is greater than the dynamic wave speeds c_{d_+} and c_{d_-} (5.4.26), and violates the stability criterion (1.2.24). This agrees with the dotted curve for $\bar{S} = 2.5$ in Figure 5.7(a) which shows long-wave instability.

To confirm the general results given above, we now consider the behaviour of the kinematic wave speed (5.4.25) and the dynamic wave speeds (5.4.26) in the limit of a thin base state ($\bar{S} \to 1^+$), and in the limit of a thick base state ($\bar{S} \to \infty$). For a thin base state

$$c_k \sim (-1 + \bar{S})^2 \quad \text{and} \quad c_{d_\pm} \sim \pm\sqrt{\frac{5\Gamma}{6Re}(-1 + \bar{S})} \quad \text{in the limit} \quad \bar{S} \to 1^+, \tag{5.4.27}$$

which satisfies the stability criterion (1.2.24) when

$$\frac{\Gamma}{Re} \geq \frac{6(-1 + \bar{S})^3}{5}, \tag{5.4.28}$$

while for a thick base state

$$c_k \sim \bar{S}^2 \log \bar{S} \quad \text{and} \quad c_{d_\pm} \sim \frac{1}{2}\bar{S}^2 \log \bar{S} \quad \text{in the limit} \quad \bar{S} \to \infty, \tag{5.4.29}$$

which violates the stability criterion (1.2.24). Thus, the stability criterion (1.2.24) is satisfied in the limit of a thin base state, but is violated in the limit of a thick base state, confirming the results given in Figure 5.7. The wave speeds in the limit

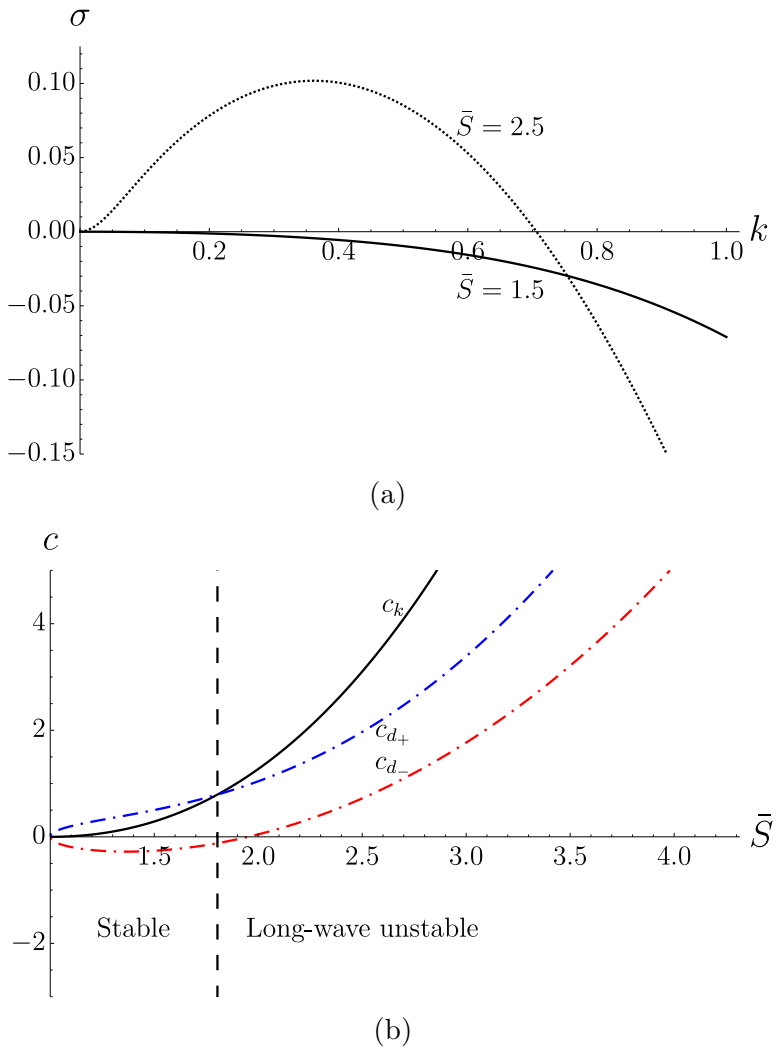

Figure 5.7: (a) The real parts of the linear growth rate σ plotted as a function of k for the $n = 1$ mode for the thick-film WRIBL equations (4.2.19) and (4.2.32) with $\bar{S} = 1.5$ (solid) and $\bar{S} = 2.5$ (dotted) for $Re = 2$ and $\Gamma = 1$. (b) The wave speed c as a function of $\bar{S}$ for the $n = 1$ mode, specifically the kinematic wave c_k (5.4.25) (solid black) and the dynamic wave speeds c_{d_+} and c_{d_-} (5.4.26) (dot-dashed blue and dot-dashed red, respectively), for $Re = 2$ and $\Gamma = 1$, where the vertical dashed line at $c_k = c_{d_+}$ (i.e. at $\bar{S} \approx 1.804$) denotes the transition from stable values of $\bar{S}$ to long-wave unstable values of $\bar{S}$.

of a thick base state for the $n = 1$ mode (5.4.29) are identical to those for the $n = 0$ mode (5.4.20), and are purely gravity driven. However, in the limit of a thin base state, only the kinematic wave speed is identical for both the $n = 1$ mode (5.4.27) and the $n = 0$ mode (5.4.19). The dynamic wave speeds in the limit of a thin base state for the $n = 1$ mode (5.4.27) are a function of Γ and Re and the $n = 1$ mode is stable in this limit when (5.4.28) is satisfied.

Again, the stability criterion (1.2.24) for the $n = 1$ mode can be recast as a stability criterion based on the ratio Γ/Re. The kinematic wave speed c_k (5.4.25) and the dynamic wave speed c_{d_+} (5.4.26) can be substituted into the stability criterion (1.2.24) to yield the stability criterion

$$\frac{\Gamma}{Re} \geq \zeta_{(1)}, \quad \text{where} \quad \zeta_{(1)} = \frac{\alpha_2}{\beta_5}\left(\left(\frac{\alpha_3}{\alpha_1} - \frac{\alpha_4}{2\alpha_2}\right)^2 + \frac{\alpha_6}{\alpha_2} - \frac{\alpha_4^2}{2\alpha_2^2}\right) \geq 0, \qquad (5.4.30)$$

for the $n = 1$ mode. In particular, equation (5.4.30) confirms that the $n = 1$ mode is stable when the effects of surface tension dominate the effects of inertia.

5.4.1.3 Mechanisms for (in)stability

We now compare the predictions of the Whitham wave hierarchy in order to determine the mechanisms for (in)stability of the $n = 0$ and $n = 1$ modes. As shown in Sections 5.4.1.1 and 5.4.1.2, the kinematic wave speed is identical for both the $n = 0$ mode (5.4.17) and the $n = 1$ mode (5.4.25), whereas the dynamic wave speeds for the $n = 0$ mode (5.4.18) and the $n = 1$ mode (5.4.26) differ by a single term, namely the second term in the square root, which corresponds to the effect of azimuthal curvature. Specifically, for the $n = 0$ mode (5.4.18) the azimuthal curvature term includes "$-\alpha_5$" which is replaced by "$+\beta_5$" for the $n = 1$ mode (5.4.26). The difference in the sign of these terms reveals the opposing effects that the azimuthal curvature has on the two modes. For the $n = 0$ mode, the azimuthal curvature decreases the speed of c_{d_+} and increases the speed of c_{d_-}, which narrows the range of stability (1.2.24), and conversely, for the $n = 1$ mode, the azimuthal curvature increases the speed of c_{d_+} and decreases the speed of c_{d_-}, which widens the range of stability (1.2.24). Therefore, the azimuthal curvature is the key mechanism for both the long-wave instability for the $n = 0$ mode and for the (in)stability of the $n = 1$ mode. This stabilising effect is confirmed by the limits of

a thin base state (5.4.27) and a thick base state (5.4.29) for the $n = 1$ mode. For the former, the azimuthal curvature is large and thus the stabilising effect on the $n = 1$ mode is amplified, whereas for the latter, the azimuthal curvature is small and thus the stabilising effect of the azimuthal curvature is diminished.

5.4.2 Wave speed for general axial wavenumbers

In Section 5.4.1, following Ruyer-Quil et al. [64], we considered the kinematic and dynamic wave speeds for small axial wavenumbers. While this has allowed us to determine that the azimuthal curvature is the key mechanism for the onset of the long-wave instability, we have not taken into account how the third and fourth-order derivatives in equations (5.4.4) and (5.4.5) affect the kinematic and dynamic wave speeds for general axial wavenumbers.

5.4.2.1 $n = 0$ mode for general axial wavenumbers

We begin by considering the $n = 0$ mode. In the same way as in Section 5.4.1, equation (5.4.4) can be rewritten as

$$\alpha_1 \left(\frac{\partial}{\partial t} + c_k \frac{\partial}{\partial z} \right) S' + Re\, \alpha_2 \left(\frac{\partial}{\partial t} + c_{d_-} \frac{\partial}{\partial z} \right) \left(\frac{\partial}{\partial t} + c_{d_+} \frac{\partial}{\partial z} \right) S' + \Gamma\, \alpha_7 \frac{\partial^4 S'}{\partial z^4} = 0. \tag{5.4.31}$$

While equation (5.4.31) is not currently of the form of equation (1.2.21), it can be recast into this form. To re-write equation (5.4.31) we set $S'(z,t) = S''(t)\mathrm{e}^{ikz}$ in order to express the fourth-order derivative as a second order derivative (i.e. by setting $\partial^4/\partial z^4 = -k^2 \partial^2/\partial z^2$) and then present the resulting equation in terms of $S'(z,t)$ to yield

$$\alpha_1 \left(\frac{\partial}{\partial t} + c_k \frac{\partial}{\partial z} \right) S' + Re\, \alpha_2 \left(\frac{\partial}{\partial t} + c_{d_-} \frac{\partial}{\partial z} \right) \left(\frac{\partial}{\partial t} + c_{d_+} \frac{\partial}{\partial z} \right) S' - k^2 \Gamma\, \alpha_7 \frac{\partial^2 S'}{\partial z^2} = 0. \tag{5.4.32}$$

Therefore, equation (5.4.32) can now be written in the form of equation (1.2.21) as

$$\alpha_1 \left(\frac{\partial}{\partial t} + c_k \frac{\partial}{\partial z} \right) S' + Re\, \alpha_2 \left(\frac{\partial}{\partial t} + c_{d_{*-}} \frac{\partial}{\partial z} \right) \left(\frac{\partial}{\partial t} + c_{d_{*+}} \frac{\partial}{\partial z} \right) S' = 0, \tag{5.4.33}$$

where the kinematic wave speed for general axial wavenumbers is identical to the kinematic wave speed for small axial wavenumbers (5.4.17) and the dynamic wave speeds for general axial wavenumbers are

$$c_{d_{*\pm}} = \frac{\alpha_4}{2\alpha_2} \pm \sqrt{\frac{\alpha_4^2}{4\alpha_2^2} - \frac{\Gamma\,\alpha_5}{Re\,\alpha_2} - \frac{\alpha_6}{\alpha_2} + k^2\frac{\Gamma\,\alpha_7}{Re\,\alpha_2}}. \tag{5.4.34}$$

The dynamic wave speeds for general axial wavenumbers (5.4.34) differs from the dynamic wave speeds for small axial wavenumbers by the addition of the k^2 term in the square root, which is due to the axial curvature. Note that the axial curvature has a dispersive effect on the dynamic waves (i.e. it causes the dynamic wave speeds to be dependent on the axial wavenumber k). In particular, the axial curvature has a stabilising effect on the $n = 0$ mode as it increases $c_{d_{*+}}$ and decreases $c_{d_{*-}}$, which widens the range of stability (1.2.24). The dynamic wave speeds for general axial wavenumbers (5.4.34) are purely real for all $\bar{S}$ when a sufficiently large k is chosen.

Figure 5.8(a) shows the real parts of the linear growth rate σ plotted as a function of k for the $n = 0$ mode for the thick-film WRIBL equations (4.2.19) and (4.2.32). Each curve in Figure 5.8(a) is long-wave unstable, but crosses the horizontal axis at different values of k. In particular, the dashed curve for $\bar{S} = 2.483$ crosses the horizontal axis at $k \approx 2.5$. Figure 5.8(b) shows the wave speed c as a function of $\bar{S}$ for the $n = 0$ mode, specifically the kinematic wave speed c_k (5.4.17) (solid black), the dynamic wave speeds for small axial wavenumbers c_{d_+} and c_{d_-} (5.4.18) (dot-dashed blue and dot-dashed red, respectively), and the dynamic wave speeds for general axial wavenumbers $c_{d_{*+}}$ and $c_{d_{*-}}$ (5.4.34) for $k = 2.5$ (dotted blue and dotted red, respectively). The dynamic wave speeds for general axial wavenumbers (5.4.34) are plotted for $k = 2.5$, however the curves in Figure 5.8(b) are typical for any $k > 0$. While the stability criterion (1.2.24) is always violated for the kinematic and dynamic wave speeds for small axial wavenumbers (when the dynamic wave speeds for small axial wavenumbers are purely real), for non-small axial wavenumbers the stability criterion (1.2.24) can be satisfied. For values of $\bar{S}$ to the left of the vertical dot-dot-dashed line at $c_k = c_{d_{*+}}$ shown in Figure 5.8(b), the kinematic wave speed c_k (5.4.17) lies between the two dynamic wave speeds for general axial wavenumbers $c_{d_{*+}}$ and $c_{d_{*-}}$ (5.4.34) for $k = 2.5$, which satisfies the stability criterion (1.2.24). This agrees with the dotted curve for $\bar{S} = 2$ in Figure

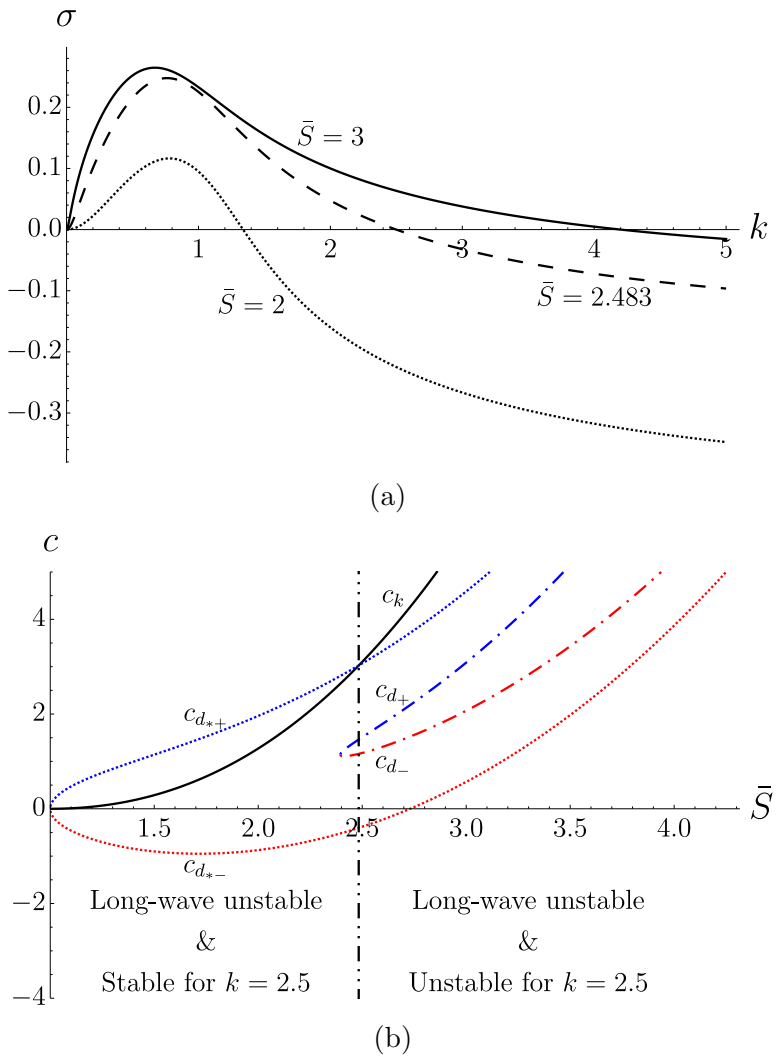

Figure 5.8: (a) The real parts of the linear growth rate σ plotted as a function of k for the $n = 0$ mode for the thick-film WRIBL equations (4.2.19) and (4.2.32) with $\bar{S} = 2$ (dotted), $\bar{S} = 2.483$ (dashed), and $\bar{S} = 3$ (solid) for $Re = 2$ and $\Gamma = 1$. (b) The wave speed c as a function of $\bar{S}$ for the $n = 0$ mode, specifically the kinematic wave speed c_k (5.4.17) (solid black), the dynamic wave speeds for small axial wavenumbers c_{d_+} and c_{d_-} (5.4.18) (dot-dashed blue and dot-dashed red, respectively), and the dynamic wave speeds for general axial wavenumbers $c_{d_{*+}}$ and $c_{d_{*-}}$ (5.4.34) for $k = 2.5$ (dotted blue and dotted red, respectively), for $Re = 2$ and $\Gamma = 1$, where the vertical dot-dot-dashed line at $c_k = c_{d_{*+}}$ (i.e. at $\bar{S} \approx 2.483$) denotes the transition from values of $\bar{S}$ which are stable for $k = 2.5$ to values of $\bar{S}$ which are long-wave unstable for $k = 2.5$.

5.8(a) which is stable for $k = 2.5$. For values of $\bar{S}$ to the right of the vertical dot-dot-dashed line at $c_k = c_{d_{*+}}$ shown in Figure 5.8(b), the kinematic wave speed c_k (5.4.17) is greater than the dynamic wave speeds for general axial wavenumbers $c_{d_{*+}}$ and $c_{d_{*-}}$ (5.4.34) for $k = 2.5$, which violates the stability criterion (1.2.24). This agrees with the solid curve for $\bar{S} = 3$ in Figure 5.8(a) which is unstable for $k = 2.5$. For $\bar{S} \approx 2.483$, i.e. on the vertical dot-dot-dashed line at $c_k = c_{d_{*+}}$ shown in Figure 5.8(b), the kinematic wave speed c_k (5.4.17) is equal to the dynamic wave speed for general axial wavenumbers $c_{d_{*+}}$ (5.4.34) for $k = 2.5$, which satisfies the stability criterion (1.2.24). This agrees with the dashed curve for $\bar{S} = 2.483$ in Figure 5.8(a) which is neutrally stable for $k \approx 2.5$.

The results described above are for the case $k = 2.5$, however we expect that the same qualitative behaviour would be observed for any $k > 0$. Specifically, the dot-dot-dashed line in Figure 5.8(b) would be located at a different value of $\bar{S}$ for a different value of $k > 0$.

5.4.2.2 $n = 1$ mode for general axial wavenumbers

Now we consider the $n = 1$ mode. Using the same procedure used to obtain equation (5.4.33), equation (5.4.5) can be rewritten in the form of equation (1.2.21) as

$$(\alpha_1 + k^2 Re\,\Gamma\,\beta_8)\left(\frac{\partial}{\partial t} + c_{k_*}\frac{\partial}{\partial z}\right)S' + Re\,\alpha_2\left(\frac{\partial}{\partial t} + c_{d_{*-}}\frac{\partial}{\partial z}\right)\left(\frac{\partial}{\partial t} + c_{d_{*+}}\frac{\partial}{\partial z}\right)S' = 0, \tag{5.4.35}$$

with kinematic wave speed for general axial wavenumbers

$$c_{k_*} = \frac{\alpha_3 + k^2 Re\,\Gamma\,\beta_9}{\alpha_1 + k^2 Re\,\Gamma\,\beta_8} \tag{5.4.36}$$

and dynamic wave speeds for general axial wavenumbers

$$c_{d_{*\pm}} = \frac{\alpha_4}{2\alpha_2} \pm \sqrt{\frac{\alpha_4^2}{4\alpha_2^2} + \frac{\Gamma\,\beta_5}{Re\,\alpha_2} - \frac{\alpha_6}{\alpha_2} + k^2\frac{\Gamma\,\alpha_7}{Re\,\alpha_2}}. \tag{5.4.37}$$

The kinematic wave speed for general axial wavenumbers (5.4.36) differs from the kinematic wave speed for small axial wavenumbers (5.4.25) by the addition of the k^2 terms in the numerator and the denominator. These terms come from the

azimuthal surface tension terms in equation (4.2.19) and have a dispersive effect on the kinematic waves (i.e. they cause the kinematic wave speed to be dependent on the axial wavenumber k). In particular, these terms have a stabilising effect on the $n = 1$ mode by slowing the speed of c_{k_*} (as β_8 grows at a greater rate than β_9 as $\bar{S}$ is increased). The dynamic wave speeds for general axial wavenumbers (5.4.37) differs from the dynamic wave speeds for small axial wavenumbers (5.4.26) by the addition of the k^2 term in the square root, which is due to the axial curvature. This difference between the dynamic wave speeds for general axial wavenumbers (5.4.37) and the dynamic wave speeds for small axial wavenumbers (5.4.26) is the same for both the $n = 0$ and $n = 1$ modes.

Figure 5.9(a) shows the real parts of the linear growth rate σ plotted as a function of k for the $n = 1$ mode for the thick-film WRIBL equations (4.2.19) and (4.2.32). Each curve in Figure 5.9(a) is long-wave unstable, but crosses the horizontal axis at different values of k. In particular, the dashed curve for $\bar{S} = 2.958$ crosses the horizontal axis at $k \approx 0.5$. Figure 5.9(b) shows curves of the wave speed c as a function of $\bar{S}$ for the $n = 1$ mode, specifically the kinematic wave speed for small axial wavenumbers c_k (5.4.25) (solid black), the dynamic wave speeds for small axial wavenumbers c_{d_+} and c_{d_-} (5.4.26) (dot-dashed blue and dot-dashed red, respectively), the kinematic wave speed for general axial wavenumbers c_{k_*} (5.4.36) for $k = 0.5$ (dotted black), and the dynamic wave speeds for general axial wavenumbers $c_{d_{*+}}$ and $c_{d_{*-}}$ (5.4.37) for $k = 0.5$ (dotted blue and the dotted red, respectively). The kinematic wave speed for general axial wavenumbers (5.4.36) and the dynamic wave speeds for general axial wavenumbers (5.4.37) are plotted for $k = 0.5$, however the curves in Figure 5.9(b) are typical for any $k > 0$. We have previously discussed the transition from stability to long-wave instability when $\bar{S}$ increases from left to right of the vertical dashed line (which corresponds to $c_k = c_{d_+}$) shown in Figure 5.9(b). For values of $\bar{S}$ to the right of the vertical dashed line at $c_k = c_{d_+}$ but to the left of the vertical dot-dot-dashed line at $c_{k_*} = c_{d_{*+}}$ shown in Figure 5.9(b), the kinematic wave speed for general axial wavenumbers c_{k_*} (5.4.36) for $k = 0.5$ is greater than the dynamic wave speeds for general axial wavenumbers $c_{d_{*+}}$ and $c_{d_{*-}}$ (5.4.37) for $k = 0.5$, which violates the stability criterion (1.2.24). This agrees with the dotted curve for $\bar{S} = 2.5$ in Figure 5.9(a) which is unstable for $k = 0.5$. For values of $\bar{S}$ to the right of the vertical dot-dot-dashed line at $c_{k_*} = c_{d_{*+}}$ shown in Figure 5.9(b), the kinematic

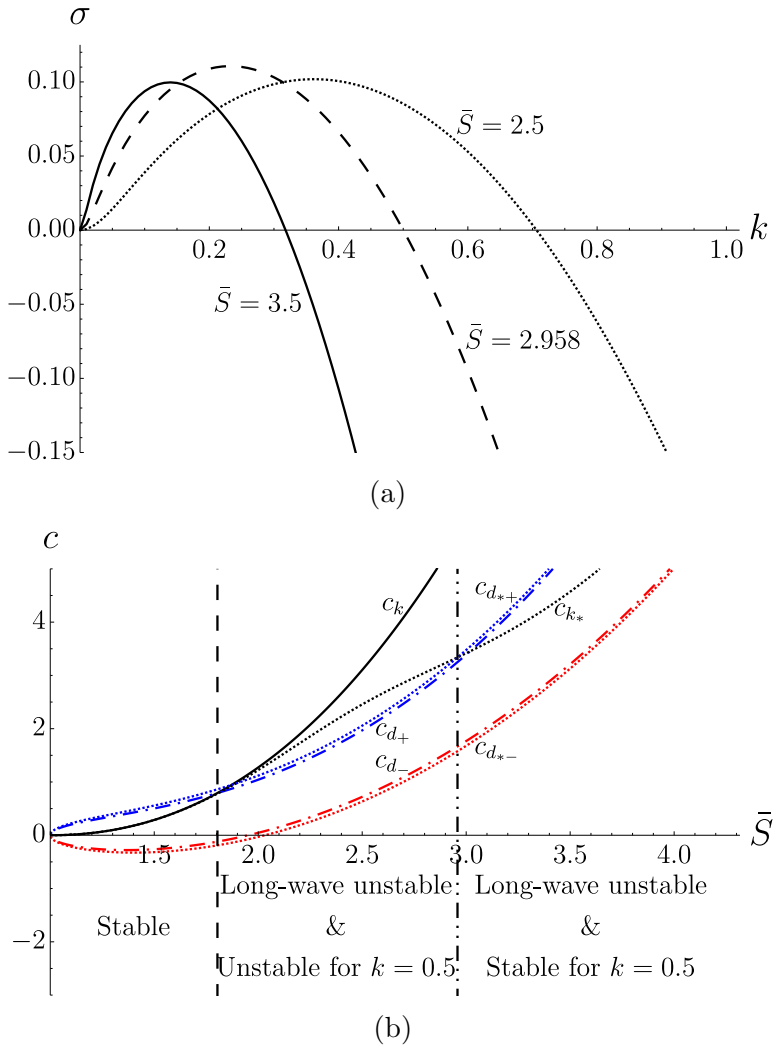

Figure 5.9: (a) The real parts of the linear growth rate σ plotted as a function of k for the $n = 1$ mode for the thick-film WRIBL equations (4.2.19) and (4.2.32) with $\bar{S} = 2.5$ (dotted), $\bar{S} = 2.958$ (dashed), and $\bar{S} = 3.5$ (solid) for $Re = 2$ and $\Gamma = 1$. (b) The wave speed c as a function of $\bar{S}$ for the $n = 1$ mode, specifically the kinematic wave speed for small axial wavenumbers c_k (5.4.25) (solid black), the dynamic wave speeds for small axial wavenumbers c_{d_+} and c_{d_-} (5.4.26) (dot-dashed blue and dot-dashed red, respectively), the kinematic wave speed for general axial wavenumbers c_{k_*} (5.4.36) for $k = 0.5$ (dotted black), and the dynamic wave speeds for general axial wavenumbers $c_{d_{*+}}$ and $c_{d_{*-}}$ (5.4.37) for $k = 0.5$ (dotted blue and dotted red, respectively), for $Re = 2$ and $\Gamma = 1$, where the vertical dashed line at $c_k = c_{d_+}$ (i.e. at $\bar{S} \approx 1.804$) denotes the transition from stable values of $\bar{S}$ to long-wave unstable values of $\bar{S}$, and where the vertical dot-dot-dashed line at $c_{k_*} = c_{d_{*+}}$ (i.e. at $\bar{S} \approx 2.958$) denotes the transition from values of $\bar{S}$ which are stable for $k = 0.5$ to values of $\bar{S}$ which are unstable for $k = 0.5$.

wave speed for general axial wavenumbers c_{k_*} (5.4.36) for $k = 0.5$ lies between the two dynamic wave speeds for general axial wavenumbers $c_{d_{*+}}$ and $c_{d_{*-}}$ (5.4.37) for $k = 0.5$, which satisfies the stability criterion (1.2.24). This agrees with the solid curve for $\bar{S} = 3.5$ in Figure 5.9(a) which is stable for $k = 0.5$. For $\bar{S} \approx 2.958$, i.e. on the vertical dot-dot-dashed line at $c_{k_*} = c_{d_{*+}}$ shown in Figure 5.9(b), the kinematic wave speed for general axial wavenumbers c_{k_*} (5.4.37) for $k = 0.5$ is equal to the dynamic wave speed for general axial wavenumbers $c_{d_{*+}}$ (5.4.37) for $k = 0.5$, which satisfies the stability criterion (1.2.24). This agrees with the dashed curve for $\bar{S} = 2.958$ in Figure 5.9(a) which is neutrally stable for $k \approx 0.5$.

The results described above are for the case $k = 0.5$, however we expect that the same qualitative behaviour would be observed for any $k > 0$. Specifically, the dot-dot-dashed line in Figure 5.9(b) would be located at a different value of $\bar{S}$ to the right of the dashed line for a different value of $k > 0$.

5.5 Nonlinear regime

In Sections 5.1, 5.3, and 5.4 we have extensively examined the behaviour of the thick-film WRIBL equations (4.2.19) and (4.2.32) in the linear regime, and now we extend our study into the nonlinear regime. Specifically, we will compare the results from our parametric study of the $n = 1$ mode in $\bar{S} - \Gamma$ parameter space in the linear regime with the results of our calculations in the nonlinear regime. Numerical simulations were performed using a well-tested C++ code (see Appendix A.2).

Figure 5.10 shows the results of our parametric study of the linear stability of the $n = 1$ mode in $\bar{S} - \Gamma$ parameter space, in which a neutral stability curve is plotted for the thick-film WRIBL equations (4.2.19) and (4.2.32). Note that the curve in Figure 5.10 is identical to the solid curve in Figure 5.4. We choose three points in Figure 5.10 which lie in the regions of linear stability (A), and long-wave instability (B and C) for the $n = 1$ mode. In particular, where point C lies close to the neutral stability curve. We show that: for point A, the results from the linear calculations are stable for the $n = 1$ mode, and the solution in the nonlinear regime has an axisymmetric free surface (corresponding to the $n = 1$ mode being stable); for point B, the results from the linear calculations are long-wave unstable for the $n = 1$ mode, and the solution in the nonlinear regime has a

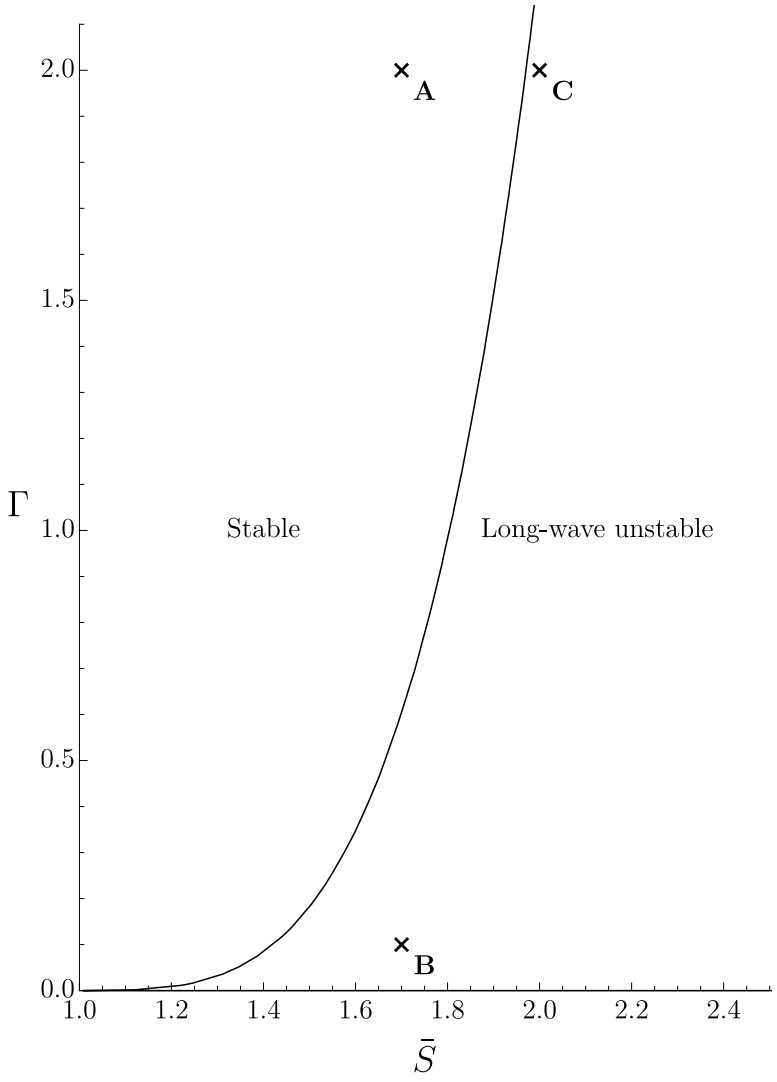

Figure 5.10: The results of our parametric study of the linear stability of the $n = 1$ mode of the flow plotted in $\bar{S} - \Gamma$ parameter space with $Re = 2$. A neutral stability curve is plotted for the thick-film WRIBL equations (4.2.19) and (4.2.32). The crossed (labelled A, B, and C) correspond to the parameter values used in the nonlinear calculations of the thick-film WRIBL equations (4.2.19) and (4.2.32) described in Section 5.5.

non-axisymmetric free surface (corresponding to the $n = 1$ mode being unstable); and for point C, the results from the linear calculations are long-wave unstable for the $n = 1$ mode, but the solution in the nonlinear regime has an axisymmetric free surface (corresponding to the $n = 1$ mode being stable).

As the initial condition for our nonlinear calculations in Sections 5.5.1–5.5.3, we use

$$q(\theta, z, 0) = 0 \tag{5.5.1}$$

for the axial flux, and

$$\begin{aligned} S(\theta, z, 0) =& \bar{S} - 0.01\left[\sin\left(2\pi\frac{\theta}{\theta_L}\right) - \sin\left(2\pi\frac{z}{z_L}\right)\right] + 0.015\left[\sin\left(4\pi\frac{\theta}{\theta_L}\right) - \sin\left(4\pi\frac{z}{z_L}\right)\right] \\ & - 0.01\left[\sin\left(6\pi\frac{\theta}{\theta_L}\right) - \sin\left(6\pi\frac{z}{z_L}\right)\right] + 0.005\left[\cos\left(8\pi\frac{\theta}{\theta_L}\right) + \cos\left(8\pi\frac{z}{z_L}\right)\right] \\ & + 0.03\cos\left(2\pi\frac{\theta}{\theta_L}\right)\cos\left(2\pi\frac{z}{z_L}\right) \end{aligned} \tag{5.5.2}$$

for the free surface, where $z_L = 20$ and $\theta_L = 2\pi$ are the domain lengths of the periodic axial and azimuthal domain, respectively. The initial condition for the free surface (5.5.2) has both small axisymmetric and small non-axisymmetric perturbations to the base-state solution. A three-dimensional plot of the initial condition for the free surface (5.5.2) is shown in Figure 5.11(a), and a top-down view of this free surface is shown in Figure 5.11(b)

We use a final computational time of $t = t_f = 6 \times 10^3$ ($t = t_f = 2.4 \times 10^4$ in Section 5.5.2) which is sufficiently long for the system to become fully developed, settling into either axisymmetric or non-axisymmetric behaviour. In order to show both axisymmetric and non-axisymmetric behaviour, we consider the absolute value of the n^{th} mode and the k^{th} mode of the Fourier transform of the free surface, i.e.

$$|\mathcal{F}_{n,k}(t)| = \left|\frac{1}{2\pi z_L}\int_0^{2\pi}\int_0^{z_L} S(\theta, z, t)\, \mathrm{e}^{-ikz - in\theta}\, \mathrm{d}z\mathrm{d}\theta\right|. \tag{5.5.3}$$

Our numerical simulations are periodic in the axial domain, therefore the axial wavenumber k is an integer, and, in general, as k increases $|\mathcal{F}_{n,k}|$ becomes smaller. In order to focus on azimuthal wavenumbers, we consider the absolute value of

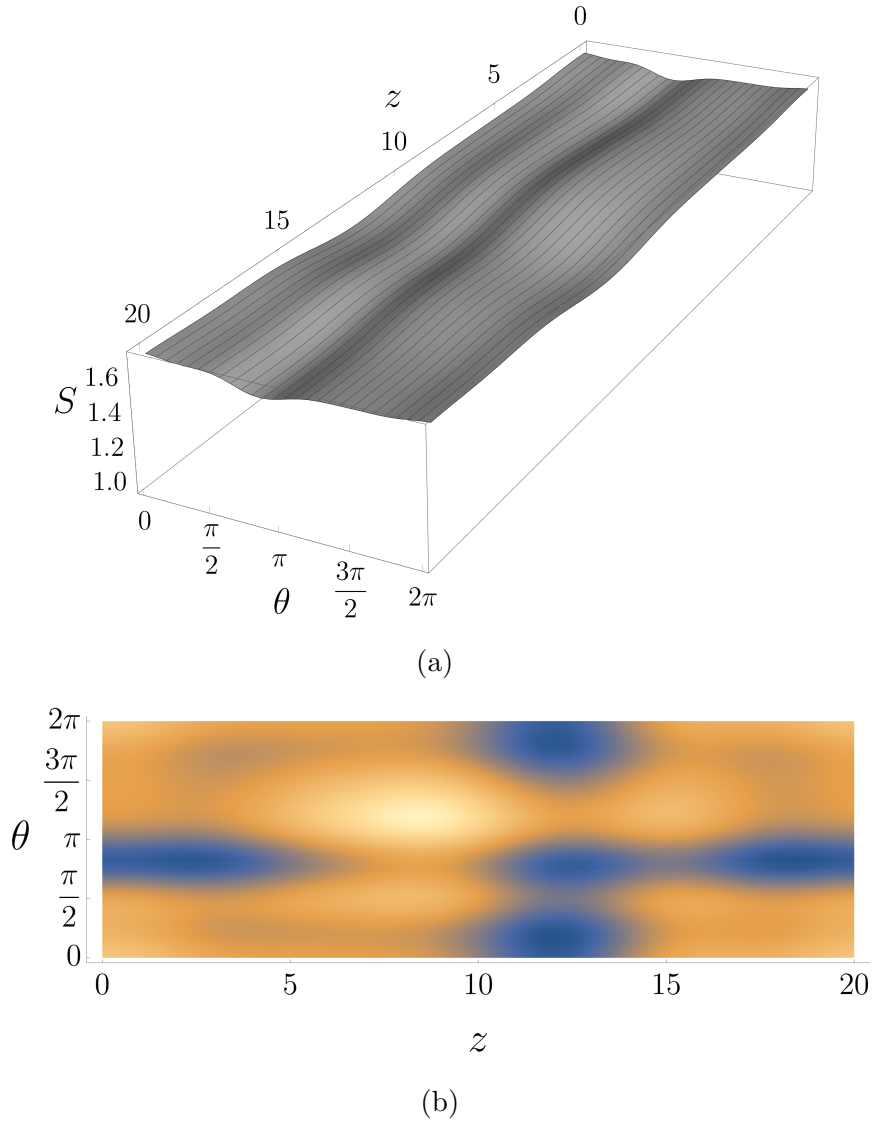

Figure 5.11: The initial condition for the free surface given by (5.5.2), with $\bar{S} = 1.7$, displayed as (a) a three-dimensional plot, and (b) a top-down view, where, in (b), lighter and darker colours represent a thicker and thinner film, respectively.

the n^{th} mode of the Fourier transform of the free surface by taking the sum of a sufficiently large number of axial wavenumbers, i.e.

$$|\mathcal{F}_n(t)| = \sum_{k=0}^{50} |\mathcal{F}_{n,k}(t)| \,, \tag{5.5.4}$$

where the axial wavenumbers we neglect (i.e. $k > 50$) are negligible. In what follows, we plot both the free surface at $t = t_f$, and $|\mathcal{F}_n|$, for the parameter values corresponding to points A, B, and C shown in Figure 5.10.

5.5.1 Flows which are axisymmetric in the linear and nonlinear regimes

We begin by considering the parameter values corresponding to point A in Figure 5.10, which lies in the region of linear stability for the $n = 1$ mode. In particular, we show that the solution in the nonlinear regime with parameter values corresponding to point A in Figure 5.10, and with initial condition (5.5.1) and (5.5.2), corresponds to an axisymmetric free surface after an initial transient phase.

In order to quantitatively classify the solutions of the nonlinear calculations as either an axisymmetric free surface or a non-axisymmetric free surface, we use the absolute value of the Fourier transform of the free surface for the $n = 1$ mode (i.e. $|\mathcal{F}_1|$) and the $n = 2$ mode (i.e. $|\mathcal{F}_2|$), given by (5.5.4), as a metric. Figure 5.12(a) shows the absolute value of the Fourier transform of the free surface for the $n = 1$ mode $|\mathcal{F}_1|$ as a function of t, with parameter values corresponding to point A in Figure 5.10. From Figure 5.12(a) we see that $|\mathcal{F}_1|$ has an initial transient phase and then decays to zero at $t \approx 2 \times 10^3$. Figure 5.12(b) shows the absolute value of the Fourier transform of the free surface for the $n = 2$ mode $|\mathcal{F}_2|$ as a function of t, with parameter values corresponding to point A in Figure 5.10. Figure 5.12(b) shows that, similarly to $|\mathcal{F}_1|$, $|\mathcal{F}_2|$ has an initial transient phase before decaying to zero at $t \approx 10^3$. The decay of $|\mathcal{F}_1|$ and $|\mathcal{F}_2|$ represents the decay of non-axisymmetric disturbances to the free surface.

Figure 5.13(a) shows a three-dimensional plot of the free surface at $t = t_f = 6 \times 10^3$, which clearly shows that the free surface is axisymmetric. Figure 5.13(b) shows a top-down view of the free surface at $t = t_f = 6 \times 10^3$. The axisymmetry of

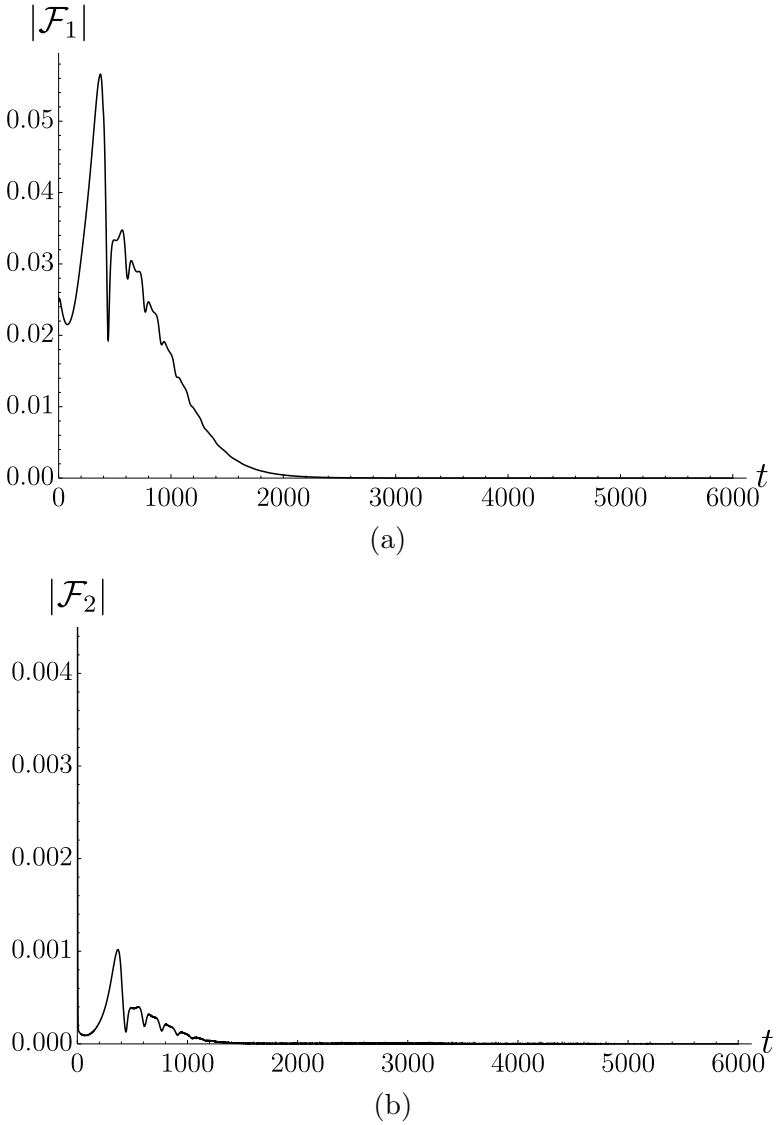

Figure 5.12: The absolute value of the Fourier transform of the free surface for (a) the $n = 1$ mode $|\mathcal{F}_1|$ and (b) $n = 2$ mode $|\mathcal{F}_2|$ as a function of t from $t = 0$ to $t = t_f = 6 \times 10^3$, with parameter values corresponding to point A in Figure 5.10 ($Re = 2$, $\Gamma = 2$, and $\bar{S} = 1.7$). Note that the scale of the vertical axis is different in each part.

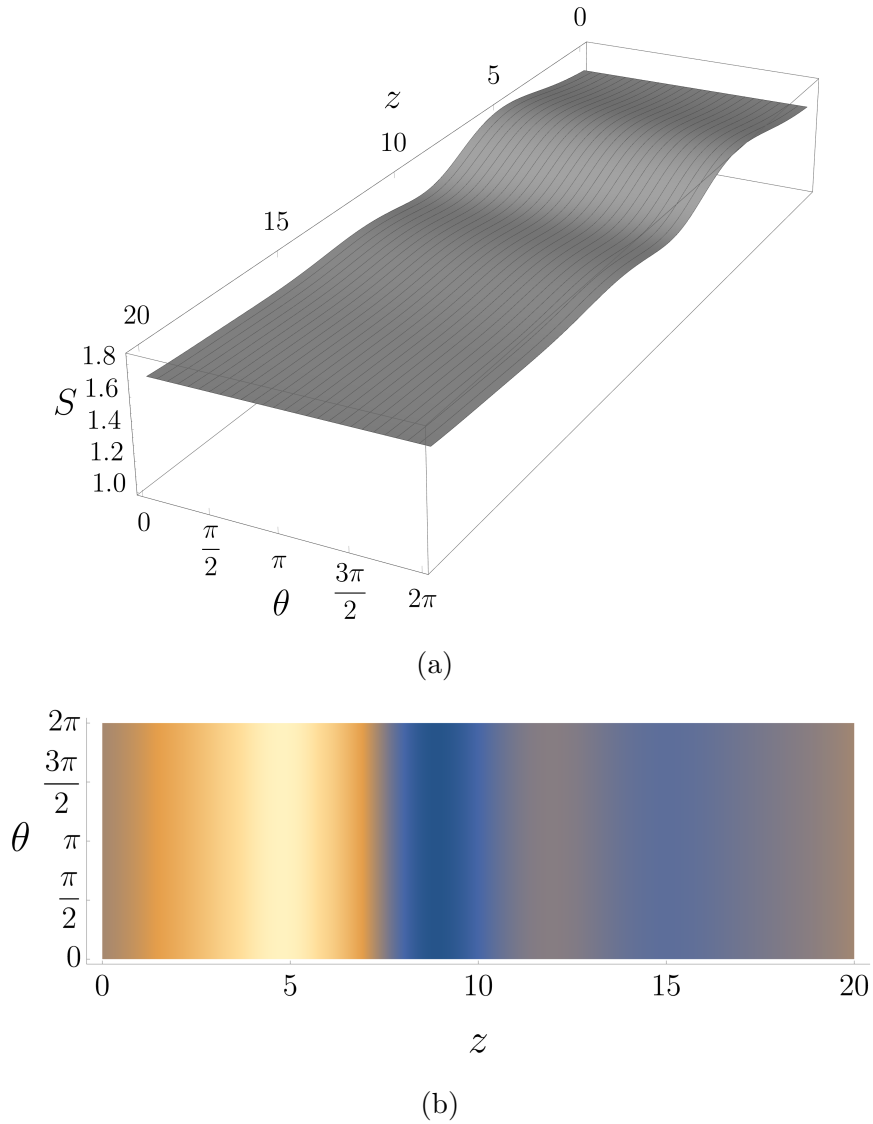

Figure 5.13: The free surface at $t = t_f = 6 \times 10^3$, with parameter values corresponding to point A in Figure 5.10 ($Re = 2$, $\Gamma = 2$, and $\bar{S} = 1.7$), displayed as (a) a three-dimensional plot, and (b) a top-down view where, in (b), lighter and darker colours represent a thicker and thinner film, respectively.

the free surface can perhaps be seen more clearly in Figure 5.13(b), as the colours are independent of θ. The decay of non-axisymmetric disturbances in Figure 5.12 results in the axisymmetric free surface at $t = t_f = 6 \times 10^3$, as shown in Figure 5.13.

Thus, we have shown that, for parameter values corresponding to point A in Figure 5.10, the results from the linear calculations are stable for the $n = 1$ mode, and the solution in the nonlinear regime has an axisymmetric free surface (corresponding to the $n = 1$ mode being stable). This demonstrates that the solution in the nonlinear regime is predicted by the linear calculations.

5.5.2 Flows which are non-axisymmetric in the linear and nonlinear regimes

Next, we consider the parameter values corresponding to point B in Figure 5.10, which lies in the region of long-wave instability for the $n = 1$ mode. In particular, we show that the solution in the nonlinear regime with parameter values corresponding to point B in Figure 5.10, and with initial condition (5.5.1) and (5.5.2), corresponds to a non-axisymmetric free surface after an initial transient phase.

Figure 5.14(a) shows the absolute value of the Fourier transform of the free surface for the $n = 1$ mode $|\mathcal{F}_1|$ as a function of t, with parameter values corresponding to point B in Figure 5.10. From Figure 5.14(a) we see that $|\mathcal{F}_1|$ does not decay to zero as in Figure 5.12. Specifically, from Figure 5.14(a), we see that $|\mathcal{F}_1|$ oscillates around a gradually decaying mean value until $t \approx 10^4$ after which $|\mathcal{F}_1|$, in general, oscillates around a constant (non-zero) mean value. Figure 5.14(b) shows the absolute value of the Fourier transform of the free surface for the $n = 2$ mode $|\mathcal{F}_2|$ as a function of t, with parameter values corresponding to point B in Figure 5.10. Figure 5.14(b) shows that, similarly to $|\mathcal{F}_1|$, $|\mathcal{F}_2|$ oscillates around a gradually decaying mean value until $t \approx 10^4$ after which $|\mathcal{F}_2|$, in general, oscillates around a constant (non-zero) mean value. In Figure 5.14 we have chosen a final computational time of $t = t_f = 2.4 \times 10^4$ (i.e. three times longer than in Figure 5.12) to show that both $|\mathcal{F}_1|$ and $|\mathcal{F}_2|$ do not decay to zero, and so, in this case, the free surface remains non-axisymmetric. Specifically, the oscillations of $|\mathcal{F}_1|$ and $|\mathcal{F}_2|$ around a constant (non-zero) mean value indicate that the significance of the $n = 1$ and $n = 2$ modes varies over time. Consequently, the non-axisymmetric

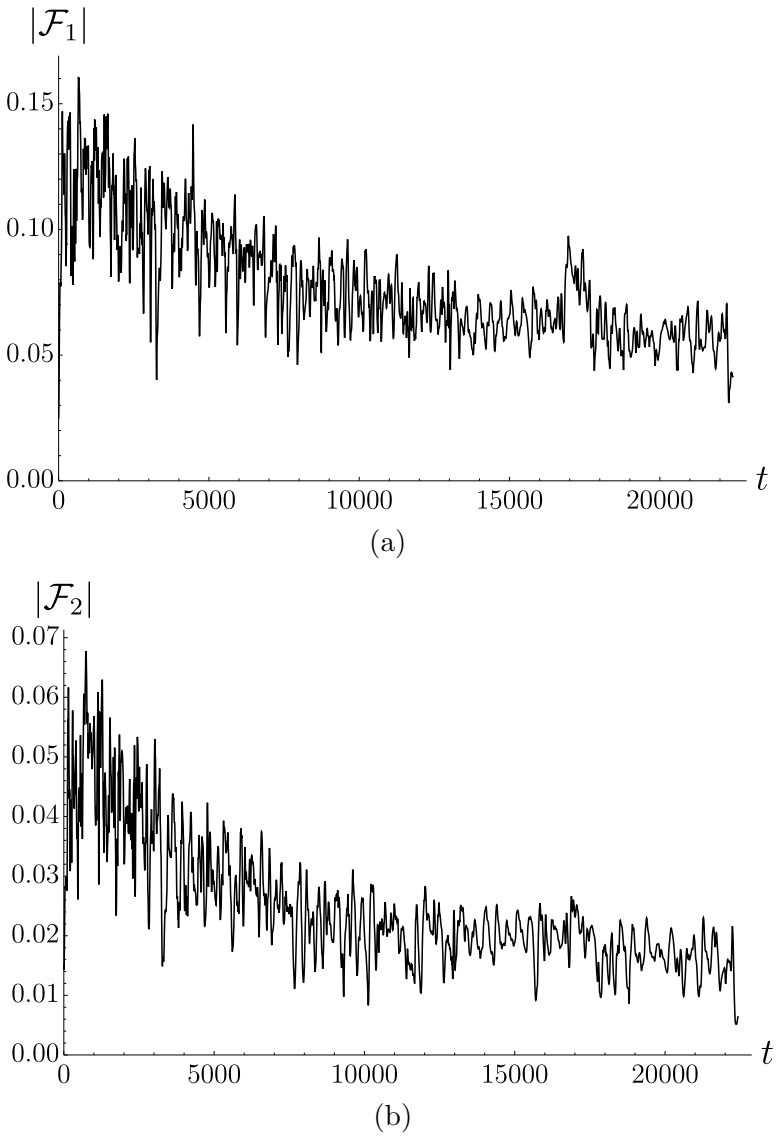

Figure 5.14: The absolute value of the Fourier transform of the free surface for (a) the $n = 1$ mode $|\mathcal{F}_1|$ and (b) $n = 2$ mode $|\mathcal{F}_2|$ as a function of t from $t = 0$ to $t = t_f = 2.4 \times 10^4$, with parameter values corresponding to point B in Figure 5.10 ($Re = 2$, $\Gamma = 0.1$, and $\bar{S} = 1.7$). Note that the scale of the vertical axis is different in each part.

disturbances to the free surface undergo periods of growth and decay as time progresses.

Figure 5.15(a) shows a three-dimensional plot of the free surface at $t = t_f = 2.4 \times 10^4$, which clearly shows that the free surface is non-axisymmetric. Figure 5.15(b) shows a top-down view of the free surface at $t = t_f = 2.4 \times 10^4$. Unlike Figure 5.13(b), the colours in Figure 5.15(b) are dependent on θ.

Thus, we have shown that, for parameter values corresponding to point B in Figure 5.10, the results from the linear calculations are long-wave unstable for the $n = 1$ mode, and the solution in the nonlinear regime has a non-axisymmetric free surface (corresponding to the $n = 1$ mode being unstable). This demonstrates that the solution in the nonlinear regime is predicted by the linear calculations.

5.5.3 Flows which are non-axisymmetric in the linear regime and axisymmetric in the nonlinear regime

Finally, we consider the parameter values corresponding to point C in Figure 5.10, which lies in the region of long-wave instability for the $n = 1$ mode, but close to the neutral stability curve. In particular, we show that the solution in the nonlinear regime with parameter values corresponding to point C in Figure 5.10, and with initial conditions (5.5.1) and (5.5.2), corresponds to an axisymmetric free surface after an initial transient phase.

Figure 5.16(a) shows the absolute value of the Fourier transform of the free surface for the $n = 1$ mode $|\mathcal{F}_1|$ as a function of t, with parameter values corresponding to point C in Figure 5.10. Figure 5.16(a) shows that $|\mathcal{F}_1|$ has an initial transient phase and then decays to zero at $t \approx 500$ (which is qualitatively the same as Figure 5.12(a)). Figure 5.16(b) shows the absolute value of the Fourier transform of the free surface for the $n = 2$ mode $|\mathcal{F}_2|$ as a function of t, with parameter values corresponding to point C in Figure 5.10. Figure 5.16(b) shows that, similarly to $|\mathcal{F}_1|$, $|\mathcal{F}_2|$ has an initial transient phase before decaying to zero at $t \approx 500$ (which is qualitatively the same as Figure 5.12(b)). The decay of $|\mathcal{F}_1|$ and $|\mathcal{F}_2|$ represents the decay of non-axisymmetric disturbances to the free surface.

Figure 5.17(a) shows a three-dimensional plot of the free surface at $t = t_f = 6 \times 10^3$, which clearly shows that the free surface is axisymmetric. Figure 5.17(b)

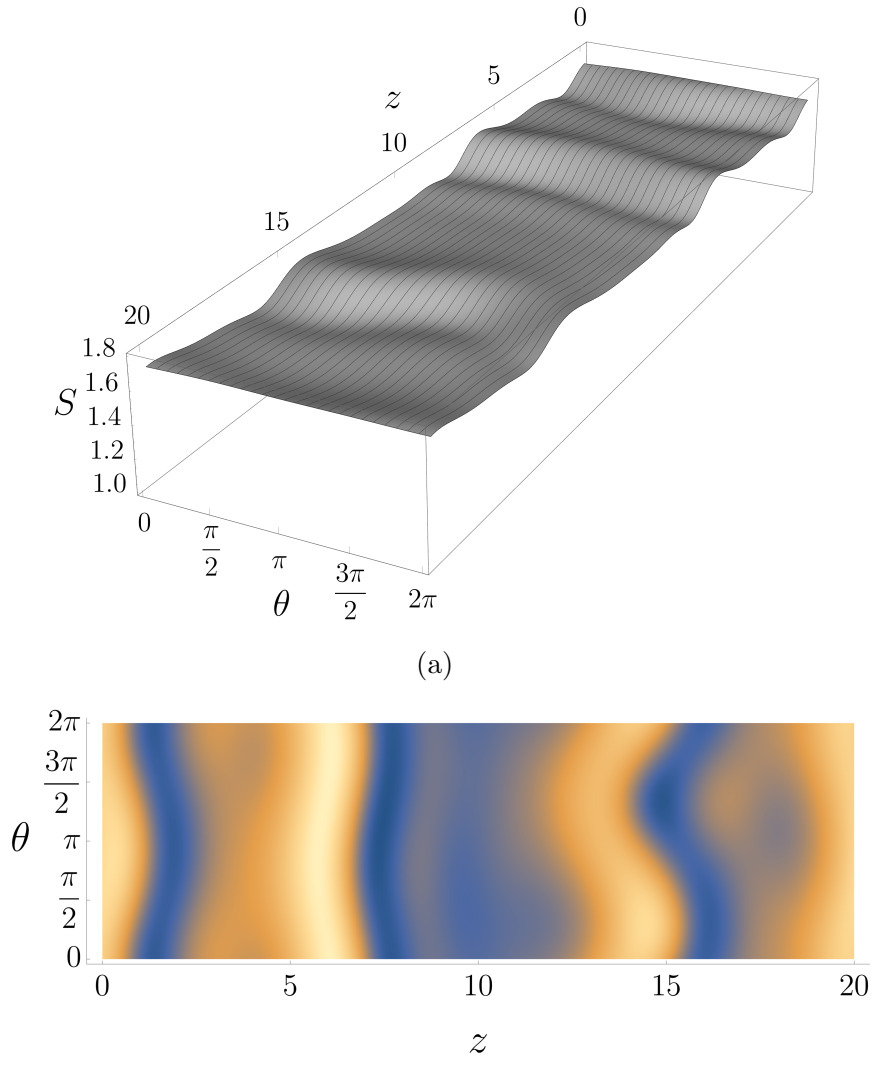

Figure 5.15: The free surface at $t = t_f = 2.4 \times 10^4$, with parameter values corresponding to point B in Figure 5.10 ($Re = 2$, $\Gamma = 0.1$, and $\bar{S} = 1.7$), displayed as (a) a three-dimensional plot, and (b) a top-down view where, in (b), lighter and darker colours represent a thicker and thinner film, respectively.

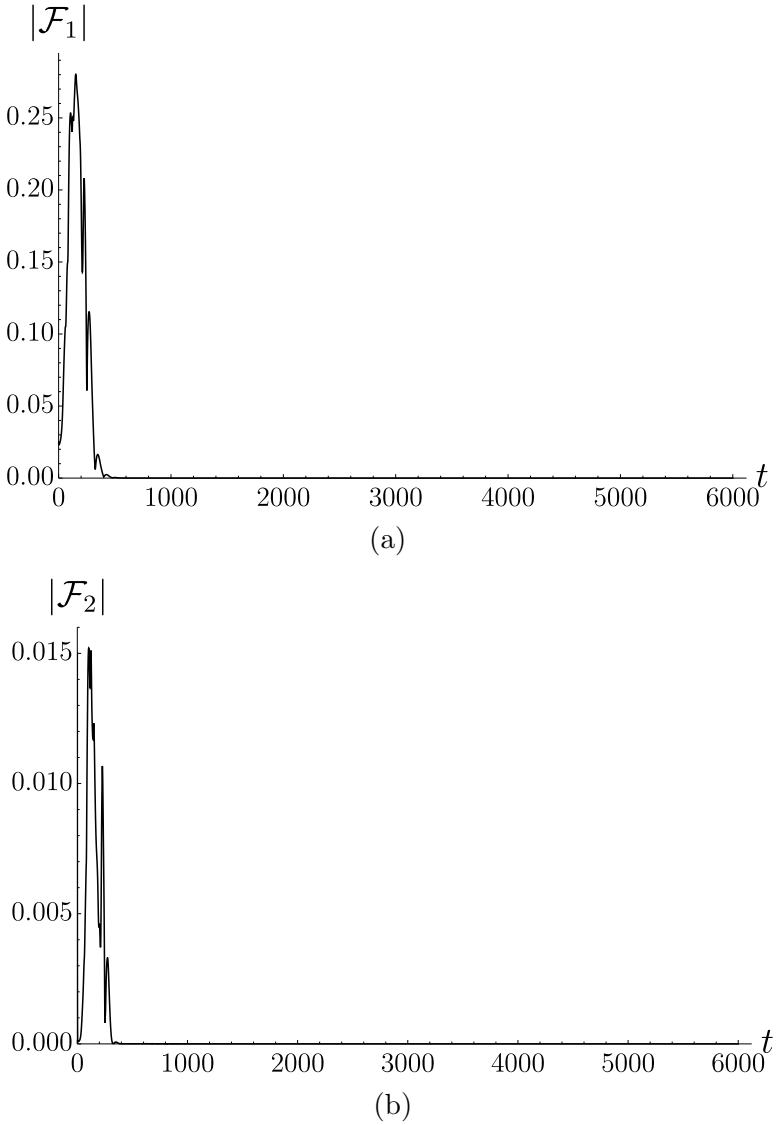

Figure 5.16: The absolute value of the Fourier transform of the free surface for (a) the $n = 1$ mode $|\mathcal{F}_1|$ and (b) $n = 2$ mode $|\mathcal{F}_2|$ as a function of t from $t = 0$ to $t = t_f = 6 \times 10^3$, with parameter values corresponding to point C in Figure 5.10 ($Re = 2$, $\Gamma = 2$, and $\bar{S} = 2$). Note that the scale of the vertical axis is different in each part.

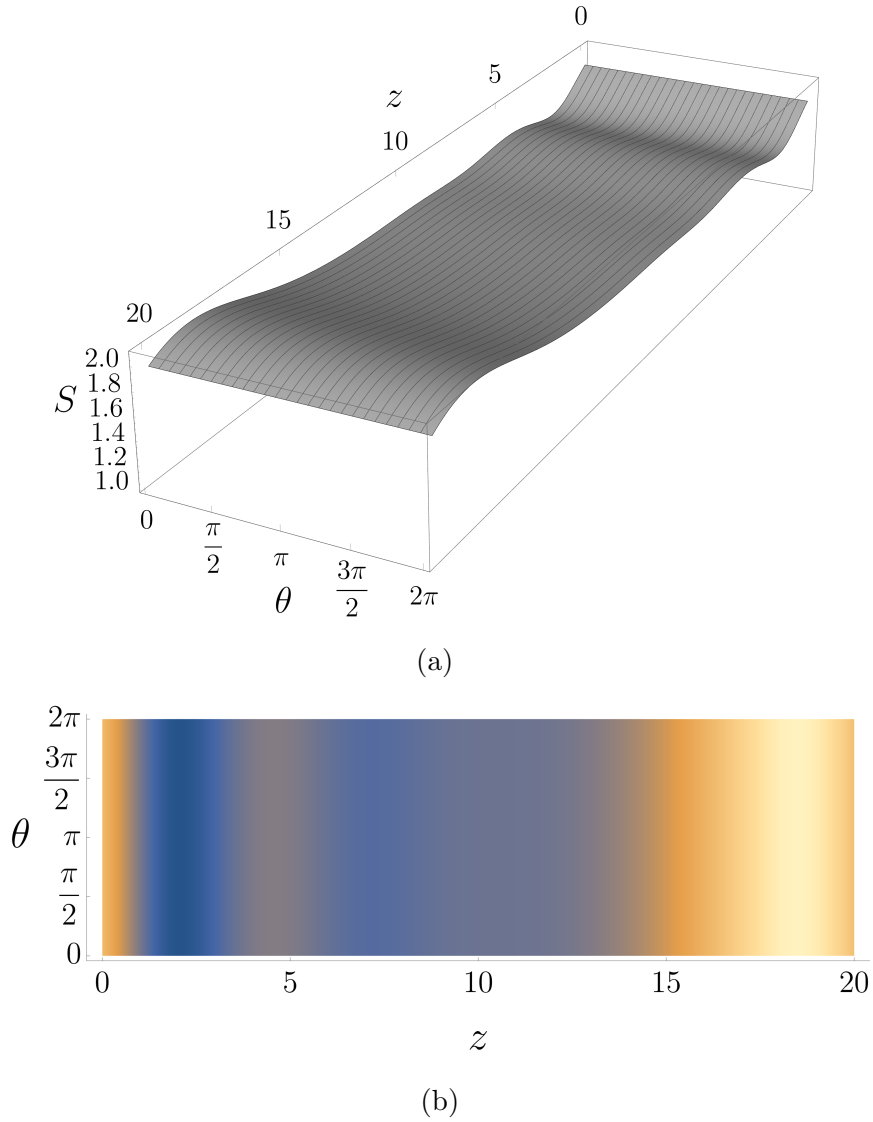

Figure 5.17: The free surface at $t = t_f = 6 \times 10^3$, with parameter values corresponding to point C in Figure 5.10 ($Re = 2$, $\Gamma = 2$, and $\bar{S} = 2$), displayed as (a) a three-dimensional plot, and (b) a top-down view where, in (b), lighter and darker colours represent a thicker and thinner free surface, respectively.

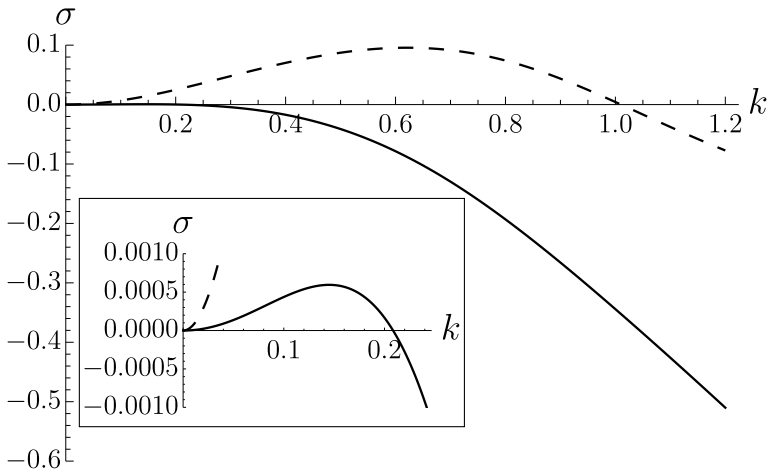

Figure 5.18: The real parts of the linear growth rate σ plotted as a function of k for the thick-film WRIBL equations (4.2.19) and (4.2.32), with parameter values corresponding to point C in Figure 5.10 ($Re = 2$, $\Gamma = 2$, and $\bar{S} = 2$), for the $n = 0$ (dashed) and $n = 1$ (solid) modes. The inset shows a zoom of the real parts of the linear growth rates near $k = 0$ mode in greater detail.

shows a top-down view of the free surface at $t = t_f = 6 \times 10^3$. The axisymmetry of the free surface can perhaps be seen more clearly in Figure 5.17(b), as the colours are independent of θ. Figure 5.17 is qualitatively the same as Figure 5.13, despite the results from the linear calculations in Figure 5.10 showing the parameter values corresponding to point C lie in the region of long-wave instability of the $n = 1$ mode.

Thus, we have shown that, for parameter values corresponding to point C in Figure 5.10, the results from the linear calculations are long-wave unstable for the $n = 1$ mode, whereas the solution in the nonlinear regime has an axisymmetric free surface (corresponding to the $n = 1$ mode being stable). This demonstrates that the linear calculations are insufficient for delineating the threshold between axisymmetry and non-axisymmetry in the nonlinear regime.

We can explain this disagreement by examining the real parts of the linear growth rates. Figure 5.18 shows the real parts of the linear growth rate σ plotted as a function of k for the thick-film WRIBL equations (4.2.19) and (4.2.32) for the $n = 0$ (dashed) and $n = 1$ (solid) modes, with parameter values corresponding to point C in Figure 5.10. The real parts of the linear growth rates are long-wave unstable for both modes, but the real parts of the linear growth rate for the $n = 1$ mode are dominated the much larger real parts of the linear growth rate

for the $n = 0$ mode. The free surface quickly evolves to the free surface shown in Figure 5.17, in which the axisymmetric bulges are formed due to the dominant $n = 0$ long-wave instability. However, these numerical solutions then imply that this saturated shape is stable to non-axisymmetric $n = 1$ perturbations, and so in the nonlinear regime this non-axisymmetric instability is suppressed, therefore, the free surface remains axisymmetric thereafter. The quick saturation is visible in both parts of Figure 5.16, in which $|\mathcal{F}_1|$ and $|\mathcal{F}_2|$ decay to zero much quicker than in Figure 5.12. Therefore, the results in the present section show that there is a region of $\bar{S} - \Gamma$ parameter space, close to the neutral stability curve for the $n = 1$ mode, for which the solution in the nonlinear regime is not predicted by the linear calculations.

5.6 Comparison with the experimental results of Gabbard and Bostwick [222]

In Section 1.6.2, we discussed the experimental results of Gabbard and Bostwick [222], and, in particular, the results of their parametric study for the transition from a non-axisymmetric flow to an axisymmetric flow, as it depends upon the fibre diameter and surface tension (Figure 1.41). In this section, we now compare our results obtained in Sections 5.1–5.5 with the experimental results of Gabbard and Bostwick [222].

Gabbard and Bostwick [222] found that decreasing the fibre diameter (while surface tension remains fixed) causes a transition from non-axisymmetric to axisymmetric flow. Decreasing the fibre diameter amplifies the effect of the azimuthal curvature which, as discussed in Section 5.4.1.3, is the key mechanism for the (in)stability of the $n = 1$ mode. This is in agreement with our results, which show that decreasing $\bar{S}$ also amplifies the effect of the azimuthal curvature, which stabilises the $n = 1$ mode, resulting in axisymmetry. Gabbard and Bostwick [222] also found that decreasing the strength of surface tension (while the fibre diameter remains fixed) causes a transition from non-axisymmetric to axisymmetric flow. This contradicts our results, which show that decreasing Γ destabilises the $n = 1$ mode, which causes the flow to become non-axisymmetric.

Despite our extensive study of the thick-film WRIBL equations (4.2.19) and

(4.2.32) in the linear regime (Sections 5.1, 5.3, and 5.4), our comparison with the real parts of the linear growth rate of the flow described by the Navier–Stokes equations (4.1.11)–(4.1.21) (Sections 5.2 and 5.3), and the solutions of the thick-film WRIBL equations (4.2.19) and (4.2.32) in the nonlinear regime (Section 5.5), we have not been able to completely recover the experimental results of Gabbard and Bostwick [222], specifically, we have not been able to recover the transition from a non-axisymmetric flow to an axisymmetric flow when the strength of surface tension is decreased. Unfortunately, Gabbard and Bostwick [222] do not give any discussion of the physical mechanism(s) which cause this transition from a non-axisymmetric flow to an axisymmetric flow as the strength of surface tension is decreased, and so we can only speculate about the reasons for this contradiction with our results. Perhaps the most likely reason for this contradiction is that Gabbard and Bostwick [222] begin their experiments by applying the fluid to the side of the fibre (i.e. they impose a highly non-axisymmetric initial condition, which is far outside the range of applicability of linear theory), whereas we have assumed that the free surface is initially almost axisymmetric with small axisymmetric and/or non-axisymmetric perturbations. Therefore, similar to the results shown in Section 5.5.3, it is possible that the disagreement is due to linear theory failing to predict the threshold between axisymmetry and non-axisymmetry in the nonlinear regime. To provide evidence to support this speculation, we consider the solution of the thick-film WRIBL equations (4.2.19) and (4.2.32) in the nonlinear regime with a highly non-axisymmetric initial condition for the free surface.

5.6.1 Highly non-axisymmetric initial condition

As the highly non-axisymmetric initial condition for the nonlinear calculations presented in this section, we use

$$q(\theta, z, 0) = 0 \tag{5.6.1}$$

for the axial flux, and

$$\begin{aligned} S(\theta,z,0) =& 1.1 + 0.493\left[1.1-\cos\left(2\pi\frac{\theta}{\theta_L}\right)\right] - 0.01\left[\sin\left(2\pi\frac{\theta}{\theta_L}\right)-\sin\left(2\pi\frac{z}{z_L}\right)\right] \\ &+ 0.015\left[\sin\left(4\pi\frac{\theta}{\theta_L}\right)-\sin\left(4\pi\frac{z}{z_L}\right)\right] - 0.01\left[\sin\left(6\pi\frac{\theta}{\theta_L}\right)-\sin\left(6\pi\frac{z}{z_L}\right)\right] \\ &+ 0.005\left[\cos\left(8\pi\frac{\theta}{\theta_L}\right)+\cos\left(8\pi\frac{z}{z_L}\right)\right] + 0.03\cos\left(2\pi\frac{\theta}{\theta_L}\right)\cos\left(2\pi\frac{z}{z_L}\right) \end{aligned} \tag{5.6.2}$$

for the free surface, where $z_L = 20$ and $\theta_L = 2\pi$ are the domain lengths of the periodic axial and azimuthal domain, respectively. The initial condition for the free surface (5.6.2) is highly non-axisymmetric with a single long bulge on one side of the fibre. Note that the combination of axisymmetric and non-axisymmetric perturbations in (5.6.2) (i.e. the second to sixth lines) is the same as in (5.5.2). A three-dimensional plot of the initial condition for the free surface (5.6.2) is shown in Figure 5.19(a), and a top-down view of this free surface is shown in Figure 5.19(b). The mean value of the initial condition for the free surface (5.6.2) is approximately 1.6423, and so we set $\bar{S} = 1.6423$, and choose parameter values which lie in the stable region of Figure (5.10) for the $n = 1$ mode, namely $Re = 2$ and $\Gamma = 0.5$. Figure 5.20 shows the real parts of the linear growth rate σ plotted as a function of k for the thick-film WRIBL equations (4.2.19) and (4.2.32) for the $n = 0$ (dashed) and $n = 1$ (solid) modes, with $Re = 2$, $\Gamma = 0.5$, and $\bar{S} = 1.6423$. For these parameter values, the $n = 0$ mode is (of course) long-wave unstable, whereas the $n = 1$ mode is stable. In what follows, we show that choosing a highly non-axisymmetric initial condition for the free surface (5.6.2) can result in a solution in the nonlinear regime which has a non-axisymmetric free surface for parameter values which lie in the region of linear stability for the $n = 1$ mode.

Figure 5.21 shows a plot of the maximum film thickness (solid) and the minimum film thickness (dashed) as a function of t, for $Re = 2$ and $\Gamma = 0.5$. Figure 5.21 shows that there are three types of behaviour that approximately correspond to $t \in [0, 10^4]$, $t \in (10^4, 1.5 \times 10^4]$, and $t \in [1.5 \times 10^4, t_f = 2.4 \times 10^4]$. For $t \in [0, 10^4]$, there is a short initial transient phase after which the maximum (minimum) film thickness monotonically decreases (increases) as the initially highly non-axisymmetric free surface becomes flatter until $t \approx 10^4$. For $t \in (10^4, 1.5 \times 10^4]$, there is a small increase (decrease) in the maximum (minimum)

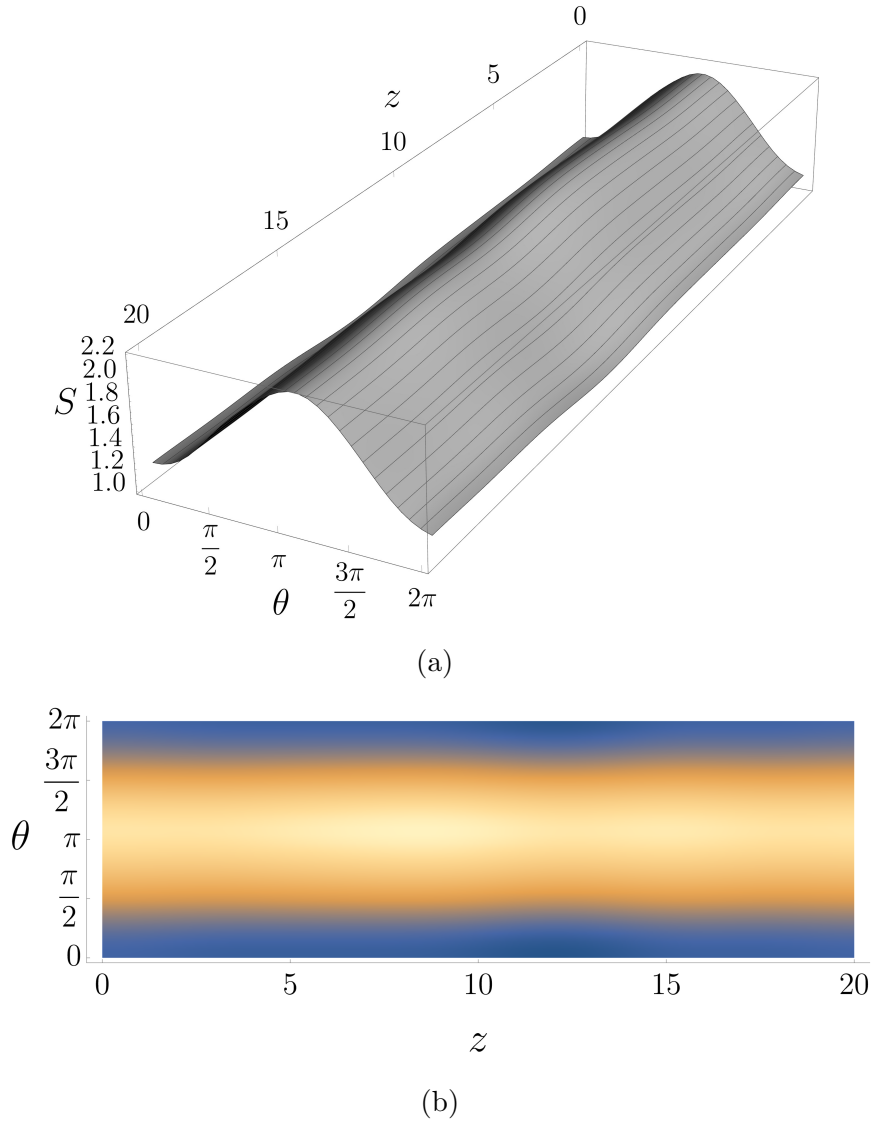

Figure 5.19: The initial condition for the free surface given by (5.6.2), displayed as (a) a three-dimensional plot, and (b) a top-down view, where, in (b), lighter and darker colours represent a thicker and thinner film, respectively.

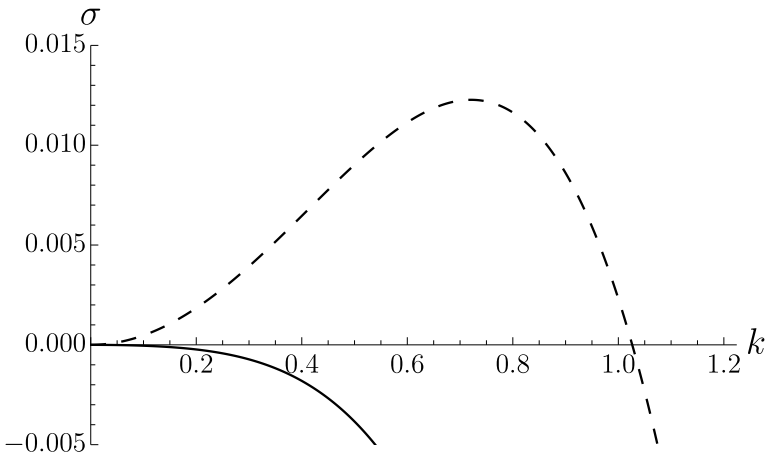

Figure 5.20: The real parts of the linear growth rate σ plotted as a function of k for the thick-film WRIBL equations (4.2.19) and (4.2.32) with $Re = 2$, $\Gamma = 0.5$, and $\bar{S} = 1.6423$, for the $n = 0$ (dashed) and $n = 1$ (solid) modes.

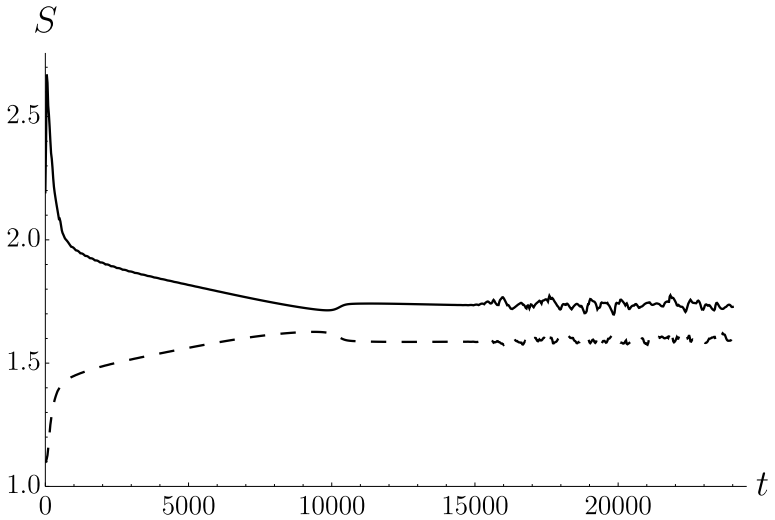

Figure 5.21: Plot of the maximum film thickness (solid) and the minimum film thickness (dashed) plotted as a function of t from $t = 0$ to $t = t_f = 2.4 \times 10^4$, with $Re = 2$ and $\Gamma = 0.5$ for the thick-film WRIBL equations (4.2.19) and (4.2.32).

film thickness, after which they remain approximately constant until $t \approx 1.5 \times 10^4$. For $t \in [1.5 \times 10^4, t_f = 2.4 \times 10^4]$, the maximum film thickness and the minimum film thickness oscillate irregularly with time.

We gain further insight into the effect of the highly non-axisymmetric initial condition for the free surface (5.6.2) on our nonlinear solutions of the thick-film WRIBL equations (4.2.19) and (4.2.32) by examining the absolute value of the Fourier transform of the free surface (5.5.4). Figure 5.22(a) shows the absolute value of the Fourier transform of the free surface for the $n = 1$ mode $|\mathcal{F}_1|$ as a function of t, with $Re = 2$ and $\Gamma = 0.5$. Figure 5.22(a) shows that there are again three types of behaviour which correspond to the same times as in Figure 5.21. For $t \in [0, 10^4]$, $|\mathcal{F}_1|$ decays, however, this decay occurs gradually over time, and not quickly as the $|\mathcal{F}_1|$ in Figures 5.12 and 5.16. Over this time interval, the maximum film thickness of the initially highly non-axisymmetric free surface decreases, which leads to this decay of $|\mathcal{F}_1|$. For $t \in (10^4, 1.5 \times 10^4]$, there is a small increase in $|\mathcal{F}_1|$, after which it begins to decay again, albeit at a slower rate, until $t \approx 1.5 \times 10^4$. Unlike in Figures 5.12 and 5.16, $|\mathcal{F}_1|$ in Figure 5.22(a) never decays to zero. For $t \in [1.5 \times 10^4, t_f = 2.4 \times 10^4]$, $|\mathcal{F}_1|$ oscillates with time in the same way as in Figure 5.14 (i.e. around a constant (non-zero) mean value), and so, in this case, the free surface remains non-axisymmetric. Specifically, the oscillations of $|\mathcal{F}_1|$ and $|\mathcal{F}_2|$ around a constant (non-zero) mean value indicate that the significance of the $n = 1$ and $n = 2$ modes varies over time. This change in the behaviour of $|\mathcal{F}_1|$ from a gradual monotonic decay to oscillation with time is due to a nonlinear non-axisymmetric instability. Figure 5.22(b) shows the absolute value of the Fourier transform of the free surface for the $n = 2$ mode $|\mathcal{F}_2|$ as a function of t, with $Re = 2$ and $\Gamma = 0.5$. The behaviour of $|\mathcal{F}_2|$ (which also never decays to zero in Figure 5.22(b)) mirrors that of $|\mathcal{F}_1|$ discussed above, however, the size of $|\mathcal{F}_2|$ is, of course, much smaller than the size of $|\mathcal{F}_1|$ due to our choice of the highly non-axisymmetric initial condition for the free surface (5.6.2).

Choosing the highly non-axisymmetric initial condition for the free surface (5.6.2) significantly increases the intricacy of the behaviour of the solutions of the thick-film WRIBL equations (4.2.19) and (4.2.32) in the nonlinear regime when compared with the initial condition for the free surface with both small axisymmetric and small non-axisymmetric perturbations to the base-state solution (5.5.2), as described in Section 5.5. We now examine the free surface in each of

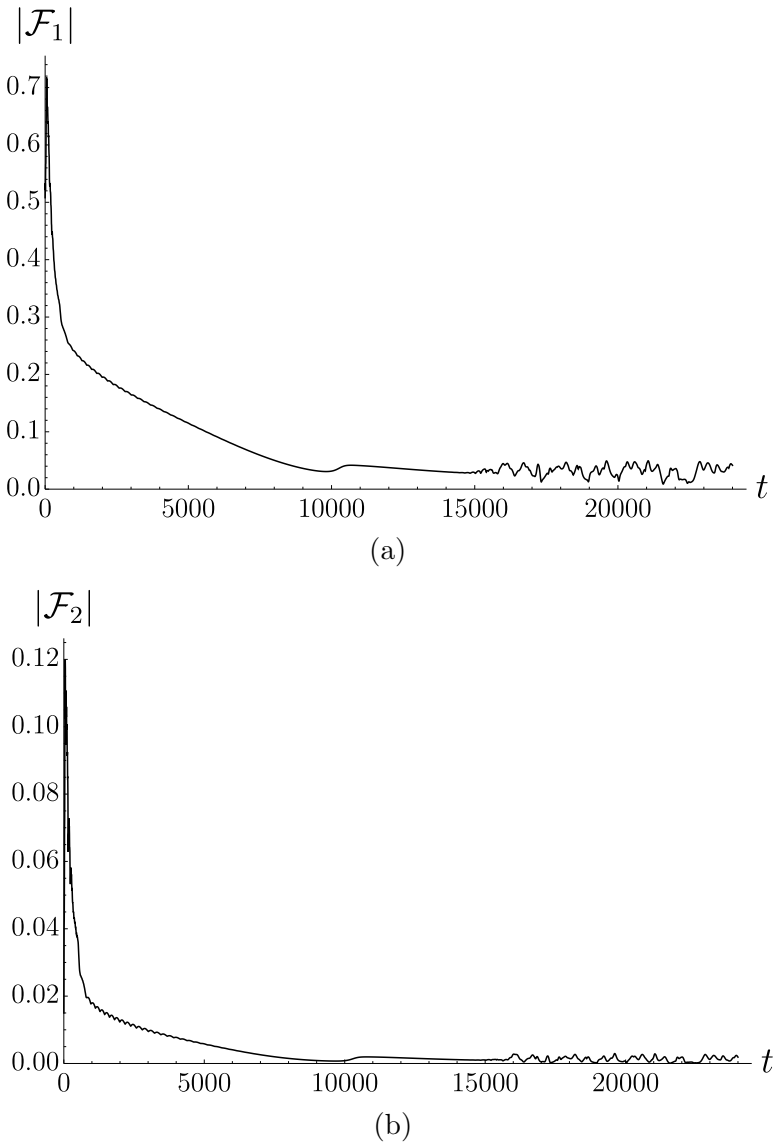

Figure 5.22: The absolute value of the Fourier transform of the free surface for (a) the $n = 1$ mode $|\mathcal{F}_1|$ and (b) $n = 2$ mode $|\mathcal{F}_2|$ as a function of t from $t = 0$ to $t = t_f = 2.4 \times 10^4$, with $Re = 2$ and $\Gamma = 0.5$. Note that the scale of the vertical axis is different in each part.

the three time intervals discussed in Figures 5.21 and 5.22. Figure 5.23(a) shows a three-dimensional plot of the free surface at $t = 7.5\times10^3$, and Figure 5.23(b) shows a top-down view of the free surface at $t = 7.5 \times 10^3$. At $t = 7.5 \times 10^3$, the highly non-axisymmetric initial condition for the free surface (5.6.2) has experienced an axisymmetric instability. Specifically, the single long bulge has broken up into two distinct bulges which flow down the same side of the fibre. This behaviour is similar to the flow patterns observed by Gabbard and Bostwick [222] (see Figure 1.40). Figure 5.24(a) shows a three-dimensional plot of the free surface at $t = 1.5 \times 10^4$, and Figure 5.24(b) shows a top-down view of the free surface at $t = 1.5 \times 10^4$. At $t = 1.5 \times 10^4$, the two bulges have "connected" in the azimuthal direction. The amplitude of the bulges remains (approximately) constant (see Figure 5.21), however, despite the flow remaining non-axisymmetric, the degree of this non-axisymmetry has diminished (see Figure 5.22). Figure 5.25(a) shows a three-dimensional plot of the free surface at $t = t_f = 2.4\times10^4$, and Figure 5.25(b) shows a top-down view of the free surface at $t = t_f = 2.4\times10^4$. At $t = t_f = 2.4\times10^4$, the two bulges have broken up due to a nonlinear non-axisymmetric instability, and the free surface reaches a configuration similar to that of Figure 5.15, in which the free surface remains non-axisymmetric, and the non-axisymmetric disturbances to the free surface undergo periods of growth and decay as time progresses.

In summary, in this section we have shown that choosing a highly non-axisymmetric initial condition for the free surface such as (5.6.2) can result in a solution in the nonlinear regime which has a non-axisymmetric free surface for parameter values which lie in the region of linear stability for the $n = 1$ mode. However, as the results presented in this section show, it appears that there exists a nonlinear non-axisymmetric instability which could be the reason for the apparent contradiction between our results and the experimental results of Gabbard and Bostwick [222].

5.7 Conclusions

In this chapter, for the non-axisymmetric coating of a vertical fibre by a thick film of fluid, in the linear regime, we analysed the analytical and numerical results of the thick-film WRIBL equations (4.2.19) and (4.2.32), the thick-film gradient-expansion equation (4.3.5), the thin-film gradient-expansion equation (4.3.7), and the Navier–Stokes equations (4.1.11)–(4.1.21). Our study was the first to explore

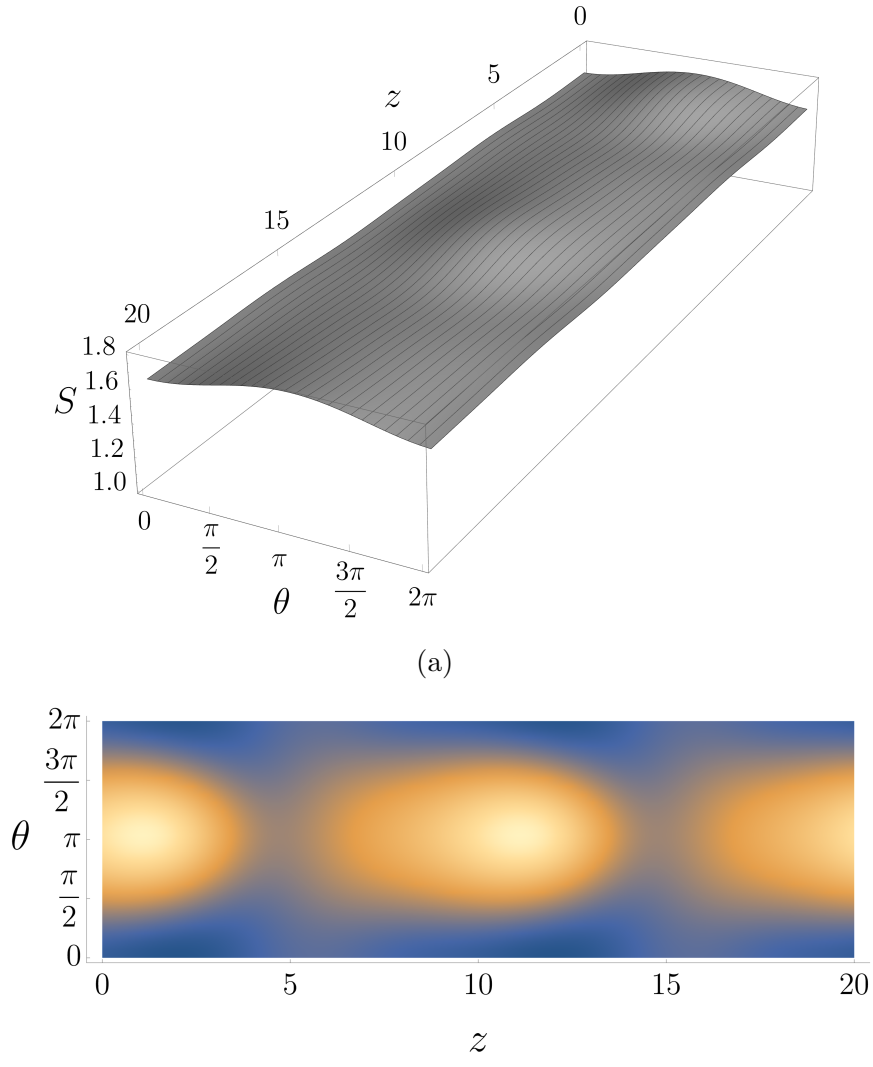

Figure 5.23: The free surface at $t = 7.5 \times 10^3$, with $Re = 2$ and $\Gamma = 0.5$, displayed as (a) a three-dimensional plot, and (b) a top-down view where, in (b), lighter and darker colours represent a thicker and thinner free surface, respectively.

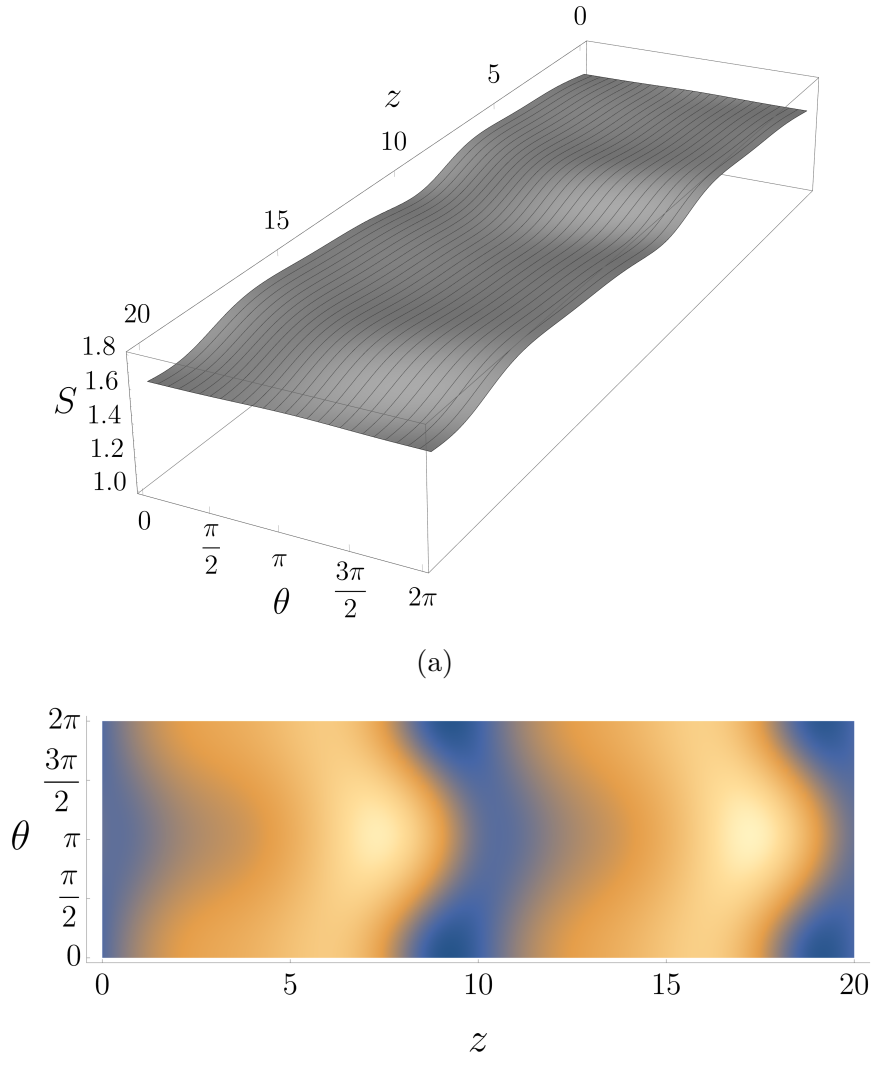

Figure 5.24: The free surface at $t = 1.5 \times 10^4$, with $Re = 2$ and $\Gamma = 0.5$, displayed as (a) a three-dimensional plot, and (b) a top-down view where, in (b), lighter and darker colours represent a thicker and thinner free surface, respectively.

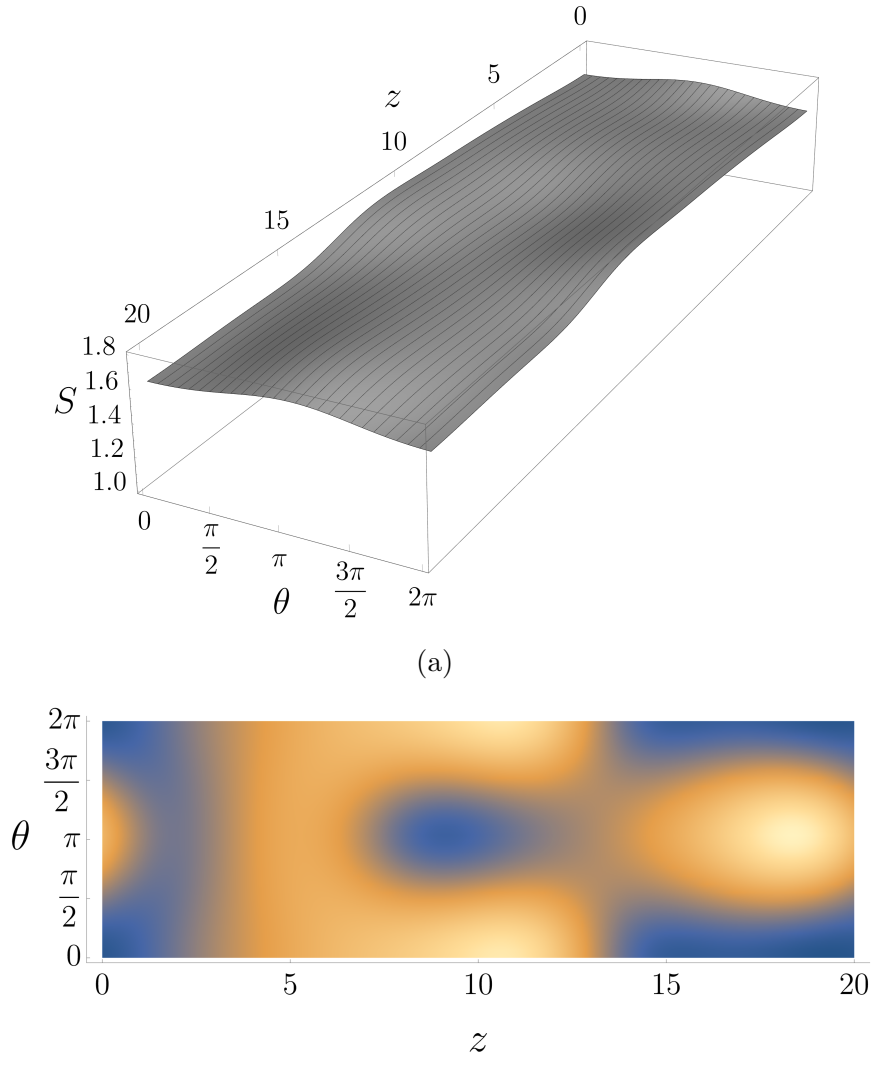

Figure 5.25: The free surface at $t = t_f = 2.4 \times 10^4$, with $Re = 2$ and $\Gamma = 0.5$, displayed as (a) a three-dimensional plot, and (b) a top-down view where, in (b), lighter and darker colours represent a thicker and thinner free surface, respectively.

the thick-film regime for non-axisymmetric flow down a vertical fibre. Additionally, we were the first to compare our results with those of the Navier–Stokes equations (4.1.11)–(4.1.21) in the linear regime for general axial wavenumbers, for non-axisymmetric flow down a vertical fibre. However, our comparisons with the results of the Navier–Stokes equations (4.1.11)–(4.1.21) in the linear regime have shown that the thick-film WRIBL equations (4.2.19) and (4.2.32) significantly overpredict the range of unstable parameter values. Furthermore, in the nonlinear regime, we analysed the numerical results of the thick-film WRIBL equations (4.2.19) and (4.2.32). Notably, we were the first to attempt to match theoretical results in both the linear and nonlinear regimes with the experimental results of Gabbard and Bostwick [222].

In Section 5.1 we performed a linear stability analysis of the flow described by the thick-film WRIBL equations (4.2.19) and (4.2.32), the thick-film gradient-expansion equation (4.3.5), and the thin-film gradient-expansion equation (4.3.7). In particular, in Section 5.1.1, we obtained an analytical expression for the linear growth rate for the $n = 0$ and $n = 1$ modes for small axial wavenumbers. For small axial wavenumbers, the stability was governed by $\sigma_{2(0)}$ given by (5.1.13), and $\sigma_{2(1)}$ given by (5.1.15), for the $n = 0$ and $n = 1$ modes, respectively. For the $n = 0$ mode, $\sigma_{2(0)}$ (5.1.13) was always positive, thus the effects of both inertia and azimuthal curvature were destabilising. For the $n = 1$ mode, the inertial terms in $\sigma_{2(1)}$ (5.1.15) were always positive (i.e. destabilising), while the azimuthal surface tension terms were always negative (i.e. stabilising).

In Section 5.2 we performed a linear stability analysis of the flow described by the Navier–Stokes equations (4.1.11)–(4.1.21). In Section 5.2.1 we provided a more comprehensive account of the analysis, which was previously summarised in a condensed form by Dávalos-Orozco and Ruiz-Chavarría [214] and Ruiz-Chavarría and Dávalos-Orozco [215]. In particular, in Sections 5.2.1.1 and 5.2.1.2, we obtained an analytical expression for the linear growth rate for the $n = 0$ and $n = 1$ modes for small axial wavenumbers, respectively. For small axial wavenumbers, the stability was governed by $\sigma_{2(0)}$ given by (5.2.61), and $\sigma_{2(1)}$ given by (5.2.97), for the $n = 0$ and $n = 1$ modes, respectively. For the $n = 0$ mode, $\sigma_{2(0)}$ (5.2.61) was identical to $\sigma_{2(0)}$ given by (5.1.13), and thus was always positive, thus the effects of both inertia and azimuthal curvature were destabilising. For the $n = 1$ mode, the azimuthal curvature terms in $\sigma_{2(1)}$ (5.2.97) were always negative (i.e. destabilising),

while the inertial terms could be either positive or negative, therefore there was a range of values of $\bar{S}$, Re, and Γ for which inertia was stabilising for the $n = 1$ mode for small axial wavenumbers.

In Section 5.3 we numerically investigated the linear stability of the flow described by the thick-film WRIBL equations (4.2.19) and (4.2.32), the thick-film gradient-expansion equation (4.3.5), the thin-film gradient-expansion equation (4.3.7), and the Navier–Stokes equations (4.1.11)–(4.1.21) for general axial wavenumbers. In Section 5.3.1 we examined the linear stability of the flow for the $n = 0$ mode for general axial wavenumbers. The flow described by the thick-film WRIBL equations (4.2.19) and (4.2.32), the thick-film gradient-expansion equation (4.3.5), the thin-film gradient-expansion equation (4.3.7), and the Navier–Stokes equations (4.1.11)–(4.1.21) was always long-wave unstable for the $n = 0$ mode. In Section 5.3.2 we examined the linear stability of the flow for the $n = 1$ mode for general axial wavenumbers. The flow described by the thick-film WRIBL equations (4.2.19) and (4.2.32), the thick-film gradient-expansion equation (4.3.5), and the thin-film gradient-expansion equation (4.3.7) was either stable or long-wave unstable for the $n = 1$ mode, and was stabilised by decreasing $\bar{S}$ and/or increasing Γ. Additionally, we observed that the flow described by the Navier–Stokes equations (4.1.11)–(4.1.21) was either stable or long-wave unstable or finite-wave unstable (see Figure 5.1), and was, in general, also stabilised by decreasing $\bar{S}$ and/or increasing Γ.

In Section 5.4 we used the thick-film WRIBL equations (4.2.19) and (4.2.32) to implement the Whitham wave hierarchy (see Section 1.2.2). In particular, we used the framework of the Whitham wave hierarchy to gain insight into the mechanisms for the (in)stability of the $n = 0$ and $n = 1$ modes. Specifically, we derived explicit expressions for the kinematic and dynamic wave speeds for these modes and determined the stability of these modes by using the stability criterion (1.2.24). In Section 5.4.1 we derived explicit expressions for the kinematic and dynamic wave speeds for small axial wavenumbers. In Section 5.4.1.3, by examining the kinematic and dynamic wave speeds, respectively, for the $n = 0$ mode (5.4.17) and (5.4.18), and the $n = 1$ mode (5.4.25) and (5.4.26), we determined that the azimuthal curvature was the key mechanism for the long-wave instability of the $n = 0$ mode and the onset of the long-wave instability of the $n = 1$ mode. Specifically, azimuthal curvature destabilised the $n = 0$ mode and stabilised the

$n = 1$ mode. In Section 5.4.2 we derived explicit expressions for the kinematic and dynamic wave speeds for general axial wavenumbers. For both the $n = 0$ and $n = 1$ modes, the axial curvature had a dispersive effect on the dynamic waves. In particular, the axial curvature had a stabilising effect on the $n = 0$ and $n = 1$ modes by widening the range of stability (1.2.24). For the $n = 1$ mode, the azimuthal surface tension terms in equation (4.2.19) had a dispersive effect on the kinematic waves. In particular, these terms had a stabilising effect on the $n = 0$ mode by slowing the kinematic wave speed for general axial wavenumbers.

In Section 5.5 we compared the results from our parametric study of the $n = 1$ mode in $\bar{S} - \Gamma$ parameter space in the linear regime with the results of our calculations in the nonlinear regime. In particular, we chose three points in Figure 5.10 which lay in the regions of linear stability (A), long-wave instability (B), and long-wave instability but close to the neutral stability curve (C). In Section 5.5.1 we showed that, for parameter values corresponding to point A in Figure 5.10, the results from the linear calculations were stable for the $n = 1$ mode, and the solution in the nonlinear regime had an axisymmetric free surface after an initial transient phase (corresponding to the $n = 1$ mode being stable). This demonstrated that the solution in the nonlinear regime was predicted by the linear calculations. In Section 5.5.2 we showed that, for parameter values corresponding to point B in Figure 5.10, the results from the linear calculations were long-wave unstable for the $n = 1$ mode, and the solution in the nonlinear regime had a non-axisymmetric free surface after an initial transient phase (corresponding to the $n = 1$ mode being unstable). This demonstrated that the solution in the nonlinear regime was predicted by the linear calculations. In Section 5.5.3 we showed that, for parameter values corresponding to point C in Figure 5.10, the results from the linear calculations were long-wave unstable for the $n = 1$ mode, whereas the solution in the nonlinear regime had an axisymmetric free surface after an initial transient phase (corresponding to the $n = 1$ mode being stable). In this case, the free surface quickly evolved to a shape which was saturated and was stable to non-axisymmetric $n = 1$ perturbations. Therefore, there was a region of $\bar{S} - \Gamma$ parameter space, close to the neutral stability curve for the $n = 1$ mode, for which the solution in the nonlinear regime was not predicted by the linear calculations.

In Section 5.6 we compared our results from Sections 5.1–5.5 with the experimental results of Gabbard and Bostwick [222]. Gabbard and Bostwick [222]

observed that the transition from a non-axisymmetric flow to a symmetric flow occurred when the fibre diameter was decreased (which agreed with our results) and/or the strength of surface tension was decreased (which contradicted our results). In their experiments, Gabbard and Bostwick [222] applied the fluid to the side of the fibre (i.e. they imposed a highly non-axisymmetric initial condition, which was far outside the range of applicability of linear theory), whereas we assumed that the free surface was initially almost axisymmetric with small axisymmetric and/or non-axisymmetric perturbations. We speculated that, similar to the results shown in Section 5.5.3, it was possible that the disagreement was due to linear theory failing to predict the threshold between axisymmetry and non-axisymmetry in the nonlinear regime. To provide evidence to support this speculation, we considered the solution of the thick-film WRIBL equations (4.2.19) and (4.2.32) in the nonlinear regime with the highly non-axisymmetric initial condition for the free surface (5.6.2) (a single long non-axisymmetric bulge) in Section 5.6.1. The mean value of the highly non-axisymmetric initial condition for the free surface (5.6.2) was approximately 1.6423, and so we chose $Re = 2$ and $\Gamma = 0.5$ such that these parameter values lay in the regions of linear stability for the $n = 1$ mode. Our nonlinear calculations revealed that choosing the highly non-axisymmetric initial condition for the free surface (5.6.2) significantly increased the intricacy of the behaviour of the solutions of the thick-film WRIBL equations (4.2.19) and (4.2.32) in the nonlinear regime when compared with the initial condition for the free surface with both small axisymmetric and small non-axisymmetric perturbations to the base-state solution (5.5.2). Initially, the highly non-axisymmetric initial condition for the free surface (5.6.2) was broken into distinct bulges due to an axisymmetric instability, which resulted in a flow pattern similar to that observed experimentally by Gabbard and Bostwick [222] (see Figure 1.40). Next, the distinct bulges were "connected" in the azimuthal direction, and despite the flow remaining non-axisymmetric, the degree of the non-axisymmetry diminished. Finally, the bulges had broken up due to a nonlinear non-axisymmetric instability, and the free surface remained non-axisymmetric. This nonlinear non-axisymmetric instability could be the reason for the contradiction between our results and the experimental results of Gabbard and Bostwick [222].

Chapter 6

Conclusions and future work

In this chapter, we conclude the work presented in this thesis. In particular, in Section 6.1 we summarise the main results of this thesis, and in Section 6.2 we outline some possible extensions to the work presented in this thesis.

6.1 Conclusions

In this thesis, we have formulated and analysed novel models for two different coating flow problems, namely the coating of a two-dimensional uniformly rotating horizontal elliptical cylinder by a thick film of fluid and a thin film of fluid, and the non-axisymmetric coating of a vertical fibre by a thick film of fluid.

In Chapter 1 we described the modelling techniques used throughout this thesis, and discussed the relationship between the length scales which arise in flow on a curved substrate in order to make precise the distinction between a thin-film approximation and a long-wave approximation. We also discussed the relevant previous works on flow on circular and elliptical cylinders, and axisymmetric and non-axisymmetric fibre flow.

In Chapter 2 we considered the coating of a two-dimensional uniformly rotating horizontal elliptical cylinder by a thick film of fluid and a thin film of fluid. We formulated the problem in the rotating frame using a body-fitted curvilinear coordinate system. We used a long-wave approximation to derive the thick-film ellipse equation (2.2.14), which incorporated the effects of cylinder eccentricity,

rotation, gravity, centrifugation, viscosity, and surface tension. We also used a thin-film approximation to derive the thin-film ellipse equation (2.3.13), which also incorporated the effects of cylinder eccentricity, rotation, gravity, centrifugation, viscosity, and surface tension. We recovered the special cases of a circular cylinder, and a rotating and inclined flat plate from both the thick-film ellipse equation (2.2.14) and the thin-film ellipse equation (2.3.13).

In Chapter 3 we analysed the analytical and numerical results of the thin-film ellipse equation (2.3.13). From the results of a parametric study on the dimensionless rotation speed, we identified four characteristic behaviours of the free surface corresponding to the rotation speed, namely the low rotation speed regime, the low-moderate rotation speed regime, the high-moderate rotation speed regime, and the high rotation speed regime. We fully explored these four regimes and determined the values of the dimensionless rotation speed for the transition between these for regimes. We then examined how these values changed when the ellipse is highly eccentric. For the special case of a stationary ellipse, we showed that when the ellipse is highly eccentric, a portion of fluid is trapped on top of the ellipse. By examining a variety of analytically tractable limits, we have shown that the behaviour of a thin film of fluid coating a two-dimensional uniformly rotating elliptical cylinder is radically different when compared to the circular case. In particular, by examining the limit of a nearly-circular ellipse, we showed that even a relatively mild departure from circularity produced significant qualitative and quantitative differences from the behaviour in the circular case.

In Chapter 4 we considered the non-axisymmetric coating of a vertical fibre by a thick film of fluid. We formulated the three-dimensional problem using a cylindrical coordinate system. We used a long-wave approximation and the WRIBL method to derive the thick-film WRIBL equations (4.2.19) and (4.2.32), which incorporated the effects of gravity, viscosity, inertia, and surface tension, and allows for variations in the film in both the axial and azimuthal directions. We performed a gradient expansion on the azimuthal flux and axial flux to reduce the thick-film WRIBL equations (4.2.19) and (4.2.32) to a single equation for the film radius, namely the thick-film gradient-expansion equation (4.3.5). We then further reduced the thick-film WRIBL equations (4.2.19) and (4.2.32) by applying a thin-film approximation to the unscaled thick-film gradient-expansion equation (4.3.5). We then neglected terms of second-order in the thin-film small aspect ratio

to obtain the thin-film gradient-expansion equation (4.3.7).

In Chapter 5 we analysed the analytical and numerical results of the thick-film WRIBL equations (4.2.19) and (4.2.32) in the linear and nonlinear regimes. In the linear regime, we showed that, in general, the results of the linear calculations of the thick-film WRIBL equations (4.2.19) and (4.2.32) correctly predicted the results of the linear calculations of the Navier–Stokes equations (4.1.11)–(4.1.21). From our linear calculations, we showed that increasing the effect of inertia and/or increasing the film radius and/or decreasing the effect of surface tension triggers the onset of a non-axisymmetric instability. By using the framework of the Whitham wave hierarchy, we determined that azimuthal curvature is the key mechanism for onset of a non-axisymmetric instability. In the nonlinear regime, we showed that, in general, the results of the linear calculations of the thick-film WRIBL equations (4.2.19) and (4.2.32) correctly predicted the solution of the thick-film WRIBL equations (4.2.19) and (4.2.32) in the nonlinear regime. Our results in the nonlinear regime revealed a nonlinear non-axisymmetric instability. We speculated that this nonlinear non-axisymmetric instability is the reason for the apparent contradiction between our results and the experimental results of Gabbard and Bostwick [222].

6.2 Future work

The work presented in this thesis motivates many potential directions for future work. An obvious direction for future work would be to compare the results in Chapters 3 and 5 with the results of DNS, however we will discuss other potential directions for future work for each of the two problems considered in this thesis in turn.

6.2.1 Future work motivated by Chapters 2 and 3

The problem of fluid coating a two-dimensional uniformly rotating elliptical cylinder has many possible extensions and directions for future work.

In Chapter 3 we extensively studied the limit of a nearly-circular ellipse ($b \to 1^-$), however we did not consider the limit of a nearly-flat ellipse ($b \to 0^+$). The

limit of a nearly-flat ellipse would be a particularly interesting limit for further study, as both Moffatt [57] and Pukhnachev [58] used a circular cylinder as a simple model for a knife (see Section 1.4.1), whereas a nearly-flat ellipse is a more accurate model for a knife.

We extensively studied the thin-film ellipse equation (2.3.13) in Chapter 3, but, due to time constraints, we did not study the results of the thick-film ellipse equation (2.2.14). It would be interesting to compare the solutions of both equations, and, in particular, the special case of a stationary ellipse could prove interesting as there is a potential for the film thickness to exceed the range of validity of the thin-film approximation (see Figure 1.10).

The circular problem has already been extended to include many other physical effects, such as the effect of an irrotational airflow [152; 153], dewetting effects [154; 155], non-isothermal effects [156; 157], the effects of a magnetic field [115], surfactant effects [114; 158], and the effect of drying on a film laden with colloidal particles [159]. We could extend the elliptical problem in the same way by including one or more of these other physical effects. In particular, including dewetting effects [154; 155] would be particularly interesting, as this would open up the possibility to study film rupture at the tips of the ellipse.

We could extend the ellipse problem to three dimensions as an elliptical cylinder and investigate how the elliptical cross-section will impact the behaviour of the free surface in the three-dimensional case. We could also extend the ellipse problem to three dimensions as an ellipsoid. Recent work on the coating of a three-dimensional rotating ellipsoid with a thin film of fluid [230] could easily be extended to consider the coating of a three-dimensional rotating ellipsoid with a thick film of fluid, using our work in Chapter 2.

We could include the effects of convective inertia and the Coriolis force, both of which we have neglected at present. To include these effects, we would need to use the WRIBL method. We could also include the effect of Euler force by introducing a time-dependent rotation speed [224, Chapter 3], which would also likely require the use of the WRIBL method.

We have shown that the geometry of an ellipse has a significant influence on the free surface, and so it would also be interesting to use control theory to control the free surface towards a desired target state [231].

6.2.2 Future work motivated by Chapters 4 and 5

The problem of the non-axisymmetric coating of a vertical fibre by a thick film of fluid also has many possible extensions and directions for future work.

In Chapter 5, our nonlinear calculations with a highly non-axisymmetric initial condition for the free surface revealed a nonlinear non-axisymmetric instability, which would be a particularly interesting topic for further study. In particular, further study of this nonlinear non-axisymmetric instability might confirm our proposed explanation for the contradiction between our results and the experimental results of Gabbard and Bostwick [222].

We could extend the thick-film WRIBL equations (4.2.19) and (4.2.32) to include the effects of viscous dispersion at second order in the long-wave approximation, i.e. extending the first-order model to the simplified second-order model (see Section 1.2.1.4). The simplified second-order model would consist of three equations, as the azimuthal flux would have an independent evolution equation (i.e. the azimuthal velocity would no longer be linked to the free surface). We expect that the simplified second-order model would improve the agreement with the Navier–Stokes equations (4.1.11)–(4.1.21) in the linear and nonlinear regimes.

It would be interesting to include other physical effects to enhance or suppress the non-axisymmetric instability. For example, we could introduce another non-axisymmetric instability-inducing effect, such as electric field [219] or thermal effects [220], or we could introduce the effect of a rotating fibre to make the $n = 1$ mode dominant [203]. We could also introduce other physical effects to stabilise all azimuthal wavenumbers, such as the electric effects studied by Wray et al. [198].

An extension of particular interest would be to consider different fibre shapes (i.e. fibres which have a non-circular cross-section). Differently shaped fibres have, at present, only been considered experimentally [232]. By using the body-fitted curvilinear coordinate system described in Chapter 2, as well as the WRIBL method, a model for a different fibre shape could be developed.

Appendix A

Numerical schemes

In this appendix, we give the details of the codes used to obtain numerical solutions of the thin-film ellipse equation (2.3.13) in Chapter 3 and the thick-film WRIBL equations (4.2.19) and (4.2.32) in Chapter 5. All numerical codes discussed in this section were implemented either in C++ or Mathematica [229], and are based on previous well-tested numerical schemes by one of the author's supervisors (Dr A. W. Wray) [55; 60; 62; 233].

A.1 Numerical solution of the thin-film ellipse equation (2.3.13)

In Chapter 3, to obtain numerical solutions of the thin-film ellipse equation (2.3.13) we used a numerical code which was implemented in C++ and is based on an existing code by Dr A. W. Wray, which is well-tested, with convergence and validity tests performed. The original code solved the thick-film gradient-expansion model (equation (3.18) from Wray and Cimpeanu [60]), and the thin-film gradient-expansion model (equation (6.13) from Wray et al. [55] and equation (3.19) from Wray and Cimpeanu [60]) for the circular problem; we replace these equations by inputting the thin-film ellipse equation (2.3.13).

The code used the method of lines in which the PDE is discretised in space using a second-order centred-finite-difference method, which results in a large number of coupled ODEs in time, and allows periodic boundary conditions to be imposed.

A second-order centred-finite-difference method is used as it offers second-order accuracy and is more accurate than a one-sided finite difference method (such as first-order forwards or first-order backwards) which only offers first-order accuracy. For time integration, a second-order implicit trapezium rule method was used. This method was used as it offers second-order accuracy for solving stiff equations which are not particularly complicated to implement, such as a single evolution equation for η in the present case. To improve the speed of computations, the code uses an adaptive time-stepping method, where the initial time step was set to be 0.001.

A uniform grid of 2000 spatial grid points was chosen, as refinement tests showed that doubling the number of spatial grid points did not result in discernible differences between the two numerical solutions, indicating convergence in space. Validity tests were performed by comparing our numerical solutions against our analytical solutions in Chapter 3.

The C++ code was tested against a separate code which was implemented in Mathematica [229] by Dr A. W. Wray. The Mathematica code also uses the method of lines, discretising the PDE in space using a second-order centred-finite-difference method. In Mathematica, the time integration is performed automatically based on desired accuracy and precision goals. Refinement and validity tests were conducted on the Mathematica code as well. The comparison confirmed the agreement between the C++ and Mathematica implementations. The Mathematica code was the initial code used, however for values of W in the high rotation speed regime and in the upper end of the high-moderate rotation speed regime, the automated time integration in Mathematica led to high memory usage, ultimately causing the code to crash before reaching the desired final time. This crash prompted us to switch to using the C++ code instead.

A.2 Numerical solution of the thick-film WRIBL equations (4.2.19) and (4.2.32)

In Chapter 5, to obtain numerical solutions of the thick-film WRIBL equations (4.2.19) and (4.2.32) we used a numerical code which was implemented in C++ and is based on an existing code by Dr A. W. Wray, which is well-tested, with convergence and validity tests performed. The original code solved the WRIBL

equations (equations (4), (5), and (10) from Wray et al. [231]) for the planar electrostatic-control problem; we replace these equations by inputting the thick-film WRIBL equations (4.2.19) and (4.2.32).

The code used the method of lines in which the PDE is discretised in space using a second-order centred-finite-difference method, which results in a large number of coupled ODEs in time and allows periodic boundary conditions to be imposed. A second-order centred-finite-difference method is used as it offers second-order accuracy and is more accurate than a one-sided finite difference method (such as first-order forwards or first-order backwards) which only offers first-order accuracy. For time integration, a first-order backwards Euler implicit method was used. This method was used as it offers greater numerical stability for solving stiff equations which are complicated to implement, such as two coupled evolution equations for S and q in the present case. To improve the speed of computations, the code uses an adaptive time-stepping method, where the initial time step was set to be 0.01. The code is multi-threaded which exploits parallel processes where one process constantly recomputes the Jacobian while another process applies it.

A uniform grid of 6000 spatial grid points (30 in the azimuthal direction and 200 in the axial direction) was chosen, as refinement tests showed that doubling the total number of spatial grid points (40 in the azimuthal direction and 300 in the axial direction to give 12000 total spatial grid points) did not result in discernible differences between the two numerical solutions, indicating convergence in space. Validity tests were performed by comparing our numerical solutions against our analytical solutions in Chapter 5.

The code was tested against a separate existing C++ code by Dr A. W. Wray which used a Runga-Kutta-45 solver in time, which was also well-tested, with convergence and validity tests performed. To avoid confusion, hereafter we will refer to the C++ code with the Runga-Kutta-45 solver in time and the C++ code with the first-order backwards Euler implicit method as simply the "RK45 code" and the "backwards Euler code", respectively. The original RK45 code solved the WRIBL equations (equations (B1)–(B12) from Wray et al. [62]) for the planar electrostatic problem, and equations (10) and (11) from Wray et al. [233] for the electrostatic suppression of the "coffee-stain effect"; we replace these equations by inputting the thick-film WRIBL equations (4.2.19) and (4.2.32). Refinement and validity tests were then performed on the modified RK45 code as well. The

comparison confirmed the agreement between the backwards Euler code and the RK45 code. The RK45 code was the initial code used, however, while accurate, the computational time was too long for the parameter values used in our calculations. The long computational time prompted us to switch to using the backwards Euler code instead.

Appendix B

Chebyshev–Tau method

The Chebyshev–Tau method is a well-known numerical method which is used to find the eigenvalues of the linearised Navier–Stokes equations [60; 62; 234–238]. We first describe the process of the Chebyshev–Tau method in general before later discussing how this was implemented and used in Chapter 5.

The Chebyshev–Tau method seeks a solution for velocity components (u, v, w) and pressure p as a series expansion involving N Chebyshev polynomials, with these polynomials serving as basis functions for each field. By substituting this expansion into the Navier–Stokes and continuity equations, we obtain a system of $4N + 1$ coupled ODEs: N coefficients for each of the linearised u, v, w, and p, and one coefficient for the linearised film thickness. To impose boundary conditions, m rows (where m represents the number of boundary conditions) are replaced within this system with the m boundary conditions. This results in a generalised eigenvalue problem which can be easily solved using Mathematica [229]. We are only interested in the behaviour of the largest eigenvalue, as this corresponds to the most unstable (or least stable) mode and thus will determine if linear perturbations to the base-state solution grow or decay. While the solution becomes more accurate as the value of N increases, the computational cost also increases.

The numerical code for the Chebyshev–Tau method was implemented in Mathematica [229] and is based on an existing implementation by Dr A. W. Wray, which is well-tested with validity tests performed. This numerical code has been successfully used in other previous works for flow on circular cylinders [60] and flow down inclined planes [62], and was modified by inputting the Navier–Stokes equations

(4.1.11)–(4.1.21). We used $N = 18$ Chebyshev polynomials, as we found that this gave the best balance between computational cost and accuracy. In our implementation of the Chebyshev–Tau method, we have $m = 7$ boundary conditions (i.e. three at the surface of the fibre (4.1.15) and four at the free surface (4.1.17)–(4.1.21)). Validity tests were performed by comparing our numerical results from this code against our analytical solutions in Section 5.2.1.

Appendix C

Stability matrices

C.1 Stability matrix $A_{0(0)}$

The matrix $A_{0(0)}$ in the matrix problem (5.2.49) is given by

$$A_{0(0)} = \begin{bmatrix} 1 & 1 & 0 & 1 & 0 \\ -1 & 1 & 1 & 3 & 0 \\ 0 & 0 & -2\bar{S} & -8\bar{S}^3 & \bar{S}^2 \\ \dfrac{i}{\bar{S}} & i\bar{S} & i\bar{S}\log\bar{S} & i\bar{S}^3 & \sigma_{1(0)} + i\dfrac{1-\bar{S}^2+2\bar{S}^2\log\bar{S}}{4} \\ 0 & 0 & 0 & 16i\bar{S}^2 & 0 \end{bmatrix}. \qquad \text{(C.1.1)}$$

C.2 Stability matrix $A_{1(0)}$

The matrix $A_{1(0)}$ in the matrix problem (5.2.59) is given by

$$A_{1(0)} = \begin{bmatrix} 1 & 1 & 0 & 1 & i\frac{Re\bar{S}}{384}\left(7+12\bar{S}^2+30\bar{s}^2\log\bar{S}\right) \\ -1 & 1 & 1 & 3 & i\frac{Re\bar{S}}{192}\left(7+12\bar{S}^2+33\bar{s}^2\log\bar{S}\right) \\ 0 & 0 & -2\bar{S} & -8\bar{S}^3 & i\frac{Re\bar{S}^4}{32}C_1 \\ \frac{i}{\bar{S}} & i\bar{S} & i\bar{S}\log\bar{S} & i\bar{S}^3 & \sigma_{2(0)}+\frac{Re\bar{S}^4}{768}C_2 \\ 0 & 0 & 0 & 16i\bar{S}^2 & -\Gamma+\frac{Re\bar{S}^3\left(1+\bar{S}^2\right)}{8} \end{bmatrix}, \tag{C.2.1}$$

where

$$C_1 = -\bar{S}^2 - 4\left(-2+\bar{S}^2\right)\log\bar{S} + 8\bar{S}^2\log^2\bar{S}, \tag{C.2.2}$$

$$C_2 = -3 - 35\bar{S}^2 - 12\left(-1+\bar{S}^2\right)\log\bar{S} + 24\left(1+\bar{S}^2\right)\log^2\bar{S}. \tag{C.2.3}$$

C.3 Stability matrix $A_{0(1)}$

The matrix $A_{0(1)}$ in the matrix problem (5.2.73) is given by

$$A_{0(1)} = \begin{bmatrix} 1 & 1 & 0 & 0 & -i & 0 & 0 \\ 0 & 0 & 1 & 1 & 1 & 0 & 0 \\ 0 & 2 & 0 & 0 & 2i & i & 0 \\ -\bar{S}^2 & -\bar{S}^4 & i\bar{S}^2 & -i\bar{S}^4 & 4i & -i\bar{S}^2 & 0 \\ 1 & -3\bar{S}^2 & -i & i\bar{S}^2 & 0 & i & \bar{S}^2 \\ i & i\bar{S}^2 & 0 & 0 & \dfrac{1}{\bar{S}^2} & -\log\bar{S} & \sigma_{1(1)} + i\dfrac{1-\bar{S}^2+2\bar{S}^2\log\bar{S}}{4} \\ 2i\bar{S} & -2i\bar{S}^3 & 2\bar{S} & -2\bar{S}^3 & \dfrac{4}{\bar{S}} & 2\bar{S} & 0 \end{bmatrix}. \tag{C.3.1}$$

C.4 Stability matrix $A_{1(1)}$

The matrix $A_{1(1)}$ in the matrix problem (5.2.95) is given by

$$A_{1(1)} = \begin{bmatrix} 1 & 1 & 0 & 0 & -i & 0 & -iRe\bar{S}^2C_3 \\ 0 & 0 & 1 & 1 & 1 & 0 & Re\bar{S}^2C_4 \\ 0 & 2 & 0 & 0 & 2i & i & iRe\bar{S}^2C_5 \\ -\bar{S}^2 & -\bar{S}^4 & i\bar{S}^2 & -i\bar{S}^4 & 4i & -i\bar{S}^2 & -iRe\bar{S}^8C_6 \\ 1 & -3\bar{S}^2 & -i & i\bar{S}^2 & 0 & i & -iRe\bar{S}^6C_7 \\ i & i\bar{S}^2 & 0 & 0 & \dfrac{1}{\bar{S}^2} & -\log\bar{S} & \sigma_{2(1)} + Re\bar{S}^6C_8 \\ 2i\bar{S} & -2i\bar{S}^3 & 2\bar{S} & -2\bar{S}^3 & \dfrac{4}{\bar{S}} & 2\bar{S} & \Gamma\bar{S}^2 + Re\bar{S}^7C_9 \end{bmatrix}, \tag{C.4.1}$$

where

$$C_3 = \frac{1}{4608\left(1+\bar{S}^2\right)\left(1+\bar{S}^4\right)^2}\Bigg[-21+49\bar{S}^2-24\bar{S}^4+58\bar{S}^6+3\bar{S}^8+51\bar{S}^{10} + 6\bar{S}^2\left(3+3\bar{S}^2+7\bar{S}^4+3\bar{S}^6+4\bar{S}^8\right)\log\bar{S}\Bigg], \tag{C.4.2}$$

$$C_4 = \frac{1}{4608\left(1+\bar{S}^2\right)\left(1+\bar{S}^4\right)^2}\Bigg[-37+49\bar{S}^2-248\bar{S}^4+310\bar{S}^6-241\bar{S}^8+51\bar{S}^{10} + 6\bar{S}^2(9-15\bar{S}^2+13\bar{S}^4-15\bar{S}^6+4\bar{S}^8)\log\bar{S}\Bigg], \tag{C.4.3}$$

$$C_5 = \frac{1}{2304\left(1+\bar{S}^2\right)\left(1+\bar{S}^4\right)^2}\Bigg[6\bar{S}^2(9-3\bar{S}^2+16\bar{S}^4+7\bar{S}^8+3\bar{S}^{10})\log\bar{S} + 34+139\bar{S}^2-13\bar{S}^4+346\bar{S}^6-68\bar{S}^8+123\bar{S}^{10}-9\bar{S}^{12}\Bigg], \tag{C.4.4}$$

$$C_6 = \frac{1}{1152\left(1+\bar{S}^2\right)\left(1+\bar{S}^4\right)^2}\Bigg[86+68\bar{S}^2-89\bar{S}^4+323\bar{S}^6-199\bar{S}^8+87\bar{S}^{10} + 3\left(101-19\bar{S}^2+142\bar{S}^4-18\bar{S}^6+41\bar{S}^8+\bar{S}^{10}\right)\log\bar{S}\Bigg], \tag{C.4.5}$$

$$C_7 = \frac{1}{384\left(1+\bar{S}^2\right)\left(1+\bar{S}^4\right)}\Bigg[144-108\bar{S}^2+183\bar{S}^4-85\bar{S}^6 + 3(-1-\bar{S}^2+23\bar{S}^4+7\bar{S}^6)\log\bar{S}\Bigg] + \frac{\log^2\bar{S}}{32}, \tag{C.4.6}$$

(C.4.7)

$$C_8 = \frac{1}{4608\left(1+\bar{S}^2\right)\left(1+\bar{S}^4\right)^2}\Bigg[6(-73+20\bar{S}^2-143\bar{S}^4+21\bar{S}^6-70\bar{S}^8+\bar{S}^{10})\log\bar{S} \\ -23+51\bar{S}^2-28\bar{S}^4+62\bar{S}^6+\bar{S}^8+53\bar{S}^{10}\Bigg]-\frac{\left(5-2\bar{S}^2+\bar{S}^4\right)\log^2\bar{S}}{128\left(1+\bar{S}^4\right)}, \tag{C.4.8}$$

$$C_9 = \frac{1}{576\left(1+\bar{S}^2\right)\left(1+\bar{S}^4\right)^2}\Bigg[6(16-20\bar{S}^2+35\bar{S}^4-9\bar{S}^6+19\bar{S}^8+11\bar{S}^{10})\log\bar{S} \\ -88+5\bar{S}^2-221\bar{S}^4+77\bar{S}^6+95\bar{S}^8-132\bar{S}^{10}\Bigg]-\frac{\log^2\bar{S}}{32}. \tag{C.4.9}$$

Bibliography

[1] R. V. Craster and O. K. Matar, "Dynamics and stability of thin liquid films", *Reviews of Modern Physics*, **81**(3), 1131–1198, 2009.

[2] A. Oron, S. H Davis, and S. G. Bankoff, "Long-scale evolution of thin liquid films", *Reviews of Modern Physics*, **69**(3), 931–980, 1997.

[3] M. Sellier, "Inverse problems in free surface flows: a review", *Acta Mechanica*, **227**(3), 913–935, 2016.

[4] D. T. Papageorgiou, "Film flows in the presence of electric fields", *Annual Review of Fluid Mechanics*, **51**, 155–187, 2019.

[5] A. J. T. M. Mathijssen, M. Lisicki, V. N. Prakash, and E. J. L. Mossige, "Culinary fluid mechanics and other currents in food science", *Reviews of Modern Physics*, **95**(2), 025004, 2023.

[6] R. W. Yeung, "Numerical methods in free-surface flows", *Annual Review of Fluid Mechanics*, **14**, 395–442, 1982.

[7] C. Duprat, "Moisture in textiles", *Annual Review of Fluid Mechanics*, **54**, 443–467, 2022.

[8] S. K. Wilson and H.-M. D'Ambrosio, "Evaporation of sessile droplets", *Annual Review of Fluid Mechanics*, **55**, 481–509, 2023.

[9] D. Brutin and V. Starov, "Recent advances in droplet wetting and evaporation", *Chemical Society Reviews*, **47**(2), 558–585, 2018.

[10] D. Lohse, "Fundamental fluid dynamics challenges in inkjet printing", *Annual Review of Fluid Mechanics*, **54**, 349–382, 2022.

[11] W.-T. Tsai and D. K. P. Yue, "Computation of nonlinear free-surface flows", *Annual Review of Fluid Mechanics*, **28**, 249–278, 1996.

[12] J. Eggers, "Nonlinear dynamics and breakup of free-surface flows", *Reviews of Modern Physics*, **69**(3), 865, 1997.

[13] H. E. Huppert, "Flow and instability of a viscous current down a slope", *Nature*, **300**(5891), 427–429, 1982.

[14] R. W. Griffiths, "The dynamics of lava flows", *Annual Review of Fluid Mechanics*, **32**, 477–518, 2000.

[15] H. E. Huppert, "The propagation of two-dimensional and axisymmetric viscous gravity currents over a rigid horizontal surface", *Journal of Fluid Mechanics*, **121**, 43–58, 1982.

[16] B. Hunt, "Newtonian fluid mechanics treatment of debris flows and avalanches", *Journal of Hydraulic Engineering*, **120**(12), 1350–1363, 1994.

[17] C. Ancey and M. Meunier, "Estimating bulk rheological properties of flowing snow avalanches from field data", *Journal of Geophysical Research: Earth Surface*, **109**(F1), F01004, 2004.

[18] K. Hutter, B. Svendsen, and D. Rickenmann, "Debris flow modeling: A review", *Continuum Mechanics and Thermodynamics*, **8**(1), 1–35, 1994.

[19] L. W. Morland and G. D. Smith, "Influence of non-uniform temperature distribution on the steady motion of ice sheets", *Journal of Fluid Mechanics*, **140**, 113–133, 1984.

[20] K. Hutter, "Dynamics of glaciers and large ice masses", *Annual Review of Fluid Mechanics*, **14**, 87–130, 1982.

[21] D. R. Baral, K. Hutter, and R. Greve, "Asymptotic theories of large-scale motion, temperature, and moisture distribution in land-based polythermal ice sheets: A critical review and new developments", *Applied Mechanics Reviews*, **54**(3), 215–256, 2001.

[22] J. Yang, P. Andreasson, P. Teng, and Q. Xie, "The past and present of discharge capacity modeling for spillways—A Swedish perspective", *Fluids*, **4**(1), 10, 2019.

[23] X. Yang and E. Miyako, "Soap bubble pollination", *iScience*, **23**(6), 101188, 2020.

[24] S. F. Ahmadi, S. Nath, C. M. Kingett, P. Yue, and J. B. Boreyko, "How soap bubbles freeze", *Nature Communications*, **10**, 2531, 2019.

[25] R. Bhardwaj and A. Agrawal, "Likelihood of survival of coronavirus in a respiratory droplet deposited on a solid surface", *Physics of Fluids*, **32**(6), 061704, 2020.

[26] G. P. Narayan, M. G. St. John, S. M. Zubair, and J. H. Lienhard V, "Thermal design of the humidification dehumidification desalination system: An experimental investigation", *International Journal of Heat and Mass Transfer*, **58**(1), 740–748, 2013.

[27] M. Damak and K. K. Varanasi, "Electrostatically driven fog collection using space charge injection", *Science Advances*, **4**(6), eaao5323, 2018.

[28] H. A. Stone, A. D. Stroock, and A. Ajdari, "Engineering flows in small devices: microfluidics toward a lab-on-a-chip", *Annual Review of Fluid Mechanics*, **36**, 381–411, 2004.

[29] T. M. Squires and S. R. Quake, "Microfluidics: Fluid physics at the nanoliter scale", *Reviews of Modern Physics*, **77**(3), 977–1026, 2005.

[30] S. J. Weinstein and K. J. Ruschak, "Coating flows", *Annual Review of Fluid Mechanics*, **36**, 29–53, 2004.

[31] T. G. Myers, "Thin films with high surface tension", *SIAM Review*, **40**(3), 441–462, 1998.

[32] K. J. Ruschak, "Coating flows", *Annual Review of Fluid Mechanics*, **17**, 65–89, 1985.

[33] A. R. Parker and C. R. Lawrence, "Water capture by a desert beetle", *Nature*, **414**(6859), 33–34, 2001.

[34] F. Fathieh, M. J. Kalmutzki, E. A. Kapustin, P. J. Waller, J. Yang, and O. M. Yaghi, "Practical water production from desert air", *Science Advances*, **4**(6), eaat3198, 2018.

[35] J. B. Grotberg, "Pulmonary flow and transport phenomena", *Annual Review of Fluid Mechanics*, **26**, 529–571, 1994.

[36] R. J. Braun, R. Usha, G. B. McFadden, T. A. Driscoll, L. P. Cook, and P. E. King-Smith, "Thin film dynamics on a prolate spheroid with application to the cornea", *Journal of Engineering Mathematics*, **73**(1), 121–138, 2012.

[37] A. Sharma and E. Ruckenstein, "An analytical nonlinear theory of thin film rupture and its application to wetting films", *Journal of Colloid and Interface Science*, **113**(2), 456–479, 1986.

[38] H. Wong, I. Fatt, and C. J. Radke, "Deposition and thinning of the human tear film", *Journal of Colloid and Interface Science*, **184**(1), 44–51, 1996.

[39] B. A. Morris, *"The science and technology of flexible packaging: multilayer films from resin and process to end use"*, William Andrew Publishing, 2016.

[40] M. A. Hayes and S. B. G. O'Brien, "The fluid profile during spin-coating over a small sinusoidal topography", *International Journal of Mathematics and Mathematical Sciences*, **2004**(43), 2279–2298, 2004.

[41] L. E. Stillwagon and R. G. Larson, "Fundamentals of topographic substrate leveling", *Journal of Applied Physics*, **63**(11), 5251–5258, 1988.

[42] B. A. Morris, "Understanding why adhesion in extrusion coating decreases with diminishing coating thickness", *Journal of Plastic Film & Sheeting*, **24**(1), 53–88, 2008.

[43] T. D. Lee and A. U. Ebong, "A review of thin film solar cell technologies and challenges", *Renewable and Sustainable Energy Reviews*, **70**, 1286–1297, 2017.

[44] C. N. Bucherl, K. R. Oleson, and H. W. Hillhouse, "Thin film solar cells from sintered nanocrystals", *Current Opinion in Chemical Engineering*, **2**(2), 168–177, 2013.

[45] H. Chen, T. Ran, Y. Gan, J. Zhou, Y. Zhang, L. Zhang, D. Zhang, and L. Jiang, "Ultrafast water harvesting and transport in hierarchical microchannels", *Nature Materials*, **17**(10), 935–942, 2018.

[46] Y. Zheng, H. Bai, Z. Huang, X. Tian, F.-Q. Nie, Y. Zhao, J. Zhai, and L. Jiang, "Directional water collection on wetted spider silk", *Nature*, **463**(7281), 640–643, 2010.

[47] L. Guo and G. H. Tang, "Experimental study on directional motion of a single droplet on cactus spines", *International Journal of Heat and Mass Transfer*, **84**, 198–202, 2015.

[48] J. Ju, H. Bai, Y. Zheng, T. Zhao, R. Fang, and L. Jiang, "A multi-structural and multi-functional integrated fog collection system in cactus", *Nature Communications*, **3**, 1247, 2012.

[49] J. Ju, X. Yao, S. Yang, L. Wang, R. Sun, Y. He, and L. Jiang, "Cactus stem inspired cone-arrayed surfaces for efficient fog collection", *Advanced Functional Materials*, **24**(44), 6933–6938, 2014.

[50] H. Bai, X. Tian, Y. Zheng, J. Ju, Y. Zhao, and L. Jiang, "Direction controlled driving of tiny water drops on bioinspired artificial spider silks", *Advanced Materials*, **22**(48), 5521–5525, 2010.

[51] M. Cao, J. Ju, K. Li, S. Dou, K. Liu, and L. Jiang, "Facile and large-scale fabrication of a cactus-inspired continuous fog collector", *Advanced Functional Materials*, **24**(21), 3235–3240, 2014.

[52] C. Ruyer-Quil and P. Manneville, "Improved modeling of flows down inclined planes", *The European Physical Journal B: Condensed Matter and Complex Systems*, **15**(2), 357–369, 2000.

[53] B. Scheid, C. Ruyer-Quil, and P. Manneville, "Wave patterns in film flows: modelling and three-dimensional waves", *Journal of Fluid Mechanics*, **562**, 183–222, 2006.

[54] T. Shlang and G. I. Sivashinsky, "Irregular flow of a liquid film down a vertical column", *Journal de Physique*, **43**(3), 459–466, 1982.

[55] A. W. Wray, D. T. Papageorgiou, and O. K. Matar, "Reduced models for thick liquid layers with inertia on highly curved substrates", *SIAM Journal on Applied Mathematics*, **77**(3), 881–904, 2017.

[56] P. L. Evans, L. W. Schwartz, and R. V. Roy, "Steady and unsteady solutions for coating flow on a rotating horizontal cylinder: Two-dimensional theoretical and numerical modeling", *Physics of Fluids*, **16**(8), 2742–2756, 2004.

[57] H. K. Moffatt, "Behaviour of a viscous film on the outer surface of a rotating cylinder", *Journal de Mécanique*, **16**(5), 651–673, 1977.

[58] V. V. Pukhnachev, "Motion of a liquid film on the surface of a rotating cylinder in a gravitational field", *Journal of Applied Mechanics and Technical Physics*, **18**(3), 344–351, 1977.

[59] S. Kalliadasis, C. Ruyer-Quil, B. Scheid, and M. G. Velarde, *"Falling Liquid Films"*, vol. 176, Springer Series on Applied Mathematical Sciences, 2012.

[60] A. W. Wray and R. Cimpeanu, "Reduced-order modelling of thick inertial flows around rotating cylinders", *Journal of Fluid Mechanics*, **898**, A1, 2020.

[61] G. R. Daly, P. H. Gaskell, and S. Veremieiev, "Gravity-driven film flow down a uniformly heated smoothly corrugated rigid substrate", *Journal of Fluid Mechanics*, **930**, A23, 2022.

[62] A. W. Wray, O. K. Matar, and D. T. Papageorgiou, "Accurate low-order modeling of electrified falling films at moderate Reynolds number", *Physical Review Fluids*, **2**(6), 063701, 2017.

[63] C. Ruyer-Quil and P. Manneville, "Further accuracy and convergence results on the modeling of flows down inclined planes by weighted-residual approximations", *Physics of Fluids*, **14**(1), 170–183, 2002.

[64] C. Ruyer-Quil, P. Treveleyan, F. Giorgiutti-Dauphiné, C. Duprat, and S. Kalliadasis, "Modelling film flows down a fibre", *Journal of Fluid Mechanics*, **603**, 431–462, 2008.

[65] A. Samanta, C. Ruyer-Quil, and B. Goyeau, "A falling film down a slippery inclined plane", *Journal of Fluid Mechanics*, **684**, 353–383, 2011.

[66] K. Zakaria and M. A. Sirwah, "Nonlinear dynamics of a liquid film flow over a solid substrate in the presence of external shear stress and electric field", *The European Physical Journal Plus*, **137**(9), 1087, 2022.

[67] D. J. Benney, "Long waves on liquid films", *Journal of Mathematics and Physics*, **45**, 150–155, 1966.

[68] A. Pumir, P. Manneville, and Y. Pomeau, "On solitary waves running down an inclined plane", *Journal of Fluid Mechanics*, **135**, 27–50, 1983.

[69] A. Oron and O. Gottlieb, "Subcritical and supercritical bifurcations of the first- and second-order Benney equations", *Journal of Engineering Mathematics*, **50**(2), 121–140, 2004.

[70] S. W. Joo, S. H. Davis, and S. G. Bankoff, "On falling-film instabilities and wave breaking", *Physics of Fluids A: Fluid Dynamics*, **3**(1), 231–232, 1991.

[71] P. Rosenau, A. Oron, and J. M. Hyman, "Bounded and unbounded patterns of the Benney equation", *Physics of Fluids A: Fluid Dynamics*, **4**(6), 1102–1104, 1992.

[72] T. R. Salamon, R. C. Armstrong, and R. A. Brown, "Traveling waves on vertical films: Numerical analysis using the finite element method", *Physics of Fluids*, **6**(6), 2202–2220, 1994.

[73] B. Ramaswamy, S. Chippada, and S. W. Joo, "A full-scale numerical study of interfacial instabilities in thin-film flows", *Journal of Fluid Mechanics*, **325**, 163–194, 1996.

[74] D. T. Papageorgiou and Y. S. Smyrlis, "The route to chaos for the Kuramoto–Sivashinsky equation", *Theoretical and Computational Fluid Dynamics*, **3**(1), 15–42, 1991.

[75] Y. S. Smyrlis and D. T. Papageorgiou, "Predicting chaos for infinite dimensional dynamical systems: the Kuramoto–Sivashinsky equation, a case study", *Proceedings of the National Academy of Sciences*, **88**(24), 11129–11132, 1991.

[76] G. I. Sivashinsky and D. M. Michelson, "On irregular wavy flow of a liquid film down a vertical plane", *Progress of Theoretical Physics*, **63**(6), 2112–2114, 1980.

[77] D. Tseluiko, S. Saprykin, C. Duprat, F. Giorgiutti-Dauphiné, and S. Kalliadasis, "Pulse dynamics in low-Reynolds-number interfacial hydrodynamics: Experiments and theory", *Physica D: Nonlinear Phenomena*, **239**(20), 2000–2010, 2010.

[78] B. S. Tilley, P. G. Petropoulos, and D. T. Papageorgiou, "Dynamics and rupture of planar electrified liquid sheets", *Physics of Fluids*, **13**(12), 3547–3563, 2001.

[79] A. P. Hooper and R. Grimshaw, "Nonlinear instability at the interface between two viscous fluids", *Physics of Fluids*, **28**(1), 37–45, 1985.

[80] D. T. Papageorgiou, C. Maldarelli, and D. S. Rumschitzki, "Nonlinear interfacial stability of core-annular film flows", *Physics of Fluids A: Fluid Dynamics*, **2**(3), 340–352, 1990.

[81] G. I. Sivashinsky, "On flame propagation under conditions of stoichiometry", *SIAM Journal on Applied Mathematics*, **39**(1), 67–82, 1980.

[82] D. M. Michelson and G. I. Sivashinsky, "Nonlinear analysis of hydrodynamic instability in laminar flames—II. Numerical experiments", *Acta Astronautica*, **4**(11), 1207–1221, 1977.

[83] G. I. Sivashinsky, "Nonlinear analysis of hydrodynamic instability in laminar flames—I. Derivation of basic equations", *Acta Astronautica*, **4**(11), 1177–1206, 1977.

[84] D. Michelson, "Stability of the Bunsen flame profiles in the Kuramoto–Sivashinsky equation", *SIAM Journal on Mathematical Analysis*, **27**(3), 765–781, 1996.

[85] Y. Kuramoto and T. Tsuzuki, "On the formation of dissipative structures in reaction-diffusion systems: Reductive perturbation approach", *Progress of Theoretical Physics*, **54**(3), 687–699, 1975.

[86] Y. Kuramoto and T. Tsuzuki, "Persistent propagation of concentration waves in dissipative media far from thermal equilibrium", *Progress of Theoretical Physics*, **55**(2), 356–369, 1976.

[87] A. Armaou and P. D. Christofides, "Feedback control of the Kuramoto–Sivashinsky equation", *Physica D: Nonlinear Phenomena*, **137**(1), 49–61, 2000.

[88] A. Armaou and P. D. Christofides, "Wave suppression by nonlinear finite-dimensional control", *Chemical Engineering Science*, **55**(14), 2627–2640, 2000.

[89] R. J. Tomlin and S. N. Gomes, "Point-actuated feedback control of multidimensional interfaces", *IMA Journal of Applied Mathematics*, **84**(6), 1112–1142, 2019.

[90] S. N. Gomes, D. T. Papageorgiou, and G. A. Pavliotis, "Stabilizing non-trivial solutions of the generalized Kuramoto–Sivashinsky equation using feedback and optimal control: Lighthill–Thwaites prize", *IMA Journal of Applied Mathematics*, **82**(1), 158–194, 2017.

[91] V. Y. Shkadov, "Wave flow regimes of a thin layer of viscous fluid subject to gravity", *Fluid Dynamics*, **2**(1), 29–34, 1967.

[92] C. Duprat, C. Ruyer-Quil, and F. Giorgiutti-Dauphiné, "Spatial evolution of a film flowing down a fiber", *Physics of Fluids*, **21**(4), 042109, 2009.

[93] F. Denner, A. Charogiannis, M. Pradas, C. N. Markides, B. G. M. van Wachem, and S. Kalliadasis, "Solitary waves on falling liquid films in the inertia-dominated regime", *Journal of Fluid Mechanics*, **837**, 491–519, 2018.

[94] M. Pradas, S. Kalliadasis, P.-K. Nguyen, and V. Bontozoglou, "Bound-state formation in interfacial turbulence: direct numerical simulations and theory", *Journal of Fluid Mechanics*, **716**, R2, 2013.

[95] S. Mukhopadhyay, C. Ruyer-Quil, and R. Usha, "Modelling falling film flow: an adjustable formulation", *Journal of Fluid Mechanics*, **952**, R3, 2022.

[96] G. B. Whitham, *"Linear and Nonlinear Waves"*, Wiley-Interscience, 1974.

[97] T. Ooshida and T. Kawahara, "Generic weakly nonlinear model equations for density waves in two-phase flows", *Physical Review E*, **56**(1), 511–519, 1997.

[98] T. Ooshida, "Surface equation of falling film flows with moderate Reynolds number and large but finite Weber number", *Physics of Fluids*, **11**(11), 3247–3269, 1999.

[99] S. V. Alekseenko, V. Y. Nakoryakov, and B. G. Pokusaev, "Wave formation on a vertical falling liquid film", *AIChE Journal*, **31**(9), 1446–1460, 1985.

[100] M. J. Lighthill and G. B. Whitham, "On kinematic waves I. Flood movement in long rivers", *Proceedings of the Royal Society of London. Series A. Mathematical and Physical Sciences*, **229**(1178), 281–316, 1955.

[101] M. K. Smith, "The mechanism for the long-wave instability in thin liquid films", *Journal of Fluid Mechanics*, **217**, 469–485, 1990.

[102] A. J. Roberts and Z. Li, "An accurate and comprehensive model of thin fluid flows with inertia on curved substrates", *Journal of Fluid Mechanics*, **553**, 33–73, 2006.

[103] R. V. Roy, A. J. Roberts, and M. E. Simpson, "A lubrication model of coating flows over a curved substrate in space", *Journal of Fluid Mechanics*, **454**, 235–261, 2002.

[104] N. M. Ribe, "Bending and stretching of thin viscous sheets", *Journal of Fluid Mechanics*, **433**, 135–160, 2001.

[105] A. Oron and C. Heining, "Weighted-residual integral boundary-layer model for the nonlinear dynamics of thin liquid films falling on an undulating vertical wall", *Physics of Fluids*, **20**(8), 082102, 2008.

[106] M. J. Miksis and M. P. Ida, "The dynamics of thin films I: General theory", *SIAM Journal on Applied Mathematics*, **58**(2), 456–473, 1998.

[107] M. J. Miksis and M. P. Ida, "The dynamics of thin films II: Applications", *SIAM Journal on Applied Mathematics*, **58**(2), 474–500, 1998.

[108] P. S. Hammond, "Nonlinear adjustment of a thin annular film of viscous fluid surrounding a thread of another within a circular cylindrical pipe", *Journal of Fluid Mechanics*, **137**, 363–384, 1983.

[109] I. L. Kliakhandler, S. H. Davis, and S. G. Bankoff, "Viscous beads on vertical fibre", *Journal of Fluid Mechanics*, **429**, 381–390, 2001.

[110] R. V. Craster and O. K. Matar, "On viscous beads flowing down a vertical fibre", *Journal of Fluid Mechanics*, **553**, 85–105, 2006.

[111] J. Eggers, "Singularities in droplet pinching with vanishing viscosity", *SIAM Journal on Applied Mathematics*, **60**(6), 1997–2008, 2000.

[112] J. Eggers and T. F. Dupont, "Drop formation in a one-dimensional approximation of the Navier–Stokes equation", *Journal of Fluid Mechanics*, **262**, 205–221, 1994.

[113] D. E. Weidner, L. W. Schwartz, and M. H. Eres, "Simulation of coating layer evolution and drop formation on horizontal cylinders", *Journal of Colloid and Interface Science*, **187**(1), 243–258, 1997.

[114] D. E. Weidner, "Suppression and reversal of drop formation on horizontal cylinders due to surfactant convection", *Physics of Fluids*, **25**(8), 082110, 2013.

[115] D. E. Weidner, "Drop formation in a magnetic fluid coating a horizontal cylinder carrying an axial electric current", *Physics of Fluids*, **29**(5), 052103, 2017.

[116] M. Heil and J. P. White, "Airway closure: surface-tension-driven non-axisymmetric instabilities of liquid-lined elastic rings", *Journal of Fluid Mechanics*, **462**, 79–109, 2002.

[117] M. Cachile, M. A. Aguirre, M. Lenschen, and A. Calvo, "Flow of a thin liquid film coating a horizontal stationary cylinder", *Physical Review E*, **88**(6), 063005, 2013.

[118] S. Kumar, "Liquid transfer in printing processes: liquid bridges with moving contact lines", *Annual Review of Fluid Mechanics*, **47**, 67–94, 2015.

[119] U. Tahir, M. A. Kamran, M. H. Jang, and M. Y. Jeong, "Thin-film coating on cylinder for fabrication of cylindrical mold: Roll-to-roll nano-imprint lithography", *Microelectronic Engineering*, **211**, 5–12, 2019.

[120] U. Tahir, J. I. Kim, S. Javeed, A. Khaliq, J.-H. Kim, D.-I. Kim, and M. Y. Jeong, "Process optimization for manufacturing functional nanosurfaces by roll-to-roll nanoimprint lithography", *Nanomaterials*, **12**(3), 480, 2022.

[121] U. Tahir, M. A. Kamran, and M. Y. Jeong, "Numerical study on the optimization of roll-to-roll ultraviolet imprint lithography", *Coatings*, **9**(9), 573, 2019.

[122] E. D. Kay, S. Hibberd, and H. Power, "Inertial effects at moderate Reynolds number in thin-film rimming flows driven by surface shear", *Physics of Fluids*, **25**(10), 102108, 2013.

[123] H. Lv, K. Yang, J. You, and S. Wang, "Operational stability analysis on the roller-coating process for a roll coating-simulation test equipment", *Machines*, **10**(5), 304, 2022.

[124] M. Schmitt, M. Baunach, L. Wengeler, K. Peters, P. Junges, P. Scharfer, and W. Schabel, "Slot-die processing of lithium-ion battery electrodes—Coating window characterization", *Chemical Engineering and Processing: Process Intensification*, **68**, 32–37, 2013.

[125] W. Li, M. S. Carvalho, and S. Kumar, "Viscous free-surface flows on rotating elliptical cylinders", *Physical Review Fluids*, **2**(9), 094005, 2017.

[126] B. R. Duffy and S. K. Wilson, "Thin-film and curtain flows on the outside of a rotating horizontal cylinder", *Journal of Fluid Mechanics*, **394**, 29–49, 1999.

[127] S. T. Thoroddsen and L. Mahadevan, "Experimental study of coating flows in a partially-filled horizontally rotating cylinder", *Experiments in Fluids*, **23**(1), 1–13, 1997.

[128] J. Ashmore, A. E. Hosoi, and H. A. Stone, "The effect of surface tension on rimming flows in a partially filled rotating cylinder", *Journal of Fluid Mechanics*, **479**, 65–98, 2003.

[129] H. Aggarwal and N. Tiwari, "Generalized linear stability of non-inertial rimming flow in a rotating horizontal cylinder", *The European Physical Journal E*, **38**(10), 111, 2015.

[130] T. C. Kumawat and N. Tiwari, "Stability analysis of the rimming flow inside a uniformly heated rotating horizontal cylinder", *Physics of Fluids*, **29**(3), 032102, 2017.

[131] T. C. Kumawat and N. Tiwari, "Hydrodynamic stability of thermoviscous liquid film inside a rotating horizontal cylinder: Heating and cooling effects", *Physics of Fluids*, **30**(3), 032103, 2018.

[132] R. E. Johnson, "Steady-state coating flows inside a rotating horizontal cylinder", *Journal of Fluid Mechanics*, **190**, 321–342, 1988.

[133] S. B. G. O'Brien and E. G. Gath, "The location of a shock in rimming flow", *Physics of Fluids*, **10**(4), 1040–1042, 1998.

[134] S. B. G. O'Brien, "Linear stability of rimming flow", *Quarterly of Applied Mathematics*, **60**(2), 201–211, 2002.

[135] S. B. G. O'Brien, "A mechanism for linear instability in two-dimensional rimming flow", *Quarterly of Applied Mathematics*, **60**(2), 283–299, 2002.

[136] I. Holland, W. Shu, and J. A. Davies, "Stratified tissue biofabrication by rotational internal flow layer engineering", *Biofabrication*, **15**(4), 045003, 2023.

[137] E. B. Hansen and M. A. Kelmanson, "Steady, viscous, free-surface flow on a rotating cylinder", *Journal of Fluid Mechanics*, **272**, 91–108, 1994.

[138] M. A. Kelmanson, "Theoretical and experimental analyses of the maximum-supportable fluid load on a rotating cylinder", *Journal of Engineering Mathematics*, **29**(3), 271–285, 1995.

[139] S. K. Wilson, R. Hunt, and B. R. Duffy, "On the critical solutions in coating and rimming flow on a uniformly rotating horizontal cylinder", *The Quarterly Journal of Mechanics and Applied Mathematics*, **55**(3), 357–383, 2002.

[140] E. J. Hinch and M. A. Kelmanson, "On the decay and drift of free-surface perturbations in viscous thin-film flow exterior to a rotating cylinder", *Proceedings of the Royal Society of London. Series A: Mathematical, Physical and Engineering Sciences*, **459**(2033), 1193–1213, 2003.

[141] E. S. Benilov and S. B. G. O'Brien, "Inertial instability of a liquid film inside a rotating horizontal cylinder", *Physics of Fluids*, **17**(5), 052106, 2005.

[142] C. J. Noakes, J. R. King, and D. S. Riley, "On the development of rational approximations incorporating inertial effects in coating and rimming flows: a multiple-scales approach", *The Quarterly Journal of Mechanics and Applied Mathematics*, **59**(2), 163–190, 2006.

[143] M. A. Kelmanson, "On inertial effects in the Moffatt–Pukhnachov coating-flow problem", *Journal of Fluid Mechanics*, **633**, 327–353, 2009.

[144] A. v. B. Lopes, U. Thiele, and A. L. Hazel, "On the multiple solutions of coating and rimming flows on rotating cylinders", *Journal of Fluid Mechanics*, **835**, 540–574, 2018.

[145] X. Xu, U. Thiele, and T. Qian, "A variational approach to thin film hydrodynamics of binary mixtures", *Journal of Physics: Condensed Matter*, **27**(8), 085005, 2015.

[146] S. D. R. Wilson and A. F. Jones, "The entry of a falling film into a pool and the air-entrainment problem", *Journal of Fluid Mechanics*, **128**, 219–230, 1983.

[147] E. S. Benilov, S. J. Chapman, J. B. McLeod, J. R. Ockendon, and V. S. Zubkov, "On liquid films on an inclined plate", *Journal of Fluid Mechanics*, **663**, 53–69, 2010.

[148] E. S. Benilov and M. S. Benilov, "A thin drop sliding down an inclined plate", *Journal of Fluid Mechanics*, **773**, 75–102, 2015.

[149] R. A. McKinlay, A. W. Wray, and S. K. Wilson, "Late-time draining of a thin liquid film on the outer surface of a circular cylinder", *Physical Review Fluids*, **8**(8), 084001, 2023.

[150] P. L. Evans, L. W. Schwartz, and R. V. Roy, "Three-dimensional solutions for coating flow on a rotating horizontal cylinder: Theory and experiment", *Physics of Fluids*, **17**(7), 072102, 2005.

[151] L. Preziosi and D. D. Joseph, "The run-off condition for coating and rimming flows", *Journal of Fluid Mechanics*, **187**, 99–113, 1988.

[152] A. J. Mitchell, B. R. Duffy, and S. K. Wilson, "Coating flow on a rotating cylinder in the presence of an irrotational airflow with circulation", *Journal of Fluid Mechanics*, **932**, A33, 2022.

[153] A. J. Mitchell, B. R. Duffy, and S. K. Wilson, "Unsteady coating flow on a rotating cylinder in the presence of an irrotational airflow with circulation", *Physics of Fluids*, **34**(4), 043105, 2022.

[154] U. Thiele, "On the depinning of a drop of partially wetting liquid on a rotating cylinder", *Journal of Fluid Mechanics*, **671**, 121–136, 2011.

[155] T.-S. Lin, S. Rogers, D. Tseluiko, and U. Thiele, "Bifurcation analysis of the behavior of partially wetting liquids on a rotating cylinder", *Physics of Fluids*, **28**(8), 082102, 2016.

[156] B. R. Duffy and S. K. Wilson, "Large-Biot-number non-isothermal flow of a thin film on a stationary or rotating cylinder", *The European Physical Journal Special Topics*, **166**(1), 147–150, 2009.

[157] B. Reisfeld and S. G. Bankoff, "Non-isothermal flow of a liquid film on a horizontal cylinder", *Journal of Fluid Mechanics*, **236**, 167–196, 1992.

[158] W. Li and S. Kumar, "Thin-film coating of surfactant-laden liquids on rotating cylinders", *Physics of Fluids*, **27**(7), 072106, 2015.

[159] C. Parrish and S. Kumar, "Simultaneous liquid flow and drying on rotating cylinders", *Physical Review Fluids*, **5**(3), 034001, 2020.

[160] D. Perizzolo, W. R. Lacefield, and D. M. Brunette, "Interaction between topography and coating in the formation of bone nodules in culture for hydroxyapatite-and titanium-coated micromachined surfaces", *Journal of Biomedical Materials Research*, **56**(4), 494–503, 2001.

[161] B. G. X. Zhang, D. E. Myers, G. G. Wallace, M. Brandt, and P. F. M. Choong, "Bioactive coatings for orthopaedic implants—recent trends in development of implant coatings", *International Journal of Molecular Sciences*, **15**(7), 11878–11921, 2014.

[162] W. R. Lacefield, "Materials characteristics of uncoated/ceramic-coated implant materials", *Advances in Dental Research*, **13**(1), 21–26, 1999.

[163] S. Wichchukit, M. J. McCarthy, and K. L. McCarthy, "Flow behavior of milk chocolate melt and the application to coating flow", *Journal of Food Science*, **70**(3), E165–E171, 2005.

[164] A. K. Sahu and S. Kumar, "Thin-liquid-film flow on a topographically patterned rotating cylinder", *Physics of Fluids*, **26**(4), 042102, 2014.

[165] W. Li, M. S. Carvalho, and S. Kumar, "Liquid-film coating on topographically patterned rotating cylinders", *Physical Review Fluids*, **2**(2), 024001, 2017.

[166] C. Parrish, L. Pham, and S. Kumar, "Thin-liquid-film flow on three-dimensional topographically patterned rotating cylinders", *Journal of Fluid Mechanics*, **918**, A12, 2021.

[167] C. Parrish, M. S. Carvalho, and S. Kumar, "Thin-film flows on rotating non-circular cylinders with large curvature variations", *Physical Review Fluids*, **7**(5), 054002, 2022.

[168] R. Hunt, "Numerical solution of the free-surface viscous flow on a horizontal rotating elliptical cylinder", *Numerical Methods for Partial Differential Equations*, **24**(4), 1094–1114, 2008.

[169] H. Chinju, K. Uchiyama, and Y. H. Mori, ""String-of-beads" flow of liquids on vertical wires for gas absorption", *AIChE Journal*, **46**(5), 937–945, 2000.

[170] K. Uchiyama, H. Migita, R. Ohmura, and Y. H. Mori, "Gas absorption into "string-of-beads" liquid flow with chemical reaction: application to carbon dioxide separation", *International Journal of Heat and Mass Transfer*, **46**(3), 457–468, 2003.

[171] H. Takahama and S. Kato, "Longitudinal flow characteristics of vertically falling liquid films without concurrent gas flow", *International Journal of Multiphase Flow*, **6**(3), 203–215, 1980.

[172] Z. Zeng, A. Sadeghpour, G. Warrier, and Y. S. Ju, "Experimental study of heat transfer between thin liquid films flowing down a vertical string in the Rayleigh-Plateau instability regime and a counterflowing gas stream", *International Journal of Heat and Mass Transfer*, **108**, 830–840, 2017.

[173] C. Yu, M. Cao, Z. Dong, K. Li, C. Yu, J. Wang, and L. Jiang, "Aerophilic electrode with cone shape for continuous generation and efficient collection of H_2 bubbles", *Advanced Functional Materials*, **26**(37), 6830–6835, 2016.

[174] S. M. Hosseini, R. Alizadeh, E. Fatehifar, and A. Alizadehdakhel, "Simulation of gas absorption into string-of-beads liquid flow with chemical reaction", *Heat and Mass Transfer*, **50**(10), 1393–1403, 2014.

[175] H. Migita, K. Soga, and Y. H. Mori, "Gas absorption in a wetted-wire column", *AIChE Journal*, **51**(8), 2190–2198, 2005.

[176] C. L. Lee, T. S. Chan, A. Carlson, and K. Dalnoki-Veress, "Multiple droplets on a conical fiber: formation, motion, and droplet mergers", *Soft Matter*, **18**(7), 1364–1370, 2022.

[177] A. Sadeghpour, Z. Zeng, H. Ji, N. D. Ebrahimi, A. L. Bertozzi, and Y. S. Ju, "Water vapor capturing using an array of traveling liquid beads for desalination and water treatment", *Science Advances*, **5**(4), eaav7662, 2019.

[178] R. Battisti, R. A. F. Machado, and C. Marangoni, "A background review on falling film distillation in wetted-wall columns: from fundamentals towards intensified technologies", *Chemical Engineering and Processing: Process Intensification*, **150**, 107873, 2020.

[179] K. Li, J. Ju, Z. Xue, J. Ma, L. Feng, S. Gao, and L. Jiang, "Structured cone arrays for continuous and effective collection of micron-sized oil droplets from water", *Nature Communications*, **4**, 2276, 2013.

[180] B. P. Dojčinović, G. M. Roglić, B. M. Obradović, M. M. Kuraica, T. B. Tosti, M. D. Marković, and D. D. Manojlović, "Decolorization of Reactive Black 5 using a dielectric barrier discharge in the presence of inorganic salts", *Journal of the Serbian Chemical Society*, **77**(4), 535–548, 2012.

[181] T. Gilet, D. Terwagne, and N. Vandewalle, "Digital microfluidics on a wire", *Applied Physics Letters*, **95**(1), 014106, 2009.

[182] M. E. R. Shanahan, "On the behavior of dew drops", *Langmuir*, **27**(24), 14919–14922, 2011.

[183] Z. Zeng, A. Sadeghpour, and Y. S. Ju, "Thermohydraulic characteristics of a multi-string direct-contact heat exchanger", *International Journal of Heat and Mass Transfer*, **126**, 536–544, 2018.

[184] R. R. Barton, K. E. VanTreeck, C. J. Duran, M. J. Schulte, and M. C. Flickinger, "A falling film bioreactor (FFBR) for generating effective gas-to-liquid mass transfer using wavy laminar flow for continuous microbial gas processing", *Chemical Engineering Science*, **219**, 115592, 2020.

[185] Lord Rayleigh, "On the instability of jets", *Proceedings of the London Mathematical Society*, **s1-10**(1), 4–13, 1878.

[186] N. B. Speirs, K. R. Langley, P. Taborek, and S. T. Thoroddsen, "Jet breakup in superfluid and normal liquid ^{4}He", *Physical Review Fluids*, **5**(4), 044001, 2020.

[187] M. S. Keith, "Mathematical modelling of electrohydrodynamic flows", PhD thesis, University of Strathclyde, 2021.

[188] A. L. Frenkel, A. J. Babchin, B. G. Levich, T. Shlang, and G. I. Sivashinsky, "Annular flows can keep unstable films from breakup: nonlinear saturation of capillary instability", *Journal of Colloid and Interface Science*, **115**(1), 225–233, 1987.

[189] S. Kalliadasis and H.-C. Chang, "Drop formation during coating of vertical fibres", *Journal of Fluid Mechanics*, **261**, 135–168, 1994.

[190] D. Quéré, "Thin films flowing on vertical fibers", *Europhysics Letters*, **13**(8), 721–726, 1990.

[191] A. W. Wray, O. K. Matar, and D. T. Papageorgiou, "Non-linear waves in electrified viscous film flow down a vertical cylinder", *IMA Journal of Applied Mathematics*, **77**(3), 430–440, 2012.

[192] Z. Ding, R. Liu, T. N. Wong, and C. Yang, "Absolute instability induced by Marangoni effect in thin liquid film flows on vertical cylindrical surfaces", *Chemical Engineering Science*, **177**, 261–269, 2018.

[193] Z. Ding, Z. Liu, R. Liu, and C. Yang, "Breakup of ultra-thin liquid films on vertical fiber enhanced by Marangoni effect", *Chemical Engineering Science*, **199**, 342–348, 2019.

[194] P. Li and Y. Chao, "Marangoni instability of self-rewetting films modulated by chemical reactions flowing down a vertical fibre", *Chemical Engineering Science*, **227**, 115936, 2020.

[195] Y. Chao, Z. Ding, and R. Liu, "Dynamics of thin liquid films flowing down the uniformly heated/cooled cylinder with wall slippage", *Chemical Engineering Science*, **175**, 354–364, 2018.

[196] S. Khanum and N. Tiwari, "Gravity-driven thermoviscous liquid film down a heated or cooled vertical cylinder", *Physical Review Fluids*, **5**(9), 094005, 2020.

[197] D. Kishal and N. Tiwari, "Role of suction pressure in the stability of a gravity-driven thermoviscous liquid film flow down the interior surface of a cylinder", *The European Physical Journal E*, **44**(7), 100, 2021.

[198] A. W. Wray, D. T. Papageorgiou, and O. K. Matar, "Electrified coating flows on vertical fibres: enhancement or suppression of interfacial dynamics", *Journal of Fluid Mechanics*, **735**, 427–456, 2013.

[199] Z. Ding, J. Xie, T. N. Wong, and R. Liu, "Dynamics of liquid films on vertical fibres in a radial electric field", *Journal of Fluid Mechanics*, **752**, 66–89, 2014.

[200] R. Liu and Q. S. Liu, "Thermocapillary effect on the dynamics of viscous beads on vertical fiber", *Physical Review E*, **90**(3), 033005, 2014.

[201] R. Liu, Z. Ding, and Z. Zhu, "Thermocapillary effect on the absolute and convective instabilities of film flows down a fibre", *International Journal of Heat and Mass Transfer*, **112**, 918–925, 2017.

[202] L. Dong, X. Li, and R. Liu, "Effect of thermocapillary on absolute and convective instability of film flow of self-rewetting fluid", *Microgravity Science and Technology*, **32**(3), 415–422, 2020.

[203] R. Liu and Z. Ding, "Instabilities and bifurcations of liquid films flowing down a rotating fibre", *Journal of Fluid Mechanics*, **899**, A14, 2020.

[204] W. Jiang and Z. Ding, "Thin liquid films down a vertical microfiber: Effect of curvature elasticity", *Physical Review E*, **105**(3), 035104, 2022.

[205] Z. Ding and Q. Liu, "Stability of liquid films on a porous vertical cylinder", *Physical Review E*, **84**(4), 046307, 2011.

[206] Z. Ding, T. N. Wong, R. Liu, and Q. Liu, "Viscous liquid films on a porous vertical cylinder: dynamics and stability", *Physics of Fluids*, **25**(6), 064101, 2013.

[207] R. Liu and Z. Ding, "Stability of viscous film flow coating the interior of a vertical tube with a porous wall", *Physical Review E*, **95**(5), 053101, 2017.

[208] M. Pradas, S. Kalliadasis, and D. Tseluiko, "Binary interactions of solitary pulses in falling liquid films", *IMA Journal of Applied Mathematics*, **77**(3), 408–419, 2012.

[209] C. Duprat, C. Ruyer-Quil, S. Kalliadasis, and F. Giorgiutti-Dauphiné, "Absolute and convective instabilities of a viscous film flowing down a vertical fiber", *Physical Review Letters*, **98**(24), 244502, 2007.

[210] Z. Ding and A. P. Willis, "Relative periodic solutions in conducting liquid films flowing down vertical fibres", *Journal of Fluid Mechanics*, **873**, 835–855, 2019.

[211] R. Liu and Z. Ding, "Coating flows down a vertical fibre: towards the full Navier–Stokes problem", *Journal of Fluid Mechanics*, **914**, A30, 2021.

[212] B. Guo and R. Liu, "The relative periodic orbit of liquid films flowing down a vertical fiber", *Microgravity Science and Technology*, **34**(1), 3, 2022.

[213] A. M. Binnie, "Experiments on the onset of wave formation on a film of water flowing down a vertical plane", *Journal of Fluid Mechanics*, **2**(6), 551–553, 1957.

[214] L. A. Dávalos-Orozco and G. Ruiz-Chavarría, "Hydrodynamic instability of a fluid layer flowing down a rotating cylinder", *Physics of Fluids A: Fluid Dynamics*, **5**(10), 2390–2404, 1993.

[215] G. Ruiz-Chavarría and L. A. Dávalos-Orozco, "Stability of a liquid film flowing down a rotating cylinder subject to azimuthal disturbances", *Journal de Physique II*, **6**(8), 1219–1227, 1996.

[216] G. Ruiz-Chavarría and L. A. Dávalos-Orozco, "Azimuthal and streamwise disturbances in a fluid layer flowing down a rotating cylinder", *Physics of Fluids*, **9**(10), 2899–2908, 1997.

[217] L. B. Smolka and M. SeGall, "Fingering instability down the outside of a vertical cylinder", *Physics of Fluids*, **23**(9), 092103, 2011.

[218] L. C. Mayo, S. W. McCue, and T. J. Moroney, "Gravity-driven fingering simulations for a thin liquid film flowing down the outside of a vertical cylinder", *Physical Review E*, **87**(5), 053018, 2013.

[219] A. W. Wray, D. T. Papageorgiou, and O. K. Matar, "Electrostatically controlled large-amplitude, non-axisymmetric waves in thin film flows down a cylinder", *Journal of Fluid Mechanics*, **736**, R2, 2013.

[220] Z. Ding and T. N. Wong, "Three-dimensional dynamics of thin liquid films on vertical cylinders with Marangoni effect", *Physics of Fluids*, **29**(1), 011701, 2017.

[221] L. W. Schwartz and T. A. Cender, "The flow of thin liquid layers on circular cylinders", *Journal of Colloid and Interface Science*, **533**, 126–135, 2019.

[222] C. T. Gabbard and J. B. Bostwick, "Asymmetric instability in thin-film flow down a fiber", *Physical Review Fluids*, **6**(3), 034005, 2021.

[223] S. Eghbali, L. Keiser, E. Boujo, and F. Gallaire, "Whirling instability of an eccentric coated fibre", *Journal of Fluid Mechanics*, **952**, A33, 2022.

[224] G. K. Batchelor, *"An Introduction to Fluid Dynamics"*, Cambridge University Press, 1967.

[225] W. Li and S. Kumar, "Three-dimensional surfactant-covered flows of thin liquid films on rotating cylinders", *Journal of Fluid Mechanics*, **844**, 61–91, 2018.

[226] C. H. Tougher, S. K. Wilson, and B. R. Duffy, "On the approach to the critical solution in leading order thin-film coating and rimming flow", *Applied Mathematics Letters*, **22**(6), 882–886, 2009.

[227] D. Takagi and H. E. Huppert, "Flow and instability of thin films on a cylinder and sphere", *Journal of Fluid Mechanics*, **647**, 221–238, 2010.

[228] J. Qin, Y.-T. Xia, and P. Gao, "Axisymmetric evolution of gravity-driven thin films on a small sphere", *Journal of Fluid Mechanics*, **907**, A4, 2021.

[229] Wolfram Research Inc., *Mathematica, Version 13.1*, Champaign, IL, 2022, URL: `https://www.wolfram.com/mathematica`.

[230] S. Duruk, R. G. Shepherd, E. Boujo, and M. Sellier, "Three-dimensional nonlinear dynamics of a thin liquid film on a spinning ellipsoid", *Physics of Fluids*, **35**(7), 072115, 2023.

[231] A. W. Wray, R. Cimpeanu, and S. N. Gomes, "Electrostatic control of the Navier–Stokes equations for thin films", *Physical Review Fluids*, **7**(12), L122001, 2022.

[232] Q. Xie, R. Liu, X. Wang, and X. Chen, "Investigation of flow dynamics of thin viscous films down differently shaped fibers", *Applied Physics Letters*, **119**(20), 201601, 2021.

[233] A. W. Wray, D. T. Papageorgiou, R. V. Craster, K. Sefiane, and O. K. Matar, "Electrostatic suppression of the "coffee-stain effect"", *Procedia IUTAM*, **15**, 172–177, 2015.

[234] H. Tu, Y. Wang, Q. Lan, W. Liu, W. Xiao, and S. Ma, "A Chebyshev-Tau spectral method for normal modes of underwater sound propagation with a layered marine environment", *Journal of Sound and Vibration*, **492**, 115784, 2021.

[235] A. J. Harfash, "Numerical methods for solving some hydrodynamic stability problems", *International Journal of Applied and Computational Mathematics*, **1**(2), 293–326, 2015.

[236] J. J. Dongarra, B. Straughan, and D. W. Walker, "Chebyshev tau-QZ algorithm methods for calculating spectra of hydrodynamic stability problems", *Applied Numerical Mathematics*, **22**(4), 399–434, 1996.

[237] M. G. Blyth and C. Pozrikidis, "Effect of inertia on the Marangoni instability of two-layer channel flow, Part II: normal-mode analysis", *Journal of Engineering Mathematics*, **50**, 329–341, 2004.

[238] S. A. Orszag, "Accurate solution of the Orr–Sommerfeld stability equation", *Journal of Fluid Mechanics*, **50**(4), 689–703, 1971.